Guangye Zhang

Chen Xie

Peng You

Shunpu Li

Introduction to Organic Electronic Devices

Introduction to Organic Electronic Devices

Guangye Zhang · Chen Xie · Peng You · Shunpu Li

Introduction to Organic Electronic Devices

Guangye Zhang
College of New Materials and New
Energies
Shenzhen Technology University
Shenzhen, China

Chen Xie
College of New Materials and New
Energies
Shenzhen Technology University
Shenzhen, China

Peng You
College of New Materials and New
Energies
Shenzhen Technology University
Shenzhen, China

Shunpu Li
College of New Materials and New
Energies
Shenzhen Technology University
Shenzhen, China

Preface

Organic materials, according to conventional wisdom, are carbon-based insulators that lack the optical, electrical, and magnetic properties of conductors or semiconductors. The discovery of conducting polymers in the late 1970s ushered in the emerging field of organic electronics. Organic electronics has since grown in importance as a research field and is still flourishing. The optical, electrical, and magnetic properties of organic materials have steadily been recognized, and researchers have advocated their use in various electronic devices. Particularly in the last 30 years, semiconductor materials and electronic devices based on organic molecules have advanced fast. They have progressed from pure scientific research to the practical stage and are moving toward industrialization. For example, organic electroluminescent materials and devices are not only used in digital cameras, mobile phone screens, thin-film large-screen displays, but also in solid-state lighting. Besides, organic semiconductor materials have also achieved rapid development in photovoltaic cells, thin-film sensors, thin-film field-effect transistors, and other devices.

The most common characteristic of organic molecular materials is that they have delocalized π electronic structures and weak intermolecular forces. The solid phase of organic materials is mainly formed due to non-bonding interactions such as van der Waals forces. Therefore, the properties of the material depend essentially on the nature of the molecule itself and the condensed structure. Compared with the limited inorganic semiconductor materials, a wide variety of molecular materials can be synthesized by chemical methods, and their functions can be rationally modulated through chemical synthesis and modification, making it easier to meet different functional requirements. Organic molecular materials can realize information display, sensing, storage, solar energy conversion, and other functions of inorganic semiconductors such as silicon. More importantly, they are relatively inexpensive and can produce lightweight and thin devices at low cost through printing methods. Most of them can be prepared on foldable flexible substrates to create thin-film devices with special shapes. This not only can complement and expand inorganic semiconductor devices, but also have unlimited potential in the application of electronic devices in the future. If these devices can be made into all organic, it will be a profound revolution in electronic devices. It will also play a huge role in developing new energy

and solving environmental pollution. In addition, since organic materials are more compatible with living organisms than inorganic materials, they can be used as a bridge between inorganic materials and biological systems.

The authors have written this book based on years of experience in research work in this field. The aim is to introduce the research status, important progress, and application prospects of organic molecular materials to readers from the perspective of materials and devices. The book systematically introduces the characteristics of molecular materials and their working mechanisms different from inorganic semiconductors. By summarizing both the results from both theoretical analysis and experimental data, it describes the application of organic molecular materials in thin-film devices such as organic electroluminescence devices, organic photovoltaics, organic field-effect transistors, and organic sensors. One of the hot topics of current research, organic–inorganic hybrid materials with perovskite crystal structure, is also systematically discussed. Chapters 1, 2, 7, and 10 of this book were written by Shunpu Li, Chaps. 3, 5, and 6 were written by Guangye Zhang, Chaps. 4, 8, and 9 were written by Chen Xie, and Chap. 11 by Peng You. We would like to thank Lihong Wang for her dedication to the drawing, formatting, and proofreading of some of the chapters this book.

The research on organic electronic materials and devices is developing rapidly. New concepts and new achievements are emerging all the time, so some of the new topics and new results may miss and mistakes certainly remain in the book. Nonetheless, we hope that this book paints a reasonable picture of what organic electronics are and can provide a reference for the researchers engaged in molecular materials and device research, as well as graduate students in colleges and universities. We sincerely hope that readers will provide valuable comments.

Shenzhen, China   Guangye Zhang
                                                                          Chen Xie
                                                                          Peng You
                                                                          Shunpu Li

Acknowledgements

Contents

Chapter 1
Electronic Process in Organic Semiconductor Materials

The nature of bonding in organic molecule semiconductors is fundamentally different from inorganic semiconductors. In polymer materials and organic crystals, the molecules are bonded by van der Waals force implying a weaker intermolecular bonding as compared to inorganic semiconductors, like silicon, where the atoms are strongly bonded covalently. The weak bonding property can be seen from their mechanical and thermodynamic properties. In organic materials, a much weaker delocalization of electronic wave functions among neighbor molecules brings a strong impact on the optical and electrical properties.

1.1 Semiconductor Property of Conjugated Polymers

1.1.1 Fermi Surface of One-Dimensional System

Organic semiconductor materials are the premise of development of organic electronics. An understanding of conducting mechanism in conjugated molecules is important for designing new organic semiconductors and device fabrication. Therefore, we start from discuss about conducting property of conjugated polymer: why is an intrinsic conjugated polymer a semiconductor, not a conductor?

Taking a one-dimensional (1D) system with length L contains N free electrons. Electrons are moving with momentum p in the system. The electron wavelength λ and momentum p follow the de Broglie relation:

$$\lambda = \frac{h}{p} \tag{1.1}$$

where h is plank constant. The wavelength is often replaced with wavenumber k.

$$k = \frac{1}{\lambda} = \frac{p}{h}, \, p = \text{hk} \tag{1.2}$$

If free electrons are moving in direction x, the wave function is a plane wave and can be expressed as:

$$\psi_p(x) = \frac{1}{L} e^{\frac{i}{\hbar} px}, \, (\hbar = h/2\pi) \tag{1.3}$$

$$\psi_k(x) = \frac{1}{L} e^{i2\pi kx} \tag{1.4}$$

When an electron is moving in a chain with length L, the wave function is satisfying the boundary condition $\psi_k(L) = \psi_k(0)$. Inserting Eq. (1.4) to the boundary condition, we have

$$e^{i2\pi kL} = 1 \tag{1.5}$$

Thus, kL can only be an integer and

$$k = m/L (m = 0, \pm 1, \pm 2 \cdots) \tag{1.6}$$

As $k = p/h$, the k (or p) can only take a series of discrete points in momentum space, and the interval between two neighbor states is:

$$\Delta k = \frac{1}{L}, \tag{1.7}$$

Kinetic energy of a free electron:

$$E(k) = \frac{p^2}{2m} = \frac{h^2 k^2}{2m} \tag{1.8}$$

From (1.8), we know that the energy (E) is a quadratic function of wavenumber (k) (Fig. 1.1). Each momentum state can be occupied by two electrons (spin-up and spin-down), N electrons in the $1D$ system will sequentially fill into these states from low momentum to high momentum, and the maximum momentum is p_F. The corresponding maximum wavenumber is k_F ($p_F = \text{hk}_F$). The p_F is named as Fermi momentum below which ($|p| \leq p_F$) all states are occupied without any holes. In contrast, all states with $|p| > p_F$ are empty (Fig. 1.1).

The electron density in the 1D system is $n = N/L$, and from Fig. 1.1, we see that the occupied region in the momentum space is $2k_F$ and the number of states occupied is $2k_F/\Delta k = 2k_F L$. The number of occupied electrons is $4k_F L = N$ (each state contains two electrons with anti-parallel spins), and we have the Fermi momentum of 1D system:

Fig. 1.1 Schematic illustration of momentum states and energy of free electrons in 1D system
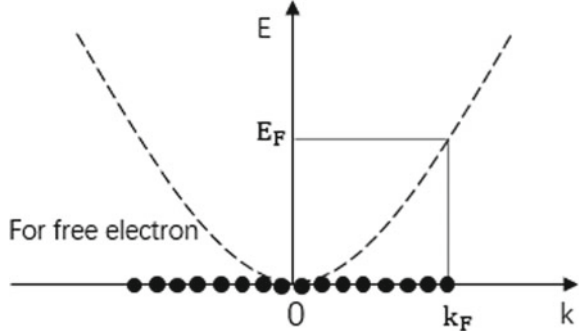
$$k_F = \frac{N}{4L} = \frac{n}{4}, \tag{1.9}$$

The corresponding maximum energy, i.e., Fermi energy, is

$$E_F = \frac{h^2 k_F^2}{2m}, \tag{1.10}$$

1.1.2 Brillouin Zone in One-Dimensional Lattice and Peierls Transition

We have discussed free electrons in one-dimensional system without lattice of crystal. In a practical material, the electrons are moving in crystal lattice and the lattice will influence the energy states of the system. We consider N atoms which are equally spaced in a line to form one-dimensional lattice. If the distance of two neighbor atoms (i.e., lattice constant) is a, then the length of the system is $L = Na$ (strictly speaking, $L = a(N-1)$, for $N >> 1$ we take $L = Na$). If each atom provides one valence electron to contribute conductance, there are N conduction electrons in the system. As described above, the wave function can only take certain discrete values. At ground state of the system, the N electrons occupy momentum space below Fermi momentum $[-k_F, +k_F]$. For the weak interaction between the electrons and lattice atoms, the energy of an electron is mainly contributed by kinetic energy (free electron):

$$E_0(k) = \frac{h^2 k^2}{2m} \tag{1.11}$$

The plot of energywavenumber has a parabolic form as depicted in Fig. 1.2a (dashed line), which is similar to the case of free electrons (Fig. 1.1). Such an energy-wavenumber relation $E(k)$ is called energy spectrum.
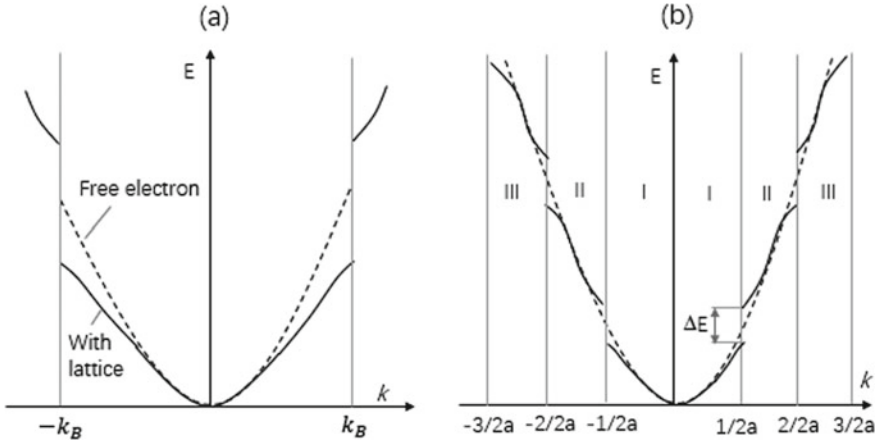
Fig. 1.2 Schematic illustration of energy spectrum of 1D crystal and Brillouin zones

When each atom provides one conduction electron, the linear density of electrons is:

$$n = \frac{N}{L} = \frac{1}{a} \tag{1.12}$$

From Eq. (1.9), we have the Fermi momentum of electrons:

$$k_F = \frac{n}{4} = \frac{1}{4a}, \tag{1.13}$$

This indicates that for such a one-dimensional system, the electrons occupy the states in the region $[-1/4a, 1/4a]$, and those states outside the region are empty.

Next, we discuss the influence on the energy spectrum caused by the atom lattice. An electron with wavelength $\lambda = 1/k$ propagates in a 1D crystal, and the plane wave experiences scattering from atoms as shown in Fig. 1.3 where the solid line expresses the forward propagated wave and the dashed lines express reflective waves from atoms in the crystal lattice. Let us examine the situation at point A. The wave paths of the waves reflected from different atoms are different. As the lattice constant is a, the path difference of reflected waves from any two neighbored atoms is $\Delta l = 2a$ [e.g., path (ACA)-path (ABA) $= 2a$]. Therefore, the phase difference between the two reflected waves from neighbored atoms is:

$$\Delta \varphi = 2\pi \frac{\Delta l}{\lambda} = 2\pi \frac{2a}{\lambda}, \tag{1.14}$$

For electrons with long wavelength, $\lambda \gg a$, $\Delta \varphi \ll 2\pi$. Hence, at point A, the phase differences for waves reflected from all atoms in the chain are distributed in the range $[0, 2\pi]$, and this leads to a cancelation of the reflected waves which means
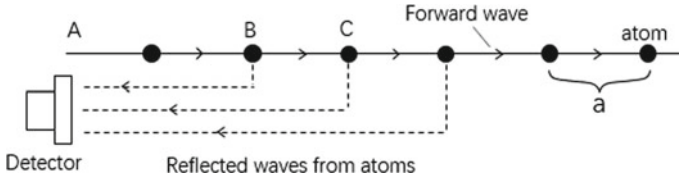
Fig. 1.3 Schematic illustration of electron wave propagation and reflection in 1D crystal

that the waves of electrons can propagate forward without attenuation by the lattice atoms. Thus, for electrons with small momentum, the energy spectrum is close to that of free electrons $E_0(k)$.

For electrons with large momentum (i.e., small wavelengths) from Eq. (1.14), one can see that the phase difference of reflected waves from two neighbor atoms $\Delta\varphi$ increases. In this case, the reflected waves will not cancel each other completely. The energy spectrum of electrons $E(k)$ start deviate from that of free electrons $E_0(k)$. In Fig. 1.2a, the solid curve expresses actual energy spectrum. When k is small, the solid cure is close to the dashed curve (free electrons). With decreasing of wavelength, the deviation between the two curves increases, especially in the case $\lambda = 2a$. From Eq. (1.14), one can see that all reflected waves are in phase and the reflected waves are strengthened by superposition. This indicates that the waves with $\lambda = 2a$ cannot propagate in the 1D lattice. The wavenumber (k_B) that corresponding to $\lambda = 2a$ defines a boundary of wave propagation.

$$k_B = \frac{1}{\lambda} = \frac{1}{2a}, \tag{1.15}$$

The electrons with wavevector k_B will experience a strong scattering from lattice atoms which leads a gap at k_B for the energy spectrum (Fig. 1.2a).

More generally, when $\lambda = 2a/m$ ($m = \pm 1, \pm 2, \pm 3, \ldots$), $\Delta\varphi = 2m\pi$ (see Eq. 1.14), the reflective waves from lattice atoms are in phase. The energy spectrum is discontinuous at following wavenumbers:

$$k_B^m = \frac{m}{2a}, \quad (m = \pm 1, \pm 2, \pm 3, \ldots) \tag{1.16}$$

It is obvious from Eq. (1.16) that because the existing of lattice atoms, there is series of special points k_B^m in the momentum space where the energy spectrum is discontinuous (Fig. 1.2b). These points define many regions in the momentum space. In each region, the energy spectrum is continuous, and at the boundary between any two neighbored regions (k_B^m), an energy gap exists. Each continuous region forms an energy band, and the energy gap between two neighbored regions is called band gap. The regions that are divided by k_B^m form Brillouin zones, where the region with small momentum is the first Brillouin zone. With increasing momentum, other regions are named second Brillouin zone, third Brillouin zone in turn.

For each Brillouin zone, the width is $1/a$, and the energy spectrum in each Brillouin zone form an energy band. The points k_B^m are the boundaries of Brillouin zones. For 1D crystal lattice, the two boundary points of the first Brillouin zone are $\pm 1/2a$, where a is the lattice constant.

Next, let us evaluate the number of states in each Brillouin zone. For 1D system, the interval of two neighbor momentum states is $\Delta k = 1/L$ in the momentum space (Eq. 1.7), while the momentum region in one Brillouin zone is $1/a$. The total state number in a Brillouin zone is:

$$\left(\frac{1}{a}\right)/\left(\frac{1}{L}\right) = \frac{L}{a} = N_c \qquad (1.17)$$

where N_c is the state number in the first Brillouin zone of 1D crystal. When the atoms are equally spaced (Fig. 1.4a), the lattice constant "a" equals the average distance of atoms "$\overline{a}$", i.e., each unit cell only contains single atom. In this case, the number of states (Eq. 1.17) equals the number of atoms $Nc = N$. As each state can occupy two electrons, 2 N electrons are needed for each Brillouin zone (or energy band) to be fully occupied. If each atom provides one free electron, only N free electrons in the system. Therefore, the fermi momentum locates in the middle of the first Brillouin zone, i.e., the corresponding energy band is partially filled, and the system is metallic. If atoms are arranged pairwise in the chain (or dimerized), one unit cell contains two atoms, $a = 2\,\overline{a}$ (Fig. 1.4b). The state number in the Brillouin zone is $N_c = L/a = L/2\,\overline{a} = N/2$, i.e., N electrons can be occupied. If each atom provides one free electron, the Fermi momentum coincides with the boundary of first Brillouin zone, i.e., the energy band is fully occupied. In this case, the 1D system is semiconductor or insulator. Such lattice change-induced transition from conductive phase to semiconductor (or insulator) phase is called Peierls transition [1].

1.2   Semiconductor Property of Conjugated Molecules

In the polyacetylene, the basic unit is CH and each CH provides one p electron as the carbon is sp^2 hybridized. In principle, such a structure is expected to behave as an intrinsic conductive polymer. However, pure polyacetylene is not conductive which is explained by the π-electron overlap in an alternating fashion, i.e., the CH units arrange pairwise in the polymer chain. In such 1D structure the first Brillouin zone (or lowest energy band) is fully occupied and the higher energy bands are empty. This specifies that the polyacetylene is intrinsic semiconductor.
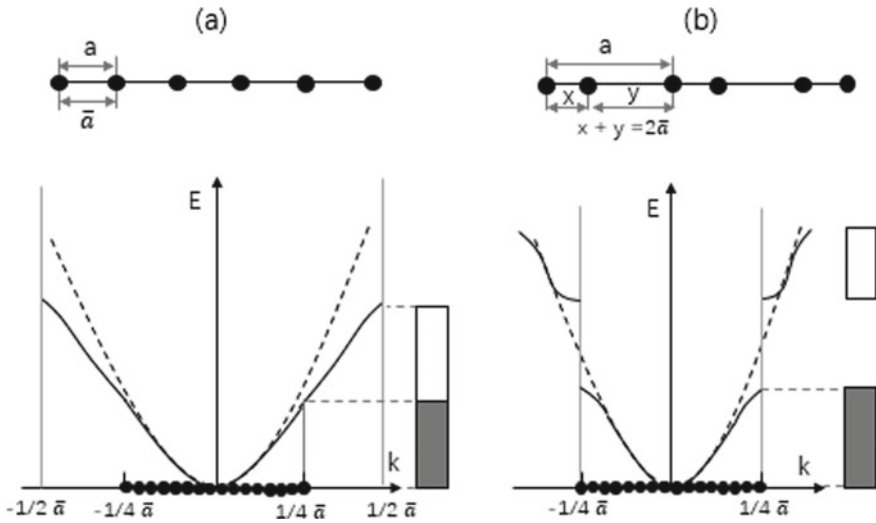
Fig. 1.4 Schematic illustration of energy spectrum of 1D crystal for equally spaced atoms (**a**) and paired atoms (**b**)

1.2.1   Solitons in Polyacetylene

As described above, polyacetylene is intrinsic semiconductor which is not conductive in pure state. After doping of donor impurity (Li, Na, K…) or acceptor impurity (Cl, I, Br, AsF_5, PF_5, BCl_3 …), it became conductive. After such doping, the conductance of polyacetylene has increased for 10 orders of magnitude from $10^{-9} (\Omega^{-1}\ cm^{-1})$ to $10\ (\Omega^{-1}\ cm^{-1})$ [2], which indicate that there are many mobile charges in the polyacetylene. If these charges are electrons or holes, one can use spin resonance technique to measure spin momentum of the charges, i.e., magnetic susceptibility $\chi > 0$. Experiment showed that when the impurity concentration is less than 6%, the magnetic susceptibility is zero as shown in Fig. 1.5 [2–4]. This indicates that the charge carriers are spinless. When the impurity concentration is larger than 6%, there is a phase transition in the system: from semiconductor to conductor and χ increases drastically. The spinless charge carriers indicate that the carriers in the polyacetylene are not electrons or holes. To understand the electrical conduction mechanism, W. Su, J. R. Schrieffer and A. Heeger have proposed a new theory [5]. It is suggested that the charge carriers are solitons which can carry positive charges and negative charges with zero spin. This theory can nicely explain many observed properties in polyacetylene.
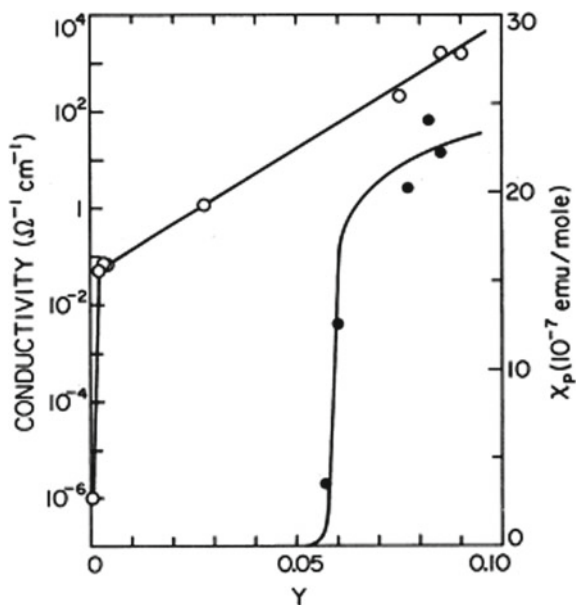
Fig. 1.5 Impurity content dependence of conductivity and susceptibility measured from trans-(CH)$_x$ doped with sodium (Adapted from ref [2])

1.2.1.1 Degenerate /Non-degenerate Ground States in Conjugated Polymers

For a given sequence of polyacetylene chain (with carbon atoms numbered as 1, 2, 3···), there are two ways of dimerization of carbon atoms as shown in Fig. 1.6.

Odd numbered atoms displace to the right direction for u$_0$, while the even numbered atoms displace to left direction for u$_0$ as shown in (a);
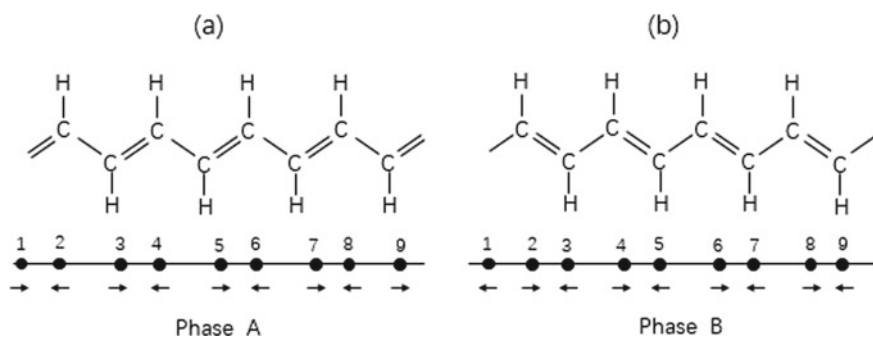
Fig. 1.6 Phase A and phase B in trans-polyacetylene
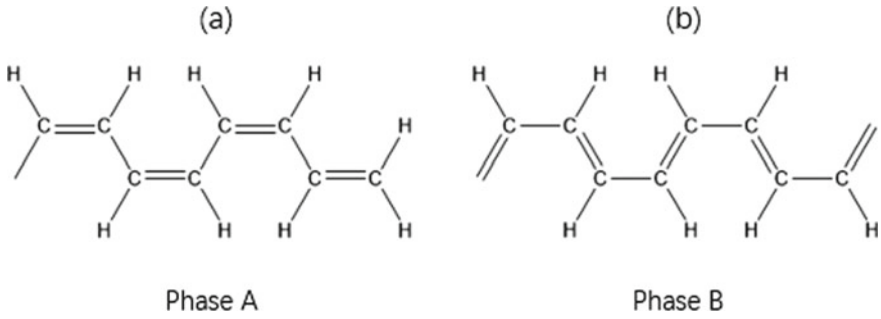
Fig. 1.7 Phase A and phase B in cis-polyacetylene

In contrast to (a), odd numbered atoms displace to the left direction for u_0, while the even numbered atoms displace to right direction for u_0 as shown in (b);

We specify the dimerization structure (a) as phase A and the structure (b) as phase B. If we interchange the positions of singe bond and double bond in phase A, it becomes phase B. The same is for the transition from phase B to phase A. For trans-polyacetylene, the two phases are shown in Fig. 1.6, while for cis-polyacetylene, the two phases are shown in Fig. 1.7. In the trans-polyacetylene, the phase A and phase B are completely equivalent and the ground energies of the two phases are degenerate. For the cis-polyacetylene, the phases A and B are inequivalent, and the energies of the two phases are non-degenerate. Therefore, the cis-polyacetylene has only one ground state which is the phase A. For other polymers, like polyparaphenylene, polythiophene, polypyrrole, etc., all have energy non-degenerate states: phase A (rings are linked by single bonds) and phase B (rings are linked by double bonds) (Fig. 1.8). For polyparaphenylene, the two phases are well known as aromatic and quinoid phase. For these polymers, the phases A and B are isomers with different structures where the energy of phase B is higher than phase A [6]. The ground state degeneracy/non-degeneracy will determine the type of excited states of a conjugated polymer. When there are degenerate ground states of phase A and B, solitons might exist in the polymer chains. In contrast, when the grounds are non-degenerate, the solitons cannot exist and polarons can be formed in the polymer chains (detailed in future sections).

1.2.1.2 Solitons in Trans-Polyacetylene

In the dimerized ground state of trans-polyacetylene (phase A or B), the displacement u_0 of any two neighbor atoms has opposite directions (Fig. 1.6). The atom displacement in a chain can be described with an order parameter ϕ_n:

$$\phi_n = (-1)^n u_n, \tag{1.18}$$
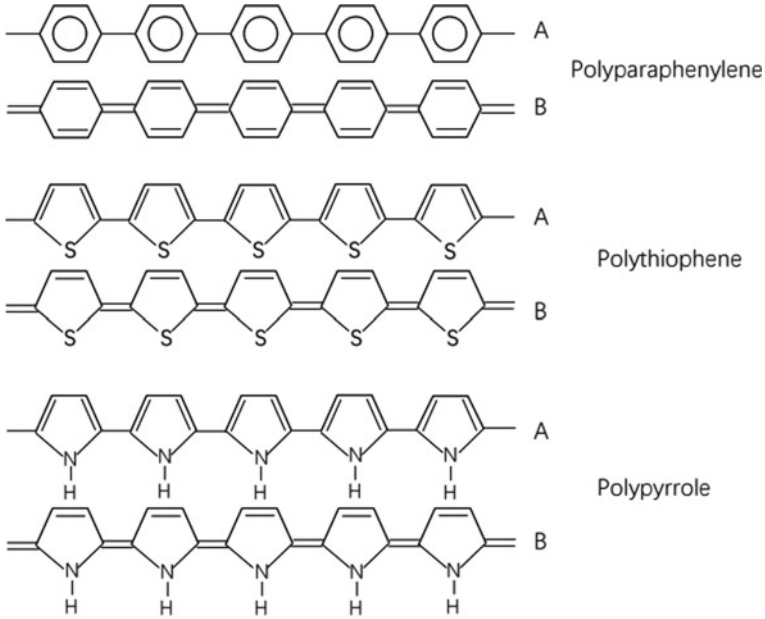
Fig. 1.8 Schematic molecule structures of phase A and phase B for polyparaphenylene, polythiophene, and polypyrrole

where u_n is the physical displacement of n-th atom. It is convenient to use ϕ_n to express a dimerized polymer chain instead of using u_n. For phase A, $\phi_n = -u_0$, and for phase B, $\phi_n = u_0$.

Assuming a trans-polyacetylene chain was in phase A originally, and a sequence of it has changed to phase B through thermal excitation or irradiation (Fig. 1.9). The excitation process requires certain energy $2E_s$. In the left part, a transition from phase A to phase B is seen, and this transition region is named as positive domain wall. Similarly, in the right part, a negative domain wall exist which is formed from transition from phase B to phase A. Because the energy degeneracy of the phases A and B, the energy spent for excitation is mainly used for domain wall formation (i.e., the energy is stored in the domain walls). The energy in the regions outside the domain walls does not change after the excitation. The domain walls are neither phase A nor phase B, where the links between carbon atoms are neither a single bond nor a double bond (indicated with dotted lines in Fig. 1.9). In a positive domain wall, the order parameter ϕ_n varies from $-u_0$ to u_0 across the domain wall (Figs. 1.10 and 1.11).

The domain wall is an elementary excitation which can move along the chain and the domain wall configuration does not change during the movement. We name such a domain wall as soliton. A positive domain wall is named as soliton (expressed as S) and negative domain wall is named as anti-soliton (expressed as $\overline{S}$).
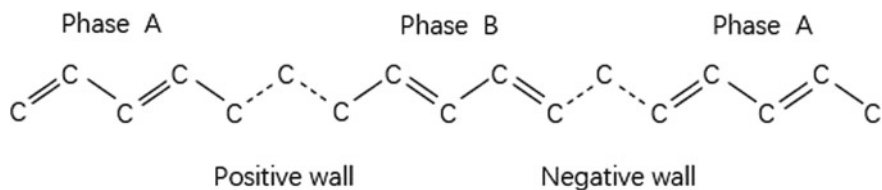
Fig. 1.9 Domain walls in trans-polyacetylene
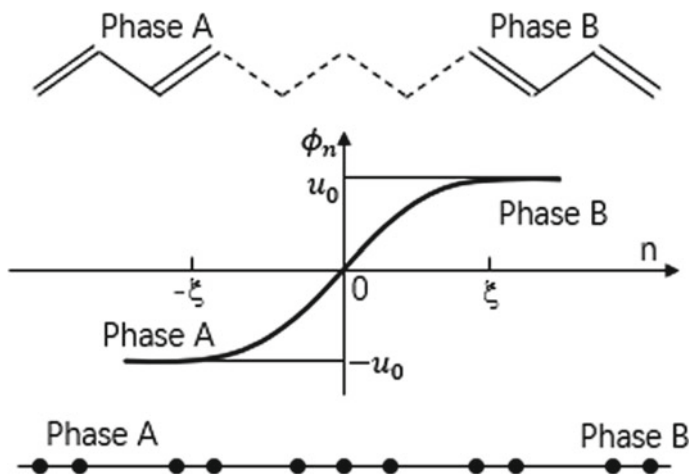
Fig. 1.10 Schematic structure of positive domain wall
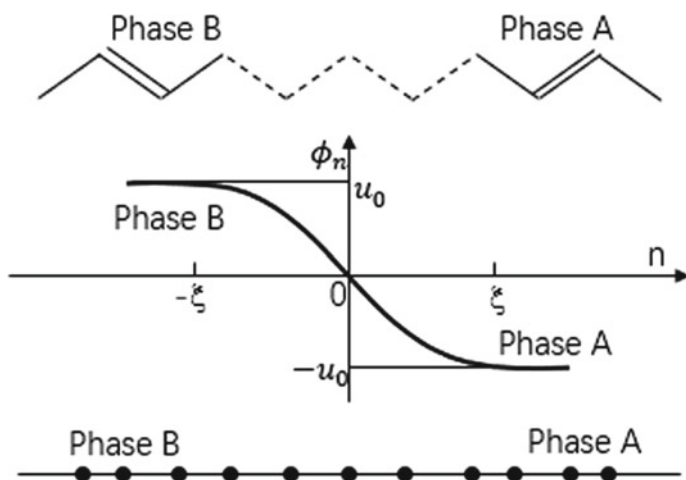
Fig. 1.11 Schematic structure of negative domain wall

In a dimerized polymer chain, a soliton as a localized distortion of lattice generates local potential, like the impurity in crystal of semiconductor. Thus, a soliton can generate a localized state around it and the energy level of the localized state is discrete and located in the middle of band gap [5, 7]. The energy level of the localized soliton state is called soliton level ε_s which has been found experimentally [8, 9].

1.2.1.3   Electrical Charge and Spin of Soliton

A polymer chain with π-electrons of N can forms N energy levels. The dimerization induces two energy bands with a band gap between them, i.e., valence band (VB) and conduction band (CB). Each band contains $N/2$ levels. Each level contains two electrical states and can be occupied by two electrons with different spin orientations (spin-up and spin-down). The valence band is fully occupied by electrons and the conduction band is empty. For clear description, we draw the band diagram separately for different spin orientations in Fig. 1.12a where each line represents one electrical state and can be occupied with one electron.

The soliton generation does not change the numbers of atoms and π-electrons in the polymer chain. The total electrical states will not change in the system owing to the soliton generation. Thus, with the soliton state generation, the valence band needs to deficit of one-half a state for each spin, as does the conduction band (Fig. 1.12b). We consider spin-up ($s = 1/2$, right) and spin-down ($s = -1/2$, left) states separately. For spin-up state (right of Fig. 1.12b), to generate a soliton state in the gap, a deficiency of one state from valence and conduction band is needed. Because the soliton state located in the middle of gap and the symmetry of the band structures, the reduced number of states from valence and conduction band are the same. This requires a reduction of "one-half state" from both valence and conduction band. For better
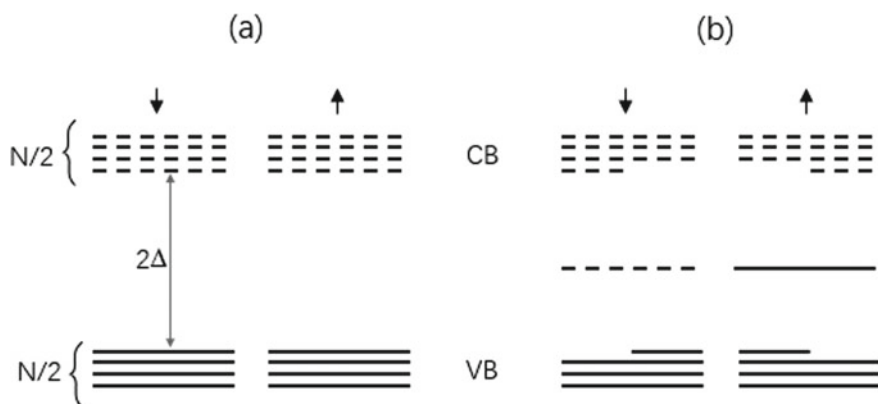
Fig. 1.12 Schematic illustration of energy level distribution for dimerized polymer molecule (**a**) and soliton energy level (**b**)

visualization, we illustrate the bottom of the conduction band with half dashed line and illustrate the top of the valence band with half solid line. These two "half states" are moved to the middle of gap to form a soliton state with spin-up oriented electron. The same is happened for the states with spin-down electrons, where a reduction of "one-half of spin-down state" from both valence and conduction band.

For pure polyacetylene, the number of π-electrons N does not change after the soliton generation. Before the soliton generation, there are N electrical states which are occupied with N electrons. After soliton generation, one state (one-half for spin-up and one-half for spin-down) is donated from valence band. Thus, only $N-1$ electrons can be accommodated in the valence band, and the remaining one electron needs to fill in the soliton state with either spin-up or spin-down. We assume that it occupies the spin-up state, therefore the spin-up soliton state is illustrated with solid line and the spin-down soliton state is illustrated with dashed line.

Let us examine the charge and spin of the soliton. Because the number of electrons does not change after the soliton generation, the system remains neural. Therefore, the soliton is non-charged. In the valence band, the occupation condition is identical for the two spin orientations and the total spin is zero. There is neither electron nor spin in the conduction band. On the soliton level, there is only one electron occupied in the spin-up state (the spin-down state is empty); hence, the total spin is $+1/2$. Therefore, the soliton has no charge but has spin 1/2, i.e., neutral soliton has spin $\pm 1/2$. Experiment showed that a kind of "defect" exists in polyacetylene which is neutral electrically, but they carry spin [10]. Such neutral defects with nonzero spin are solitons.

From Fig. 1.12b, we see that in pristine trans-polyacetylene, only one soliton state from the two is occupied. Therefore, the empty soliton state can be occupied with the electron donated by the donor impurity, if donor impurity exists in the polyacetylene. In this case, the two soliton states are illustrated with two solid lines (Fig. 1.13a). In this case, at all energy levels (valence band, conduction band, soliton level), the electron occupation conditions are identical for both spin-up and spin-down states. The total spin is zero which indicates that the negatively charged soliton has zero spin.

If an acceptor impurity is introduced into the polyacetylene, the impurity will remove the electron from the soliton and the two soliton states became empty as shown in Fig. 1.13b. The two empty states of the soliton level are illustrated with two dashed lines. As an electron is taken, the soliton is positively charged, and the net spin is zero. A summary of charge/spin of soliton is listed in Table 1.1 along with the electron/hole for comparison.

It seems that the above mentioned "one-half state" violated the basic principle of quantum mechanics. An electron is described by a quantum state and cannot occupy one-half state. The reason is that the anti-soliton $\overline{S}$ needs to be considered here, as the soliton and anti-soliton are paired in the polymer chain. The soliton and anti-soliton can be treated as two wave packages in a whole state. Consider a soliton and anti-soliton pair (Fig. 1.14), where the left part is energy band structure for the soliton, while the right part is the energy band structure for the anti-soliton. In the valence band there are four "half state" (two with soliton and another two with anti-soliton),
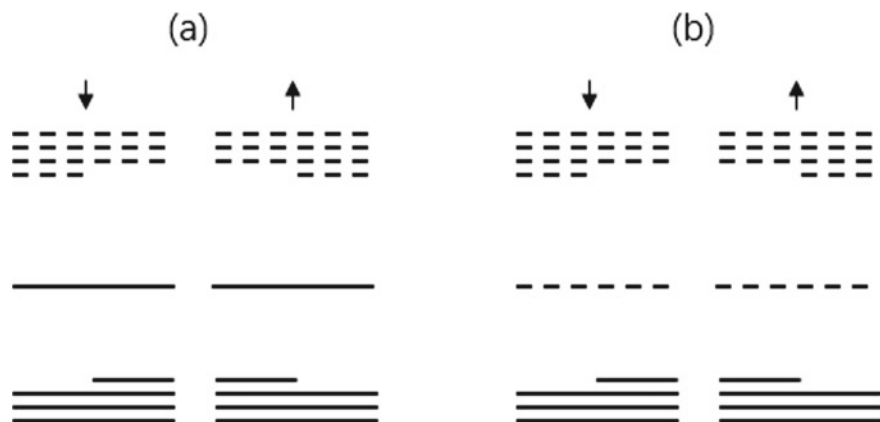
Fig. 1.13 Schematic illustration of energy levels for negative soliton $q = -e$ and $s = 0$ (**a**), and positive soliton $q = +e$ and $s = 0$ (**b**)

Table 1.1 The charge and spin of soliton

	Charge q	Spin S
Neutral soliton	0	$\pm\frac{1}{2}$
Positive soliton	$+e$	0
Negative soliton	$-e$	0
Electron	$-e$	$\pm\frac{1}{2}$
Hole	$+e$	$\pm\frac{1}{2}$

and two of them are occupied with spin-up electron and another two with spin-down electron. Two from the four "half state" form a whole spin-up state, and other two form a spin-down state. The two spin-up "half state" represent two wave packages of one wave function, i.e., the two spin-up "half state" form one whole spin-up state. The same description is applied for the two spin-down "half state." The two "half state" are coupled together and occupied by one electron which is indicated with dashed curves in Fig. 1.14.

1.2.2 Polarons in Conjugated Polymers

1.2.2.1 The Formation of Polarons

Soliton and anti-soliton are simultaneously generated in a polymer chain. When they get close to each other an interaction is expected. The soliton and anti-soliton have three charging conditions which possess different interaction between the soliton and
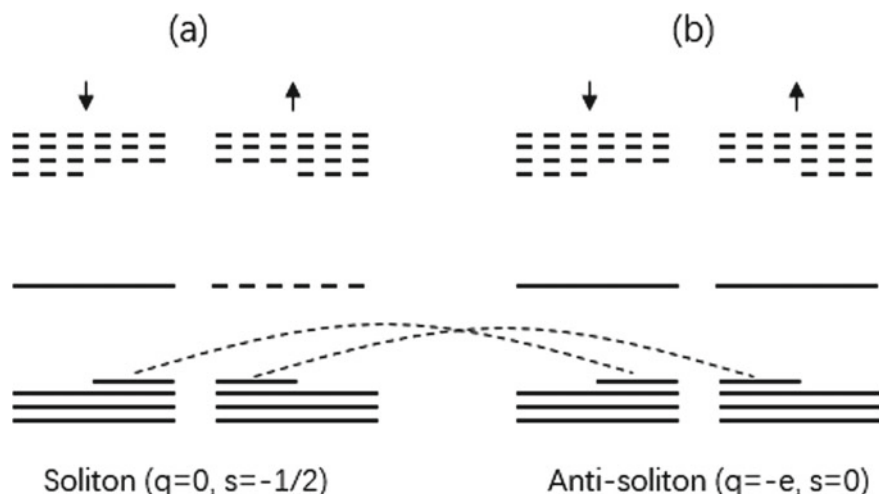
Fig. 1.14 State distribution of a $S - \bar{S}$ pair

anti-soliton. According to the total charges carried by the $S - \bar{S}$ pair, three different situations can be considered for investigating the soliton/anti-soliton interaction:

(i) The $S - \bar{S}$ pair has zero total charge, where soliton and anti-soliton carry opposite charges, or both are neutral.
(ii) The $S - \bar{S}$ pair has total charges $\pm 2e$, where the soliton and anti-soliton carry charges with the same sign.
(iii) The $S - \bar{S}$ pair has total charges $\pm e$, where one carries charge (e or $-e$) and another is neutral for soliton and anti-soliton.

In the case (i), the soliton and anti-soliton attract each other. They approach each other under attraction force to reduce phase B gradually, and the soliton and anti-soliton annihilate eventually as shown in Fig. 1.15.

In the case (ii), as the soliton and anti-soliton carry charges with same sign, they repel each other. Therefore, no new local state will form.

In the case (iii), when the soliton and anti-soliton are apart with far distance, they attract each other, and the system energy is the total energy of soliton and anti-soliton $4\Delta_0/\pi$ (Δ_0 is the energy required to generate a hole). However, when
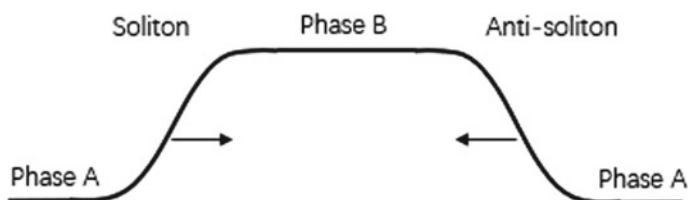
Fig. 1.15 Annihilation of soliton and anti-soliton

they are very close, a repelling force exists. Therefore, a balanced distance ($1.24 \xi_0$, where ξ_0 is called half width of the soliton) exists at which the net force between the soliton and anti-soliton is zero. While, the energy of the system is minimized which is $2\sqrt{2}\Delta_0/\pi$ [11, 12]. If the soliton and anti-soliton overlap for any reason to become single phased chain. The dimerized A (or B) phase will carry one charge (hole or electron) which will increase the energy of the system to Δ_0. Thus, soliton and anti-soliton can form a bound state with energy $2\sqrt{2}\Delta_0/\pi$. For this bound state the distance between the soliton and anti-soliton is $1.24 \xi_0$, and the overlap between the soliton and anti-soliton is so huge that the profiles of the individual soliton and anti-soliton cannot be recognized. This newly formed bound state is stable and is termed as polaron.

1.2.2.2   The Structure and Property of Polarons

Polaron is a bound state formed with soliton and anti-soliton. Therefore, the polaron structure could be evolved from the structures of soliton and anti-soliton. The structure of polaron includes two aspects: distribution of atoms and energy band structure.

(1)   The distribution of atoms in polaron

As stated earlier, the distribution of atoms is described with order parameter $\phi_n = (-1)^n u_n$. The coordinates at the centers of soliton and anti-soliton are x_0 and $-x_0$, respectively. When the length of $S-\overline{S}$ pair $2x_0$ is much large than width of soliton($2x_0 \gg 2\xi_0$), there is no overlap between the soliton and anti-soliton. Three regions exist on the chain as shown in Fig. 1.16a which is assumed that phase A is excited in phase B. If one is charged in the $\overline{S} - S$ pair, the soliton and anti-soliton attract each other, and the region A is shrinking as shown in Fig. 1.16b. At $2x_0 = 2\xi_0$, the soliton and anti-soliton overlap, the phase A disappears as shown in Fig. 1.16c. With further narrowing the phase A, an equilibrium position $2x_0 = 1.24\xi_0$ is reached where the ϕ_n is no longer being negative (Fig. 1.16d). Under this condition, the ϕ_n represents the order parameter of polaron. From the shape of ϕ_n, one can see that after the formation of polaron the chain is in single phase. The dent on the curve represents a small charged region with structure deformation from equilibrium, i.e., polaron. In the polaron formation process described in Fig. 1.16, the phase A is generated in phase B where anti-soliton is on the left and the soliton on the right. The polaron is formed in the phase B. Similarly, a polaron can be created in phase A and the process is shown in Fig. 1.17. In this case, the soliton is on the left and the anti-soliton on the right. The order parameter of the polaron is negative.

Polaron is a local lattice distortion in a uniform dimerized chain. The region of the distortion is around $4\xi_0$ where the displacements of atoms are not uniform (the values of u_n are different). Such a lattice distortion forms bound state located in the energy gap between the valence and conduction bands.

Fig. 1.16 Schematic illustration of polaron formation and polaron structure in phase B
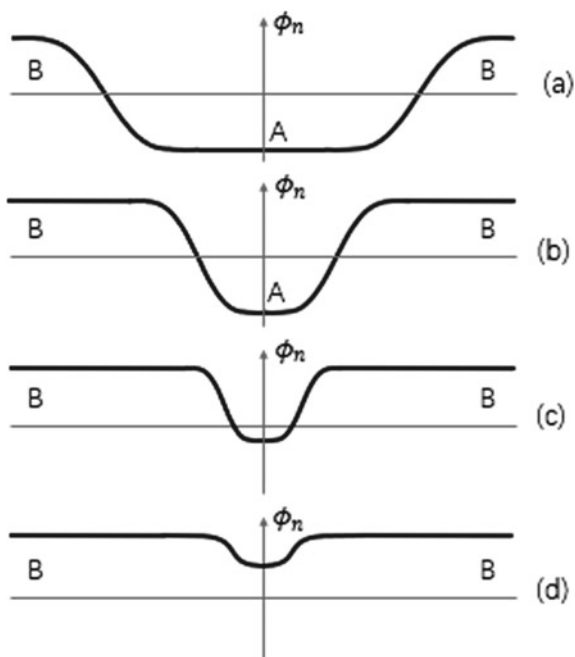
Fig. 1.17 Schematic illustration of polaron formation and polaron structure in phase A
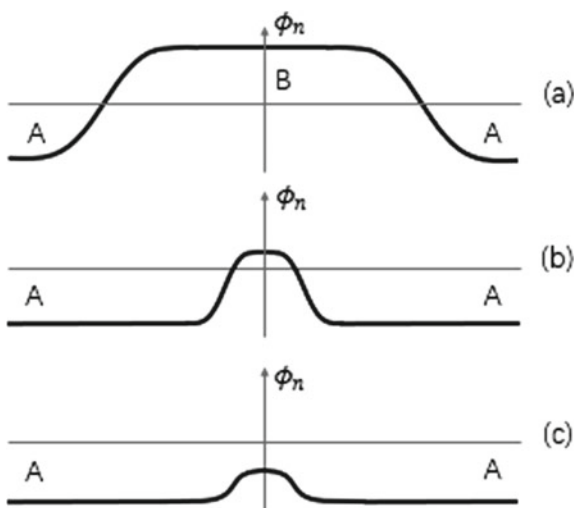
(2)   The energy levels of polaron

As the polaron can be viewed as a bound state of a $S - \bar{S}$ pair, the energy levels of the polaron could be evolved from soliton states. We examine the states of a $S - \bar{S}$ pair as shown in Fig. 1.18. For simplicity, only the spin-up states are considered (for the
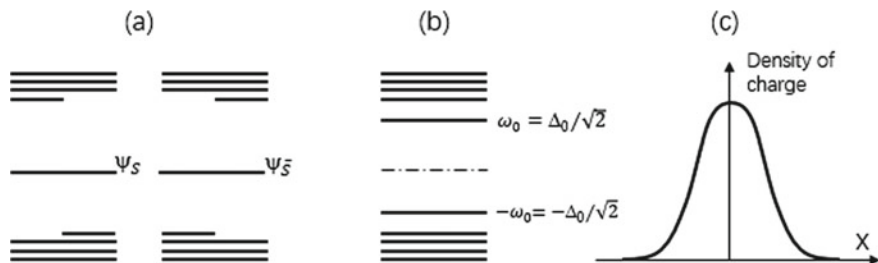
Fig. 1.18 Electrical spectrum and charge density distribution of polaron

spin-down states, the energy spectrum is symmetric with the spin-up states). When the soliton and anti-soliton are far apart ($2x_0 \gg 4\xi_0$) they are less interacted, and the state of the soliton (ψ_S) and the state of anti-soliton ($\psi_{\bar{S}}$) are located in the center of energy gap (Fig. 1.18a, only spin-up state is drawn). Each state of the ψ_S and $\psi_{\bar{S}}$ is formed by splitting off one-half state from the valence band and conduction band. The states ψ_S and $\psi_{\bar{S}}$ are degenerate when the soliton and anti-soliton are far apart. When the soliton and anti-soliton approach to each other and partially overlapped, because the overlap of the wave packages of the soliton and anti-soliton, the two "one-half states" on the two conduction band edges of soliton and anti-soliton will merge together to become a whole state of the conduction band. The same is happened for the valence band. Therefore, in the polaron no "one-half state" exist as shown in Fig. 1.18b. The overlap of soliton and anti-soliton will bring huge impact to the gap states ψ_S and $\psi_{\bar{S}}$. The states ψ_S and $\psi_{\bar{S}}$ are degenerate when the soliton and anti-soliton are well apart. When the soliton and anti-soliton overlap, the interaction of them will cause the splitting of the degenerated ψ_S and $\psi_{\bar{S}}$, i.e., the ψ_S and $\psi_{\bar{S}}$ will mix and form two new states: bonding state and anti-bonding state. The bonding and anti-bonding states have different energies which appear as two separated energy levels in the band gap. As the soliton and anti-soliton are mirror symmetric the newly formed bonding and anti-bonding states are symmetrical about the gap center. The bonding state is below the gap center line for ω_0, and the anti-bonding is above the line for ω_0. Thus, for the polaron there two separated energy levels in the energy gap which are ω_0 and $-\omega_0$. The value of the ω_0 is $\Delta_0/\sqrt{2}$ [7]. These two localized states are bound states of electron in the potential of the lattice distortion, and the charge localization is schematically shown in Fig. 1.18c.

1.2.2.3   The Charge and Spin of the Polaron

From the energy spectrum shown in Fig. 1.18, we can discuss the charge and spin of the polaron. The two energy levels $-\omega_0$ and $+\omega_0$ in the energy gap are split off from the valence and electron band, respectively. For the neutral ground state, the states in valence band and $-\omega_0$ level are occupied completely, while the $+\omega_0$ level and conduction band are empty. For trans-polyacetylene, a stable polaron can
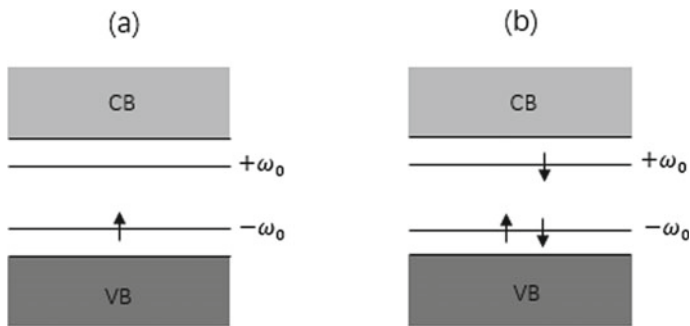
Fig. 1.19 Schematic illustration of polaron state occupation. **a** p-polaron, $q = +e$, $s = 1/2$ (or $-1/2$); **b** n-polaron, $q = -e$, $s = -1/2$ (or $1/2$)

only carry charge $+e$ or $-e$. For a positive polaron one electron is missing in the system, therefore, the $-\omega_0$ level is occupied by one electron only and the spin is 1/2 (Fig. 1.19a). The charge and spin have normal relation in the polaron, like a hole. For negative polaron, the system receives an additional electron occupied on the $+\omega_0$ level (Fig. 1.19b) and the spin is $s = 1/2$ (or $s = -1/2$) which indicates a normal charge/spin relation for the negative polaron, like an electron.

The existence of polaron can be proved with experiments, for instance, one can measure the absorption spectra of the materials. For the polymer with polarons, two discrete energy levels $\pm\omega_0$ locate in the energy gap which can induce a transition between the two levels, and an absorption at $2\omega_0 = \sqrt{2}\Delta_0$ can be observed [13].

Experiment has shown that when dopant concentration is less than 1%, spin signal can be observed in the doped polyacetylene. However, the magnetic signal has disappeared when the doping concentration was large than 1% [10]. This was explained with the formation of polarons. Although the excitation energy of single soliton Es ($2\Delta_0/\pi$) is lower than that of polaron Ep ($2\sqrt{2}\Delta_0/\pi$), the soliton-creation requires generation of $S - \bar{S}$ pair which needs energy of 2Es [7, 14]. Furthermore, the energy for creation of polaron is less than the excitation energy of hole or electron (Δ_0). Thus, in the trans-polyacetylene, the easiest elemental excitation is the polaron excitation, and the polaron will be generated at low dopant concentration. The polaron carries charge and spin which is conductive possess magnetic property. As the conjugation length is limited (several tens and hundreds of carbon atoms), each chain might have chance to receive (from donor dopant) or donate (to acceptor dopant) one electron which excites the carbon chain at low dopant concentration. With increasing dopant concentration, two charges might be created in a carbon chain. However, in trans-polyacetylene, a polaron cannot carry two charges, and two elemental excitations are needed. In such case, the $S - \bar{S}$ pair generation is energetically favorable, and the charge carriers became $S - \bar{S}$ pairs with zero net spins.

1.2.2.4   Bipolaron

As described above that the conjugated polymers can be divided into two categories which are (i) polymers with degenerate ground states and (ii) those with non-degenerate ground states. In previous section, polaron structure and property in trans-polyacetylene, a polymer with degenerate ground states, were discussed. In this section we discuss conjugated polymers with non-degenerate ground states.

We assume that the phase A is in ground state and the energy of each structure unit of the polymer is ε_A. Phase B is generated by interchange single bond and double bond in the chain, and the energy of the structure unit in phase B (ε_B) is higher, i.e., $\delta\varepsilon = \varepsilon_B - \varepsilon_A > 0$. We take polyparaphenylene as example to illustrate why soliton cannot be generated in such non-degenerate systems. In the polyparaphenylene, the aromatic phase A is the ground state (Fig. 1.20a). A soliton can be generated in the chain (Fig. 1.20b), while an anti-soliton will also be generated in distance (not shown). As the energy of a quinoid ring is higher than the energy of aromatic ring for $\delta\varepsilon = 0.35$ eV, the B phase generation will increase energy for $N_B\delta\varepsilon$ which is very high if the N_B is not very small (N_B is the number of quinoid rings generated). This is a fundamental difference between the two types of polymers with degenerate and non-degenerate ground states in terms of elemental excitation. For polymers with degenerate ground states, like polyacetylene, the soliton formation only requires a little energy spent onto the formation domain wall between the two phases with equal energy. Therefore, the soliton can only form in the conjugated polymers with degenerate ground states.

Although solitons cannot be formed in conjugated polymers with non-degenerated ground states, polarons can still be generated. Both singly charged and doubly charged polarons can be formed in such type of polymers. A doubly charged polaron
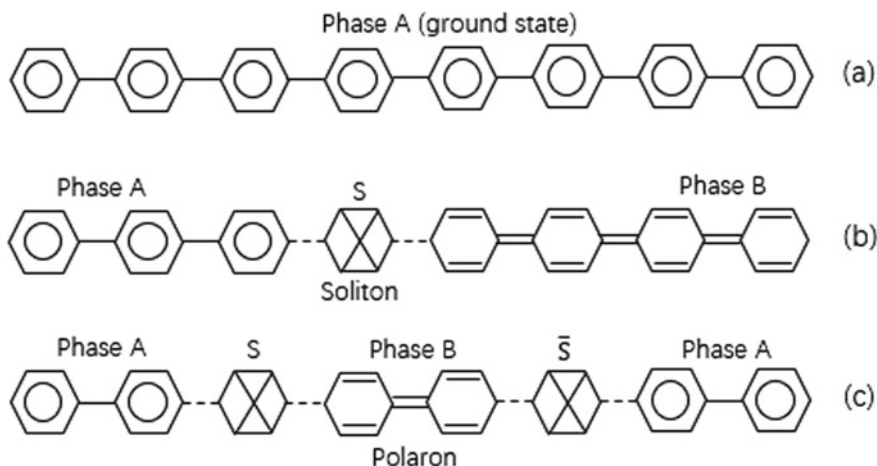
Fig. 1.20 Schematic illustration of confinement effect of $S - \bar{S}$ pair in polymer with non-degenerate ground states

is named as bipolaron. A polaron can be treated as closely bounded $S - \bar{S}$ pairs where the length of phase B is very small (for phase A polymer). Conversion of few aromatic rings into quinoid phase in a chain of phase A (Fig. 1.20c) is possible as the energy required is small due to the small number of N_B. An interesting phenomenon is that an attraction force exists between the soliton and anti-soliton. Let the length of each ring is d_0, then, the length of phase B is $l = N_B d_0$. As the formation of each quinoid ring requires energy $\delta\varepsilon$, the energy needed to form phase B with length l is:

$$E(l) = N_B \delta\varepsilon = l\delta\varepsilon/d_0 \tag{1.19}$$

The energy is proportional to the length of reversed domain between the soliton and anti-soliton l which is similar to the elastic potential energy of a spring where the elastic potential is increased with length elongation caused by the restoring force. In likewise, the increasing $E(l)$ with l indicates that an attraction force (f) exists between the soliton and anti-soliton.

$$f = \frac{\mathrm{d}E(l)}{\mathrm{d}l} = \frac{\delta\varepsilon}{d_0} \tag{1.20}$$

One can see that the attraction force is a constant which is not weaken with the increasing of the distance between the soliton and anti-soliton. The attraction force is originated from the energy non-degeneracy between the phase A and B. The constant attraction force results a strong bounding of the $S - \bar{S}$ pairs, i.e., a bound state is formed. This phenomenon is called "confinement effect." From the confinement effect, we can see that no matter what kind of charge the soliton/anti-soliton carry (even charges with the same sign), they still can bound together. When the soliton and anti-soliton carry charge with same sign a repelling force exists between them. Such repelling force is weakening with increasing distance between the soliton and anti-soliton, but the attraction force does not change. Therefore, the repelling force will be balanced by the attraction force eventually at a small increased distance between the soliton and anti-soliton, and the bound state still maintains. This shows that in conjugated polymer with non-degenerate ground states, polaron with charge ($\pm 2e$) can exist which is termed as bipolaron. Table 1.2 shows the summary of the possible elemental excitations in conjugated polymers with both degenerate and non-degenerate ground states. Figure 1.21 shows a schematic illustration of polaron state occupation.

1.3 Small Molecular Semiconductor Materials

Molecular semiconductors have been widely studied and used because they are easy to form crystalline films for fabrication of devices with high quality. Many small molecular semiconductor materials with high charge mobility have been synthesized such as pentacene, rubrene, C8-BTBT, etc. The crystalline materials are not only

Table 1.2 Possible elemental excitations in conjugated polymers with degenerate and non-degenerate ground states

Conjugated polymer	With degenerate ground states	With non-degenerate ground states
Soliton $\begin{pmatrix} q = \pm e, & s = 0 \\ q = 0, & s = 1/2 \end{pmatrix}$	Yes	No
Polaron (s = 1/2)	Yes	Yes
Bipolaron (s = 0)	No	Yes
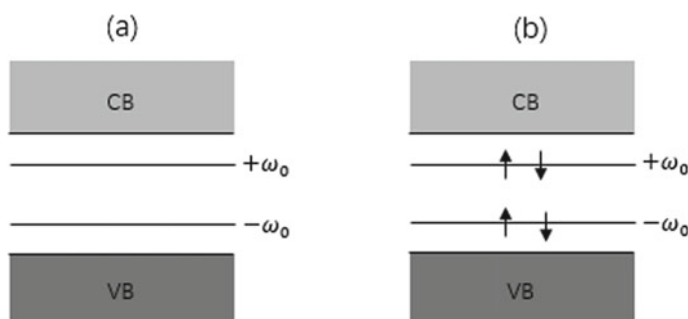
Fig. 1.21 Schematic illustration of bipolaron state occupations. **a** p-bipolaron, q = + 2e, s = 0; **b** n-bipolaron, q = − 2e, s = 0

beneficial to practical applications, but also valuable for fundamental research. The intrinsic properties of organic semiconductors can be tracked by using their single crystals because organic crystals provide highly ordered structures with minimized traps and free from grain boundaries.

At low temperature, the charge mobility of organic semiconductor single crystal is decreasing with elevating temperature because of the increased scattering probability by phonons which signifies a band-like conduction mechanism. At increased temperature, the weak inter molecule interaction leads to enhanced molecule and lattice distortions. The thermally activated variation of relative positions of adjacent molecules induces a fluctuation in transfer integrals. This will eventually induce a charge-carrier localization. Therefore, at high temperature, a localized charge hopping picture is more appropriate conduction mechanism. Since the high-temperature (like room temperature) mobility is very important for real application, the hopping description of charge transport based on the localized picture has brought increased attention. This mechanism has been widely used to interpret experimental data and to design new molecular semiconductors.

The charge transport is mainly determined by the molecular structure and crystal structure [15–17]. There are four different types of packing motifs as shown in Fig. 1.22 [18]. (i) Herring-bone packing (face-to-edge) without π-π overlap between adjacent molecules; (ii) Herringbone packing with π-π overlap between adjacent
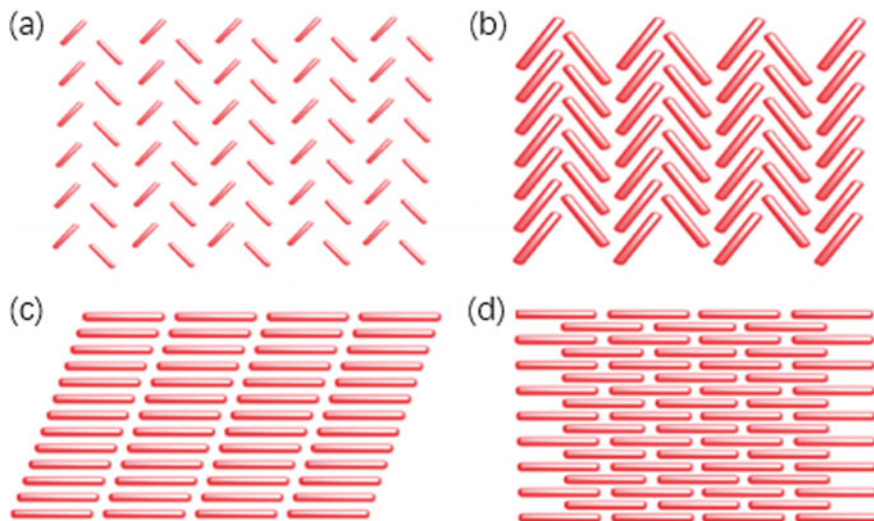
Fig. 1.22 Molecular packing motifs in crystals. **a** Herring-bone packing (face-to-edge) without π-π overlap between adjacent molecules; **b** Herringbone packing with π-π overlap between adjacent molecules; **c** Lamellar packing, one-dimension π-stacking, and **d** lamellar packing, two-dimension π-stacking. (Adapted from ref [18])

molecules; (iii) Lamellar packing, one-dimension π-stacking, and (iv) lamellar packing, two-dimension π-stacking. From the four types of molecular packing, the lamellar packing (2D-π-stacking) is believed to be the most efficient charge transport because it can increase the transfer integral more efficiently [16].

1.3.1 Marcus Charge-Transfer Theory

A classical theory that is widely used to describe charge transfer in molecular system is Marcus theory where the charge-transfer rate is expressed as:

$$k = \frac{J^2}{\hbar} \sqrt{\frac{\pi}{\lambda k_B T}} \exp\left(-\frac{\left(\lambda + G^0\right)^2}{4\lambda k_B T}\right) \tag{1.21}$$

where J is the transfer integral between the initial and final states of the two molecules that involved the charge transfer, λ is the reorganization energy which is defined using the energy change associated with geometry relaxation during the charge transfer, and ΔG^0 is the relevant change of total Gibbs free energy. In a crystal formed with one type of molecules, the $\Delta G^0 = 0$, and the equation becomes:

$$k = \frac{J^2}{\hbar}\sqrt{\frac{\pi}{\lambda k_B T}}\exp\left(-\frac{\lambda}{4 k_B T}\right) \qquad (1.22)$$

In this case, the thermal activation energy barrier for charge transfer is $\lambda/4$.

1.3.1.1   Reorganization Energy and Transfer Integral

From Marcus equation, we know that there two key factors that influence the charge-transfer rate: the reorganization energy (λ) and the transfer integral (J). The reorganization energy has both internal and external contributions. The internal contribution arises from changes in the geometry of the molecules when the electron transfer takes place. External contribution arises from change in the surrounding media that accompany the charge transfer. In organic crystal, the internal contribution plays dominant role and the external part is often neglected. This contrasts with the case of charge transfer in solution where the external part dominates because the reorganization of the surrounding solvent molecules. The internal contribution includes two parts: (i) the energy difference between the neutral molecule with its optimal charged geometry (i.e., after turning to neutral, the molecule geometry remains as it was charged before relaxation to equilibrium) and in the equilibrium neutral geometry (λ^{I}), and the energy difference of the charged molecule in these two geometries (λ^{II}) as sketched in Fig. 1.23.

Fig. 1.23 Schematic representation of potential energies of a molecule in neutral and charged states. The internal reorganization energy is the sum of the two relaxation energies λ^{I} and λ^{II}
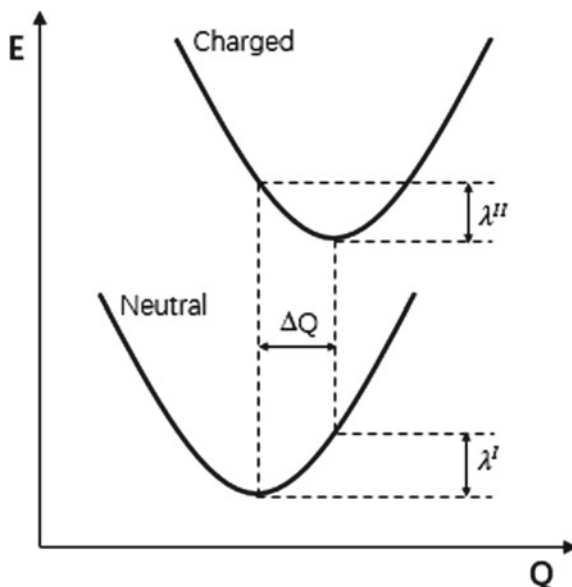
There are several methods have been used to evaluate the transfer integral of molecule dimmer such as energy level splitting (ELS) [19], minimized energy splitting along reaction path (MES) [20], site-energy correction (SEC) [21], and direct evaluation (DE) [22]. The transfer integral strongly depends on the overlap of frontier orbitals of the neighbored molecules. Therefore, optimizing relative orientation between molecules (i.e., the way of molecule packing) is important for designing new materials. The computation on pentacene dimmer with different tilt angles from parallel to perpendicular shows that the transfer integral varies from maximum at parallel configuration to minimum at tilt angle around 60°, and increases again with enlargement of the angle [23].

The molecule staking in a crystal can be tuned by delicate design of molecule derivatives. For instance, in polyacene crystals, the balance between the π-π interaction and the electrostatic repulsion can result in a herringbone angle between neighboring molecules. If polar groups are introduced into the molecule structure, a new balance can be achieved with the result of shifting molecule packing, for instance, from herringbone to lamellar stacking [16]. According to the Marcus theory, a small internal reorganization energy and large intermolecular transfer integral are helpful to speed up the charge conduction in the materials.

1.3.1.2 Methods to Reduce the Internal Reorganization Energy

The internal reorganization energy originates from molecule deformations upon charging. Therefore, rigid molecules should have smaller λ value than that for flexible molecules. Other strategies that can extend delocalization of charges in molecules have also been used to lessen the molecule distortion and in turn to reduce internal reorganization energy.

Triphenylamine is a well-renowned hole transporting material. To further improve the conductive property, one could construct proper molecule configuration, for example, to form a macrocycle (M1) or a linear chain (M2) with triphenylamine units (Fig. 1.24). Intuitively, the chain molecules should be more conductive since the extended conjugation length. Quantum chemistry computation shows that λ of molecule M1 (173 meV) is much smaller than the λ of molecule M2 (317 meV) [24]. The disparity arises from the difference in molecule geometry change occurred from neutral to positively charged equilibrium form. It is found that the rotation of the phenyl group is restricted in M1, while a large relaxation of the biphenyl core is observed in M2. Since the transfer integrals are found to be very close for the two molecules and the room temperature hole mobility for M2 was calculated to be 1.9×10^{-3} cm^2 V^{-1} s^{-1} which is one order of magnitude smaller than that of 1, 2.7×10^{-2} cm^{2}V^{-1} s^{-1} for M1. This is mainly arising from the difference of the λ values [24]. These results compare well with the experimental results of 1.5×10^{-2} cm^2 V^{-1} s^{-1} and 2×10^{-4} cm^2 V^{-1} s^{-1} for the two molecules [25].

It is found that λ decreases with the number of thiophene rings of oligothiophene (nT, M3 in Fig. 1.24) from about 360 meV for 2 T to 210 meV for 8 T [26, 27].

Fig. 1.24 Molecule structures of macrocycle (M1) and linear chain (M2) with triphenylamine units and oligothiophene nT (M3)

Similar trend was also observed in other system, e.g., oligoacenes, [28], oligothienoacenes [29], and other molecules [30]. Hutchison and coauthors argued that the positive charge becomes more delocalized in longer conjugated oligomers, therefore the internal reorganization energy is getting smaller due to decreased geometric change with the charge transfer [30]. Another strategy can be used is substitution. It is found that cyanation can effectively reduce λ for pentacene. The cyano-groups are found to further extend the charge delocalization and leads to a smaller reorganization energy [31].

1.3.1.3 Methods to Increase the Intermolecular Transfer Integrals

In contrast to the reorganization energy which describes an internal energy change of molecules, the transfer integrals are strongly related to the intermolecular interaction. Brédas et al. have systematically studied the evolution of the transfer integrals with respect to the intermolecular displacement and relative orientations for various organic compounds [32–36]. The research results indicate that large variations in the transfer integrals resulted from small distortions in the configuration relationship between molecules. This brings promising opportunities to optimize intermolecular position through modification of the molecule structures or changing the environmental conditions to increase the intermolecular electron coupling. A representative example is rubrene, which is a tetraphenyl derivative of tetracene. The phenyl substitution improves the molecule packing in rubrene crystal, and intermolecular transfer integral is considerably increased from 71 meV for tetracene to 102 meV for rubrene which is attributed to an intermolecular displacement [37]. Although the reorganization energy of rubrene is large than that for tetracene (150 meV vs 105 meV), the hole mobility for the former is much large [38]. Very similar situation is in pentacene derivatives, and a charge mobility more than 35 $cm^2V^{-1} s^{-1}$ has been predicted [31].

A simple and straight forward way to increase intermolecular transfer integrals is to change crystal packing without modifying the molecular structure. Many efforts
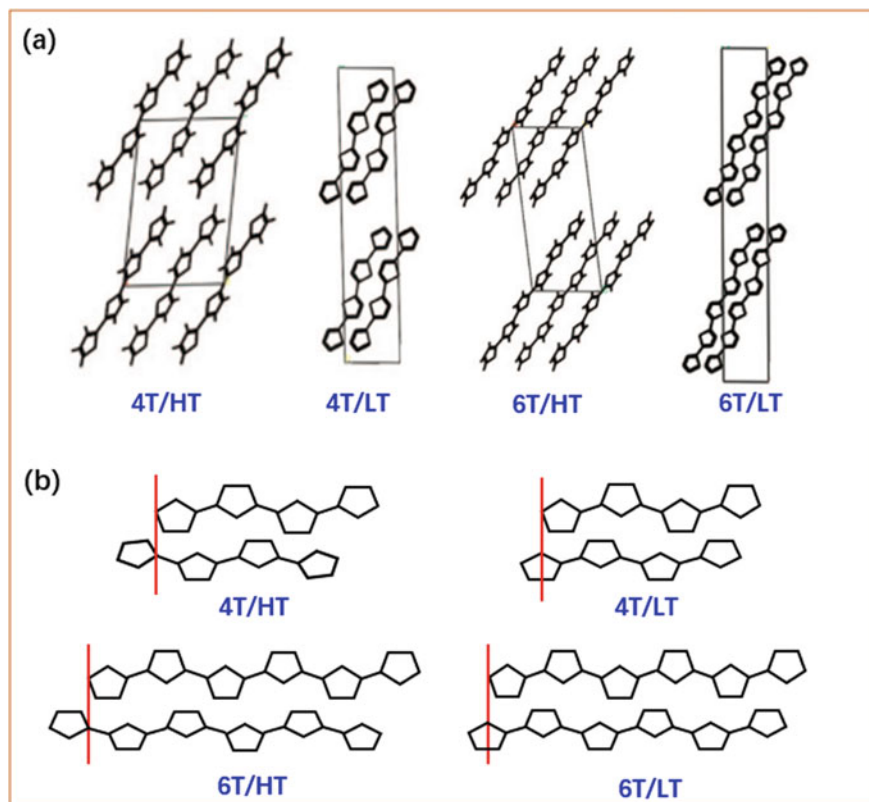
Fig. 1.25 **a** Crystal structures of 4 T/HT, 4 T/LT, 6 T/HT and 6 T/LT. **b** Intermolecular displacements taken from the crystal packing along the long axis of thiophenes for the dominant pathway of 4 T and 6 T. (Adapted from ref [42])

were made with this purpose, like using different substrates, different deposition methods, etc. A molecular material may have several polymorphs in the crystal form. For example, depending on the sublimation temperatures both 4 T and 6 T (M3 in Fig. 1.24) molecules can have two typical polymorphs, i.e., low-temperature phase (LT) and high-temperature phase (HT) [39–42]. For the HT phase, there are two molecules in the unit cell, while for the LT phase each unit cell has four molecules (Fig. 1.25a). The small difference in the crystal packing causes a dramatic different transfer integral. For the HT phase, the transfer integral is 40 meV and 36 meV for 4 T and 6 T molecules, respectively. These values are about twice of that for LT phase which is 18 meV for both 4 T and 6 T molecules. It was found that there is a displacement of about half a thiophene ring between the dominant dimmers for the LT phase, while, for the HT phase, the displacement is around one thiophene ring (Fig. 1.25b). Since the sign of the HOMO orbitals has a period of half a thiophene

ring, the different displacement in HT and LT phases results in huge different inter-molecular coupling strengths. Consequently, the calculated hole mobility of the HT phase is about four times large than that of the LT phase.

1.3.1.4   Charge-Transport Network in Crystals

Besides optimized reorganization energy and transfer integral, a proper charge-transport network in the crystals is crucial for materials with high charge mobility. Figure 1.26b, c show crystal packing of two β-trithiophene based compounds (Fig. 1.26a). For compound-I, the crystal has a sandwich-herringbone arrangement (Fig. 1.26b), while the compound-II molecules stack in the normal herringbone struc-ture (Fig. 1.26c). For hole transport, the values of transfer integrals between neighbor molecules in compound-II are ranging from 11.3 to 35.4 meV [43]. The maximum transfer integral of that in the compound-I can be as large as 62.2 meV since the cofa-cial configuration of dimers. However, the transfer integrals between the molecule (red highlighted) and non-cofacial molecules around are less than 7.4 meV which means that charges are highly localized in the dimer and hardly to contribute to the overall mobility. For the compound-II crystal, a charge can always find a way to travel in the crystal and probability to move in different directions are similar. This results a large difference of charge mobilities between the two compounds.
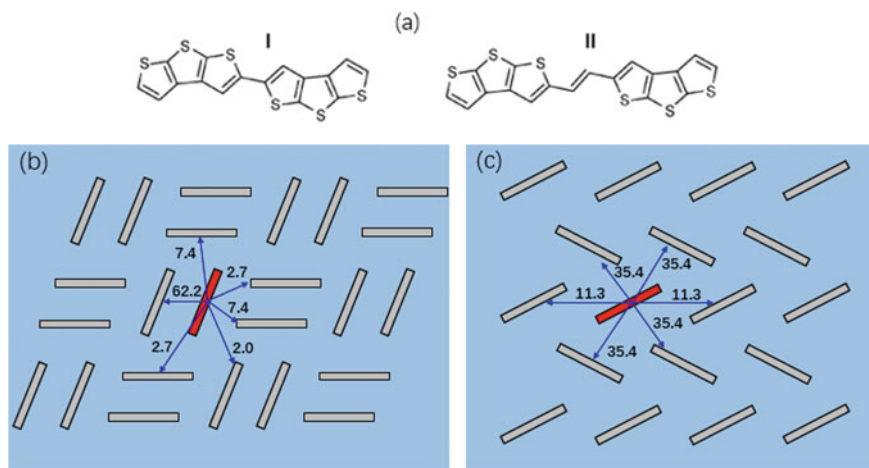
Fig. 1.26 Molecule structure (**a**) and crystal packing (**b**, **c**) of two β-trithiophene-based compounds. The arrows indicate the nearest neighbors of the red-highlighted molecule. The values marked are the corresponding transfer integrals in meV

References

1. Ono S, Shima H (2011) Flexible control of the Peierls transition in metallic C60 polymers. Euro Phys Lett 96:207011
2. Chung TC, Moraes F, Flood JD, Heeger AJ (1984) Solitons at high density in trans-(CH)x: collective transport by mobile, spinless charged solitons. Phys Rev B 29:2341–2343
3. Ikehata S, Kaufer J, Woerner T, Pron A, Druy MA, Sivak A, Heeger AJ, MacDiarmid AG (1980) Phys Rev Lett 45:1123–1126
4. Moses D, Denenstein A, Chen J, Heeger AJ, McAndrew P, Woerner T, MacDiarmid AG, Park YW (1982) Effect of nonuniform doping on electrical transport in trans-$(CH)_x$: studies of the semiconductor-metal transition. Phys Rev B 25:7652–7660
5. Su WP, Schrieffer J, Heeger A (1979) Solitons in polyacetylene. Phys Rev Lett 42:1698–1701
6. Bredas JL, Themans B, Fripiat J, Andre JM, Chance RR (1984) Highly conducting polypara-phenylene, polypyrrole, and polythiophene chains: an ab initio study of the geometry and electronic-structure modifications upon doing. Phy Rev B 29:6761–6773
7. Heeger AJ, Kivelson S, Schrieffer JR, Su WP (1988) Solitons in conducting polymers. Rev Mod Phys 60:781–850
8. Suzuki N, Ozaki M, Etemad S, Heeger AJ, MacDiarmid AG (1980) Solitons in polyacetylene: effect of dilute doping on optical absorption spectra. Phys Rev Lett 45:1209–1213
9. Kivelson S, Lee T-K, Liu YRL, Peschel I, Yu L (1982) Boundary conditions and optical absorption in the soliton model of polyacetylene. Phys Rev B 25:4173–4184
10. Weinberger BR, Kaufer J, Heeger AJ, Pron A, MacDiarmid AG (1979) Magnetic susceptibility of doped polyacetylene. Phys Rev B 20:223–230
11. Campbell DK, Bishop AR (1981) Solitons in polyacetylene and relativistic-field-theory models. Phys Rev B 24:4859–4862
12. Zhang C, Ma Y, Sun X, Ye C (1999) Electron interaction and the polaron in polymers. Acta Physica Sinica 48:917–925
13. Fesser K, Bishop AR, Campbell DK (1983) Optical absorption from polarons in a model of polyacetylene. Phys Rev B 27:4804–4825
14. Campbell DK, Bishop AR, Fesser K (1982) Polarons in quasi-one-dimensional systems. Phys Rev B 26:6862–6874
15. Wurthner F, Schmidt R (2006) Electronic and crystal engineering of acenes for solution-processible self-assembling organic semiconductors. Chem Phys Chem 7:793–797
16. Wang C, Dong H, Li H, Zhao H, Meng Q, Hu W (2010) Dibenzothiophene derivatives: from herringbone to lamellar packing motif. Cryst Growth Des 10:4155–4160
17. Dong H, Wang C, Hu W (2010) High performance organic semiconductor for field-effect transistors. Chem Commun 46:5211–5222
18. Wang C, Dong H, Hu W, Liu Y, Zhu D (2012) Semiconducting π-conjugated systems in field-effect transistors: a material odyssey of organic electronics. Chem Rev 112:2208–2267
19. Hutchison GR, Ratner MA, Marks TJ (2005) Intermolecular charge transfer between hetero-cyclic oligomers. Effect of heteroatom and molecular packing on hopping transport in organic semiconductors. J Am Chem Soc 127:16866–16881
20. Li XY (2001) Electron transfer between tryptophan and tyrosine: theoretical calculation of electron transfer matrix element for intramolecular hole transfer. J Comput Chem 22:565–579
21. Valeev EF, Coropceanu V, da Silva FDA, Salman S, Bredas J-L (2006) Effect of electronic polarization on charge-transport parameters in molecular organic semiconductors. J Am Chem Soc 128:9882–9886
22. Troisi A, Orlandi G (2002) Hole migration in DNA: A theoretical analysis of the role of structural fluctuations. J Phys Chem B 106:2093–2101
23. Nan GJ, Wang LJ, Yang XD, Shuai Z, Zhao Y (2009) Charge transfer rates in organic semiconductors beyond first-order perturbation: from weak to strong coupling regimes. J Chem Phys 130:024704

24. Yang XD, Li QK, Shuai Z (2007) Theoretical modelling of carrier transports in molecular semiconductors: molecular design of triphenylamine dimer systems. Nanotechnology 18:424029
25. Song YB, Di CA, Yang XD, Li SP, Xu W, Liu YQ, Yang LM, Shuai Z, Zhang DQ, Zhu DB (2006) A cyclic triphenylamine dimer for organic field-effect transistors with high performance. J Am Chem Soc 128:15940–15941
26. Coropceanu V, Cornil J, da Silva FDA, Olivier Y, Silbey R, Bredas J-L (2007) Charge transport in organic semiconductors. Chem Rev 107:926–952
27. Yang XD, Wang LJ, Wang CL, Long W, Shuai Z (2008) Influences of crystal structures and molecular sizes on the charge mobility of organic semiconductors: oligothiophenes. Chem Mater 20:3205–3211
28. Deng WQ, Goddard WA (2004) Predictions of hole mobilities in oligoacene organic semiconductors from quantum mechanical calculations. J Phys Chem B 108:8614–8621
29. Zhang YX, Cai X, Bian YZ, Li XY, Jiang JZ (2008) Heteroatom substitution of oligothienoacenes: from good p-type semiconductors to good ambipolar semiconductors for organic field-effect transistors. J Phys Chem C 112:5148–5159
30. Hutchison GR, Ratner MA, Marks TJ, Marks TJ (2005) Hopping transport in conductive heterocyclic oligomers: reorganization energies and substituent effects. J Am Chem Soc 127:2339–2350
31. Kuo MY, Chen HY, Chao I (2007) Cyanation: providing a three-in-one advantage for the design of n-type organic field-effect transistors. Chem Eur J 13:4750–4758
32. Brédas J-L, Beljonne D, Coropceanu V, Cornil J (2004) Charge-transfer and energy-transfer processes in π-conjugated oligomers and polymers: a molecular picture. Chem Rev 104:4971–5003
33. Brédas JL, Calbert JP, da Silva FDA, Cornil J (2002) Organic semiconductors: a theoretical characterization of the basic parameters governing charge transport. Proc Natl Acad Sci 99:5804–5809
34. Cornil J, Lemaur V, Calbert JP, Brédas JL (2002) Charge transport in discotic liquid crystals: a molecular scale description. Adv Mater 14:726–729
35. Lemaur V, da Silva FDA, Coropceanu V, Lehmann M, Geerts Y, Piris J, Debije MG, van de Craats AM, Senthilkumar K, Siebbeles LDA, Warman JM, Brédas J-L, Cornil J (2004) Charge transport properties in discotic liquid crystals: a quantum-chemical insight into structure-property relationships. J Am Chem Soc 126:3271–3279
36. Norton JE, Brédas JL (2008) Theoretical characterization of titanyl phthalocyanine as a p-type organic semiconductor: Short intermolecular π-π interactions yield large electronic couplings and hole transport bandwidths. J Chem Phys 128:034701
37. Nan GJ, Yang XD, Wang LJ, Shuai Z, Zhao Y (2009) Nuclear tunneling effect of charge transport in rubrene, tetracene, and pentacene. Phys Rev B 79:115203
38. Wang L, Nan G, Yang X, Peng Q, Li Q, Shuai Z (2010) Computational methods for design of organic materials with high charge mobility. Chem Soc Rev 39:423–434
39. Antolini L, Horowitz G, Kouki F, Garnier F (1998) Polymorphism in oligothiophenes with an even number of thiophene subunits. Adv Mater 10:382–385
40. Siegrist T, Kloc C, Laudise RA, Katz HE, Haddon RC (1998) Crystal growth, structure, and electronic band structure of α-4T polymorphs. Adv Mater 10:379–382
41. Horowitz G, Bachet B, Yassar A, Lang P, Demanze F, Fave JL, Garnier F (1995) Growth and characterization of sexithiophene single crystals. Chem Mater 7:1337–1341
42. Yang X, Wang L, Wang C, Long W, Shuai Z (2008) Influence of crystal structure and molecular sizes on the charge mobility of organic semiconductors: oligothiophenes. Chem Mater 20:3205–3211
43. Tan L, Zhang L, Jiang X, Yang XD, Wang LJ, Wang ZH, Li LQ, Hu WP, Shuai Z, Li L, Zhu DB (2009) A densely and uniformly packed organic semiconductor based on annelated β-trithiophenes for high-performance thin film transistors. Adv Funct Mater 19:272–276

Chapter 2
The Fundamentals of Organic Photophysics and Photochemistry

To understand material and device properties of organic electronics, some knowledge about organic photochemistry and photophysics is crucial. We do not attempt to cover many contents in this field due to space limitation, only several points, closely related to the devices described in this book, are introduced in this chapter, like energy quantization of molecule vibration, frontier molecular orbitals, excitons, typical photochemical reaction, etc.

2.1 Singlet and Triplet States

According to the theory of quantum mechanics, in a system formed with two particles of spin half (1/2), the wave functions of spin states can be expressed with 4 equations. If we use Dirac expression to express the quantum spin states χ of the two particles, then the four states are:

$$\chi_{11} = |\uparrow\uparrow\rangle$$

$$\chi_{10} = \frac{1}{\sqrt{2}}(|\uparrow\downarrow\rangle + |\downarrow\uparrow\rangle)$$

$$\chi_{1-1} = |\downarrow\downarrow\rangle$$

$$\chi_{00} = \frac{1}{\sqrt{2}}(|\uparrow\downarrow\rangle - |\downarrow\uparrow\rangle)$$

where the first subscript of χ is quantum number of spin angular momentum (S), while the second subscript is magnetic quantum number (m_s). When $S = 1$, $m_s = 1, 0, -1$ and when $S = 0$, $m_s = 0$. Figure 2.1 shows a schematic illustration of

spin configurations of the two-particle system. In the case of molecule excitation, $S = 0$ corresponds to singlet excitation where the spins of charges (two electrons at different energy levels) are anti-parallel, while $S = 1$ corresponds to triplet excitation where the spins of charges are parallel (Fig. 2.2). The transition between ground state S_0 and singlet states (S_1, S_2 $\cdots$) is spin-allowed transition which is fast and efficient. In contrast, the transition between ground state S_0 and triplet states (T_1, T_2 $\cdots$) are spin-forbidden transition which is much slow and inefficient. When the excited singlet decays through radiation, a fluorescence is observed. If the light emission is caused by a transition from excited triplet state to the ground state, the relaxation process is named as phosphorescence. The singlet has very short lifetime (~nanoseconds); therefore, the fluorescence takes place much more rapidly than the phosphorescence (microseconds or much longer). The triplet state is energetically favorable state which has lower energy level than singlet (e.g., $E(S_1) > E(T_1)$) because the higher multiplicity of the triplet according to the Hund's rule.
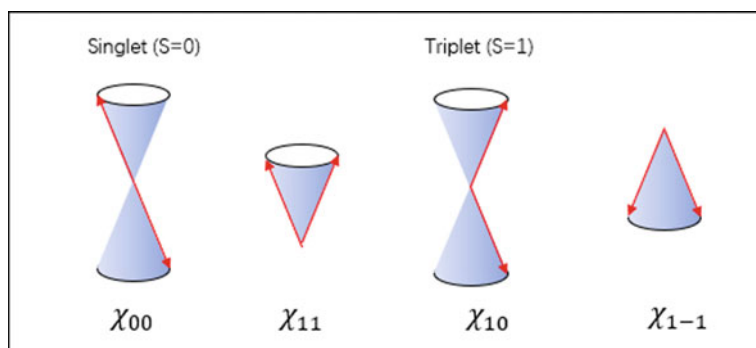
Fig. 2.1 Schematic illustration of spin configurations of two coupled particles with spin 1/2
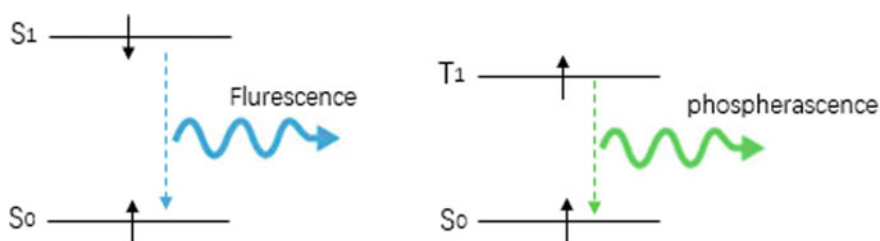
Fig. 2.2 Singlet excitation and fluorescence emission (left), triplet excitation and phosphorescence emission (right)

2.2 Quantized Energy Levels of Molecule Vibration

A simple model is a diatomic molecule of atom A and atom B (Fig. 2.3). The molecule can be viewed as a harmonic oscillator formed with two atoms of mass m_1 and m_2 linked with a spring-like bond. The reduced mass is $\mu = m_1 m_2/(m_1 + m_2)$. If the instant distance and equilibrium distance between the two atoms are x' and L_0, then $x = x' - L_0$ is the deviation from the equilibrium distance. The elastic force experienced by the two atoms is $f = -kx$, where k is elastic coefficient of the bond that links the two atoms. The potential energy $V(x) = kx^2/2$ which can be rewritten with following form by taking $k = \mu\omega^2$ ($\omega > 0$):

$$V(x) = \frac{1}{2}\mu\omega^2 x^2 \tag{2.1}$$

Under such an elastic potential, the system can be described with classical mechanics as:

$$x(t) = A\sin(\omega t + \varphi) \ (A \text{ is amplitude})$$

$$v(t) = \frac{dx}{dt} = \omega A\cos(\omega t + \varphi) \tag{2.2}$$

The total energy is the sum of kinetic and potential energy

$$E = T + V = \frac{1}{2}\mu\left(v^2 + \omega^2 x^2\right) = \frac{1}{2}\mu\omega^2 A^2 \tag{2.3}$$

In quantum mechanics, the Hamiltonian of the system is

Fig. 2.3 Energy variation with displacement of atom B (taking atom A as static reference and equilibrium point of B as origin). Bulk curve—classic potential; dashed lines—quantized energy levels
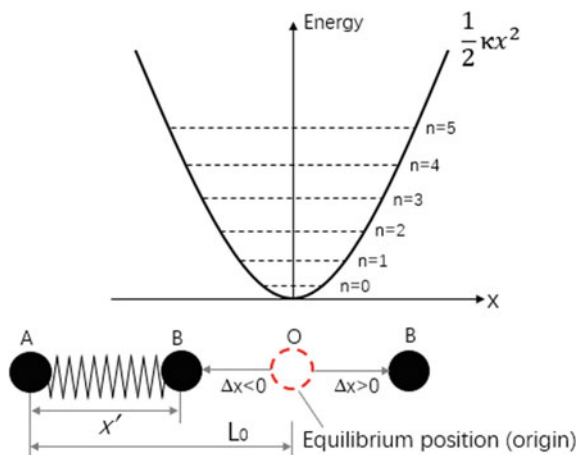
$$\widehat{H} = \widehat{T} + V = -\frac{\hbar^2}{2\mu}\frac{d^2}{dx^2} + \frac{1}{2}\mu\omega^2 x^2 \tag{2.4}$$

The Schrödinger equation is

$$\left(\widehat{H} - E\right)\psi = \left(-\frac{\hbar^2}{2\mu}\frac{d^2}{dx^2} + \frac{1}{2}\mu\omega^2 x^2 - E\right)\psi = 0 \tag{2.5}$$

The average potential is

$$\overline{V} = \int_{-\infty}^{\infty} V(x)|\psi(x)|^2 dx = \frac{1}{2}\mu\omega^2 \int_{-\infty}^{\infty} |x\psi(x)|^2 dx \tag{2.6}$$

When $x \to \pm\infty$, $V \to \infty$ and $\psi \to 0$. In the range $(-\infty, \infty)$, the $|x\psi(x)|^2$ is integrable and all the states must be localized.

$$\text{Let } x_0 = \sqrt{\hbar/\mu\omega}, \alpha = 1/x_0 = \sqrt{\mu\omega/\hbar}, \lambda = 2E/\hbar\omega \tag{2.7}$$

$$\xi = \alpha x = x/x_0 = x\sqrt{\mu\omega/\hbar} \tag{2.8}$$

Use above relations, the Eq. (2.5) can be expressed as

$$\frac{d^2}{d\xi^2}\psi + \left(\lambda - \xi^2\right)\psi = 0 \tag{2.5'}$$

where ξ is spatial coordinate with x_0 as unit, while λ is energy with $\hbar\omega/2$ as unit.

When $\xi \to \pm\infty$, Eq. (2.5') can be approximated as

$$\frac{d^2}{d\xi^2}\psi \approx \xi^2\psi$$

and its asymptotic solutions are $\psi \sim e^{\xi^2/2}, e^{-\xi^2/2}$.

Since $\xi \to \pm\infty$, $\psi \to 0$, only $\psi \sim e^{-\xi^2/2}$ is the proper form of the possible solutions.

Based on this argument, we express the solution as

$$\psi = u(\xi)e^{-\xi^2/2} \tag{2.9}$$

By inserting (2.9) to (2.5') an equation about $u(\xi)$ is

$$u'' - 2\xi u' + (\lambda - 1)u = 0 \tag{2.10}$$

$\lambda = 2E/\hbar\omega$ is the parameter to be determined. Some simple solutions of the equation can be easily observed directly, for instance

$$u = 1, \lambda = 1, E = \hbar\omega/2$$

$$u = \xi, \lambda = 3, E = 3\hbar\omega/2$$

$\xi = 0$ is a rational point in (2.10), $\xi \to \pm\infty$ is the only singularity point of Eq. (2.10). According to differential equation theory, $u(\xi)$ can be expressed with a positive power series

$$u(\xi) = \sum_{\nu=0}^{\infty} a_\nu \xi^\nu \tag{2.11}$$

As the $V(x)$ has even parity, ψ should be a real function with explicit parity. From Eq. (2.9), we know that ψ and u have the same parity. Therefore, formula (2.11) is formed either with all even terms or all odd terms.

$$u(\xi) = a_0 + a_2\xi^2 + a_4\xi^4 + \cdots$$

or

$$u(\xi) = a_1\xi + a_3\xi^3 + a_5\xi^5 + \cdots \tag{2.11'}$$

By inserting (2.11') into (2.10) and comparing the coefficients of terms of the same power, we have

$$a_{\nu+2} = a_\nu(2\nu + 1 - \lambda)/(\nu + 1)(\nu + 2) \tag{2.12}$$

Use this *recurrence relation all coefficients in the* (2.11') *can be calculated.* a_0 or a_1 are treated as normalization coefficients. *From* (2.12), *we see that for states with even parity, if $\lambda = 1$, $a_2 = a_4 = \cdots = 0$, $u = a_0$; for states with odd parity, if $\lambda = 3$, $a_3 = a_5 = \cdots = 0$, $u = a_1\xi$. One can generalize the values of λ, for instance*

$$\lambda = 2n + 1, \ n = 0, 1, 2, \cdots \tag{2.13}$$

Then $a_{n+2} = a_{n+4} = \cdots = 0$, $u(\xi)$ is a polynomial of degree n.
The energy E_n can be expressed as

$$E_n = \frac{\lambda}{2}\hbar\omega = \left(n + \frac{1}{2}\right)\hbar\omega, \ n = 0, 1, 2, \cdots \tag{2.14}$$

Therefore, the vibration energy of a molecule is quantized as shown in Fig. 2.3.

2.3   Frontier Molecular Orbitals

The electronic structure of a single atom is described by discrete energy levels, while the electronic structure of a solid material which contains massive atoms is well described with energy band theory. For a molecule, like a dye molecule, which contains limited number of atoms, molecule orbital theory is applied. In 1950s, Fukui Kenich suggested that the electron cloud of a molecule can be described with different energy levels which are called molecule orbitals. Like the case of single atom, electrons occupy from lower orbitals to higher orbitals sequentially, until to an orbital which is named as highest occupied molecule orbital (HOMO) the occupation is completed. The HOMO and the lowest unoccupied molecule orbital (LUMO) are the two most important orbitals for any reaction (physical or chemical reaction), while other orbitals are less important and can be ignored usually. The HOMO and LUMO are the frontier orbitals of molecules.

2.3.1   Orbitals of a Molecule Formed with Two Atoms with 1s Valence Electrons

The simplest example is hydrogen molecule formed with two hydrogen atoms. The ground state of a hydrogen atom (1s orbital) is described with wave function $\varphi_{1s} \sim e^{-r/a}$, where r is the length of radial vector and a is Bohr radius. When two atoms are brought together to form a molecule, the wave function of molecule ψ is formed by linear combinations of the two φ_{1s} from the two atoms. Two molecule orbitals (ψ_1, ψ_2) are formed through linear combinations of the two atomic orbitals (φ_1, φ_2) of the two atoms: $\psi_1 \sim \varphi_1 + \varphi_2$ and $\psi_2 \sim \varphi_1 - \varphi_2$. The ψ_1 and ψ_2 are called bonding and anti-bonding orbitals (Figs. 2.4 and 2.5). In the case of bonding, the density of negatively charged electrons between the two positively charged nuclei is high which attracts the two atoms. In contrast, in the anti-bonding state, the electron density between the two nuclei is low and the two atoms repel each other. The bonding state is a lower-energy state which is occupied by the two electrons with anti-parallel spin configuration. The number of bonds that link the two atoms can be calculated by:

Bond number $N = 0.5 \times$ (number of electrons in bonding orbitals—number of electrons in anti-bonding orbitals). For hydrogen molecule as shown in Fig. 2.5a, the bond number $N = 0.5 \times (2-0) = 1$. If we bring two helium atoms together, a very similar molecule orbitals will form because the expected involvement of 1s orbitals (Fig. 2.5b). However, each helium atom has two electrons in the 1s orbital, and the total 4 electrons will fully occupy the bonding and anti-bonding orbitals. In this case, the bond number $N = 0.5 \times (2-2) = 0$ which means that diatomic molecule of helium (He_2) cannot form.
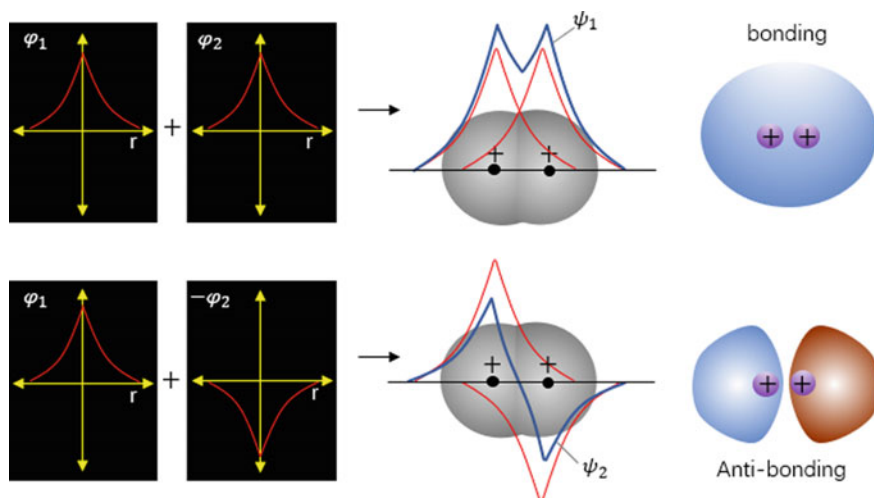
Fig. 2.4 Schematic illustration of the formation of hydrogen molecular orbitals by linear combinations of 1s orbitals from two hydrogen atoms
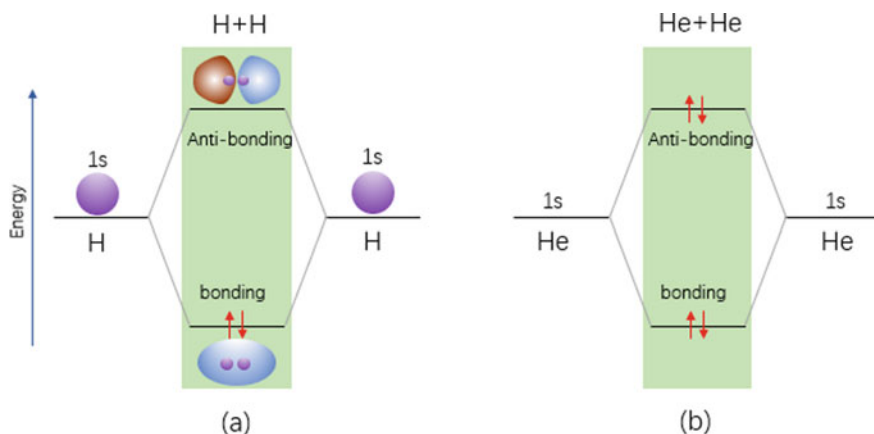
Fig. 2.5 Schematic illustration of molecular orbital formation for hydrogen (**a**) and helium (**b**), and the electron occupation of the orbitals

2.3.2 Orbitals of Molecule Formed with Two Atoms with p Valence Electrons

For a molecule formed with atoms A and B from second periodic elements in the periodic table, we assume that only top shell electrons (i.e., 2s and 2p valence electrons) involve the formation of chemical bonds. The valence electrons of the elements A and B are from atomic orbitals 2s, $2p_x$, $2p_y$, $2p_z$ (Fig. 2.6).

Fig. 2.6 Schematic
representation of compound
AB formed with atoms A
and B from second periodic
elements
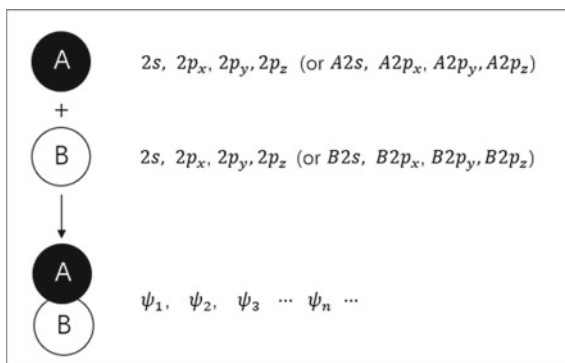
The molecule orbitals (ψ_1, ψ_2, ψ_3 ⋯) of the compound AB are formed through linear combinations of the atomic orbitals of the A and B.

$$\psi_i = c_1 A2s + c_2 A2p_x + c_3 A2p_y + c_4 A2p_z + c_5 B2s + c_6 B2p_x$$
$$+ c_7 B2p_y + c_8 B2p_z \qquad (2.15)$$

where $c_1, c_2, c_3 \cdots c_8$ are constants, and 8 molecular orbitals $\psi_i (i = 1, 2, \cdots, 8)$ can be defined, i.e., the number of formed molecule orbitals equals to the total number of atomic orbitals involved. Figure 2.7 shows schematic illustration of the obtained molecule orbitals. There are four bonding orbitals (σ_{2s}, σ_{2p}, and two degenerate π_{2p}) and four anti-bonding orbitals (σ_{2s}^*, σ_{2p}^*, and two degenerate π_{2p}^*) formed through overlapping of atomic orbitals of 2s and 2p from the two atoms. The σ-bond is formed by head to head overlap of two orbitals from the two atoms, and the π-bond is formed by side by side overlap of two p-orbitals of the two atoms. The molecule orbitals of σ_{2s} and σ_{2s}^* are similar to the case shown in Fig. 2.5. Other molecule orbitals are formed through p-orbitals of the two atoms as shown in Fig. 2.8. For organic semiconductors, the role of π and π^* orbitals is more significant.

The relative energy levels of the molecular orbitals shown in Fig. 2.7 are modified depending on the elements in the periodic table. Figure 2.9 shows the orbitals of diatomic systems consisting of the same kind of atoms (A_2) from second periodic elements. Quantum calculations showed that for O_2 and F_2 the sequence of energy levels remains as Fig. 2.7 (redrawn in Fig. 2.9b), while for the B_2, C_2, N_2 the energy levels of σ_{2p} and π_{2p} are interchanged (Fig. 2.9a). This is caused by the intermixing of σ_{2s}^* and σ_{2p} orbitals. At the center region of σ_{2s}^* orbital (see anti-bonding orbital in Fig. 2.5a), the density of electrons is low which will reduce the electron density at the center of σ_{2p} orbital and lifts its energy to the level higher than the energy of π_{2p}.

Using molecular orbitals shown in Fig. 2.9, some properties of simple diatomic molecules can be discussed, for instance, diatomic oxygen and nitrogen molecules. The electronic structure of oxygen atom is O:1s(2)2s(2)2p(4) from which 6 electrons

Fig. 2.7 Schematic illustration of molecular orbitals of compound AB formed from second periodic elements A and B
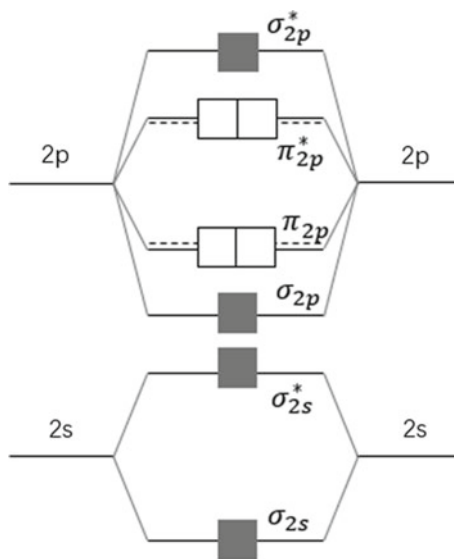
from shell-2 will participate to form molecule orbitals. For a diatomic molecule (O_2), there are 12 electrons occupy the molecular orbitals in sequence from low energy to high energy levels as shown in Fig. 2.10a. The last two electrons occupy the two degenerate orbitals with the same spin orientation (Hund's rule). Then, bond number is $0.5 \times (8–4) = 2$ which is the case for the existing oxygen molecules. The two unpaired spins indicate that the oxygen molecules are paramagnetic and this agrees with experiments [1]. For the nitrogen, the top shell electrons in an atom are 2s(2)2p(3), and there are 10 electrons occupy the molecule orbitals as shown in Fig. 2.10b. The number of bonds is $0.5 \times (8–2) = 3$ which is in line with the actual situation. All electrons are paired without net spin which indicate the N_2 is non-magnetic.

2.3.3 Orbitals of Ethene Molecule ($CH_2=CH_2$)

For the ethene molecule, each carbon has four valence orbitals $2s2p_x2p_y2p_z$, and each hydrogen has one valence orbital 2s. Thus, the ethene molecule will have 12 molecule orbitals formed. The number of valence electrons from the 6 atoms is 12 (4 from each carbon atom and 1 from each hydrogen atom), and they occupy the molecule orbitals in sequence from low energy to high energy levels as shown in Fig. 2.11. Six orbitals with lower energy are fully occupied with paired 12 electrons. The HOMO and LUMO are the π and π^* orbitals formed with p-orbitals of carbons in parallel and anti-parallel configurations. The charge conduction of the π/π^* orbitals and interorbital transitions are important for conjugated molecules.
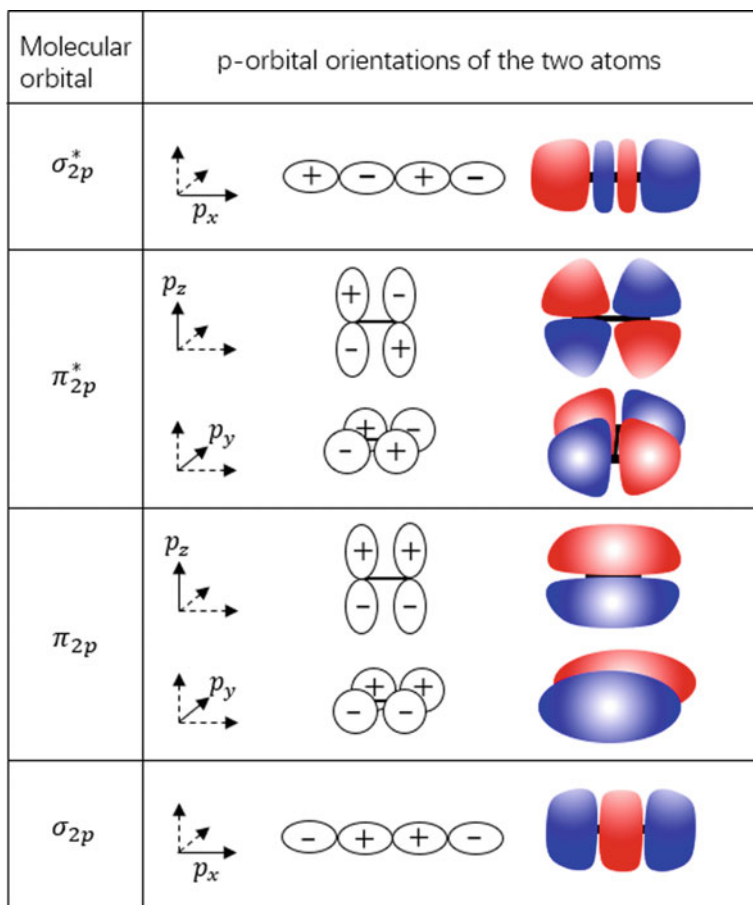
Fig. 2.8 Schematic illustration of several molecule orbitals of compound AB formed from second periodic elements A and B

2.4 Optical Transitions in Organic Materials

2.4.1 Jablonski Energy Diagram

When a photon is absorbed by a molecule, the molecule is in its excited state with higher energy. The photon absorption generates an electron–hole pair (exciton) and the absorption process is efficient when the photon's energy is close to (or large than) the gap between the HOMO and LUMO. The concept of exciton plays important role in the material and device physics of organic electronics. There are two types of excitons: singlet excitons and triplet excitons. A singlet exciton is formed by electron–hole pair with anti-parallel spins, whereas the triplet exciton comprises an
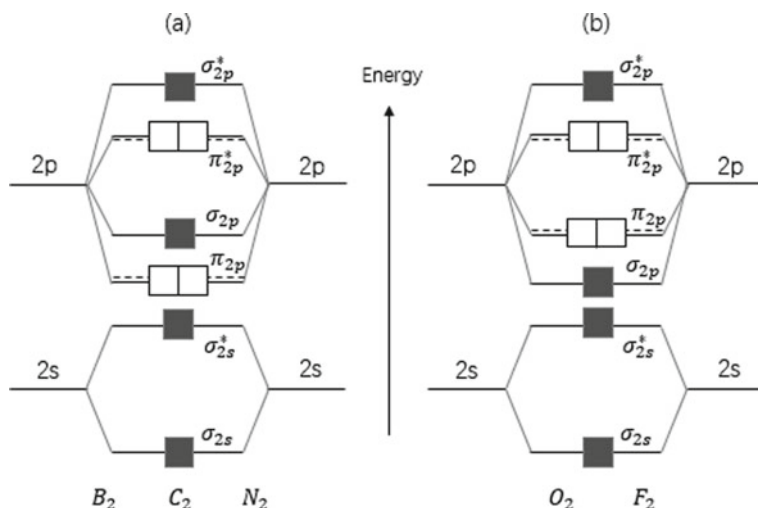
Fig. 2.9 Schematic illustration of orbital energy levels of diatomic systems consisting of the same kind of atoms from the second periodic elements. **a** For B_2, C_2, N_2 and **b** for O_2, F_2
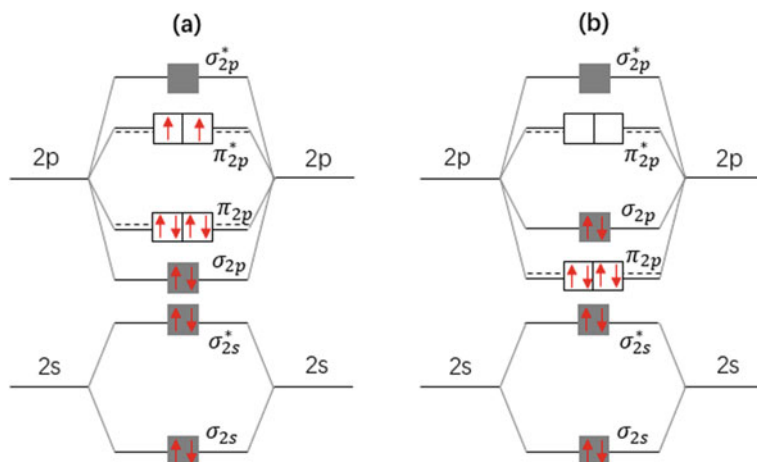
Fig. 2.10 Schematic illustration of energy levels of oxygen (**a**) and nitrogen (**b**) molecule orbitals

electron–hole pair with the spins pointing in the same orientation. In the process of molecular excitation, the motion of electrons can be described separately from the motion of nuclei as the nucleus of an atom is much heavier than an electron [2, 3]. This allows us to determine energy levels of a molecule by calculating the energy of the electrons with freezing atomic positions in the molecule. A molecule, in its ground state and in its excited state, has different equilibrium arrangement of atoms.
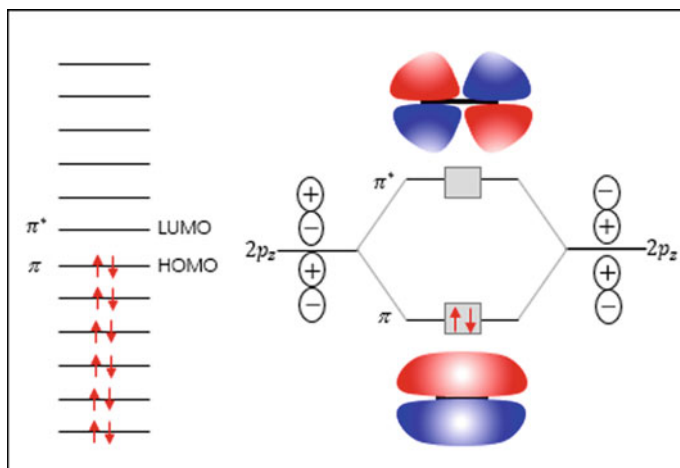
Fig. 2.11 Schematic illustration of energy levels of ethene molecule and its HOMO/LUMO orbitals

Therefore, the curve of the molecular energy potential as function of the molecule configuration can be plotted as Fig. 2.12.

When a photon is absorbed, a transition from the ground state to an excited state occurs, as indicated by a vertical line linking the two states. The excitation causes a modification of geometric form of the molecule. This geometric change of molecule is indicated by a change in the atomic coordinates during the S_0 to S_1 transition.

The transition between the vibrational levels at different states (S_0, S_1 ...) is governed by Franck–Condon principle, which indicates that electron transition is sufficiently quick to take place with no alteration of the nuclear coordinate associated with the positions of the atoms. The probability that the molecule is found at a particular vibrational level is proportional to the square of the overlap between the vibrational wave functions of the initial and final states [4–6]. The different energy levels and energy transitions resulting from absorption of a photon by an organic

Fig. 2.12 Energy curves of molecule potentials for the ground state S_0 and the excited state S_1. The position shift of the curve for excited state is caused by excitation-induced atomic position change
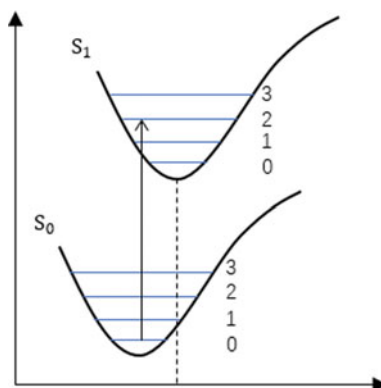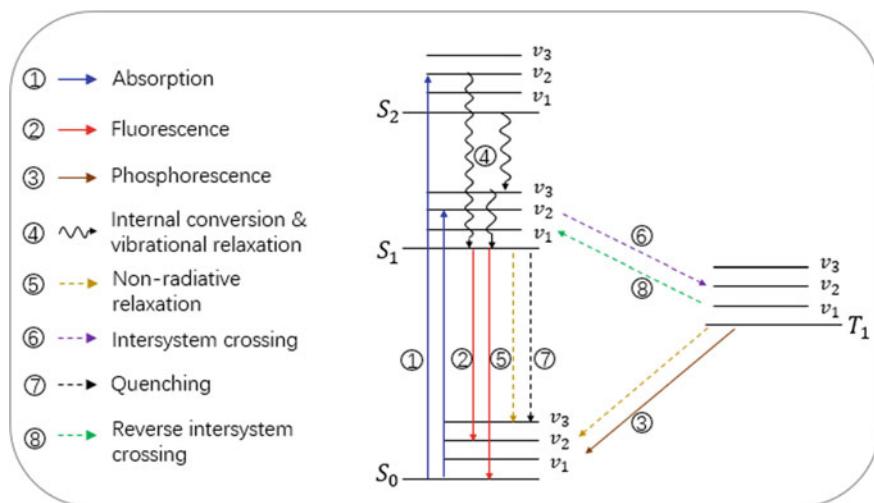
Fig. 2.13 Jablonski energy diagram

molecule are visually displayed with Jablonski energy diagram (Fig. 2.13) [7]. In this diagram, the states are represented vertically with energy levels, and grouped horizontally with their multiplicity, like singlet and triplet. A triplet state has lower energy than the corresponding singlet state owing to the exchange interaction [8].

The thin horizontal lines represent the vibrational states. The radiative transition is represented by a straight arrow and non-radiative transition by a wavy arrow. Molecule at ground state (V_0 of S_0) is excited to an excited state by absorption of a photon. Such an excited state can release its energy by different decay mechanisms. The molecule can decay trough radiative transition to different vibration levels of the ground state. If the decay process is directly from singlet state (like S_1) to ground state, the obtained emission spectrum is called fluorescence. The spectrum appears in the form of radiation bands because the excited molecule can return to whatever vibrational levels of the state S_0. The lifetime of the singlet state S_1 is very short, in the order of 10^{-9} to 10^{-7} s. If the excited singlet state can evolve, becoming a triplet state in a non-radiative way, the process is called intersystem cross (ISC). If the photoemission occurs between two states of different multiplicity (e.g., from triplet to S_0), the process is called phosphorescence whose lifetime is much longer than fluorescence, with the order of 10^{-3} to 10^2 s. The transition from the triplet to the ground state is generally a non-radiative relaxation because of its long lifetime and the possible interaction with other molecules around. A molecule can be excited to a state higher than the first excited state (S_1) which is termed as second excited state, third excited state… in turn. When a molecule decays from a higher excited state to a lower excited state, the energy is normally converted into heat. This process occurs in a very short time (10^{-14} to 10^{-11} s) and is called internal conversion (IC). In addition, it is possible to have vibrational relaxations in an excited state from higher vibrational level (V_n) to the lowest vibrational level (V_0). This process is very quick

($<10^{-12}$ s) and non-radiative. Another non-radiative process is called "quenching": relaxation occurred following the collision between an excited molecule and another molecule. The quenching is one of the main reasons of decreasing fluorescence in organic materials.

2.4.2 Stokes Shift

An organic molecule can be excited to different vibration energy levels in the excited state by absorbing photons with different energies (Fig. 2.14). This is seen from a series of equally spaced peaks in absorption spectra of molecules. Following absorption of a photon the excited molecule first relaxes to the lowest vibration level of the excited state by non-radiative process. The molecule then returns to the ground state either by the light emission or by internal or external conversion (collision with other molecules). The molecule relaxes from the lowest vibrational level in the excited state to various vibration levels in the ground state which is clearly indicated by the multiple peaks in the fluorescence spectra [9]. The emission wavelength depends on the vibration levels of the ground state that the molecule relaxes into. This explains why the fluorescence spectrum of an organic material is symmetric to its absorption spectrum and is shifted toward red. The shift of an emission spectrum relative to the absorption spectrum is called Stokes shift.

2.5 Energy Transfer

An excited molecule (termed as donor D^*) can pass its excitation energy to a neighboring molecule (termed as acceptor A) in a non-radiative fashion by coupling
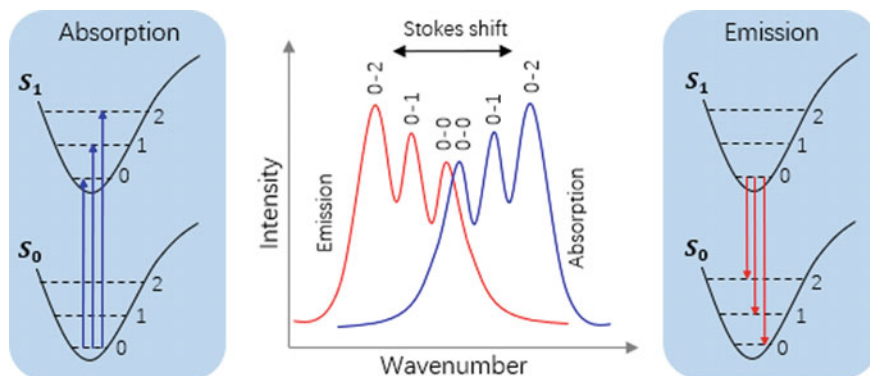
Fig. 2.14 Schematic illustration of the relation between absorption and fluorescence in organic semiconductor materials

between electron orbitals of the two molecules. The phenomenon is known as resonance energy transfer and can be described with following formula:

$$D^* + A \rightarrow D + A^*$$
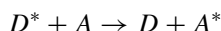
This phenomenon has been used to improve light emission property of OLED device through a host–guest systems [10, 11]. In such system, excitation can be transferred from a host molecule (matrix material) to a guest molecule (doping agent). Such energy transfer may take place by different mechanisms: Förster long-range resonant energy transfer or short-range Dexter energy transfer.

2.5.1   Förster Transfer

The Förster mechanism is a non-radiative resonant dipole–dipole transition between a molecule with singlet excited state and a molecule of ground state. The Förster resonance energy transfer mechanism (also known as fluorescence resonance energy transfer, FRET) is illustrated in Fig. 2.15, where an excited donor molecule (D^*) transfers its energy to a neighboring acceptor (A).

Förster transfer is described with Fermi's golden rule, where the transfer rate Γ_{mn} from a donor state m to an acceptor state n is written as:

$$\Gamma_{mn} = \frac{2\pi}{\hbar}|V_{mn}|^2\delta(E_n - E_m)$$

where V_{mn} is the transfer matrix between the two states m and n, with energy levels E_m and E_n, respectively. The Dirac δ-function indicates that the energy of the two states need to be balanced for the transfer to take place. Thus, a spectral overlap between the emission spectrum of the donor and the absorption spectrum of the acceptor is needed for the Förster transfer. The transfer rate from donor to acceptor molecule can be expressed as:

$$\Gamma_{da} \sim \frac{1}{\tau_d}\left(\frac{r_0}{r}\right)^6$$
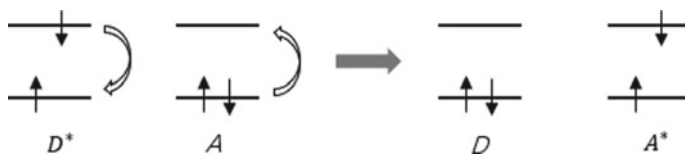
Fig. 2.15   Diagram of the Förster transfer

where r is the distance between the donor and the acceptor, τ_d is the lifetime of the excited state of the donor, and r_0 is the Förster radius. The transfer rate decrease as a function of r^{-6}, and the transfer happens in a distance range of 10 nm [12].

2.5.2   Dexter Transfer

Another energy transfer mechanism is Dexter mechanism. For the Dexter transfer, the exciton diffuses from the excited donor to a ground-state acceptor through which the acceptor became excited. In this process, a direct charge transfer between the donor and acceptor occurs as illustrated in Fig. 2.16. An electron is transferred from the LUMO of the donor to the LUMO of the acceptor, while an electron in HOMO of the acceptor is transferred to the HOMO of the donor. This mechanism can also be applied to the transfer of triplet excitons. The Dexter transfer rate is proportional to e^{-2r}, where r is the distance between the donor and acceptor [13]. The exponential function dependence makes the Dexter mechanism takes place at very short range, i.e., ~2 nm.

2.6   Excitons and Exciton Dynamics

An exciton is electron–hole pair held together by their mutual Coulomb interaction. There are two types of excitons in semiconductor materials: Frenkel exciton and Wannier exciton. When the electron–hole pair is strongly coupled together (the bonding energy is ~1 eV), the exciton is called Frenkel exciton. The excitons in organic semiconductor belong to this type as the Coulomb force is inversely proportional to the dielectric constant of the medium in which the electron and hole are located. The distance between the electron and hole is in the range of 1 nm. In contrast, the excitons in inorganic semiconductors belong Wannier type where the electron–hole binding energy is on the order of 10 meV and the electron–hole distance can be as large as ~10 nm. The large binding energy of the excitons in organic semiconductors has great impact on the design of devices, for instance, delicate exciton separation strategy is required in organic solar cell preparation.

Fig. 2.16   Diagram of Dexter transfer

Understanding of exciton dynamics in organic semiconductor materials/devices, like exciton quenching, fusion, fission/splitting, etc. is important for both research and development.

2.6.1 Singlet–Singlet Interaction

The interaction between two singlet excitons (S_1) can cause exciton annihilation which has two main processes:

(a) To generate hot exciton and ground-state molecule

$$S_1 + S_1 \rightarrow S_1^* + S_0 \rightarrow S_1 + S_0 + \text{Phonon}$$

(b) Autoionization
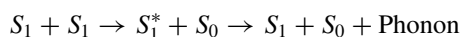
$$S_1 + S_1 \rightarrow e + \text{cationic radical} + S_0$$
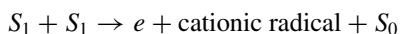
where S_1^* is singlet exciton at high vibration level (hot exciton). The cationic radical is also called autoionization state which is highly unstable.

2.6.2 Triplet–Triplet Interaction

Since the lifetime of triplet is much longer than the singlet lifetime, the collision between triplets is an important annihilation process in organic materials. A representative process is triplet fusion where two triplet excitons with low energy combine and form one exciton with high energy as illustrated in Fig. 2.17 [14]. The fusion may undergo through different mechanism: with and without photoemission.

(a) $T_1 + T_1 \rightarrow +S_1^* + S_0 \rightarrow S_1 + S_0 + \text{Phonon}$
(b) $T_1 + T_1 \rightarrow T_2 \left(\text{or } T_1^* \right) + S_0 \rightarrow T_1 + S_0 + \text{Phonon}.$

Fig. 2.17 Schematic illustration of triplet fusion process
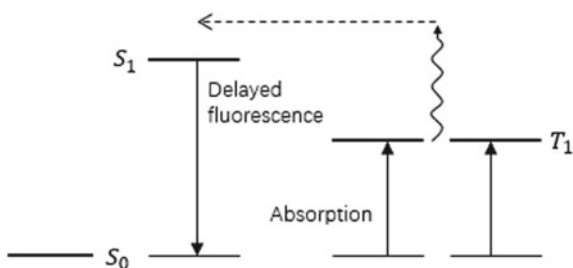
The fusion may result S_1, even higher excited singlet or triplet state. Then, the molecule relaxes to S_1 or T_1 and decays further with the inherent mechanism with the state, illumination, or heat releasing. The fusion generated fluorescence has very long apparent lifetime, i.e., delayered fluorescence, which includes the time spending on transition from triplet to singlet and singlet fluorescence. The lifetime of fluorescence is 10^{-9} to 10^{-7} s, and the lifetime of delayed fluorescence is in the scale of millisecond.

2.6.3   Singlet–Triplet Interaction

When a singlet is annihilated by a triplet, a triplet state with higher energy or photocharge can be generated.

(a) $S_1 + T_1 \rightarrow T_1^* + S_0$ or $T_2 + S_0$
(b) $S_1 + T_1 \rightarrow e + \text{cationic radical} + S_0$

2.6.4   Singlet Fission

When a singlet collides with a molecule of ground state, two triplets can be generated:

$$S_1 + S_0 \rightarrow T_1 + T_1$$
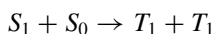
This is an inverse process of the triple fusion as shown in Fig. 2.18. If the energy of singlet is slightly less than the twice of the triplet energy, the fission requires additional thermal energy $\Delta E \geq (2E_{T1} - E_{S1})$, and the fission process is written as $S_1 + S_0 + \Delta E \rightarrow T_1 + T_1$. For example, the singlet fission process can occur in tetracene material [15], where the energy of first singlet (2.4 eV) is slightly lower than the twice of the energy of the first triplet (1.28 eV). With the assistance of thermal energy, one singlet can convert to two triplets. There is a competition between singlet fission and direct decay through fluorescence which reduces the efficiency of the fluorescence emission. The singlet fission produced triplets can decay through non-radiative emission or phosphorescence emission.

2.6.5   The Interaction Between Excitons and Traps

There are randomly distributed traps which can capture excitons in organic materials.

(a)   Interaction between singlets and traps

$$S_1 + \text{trap} \rightarrow S_{1t} + S_0 + \text{Phonon}$$
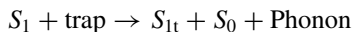
Fig. 2.18 Schematic illustration of singlet fission, where ΔE is the required additional thermal energy for the process
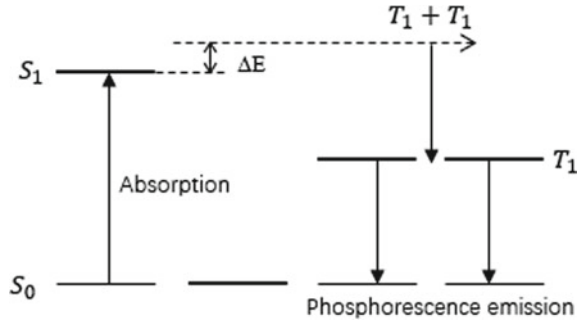
S_{1t} is the trapped singlet, and it can return back to ground state through radiative or non-radiative decay.

(b) Fission of the trapped singlet (S_{1t})

$$S_{1t} + S_0 \rightarrow T_1 + T_{1t}$$
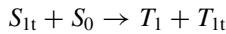
T_{1t} is trapped triplet.

(c) Interaction between a triplet and trapped triplet (T_{1t})

$$T_1 + T_{1t} \rightarrow S_{1t}^* + S_0 \text{ or } T_{1t}^* + S_0$$
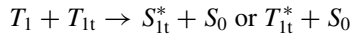
The $T_1 - T_{1t}$ interaction may produce a hot trapped singlet S_{1t}^* or hot trapped triplet T_{1t}^*.

2.6.6 Interaction Between Excitons and Charges

The interaction between excitons (singlet, triplet) and charges (electron (e), hole (h)) may lead to the following results:

(a) $S_1 + e/h \rightarrow S_0^* (\text{or } T_0^*) + e/h$
(b) $S_1 + e_t/h_t \rightarrow S_0^* (\text{or } T_1^*) + e/h$
(c) $T_1 + e/h \rightarrow S_0^* + e/h$
(d) $T_1 + e_t/h_t \rightarrow S_0^* + e/h$.

The processes (b) & (d) indicate that exciton can de-trap the trapped electron (e_t) or hole (h_t). Thus, the process can increase photocurrent of organic materials. The interaction between the excitons and charge carriers can lead a reduction of fluorescence intensity and lifetime of excitons. All processes are resulted from energy transfer from excitons to charges.

2.6.7   The Interaction Between Excitons and Surfaces/Interfaces

(a) Electron of an exciton can migrate to surface traps and a free hole is generated in the semiconductor consequently. For instance, the oxygen molecules adsorbed on the surfaces of materials can act as traps of electrons.
(b) Heterojunction formed by donor and acceptor can separate excitons to free electrons and holes (see the solar cell chapter).
(c) At interface between metal electrode and semiconductor the metal can strongly influence on the electronic states of the molecules. The position of energy levels are modified by the electrode and the energy of certain excitons is modified accordingly. The metal electrodes also have an impact on the lifetime of excitons at the metal/semiconductor interface.

2.6.8   Interaction Between Excitons and Photons

The interaction of photons with excitons can induce photoionization:

$$S_1 + h\gamma \rightarrow S_0^+ + e$$

$$T_1 + h\gamma \rightarrow S_0^+ + e$$
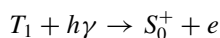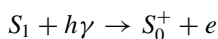
It is known that the exciton–exciton interaction is an important mechanism for charge generation. When the light intensity is high, the exciton–photon interaction mechanism can compete with the exciton–exciton colliding for charge generation.

2.7   The Photophysical Properties of Organotransition Metal Compounds (OTMC)

Perceptually speaking, spin–orbit coupling (SOC) is the interaction between the spin of an electron and the electrical movement in an orbital around the nucleus of atom. When an electron travels along its orbital around the nucleus, the nucleus is moving around electron equivalently if we take the electron as the reference. As the nucleus carries charge, it generates a magnetic field H. The strength of the magnetic field is proportional to orbital angular momentum $\mathbf{L}$, i.e., $\mathbf{H} = c\,\mathbf{L}$ (c is a constant). In the sense of classical physics, if an electron with magnetic moment $\boldsymbol{\mu}_s$ is placed in a magnetic field $\mathbf{H}$, the interaction between the magnetic moment and the magnetic field will induce an energy change $\Delta E = -\boldsymbol{\mu}_s \cdot \mathbf{H}$. Thus, the SOC will induce a change of electrical energy levels in a molecule. Meanwhile, the SOC can induce a change of selection rule of molecule radiation.

For OTMC molecules, like Ir(ppy)₃, Pt(thpy)₂, [Ru(bpy)₃]²⁺, [Os(bpy)₃]²⁺ etc., a number of excitations between various molecular orbitals (MO) contribute to their optical properties. Such excitations include:

- Ligand-centered (LC) excitation, i.e., π–π* transition in the ligands of the OTMC.
- Metal-centered (MC) excitation, i.e., d–d* transition in the metal atom of the OTMC.
- Metal-to-ligand charge transfer (MLCT), i.e., d–π* excitation between the d-orbital of the transition metal atom and the LUMO of the ligand.

Figure 2.19a illustrates a simplified energy diagram of OTMC and possible energy transitions. The main transitions are π–π* transition in ligand (LC) and the transition between metal and ligand (MLCT). As d*-orbital is located at high energy, the d–d* excitation normally does not happen. Figure 2.19b shows the transition energy levels which include singlet/triplet excitation of MLCT (^{1,3}d–π*), and singlet/triplet excitation of LC ($^{1,3}\pi$–π*). Each triplet contains three states and there are eight states depicted. All these states can experience substantial quantum mechanical mixing due to configuration interaction (CI) and spin–orbit coupling (SOC). The SOC effect induces a zero-field splitting (ZFS) of the triplet. After such quantum mechanical mixing, the states, like ^{1,3}LC and ^{1,3}MLCT, cannot be understood as "pure" singlets or triplets. Such electron–electron interaction caused by excited state population can induce a splitting between the singlet and triplet energy levels $\Delta E(S–T)$ (originated from exchange effect). The $\Delta E(S–T)$ value is about twice of the exchange integral [16].

$$K = \mathrm{const} \left[\pi(r_1)\pi^*(r_2) \left| \frac{1}{r_{12}} \right| \pi(r_2)\pi^*(r_1) \right]$$

where π and π* are the wave functions of HOMO and LUMO, r_1 and r_2 represent the coordinates of the electrons, and r_{12} is the separation between the two electrons. The exchange interaction takes the spin correlation into account. The two electrons with opposite spin orientations (singlet) have a large chance of being found with short distance, while the electrons with same spin orientations have the tendency to avoid each other. Thus, the triplet has a lower energy than the singlet. A small admixture of metal d-orbital or MLCT character to the LC state will increase the spatial extension of the wave functions and reduce the exchange integral, i.e., singlet–triplet splitting between the perturbed ^{1}LC($\pi\pi$*) and ^{3}LC ($\pi\pi$*) states will change.

There are two typical types of ligand coordination with the metal ions in the OTMC. One is octahedral coordination with Oh symmetry, where the crystal field generated by the ligands splits the five d-orbitals into two groups, i.e., the higher energy e_g and lower energy t_{2g} (Fig. 2.20a). Another type is the square-planar coordination and the arrangement of its d-orbital energies is more complicated (Fig. 2.20b). Figure 2.21 illustrates the simplified models of orbital levels for the two types of coordination which show a dramatical difference of photophysical properties. For the octahedral coordination it contains $^3\pi\pi$* excitation of ligand, transitions between
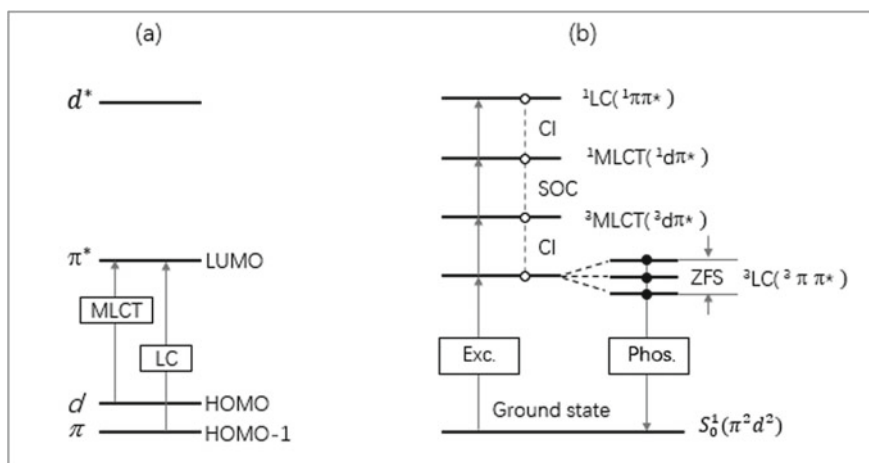
Fig. 2.19 **a** MO model for a compound with single π, d, and π* orbitals and the respective MLCT and LC transitions. It is assumed that the d*-orbital is located at a significantly higher energy and it does not lead to low-lying energy transition; **b** eight energy states obtained from the MLCT and LC transitions, i.e., two singlets: ^{1}LC and ^{1}MLCT, and three substates for both ^{3}LC and ^{3}MLCT. The states experience a substantial quantum mechanical mixings due to CI and SOC as indicated by the vertical dashed line. The SOC induces the zero-field splitting (ZFS) of triplets. After these quantum mechanical mixings, the meaning of singlet/triplet of the LC and MLCT can no longer be regarded as conventional classifications

d-orbitals (d_1, d_2) of t_{2g} and π* orbital ($^1d_2\pi^*$ and $^3d_1\pi^*$). The OTMC with square-planar coordination contains transitions between d-orbitals with higher-energy and π* orbital ($^1 d_{z^2} \pi^*$ and $^3 d_{z^2} \pi^*$), and transition between d-orbitals with lower-energy and π* orbital $\left[^{1,3}(d_{xz}d_{yz})\pi^*\right]$.

The transitions between different orbitals brings different SOC effect and ZFS. For the octahedral coordination both SOC and ZFS are large, thereby the decay time from the lowest triplet (T_1) to ground state (S_0) is shorter than the case of square-planar coordination. This indicates that the molecules with octahedral coordination are more suitable for OLED applications. Form Fig. 2.19 one can see that the triplet can split to 3 substates which is important for OTMC applications. The ZFS of the triplet $^3\pi\pi^*$ is mainly induced by spin–spin interaction of the two unpaired electrons. Such interaction-induced ZFS value of the ^{3}LC is around ~10^{-5} eV. Although the ZFS value of ^{3}LC in an OTMC is hard to be effected by small external disturbance (similar to pure ligand molecules), the existence of transition metal atom can dramatically increase the radiative (or non-radiative) decay rate owing to the SOC. For instance, it can increase the value of ISC to ~100%. For ^{3}LC emission compounds, like Pd(thpy)$_2$ and Pt(qol)$_2$, the transition time of ISC (τ_{isc}) can reach 800 fs and 500 fs, respectively [16, 17]. The T_1–S_0 radiative decay rate is faster for several orders of magnitude than the "pure" organic molecules, i.e., the radiative decay can surpass non-radiative decay process and high quantum yield is achieved.
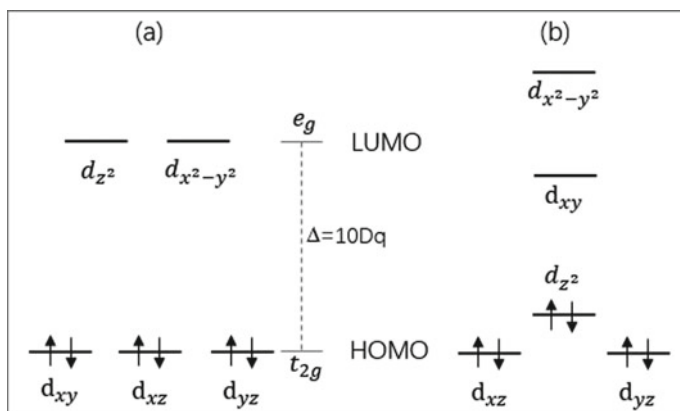
Fig. 2.20 Schematic illustration of the d-orbital energy levels for OTMC with octahedral (**a**) and square-planar (**b**) coordination. In the case of octahedral OTMC, three low degenerate orbitals are occupied by 6 electrons, while in the case of square-planar coordination, the three occupied orbitals are non-degenerate
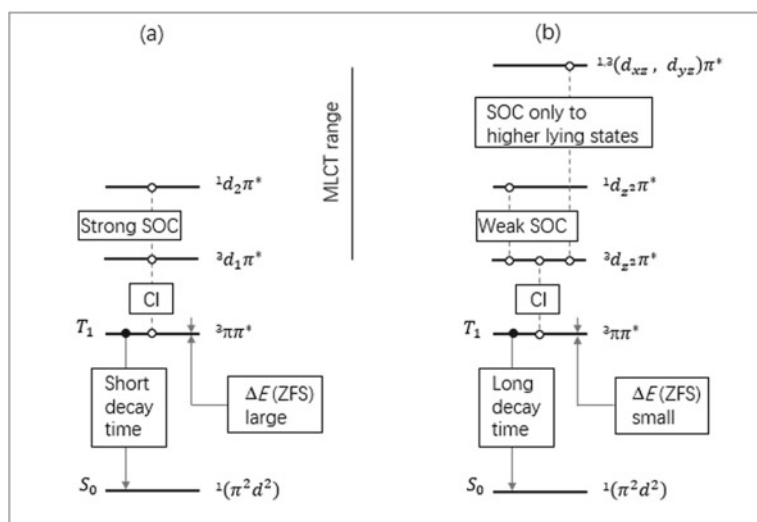
Fig. 2.21 Simplified models of energy states for the OTMC with octahedral (**a**) and the square-planar (**b**) coordination

ZFS also exists for the lowest excited triplet with MLCT transition, and its value can be used as an important measure to evaluate the quality of luminescence materials. For OLED application the ZFS value should be larger than 1.2×10^{-3} eV. The luminescence from lowest triplet of OTMC depends on the characteristics and allowness of the transition between substates of T1 and ground state S_0. The allowness of the transition is mainly controlled by the involvement of the higher excited

[1]MLCT singlet. The probability of transition from substates of the triplet (I, II, III) to ground state are different. Even a small amount of singlet is mixed into the [3]LC can induce a drastic enhancement of radiative transition. For Pt(thpy)$_2$ compound, because a relatively large proportion of mixing MLCT into the lowest [3]LC state, the decay time of the Pt(thpy)$_2$ is 6–7 orders of magnitude smaller than the pure organic compounds, and the radiative lifetime is shorten to ~1 μs [18].

For quantitative understanding of photophysics of the OMTC theoretical calculations are required, for instance, time-dependent density functional theory (TDDFT) [19, 20] or CASSCF/CASPT2 calculation [21] etc. can be used.

2.8   Photochemical Reaction

In photochemistry, the chemical reaction occurs through photoexcitation where the reactant molecules are excited to excited states by absorbing photoenergy. The energy absorbed to excite a molecule from its ground state to an excited state can be much higher than the energy required for thermochemical reaction sometimes. Therefore, organic photochemical synthesis can complete tasks that are difficult in thermochemical reaction. The bond energy of organic compounds is normally around 200–500 kJ.mol^{-1}. When photons with wavelength 239–600 nm are absorbed, they can break chemical bonds and cause chemical reactions to proceed.

2.8.1   Types of Excitations

At ground state of a molecule the valence electrons normally occupy in σ-orbitals, π-orbitals, and non-bonding orbitals (n). When the molecule is excited an electron is promoted into the lowest unoccupied molecular orbital (LUMO), although promotion to higher orbitals is also possible. There are four types of electronic excitations are possible as shown in Fig. 2.22.

Fig. 2.22 Possible orbitals and transitions in organic photochemistry
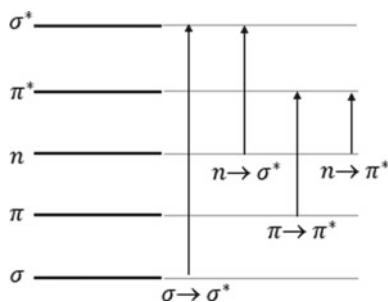
σ → σ*: Molecules, like alkanes etc., have no n or π electrons, can be excited through this way.

n → σ*: Alcohols, amines, ethers, etc. can be excited in this manner (n: orbital of lone pair electrons).

π → π *: Applicable for alkenes, aldehydes, carboxylic esters, etc.

n → π *: Applicable for aldehydes, ketones, carboxylic esters, etc.

2.8.2 Sensitization and Quenching in Photochemical Reaction

For molecules (M), there is no reaction occur (or low reaction quantum yield) under illumination with light of wavelength λ. If the reaction can happen (or reaction quantum yield increases) with introduction of another type of molecules (S), we call the introduced material sensitizer and this effect is called sensitization. There are two important sensitization mechanisms: Photoreaction is processed through (i) production of free radicals and (ii) through energy transfer. In the first case, the sensitizer absorbs light and forms free radical. After reaction with the reactant molecules (M), the free radical becomes sensitizer again. The resulted product is the same as that produced from direct irradiating the reactant molecules with light. The sensitization via energy transfer is a physical process where the sensitizer is excited by light absorption S^*. The excited sensitizer passes the energy to reactant molecule to excite the molecule M^* and the sensitizer comes back to ground state. The process is expressed as:

$$S \xrightarrow{h\gamma} S^*$$

$$S^* + M \rightarrow S + M^*$$

$$M^* \rightarrow P\,(\text{product})$$
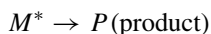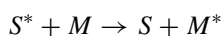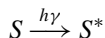
There are two energy transfer mechanisms with the reaction: triplet–triplet energy transfer and singlet–singlet energy transfer. The former is photoexciting the sensitizer to triplet excited state, and subsequently the triplet excitation is transferred to the reactant. The latter is photoexciting the sensitizer to singlet excited state, and subsequently the singlet excitation is transferred to reactant. The triplet–triplet energy transfer can be used to explain the sensitization of benzophenone to naphthalene as shown in Fig. 2.23. As the first singlet (S_1) of the benzophenone is lower than that of naphthalene, the benzophenone can be excited to S_1 with longer light wavelength. Because the ISC in the benzophenone is highly efficient, the benzophenone quickly turns to triplet (T_1). The triplet energy of benzophenone is higher than that

Fig. 2.23 Schematic illustration of triplet–triplet energy transfer, where ISC, ET, and Vr represent inter system cross, energy transfer, and vibration decay, respectively
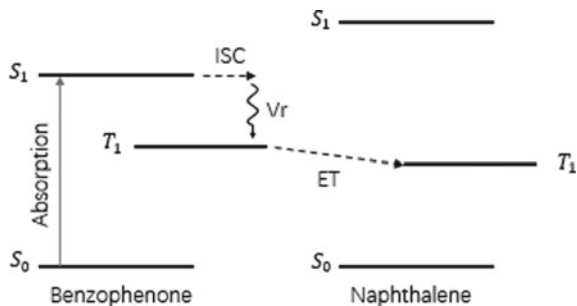
of the naphthalene, the energy is transferred immediately to naphthalene, and the naphthalene becomes triplet excited.

The quenching is an opposite process of sensitization. If a mater Q is added to reactant mater M, the Q can stop or attenuate the reaction, and then, the mater Q is called quencher. The main quenching mechanisms are oxygen-induced quenching and quenching caused by energy transfer. The oxygen can capture the free radicals and stop the progress of the reaction.

2.8.3   Several Types of Photochemical Reaction

a.   Photolysis reaction

The explosion of hydrogen-chlorine mixture under photoillumination is typical example of the photolysis. In the photoexcited chlorine molecule the σ-bond is much weaker than that of the ground-state molecule. Under photoillumination the chlorine molecule is cleaved to two free radicals. Then, the chlorine-free radical reacts with hydrogen molecule to form hydrogen chloride and hydrogen-free radical. Afterward, the hydrogen-free radical reacts with chlorine molecule to generate hydrogen chloride and chlorine-free radical again. Such a chain reaction is processed and one photon can consume 10^4 to 10^5 hydrogen or chlorine molecules.

$$Cl-Cl \xrightarrow{h\gamma} Cl \cdot + \cdot Cl$$

$$Cl \cdot + H-H \rightarrow HCl + H\cdot$$

$$H \cdot + Cl-Cl \rightarrow HCl + Cl\cdot$$
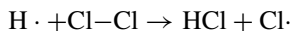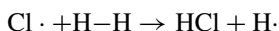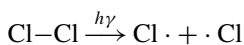
Photolysis of azo compound is another typical example, for instance

$$R-N=N-R \xrightarrow{h\gamma} R \cdot + N_2 + \cdot R$$
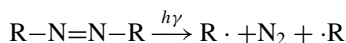
where the two adjoining bonds of the azo group are cleaved, and two free radicals and nitrogen molecule are formed.

b. **Photorearrangement**

Under photoillumination, bond cleavage happens and pair of free radicals is generated. This results a relocation of functional groups in the molecule. The photorearrangement is an intramolecule reaction process. An example is photo-Fries rearrangement of phenyl ester. Under photoillumination, an O–C bond is cleaved and form phenoxy and benzoyl radicals. Benzoyl located in the solvent "cage" is transfered to ortho position or para position. Meanwhile, the phenoxy radicals that diffused out from the solvent cage will extract hydrogen to form phenol. Photorearrangement of benzoic acid phenyl ester can be illustrated below:
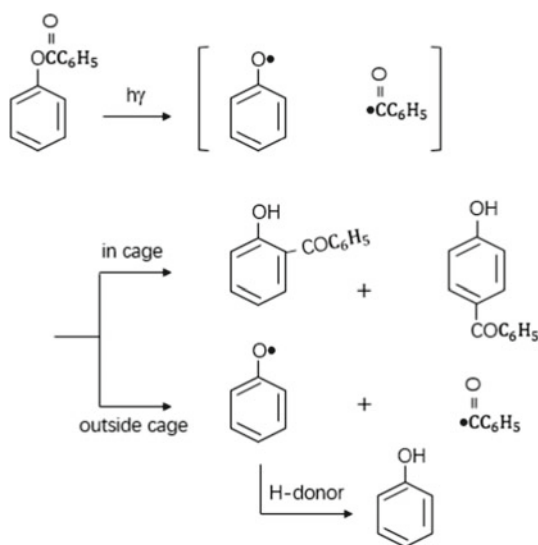
c. **Photoisomerization**

Some molecules can undergo a trans–cis or cis–trans isomerrization under photoillumination where the molecule composition does not change. It is an intramolecular reaction. The most common reaction is the trans–cis structure interchange with ethylene type molecule.
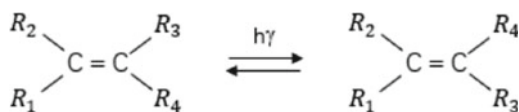
This is resulted from π-π^* transition under photoillumination. At excited state, the π-bond is broken and the remaining σ-bond is free to rotate. An isomerization can be realized as schematically represented below:
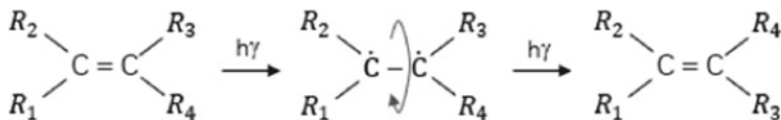
Normally, the trans-structure is thermodynamically stable, i.e., the proportion of trans-structure is larger. But, the photoisomerization can induce more cis-structure. Thus, photoillumination is an effective way to produce cis-structure. A typical example is the isomerization of stilbene. When stilbene solution in benzene is illuminated with light of 313 nm wavelength, the production contains 93% cis-stilbene and 7% trans-stilbene. This is mainly because the difference of absorption property of the trans- and cis-structures. Under illumination of 313 nm light, the absorption coeffecients are 2280 and 16,300 (L mol^{-1} cm^{-1}) for the cis- and trans-stilbene, respectively. Consequently, more trans-structure molecules will be excited and have more chance to transfer to cis-structure.

Trans-stilbene   Intermediate   Cis-stilbene
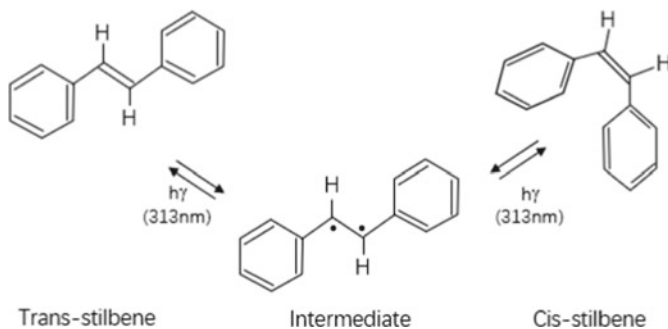
d. **Photoaddition reaction**

One mechanism of the photoaddition reaction is that first to excite molecule M to its excited state M* with light, then, the M* is added to molecule N of ground state, and the process is:

$$M + h\gamma \rightarrow M^*$$

$$M^* + N \rightarrow (MN)^* \rightarrow MN$$
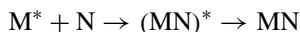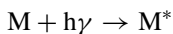
The (MN)* denotes a short-lived intermediate state. When the M and N are the same type of molecules, the (MN)* is termed as excimer. If the M and N are not the

same type of molecules, the (MN)* is known as exciplex. The final product is MN. A representative example is the addition reaction of a ketone to alkene.

Exciplex
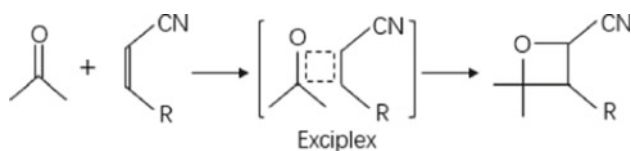
Another mechanism is that the reaction starts with photogeneration of free radicals, and addition reaction of the free radical to another molecule occurs subsequently. For instance, the photoaddition reaction of hydrogen halide (HX) to alkene.

$$H - X \xrightarrow{h\gamma} H \cdot + \cdot X$$

$$X \cdot + RCH{=}CH_2 \rightarrow R\dot{C}HCH_2X$$

$$R\dot{C}HCH_2X + H{-}X \rightarrow RCH_2CH_2X + X\cdot$$
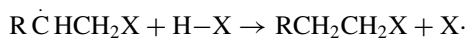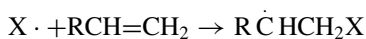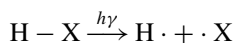
e. **Photooxidation**

Photooxidation of organic molecules is photoaddition reaction of oxygen to organic molecules. There are two mechanisms with the photooxidation: addition reaction of excited molecules M* to oxygen molecules, and addition reaction of excited oxygen molecules to molecules M of ground state.

(i) $M \xrightarrow{h\gamma} M^* \xrightarrow{O_2} MO_2$
(ii) $O_2 * + M \rightarrow MO_2$
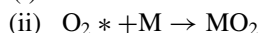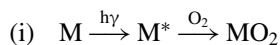
For instance, the photoexcited anthracene can be oxidized with oxygen:
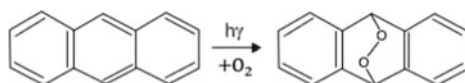
The oxygen molecule is added to the excited double bonds to form peroxide. There are many ways of photooxidations with excited oxygen molecules O_2^*, for instance, addition reaction to compounds with double bond to form hydroperoxide.
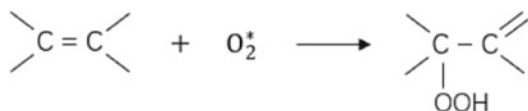
Another type of reaction is oxidative cyclization through photooxidation of double bond, such as photooxidation of butadiene.

$$CH_2{=}CH{-}CH{=}CH_2 \quad + \quad O_2^{\cdot} \quad \longrightarrow \quad$$
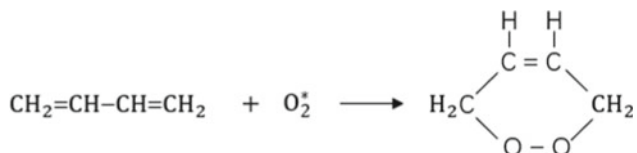
f. Photoreduction

Photoreduction is chemical reduction under the influence of radiant energy. It is an addition reaction of a hydrogen atom or an electron to a molecule. An addition reaction of hydrogen atom to a molecule is accompanied by a dehydrogenation of another molecule. Therefore, such reaction is also called hydrogen abstraction reaction. An example is the reduction of ketone or aldehyde molecules in alcohol or other hydrogen donors (HZ) (see the illustration below). The excited ketone abstracts a hydrogen atom from HZ to form a free radical, while the HZ losses a hydrogen to form another radical. During the secondary reaction, the radicals may form dimmers or react to other molecules to form final products. The efficiency of hydrogen abstraction depends on the distribution of electrons in the carbonyl compounds. For compounds with $n \rightarrow \pi^*$ excitation, the efficiency of hydrogen abstraction is high (acetophenone, benzophenone, acetone, etc.). In contrast, for compounds with $\pi \rightarrow \pi^*$ excitation, the efficiency is low (naphthalene formaldehyde, naphthalene acetaldehyde, p-phenyldiphenyl ketone, etc.). This is because the $n \rightarrow \pi^*$ transition induces a reduction of electron density around oxygen atom in the carbonyl, and the oxygen has stronger electrophilicity for abstracting hydrogen atom. With the $\pi \rightarrow \pi^*$ transition, the π^* orbital is more closer to the oxygen atom than the π orbital. The increased density of electrons around the oxygen atom makes it has better nucleophilic which is unfavorable for hydrogen abstraction.
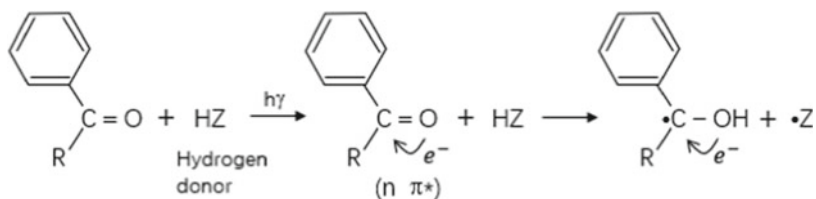
g. Photodimerization

Photodimerization is the photoaddition reaction of two identical molecules. For instance, the formation of anthracene dimer is realized through reaction of a singlet state molecule with another ground-state molecule.

(π, π^*)
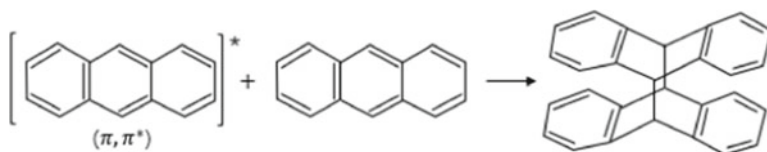
Another interesting example is dimerization of linear alkene molecules which is useful for application of photosensitive polymers. The photoabsorption wavelength depends on the detailed molecule structures. For simple alkene, dimerization can only be carried out with short wavelength light (180–210 nm), because there is only $\pi–\pi^*$ transition to absorb light in the molecules. When there are functional groups with lone pair electrons in the molecules, longer wavelength absorption occurs through $n–\pi^*$ transition, and the photoreaction becomes easier, like cinnamic acid and its derivatives. The double bond is affected by the oxygen in the carboxyl group and the phenyl group which have electron-withdrawing property. Under photoillumination, the π-bond is open and two molecules form a dimer through cyclobutene structure (see figure below). For this reaction, two σ-bonds are formed through opening of the two π-bonds. The transition from π-bond to σ-bond requires an orbital hybridization process.
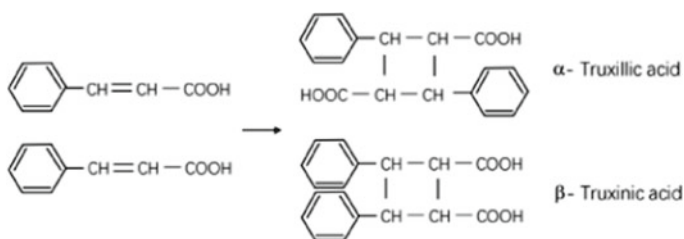
h. **Photopolymerization**

Photopolymerization is the process to form polymers with small molecular monomers/oligomers under photoillumination. Normally, the process requires photoinitiator which absorbs light and generates free radicals or ions to initiate polymerization. Generally, to complete a polymerization process, following steps are followed:

(i) Sensitizer (S) absorbs light and excites initiator (I) to its excited state, or the initiator is excited by absorbing light directly:

$$S + h\gamma \rightarrow S^*$$

$$S^* + I \rightarrow S + I^*$$

$$\text{or } I + h\gamma \rightarrow I^*$$
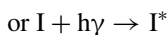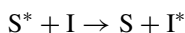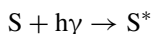
(ii) The photoexcited initiator molecule decomposes into free radicals:

$$I^* \rightarrow R' \cdot + R'' \cdot$$

$$\text{or } I^* + RH \rightarrow HI \cdot + R \cdot$$
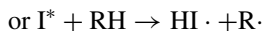
It is possible to form biradicals or ions.

(iii) Once the free radicals are formed, small molecule monomers (M) react to form polymer, and the process is:

$$R \cdot + nM \rightarrow RM \cdot + (n-1)M \quad \text{(to initiate reaction)}$$
$$RM \cdot + (n-1)M \rightarrow RM_2 \cdot + (n-2)M \quad \text{(reaction continues)}$$
$$RM_2 \cdot + (n-2)M \rightarrow RM_3 \cdot + (n-3)M \quad \text{(reaction continues)}$$
$$\cdots$$
$$RM_{(m-1)} \cdot + (n-m+1)M \rightarrow RM_m \cdot + (n-m)M \quad \text{(reaction continues)}$$
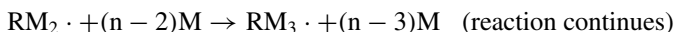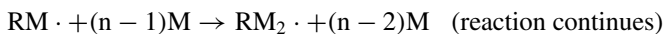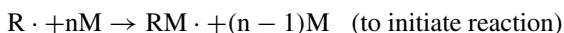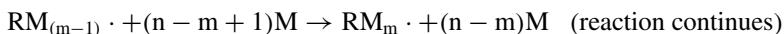
(iv) The activity of free radicals can fade away through radical combination. Radical–radical coupling or hydrogenation/dehydrogenation reaction through deprotonation:

$$2RM_m \cdot \rightarrow RM_m - M_m R (\text{radical}-\text{radical coupling})$$

$$RM_m \cdot + R'H \rightarrow RM_m H + R' \cdot$$
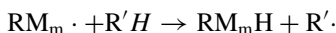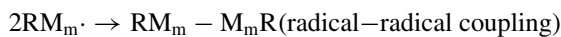
R' is inactive free radical which forms inactive product and the reaction is terminated. If there are oxygen or other inhibitors contained in the system, the polymerization will be terminated due to the vanishing of free radicals.

$$RM_m \cdot + O_2 \rightarrow R - M_m - O - O \cdot (\text{inactive}).$$

References

1. Schmid U, Seidel H, Mueller G, Becker Th (2006) Theoretical consideration on the design of miniaturized paramagnetic oxygen sensor. Sens Actuators B 116:213–220
2. Born M, Oppenheimer R (1927) Zur quantentheorie der molekeln. Ann Phys 84:457–484
3. Tully JC (2000) Perspective on "Zur quantentheorie der molekeln." Theor Chem Acc 103:173–176
4. Franck J (1926) Elementary processes of photochemical reactions. Trans Faraday Soc 21:536–542
5. Condon E (1928) Nuclear motions associated with electron transitions in diatomic molecules. Phys Rev 32:858–872

6. Doktorov EV, Malkin IA, Manko VI (1975) Dynamical symmetry of vibronic transitions in polyatomic molecules and the Franck-Condon principle. J Mol Spectrosc 56:1–20
7. Frackowiak D (1988) The Jablonski diagram. J Photoch Photobio B 2:399–408
8. Kimura K, Miwa K, Imada H, Imai-Imada M, Kawahara S, Takeya J, Kawai M, Galperin M, Kim Y (2019) Selective triplet exciton formation in a single molecule. Nature 570:210–213
9. Alia JD, Flack JA (2020) Unspecified verticality of Franck-Condon transitions, absorption and emission spectra of cyanine dyes, and a classically inspired approximation. RSC Adv 10:43153–43167
10. Jeon WS, Park TJ, Kim SY, Pode R, Jang J, Kwon JH (2009) Ideal host and guest system in phosphorescent OLEDs. Org Electron 10:240–246
11. Liu B, Luo D, Gao D, Wang X, Xu M (2015) An ideal host-guest system to accomplish high-performance greenish yellow and hybrid white organic light-emitting diodes. Org Electron 27:29–34
12. To T-L, Fadul MJ, Shu X (2014) Singlet oxygen triplet energy transfer-based imaging technology for mapping protein–protein proximity in intact cells. Nat Commun 5:4072
13. Rudolf M, Kirner SV, Guldi DM (2016) A multicomponent molecular approach to artificial photosynthesis–the role of fullerenes and endohedral metallofullerenes. Chem Soc Rev 45:612–630
14. Brenner H, Gilbert SA (1991) Delayed fluorescence ODMR as a probe of triplet-triplet fusion probability. Appl Magn Reson 2:241–256
15. Wu TC, Thompson NJ, Congreve DN, Hontz E, Yost SR, Voorhis TV, Baldo MA (2014) Singlet fission efficiency in tetracene-based organic solar cells. Appl Phys Lett 104:193901
16. Yersin H (2008) Highly efficient OLEDs with phosphorescent materials. Wiley-VCH Verlag GmbH & Co., Weinheim
17. Donges D, Nagle JK, Yersin H (1997) Intra-ligand charge transfer in Pt(qol)$_2$, characterization of electronic states by high-resolution Shpolskii specreoscopy. Inorg Chem 36:3040–3048
18. Yersin H, Donges D (2001) Low lying electronic states and photophysical properties of organometallic Pd(II) and Pt(II) compounds. Modern research trends presented in detailed case studies. Top Curr Chem 214:81–186
19. Hay PJ (2002) Theoretical studies of the ground and excited electronic states in cyclo-metalated phenylpyridine Ir(III) complexes using density functional theory. J Phys Chem A 106:1634–1641
20. Abedin-Siddique Z, Yamamoto Y, Ohno T, Nozaki K (2003) Structure-dependent photophysical properties of singlet and triplet metal-to-ligand charge transfer state in Copper (I) bis(diimine) compounds. Inorg Chem 42:6366–6378
21. Pierloot K, Ceulemans A, Merchán M, Luis S-A (2000) Electronic spectra of the cyclometalated complexes M(2-thienylpyridine)$_2$ with M=Pd, Pt: a theoretical study. J Phys Chem A 104:4374–4382

Chapter 3
Organic Light-Emitting Diodes (OLEDs)

Organic light-emitting diodes (OLEDs) rely on the electroluminescence of organic semiconductors, which refers to the phenomenon that organic, typically polymeric and small molecular materials with semiconductor characteristics emit light under the excitation of electric field. OLEDs can be made into lightweight, ultrathin devices with flexible substrates that have a number of advantageous characteristics, including low driving voltage, high luminous efficiency, fast response speed, active light-emitting, all-solid-state, non-vacuum processing, low-temperature resistance, and flexibility. These benefits endowed OLEDs with very broad application prospects in industries including flat-panel display, flexible surface lighting, and solid-state lighting.

According to the working principle of the device, the research of organic electroluminescent materials and devices primarily includes the following several directions: active layer materials (the three primary color light-emitting materials, red, green, and blue, including fluorescent materials and phosphorescent materials), compatible materials for device fabrication (hole and electron injection and transport materials), interface materials (anode and cathode interface modification materials), electrode materials (ITO electrodes, metal electrodes), device engineering, driving technologies (polysilicon TFT, metal oxide TFT, organic TFT, etc.), and encapsulation technology (for glass substrates, flexible substrates, etc.). Luminous efficiency, color purity, and device stability are important parameters for evaluating the overall performance of organic electroluminescent materials and devices. In terms of commercialization, the yield and cost are two additional important considerations.

We should mention that in this chapter, we utilize OLED(s) as the unified language to designate all light-emitting devices based on organic semiconductors. In some other books/articles, researchers distinguish between small molecules and polymers, with OLEDs referring only to those based on small molecules and PLEDs referring to those based on polymers. According to the route of process technology, devices based on small molecules and polymers are different. The former employs red, green, and blue, the three primary color organic small molecule light-emitting compounds as raw materials and vacuum evaporation technology as the main approach to prepare

light-emitting devices. It has the advantage of being suitable for small and medium-sized displays. The technology is relatively developed when compared to the PLED printing process, and representative products include smartphone displays and high-definition TV screens. The latter (PLEDs) prepare displays primarily using trichromatic polymer luminous materials as basic materials and inkjet printing technology. The benefits include low cost and the potential in making large-size and flexible displays. However, in comparison with the former, which uses a vacuum evaporation technique, PLED manufacturing technology lags behind, resulting in device performance that is not competitive enough for mass-produced products.

This chapter briefly introduces the light-emitting principle and basic structure of OLEDs, classifies representative luminescent OLED materials, and discusses the development and application prospects of OLED materials and devices. Finally, the possible development direction of OLED is proposed.

3.1   Introduction to OLED Devices

With the rapid development of science and technology and the continuous growth of daily requirements for more convenient lifestyle, electronic products have developed rapidly. Among many electronics, the display technology is one of the archetypes. After the large-scale application of plasma display panels, researchers have discovered that OLEDs could be the next-generation technology. Compared with previous display materials, OLED materials have a wide viewing angle, decent flexibility, low power consumption, fast response time (within tens of nanoseconds), large spectral width (complete coverage in the visible light region), "true-black" color, self-luminous properties, and simple preparation process, which allow them to meet requirements by the display industry such as large area, flexibility, ultrathin, and low cost.

Before discussing the application and industrialization, this section first introduces the basic working principle of OLED and the general device structure. To that aim, we must first comprehend the meaning of various terminology used in the field of OLEDs, namely, which adjectives reflect which categorization of OLEDs. First, according to the materials used in the light-emitting layer, OLEDs can be divided into small molecule based and polymer-based categories, and according to the different light-emitting mechanisms of these materials, they can be further divided into fluorescence OLEDs, phosphorescence OLEDs, TADF OLEDs, etc. Secondly, from the perspective of device structure, according to the different light emission channels, OLEDs can be divided into top and bottom emission OLEDs and transparent OLEDs. Finally, depending on the driving method, OLEDs can be divided into passive matrix OLEDs and active matrix OLEDs (Fig. 3.1).
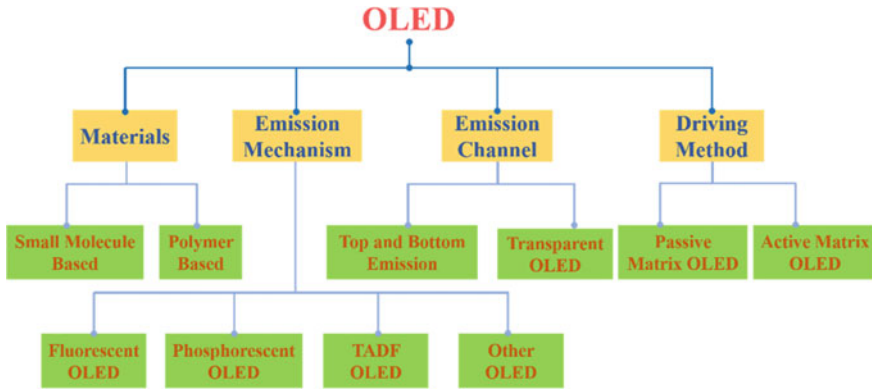
Fig. 3.1 The categorization of OLEDs

3.1.1 Introduction to the Light-Emitting Principle of OLED Devices

OLED devices mainly obtain electrons from the anode and holes from the cathode under the action of the voltage provided by the external electric field. Next, the electrons and holes migrate through the electron and hole transport layers, respectively, before an electron and a hole combine in the organic active layer to form an exciton. In working OLEDs, the excitons are extremely unstable and will soon release its energy, and the electroluminescence (EL) occurs as these excitons relax radiatively from the excited state to the ground state.

Researchers currently agree that electrons and holes migrate on the HOMO and LUMO of organic molecules, respectively, which means that under external voltage, electrons from the cathode will reach the LUMO of the organic material, while holes from the anode will reach the HOMO of the organic material [1, 2]. Electrons and holes combine with each other in the recombination region to obtain extremely unstable excitons, which transfer energy to the luminescent molecules, which in turn leads to the transition of the luminescent molecules to the excited state, and finally, the luminescent molecules in the excited state will radiate back to the original state. In this process, the luminescence phenomenon occurs. The energy difference between the excited and ground states of the luminescent molecule defines the photon's wavelength and, consequently, the color of the light that is emitted (Figs. 3.2, 3.3 and 3.4).

Once the electron and hole are in the active layer, there are generally two ways to realize photon emission [4]: One is that the two carriers are directly captured by the host, and after the recombination between the two, the energy is transferred to the host molecule, leaving it in an excited state, which is followed by the energy transfer from the host molecule to the dopant molecule, causing the dopant to excite, and the transition of the dopant then emits light; the other is that the two carriers are captured by the dopant material without passing through the host material, and the
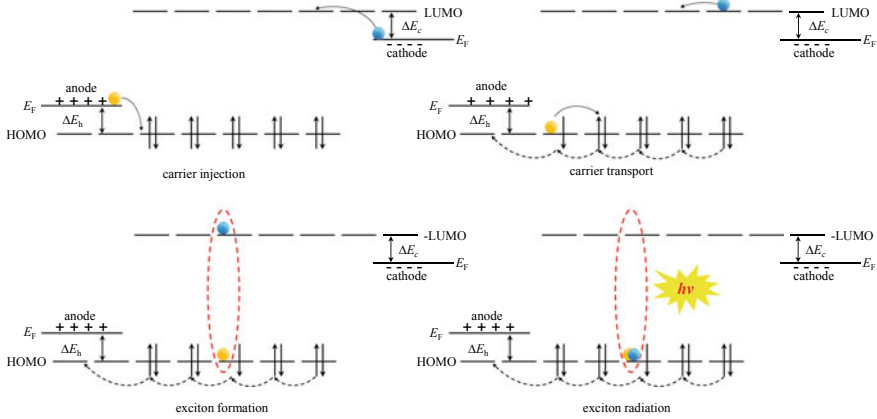
Fig. 3.2 Organic electroluminescence mechanism
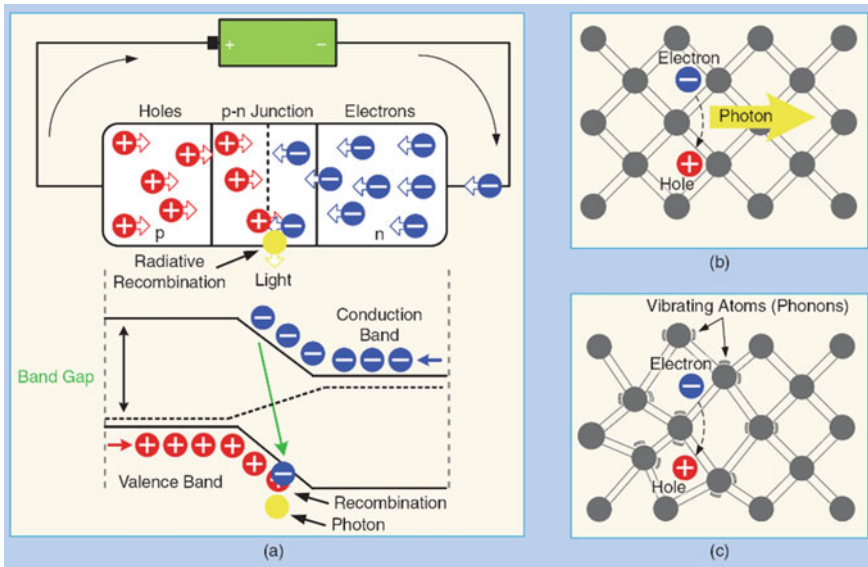
Fig. 3.3 **a** The LED operation principle. **b** Radiative recombination of an electron–hole pair accompanied by the emission of a photon. **c** Non-radiative recombination: the energy is converted to phonons

recombination of the two occurs in the dopant material. In this route, the intermediate energy transfer process is omitted, and the energy is directly transferred to the dopant molecule, resulting in its excitation, transition, and emission of light.

In the process of exciton formation, since electrons and holes have two possible spin states, namely α and β, there are 4 spin states for the exciton, including the
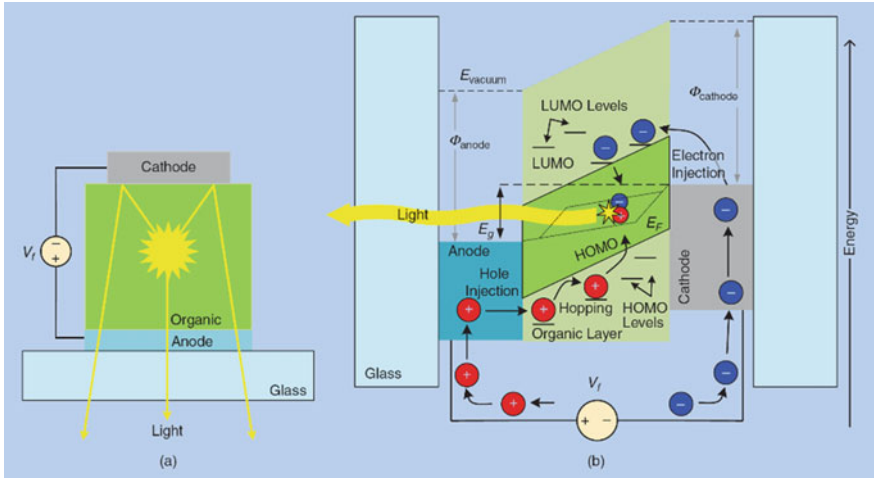
Fig. 3.4 The OLED operation principle: **a** a simple OLED structure and **b** an energy diagram of an OLED. Adapted from Ref. [3]

three triplet states, namely $\alpha(1)\,\alpha(2)$, $\beta(1)\,\beta(2)$, $\frac{1}{\sqrt{2}}[\alpha(1)\beta(2) + \beta(1)\alpha(2)]$, and the singlet state of $\frac{1}{\sqrt{2}}[\alpha(1)\,\beta(2) - \beta(1)\,\alpha(2)]$, whose vector representations are shown in Fig. 3.5. Since each case occurs with equal probability, 25% of singlet excitons and 75% of triplet excitons can be generated under electrical excitation in theory.
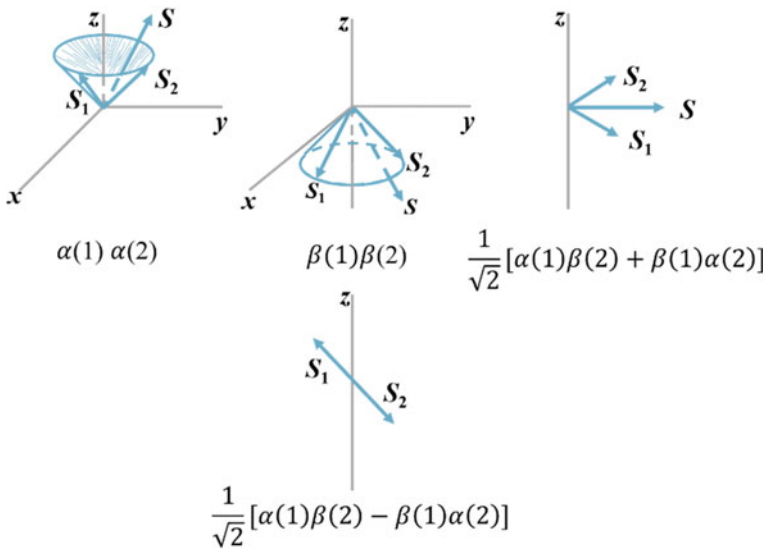
Fig. 3.5 Spin situation of electro-generated excitons. Adapted from Ref. [2]

As a result of the different spin states of the exciton, the light emitted by OLED is divided into fluorescence and phosphorescence. The light emitted by the energy of the excitons in the singlet state is fluorescence, and that by the energy of the excitons in the singlet state and triplet state at the same time is phosphorescence. Because the number of singlet states and triplet states formed by excitons has a fixed ratio of 1:3, from a theoretical point of view, the internal quantum efficiency of fluorescent devices that only use singlet excitons is 25% while emitting phosphorescence has a maximum internal quantum efficiency of 100% [5].

For phosphorescent electroluminescent devices, if the concentration of the luminescent material is too high, concentration quenching and triplet–triplet annihilation often occur, thereby reducing the luminous efficiency. Therefore, host–guest doping is often used in phosphorescent devices, which leads to two different light-emitting mechanisms in the hybrid system: One is that the excitons are directly captured by the guest molecules, and the guest molecules emit light directly [6]; the other is that the excitons are captured by the host molecules, and the host molecules transfer energy to the guest molecules, which then emit light [7]. Since the concentration of the guest molecules is often below 20%, the energy transfer mechanism dominates in such systems. Therefore, the effective energy transfers between the host and guest molecules. Electroluminescence efficiency is very important. There are two common energy transfer mechanisms: intramolecular Förster resonance energy transfer and intermolecular Dexter electron energy exchange [8]. Förster resonance energy transfer means that the host molecule transfers energy to the guest molecule through dipole–dipole interaction. Since it is an electronic transition within the molecule, this energy transfer is a relatively long-range interaction with a distance of ≤10 nm. For Förster energy transfer to take place, several conditions generally need to be met: First, the energy of the host molecule is higher than that of the guest molecule; second, the spins of the host molecule and the guest molecule remain unchanged before and after energy transfer; and third, the emission spectrum of the host molecule and the absorption spectrum of the guest molecule have a certain spectral overlap or transition coupling between them. For Dexter energy transfer, it is the process of electron exchange between the host molecule and the guest molecule. Since electrons are exchanged between different molecules, the distance between the two molecules is important for Dexter energy transfer. The host and guest molecules must be close enough to allow energy transfer to occur. Generally, the distance between the molecules should be <1 nm. In addition, the occurrence of Dexter energy transfer also requires the following conditions: First, the energy of the host molecule must be higher than that of the guest molecule; secondly, the total spin of electrons before and after energy transfer must be conserved; that is, the sum of the spins of the host and guest molecules before and after energy transfer remain unchanged; and finally, in addition to requiring a certain spectral overlap or transition coupling between the emission spectrum of the host molecule and the absorption spectrum of the guest molecule, there should also be a certain overlap of the orbital wave functions between the host and guest molecules.

3.1.2 Characteristics of an OLED Device

To characterize an OLED device, there are different parameters that can be obtained from different measurements. For the efficiency of an OLED device, researchers sometimes use luminescence efficiency to describe the overall performance, which typically involves three more specific efficiencies.

The first is quantum efficiency, which refers to the ratio of the number of photons emitted from the device to the number of injected electron–hole pairs. This can further be divided into internal quantum efficiency (IQE) and external quantum efficiency (EQE). IQE (η_{int}) is defined by the ratio of the number of all photons generated by the device to the number of injected electron–hole pairs while EQE (η_{ext}) refers to the ratio of the number of photons emitted by the device in the full space N_p to the number of injected electron–hole pairs N_c.

The second is lumen efficiency (η_l), which is defined by $A \cdot L / I_{oled}$, where A is the effective area of the device, L the device's luminous brightness, and I_{oled} the operating current of the organic light-emitting device when the luminous brightness is L.

The last is optical power efficiency (η_p), which is defined by $L_p/(I_{oled} \cdot V)$, where L_p is the light power emitted from the device, and $I_{oled} \cdot V$ is the total electrical power of the device driven by the voltage V.

The efficiency of an OLED device can be measured with an integrating sphere photometer. However, this is an ideal model whose measurement results need correction. The luminescence efficiency is typically measured by the integrating sphere photometer with the aid of a spectrometer.

Luminance, L_v, is defined by $k_m \int_\lambda L_{e,\lambda} V(\lambda) d\lambda$, where k_m is the mechanical equivalent of light, $L_{e,\lambda}$ the radiation luminance, and $V(\lambda)$ the luminous efficacy under bright conditions (photopic vision). The dependence of L on the viewing direction (θ) is $L_\theta = I_\theta/(dA \cdot \cos\theta)$, where I_θ is the light intensity in the direction, and dA is a luminous surface. Luminance is generally measured with luminometers, which measure the illumination produced on the surface of the photoelectric device by the image formed on the surface of the light source being measured. The illumination of the surface of the image is directly proportional to the luminance of the light source, not changing with the distance between the photometer and the light body.

The chromaticity of an OLED device is usually measured with a spectroradiometer, such as PR-705. The current–voltage curve of the device can be measured using a typical I–V testing method. To understand the photoelectric properties of the devices, a simple way is to measure the luminance-voltage curve and analyze the relationship between them.

To measure the emission spectrum, the general procedure is to make fluorescent or phosphor light pass through the monochromator and then irradiate it on the detector, scan the emission monochromator and detect the corresponding luminous intensity at various wavelengths, and then record the monochromatic curve of the luminous intensity against the emission wavelength by the recorder to obtain the emission spectrum.

To assess the stability of an OLED device, lifetime measurements need to be conducted. T50 is usually used to describe lifetime, which is the time experienced for the device's luminous brightness to go down to 50% of the original brightness. Because the device lifetime is usually very long, the lifetime is sometimes obtained through the analysis of the brightness-time–voltage curve.

3.1.3   Structure of OLED Devices

Most organic dyes alone cannot meet the demands of an efficient OLED device due to issues such as concentration quenching in the solid state, resulting in broadened emission peaks, redshifted emissions, and decreased fluorescence quantum efficiency. Therefore, they are generally doped in the host at the lowest concentration so that a small number of organic dyes (dopants) are dispersed in the matrix of the main luminophore (host) and the dopant molecules can emit light by energy transfer. This pair of host and dopant is typically called an emitter.

As shown in Fig. 3.6, most of the state-of-the-art OLED devices adopt a stacked structure [9]. The simplest OLED device is a single-layer device, originally proposed by Pope, and its structure is shown in Fig. 3.6a: A single-layer organic layer is placed between the cathode and anode. This structure has mostly been used in the early stage of OLED development. Because there is only one layer of organic substances in this structure, the organic material(s) must have a variety of excellent properties at the same time in order to realize various functions in the device, which is typically not possible. For instance, the transport of carriers is often unipolar, so it is almost impossible to achieve balanced charge transport. Therefore, unipolar devices are only used as a material-testing structure nowadays. More efficient devices consist of two or more layers sandwiched between the cathode and anode.

The first double-layer OLED device was reported in 1987. It largely addressed the limitations imposed by the single-layer devices and improved the luminescence and thus the display performance [11]. This structure is shown in (b) and (c) of Fig. 3.6. In order to achieve more balanced charge transport, another organic material is added as a functional layer on the basis of a single-layer device. The organic functional layers are divided into hole-type and electron-type according to the charge transport properties of the materials. For example, in Fig. 3.6b, the light-emitting material itself can transport holes effectively, so it needs another organic functional layer that can transport electrons, while the structure in Fig. 3.6c is the opposite that contains a hole transport layer.

Since then, researchers have been more and more in depth in the research of multilayer structures. Figure 3.6d shows a three-layered device structure consisting of a hole transport layer (HTL), an emissive layer (EL), and an electron transport layer (ETL) [12]. With the deepening of research, researchers employed more organic functional layers with different characteristics to make the device. In such a multilayer structure, each organic functional layer has a more refined function according to its own characteristics, and the cooperation of these layers could effectively limit the
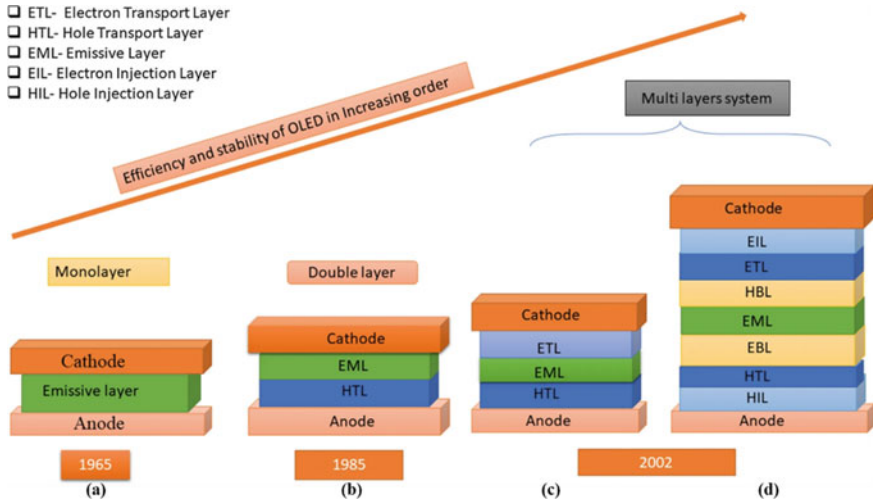
Fig. 3.6 Typical structures of OLED device. Adapted from Ref. [10]

recombination range of charge carriers. As a result, the recombination probability is greatly increased, and the performance of the device is improved [13]. Figure 3.6 shows the structure of the multilayer OLED device. This multilayer structure is the most widely used structure to make efficient OLED devices nowadays.

As we discussed previously, the structure of OLED may also be categorized based to the driving technique and the emission channel. As demonstrated in Fig. 3.7, the typical architectures of the OLED devices under these classification conditions are shown.

3.2 OLED Materials

In the preparation and optimization of OLEDs, the judicious design of the emissive layer that holds the emitter system is the key to realizing high efficiency in OLED devices. Therefore, the selection of luminescent material is crucial, and its properties are one of the most important factors in determining the device's performance. After more than 30 years of in-depth research, a variety of electroluminescent materials have been developed, and the performance of OLED devices has been significantly improved. Among the three primary colors of red, green, and blue that are required for full-color display, green OLED has demonstrated the best luminous efficiency. With continuous research, the types and quantities of red-light materials and devices have been greatly enhanced, and thus the efficiency of red-light devices has largely increased. In comparison, blue light materials have large band gaps, which are more difficult to obtain compared to red and green light materials. Common conjugates such as alkene, alkyne, and fluorene are often located in the blue-violet region due
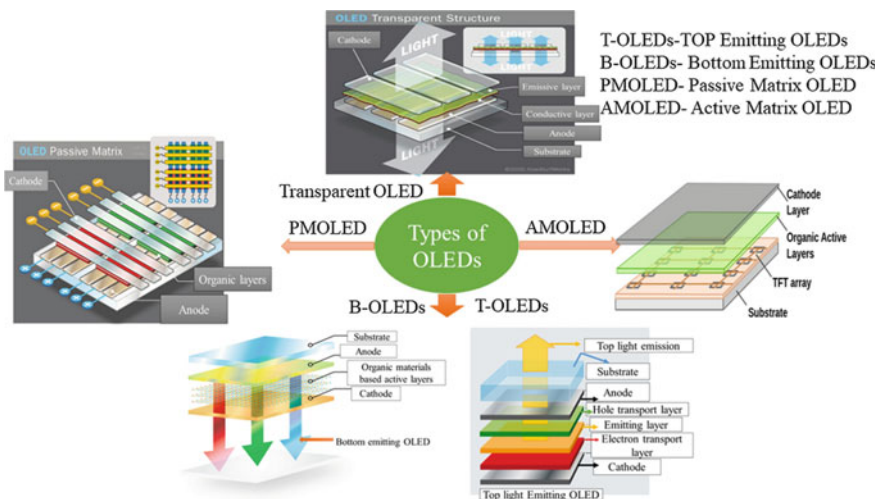
Fig. 3.7 Types of OLED device. Adapted from Ref. [10]

to the limited degree of self-conjugation and must be connected with other conjugated units to redshift the spectrum to the blue light region. At present, challenges such as stability, color purity, and quantum efficiency also need to be addressed for novel blue light materials to make them applicable for flat-panel displays and other products. Therefore, the performance of blue light OLED devices has much room for improvement, and research on blue materials is one of the most active research areas.

Typically, matrix materials are used to dilute the emitting materials, with the doping concentrations hovering around 10%. These "host materials" are frequently identical to or very comparable to the previously presented materials that transport electrons and holes. Hole and electron-transporting functional groups are frequently combined in one molecule to form so-called ambipolar host materials. In this section, we will focus on the materials that actually emit light, and we call these "emitter materials."

Generally speaking, emitter materials can be classified according to their chemical structure, such as small molecules and polymers (which can be divided into more subcategories), and can also be divided into fluorescence materials, phosphorescent materials, TADF materials, and next-generation materials according to the approximate time sequence of OLED device development. In this section, the research progress of OLED electroluminescent materials, along with typical charge transport materials and electrode materials, is briefly reviewed with a focus on the most recent high-performance representatives.

3.2.1 Fluorescent OLED Materials

In 1963, Pope et al. [14] observed electroluminescence in single crystal anthracene. They first prepared anthracene single crystals with a thickness of 10–20 m by sublimation and solution methods. Using silver paste (epoxy resin-based) electrodes, the first realization of electroluminescence by anthracene single crystals at a DC voltage of about 400 V was achieved. As we discussed in previous chapters, a fundamental difference between organic and inorganic electronic materials is that charge is transported via hopping between localized states in organic materials contrasted to the more delocalized energy bands in crystalized inorganic semiconductors. This causes the charge-carrier mobility and consequently conductivity of organic matter to be substantially lower and is the main reason why Pope et al. had to utilize 400 V to create emission. However, the intrinsically lower charge-carrier mobility of organic substances did not prevent researchers from researching the fascinating light-emitting phenomena in organic material-based systems.

Through the analysis of the relationship between brightness and voltage, Piper et al. [15] introduced the acceleration-collision excitation mechanism for the first time to explain this phenomenon and proposed that carriers are first generated inside anthracene crystals, accelerated by the electric field, collide with each other that had a high kinetic energy to generate electron–hole pairs, and finally the electron–hole pairs recombine and emit light [14, 15].

In the next ~10 years, the electroluminescence phenomenon has been intensively studied around the crystalized small molecules with high fluorescence efficiency. Some of the representative works are the study on anthracene crystal-based electroluminescence [16, 17] and the investigations on the electrode materials in the following years [17–23].

During this time period, the structure, fabrication, and packaging of some of the diodes were already similar to those used in the commercial market today, but the driving voltage used in these systems was very high (hundreds of volts). The main reasons were that the luminous efficiency of the device was low and that the minimum thickness of crystalline anthracene was high (m level). Furthermore, the conditions for crystal preparation, such as temperature changes, will cause differences in lattice defects and thus the electroluminescence spectrum. These problems hindered the further development of organic light-emitting diodes at the time. It was not until the Langmuir–Blodgett (LB) film and vacuum vapor deposition [24, 25] techniques were applied to organic electroluminescent devices that this impasse was broken, and the use of organic thin films reduced the thickness of the device. In 1979, Roberts et al. [24] observed electroluminescence in multilayer LB films of anthracene derivatives for the first time. Compared with single crystal anthracene, these short-chain anthracene multilayer films have higher thermal stability and a higher refractive index. The 0.6-m anthracene film greatly reduced the driving voltage of electroluminescence to 30 V. In the following few years, electroluminescence was observed in other small molecular or even polymeric organic thin films such as anthracene-doped tetracene [26], octaethylporphyrin [27], or polyvinylcarbazole [27, 28]. These

results show that the organic thin films all have similar properties. Although the use of organic thin films significantly reduces the driving voltage of the device, the driving voltage and the luminous efficiency were still not low enough due to the inefficient electron injection, unfavorable and unstable film morphology, and unstable morphology.

A breakthrough came in the year of 1987, when Tang et al. [29] first reported a green electroluminescent device made of double-layer organic thin film. The device used indium tin oxide (ITO) as the anode, and a layer of amorphous pinhole-free aromatic diamine thin film with a thickness of only 75 nm was evaporated on the anode, which was used as a hole transport layer. Then, an 8-hydroxyquinoline aluminum (Alq_3) film with a thickness of only 60 nm was evaporated on the aromatic diamine film, which was used as an electron transport layer and a light-emitting layer. A magnesium-silver alloy was used as the cathode. This double-layer film structure successfully reduced the turn-on voltage to 5.5 V. An external quantum efficiency of 1.0% and high radiative luminescence (>1000 cd m^{-2}) were achieved at a wavelength of 550 nm. This development made organic materials a realistic candidate for displays and quickly set off a research upsurge in OLEDs. Since then, research and development of OLED technology has continuously evolved in academia as well as in industry.

For blue light emission, early exploration was mainly based on anthracene derivatives. These materials typically exhibit excellent charge transport properties, broad bandgap, decent chemical, and thermal stability [30]. The emission color is changed from blue to deep blue by adding bulky substituents to the 9- or 10-position. An EQE of 2.82%, an emission wavelength of 452 nm, and CIE coordinates of for a non-doped device based on the fluorescent emitter 2PAn are presented in Fig. 3.8. (0.71, 0.21) [31].

In addition to organic small molecules, conjugated polymeric materials have also been employed with the expectation of enhancing charge transport and quantum efficiency. In 1990, Burroughes et al. [32] employed polyparaphenylene vinylene (PPV) as the emitter material and obtained yellow-green light emission at a DC voltage of about 14 V with a quantum efficiency of 0.05%. PPV is the first polymer reported to be used as a luminescent material for the preparation of electroluminescent devices. PPV is also the most studied, widely and intensively studied polymer and is considered promising as heterogeneous polymer electroluminescent materials. The classical PPV materials are insoluble and non-melting, which cannot meet the requirements of light-emitting devices. Design and synthesis of PPVs with different structures and properties through chemical and physical modifications have then become popular. For instance, a famous PPV derivative, poly-2-methoxy-5-(2′-ethylhexyloxy)-1,4-phenylethene (MEH-PPV), was reported by Braun et al. [33] to make an orange-yellow light-emitting OLED device at an AC voltage of 3 V in 1991. In 1992, Gustafsson et al. [34] used polyethylene terephthalate (PET) as a flexible substrate and doped polyaniline (PANI) as a hole-injecting transparent electrode, MEH-PPV as the light-emitting layer, and calcium as the electron injection electrode to prepare a flexible and bendable OLED device. Under the voltage of 2–3 V, orange-yellow light was observed, and the EQE was about 1.0%. This demonstrated the capability
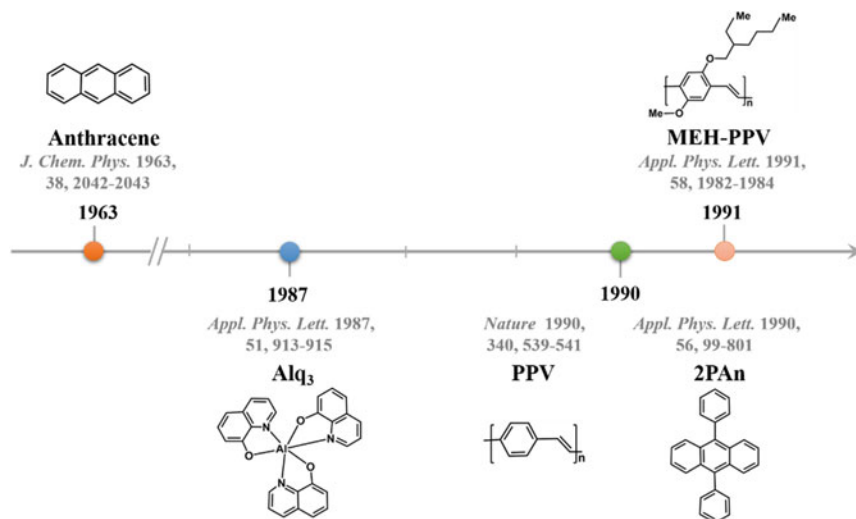
Fig. 3.8 Several fluorescent materials developed in the early stage of OLED development

of OLEDs to make flexible devices, which marks a new field for the application of OLEDs.

The results during this time period (late 1980s to early 1990s) have made this field a research hotspot. In the research of new emitter materials and devices, the exploration of small molecule and polymer materials and devices has become a very active field in the international arena and was rated as one of the top ten achievements in chemistry in 1992 by the United States. Many academic institutions and some internationally famous electronic and chemical companies have invested in research in this field.

In 1994, Kido et al. [35] first reported a white light-emitting organic electroluminescent device. They blended blue, green, and orange fluorescent dyes in poly-N-vinylcarbazole (PVK) thin films to make the hole transport layer and also the emitter at the same time. They employed 1,2,4-triazole derivative (TAZ) as the hole-blocking layer and Alq$_3$ as the electron transport layer. The device adopted a multilayer structure of glass/ITO/PVK/TAZ/Alq$_3$/Mg:Ag, which produced white light emission covering a wide range of visible light regions and brightness up to 3400 cd·m^{-2} under a driving voltage of 14 V. This high-brightness white light emission was achieved by doping the polymer film with fluorescent compounds of various colors to form a single light-emitting layer. This result shed light on the application of OLEDs in the commercial lighting field and substantially promoted the further development of OLEDs.

3.2.2 Phosphorescent OLED Materials

The luminescent materials studied in the early stage are all fluorescent materials. Since only singlet excitons can be utilized to emit light, the theoretical maximum internal quantum efficiency is only 25%, while 75% of triplet excitons lost their energy through non-radiative transitions. Based on this, researchers began to study how to take advantage of triplet excitons and improve the utilization rate of excitons. Since then, OLEDs have entered the era of phosphorescence.

In 1996, Hoshino et al. [36] doped benzophenone (BP) in the film of inert polymethyl methacrylate (PMMA) and found that the electroluminescence spectrum was the same as the phosphorescence spectrum of benzophenone, which indicated that it was the triplet excitons in benzophenone that emitted light. However, because the source of the triplet excitons cannot be determined, it had not attracted widespread attention. By 1998, Ma et al. [37] incorporated the complexes containing the heavy metal atom osmium (II) into PVK thin film to form the emitter, used 2-(4-biphenyl)-5-(4-tert-butylphenyl)-1,3,4-oxadiazole (PBD) as the electron transport layer, and make an OLED device with a structure of ITO/Os:PVK/PBD/Al. Red electroluminescence was observed at a DC voltage of 10 V. Although the electroluminescence efficiency was less than 1%, the experiments proved that transition metal materials with high triplet EL efficiencies can be used to make light-emitting layer of organic electroluminescent devices, thus creating a precedent for heavy metal phosphorescent electroluminescent devices and opening up a new way to improve electroluminescence efficiency. In the same year, Baldo et al. [38] successfully fabricated an electrophosphorescent device using Alq_3 doped with platinum octaethylporphyrin (PtOEP). When the doping concentration of PtOEP was 6%, the EQE reached 4%, which was much higher than the red fluorescent organic electroluminescent devices at the time. One year later, Baldo et al. [39] used 4,4′-N,N′-dicarbazole biphenyl doped with tris(2-phenylpyridine) (Ir(ppy)3) (CBP) and made a green electrophosphorescent device, which achieved a maximum EQE of 8.0% and a peak brightness of 100,000 cd·m^{-2}. In 2001, Universal Display Corporation and Baldo et al. [40] reported blue phosphorescent organic electroluminescence device (FIrpic). They introduced 2 electron-withdrawing groups (fluorine) on the benzene ring of the 2-phenylpyridine ligand to increase the energy of the triplet excitons of the iridium complex, thereby obtaining an OLED device with a sky blue (wavelength of 475 nm) whose color coordinates were (0.16, 0.29). The external quantum efficiency for the device was $(5.7 \pm 0.3)\%$.

Since then, continuous efforts have been devoted to optimizing the device structure. By 2016, Kim et al. [41] increased the EQE using FIrpic as luminescent material to 34.1%. The higher EQE was attributed to the strong spin–orbit coupling effect caused by heavy metal atoms, which increased the rate of intersystem crossing, and singlet excitons can be converted into triplet excitons. In theory, the internal quantum efficiency of such phosphorescent materials can reach 100.0%, and the maximum external quantum efficiency is 30.0–40.0% [42]. This experiment also

proved that the phosphorescent materials with triplet excitons involved make it possible to significantly improve the electroluminescence efficiency.

3.2.3 TADF OLED Materials

The second-generation light-emitting material, phosphorescent materials, has solved the problem of omitting T1 exciton energy, which effectively improved the performance of OLEDs. On the other hand, phosphorescent materials still have many problems in blue light devices. For instance, as discussed in Sect. 3.2.2, phosphorescent devices have significant triplet–triplet annihilation (TTA), resulting in a reduction in device efficiency and stability. From a structural point of view, phosphorescent materials are mainly composed of 4d and 5d transition metal atoms and organic frameworks. These complexes containing heavy metal atoms mainly include platinum (II) with a planar structure [38], palladium (II) [43], gold (III) [44], osmium (II) [37], ruthenium (II) [45], iridium (III) [39], etc., with an octahedral structure. The color of the compound depends largely on the energy of the cyclometallic ligand [46], so the luminescent color of the device can be regulated by changing the cyclometallic ligand and auxiliary ligands. However, the noble metals used in phosphorescent electroluminescence devices are not renewable [47, 48], which is unfavorable for cost reduction and sustainable development and thus limits the application of phosphorescent OLEDs. Along with the relatively short lifetime, these issues make typical phosphorescent materials unable to meet the stability, color purity, and brightness requirements during device preparation, meanwhile limiting the application of phosphorescent materials in the field of white lighting and full-color display. In order to effectively solve these problems, researchers began to explore different methods to improve the utilization of T1 excitons in fluorescent OLEDs. So far, there are several ways that can enhance T1 exciton utilization in small molecule fluorescent materials. Three major ones are triplet–triplet state annihilation (TTA), thermally delayed fluorescence (TADF), and local charge-transfer hybrid excited state (HLCT). We will discuss the most representative and most widely studied, TADF, in this section.

In 2012, Adachi's group [49] reported a series of compounds based on carbazolyl dicyanobenzenes (CDCBs) that generate additional light on a microsecond timescale, known as delayed fluorescence (DF). The luminescent color of the device can be tuned by changing the number of carbazole groups or substituents. The maximum EQEs of the green, orange, and sky blue electroluminescent device were (19.3 ± 1.5)%, (11.2 ± 1.0)%, and (8.0 ± 1.0)%, respectively. In terms of luminescence, these materials are called thermally activated delayed fluorescence (TADF) materials. Due to the excellent light-emitting properties of OLED devices made of TADF materials, they have attracted extensive attention from researchers in different fields and are considered the third-generation OLED materials. Figure 3.9 shows the third generation of organic luminescent materials. TADF molecules refer to those that have a small energy gap between the lowest-lying singlet state S1 and lowest-lying triplet state T1. When the lifetime for the T1 excitons is sufficiently long, the (formally)

Fig. 3.9 Chemical structures of some typical wavelength-tunable metal complexes. Adapted from Ref. [2]

spin-forbidden reverse intersystem crossing (RISC) process can be thermally activated and the triplet excitons can upconvert into the S1 state through which they radiatively relax to the ground state. This leads to a theoretical IQE of 100%.

Several conditions need to be considered to design an ideal donor–acceptor-based TADF material system: (1) There is a small energy level difference (EST) between the singlet and triplet states, which makes the RISC process more efficient; (2) appropriate HOMO and LUMO: While less overlap between HOMO and LOMO may reduce EST, according to the Franck–Condon principle, it also reduces the radiative transition rate; (3) a high singlet energy level and a stable triplet energy level can reduce the energy of the triplet state to transfer back to the ground state, so as to make full use of the singlet state luminescence; (4) appropriate steric hindrance and steric distortion between the donor and acceptor can improve the separation of HOMO and LUMO energy levels; (5) good film-forming properties; and (6) excellent photo- and electrochemical stability.

As mentioned earlier, the first TADF system was reported by Adachi's group from Japan in 2009 [50]. By doping SnF_2-OEP complexes in polyvinylcarbazole (PVCz) films, they studied the TADF behavior of six types of tin difluoride (IV) porphyrin complexes. The researchers discovered that the fraction of TADF increased significantly as temperature increased, with a strong TADF phenomenon observed at 400 K. Despite the relatively low luminous quantum efficiency (2.43%) and EQE (0.3%) at the time, it marks the beginning of a new generation of OLED materials.

One year later, Deaton et al. [51] reported the TADF phenomenon in bis(phosphine) diarylamide-based binuclear copper(I) complexes. They used vapor deposition techniques and fabricated OLED devices with a 4,4′-di(9H-carbazol-9-yl)-1,1′-biphenyl (CBP) host that contained 25% [N,N-di(p-toly)amino]phenyl]cyclohexane (TAPC). A maximum EQE of 16.1% was demonstrated at low current density, which showed that triplet excitons can be efficiently utilized by TADF. Subsequently, Adachi et al. reported TADF OLED devices based on metal-free pure organic materials, which have attracted much attention [49]. In this work, they proposed the design concept: One is to separate the electron wave function and hole wave function of the material to obtain a smaller ΔE_{ST} to facilitate RISC under thermal activation; the second is to use donor–acceptor units that are more tightly arranged to increase orbital overlap and the structure stiffness with an aim to suppress non-radiative transition and increase luminous efficiency.

In 2015, the research group of Lee [52] used 3-3-(carbazol-9-yl)phenyl)pyridinyl[3′,2′:4,5]furo[2,3-b]pyridine (3CzPFP) as a bipolar host

material for (4 s,6 s)-2,4,5,6-tetrakis(9H-carbazol-9-yl)-isophthalonitrile (4CzIPN). At a low doping concentration of 1%, a green TADF device with an EQE as high as $(31.2 \pm 0.5)\%$ was obtained. One year later, the research group of Wu reported blue TADF molecules based on the structure of spirocyclic acridinetriazine [53]. The device showed a maximum. Following that, Liao's group designed and synthesized the red TADF material 11,12-Bis(4-(diphenylamino) phenyl) dibenzo[a, c] phenazine-3,6-dicarbonitrile (TPA-PZCN) in 2019. The OLED devices based on TPA-PZCN achieved a maximum EQE of 28.1% [54] (Fig. 3.10).

As the generally considered "third-generation" OLED materials, TADF materials have seen tremendous development and have been successfully applied to high-performance OLEDs. So far, high-efficiency fluorescent OLEDs with an EQE greater than 30% have been successfully fabricated by using pure TADF organic materials. The efficiency is comparable to that of the commercialized emitters based on phosphorescent noble metal Ir, making TADF-based OLEDs not only cost-competitive in terms of materials but also performance comparable. Furthermore, the chemical structure of organic TADF material is diverse and easily tunable, which are additional advantages for use in OLED and solid-state lighting technologies. However, obtaining efficient TADF organic molecules by intramolecular charge transfer is still challenging due to the strong localization of excitons and high electron exchange energy.
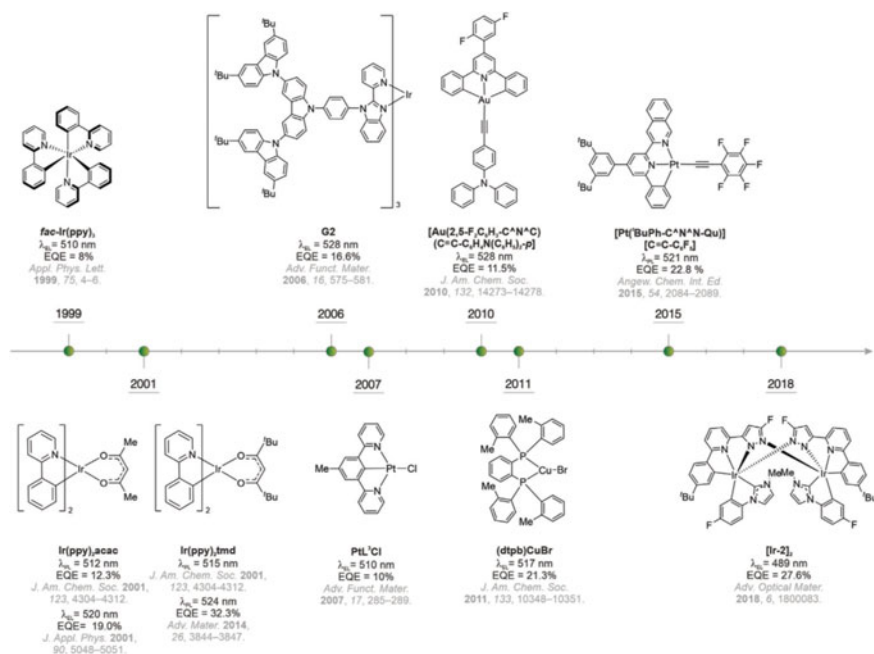
Fig. 3.10 3rd-Generation organic electroluminescent materials. Adapted from Ref. [55]

In designing TADF molecules, new donors and acceptors and their bridging groups need to be explored to not only enlarge the library of materials, but also facilitate the understanding of the fundamental photophysics of the molecules, including the role of conformational effects. Molecular structure optimization will result in smaller ΔE_{ST}, shorter DF lifetimes, higher PLQY, and narrower full width at half maximum. In the case of dendrimers, the effect of different dendrites on the same TADF core should be investigated. Furthermore, due to the good solubility and lower viscosity of hyper-branched polymers, which can improve the processability of materials compared to linear polymeric TADF materials, hyperbranched polymers incorporating D-A building blocks should be further designed and investigated [56].

For polymeric TADF materials, research has focused on copolymers and homopolymers designed to emit white light or specific colors. In copolymeric TADF, monomers without TADF properties are usually copolymerized with TADF monomers to separate TADF units, thereby preventing concentration quenching. Therefore, in addition to the choice of TADF monomers, the type of spacer and its electronic properties such as hole or electron transport behavior should be carefully considered to optimize the TADF properties of the copolymers [57]. Furthermore, compared to the material and device physics that is already difficult to fully under-stand, the photophysical mechanism of polymer TADF materials and their devices is even more complex and deserves further study. For example, the effect of systematic changes in the structural conformation of molecular chains and end groups on the material properties of polymeric TADFs is the subject of future research. Besides chemical structure, the effect of the condensed state of the polymer film on the properties of TADF needs to be clarified: The stacking of polymer chains, the crys-tallization of polymers, and the orientation of polymer chains in films can affect the overall morphology and in turn the TADF properties and device performance [58–60].

In addition, in-depth computational prediction and optimization of TADF mate-rials could make a significant contribution to the future development of this field. For example, quantum chemical calculations can screen inefficient molecules and allow experimental efforts to focus on more promising molecular candidates. For quantum chemical calculations, density functional theory is usually used to predict the singlet and triplet transition energies of TADF molecules, and the optimal adjustment of the separation function is a promising method to more effectively predict the transition energy of TADF systems [59].

Finally, from the perspective of electroluminescent devices, TADF materials can achieve high external quantum efficiency, but the relationship between the singlet triplet energy gap and electroluminescence efficiency is not clear in all systems. Another strategy to utilize triplet excitons is through triplet–triplet annihilation (TTA). Singlet excitons are generated to improve exciton utilization, but both TTA and TADF have similar problems, so the phosphorescent electroluminescent mate-rials in the commercial field are still considered more reliable choices. TADF mate-rials still have many problems to be solved urgently before they can achieve a combi-nation of low efficiency roll-off, good color stability, and long device lifetime [55, 61]. These factors will determine the commercial prospects of TADF materials.

Moreover, the realization of high-performance solution-processable undoped devices remains a challenge. In this regard, TADF dendrimers and polymers with blue, red, and white emission colors are particularly desirable. Energy transfer using TADF-assisted dopants in combination with conventional fluorescent emitter dopants (in small molecule and polymer devices) is an emerging strategy to improve OLED performance [62].

3.2.4 Next-Generation OLED Materials

Triplet–triplet annihilation (TTA)

In addition to fluorescence, phosphorescence, and thermally activated delayed fluorescence, several other mechanisms have been proposed in recent years to improve the exciton utilization of organic electroluminescent devices. As we mentioned earlier, triplet–triplet annihilation (TTA) phenomenon mainly exists in anthracene derivatives, which are characterized by T1 exciton fusion [63], and the energy level distribution of such molecules can generally meet the requirements [64, 65], and the mechanism of its generation is shown in Fig. 3.11 [66]. The energy released during the fusion of T1 excitons can form an S1 exciton without producing a T_n exciton, and the other exciton will return to the ground state S0. After the TTA energy conversion process, the ratio of S1 excitons can reach up to 62.5%, where the utilization rate of T1 excitons is 50% [62, 65, 67]. In this process, the concentration of S1 excitons generated and the concentration of T1 excitons are quadratically and exponentially positively correlated, and thus the brightness and efficiency of OLEDs are significantly increased with the increase of TTA energy conversion efficiency [68].

Anthracene derivatives have been used earlier as light-emitting materials for blue OLEDs. Due to that, its T1 energy level is about 1.85 eV, and after the TTA energy conversion process, the S1 exciton energy level is about 3.0 eV, which can achieve blue light emission and also break the barrier of low quantum efficiency in traditional fluorescent materials, but the deep mechanism of this phenomenon has been obscured. Kondakov suggested that the enhancement of EQE is inextricably linked to the TTA process [69]. The EQE of the fluorescent OLEDs designed by the team in 2009 using PADN, an anthracene derivative, as the host material was 9.1%, and TTA contributed about 32% of S1 excitons to the efficiency enhancement. Hu et al. [70] synthesized a series of anthracene-based luminescent materials with high TTA energy conversion efficiency, among which BD3 produced an EQE as high as 12% and a color coordinate (CIE) located at (0.15, 0.06), which meets the performance index of blue light material in full-color display technology. Chou et al. [62, 68] also observed the TTA in the devices of pyrene and benzophenanthrene luminescent materials. They chose DMPPP as the host material and a 2-styryltriphenylene derivative named TSTA as the emitting material to prepare blue light devices with EQE of 10.2% at 15 V. The EQE-brightness curves of this class of materials exhibit anomalous efficiency roll-offs. This is mainly due to the enhanced energy conversion
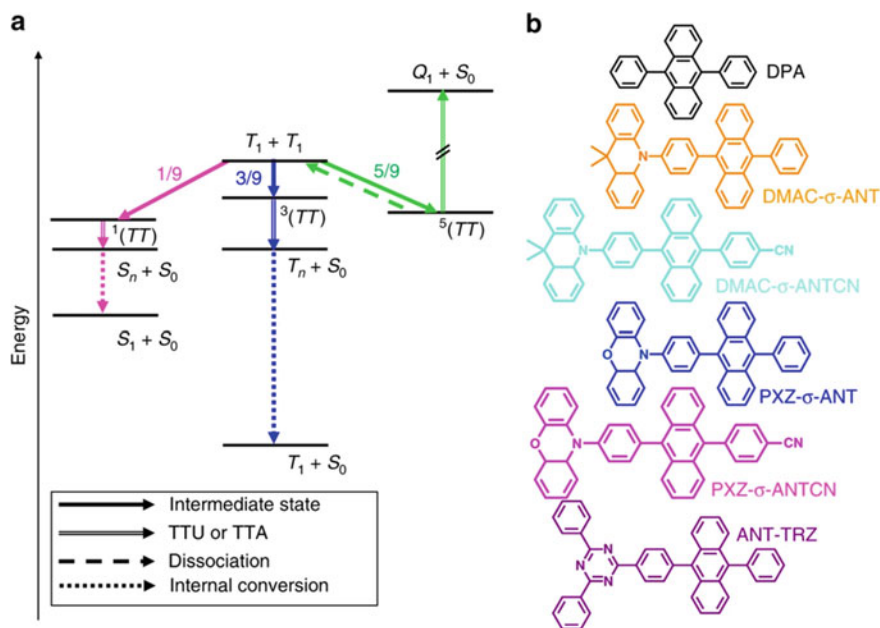
Fig. 3.11 Conventional triplet–triplet upconversion mechanism. **a** Energy-level diagram illustrating the mechanisms of triplet–triplet upconversion (TTU) and triplet–triplet annihilation (TTA). The 1(TT), 3(TT), and 5(TT) are singlet, triplet, and quintet intermediate states. The S1, T1, and S0 are singlet excitons, triplet excitons, and ground states. The S_n and T_n are higher singlet and triplet states. **b** Chemical structures of the anthracene derivatives. Adapted from Ref. [66]

efficiency of TTA at high current density [62]. Usually, in order to improve the energy conversion efficiency of TTA, it is necessary to increase the driving voltage and the doping of the luminescent material, which will increase the efficiency roll-off rate of the device exponentially [71].

Hybrid local charge transfer (HLCT)

In 2012, Ma Yuguang's group [72] proposed the hybrid local charge-transfer excited state theory and applied it to electroluminescent devices. They found that the twisted donor–acceptor molecule composing triphenylamine (TPA) and 1,2-diphenyl-1H-phenanthrene[9,10-d]imidazole (PPI) showed coupled charge-transfer (CT) and localized (LE) excited states, which form hybrid local charge-transfer state (HLCT): On the one hand, for the charge-transfer state, the energy level difference between the singlet and triplet states is small, and the triplet excitons are easily converted into singlet states, thus ensuring a high proportion of singlet excitons; on the other hand, for the local excited state, the large transition moment and orbital overlap ensure the efficient generation of fluorescence. The coexistence of the two states enables the compatibility between the high $T_1 \rightarrow S_1$ conversion rate and the high $S_1 \rightarrow S_0$

radiation rate, which results in high fluorescence quantum yield, and the maximum quantum efficiency can reach 7.8% [73].

In the HLCT system, the rapid decay of excitons leads to the inability to observe delayed fluorescence, which is an important feature to distinguish the HLCT and TADF. Theoretically, it is also possible to achieve 100% IQE in HLCT, but it is difficult to convert all T_n exciton energy into S_n exciton energy, and there are not many materials with suitable high excited state energy levels, which also limits the application of HLCT in OLEDs [74, 75]. HLCT molecules generally have a D-A-D structure. Compared with TADF materials, HLCT molecules require milder donor and acceptor groups in order to achieve a balanced distribution of LE excitons and CT excitons, which is important for the energy conversion process of HLCT [74]. On the other hand, the D-π-A conformation plays a crucial role in the formation of the HLCT excited states. Related studies have shown that the linkage suitable donor and acceptor within the TADF molecule is sp^3 hybridization, but this is not suitable for the HLCT molecule [76]. This is because this type of linkage would make the properties of the LE excited state of the HLCT molecule disappear, and the appropriate way for the donor and acceptor moieties to link in HLCT molecule is through the single bond to spatially large groups [77].

Others

Other mechanisms such as singlet fission [78, 79], neutral π radicals [79, 80], triplet-polaron interaction (TPI) [80], hyperfluorescence, sequential processing of emissive layer, TADF-sensitized fluorescent OLED (FOLED), multicomponent system (combination of TADF and fluorescent molecules), cascade singlet harvesting (CSH), and direct singlet harvesting (DSH) are also explored in organic electroluminescent devices. We note that the development of OLED materials is ever-evolving, and most of these new concepts are still under intensive research studies with various questions to be answered. The discussion of the details of the mechanisms behind these materials and their device working principles is beyond the scope of this book. Readers with interest in OLED research can find more information in the reference.

3.2.5   *Charge Transport/Injection Materials*

The emitter materials are the most important and most fundamental component for an OLED device. However, to better realize the potential of them, choosing appropriate charge transport and charge injection materials is as crucial.

Hole injection

Typical methods to improve the hole injection include: (1) substrate treatment with oxygen plasma or UV ozone; (2) insertion of hole injection layer(s); (3) partial oxidation of hole transport materials; and (4) anode interface treatment such as ITO electrodes self-assembled by triamine hole transport materials containing silicon, or using

inorganic interlayers between the hole transport layer and the emitter. For instance, for ITO/PEDOT:PSS-based anodes, adding a divalent transition metal compounds or oxides-based layer can modify the surface properties and block electrons to make the electrode more selective.

Since scientists discovered that polyparastyrene (PPV) has good electroluminescence properties in 1990, the filed has shown great interest in polymer light-emitting diodes. Traditional poly[2-methoxy-5-(2′-ethylhexyloxy)-1,4-styrene vinylene] (MEH-PPV) is widely used in polymer light-emitting materials. However, for most light-emitting copolymers including MEH-PPV, the high LUMO energy levels are more conducive to the injection and transport of holes, resulting in an unbalanced injection rate of holes and electrons, thus reducing the luminous efficiency of the device.

Wu et al. [81] found that blending bipolar fluorene copolymers with MEH-PPV could significantly improve the luminous efficiency of electroluminescent devices. This enhancement does not require complicated structural modification, but can be obtained by the simplest way of blending with functional polymers. The authors synthesized a fluorene containing bipolar units by directly linking the hole-transporting triphenylamine and electron-transporting 1,2,4-triazole to the polymer chain of the fluorene copolymer through Suzuki coupling reaction. Bipolar fluorene copolymers enhance the ability of electron and hole injection because they contain structural units that can transport holes and electrons, respectively. This not only effectively prevents π stacking between polymer chains, but also inhibits the formation of excimers in bipolar units due to the non-planar structure. After mixing it with conventional MEH-PPV, the performance of the device has been significantly improved due to the improved electron and hole injection rates.

In 2010, Park et al. [82] used phenothiazine and phenoxazine to synthesize a new type of hole injection material for OLEDs named 1-PNA-BPBPOX. It was found that its glass transition temperature is higher than that of tris(N-(naphthalene-2-yl)-N-phenylamino)triphenylamine (2-TNATA), rendering better stability for 1-PNA-BPBPOX. The HOMO energy level of 1-PNA-BPBPOX is 4.9 eV, which is in the middle between the HOMOs of the widely used ITO (4.8 eV) and NPB (5.4 eV). Using it as a hole injection material for OLED devices, the device efficiencies reached 2.8 lm/W (1-PNA-BPBPOX), higher than the 2.1 lm/W by 2-TNATA.

Compared with inorganic semiconductors, organic semiconductors can be more easily processed using solution-based techniques and have better flexibility, but they typically have weak intermolecular interactions and low intrinsic carrier density, resulting in low electrical conductivity of their thin films. In order to solve these problems, researchers mainly adopt the method of doping high-performance guest materials to improve the conductivity of organic thin films and increase the carrier density. So far, in OLED devices, organic radical precursors are mainly used as electron transport materials to enhance electron conductivity and enhance electron injection performance, but their application in hole transport materials has not been paid much attention. In 2017, Guo et al. [83] used stable organic radical precursors as a new type of dopant for the first time to promote hole injection and improve device performance. The authors found using HAT-CN, a widely used hole-injecting

material, doped with a stable organic radical TTM-1Cz as the hole injection layer, high-efficiency OLED devices with extremely low turn-on voltage can be obtained. Furthermore, the authors demonstrated that the key to electron extraction and hole injection lies in the efficient charge transfer between organic radicals and organic semiconductors. In addition, the study showed that the hole injection efficiency of OLED devices can be further improved by adjusting the energy level of organic radicals.

Ohisa et al. [84] studied hole injection layers composed of heteropolyacid-phosphomolybdic acid (PMA) containing MoO_3 units in OLEDs. The study found that PMA has many excellent properties. It has good solubility in organic solvents, can form smooth films, and has high transparency in the visible light region, as well as a suitable work function (WF). The study also found that these properties are related to the annealing atmosphere and film-forming temperature. Compared with OLED devices using traditional hole-injecting materials such as poly(3,4-ethylenedioxythiophene), poly(4-styrenesulfonate), and evaporated MoO_3, their optimized OLED devices showed lower driving voltage and higher stability. Because PMA is a commercially available and cost-effective material, it became a commonly used hole injection material in the production of OLED devices.

Other potential candidates include transition metal dichalcogenides (TMDC) monolayers, functionalized graphene, or graphene oxides. These materials have excellent physical and semiconductor properties and have been adopted in different electronics. Once the electrical and morphological properties of them or compounds with them mixed with other functional materials are properly adjusted, they could have broad application prospects.

Hole transport

Hole transport materials (HTMs) are mainly used to improve the transport rate of holes in devices and block electrons in the light-emitting layer to achieve maximum recombination of carriers. At the same time, an ideal hole transport material should also serve the roles of reducing the energy barrier of holes in the injection process and thus increasing injection efficiency and improving the brightness and lifetime of the device.

On the materials side, hole transport materials usually include: (1) aromatic triamines: These compounds have low ionization energy, and the structural reorganization energy of the customer service in the transfer process is low, which is conducive to cavity transport. However, their glass transition temperature is low. Therefore, in recent years, high melting point and high glass transition temperature have generally been used for hole transport materials, and compounds with specific spatial configurations such as paired coupling, star, spiral, and branching can increase the glass transition temperature, good film formation, and high-hole transport ability; (2) triarylamine-containing conjugated polymers with a high glass transition temperature; (3) carbazole compounds: These compounds have a very high-hole transport capacity due to their specific topology; (4) organosilicon hole transport

materials: Their films formed on ITO improve electrode flatness significantly; and (5) organometallic complexes.

Polystyrene sulfonate-doped poly(3,4-ethylenedioxythiophene) (PEDOT-PSS) is one of the most commonly used HTL materials. However, it suffers from low device stability due to multiple reasons such as interfacial chemical reaction with substrate, electronic property degradation, and long-term air instability. Other HTLs with an aim to replace PEDOT:PSS have been developed over the years. For instance, organic solvent-resistant cross-linked perfluorocyclobutane (PFCB) was synthesized by radical-mediated thermal cyclic polymerization of trifluorovinyl ether (TFVE). PFCB polymers can effectively improve the processability, chemical resistance, durability, thermal stability, and optical properties of devices as HTL materials [85].

In recent years, with the introduction of various substituent groups into the polymer chains of polyphenylene vinylene, these polymers have special properties such as charge transport and carrier blocking, which can reduce the interaction between polymer chains and prevent excitons from self-quenching. In 2004, Kimoto et al. [86] reported a polymer hole transport material with benzylamine as a structural unit coordinated with metal ions and found that it only needs to coordinate with metal ions to obtain higher EL efficiency.

Trimeric indene and its derivatives have also been used as HTMs due to their good energy level matching properties and high-hole mobility [87]. Inorganic hole transport material such as CuSCN has also been shown to improve device performance [88].

Besides experimental exploration, Maebienne et al. [89] used the LC-ωPBE principle to calculate the relationship between the ground state oxidation potential and the HOMO energy of tetraphenylbenzidine (TPB)-based hole transport materials (HTMs). The calculation shows that the trends of the excitation energy and hole reorganization energy of the HTMs are consistent with the trend of the energy level and hole mobility obtained from the experiment. Using these relationships, they analyzed the energetics of new TPB-based HTMs materials. Compared with TPB, the TPB derivatives with fluorene groups such as TPBC possessed lower hole reorganization energy and lower HOMO energy level. In addition, the molar extinction coefficient of TPBC in the same absorption region is lower, resulting in its lower absorbance in the visible region. More interestingly, this material has an improved hole mobility over TPB, which can effectively improve the luminescence performance of the device.

In the past 1–2 decades, due to the surge in the power conversion efficiency of organic solar cells and perovskite solar cells, various electron and hole transport materials have been developed for photovoltaic devices. The electrochemical, photophysical, and morphological properties of some of these transport materials could meet the requirements of electroluminescence devices. Therefore, researchers should examine the compatibility of these materials in OLEDs devices, which could potentially increase the device performance.

Electron transport

Electron transport materials (ETMs) are used to transport electrons and block holes. However, compared to the various choices of HTMs that have shown decent transport properties, the electron mobility of typical current electron transport materials is generally one to two orders of magnitude lower than the hole mobility of commonly used hole transport materials. Therefore, the development of electron transport materials with stable performance and high electron mobility is of great significance. Both inorganic and organic ETMs have been explored during the past few decades. These materials usually include: (1) planar aromatic compounds with large conjugate structures: They have good electron-accepting ability and can effectively transport electrons under a certain forward bias; (2) metal complexes such as Alq_3, which have high E_a and I_p and good thermal stability and film-forming properties. A series of compounds synthesized by chemical modification can have better performance; (3) oxadiazoles: Organic small molecule oxadiazoles have a high E_a and electron mobility; stellate oxadiazoles have a high glass transition temperature as well as a high E_a and I_p; and oxadiazole polymers have a high glass transition temperature, are difficult to crystallize but easy to dope, and are easily dissolved in organic solutions; (4) nitrogen-containing five- and six-membered heterocyclic compounds; (5) cyano and imine-containing electron-transporting materials; (6) perfluorinated electron-transporting materials; (7) organoboron electron-transporting materials; and (8) thiophene oligopolymers.

Porous anatase nanocrystals (nano-TiO_2) prepared from titanium-based metal–organic frameworks (MOFs), MIL-125, as an inorganic ETM showed good carrier transport properties. The good stability of inorganic materials is beneficial for obtaining high-performance and reliable OLED devices [90]. Among different types of ETMs, the focus of recent research has shifted to organic materials due to their flexible synthesis, easy-to-tune properties, and simple film formation processes. The design and synthesis of organic π-conjugated systems with strong electron-withdrawing groups are important for the preparation of organic electron transport materials.

In 2011, Sun et al. [91] synthesized a new organic small molecule named triaryl-boronyltriazine (B3T), which is a promising ETM for phosphorescent electrolumi-nescence devices. The molecule has three electron-accepting boron centers and has a very high triplet energy level (3.07 eV), while the HOMO energy level (6.73 eV) and the LUMO energy level (3.25 eV) are both relatively low. Phosphorescent OLED devices fabricated using this material as an electron transport layer showed external quantum efficiencies reaching brightness levels suitable for display applications.

Ruden et al. [92, 93] synthesized two new electron transport materials containing phenylphosphoryl: 2,6-bis(4-(diphenylphosphoryl)phenyl)pyridine (BM-A11) and 2,4- bis(4-(diphenylphosphoryl)phenyl)pyridine (BM-A10). It was found that the two molecules have sufficiently low HOMO energy levels to block holes and sufficiently high triplet energy levels to prevent exciton quenching, which make them excellent electron transport/hole-blocking materials. Although the two materials have similar structures and similar electronic properties, there are significant differences in the

performance of the OLED devices employing them as electron transport layers. The reason was that the positions that connect the central pyridine ring and the benzene rings were different, which led to the difference in the spatial arrangement and thus the degree of overlap of the π-conjugated systems of the two molecules. This leads to a big difference between the two in terms of electron transport characteristics and overall device performance.

In 2021, Chen et al. [93] combined 1,3-phenylene, 4,6-diphenyl-1,3,5-triazine-2-based units with 10-(naphthyl-2-yl)-anthracene-9-yl through coupling reaction and obtained an ETM, namely NaAN-m-TRZ, which showed low molecular weight, high glass transition temperature, and high electron mobility. The results from ultraviolet photoelectron spectroscopy showed that the HOMO energy level of NaAN-m-TRZ was −5.76 eV, and its LUMO energy level was −2.84 eV. Using space charge limited current model, the electron mobility of NaAN-m-TRZ doped with 50% Liq was as high as ~7.2×10^{-4} cm^2 V^{-1} s^{-1}, which could suppress the triplet-polaron annihilation in phosphorescent OLED devices. The green phosphorescent devices prepared using this HTM exhibited improved luminous efficiency and power efficiency along with high device stability.

3.2.6 Charge Blocking Materials

In order to better confine the charge carriers in the OLED device in the light-emitting layer and prevent the carriers from entering other layers without recombination, which leads to the reduction of the luminous efficiency, it is necessary to introduce a charge blocking material into the device, which is also known as selective contacts. Charge blocking materials and charge transport materials are closely related. Generally speaking, the charge transport material has a wide band gap to avoid absorbing the luminescence through energy transfer. Meanwhile, the charge transport material is also required to have a suitable energy level to facilitate the injection of carriers from the corresponding electrodes. Therefore, the LUMO energy level of HTMs is usually high to serve the role of electron blocking to a certain extent, while the HOMO energy level of ETMs is generally low to serve the role of hole blocking to a certain extent. However, not all charge transport materials can serve the dual roles concurrently, i.e., some of them have decent charge transport properties but poor opposite charge blocking ability. Therefore, adding a charge blocking layer can effectively improve the luminous efficiency of the device.

Generally speaking, a good hole-blocking material requires: (1) a low HOMO energy level to effectively block the hole so that the exciton recombines only in the light-emitting layer; (2) a large electron affinity and high electron mobility; and (3) good stability can form a uniform dense film.

Examples of commonly used hole-blocking materials are as follows: (1) BCP can block exciton/hole transport to the electron transport layer; (2) TPBI, with low Ea, high Ip, a great improvement over BCP; and (3) organic boron hole-blocking materials: TBB, FTBB, TFBD, TFPB, and other materials and some compounds

with hole transport capabilities such as F2PA and TPD to form a multilayer structure EL devices can effectively block the hole in the light-emitting layer.

Easy-to-process and flexible polymers have attracted extensive attention as charge blocking or transport layers due to their high heat resistance, good stability, tunable luminescence color, and good compatibility with other polymers in advanced lightweight polymer light-emitting diodes. So far, copolymers such as polyfluorene (PF), poly-p-phenylene terephthalamide (PPP), polythiophene (PT), and their soluble derivatives have been adopted to synthesize electron or hole transport materials. PF and its derivatives with high fluorescence quantum efficiency are one of the most widely used blue light polymers, but their shortcomings are also obvious. The spectral stability of such materials is poor, mainly because ketone defects or long-wavelength excitons are easily formed in their solid states. Therefore, it is necessary to maintain the balance of the polymer in the injection and transport of holes and electrons in the light-emitting layer to obtain high-efficiency light-emitting devices. Based on the fact that PT and PF are both electron-rich and hole-transporting, in order to obtain a larger electron affinity, electron-withdrawing groups must be introduced into the main chain or side chain. Based on the above analysis, Yang et al. [94] studied the most widely used electron injection and hole-blocking materials, 5-diphenyl-1,3,4-oxadiazole (OXD) derivatives, and found that they have high fluorescence quantum yield, excellent electron affinity, and good chemical and thermal stability. The performance of the device was significantly improved when OXD was used as the hole-blocking layer.

Okumoto et al. [95] designed and synthesized a new class of amorphous hole-blocking small molecular materials: TBB, FTBB, TFB, and TFPB. It was found that they have characteristics such as high oxidation potential and a large HOMO–LUMO energy gap and can be used as good hole-blocking materials in OLEDs.

One of the main factors causing the low EQE of some OLED devices is the unbalanced charge injection and transport of the luminescent material. This imbalance is mainly caused by the different energy barriers between the HOMO of the luminescent material and the work function of the ITO and between the LUMO molecular orbital of the luminescent material and the work function of the metal cathode. Molecular and polymeric 1,3,4-oxadiazole (OXD) derivatives are among the most widely studied electron injection and hole-blocking materials with high fluorescence quantum yield and high thermal and chemical stability. Among these, 1,3-bis(2-(4-tert-butylphenyl)-1,3,4-oxadiazol-5-yl)benzene (OXD-7) has seen widespread use in LED devices containing various luminescent materials. On the basis of OXD-7, Wang et al. [96] studied a new hole-blocking material based on a pyridine-containing dioxygen compound system, PDPyDP. The authors showed that when MEH-PPV was used as the light-emitting material, the OLED devices with PDPyDP as the electron transport/hole-blocking layer, prepared by the thermal evaporation method, showed better luminescence performance than the device using OXD-7.

3.3 OLED Application Status and Prospects

3.3.1 Overview of OLED Industry

Despite decades of laboratory research and academic achievements, the commercialization of OLEDs is still in an early stage. However, with the rapid development of the technology, the advantages of OLED compared with other display and lighting technologies are becoming increasingly prominent, while the disadvantages of high price, maintenance cost, and short lifespan are gradually being overcome. At present, the luminous efficiency and stability of OLED can already meet the requirements of certain types of small and medium-sized displays and are widely used in the field of instruments and smartphones. Besides, OLEDs have begun to be gradually commercialized in the field of large-size flat-panel displays owing to their advantages of wide viewing angle, ultrathin, fast response, and high luminous efficiency. More and more voices have begun to show that OLED is the next-generation mainstream display after liquid crystal. At the same time, due to its characteristics of large-area film formation and low power consumption, OLED is also an ideal flat light source and has broad application prospects in the field of energy-saving and environmentally friendly lighting. Furthermore, because OLEDs are all-solid-state thin-film devices and are prepared from organic and amorphous materials, they have natural advantages in flexible devices, making them ideal candidates for wearable smart devices.

According to the current analysis of the OLED industry, OLED materials are gradually developing in the direction of increasing size and improving performance. OLED will develop in three major aspects: display screens for popular and special products; lighting-related products; and wearable electronics.

3.3.1.1 Display Industry

At present, the global consumer electronics industry is facing transformation and upgrading, and display technology is also in a stage of rapid development. The new display technology and industry represented by OLED are changing with each passing day. The most prominent features of OLED are ultrathin, flexible, rich colors, high contrast, fast response, and low energy consumption. It is regarded by the industry as one of the new display technologies to replace the current mainstream LCD panels. Samsung Display and LG Display have invested a vast amount of time and money in research and development of both small and large-sized OLEDs. In particular, the latest generations of smartphones by leading companies such as Apple Inc. use OLED displays, which makes the global OLED market size grow dramatically.

The application of OLEDs in the display industry is considered promising, especially in popular electronic products and special display products. Popular electronics

are mainly represented by mobile phones, computers, and home TVs. These products do not require high flexibility for OLED materials. Compared with flexible screens, they are called rigid displays. The display screen of special products is a product that can best display the characteristics of OLED, which can be realized in the future, which is probably not too distant. These future OLEDs may achieve: first, a free flexible display which can be folded or even rolled with the overall thickness as thin as paper; the second is that the display screen has both transparency and double-sidedness. In addition to being able to see images outside the screen, double-sidedness means that people can accurately see the images on both sides without affecting each other; finally, the display screen must be able to have good resistance to shock and impact and work in a wide range of temperatures to meet the needs of special demands such as defense and aerospace applications.

3.3.1.2 Lighting Industry

Today, the brightness of a white OLED display is over three times that of ordinary lighting, and the lifetime of OLED has exceeded 80,000 h. The unique properties of OLED also determine the wide application of materials in lighting equipment. In the near future, OLED lighting equipment will gradually replace the current LED equipment, which has a good application prospect [19]. In the past few years, large-scale enterprises focusing on the research of the OLED lighting industry, such as OSRAM GmbH and Philips, have begun to mass-produce OLED lighting equipment. In 2015, the global OLED lighting market reached 12.1 billion US dollars, three years earlier than the US Department of Energy expected in 2010.

The demand for OLED lighting products is expected to be greatly stimulated with the enhancement of people's awareness of environmental protection and the gradual reduction of the cost of OLED products. Of course, the characteristics of OLED lighting products such as extending the lifespan and reducing the cost of OLED materials are also the technical breakthrough directions that enterprises need to focus on.

3.3.2 OLED for Flexible Applications

As solid-state light-emitting devices, OLEDs have great potential to be applied in the fields of wearable electronics thanks to their low driving voltage, low power consumption, and flexibility. With the rise of wearable devices, the demand for flexible OLED devices has been increasing over the past years, accompanied by the surge in potential market scale. At present, personal consumer electronic devices represented by smartphones and watches have already employed OLED technology to prepare their displays. On the basis of general requirements for LEDs such as luminous efficiency and color purity, flexible and wearable applications require the device to have strong bending resistance or wear resistance, which puts higher requirements

on the mechanical properties of the thin film materials of the device. One of the recent examples demonstrating the ultraflexibility of OLED together with OPD devices is done by Yokota et al. [97]. As shown in Fig. 3.12, the authors have demonstrated a smart e-skin system comprising health-monitoring sensors, displays, and ultra-flexible polymer-based OLEDs, which is referred as PLEDs. Figure 3.13 shows the structure and performance of the devices. They create optoelectronic skins (oe-skins), which add several electronic features like sensing and displays to the surface of human skin, using ultraflexible and conformable three-color, extremely efficient PLEDs and organic photodetectors. The devices are just 3 mm thick overall, an order of magnitude thinner than the epidermal layer of human skin. This thickness includes the substrate and encapsulating layer. By merging green, red, and OPDs with PLEDs, we were able to produce an ultraflexible reflecting pulse oximeter. When laminated on a finger, the gadget discretely detects the blood's oxygen content. Data is shown on the body using color indicator scans and on-skin seven-segment digital displays.

The development of flexible displays can be divided into three phases: bendable screens, foldable screens, and free-bending screens. At present, the mainstream of OLED display technology is still based on Active Matrix OLED (AMOLED) tech-nology. Most of the flexible OLED products are still in the primary bendable screen phase, and the research and development at this stage mainly revolve around the key technical points of flexible substrates, flexible TFT backplanes, flexible light-emitting layers, and thin-film packaging. In general, flexible anode materials that can replace ITO, transparent TFT materials, diverse flexible substrate materials, and curl-resistant devices with a radius of curvature less than 3 mm have been the focus of research in recent years. Devices prepared with special materials such as cloth and metal wires as substrates may be promising in the field of wearable devices because they can be combined with textiles and clothing and are also a research topic worthy of exploration. In addition, the stability of the OLED light-emitting layer film itself under the mechanical action of curling and folding is also a topic that can be deeply studied in theory and experiment. This subsection summarizes the developing trends of flexible substrate material, flexible thin-film transistor material, flexible light-emitting layer, and flexible thin-film encapsulation. Emerging flexible device fabrication technologies, such as flexible fabric substrate, polymer fiber-based light-emitting cell, the symmetric panel stacking device structure, and slot-die coating technology are also discussed.

3.3.2.1 Substrates for Flexible OLEDs

Flexible substrates include metal foils, thin glass, plastic substrates, etc. Metal foil is limited in use due to its poor light transmittance, while the problem with thinned glass is that it is easily broken. Polyimide-based plastic materials have become the most popular materials for preparing flexible substrates in the industry because they are transparent and mechanically robust. However, the use of plastic materials on flexible substrates also faces several technical challenges, including whether the performance of the substrate itself in terms of heat resistance, optical and mechanical
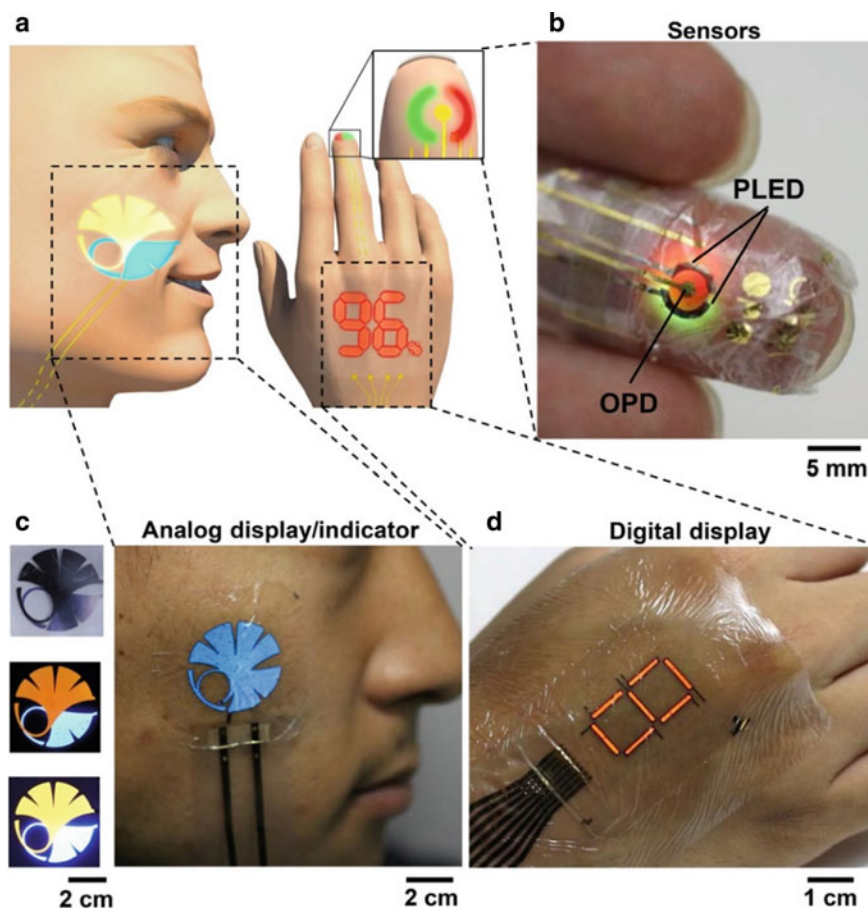
Fig. 3.12 Smart e-skin system comprising health-monitoring sensors, displays, and ultraflexible PLEDs. **a** Schematic illustration of the optoelectronic skins (oe-skins) system. **b** Photograph of a finger with the ultraflexible organic optical sensor attached. **c** Photographs of a human face with a blue logo of the University of Tokyo and a two-color logo. The brightness can be changed by the operation voltage. **d** Photograph of a red seven-segment PLEDs displayed on a hand. Adapted from Ref. [97]

properties, and resistance to water and oxygen penetration can meet the needs of device applications. First, the heat-resistant properties of plastic substrates include several different aspects, such as the thermal cracking temperature, glass transition temperature, and thermal expansion coefficient.
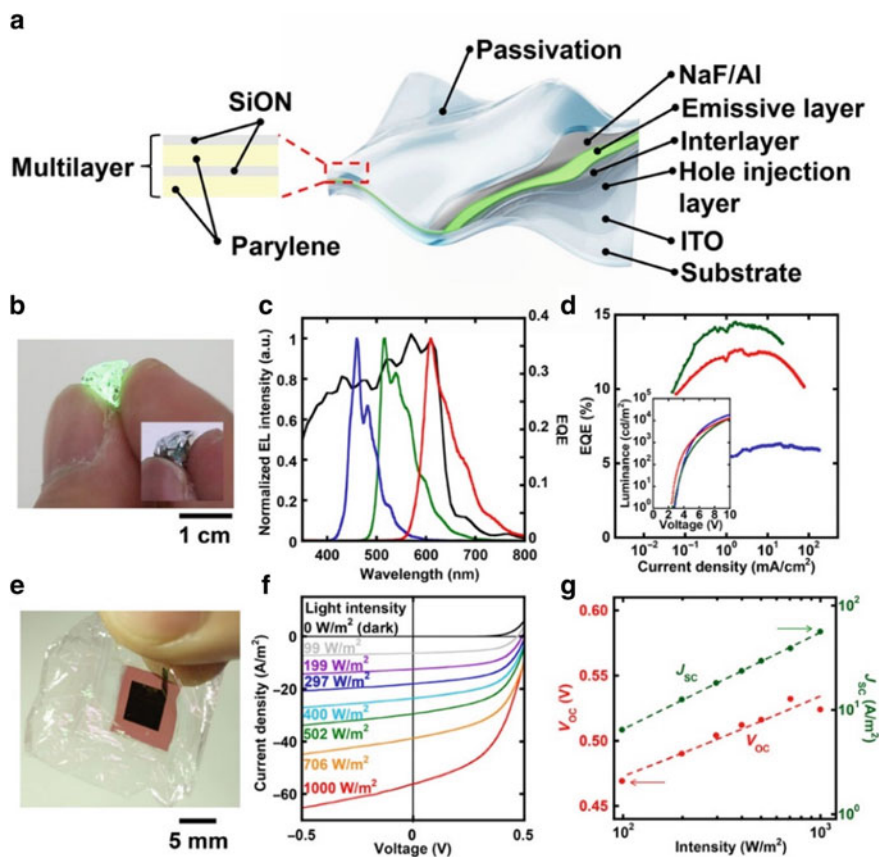
Fig. 3.13 Characteristics of ultraflexible PLEDs and OPDs. Note that all the measurements were performed in air. **a** Structure of the ultraflexible PLED. The passivation layer was composed of alternating organic (500-nm-thick Parylene) and inorganic (200-nm-thick SiON) layers. **b** Picture of the ultraflexible green PLED that was crumpled. **c** The EQE of the OPD (black line) with the normalized electroluminescence (EL) spectra of blue (blue line), green (green line), and red (red line) PLEDs. a.u., arbitrary unit. **d** Current density-dependent EQE characteristics of the ultraflexible PLEDs. The inset figure shows L–V curves of ultraflexible PLEDs. **e** Picture of the freestanding ultraflexible OPD. **f** Light intensity-dependent J–V characteristics of the OPD under simulated solar illumination. Red, orange, green, light blue, blue, purple, gray, and black represent the light intensity of 1000, 706, 502, 400, 297, 199, and 99 W/m² and the dark condition, respectively. **g** Characteristics of the ultraflexible OPD, measured using a solar simulator. Light intensity-dependent Voc of the OPD (red) and light intensity-dependent Jsc of the OPD (green). Adapted from Ref. [97]

3.3.2.2   Flexible Thin-Film Transistor (TFT)

The flexible TFT backplane is the most critical technology for driving flexible AMOLED panels. The technologies developed at this stage include silicon-based transistors (SiTFT), organic transistors (OTFT), and metal oxide semiconductor transistors (MOxTFT). In order to fabricate TFTs on flexible substrates, the process

temperature must meet the temperature limit that the substrate can withstand, and the three technologies of SiTFT, OTFT, and MOxTFT can be produced at low temperatures, so they can be matched with flexible plastic substrates.

Meanwhile, the intrinsic stress of the film grown at a low temperature is small, which is more suitable for the use of flexible devices. However, the film deposited at a low temperature typically exhibits more defects than that deposited at a high temperature, which affects the electrical performance and reliability of the device. Therefore, the process temperature must also take into account the electrical characteristics of the film and cannot be reduced indefinitely. Since silicon-based technology is relatively mature compared to other materials, flexible silicon-based TFT backplane technology is still the most common, mainly including amorphous silicon (a-Si) TFT and low-temperature polysilicon (LTPS) TFT.

3.3.2.3   Flexible OLED Light-Emitting Layer

As far as the OLED light-emitting layer is concerned, the processes of the flexible substrate and the traditional glass substrate are basically compatible. However, the conductive anode material, ITO, of traditional AMOLED devices is unable to adapt to flexible display applications due to its propensity to fracture, which leads to device failure in bending or curling conditions. Consequently, finding new conductive materials to replace ITO has become an important research topic in flexible display. In flexible displays, in addition to transparency, work function, and electrical conductivity, new alternative materials also require very good material ductility. Current research mainly focuses on ultrathin metal anodes, silver nanowires, and graphene-based materials.

3.3.2.4   Thin-Film Encapsulation of Flexible Devices

The encapsulation for traditional AMOLED device is realized by glass cover, epoxy resin sealing, and desiccant to absorb moisture, which can greatly improve the life of the device. But for flexible displays, this approach is very limited due to the rigidity of glass. Therefore, the industry has developed a flexible packaging form based on thin-film encapsulation (TFE) for flexible displays. The current mainstream TFE technology is to use a film layer with high water and oxygen barrier ability, that is, a barrier layer (mostly dense oxide materials such as Al_2O_3, SiO_2, and Si_3N_4) [98]. The barrier ability of such materials increases with the thickness of the film layer, but after reaching a certain thickness, it will no longer increase. In order to make the encapsulation capacity up to the standard, a film layer with flattening ability is generally used to "repair" the surface, eliminating surface defects before depositing the barrier layer.

Thin-film packaging has relatively high requirements on equipment and processes, and the corresponding low yield keeps costs high. Therefore, a new packaging solution has been developed in the industry, that is, the combination of thin-film packaging

and high-performance water-blocking film [98]. By depositing single-layer or multi-layer high-performance water-blocking films on thin film that is flexible substrates, the WVTR can reach the order of magnitude of 10^{-4} g/m^2/day. The film layer can also be used for the packaging of flexible display devices, but its own WVTR is not enough to realize OLED packaging. Considering the high cost of TFE, a single or multilayer high-barrier water barrier is usually deposited on the OLED surface during the production of flexible displays, followed by covering with a high-performance water-blocking film to achieve a balance of performance and cost.

3.3.2.5   Other Flexible Device Technologies

The merit of a foldable screen is that it can be folded along a certain center line with a very small radius of curvature (generally less than 3 mm), so it is easier to carry. This kind of display device has higher requirements for curvature. At present, AMOLED is still the technology with the greatest potential to realize foldable screens. The technical difficulties that foldable screens need to overcome compared to bendable screens are tracelessness and bending-resistant packaging at the soft and hard splicing fold lines of the substrate.

The main characteristic of a free flexible screen is that it can be bent freely as a whole. The number of times bending should be more than 100,000 times, and the thickness of the product is less than 0.5 mm, so it is easier to wear. This technology puts higher requirements on the material fatigue characteristics, so breakthroughs in materials and design are required.

Figure 3.14 is the demonstration of a freeform shaped AMOLED display based on low-temperature polycrystalline silicon technology by Hong et al. The authors demonstrate that their stretchable AMOLEDs, created with a special pixel structure, can endure being stretched into a variety of desired forms without losing picture quality or device attributes. We used a low-temperature thermoforming method to show off the unusual convex/concave curve of the 9.1-inch AMOLED panel.
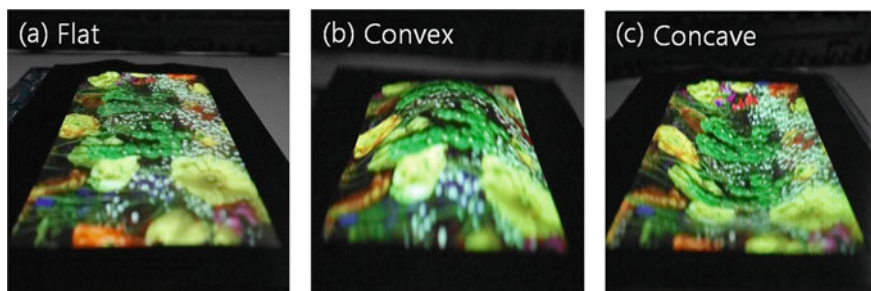
Fig. 3.14 Photographs of fabricated 9.1-inch AMOLED display prototype. **a** A flat AMOLED panel before applying thermoforming process. **b** A convex and **c** A concave shaped panel produced through the thermoforming process. Adapted from Ref. [99]

3.4   Summary and Outlook

To sum up, since the organic electroluminescence phenomenon was reported in 1953, polymer-based OLEDs, flexible OLEDs, and white light OLEDs have been reported one after another. Today, OLEDs have already been successfully promoted to commercialization. The wide application of organic electroluminescent devices in electronic products makes them expected to become a new generation of mainstream display and lighting devices, especially based on the development of flexible substrates and stretchable devices, which has given birth to the emergence of new technologies such as flexible screens, electronic newspapers, wearable displays, and OLED lighting 100. From a research point of view, the way to utilize excitons in OLEDs has experienced an evolution from fluorescence, phosphorescence, and thermally activated delayed fluorescence to new mechanisms such as hybrid local charge transfer 101.

So far, organic electroluminescence has experienced almost 70 years of development, but there are still some problems to be solved in both research and commercialization aspects. Fundamental research on the luminescence mechanism, materials and devices related to full-color displays, material physics of state-of-the-art luminescent materials, improvement of efficiency/brightness/lifetime, and so on. On the trend of current research and development, organic electroluminescent materials and devices may achieve major breakthroughs in the following research directions:

(1) Blue phosphorescent materials that are efficient and stable. At present, the development of green and red phosphorescent materials is relatively mature, but the stability of blue phosphorescent materials has not been fundamentally resolved, and there is a lack of effective solutions. This is partly due to the fact that blue light emission requires the most energy. To improve the stability of blue phosphorescent materials, it is necessary to study the chemical stability of materials and fully understand the aging mechanisms of materials and their inhibition mechanisms. Given that the chemical stability of transport materials and host materials is closely related to the chemical stability of phosphorescent dye molecules, it is necessary to develop host materials and transport materials that match blue phosphorescent dyes.

(2) Organic fluorescent light-emitting materials with a new exciton utilization mechanism. Metal–organic complex phosphorescent materials can utilize both singlet excitons and triplet excitons and have the outstanding advantage of high luminous efficiency, but the use of noble metals leads to high prices. Using other mechanisms to utilize excitons such as TADF or HLCT to develop high-efficiency and low-cost organic fluorescent materials is undoubtedly the future development direction of the material theme, for example, by establishing the relationship between high exciton utilization and high luminous efficiency of delayed fluorescence systems, developing organic materials with TADF properties, and elucidating thermal exciton fluorescence systems to obtain hybrid excited state photoluminescence, revealing the performance relationship

between efficiency and exciton utilization efficiency, exploring methods and approaches to precisely control the properties of hybrid excited states, etc.

(3) Organic electroluminescent materials and devices for printing processes in their entirety. The outstanding advantage of preparing organic, in particular, polymer-based display and lighting devices by inkjet printing and other printing processes is that it can significantly reduce production costs. However, the current device performance prepared by such processes is still lower than that of OLED devices prepared by vacuum evaporation methods. At the same time, due to the dissolution between materials in wet preparation processes, it is difficult to fabricate multilayer structures with decent interfacial properties as in vapor-deposited techniques. Therefore, it is necessary to develop high-performance red, green, and blue OLED materials, as well as compatible charge transport/blocking materials for printing processes. Compared with small molecule electroluminescent materials, polymer electroluminescent materials have these advantages for these purposes and could receive more attention in this respect.

(4) Lightweight materials and devices that are efficient and stable. The theoretical efficiency of white light OLED devices can be as high as 250 lm/W, but the power efficiency of current uncoupled white light OLED devices is generally less than 100 lm/W, which undoubtedly leaves a great room for innovation. Improving the power efficiency of organic OLED devices requires addressing three issues: luminescent material, device structure, and optical coupling technology. The fabrication of high-performance white light OLED devices faces three technical challenges, including high current injection, effective exciton utilization, and coupling-out technology. The realization of white light emission requires the combination of two (blue light + orange light) and three (blue light + green light + red light) emission spectra. Therefore, it is necessary to develop organic light-emitting materials for evaporation processes and solution processing technology, especially materials for triplet energy level matching, such as host materials and transport materials. It is also necessary to develop high-efficiency interfacial doping technology and organic heterojunction injection technology to solve the problem of high current injection in OLED devices. The stacked structure is the most effective structure for the efficient and multiplied utilization of excitons in OLED devices, but the common stacked devices still have the problems of high operating voltage and difficult-to-improve power efficiency. Thus, a charge generation layer with new mechanisms, e.g., organic heterojunction, needs to be developed to solve the problem.

(5) Machine learning could be more and more used for high-throughput material screening to explore the potential of novel structures. However, as a data-driven technique, its performance largely depends on the quantity and quality of data. How to generate and collect on a large scale, how to automatically identify and correct bad data in a dataset, and how to get a description that is more in line with the physical and chemical properties of the material are all issues to be further resolved.

For industrialization, the most urgent task is to analyze the technical production problems encountered in the process of large-scale industrialization; to develop packaging technology; to bridge the gap between novel lab-scale materials and mass-produced materials and their quality differences; between the lab-scale efficiency and the overall efficiency of a commercial product; etc.

References

1. Yunlong J, Yi F (2017) Design and optimization of organic light-emitting diodes based on iridium complexes
2. Liu L, Chen X (2021) Organic electroluminescence: past, present and future. J Beijing Normal Univ (Nat Sci) 57:671–680
3. Meerheim R, Lüssem B, Leo K (2009) Efficiency and stability of p-i-n type organic light emitting diodes for display and lighting applications. Proc IEEE 97:1606–1626. https://doi.org/10.1109/JPROC.2009.2022418
4. Lingling D, Chen Shufen, Huang Wei (2015) Studying on the microcavity effect for improving performances of blue and white top-emitting organic light-emitting diodes
5. Baiquan L, Jian W, Junbiao P (2016) High-performance white organic light-emitting diodes via controlling charges and excitons distribution
6. Holmes RJ, D'Andrade BW, Forrest SR, Ren X, Li J, Thompson ME (2003) Efficient, deep-blue organic electrophosphorescence by guest charge trapping. Appl Phys Lett 83:3818–3820. https://doi.org/10.1063/1.1624639
7. Holmes RJ, Forrest SR, Tung YJ, Kwong RC, Brown JJ, Garon S, Thompson ME (2003) Blue organic electrophosphorescence using exothermic host-guest energy transfer. Appl Phys Lett 82:2422–2424. https://doi.org/10.1063/1.1568146
8. Dexter DL (1953) A theory of sensitized luminescence in solids. J Chem Phys 21:836–850. https://doi.org/10.1063/1.1699044
9. Yunxia G, Lijia C, Ping C, Xiaoqiang F, Lianbin N (2016) Influence of MnO, on photoelectric performance in organic light emitting diodes. Spectrosc Spectral Anal 36:648–652
10. Bauri J, Choudhary RB, Mandal G (2021) Recent advances in efficient emissive materials-based OLED applications: a review. J Mater Sci 56:18837–18866
11. Xia L, Suidong W (2016) Study on electron injection in inverted bottom-emitting organic light-emitting diodes
12. Qingyang Y, Kang L (2014) Investigation on increasing light-emittine efficiency of light-emitting diodes by using nano dielectric structures
13. Yu Y, Ying-xia JIN, Deng-ke W, Jie Y, Chong W, Zheng-hong LU (2013) Progress of infrared light-visible light converter integrated semiconducting quantum dots with OLED. Infrared Technol 35:599–606+649
14. Pope M, Kallmann HP, Magnante P (1963) Electroluminescence in organic crystals. J Chem Phys 38:2042–2043. https://doi.org/10.1063/1.1733929
15. Piper WW, Williams FE (1955) The mechanism of electroluminescence of zinc sulphide. Br J Appl Phys 6:S39–S44. https://doi.org/10.1088/0508-3443/6/s4/315
16. Helfrich W, Schneider WG (1965) Recombination radiation in anthracene crystals. Phys Rev Lett 14:229–231. https://doi.org/10.1103/PhysRevLett.14.229
17. Williams DF, Schadt M (1970) A simple organic electroluminescent diode. Proc IEEE 58:476. https://doi.org/10.1109/PROC.1970.7655
18. Gu J, Kawabe M, Masuda K, Namba S (1977) Electroluminescence of anthracene with powdered graphite electrodes and ambient gas effects on the electrodes. J Appl Phys 48:2493–2494. https://doi.org/10.1063/1.324014

19. Schadt M, Williams DF (1969) Low-temperature hole injection and hole trap distribution in anthracene. J Chem Phys 50:4364–4368. https://doi.org/10.1063/1.1670904
20. Kawabe M, Namba S, MK (1977) Electroluminescence of green light region in doped anthracene. Japan J Appl Phys 16:643–644
21. Dresner J, Goodman AM (1970) Anthracene electroluminescent cells with tunnel-injection cathodes. Proc IEEE 58:1868–1869. https://doi.org/10.1109/PROC.1970.8049
22. Williams WG, Spong PL, Gibbons DJ (1972) Double injection electroluminescence in anthracene and carrier injection properties of carbon fibres. J Phys Chem Solids 33:1879–1884. https://doi.org/10.1016/S0022-3697(72)80485-2
23. Kunkel HP, Kao KC (1976) Electroluminescence in anthracene crystals under time-varying electric fields. J Phys Chem Solids 37:863–866. https://doi.org/10.1016/0022-3697(76)90062-7
24. Roberts GG, McGinnity M, Barlow WA, Vincett PS (1979) Electroluminescence, photoluminescence and electroabsorption of a lightly substituted anthracene langmuir film. Solid State Commun 32:683–686. https://doi.org/10.1016/0038-1098(79)90728-2
25. Vincett PS, Barlow WA, Hann RA, Roberts GG (1982) Electrical conduction and low voltage blue electroluminescence in vacuum-deposited organic films. Thin Solid Films 94:171–183. https://doi.org/10.1016/0040-6090(82)90509-0
26. Kalinowski J, Godlewski J, Dreger Z (1985) High-field recombination electroluminescence in vacuum-deposited anthracene and doped anthracene films. Appl Phys A 37:179–186. https://doi.org/10.1007/BF00617504
27. Kampas FJ, Gouterman M (1977) Porphyrin films. Electroluminescence of octaethylporphin. Chem Phys Lett 48:233–236. https://doi.org/10.1016/0009-2614(77)80305-9
28. Partridge RH (1983) Electroluminescence from polyvinylcarbazole films: 3. Electroluminescent devices. Polymer (Guildf) 24:748–754. https://doi.org/10.1016/0032-3861(83)90014-9
29. Tang CW, VanSlyke SA (1987) Organic electroluminescent diodes. Appl Phys Lett 51:913–915. https://doi.org/10.1063/1.98799
30. Huang J, Su JH, Tian H (2012) The development of anthracene derivatives for organic light-emitting diodes. J Mater Chem 22:10977–10989
31. Adachi C, Tsutsui T, Saito S (1990) Blue light-emitting organic electroluminescent devices. Appl Phys Lett 56:799–801. https://doi.org/10.1063/1.103177
32. Burroughes JH, Bradley DDC, Brown AR, Marks RN, Mackay K, Friend RH, Burns PL, Holmes AB (1990) Light-emitting diodes based on conjugated polymers. Nature 347:539–541. https://doi.org/10.1038/347539a0
33. Braun D, Heeger AJ (1991) Visible light emission from semiconducting polymer diodes. Appl Phys Lett 58:1982–1984. https://doi.org/10.1063/1.105039
34. Gustafsson G, Cao Y, Treacy GM, Klavetter F, Colaneri N, Heeger AJ (1992) Flexible light-emitting diodes made from soluble conducting polymers. Nature 357:477–479. https://doi.org/10.1038/357477a0
35. Kido J, Hongawa K, Okuyama K, Nagai K (1994) White light-emitting organic electroluminescent devices using the poly(N-vinylcarbazole) emitter layer doped with three fluorescent dyes. Appl Phys Lett 64:815–817. https://doi.org/10.1063/1.111023
36. Hoshino S, Suzuki H (1996) Electroluminescence from triplet excited states of benzophenone. Appl Phys Lett 69:224–226. https://doi.org/10.1063/1.117379
37. Ma Y, Zhang H, Shen J, Che C (1998) Electroluminescence from triplet metal—ligand charge-transfer excited state of transition metal complexes. Synth Met 94:245–248. https://doi.org/10.1016/S0379-6779(97)04166-0
38. Baldo MA, O'Brien DF, You Y, Shoustikov A, Sibley S, Thompson ME, Forrest SR (1998) Highly efficient phosphorescent emission from organic electroluminescent devices. Nature 395:151–154. https://doi.org/10.1038/25954
39. Baldo MA, Lamansky S, Burrows PE, Thompson ME, Forrest SR (1999) Very high-efficiency green organic light-emitting devices based on electrophosphorescence. Appl Phys Lett 75:4–6. https://doi.org/10.1063/1.124258

40. Adachi C, Kwong RC, Djurovich P, Adamovich V, Baldo MA, Thompson ME, Forrest SR (2001) Endothermic energy transfer: a mechanism for generating very efficient high-energy phosphorescent emission in organic materials. Appl Phys Lett 79:2082–2084. https://doi.org/10.1063/1.1400076

41. Shin H, Lee J-H, Moon C-K, Huh J-S, Sim B, Kim J-J (2016) Sky-blue phosphorescent OLEDs with 34.1% external quantum efficiency using a low refractive index electron transporting layer. Adv Mater 28:4920–4925. https://doi.org/10.1002/adma.201506065

42. Kim K-H, Ahn ES, Huh J-S, Kim Y-H, Kim J-J (2016) Design of heteroleptic Ir complexes with horizontal emitting dipoles for highly efficient organic light-emitting diodes with an external quantum efficiency of 38%. Chem Mater 28:7505–7510. https://doi.org/10.1021/acs.chemmater.6b03428

43. Fleetham T, Li G, Li J (2017) Phosphorescent Pt(II) and Pd(II) complexes for efficient, high-color-quality, and stable OLEDs. Adv Mater 29:1601861. https://doi.org/10.1002/adma.201601861

44. Beucher H, Kumar S, Kumar R, Merino E, Hu W-H, Stemmler G, Cuesta-Galisteo S, González JA, Bezinge L, Jagielski J, Shih C-J, Nevado C (2020) Phosphorescent κ3-(N^C^C)-Gold(III) complexes: synthesis, photophysics, computational studies and application to solution-processable OLEDs. Chem—A Eur J 26:17604–17612. https://doi.org/10.1002/chem.202003571

45. Zhu Y, Gu C, Tang S, Fei T, Gu X, Wang H, Wang Z, Wang F, Lu D, Ma Y (2009) A new kind of peripheral carbazole substituted ruthenium(II) complexes for electrochemical deposition organic light-emitting diodes. J Mater Chem 19:3941–3949. https://doi.org/10.1039/B900481E

46. Lamansky S, Djurovich P, Murphy D, Abdel-Razzaq F, Kwong R, Tsyba I, Bortz M, Mui B, Bau R, Thompson ME (2001) Synthesis and characterization of phosphorescent cyclometalated iridium complexes. Inorg Chem 40:1704–1711. https://doi.org/10.1021/ic0008969

47. Yook KS, Lee JY (2012) Organic materials for deep blue phosphorescent organic light-emitting diodes. Adv Mater 24:3169–3190. https://doi.org/10.1002/adma.201200627

48. Xu H, Chen R, Sun Q, Lai W, Su Q, Huang W, Liu X (2014) Recent progress in metal–organic complexes for optoelectronic applications. Chem Soc Rev 43:3259–3302. https://doi.org/10.1039/C3CS60449G

49. Uoyama H, Goushi K, Shizu K, Nomura H, Adachi C (2012) Highly efficient organic light-emitting diodes from delayed fluorescence. Nature 492:234–238. https://doi.org/10.1038/nature11687

50. Endo A, Ogasawara M, Takahashi A, Yokoyama D, Kato Y, Adachi C (2009) Thermally activated delayed fluorescence from Sn4+–porphyrin complexes and their application to organic light emitting diodes—A novel mechanism for electroluminescence. Adv Mater 21:4802–4806. https://doi.org/10.1002/adma.200900983

51. Deaton JC, Switalski SC, Kondakov DY, Young RH, Pawlik TD, Giesen DJ, Harkins SB, Miller AJM, Mickenberg SF, Peters JC (2010) E-type delayed fluorescence of a phosphine-supported Cu2(μ-NAr2)2 diamond core: harvesting singlet and triplet excitons in OLEDs. J Am Chem Soc 132:9499–9508. https://doi.org/10.1021/ja1004575

52. Lee DR, Kim BS, Lee CW, Im Y, Yook KS, Hwang S-H, Lee JY (2015) Above 30% external quantum efficiency in green delayed fluorescent organic light-emitting diodes. ACS Appl Mater Interfaces 7:9625–9629. https://doi.org/10.1021/acsami.5b01220

53. Lin T-A, Chatterjee T, Tsai W-L, Lee W-K, Wu M-J, Jiao M, Pan K-C, Yi C-L, Chung C-L, Wong K-T, Wu C-C (2016) Sky-blue organic light emitting diode with 37% external quantum efficiency using thermally activated delayed fluorescence from spiroacridine-triazine hybrid. Adv Mater 28:6976–6983. https://doi.org/10.1002/adma.201601675

54. Zhang Y-L, Ran Q, Wang Q, Liu Y, Hänisch C, Reineke S, Fan J, Liao L-S (2019) High-efficiency red organic light-emitting diodes with external quantum efficiency close to 30% based on a novel thermally activated delayed fluorescence emitter. Adv Mater 31:1902368. https://doi.org/10.1002/adma.201902368

55. Chen XK, Zhang SF, Fan JX, Ren AM (2015) Nature of highly efficient thermally activated delayed fluorescence in organic light-emitting diode emitters: nonadiabatic effect between excited states. J Phys Chem C 119:9728–9733. https://doi.org/10.1021/acs.jpcc.5b00276

56. Wu W, Tang R, Li Q, Li Z (2015) Functional hyperbranched polymers with advanced optical, electrical and magnetic properties. Chem Soc Rev 44:3997–4022. https://doi.org/10.1039/c4cs00224e

57. Li C, Wang Y, Sun D, Li H, Sun X, Ma D, Ren Z, Yan S (2018) Thermally activated delayed fluorescence pendant copolymers with electron- and hole-transporting spacers. ACS Appl Mater Interfaces 10:5731–5739. https://doi.org/10.1021/acsami.8b00136

58. Nikolaenko AE, Cass M, Bourcet F, Mohamad D, Roberts M (2015) Thermally activated delayed fluorescence in polymers: a new route toward highly efficient solution processable OLEDs. Adv Mater 27:7236–7240. https://doi.org/10.1002/adma.201501090

59. Peng Q, Fan D, Duan R-H, Yi Y, Niu Y, Wang D, Shuai Z (2017) Theoretical study of conversion and decay processes of excited triplet and singlet states in a thermally activated delayed fluorescence molecule

60. Xie Y, Li Z (2017) Thermally activated delayed fluorescent polymers. J Polym Sci, Part A: Polym Chem 55:575–584

61. Marian CM (2016) Mechanism of the triplet-to-singlet upconversion in the assistant dopant ACRXTN. J Phys Chem C 120:3715–3721. https://doi.org/10.1021/acs.jpcc.6b00060

62. Fukagawa H, Shimizu T, Ohbe N, Tokito S, Tokumaru K, Fujikake H (2012) Anthracene derivatives as efficient emitting hosts for blue organic light-emitting diodes utilizing triplet-triplet annihilation. Org Electron 13:1197–1203. https://doi.org/10.1016/j.orgel.2012.03.019

63. Nakayama T, Kubo O, Shingaya Y, Higuchi S, Hasegawa T, Jiang CS, Okuda T, Kuwahara Y, Takami K, Aono M (2012) Development and application of multiple-probe scanning probe microscopes. Adv Mater 24:1675–1692. https://doi.org/10.1002/adma.201200257

64. Lyu YY, Kwak J, Kwon O, Lee SH, Kim D, Lee C, Char K (2008) Silicon-cored anthracene derivatives as host materials for highly efficient blue organic light-emitting devices. Adv Mater 20:2720–2729. https://doi.org/10.1002/adma.200602885

65. Zhou J, Chen P, Wang X, Wang Y, Wang Y, Li F, Yang M, Huang Y, Yu J, Lu Z (2014) Charge-transfer-featured materials—promising hosts for fabrication of efficient OLEDs through triplet harvesting via triplet fusion. Chem Commun 50:7586–7589. https://doi.org/10.1039/c4cc00576g

66. Ieuji R, Goushi K, Adachi C (2019) Triplet–triplet upconversion enhanced by spin–orbit coupling in organic light-emitting diodes. Nat Commun 10. https://doi.org/10.1038/s41467-019-13044-1

67. Wang J, Lou X, Liu Y, Zhao G, Islam A, Wang S, Ge Z (2015) Controllable molecular configuration for significant improvement of blue OLEDs based on novel twisted anthracene derivatives. Dyes Pigm 118:137–144. https://doi.org/10.1016/j.dyepig.2015.03.005

68. Hansson R, Ericsson LKE, Holmes NP, Rysz J, Opitz A, Campoy-Quiles M, Wang E, Barr MG, Kilcoyne ALD, Zhou X, Dastoor P, Moons E (2015) Vertical and lateral morphology effects on solar cell performance for a thiophene-quinoxaline copolymer:PC70BM blend. J Mater Chem A 3:6970–6979. https://doi.org/10.1039/c5ta00683j

69. Deaton JC, Switalski SC, Kondakov DY, Young RH, Pawlik TD, Giesen DJ, Harkins SB, Miller AJM, Mickenberg SF, Peters JC (2010) E-type delayed fluorescence of a phosphine-supported cu 2(μ-nar 2) 2 diamond core: harvesting singlet and triplet excitons in OLEDs. J Am Chem Soc 132:9499–9508. https://doi.org/10.1021/ja1004575

70. Hu JY, Pu YJ, Satoh F, Kawata S, Katagiri H, Sasabe H, Kido J (2014) Bisanthracene-based donor-acceptor-type light-emitting dopants: highly efficient deep-blue emission in organic light-emitting devices. Adv Func Mater 24:2064–2071. https://doi.org/10.1002/adfm.201302907

71. Lee KH, Kang LK, Lee JY, Kang S, Jeon SO, Yook KS, Lee JY, Yoon SS (2010) Molecular engineering of blue fluorescent molecules based on silicon end-capped diphenylaminofluorene derivatives for efficient organic light-emitting materials. Adv Func Mater 20:1345–1358. https://doi.org/10.1002/adfm.200901895

72. Li W, Liu D, Shen F, Ma D, Wang Z, Feng T, Xu Y, Yang B, Ma Y (2012) A twisting donor-acceptor molecule with an intercrossed excited state for highly efficient, deep-blue electroluminescence. Adv Funct Mater 22:2797–2803. https://doi.org/10.1002/adfm.201200116

73. Zhang S, Yao L, Peng Q, Li W, Pan Y, Xiao R, Gao Y, Gu C, Wang Z, Lu P, Li F, Su S, Yang B, Ma Y (2015) Achieving a significantly increased efficiency in nondoped pure blue fluorescent OLED: a Quasi-equivalent hybridized excited state. Adv Funct Mater 25:1755–1762. https://doi.org/10.1002/adfm.201404260

74. Gao Y, Zhang S, Pan Y, Yao L, Liu H, Guo Y, Gu Q, Yang B, Ma Y (2016) Hybridization and de-hybridization between the locally-excited (LE) state and the charge-transfer (CT) state: a combined experimental and theoretical study. Phys sChem Chem Phys 18:24176–24184. https://doi.org/10.1039/c6cp02778d

75. Zhang S, Li W, Yao L, Pan Y, Shen F, Xiao R, Yang B, Ma Y (2013) Enhanced proportion of radiative excitons in non-doped electro-fluorescence generated from an imidazole derivative with an orthogonal donor-acceptor structure. Chem Commun 49:11302–11304. https://doi.org/10.1039/c3cc47130f

76. Jankus V, Chiang CJ, Dias F, Monkman AP (2013) Deep blue exciplex organic light-emitting diodes with enhanced efficiency; P-type or E-type triplet conversion to singlet excitons? Adv Mater 25:1455–1459. https://doi.org/10.1002/adma.201203615

77. Zhang S, Yao L, Peng Q, Li W, Pan Y, Xiao R, Gao Y, Gu C, Wang Z, Lu P, Li F, Su S, Yang B, Ma Y (2015) Achieving a significantly increased efficiency in nondoped pure blue fluorescent OLED: a Quasi-equivalent hybridized excited state. Adv Func Mater 25:1755–1762. https://doi.org/10.1002/adfm.201404260

78. Tang X, Hu Y, Jia W, Pan R, Deng J, Deng J, He Z, Xiong Z (2018) Intersystem crossing and triplet fusion in singlet-fission-dominated rubrene-based OLEDs under high bias current. ACS Appl Mater Interfaces 10:1948–1956. https://doi.org/10.1021/acsami.7b17695

79. Peng Q, Obolda A, Zhang M, Li F (2015) Organic light-emitting diodes using a neutral π radical as emitter: the emission from a doublet. Angew Chem Int Edit 54:7091–7095. https://doi.org/10.1002/anie.201500242

80. Obolda A, Peng Q, He C, Zhang T, Ren J, Ma H, Shuai Z, Li F (2016) Triplet–polaron-interaction-induced upconversion from triplet to singlet: a possible way to obtain highly efficient OLEDs. Adv Mater 28:4740–4746. https://doi.org/10.1002/adma.201504601

81. Wu C-S, Chen Y (2009) Copolyfluorenes containing bipolar groups: synthesis and application to enhance electroluminescence of MEH−PPV. Macromolecules 42:3729–3737. https://doi.org/10.1021/ma9004617

82. Park Y, Kim B, Lee C, Hyun A, Jang S, Lee J-H, Gal Y-S, Kim TH, Kim K-S, Park J (2011) Highly efficient new hole injection materials for OLEDs based on dimeric phenothiazine and phenoxazine derivatives. J Phys Chem C 115:4843–4850. https://doi.org/10.1021/jp108719w

83. Bin Z, Guo H, Liu Z, Li F, Duan L (2018) Stable organic radicals as hole injection dopants for efficient optoelectronics. ACS Appl Mater Interfaces 10:4882–4886. https://doi.org/10.1021/acsami.7b17385

84. Ohisa S, Kagami S, Pu Y-J, Chiba T, Kido J (2016) A solution-processed heteropoly acid containing MoO_3 units as a hole-injection material for highly stable organic light-emitting devices. ACS Appl Mater Interfaces 8:20946–20954. https://doi.org/10.1021/acsami.6b06723

85. Lim B, Hwang J-T, Kim JY, Ghim J, Vak D, Noh Y-Y, Lee S-H, Lee K, Heeger AJ, Kim D-Y (2006) Synthesis of a new cross-linkable perfluorocyclobutane-based hole-transport material. Org Lett 8:4703–4706. https://doi.org/10.1021/ol061642f

86. Kimoto A, Masachika K, Cho J-S, Higuchi M, Yamamoto K (2004) Synthesis and electroluminescence properties of novel main chain poly(p-phenylenevinylene)s possessing pendant phenylazomethine dendrons as metal ligation sites. Chem Mater 16:5706–5712. https://doi.org/10.1021/cm049241m

87. Lin K-H, Prlj A, Corminboeuf C (2017) A rising star: truxene as a promising hole transport material in perovskite solar cells. J Phys Chem C 121:21729–21739. https://doi.org/10.1021/acs.jpcc.7b07355

88. Madhavan VE, Zimmermann I, Baloch AAB, Manekkathodi A, Belaidi A, Tabet N, Nazeeruddin MK (2020) CuSCN as hole transport material with 3D/2D perovskite solar cells. ACS Appl Energy Mater 3:114–121. https://doi.org/10.1021/acsaem.9b01692

89. Gapol MAB, Balanay MP, Kim DH (2017) Molecular engineering of tetraphenylbenzidine-based hole transport material for perovskite solar cell. J Phys Chem A 121:1371–1380. https://doi.org/10.1021/acs.jpca.6b12651

90. Zhao X, Zhao J, He J, Li B, Zhang Y, Hu J, Wang H, Zhang D, Liu Q (2020) Porous anatase TiO_2 nanocrystal derived from the metal-organic framework as electron transport material for carbon-based perovskite solar cells. ACS Appl Energy Mater 3:6180–6187. https://doi.org/10.1021/acsaem.0c00085

91. Sun C, Hudson ZM, Helander MG, Lu Z-H, Wang S (2011) A polyboryl-functionalized triazine as an electron transport material for OLEDs. Organometallics 30:5552–5555. https://doi.org/10.1021/om2007979

92. von Ruden AL, Cosimbescu L, Polikarpov E, Koech PK, Swensen JS, Wang L, Darsell JT, Padmaperuma AB (2010) Phosphine oxide based electron transporting and hole blocking materials for blue electrophosphorescent organic light emitting devices. Chem Mater 22:5678–5686. https://doi.org/10.1021/cm1013653

93. Ling-ling C, Lin-ye W, Xu-hui ZHU, Shu X, Dong-ge MA, Jian-hua ZOU (2021) Triazine-based electron-transport material for stable phosphorescent organic light-emittingdiodes. Chin J Liq Cryst Displays 36:53–61

94. Yang Q, Jin H, Xu Y, Wang P, Liang X, Shen Z, Chen X, Zou D, Fan X, Zhou Q (2009) Synthesis, photophysics, and electroluminescence of mesogen-jacketed 2D conjugated copolymers based on fluorene−thiophene−oxadiazole derivative. Macromolecules 42:1037–1046. https://doi.org/10.1021/ma802414s

95. Okumoto K, Shirota Y (2003) New class of hole-blocking amorphous molecular materials and their application in blue-violet-emitting fluorescent and green-emitting phosphorescent organic electroluminescent devices. Chem Mater 15:699–707. https://doi.org/10.1021/cm020849+

96. Wang C, Jung G-Y, Hua Y, Pearson C, Bryce MR, Petty MC, Batsanov AS, Goeta AE, Howard JAK (2001) An efficient pyridine- and oxadiazole-containing hole-blocking material for organic light-emitting diodes: synthesis, crystal structure, and device performance. Chem Mater 13:1167–1173. https://doi.org/10.1021/cm0010250

97. Yokota T, Zalar P, Kaltenbrunner M, Jinno H, Matsuhisa N, Kitanosako H, Tachibana Y, Yukita W, Koizumi M, Someya T (2016) Ultraflexible organic photonic skin. Sci Adv 2. https://doi.org/10.1126/sciadv.1501856

98. Park J-S, Chae H, Chung HK, Lee SI (2011) Thin film encapsulation for flexible AM-OLED: a review. Semicond Sci Technol 26:34001. https://doi.org/10.1088/0268-1242/26/3/034001

99. Hong JH, Shin JM, Kim GM, Joo H, Park GS, Hwang IB, Kim MW, Park WS, Chu HY, Kim S (2017) The first 9.1-inch stretchable AMOLED display based on LTPS technology. In: Digest of technical papers—SID international symposium. Blackwell Publishing Ltd., pp 47–50

100. Hong G, Gan X, Leonhardt C, Zhang Z, Seibert J, Busch JM, Bräse S (2021) A brief history of OLEDs—Emitter development and industry milestones. Adv Mater 33

101. Meng L, Wang H, Wei X, Liu J, Chen Y, Kong X, Lv X, Wang P, Wang Y (2016) Highly efficient nondoped organic light emitting diodes based on thermally activated delayed fluorescence emitter with quantum-well structure. ACS Appl Mater Interfaces 8:20955–20961. https://doi.org/10.1021/acsami.6b07563

Chapter 4
Organic Field-Effect Transistors

Besides OLEDs, the semiconducting properties of conjugated molecules allow realization of another electronic device called organic field-effect transistors (OFETs).

The first OFETs were developed during 1980s. Since then, device performance has radically improved, combining with a better understanding of the properties of organic semiconductors. OFETs act as excellent devices for investigation of charge transport in organic semiconductor (OSC) materials [1]. Compared to conventional silicon-based transistors, OFET with conjugated small molecules or polymers can be conveniently fabricated at a low temperature as well as cost [2–4]. Particularly, polymeric semiconductors for OFETs are mechanically deformable and usually processed through solvents, demonstrating potential for large-area processing of flexible and stretchable electronics, such as integrated circuits, sensors, and light-emitting displays [5–7]. The performance of OFETs has steadily improved in the past decades through the development of new materials, optimization of the organic semiconductor microstructure, and enhanced control of the processes for optimizing film morphology as well as interfaces of semiconductor-dielectric and semiconductor-electrode. In this chapter, we firstly discuss the advantages of OFET in comparison with traditional inorganic FET and then introduce the working principles, including charge transport theory in OFETs, OFET architectures, and parameters. The next part discusses the development of materials, fabrication techniques, and applications of OFETs. After that, state-of-the-art strategy for high-performance OFET and OFET's lab-to-fab conversion is discussed in the last part.

4.1 A Brief Introduction of OFET

The principle of the field-effect transistor (FET) was first proposed by Lilienfeld in 1930. The invention of the transistor in 1947 by John Bardeen, William Shockley, and Walter Brattain is regarded as one of the greatest discoveries of the twentieth century since it is the basic component in modern electronics. Since the first Ge-based device

a few centimeters in size, the microelectronics industry has developed rapidly, and microprocessors with millions of transistors are currently fabricated. However, due to the fact that inorganic electronics have some technological limitations, organic-based devices have recently emerged in the market, beginning to replace amorphous silicon in some applications, and also have great possibility to find their place in a wide range of new applications.

Organic-based FETs (named OFETs) have emerged as a new application in FET family due to their distinctive properties such as good solution processability, low-temperature deposition, low cost, compatibility with large-area printing technology, and tunability of organic semiconductor materials. Although the amorphous silicon semiconductors have achieved much progress, the thin-film deposition usually needs high temperature process and dustless conditions which significantly increase the fabricating cost. Most importantly, the silicon-based materials are rare to be processed on flexible substrates due to their poor stretching characteristics. Due to the solution processability, organic materials offer the possibility to fabricate low-cost and flexible devices and are also suitable for large-area applications. In addition, the versatility of organic synthesis allows for the preparation of customized materials. That is, since by chemically modifying their molecular structure and functionality the solid-state structure and the resulting macroscopic properties are altered, it is feasible to synthesize tailored materials for specific uses.

After decades of development of material and device processing, the records of carrier mobility in OFETs have exhibited a rapid refreshing [8]. Carrier mobilities have exceeded 1 or even 10 cm^2 V^{-1} s^{-1} during last decade, which means that the performance of OFET devices is close to that of silicon-based FETs. To understand how the tremendous performances of OFETs come from, we need to learn the working principle of organic transistors.

4.2   Working Principles of OFET

4.2.1   Device Architecture

OFET is composed of several electro-active films arranged on one substrate. As shown in Fig. 4.1, those layers are organic semiconductor, gate medium (insulator), and electrode (contact). Electrode includes gate, source, and drain. Based on the sequence of layer deposition, OFETs devices can be classified into 4 different device architectures: bottom gate, bottom contacts [BGBC—Fig. 4.1a]; bottom gate, top contacts [BGTC—Fig. 4.1b]; top gate, bottom contacts [TGBC—Fig. 4.1c]; and top gate, top contacts [TGTC—Fig. 4.1d]. When organic semiconductors are structured in the form of thin films, OFET devices are called organic thin-film transistors (OTFTs). These four structures have their own advantages and disadvantages, and the reason for adopting each structure is based on its intention. For example, BGBC structure is suitable for the rapid detection of new materials and processing approaches,
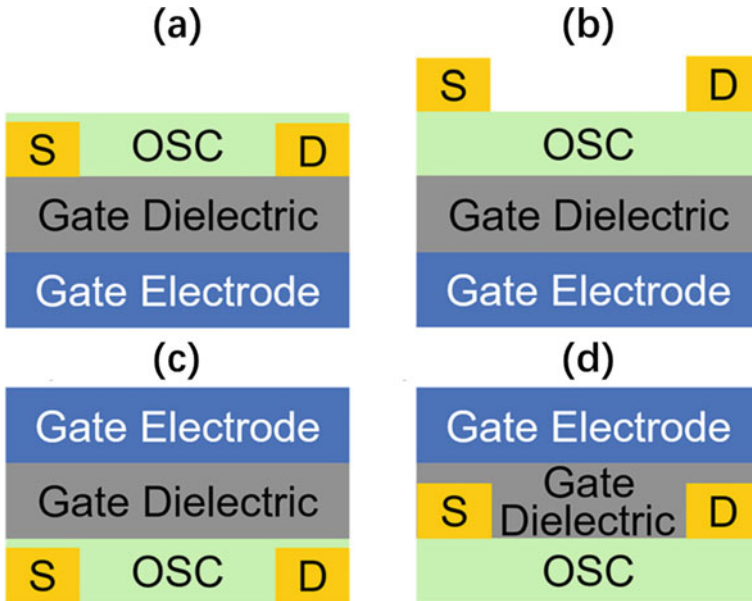
Fig. 4.1 OFET device architectures: **a** BGBC, **b** BGTC, **c** TGBC, and **d** TGTC. Figures are adapted from Ref. [9] Copyright 2019, AIP publishing

because the semiconductor is the last layer to be deposited after processing gate electrode, dielectric, source, and drain electrode. However, BGBC structure will also cause some problems, such as exposing organic semiconductors to ambient environment may cause a quick degradation and affect the life of OFET devices. The structure with top-gate electrode, such as TGBC and TGTC, is able to improve the stability of semiconductors in ambient condition, because dielectrics also act as packaging layers, but dielectrics must be carefully selected to maintain the integrity of organic semiconductor layers.

4.2.2 Charge Transport in OFET

The operation of OFETs is based on two potentials, one at the drain and the other at the gate, combining with the source electrode at the ground. The two generated voltages are gate–source voltage (V_{GS}) and drain–source voltage (V_{DS}). In the following discussion, OFET channels are composed of organic semiconductors, in which one type of carrier can be injected and transmitted. For p-type materials, holes are the carriers, while electrons are the carriers for n-type materials which polarities are just the opposite. If V_{GS} is not applied, charge is not accumulating at the interface between semiconductor and dielectric. Thus, the device is at the state of "turned off." When the device is "on", the V_{GS} is applied to polarize the dielectric, resulting in the
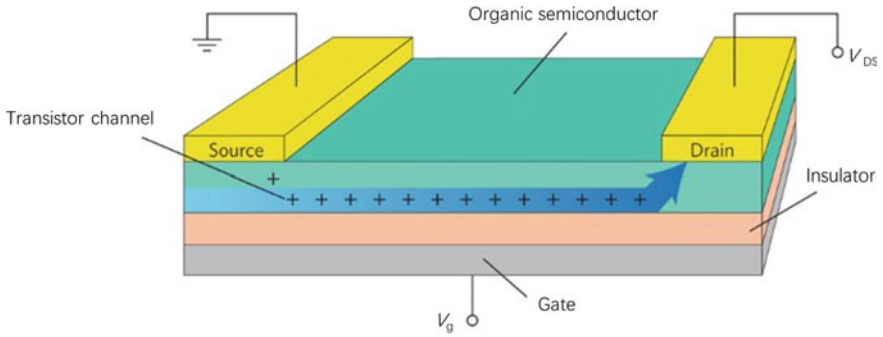
Fig. 4.2 Schematic charge transport in OFET. Adapted from Ref. [10] Copyright 2016, Springer Nature

accumulation of carriers on the interface of semiconductor and dielectric. As shown in Fig. 4.2, the applied V_{DS} induces a transmission of these accumulated charge carriers from the source to the drain, where the drain current (I_D) is measured. The applied field, V_{GS}, modulates the charge density, thereby regulating the current in the transistor channel, so there is the term "field effect."

In order to analyze the electrical characteristics of OFETs, the gradual channel approximation method is applied. In the case of this model, the potential between source and gate electrode is much higher than that between source and drain. This is usually accompanied by ensuring that the gate dielectric thickness, d, and the channel length, L, meet the relationship of $L/d \geq 10$. Otherwise, when the channel length is not enough, some problems may occur with the devices. With this relationship, the magnitude of V_{GS} determines the charge density in the semiconductor-dielectric interface. The density of charge in the channel can be given by Eq. (4.1) and Eq. (4.2), where x represents the distance across the channel between the source and the drain electrode:

$$Q = -C_{diel} V_{total}(x) \tag{4.1}$$

$$V_{total} = V_{GS} - V(x) \tag{4.2}$$

where $V_{total}(x)$ is the total potential in the channel resulting from an applied V_{DS} and V_{GS}, and C_{diel} is the gate dielectric capacitance per unit area.

In practical devices, a small V_{GS} is usually needed to fill the charge traps of the interface between semiconductor and dielectric before the accumulation of free carriers occurs in the channel. This potential for filling traps is named as threshold voltage (V_{Th}), which can be generated by interface roughness, crystal defects, and impurities. Thus, the density of mobile charge in OFET channel can be given as Eq. (4.3),

$$Q_{\mathrm{mobile}} = -C_{\mathrm{diel}}(V_{\mathrm{GS}} - V(x) - V_{\mathrm{Th}}) \tag{4.3}$$

Generally, V_{Th} is a voltage that counteracts the applied field V_{GS} between the source and the gate, representing the minimal voltage required for opening of the channel in the channel region.

Figure 4.3a is "output characteristic" of OFETs, where the gate–source potential is fixed and the drain current is increasing under a negative drain–source voltage. When $V_{\mathrm{DS}} < |V_{\mathrm{GS}} - V_{\mathrm{Th}}|$, as shown in Fig. 4.3b, the drain current is linearly increasing under the application of the drain–source voltage. When the magnitude of V_{DS} reaches that of V_{GS}, the two interacting potentials will cause a change of the channel, and threshold voltage acts as an important role on this transition. At the critical point of $V_{\mathrm{DS}} = |V_{\mathrm{GS}} - V_{\mathrm{Th}}|$, the free carriers in the region near the drain are depleted (Fig. 4.3c). A saturation of I_{D} occurs during further increase of V_{DS}, resulting in a enhanced depletion region at the side of drain (Fig. 4.3d), leading to the saturation regime. During this process, the I_{D} created by the mobile charges between the source and drain electrodes can be described as Eq. (4.4)

$$I_{\mathrm{D}} = \mu Q W E_x, \quad E_x = -\frac{dV}{dx} \tag{4.4}$$

where E_x is the electric field in the direction of current flow, W is the channel width, and μ is the charge-carrier mobility. The μ is charge-carrier mobility, representing the measure of how quickly charge carriers move in response to an external electric
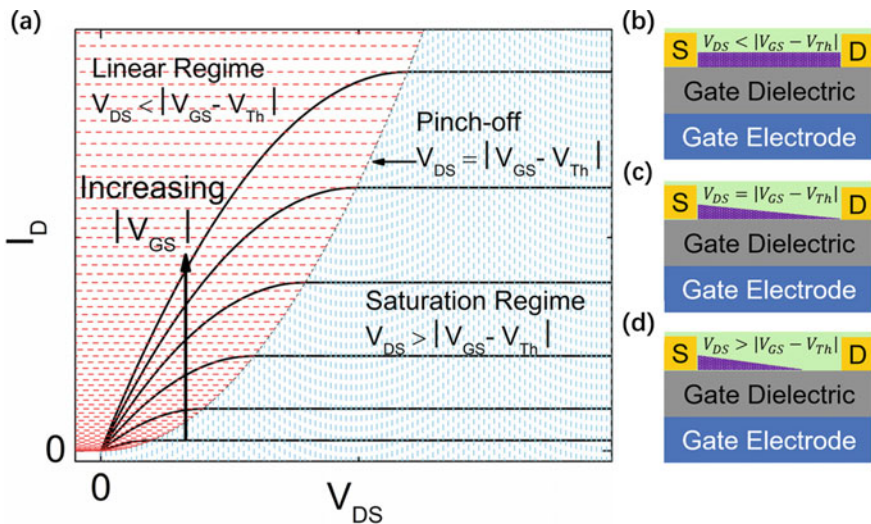
Fig. 4.3 a Ideal OFET output characteristics, b–d BGBC structures with the conduction channel in purple, (b) in the linear regime, (c) at pinch-off, and (d) in the saturation regime. Figures are adapted from Ref. [9] Copyright 2019, AIP publishing

field. The relation between μ and voltages in OFET can be observed from Eq. (4.5) by substituting Eq. (4.3):

$$I_D dx = W\mu C_{\text{diel}}(V_{\text{GS}} - V(x) - V_{\text{Th}})dV \qquad (4.5)$$

Assuming that the μ is independent from the applied electric field, integrating Eq. (4.5) along the channel from $x = 0$ to the channel length L, and from $V = 0$ to V_{DS} as such

$$\int_0^L I_D dx = W\mu C_{\text{diel}} \int_0^{V_{\text{DS}}} (V_{\text{GS}} - V(x) - V_{\text{Th}})dV \qquad (4.6)$$

results in

$$I_{D,\text{lin}} = \frac{W}{L}\mu C_{\text{diel}}\left[(V_{\text{GS}} - V_{\text{Th}})V_{\text{DS}} - \frac{1}{2}V_{\text{DS}}^2\right] \qquad (4.7)$$

Equation (4.7) is valid in the linear regime. However, as shown in Fig. 4.3a, the drain current in the linear and saturation regimes will follow different relations due to the pinch-off at saturation which results in an effective maximum drain–source voltage of $V_{\text{DS}} = V_{\text{GS}} - V_{\text{Th}}$. Saturation drain current is given by substituting this equation for V_{DS} into Eq. (4.8):

$$I_{D,\text{sat}} = \frac{W}{2L}\mu C_{\text{diel}}(V_{\text{GS}} - V_{\text{Th}})^2 \qquad (4.8)$$

Equations (4.7) and (4.8) are commonly used equations for characterization and expressing the behavior of OFETs. The voltage dependence drain–source current is usually described by transfer characteristics ($I_D - V_{\text{GS}}$ dependence for constant V_{DS}) or output characteristics ($I_D - V_{\text{DS}}$ dependence for constant V_{GS}) as depicted in Figs. 4.3a and 4.4, respectively.

4.2.3 Characterization of OFET Device

4.2.3.1 Charge-Carrier Mobility

Characterization of the performance of OFETs requires the evaluation of specific electrical properties and parameters. The charge-carrier mobility of OFETs, representing the speed (cm s^{-1}) at which the charge carriers move in organic semiconductors under an applied electric field (V cm^{-1}), can be calculated from the relationship between I_D and V_{GS}. The main characterizations for OFETs include the output characteristics in Fig. 4.3a and transfer characteristics in Fig. 4.4. The black curves in Fig. 4.4a, b show the drain current on a logarithmic scale as a function of V_{GS} with
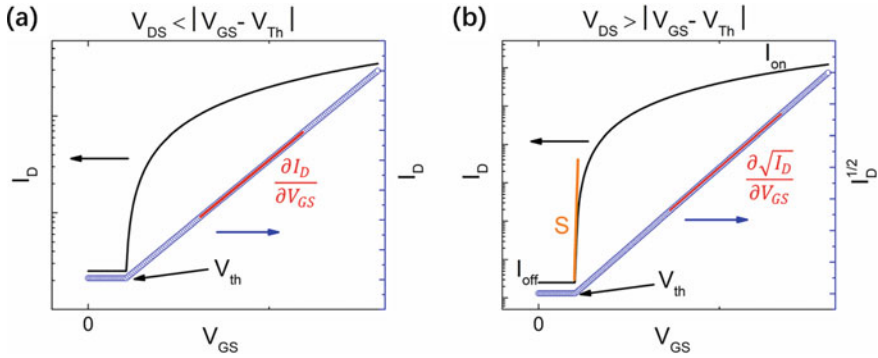
Fig. 4.4 Evolution of I_D at fixed, negative, V_{DS} as a function of increasingly negative V_{GS} in **a** the linear regime and **b** the saturation regime. Figures are adapted from Ref. [9]. Copyright 2019, AIP publishing

V_{DS} held constant in the linear and saturation regimes, respectively. In blue, Fig. 4.4a, b show the I_D on a linear scale and the square root of I_D on a linear scale, respectively. This type of characterization is known as the "transfer characteristics." For the linear regime, the charge-carrier mobility is calculated from the slope in Fig. 4.4a, which is $\partial I_D / \partial V_{GS}$. From the slope of the red line in Fig. 4.4b, the μ is $\partial \sqrt{I_D}/\partial V_{GS}$ for the saturation regime. Then, taking the derivative with respect to V_{GS} and rearranging Eqs. (4.7) and (4.8) gives the following equation for the investigation of the μ in the linear and saturation regimes, respectively,

$$\mu_{\text{lin}} = \frac{L}{C_{\text{diel}} W V_{DS}} \frac{\partial I_D}{\partial V_{GS}}, \tag{4.9}$$

$$\mu_{\text{sat}} = \frac{2L}{W C_{\text{diel}}} \left(\frac{\partial \sqrt{I_D}}{\partial V_{GS}} \right), \tag{4.10}$$

In principle, the values of μ_{lin} and μ_{sat} are identical in ideal OFET devices. However, the real devices with contact resistance exhibit lower value of μ_{lin} than that of μ_{sat}. Any resistance at the contacts will result in a reduced effective V_{DS}.

4.2.3.2 Threshold Voltage

Another important value which can be extracted from Fig. 4.4 is the threshold voltage, V_{Th}, which is calculated by finding the intercept of $I_D = 0$ and the red line [11]. Transfer characteristics and Eq. (4.8) can be used to estimate the value of V_{Th}. Furthermore, it provides an indication of the threshold voltage that is reasonable in the estimation of current (i.e., V_{GS} needs to exceed V_{Th} to open the channel and transport charge carriers). As mentioned in last section, V_{Th} is an indication of trap states in the semiconductor layer. Those traps are first filled by the applied $V_{GS,}$ and

then, free charge carriers contribute to the drain current. In some special cases, small amounts of dopants in the semiconductor and surface dipoles can result in a positive V_{Th} wherein the device is already "on" at $V_{GS} = 0$ V and requires a positive V_{GS} to reach the "off" state. In most cases, the density of trap states is inversely correlated with temperature (unless the dielectrics of device exhibit a dielectric constant which is variable with temperature, such as ferroelectrics), [12, 13] and thus, V_{Th} is dependent on temperature, allowing an estimation of the density of interfacial trap states, N_{it}, through measurements at varying temperature and application of the below equation [14].

$$N_{it} = \frac{C_{diel}}{k_B q} \frac{\partial V_{Th}}{\partial T} \tag{4.11}$$

where k_B is Boltzmann's constant, T is the temperature, and q is the elementary charge.

4.2.3.3   Subthreshold Swing

In addition to the threshold voltage, another presence of charge traps can be indicated by another parameter called subthreshold swing (S), which is presented as the inverse slope of the orange line in Fig. 4.4b. When the gate–source voltage V_{GS} is below the threshold voltage V_{Th}, the OFET channel should be closed with no current flow. However, a small current can still be recorded, which is called the subthreshold current. The subthreshold region plays a particularly important role in device performance since it indicates transition behaviors when switching from the off state to the on state, meaning how rapidly I_D increases with V_{GS} at fixed V_{DS}, and the slope of the drain–source current is defined as subthreshold slope. Usually, a high subthreshold slope suggests a good application prospect for devices. S has units of V/decade and shows the increase in V_{GS} to cause an I_D increase

$$S = \frac{\partial V_{GS}}{\partial \left(\log_{10}(I_D) \right)} \tag{4.12}$$

S is determined by the trap states on interface, and the gate dielectric is defined in the following equation:

$$S = \frac{k_B T \ln(10)}{q} \left(\frac{N_{it} q^2}{C_{diel}} + 1 \right) \tag{4.13}$$

When the first term in Eq. (4.13) tends to zero, the smaller the value of S, the sharper turn-on of the device. Hence, the presence of charge traps will increase the subthreshold swing (decreasing subthreshold slope).

4.2.3.4   On/Off Ratio

Besides the subthreshold swing, the on/off ratio, representing the ratio between the "on" current (I_{on}) and "off" current (I_{off}), is also used for characterization of the switching capabilities of OFET (Fig. 4.4). A large on/off ratio is good for OFET devices, which means that the "on" state and the "off" state can be clearly distinguished. In other technologies, in order to minimize the value of I_{off}, the selection of dielectric material and processing the semiconductor and the gate electrode are very important. I_{on} is determined by the many parameters such as the operating voltages, the mobility of the semiconductor, the capacitance of the gate, and the trap density at the interface of semiconductor and dielectric.

In summary, the abovementioned mobility, threshold voltage, subthreshold swing, and the on/off ratio are the most basic parameters for estimation of OFET performances. A high mobility is a symbolization of good performance since its value dictates the applications of OFETs. The on/off ratio should be maximized since a clear difference between the "on" state and the "off" state is crucial for an OFET device to realize an on/off switch: An ideal on/off value is above 10^6. The value of threshold voltage determines the operating voltages of an OFET device. A cost-efficient OFET should minimize its V_{Th} value. The value of S indicates switching speed of the device. The value of subthreshold swing should be lower than $1\ V\ dec^{-1}$, which is essential to many applications. Some high-performance devices even delivered an S value less than $0.5\ V\ dec^{-1}$. In order to obtain a OFET device with high performance, development of organic semiconductors with high mobility and optimization of device is important. Various materials have been developed for improving the performance of OFETs.

4.3   Organic Semiconductors for OFETs

After decades of development of material research and fabricating process, OFET devices with rapidly improving performance have been reported and the carrier mobility records have been refreshing year after year. The thriving development of mobility has been observed from $10^{-5}\ cm^2\ V^{-1}\ s^{-1}$ as originally reported for polythiophene (P3HT) in 1986 to over $20\ cm^2\ V^{-1}\ s^{-1}$ recently, even surpassing those of amorphous silicon devices.

Organic semiconductors in OFETs are basically classified into two broad categories: small molecules and polymers. Small molecules are oligomers made up of a finite number of conjugated monomer units, while polymers consist of several conjugated monomer units forming long chains and sometimes more complicated structures. Processability and properties of polymers are determined by their structure of the fundamental repeating monomer units. Moreover, these materials for OFETs can be further subclassified as p-type, n-type, and ambipolar materials, depending

on the type of charge carriers that they predominantly transport. The n-type (p-type) materials have significantly higher electron (hole) mobility than the hole (electron) mobility. Ambipolar materials have comparable values of electron and hole mobilities. Some materials show different charge transport properties in different conditions. For instance, pentacene exhibits p-type conductivity in ambient conditions, while ambipolar behavior is possible in vacuum [15]. Furthermore, the devices with ambipolar charge transport require electrodes sufficiently matching with charge transport energy levels. This section will provide a brief overview on the evolution and highlight the milestone developments of materials for the semiconductor layer in OFETs.

4.3.1   Small Molecule Organic Semiconductors

In addition to polymers, small organic molecules with definite chemical structures show certainties in some inherent properties, such as the energy of the HOMO and the LUMO. Unlike polymers, small organic molecules do not need to endure complex conformational or energy disorders caused by intrachain or interchain interactions [9, 16, 17]. Therefore, small molecular chains have relatively determined crystal structures. Thus, the films treated with small molecules always have high crystallinity. In addition, small molecules can obtain ultrahigh purity single crystals and low trap density, indicating that the improvement of carrier mobility is strongly affected by the crystallinity, defects, and traps of the film [18].

In terms of preparation approaches, organic small molecule films can be deposited by thermal evaporation. Because small molecules have the same molecular structure and crystal structure, the thermodynamic properties of their materials are certain and even predictable [19, 20]. Therefore, the processing conditions during the evaporation of organic small molecules can be accurately controlled, and the growth rate and film thickness can be monitored and tracked in real time. The good evaporation performance of small organic molecules enables the formation of organic semiconductor films with optimized morphology and uniformity, which suppresses the uncertainty of device performance caused by poor film quality, even though the problems of surface roughness and the formation of polymorphs occur during the evaporation process [21, 22].

We also divide organic small molecule OFET materials into 3 types: p-type, n-type, and ambipolar. It should be noted that the ambipolar or n-type behavior is usually observed only in inert condition, while small molecules prefer p-type conductivity in ambient environment [23]. The most common p-type small molecule organic semiconductors in OFETs are based on polyacenes and heteroacenes; those molecules as function of OFET channel that have gained a lot of attention are shown in Fig. 4.5. In 1997, OFETs based on pentacene films achieved a mobility beyond that of amorphous silicon (0.5 cm^2 V^{-1} s^{-1}), which can be considered as the first milestone of small molecule materials [24]. The solubility of pentacene can be improved by introducing triisopropyl-silylethynyl (TIPS) groups

onto the pentacene molecule structure, which enables solution processing of small molecule devices [25]. In the early 2000s, rubrene [26] and copper phthalocyanine (CuPc) were frequently studied. The second breakthrough occurred when rubrene microcrystals with a high degree of molecular ordering and low densities of defects boosted the mobility of device to more than 20 cm^2 V^{-1} s^{-1} in 2004 [27]. In recent years, a new series of p-type organic small molecule semiconductors have been developed. Some of the representatives include 2,7-dioctyl[1]benzothieno[3,2-b][1]benzothiophene (C8-BTBT), [28] dinaphtho[2,3-b:20,30-f]thieno[3,2-b]thiophene (DNTT), [29] 2,7-dihexyl-dithieno[2,3-d;20,30-d0]benzo[1,2-b;4,5-b0]dithiophene (DTBDT-C6), [30] 3,11-dioctyldinaphtho[2,3-d:20,30-d0]benzo[1,2-b;4,5-b0]dithiophene (C$_8$-DNBDT-NW), [31] and 2,8-difluoro-5,11-bis(triethylsilylethynyl)anthradithiophene (diF-TES-ADT) [32]. It has been noticed that these materials with high performance all have a fused benzene-thiophene structure. This is because thiophene ring is a strong electron donor, which makes the molecule have higher p-type conductivity.

Compared to p-type counterparts, n-type organic small molecules with both high performance and stability are not easy to be found. That is because the high LUMO energy of organic semiconductors is not easy for electron injection, and traps are caused by oxygen and water in ambient air, thus suppressing the electron transport [33, 34]. The other reason is that, high work functions of the commonly used, air-stable metals result in a high Schottky barrier between the metal/semiconductor contacts, which are not appropriate for electron injection. In order to realize OFETs with n-type materials, researchers have been trying to synthesize materials with low LUMO level to make them consistent with the work function of air-stable metals. Fullerenes and their derivatives phenyl C61 methyl butyrate (PCBM) have high electron affinity and can be used to prepare n-channel transistors with high electron mobility [35, 36]. By addition of strong electron absorbing groups to the core of small molecules, the electron affinity is able to be dramatically improved. Naphthalene tetracarboxylic diimide (NTCDI) and its derivatives [37, 38] and perylene tetracarboxylic diimide (PTCDI) and its derivatives [39–43] are some examples of functionalized small molecules, which have been proved to be stable n-type materials.

4.3.2 Polymer Organic Semiconductors

Polymer-based organic semiconductor is another category in OFET materials. Polymers usually exhibit low crystallinity and poor performance compared with small molecule semiconductors.

For p-type polymers, most solution-processable materials incorporated in OFETs are based on polythiophenes, as shown in Fig. 4.6. Alkyl substituted polythiophenes such as the classical poly (3-hexyl thiophene) (P3HT) [44]. have delivered hole mobilities over 0.1 cm^2 V^{-1} s^{-1}. Other alkyl-substituted polythiophenes such as poly(2,5-bis(3-alkylthiophen-2-yl)thieno[3, 2-b]thiophene (PBTTT) and poly(3,3000-didodecylquaterthiophene) (PQT-12) [45] also show hole mobilities
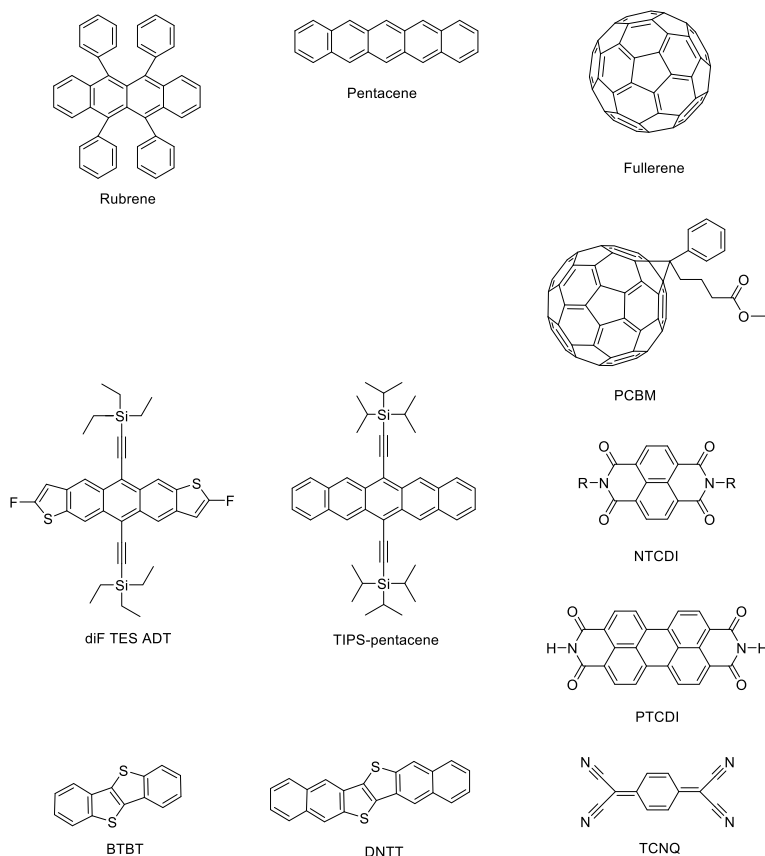
Fig. 4.5 Chemical structures of small molecules in OFETs

higher than 0.1 cm^2 V^{-1} s^{-1}, combining with good solution processability and stability.

Recently, the performance of polymer-based OFETs is reaching that of small molecules with high molecular crystals. Over 10 cm^2 V^{-1} s^{-1} of mobility has been achieved by diketopyrrolopyrrole (DPP)-based polymers after engineering side chains [46]. Luo et al. used the polymer poly[4-(4,4-dihexadecyl-4H-cyclopenta[1,2-b:5,4-b0]dithiophen-2-yl)-alt-[1,2,5]thiadiazolo-[3,4-c]pyridine] (PCDTPT) to deliver hole mobilities over 36 cm^2 V^{-1} s^{-1} [47]. One example of n-type polymers for OFETs is poly(benzimidazobenzophenanthroline) (BBL) with electron mobilities of 0.1 cm^2 V^{-1} s^{-1} [48]. A selenophene containing polymer PNBS was used to fabricate a n-type OFET with electron mobilities higher than 8.5 cm^2 V^{-1} s^{-1} [49].

Donor–acceptor copolymers polymerized by two or more oligomers have become a new category of polymer-based OFET materials. Despite the lack of long-range
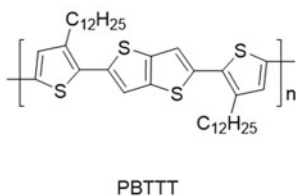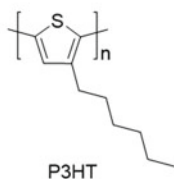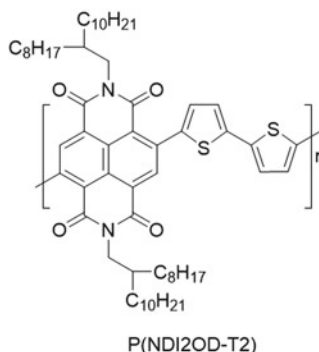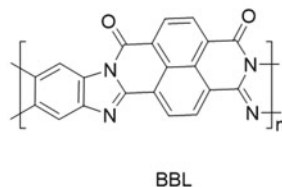
Fig. 4.6 Chemical structures of polymers in OFETs

order, the properties of these polymers are better than some highly ordered semiconductor polymers synthesized at present. For instance, copolymer cyclopentadithiophene and benzothiadiazole (CDT-BTZ) achieved hole mobilities as high as 3.5 cm^2 V^{-1} s^{-1} [50]. In addition, C$_{20}$CDT-BTZ delivered hole mobilities of 8.4 cm^2 V^{-1} s^{-1} [51]. Other types of copolymers such as isoindigo (IID) and indacenodithiophene (IDT) [52] and indacenodithiophene–benzothiadiazole copolymer (IDT-BT) [53] can realize hole mobilities of 3.6 cm^2 V^{-1} s^{-1} 14.4 cm^2 V^{-1} s^{-1} [54], respectively. One of the classical n-type polymers (PNDI2OD-T2) has achieved electron mobilities close to 1 cm^2 V^{-1} s^{-1} [34], and p2FIId-2FBT shows an electron mobilities of 9.7 cm^2 V^{-1} s^{-1} [55].

4.4 Strategies for Better Performance of OFET

This article will discuss general strategies and recent studies in OFET performance enhancement. The factors for high-performance OFETs mainly include molecular design of organic semiconductors, fabrication strategy, and interface engineering.

4.4.1   Material Design for High-Performance OFETs

It is imperative to process the OFETs with solution-based techniques and, hence, to develop what is known as printed electronics. Here, we introduce the recent advances in high-performance organic semiconductors, including small molecules, p-type, ambipolar, or n-type polymers. Backbone planarity and energy levels are the key factors for high-performance OFETs.

4.4.1.1   Small Molecules

Compared to polymers, solution-processable small molecules have unique advantages, including high purity, massive and repeatable production, and feasible structure modification. Hence, they have played important roles in designing and developing high-performance OFETs. Many small molecules exhibit very impressive charge-carrier mobilities. Among those small molecules, a versatile strategy for acquiring high-performance small molecule-based OFETs is synthesizing molecules with large planarity [56]. For instance, benzothiophene (BTh) [30] and diben-zothiophene (DBTh) [57] fused heterocyclic derivatives have been studied due to their high stability and hole mobility. In addition to the main backbone, side chain determines solubility, molecular packing, polarity, and film forming properties of organic semiconductors; thus, the side chain engineering is also important for OFET performance. Among those properties, molecular packing is greatly affected by alkyl chain length and branching point position. For example, Minari et al. [58] studied the alkyl chain length dependence of OFET performance. Compared to branched alkyl chains, linear alkyl chains generally promote closer molecular packing due to interchain interdigitation [59].

4.4.1.2   Polymers

High-performance p-type polymers have several common characteristics: high molecular weight (Mn), good main chain conjugation and coplanarity, and appropriate HOMO and LUMO energy levels. Polymers with high molecular weight also accompanied with high crystallinity and high connection between domains, thus resulting in an increased mobility [60, 61]. However, high molecular weight also means low solubility in organic solvent and increased difficulty in device fabrication. Therefore, under the condition of ensuring solubility, high molecular weight is an effective way to improve mobility. The conjugation of the main chain of polymers depends on the specific molecular structure and its coplanarity, which is similar to small molecules. Enhanced coplanarity will lead to more effective backbone conjugation and tighter π–π stacking, thereby improving mobility [62]. For unipolar p-type polymers, the HOMO of polymer should be aligned with the work function of

electrode [63]. At the same time, the LUMO level should block the electron injection of the electrode [64]. Furthermore, polymer films with high crystallinity and interconnected morphology are crucial to achieve high mobility. The introduction of hyperbranched, long linear, or spacer side chains can improve the crystallinity and achieve significant properties [46, 52, 65, 66]. Well-aligned films can be obtained through unique device manufacturing technology, which will be discussed in the next section.

Compared to p-type OFETs, the n-type polymer OFETs are suffering from low electron mobility and poor device stability. The LUMO energy level of most D-A polymers is far from that of electrode work function. Therefore, lowering the LUMO level of polymer is the key approach to realize n-type or ambipolar molecule-based OFETs. The lowered LUMO level promotes effective electron injection and improves the oxidation resistance of the device. Two strategies are used to reduce the LUMO energy level. The first is to introduction of EWGs into the backbone of polymers. The second strategy is called receptor dimerization [67]. This strategy introduces acceptor dimers which exhibits strong electron-withdrawing ability. In addition, side chain engineering is another approach to modify the energy level of n-type polymers [68, 69]. As for the device stability, it is important to significantly reduce lowering the energy level of LUMO. Furthermore, the realization of highly crystalline polymers is a feasible method to improve the mobility and stability of devices at the same time.

4.4.2 Fabrication Strategy

The technology of depositing materials selected in the fabrication process plays a crucial role in determining the performance of different OFETs, even though similar materials are used to process them. The main fabrication techniques for OFET can be classified as electron-beam/thermal vacuum evaporation [70], liquid deposition [71], and thin-film alignment [2, 72–74].

4.4.2.1 Vacuum Evaporation

It has been mentioned that the semiconductor film deposited by vacuum evaporation results in a superior charge-carriertransport property. [19, 20] In principle, high molecular weight organic semiconductors cannot be deposited by this way. The performance of an OFET primarily depends on the purity of organic material, substrate cleaning, and the rate of deposition. The mean free path of organic semiconductor particles and occurrence of redundant molecules near the substrate play a crucial role in achieving a high-performance film. Vacuum deposition techniques are advantageous in terms of achieving highly ordered films with a precise control on the thickness. Its major deficiency is that it requires complicated instruments. This is different with the solution processing technique which is simple and low cost.

4.4.2.2 Liquid Deposition

Liquid deposition process is beneficial in realizing large-area electronic circuits at considerably low temperature and, therefore, at lower cost too. The common deposition methods such as spin-coating, drop-casting, dip-coating, spray-coating, and roll coating techniques are regularly used cost-effective techniques [75].

Spin-coating is the most commonly used method for depositing organic semiconductors with uniform thickness. The modification of traditional spin-coating has been used to prepare devices with high performance, for example, using the "off-center" method through placing the substrate for processing 20–40 mm away from the central rotation axis [76].

Drop-casting refers to casting an organic semiconductor solution and then evaporating the solvent to precipitate and deposit a single crystal or film. For semiconductors with strong self-organization behavior, single crystals can be obtained directly by drop-casting or another recrystallization process. An improved drop-casting method is drop pinning [75]. In the case of drop-casting with nails, the solution droplets cannot move on the substrate, and the decay of the contact line becomes regular, resulting in stable and uniform deposition [77].

Printing comprises a family of techniques and can simultaneously deposit and pattern a target material. This technique mainly contains ejected drop printing, contact stamp printing, indirect and offset printing methods, and capillary stylus dispensing. The advantages and disadvantages of those techniques have been reported by some comprehensive reviews [75, 78].

4.4.2.3 Thin-Film Alignment

Since charge carriers are preferentially transported along the π–π stacking direction in organic semiconductors, macroscopically aligned organic films have potentially higher mobilities and provide more unusual properties, such as optically and electrically anisotropic characteristics. Therefore, many deposition techniques have been investigated for patterning and alignment of organic semiconductors [78]. Those techniques include (i) mechanical forces alignment, such as friction-transfer, nanoimprinting, and the Langmuir–Blodgett (LB) technique; (ii) depositing the organic semiconductors directly on the alignment layers prepared by different methods, such as rubbing and photoirradiation; (iii) growing the organic semiconductors on inorganic single crystals; (iv) using magnetic or electric field-induced alignment; and (v) using solution-processed technique to align organic semiconductors on isotropic substrates.

Some of those methods have been used to overcome issue of the traditional spin-coating and drop-casting techniques, which are not able to control the thin-film orientation. Zone-casting uses a nozzle to deposit a continuously supplied hot solution onto a moving, thermally controlled support. Thus, a stationary gradient of concentration is formed within the meniscus, which gives rise to directional crystallization [79]. Dip-coating can be controlled by the substrate lift rate, solvent evaporation,

and capillary flow, which is able to give a better thin-film alignment [80, 81]. In addition, solution-sheared deposition such as doctor blading and slot-die coating can deposit highly crystalline and aligned thin films on isotropic substrates [82]. Those techniques save raw materials and control film uniformity reliably, accurately, and reproducibly [83].

4.4.3 Interface Engineering

In order to improve the performance of devices and even build new functions, interface engineering is currently a research hotspot. Generally speaking, the interface in the semiconductor layer contains traps, grain boundaries, and other defects, which provide scattering points for carriers and are facilitated to charge transmission [84]. In order to obtain high-quality thin films, several strategies have been developed to provide OFET that can be used to build future OFET-based integrated devices.

Semiconductor/electrode interface is the most discussed interface in OFETs, which is the key interface for determination of charge-carrier injection and extraction [85–87]. The charge insertion layer (CIL) or self-assembled monolayer (SAM) was introduced to modify metal electrodes. By fine tuning the charge injection barrier on the interface, the contact resistance between the semiconductor and the electrode can be significantly reduced, thus improving the performance of the device.

In improving the efficiency of hole/electron injection, the modification of CIL has attracted more and more attention. Various materials such as inorganic compounds (metal oxides and inorganic salts) and organic compounds (small molecules and polymers) have been used as CILs. Metal oxides CILs have wide range of work functions [88]. Especially in transition metal oxides, their working functions range from very low (around 3 eV for ZrO_2) to significantly high (around 7 eV for V_2O_5), which is suitable for modifying the energy levels matched by different metals [89]. The mechanism of metal salts is similar to that of metal oxides. One of the advantages of metal salts is that they are compatible with solution preparation. Small organic molecules as CILS cause direct charge transfer at the interface between organic CILS and semiconductors, which helps to reduce the contact resistance through additional interface dipoles. Organic polymers with dipolar groups can also be used as electrode surface modifiers to realize low work function electrodes [85, 90]. Polyelectrolytes, including groups that can carry cations or anions, have recently proved to be a promising CIL that can achieve ohmic contact (3.0–5.8 eV) with a wide range of working functions [85].

SAMs were applied for modification of electrodes and dielectrics in OFETs. SAMs for electrodes are not only for surface property modification [91, 92] but also providing more functionalities [92, 93]. Commonly used SAM molecules are thiol derivatives, which form metal–sulfur interactions through the sulfur lone-pair electrons. The structure of thioketone is similar to pentacene. Before pentacene deposition, thioketone was used to modify Au electrode, which led to the complementary surface of pentacene growth and reduced contact resistance [94]. In addition,

dithiocarbamate-based molecules have been observed to be able to stably attached on metals under different environmental conditions [95] and could reduce the work function of precious metals (Au and Ag) to an ultralow value [96]. Recently, as a multifunctional surface modification material, N-heterocyclic carbene shows high stability [97, 98].

Apart from those strategies above, there is still much room to develop effective surface modification methods to optimize the surface of flexible substrates and improve device performance.

4.5 Summary and Outlook

During the past several years, the field of OFET has seen much progress based on. Both small molecule and polymer FETs have achieved mobilities of more than 10 cm^2 V^{-1} s^{-1}. The small molecule with large planarity forms semiconductor layers with high crystallinity. Backbone and side chain determine solubility, molecular packing, polarity, and film forming properties of small molecules. In order to improve the performance of bipolar or n-type polymers, several effective strategies have been adopted, including EWG substitution, receptor dimerization, and side chain engineering. In order to realize the solution processability of organic semiconductors, many preparation technologies have been developed. Printing technology is a promising manufacturing technology, which has the advantages of low cost, high efficiency, easy to be fabricated on a large area of substrate, and so on.

On the other hand, the commercialization of OFET still needs to solve some problems. For example, according to the current strategy, achieving large-scale production of semiconductor polymers is still a challenge. In addition, a general standard for understanding the charge transport mechanism and obtaining accurate mobility should be developed. Moreover, it is necessary to realize ambipolar or n-type OFET devices with high mobility and stability, which are compatible with p-type devices in application. Similarly, it is still challenging for using printing technology to fabricate films with high resolution, submicron pattern, and large-area uniformity.

Although there are still some problems with OFETs, they have indeed made great contributions to the development of organic electronics. It is very attractive to solve the implementation of processable and flexible OFET devices. While solving these remaining problems, OFET finally brings bright prospects for organic electronics.

References

1. Bao Z, Locklin J (2007) Organic field-effect transistors. Bova Raton, FL, USA
2. Horowitz BG (1998) Organic field-effect transistors. Adv Mater 365–377
3. Paterson AF, Singh S, Fallon KJ et al (2018) Recent progress in high-mobility organic transistors: a reality check. Adv Mater 30:1801079

4. Sirringhaus H (2014) 25th anniversary article: organic field-effect transistors: the path beyond amorphous silicon. Adv Mater 26:1319–1335

5. Baeg KJ, Caironi M, Noh YY (2013) Toward printed integrated circuits based on unipolar or ambipolar polymer semiconductors. Adv Mater 25:4210–4244

6. Fukuda K, Takeda Y, Yoshimura Y et al (2014) Fully-printed high-performance organic thin-film transistors and circuitry on one-micron-thick polymer films. Nat Commun 5:5–12

7. Yao Y, Dong H, Hu W (2016) Charge transport in organic and polymeric semiconductors for flexible and stretchable devices. Adv Mater 28:4513–4523

8. Yan Y, Zhao Y, Liu Y (2021) Recent progress in organic field-effect transistor-based integrated circuits. J Polym Sci 60:1–17

9. Phys JA, Jurchescu OD (2019) Tutorial: organic field-effect transistors: materials, structure and operation. J Appl Phys 124:071101

10. Eslamian M (2017) Inorganic and organic solution-processed thin film devices. Nano-Micro Lett 9:3

11. Boudinet D, Le BG, Serbutoviez C (2018) Contact resistance and threshold voltage extraction in-channel organic thin film transistors on plastic substrates thin film transistors on plastic substrates. J Appl Phys 084510:084510

12. Senanayak SP, Guha S, Narayan KS (2012) Polarization fluctuation dominated electrical transport processes of polymer-based ferroelectric field effect transistors. Phys Rev B 85:115311

13. Laudari A, Guha S (2015) Polarization-induced transport in ferroelectric organic field-effect transistors. J Appl Phys 117:105501

14. Smith J, Hamilton R, Qi Y et al (2010) The influence of film morphology in high-mobility small-molecule : polymer blend organic transistors. Adv Funct Mater 20:2330–2337

15. Schidleja M, Melzer C, von Seggern H (2009) Electroluminescence from a pentacene based ambipolar organic field-effect transistor. Appl Phys Lett 94:123307

16. Schweicher G, D'Avino G, Ruggiero MT et al (2019) Chasing the "Killer" phonon mode for the rational design of low-disorder, high-mobility molecular semiconductors. Adv Mater 31:1902407

17. Lazzaroni R, Sirringhaus H, Beljonne D et al (2019) Resilience to conformational fluctuations controls energetic disorder in conjugated polymer materials: insights from atomistic simulations'. Chem Mater 31:6889–6899

18. Jurchescu OD, Baas J, Palstra TTM (2004) Effect of impurities on the mobility of single crystal pentacene. Appl Phys Lett 84:3061

19. Hilal SH, Karickhoff SW (2003) Prediction of the vapor pressure boiling point, heat of vaporization and diffusion coefficient of organic compounds & combinatorial. Science 22:565–574

20. Yakubovich AV, Son WJ, Kwon O et al (2020) Accurate vapor pressure prediction for large organic molecules: application to materials utilized in organic light-emitting diodes. J Chem Theory Comput 16:5845–5851

21. Mattheus CC, Dros AB, Baas J et al (2003) Identification of polymorphs of pentacene. Synth Matals 138:475–481

22. Mattheus CC, Dros AB, Baas J et al (2001) Polymorphism in pentacene. Org Compd 17:939–941

23. You A, Be MAY, In I (2006) Ambipolar organic field-effect transistors based on rubrene single crystals. Appl Phys Lett 88:033505

24. Lin Y, Gundlach DJ, Nelson SF, Jackson TN (1997) Stacked pentacene layer organic thin-film transistors with improved characteristics. 18:606–608

25. Anthony JE, Brooks JS, Eaton DL et al (2001) Functionalized pentacene : improved electronic properties from control of solid-state order. J Am Chem Soc 123:9482–9483

26. Podzorov V, Pudalov VM, Gershenson ME (2003) Field-effect transistors on rubrene single crystals with parylene gate insulator. Appl Phys Lett 82:1739–1741

27. Podzorov V, Menard E, Borissov A et al (2004) Intrinsic charge transport on the surface of organic semiconductors. Phys Rev Lett 93:086602

28. Ebata H, Izawa T, Miyazaki E et al (2007) Highly soluble [1]benzothieno[3,2-b]benzothiophene (BTBT) derivatives for high-performance, solution-processed organic field-effect transistors. J Am Chem Soc 129:15732–15733
29. Yamamoto T, Takimiya K (2007) Facile synthesis of highly π-extended heteroarenes, application to field-effect transistors. J Am Chem Soc 129:2224–2225
30. Gao P, Beckmann D, Tsao HN et al (2009) Dithieno[2,3-d;2′3′-d′]benzo[1,2-b;4,5-b′] dithiophene (DTBDT) as semiconductor for high-performance, solution-processed organic field-effect transistors. Adv Mater 21:213–216
31. Mitsui C, Okamoto T, Yamagishi M et al (2014) High-performance solution-processable N-shaped organic semiconducting materials with stabilized crystal phase. Adv Mater 26:4546–4551
32. Subramanian S, Sung KP, Parkin SR et al (2008) Chromophore fluorination enhances crystallization and stability of soluble anthradithiophene semiconductors. J Am Chem Soc 130:2706–2707
33. Zaumseil J, Sirringhaus H (2007) Electron and ambipolar transport in organic field-effect transistors. Chem Rev 107:1296–1323
34. Yan H, Chen Z, Zheng Y et al (2009) A high-mobility electron-transporting polymer for printed transistors. Nature 457:679–686
35. You A, Be MAY, In I (2006) Fabrication and characterization of film transistors with high field-effect mobility. 4581:80–83
36. Chikamatsu M, Nagamatsu S, Yoshida Y et al (2005) Solution-processed n-type organic thin-film transistors with high field-effect mobility. Appl Phys Lett 87:1–3
37. Dewetting G (2000) A soluble and air-stable organic semiconductor with high electron mobility 404:478–481
38. Katz HE, Johnson J, Lovinger AJ, Li W (2000) Naphthalenetetracarboxylic diimide-based n-channel transistor semiconductors: structural variation and thiol-enhanced gold contacts. J Am Chem Soc 122:7787–7792
39. Jones BA, Ahrens MJ, Yoon MH et al (2004) High-mobility air-stable n-type semiconductors with processing versatility: Dicyanoperylene-3,4:9,10-bis(dicarboximides). Angew Chem—Int Ed 43:6363–6366
40. Weitz RT, Amsharov K, Zschieschang U et al (2009) The importance of grain boundaries for the time-dependent mobility degradation in organic thin-film transistors. Chem Mater 21:4949–4954
41. Schmidt R, Oh JH, Sen SY et al (2009) High-performance air-stable n-channel organic thin film transistors based on halogenated perylene bisimide semiconductors. J Am Chem Soc 131:6215–6228
42. Bao Z, Lovinger AJ, Brown J (1998) New air-stable n-channel organic thin film transistors. J Am Chem Soc 7863:207–208
43. Facchetti BA, Mushrush M, Katz HE, Marks TJ (2003) n-type building blocks for organic electronics. Adv Mater 15:33–38
44. You A, Be MAY, In I (1988) Field-effect mobility of poly (3-hexylthiophene). Appl Phys Lett 53:195
45. Ong BS, Wu Y, Liu P, Gardner S (2004) High-Performance semiconducting polythiophenes for organic thin-film transistors. J Am Chem Soc 126:3378–3379
46. Kang I, Yun H, Chung DS et al (2013) Record high hole mobility in polymer semiconductors via side- chain engineering. J Am Chem Soc 135:14896–14899
47. Luo C, Kyaw AKK, Perez LA et al (2014) General strategy for self-assembly of highly oriented nanocrystalline semiconducting polymers with high mobility. Nano Lett 14:2764–2771
48. Babel A, Jenekhe SA (2003) High electron mobility in ladder polymer field-effect transistors. J Am Chem Soc 125:13656–13657
49. Zhao Z, Yin Z, Chen H et al (2017) High-performance, air-stable field-effect transistors based on heteroatom-substituted naphthalenediimide-benzothiadiazole copolymers exhibiting ultrahigh electron mobility up to 8.5 cm V−1 s−1. Adv Mater 29:1602410

50. Tsao HN, Cho D, Andreasen JW et al (2009) The influence of morphology on high-performance polymer field-effect transistors. Adv Mater 21:209–212
51. Yamashita Y, Hinkel F, Marszalek T et al (2016) Mobility exceeding 10 cm^2/(V·s) in donor-acceptor polymer transistors with band-like charge transport. Chem Mater 28:420–424
52. Mei J, Kim DH, Ayzner AL et al (2011) Siloxane-terminated solubilizing side chains: bringing conjugated polymer backbones closer and boosting hole mobilities in thin-film transistors. J Am Chem Soc 133:20130–20133
53. Zhang X, Bronstein H, Kronemeijer AJ et al (2013) Molecular origin of high field-effect mobility in an indacenodithiophene- benzothiadiazole copolymer. Nat Commun 4:2238
54. Kim G, Kang SJ, Dutta GK et al (2014) A thienoisoindigo-naphthalene polymer with ultrahigh mobility of 14.4 cm^2/V·s that substantially exceeds benchmark values for amorphous silicon semiconductors. J Am Chem Soc 136:9477–9483
55. Yang J, Zhao Z, Geng H et al (2017) Isoindigo-based polymers with small effective masses for high-mobility ambipolar field-effect transistors. Adv Mater 29:1702115
56. Tang ML, Okamoto T, Bao Z (2006) High-Performance organic semiconductors: asymmetric linear acenes containing sulphur. J Am Chem Soc 128:16002–16003
57. Yamamoto T, Nishimura T, Mori T et al (2012) Largely π-extended thienoacenes with internal thieno[3,2-b]thiophene substructures: synthesis, characterization, and organic field-effect transistor applications. Org Lett 14:4914–4917
58. Minari T, Miyata Y, Terayama M et al (2006) Alkyl chain length dependent mobility of organic field-effect transistors based on thienyl-furan oligomers determined by the transfer line method. Appl Phys Lett 88:083514
59. Lim B, Baeg KJ, Jeong HG et al (2009) A new poly(thienylenevinylene) derivative with high mobility and oxidative stability for organic thin-film transistors and solar cells. Adv Mater 21:2808–2814
60. Tsao HN, Cho DM, Park I et al (2011) Ultrahigh mobility in polymer field-effect transistors by design. J Am Chem Soc 133:2605–2612
61. Guo X, Ortiz RP, Zheng Y et al (2011) Bithiophene-imide-based polymeric semiconductors for field-effect transistors: synthesis, structure-property correlations, charge carrier polarity, and device stability. J Am Chem Soc 133:1405–1418
62. Guo X, Facchetti A, Marks TJ (2014) Imide- and amide-functionalized polymer semiconductors. Chem Rev 114:8943–9021
63. Li J, Zhao Y, Tan HS et al (2012) A stable solution-processed polymer semiconductor with record high-mobility for printed transistors. Sci Rep 2:754
64. Chen H, Guo Y, Yu G et al (2012) Highly π-extended copolymers with diketopyrrolopyrrole moieties for high-performance field-effect transistors. Adv Mater 24:4618–4622
65. Back JY, Yu H, Song I et al (2015) Investigation of structure-property relationships in diketopyrrolopyrrole-based polymer semiconductors via side-chain engineering. Chem Mater 27:1732–1739
66. Mei J, Bao Z (2014) Side chain engineering in solution-processable conjugated polymers. Chem Mater 26:604–615
67. Zhu C, Zhao Z, Chen H et al (2017) Regioregular Bis-Pyridal[2,1,3]thiadiazole-based semiconducting polymer for high-performance ambipolar transistors. J Am Chem Soc 139:17735–17738
68. Lee J, Han AR, Kim J et al (2012) Solution-processable ambipolar diketopyrrolopyrrole-selenophene polymer with unprecedentedly high hole and electron mobilities. J Am Chem Soc 134:20713–20721
69. Kang B, Kim R, Lee SB et al (2016) Side-chain-induced rigid backbone organization of polymer semiconductors through semifluoroalkyl side chains. J Am Chem Soc 138:3679–3686
70. Puigdollers J, Voz C, Martin I et al (2004) Pentacene thin-film transistors on polymeric gate dielectric: device fabrication and electrical characterization. J Non Cryst Solids 338–340:617–621
71. Raval HN, Tiwari SP, Navan RR et al (2009) Solution-processed bootstrapped organic inverters based on P3HT with a high-κ gate dielectric material. IEEE Electron Device Lett 30:484–486

72. Wu M, Alivov YI, Morkoç H (2008) High-κ dielectrics and advanced channel concepts for Si MOSFET. J Mater Sci Mater Electron 19:915–951
73. Gupta D, Katiyar M, Gupta D (2009) An analysis of the difference in behavior of top and bottom contact organic thin film transistors using device simulation. Org Electron 10:775–784
74. Klauk H, Zschieschang U, Halik M (2007) Low-voltage organic thin-film transistors with large transconductance. J Appl Phys 102:074514
75. Diao Y, Shaw L, Mannsfeld SCB (2014) Morphology control strategies for solution-processed organic semiconductor thin films. Energy Environ Sci 7:2145–2159
76. Yuan Y, Giri G, Ayzner AL et al (2014) Ultra-high mobility transparent organic thin film transistors grown by an off-centre spin-coating method. Nat Communcations 5:3005
77. Self-assembly NE, Zhang BC, Zhang X et al (2008) Facile one-step growth and patterning of aligned squaraine. Adv Mater 20:1716–1720
78. Liu S, Wang WM, Briseno AL et al (2009) Controlled deposition of crystalline organic semiconductors for field-effect-transistor applications. Adv Mater 21:1217–1232
79. Duffy CM, Andreasen JW, Breiby DW et al (2008) High-mobility aligned pentacene films grown by zone-casting. Chem Mater 20:7252–7259
80. Jang J, Nam S, Im K et al (2012) Highly crystalline soluble acene crystal arrays for organic transistors: mechanism of crystal growth during dip-coating. Adv Funct Mater 22:1005–1014
81. Sele BCW, Kjellander BKC, Niesen B et al (2009) Controlled deposition of highly ordered soluble acene thin films: effect of morphology and crystal orientation on transistor performance. Adv Mater 21:4926–4931
82. Becerril HA, Roberts ME, Liu Z et al (2008) High-performance organic thin-film transistors through solution-sheared deposition of small-molecule organic semiconductors. Adv Mater 20:2588–2594
83. Chang J, Chi C, Zhang J, Wu J (2013) Controlled growth of large-area high-performance small-molecule organic single-crystalline transistors by slot-die coating using a mixed solvent system. Adv Mater 25:6442–6447
84. Kolesov VA, Fuentes-Hernandez C, Chou WF et al (2017) Solution-based electrical doping of semiconducting polymer films over a limited depth. Nat Mater 16:474–481
85. Tang CG, Ang MCY, Choo K et al (2016) Doped polymer semiconductors with ultrahigh and ultralow work functions for ohmic contacts. Nature 539:536–540
86. Liu C, Xu Y, Noh Y (2015) Contact engineering in organic field-effect transistors. Mater Today 18:79–96
87. Allain A, Kang J, Banerjee K, Kis A (2015) Electrical contacts to two-dimensional semiconductors. Nature 14:1195–1205
88. Greiner MT, Lu ZH (2013) Thin-film metal oxides in organic semiconductor devices: their electronic structures, work functions and interfaces. NPG Asia Mater 5:e55
89. Greiner MT, Chai L, Helander MG et al (2012) Transition metal oxide work functions: the influence of cation oxidation state and oxygen vacancies. Adv Funct Mater 22:4557–4568
90. Seah W, Tang CG, Png R et al (2017) Interface doping for ohmic organic semiconductor contacts using self-aligned polyelectrolyte counterion monolayer. Adv Funct Mater 27:1606291
91. Vericat C, Vela ME, Benitez G et al (2010) Self-assembled monolayers of thiols and dithiols on gold: new challenges for a well-known system. Chem Soc Rev 39:1805–1834
92. Petit M, Janvier P, Knight DA, Bujoli B (2012) Surface modification using phosphonic acids and esters. Chem Rev 112:3777
93. Chen H, Guo X (2013) Unique role of self-assembled monolayers in carbon nanomaterial-based field-effect transistors. Small 9:1144–1159
94. Tulevski GS, Miao Q, Afzali A et al (2006) Chemical complementarity in the contacts for nanoscale organic field-effect transistors. J Am Chem Soc 128:1788–1789
95. Zhao Y, Pe W, Shi Q et al (2005) Dithiocarbamate assembly on gold. J Am Chem Soc 127:7328–7329
96. Ford WE, Gao D, Knorr N et al (2014) Organic dipole layers for ultralow work function electrodes. ACS Nano 9:9173–9180

97. Wang G, Rühling A, Amirjalayer S et al (2017) Ballbot-type motion of N-heterocyclic carbenes on gold surfaces. Nat Chem 9:152
98. Engel S, Fritz E, Ravoo BJ, Fritz E (2017) New trends in the functionalization of metallic gold: from organosulfur ligands to N-heterocyclic carbenes. Chem Soc Rev 46:2057–2075

Chapter 5
Organic Photovoltaic Devices

As discussed in the previous chapters, organic semiconductors with tailored chemical structures can achieve decent charge transport properties and can be used to make OTFT devices. In addition to charge transport properties, some organic semiconductors can also realize high-light-absorption coefficients, which makes them candidates for photovoltaic applications. Considering the ease and flexibility of their synthesis, organic semiconductors can be rationally designed to have the desired optical and electronic properties along with good solution processability. As a matter of fact, photovoltaics based on organic active layers, known as organic photovoltaics (OPVs), are an important branch of organic electronics research and are one of the most promising emerging PV technologies. Unlike PVs based on inorganic materials whose active layers have limited material choices, the field of OPVs has witnessed several generations of materials with thousands of molecular structures developed to date. Along with the optimization of device architectures, the performance of OPV devices has improved dramatically in recent years, and the field is on the verge of industrialization. This chapter will begin with discussing the advantages of OPVs compared to other types of PVs and introduce the basic working principle of OPV devices, followed by the development of OPV materials with a focus on the new generation of non-fullerene acceptors that have been dominating the field in most recent years. Last, we discuss the cutting-edge concepts for improving the performance of OPVs and the problems to be addressed for the goal of commercialization.

5.1 Advantages of Organic Semiconductors for Photovoltaic Applications

The Paris agreement aims to achieve global peaking of greenhouse gas emissions as soon as possible and carbon neutrality by the mid-twenty-first century. To this end, the European Parliament backed climate neutrality by 2050 and a 60% carbon
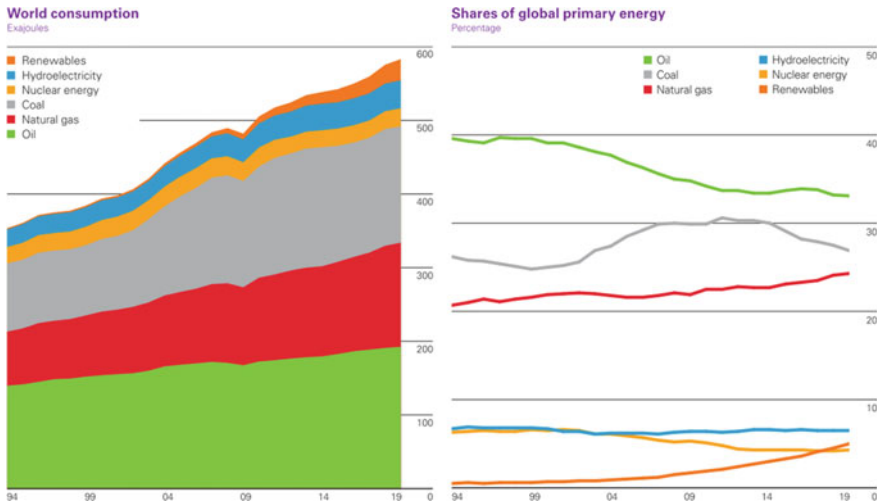
Fig. 5.1 World energy consumption between 1994 and 2019. Adapted from "Statistical Review of World Energy 2020" by British Petroleum

emission reduction by 2030; China also announced its carbon-peak and carbon-neutrality timeline—2030 and 2060, respectively, in a recent government report. However, according to the BP Energy Outlook (2020 edition) [1], world energy consumption will continue to rise for at least the next few decades, and as shown in Fig. 5.1, even in 2019, traditional sources still account for 84.3% of the total global energy consumption including a 33.1% from oil, a 27% from coal, and a 24.2% from natural gas [2]. To fulfill the goal of rapidly reducing carbon emissions while meeting global energy demand, investing in clean energy technologies is inevitable. This includes increasing the energy efficiency of current technologies, and more importantly, developing novel renewable energy technologies in the meantime.

As the most abundant, sustainable, and carbon–neutral energy source, solar energy that strikes our planet in an hour can cover the global energy demand in a year. Therefore, converting solar energy into electricity is one of the most straightforward yet effective approach for the energy transition. Calculations show that energy converted by solar cells that have an efficiency of ~15% in a total area of just ~115 km^2 (~1/10 of the area of New York City) is enough to supply the annual energy consumption in the United States—the world's largest economy [3].

The most mature photovoltaic technology nowadays is based on crystalline Si, which provides decent solar cell efficiency and has witnessed rapid cost reduction in recent years. However, the recent promotion of distributed PV has provided more opportunities for emerging PV technologies. For instance, the government work white paper issued by the State Council of China at the end of 2020 proposes to promote the diversified use of solar energy and to encourage PV installation in both a centralized and distributed manner. By letting the PV power generated be consumed in the same or nearby location, distributed PV systems can reduce the

loss of long-distance power transmission while solving the power fluctuation issue brought by grid-connected PV. Therefore, it is ideal for modern cities with dense high-rise buildings, which have the highest electricity demand. With the progress of urbanization worldwide, the pace of distributed photovoltaics entering the city is accelerating year by year. However, unlike deserts and plains with vast open areas for centralized PV systems, the application scenarios in cities have put new demands on the photovoltaic industry. For example, emerging markets such as building integrated photovoltaics (BIPVs), vehicle-integrated photovoltaics, and millions of sensors for Internet of things applications in smart cities that currently rely on batteries but have a desperate need for alternative power solutions provide large potential markets for distributed PVs, but these markets require photovoltaic technologies with certain features, including but not limited to lightweight, flexibility, semitransparency, color tunability, or indoor light spectrum compatibility. These additional demands have led to the development of a new generation of photovoltaic materials and devices.

As one of the most promising emerging PV technologies, organic photovoltaics (OPVs), also known as organic solar cells, utilize synthetic organic compounds as their active components to convert solar energy. As discussed in detail in the later section, the organic semiconductors for OPVs are mostly conjugated polymers, small molecules, or fullerene derivatives, whose building blocks are based on earth abundant non-toxic materials. These organic materials can be synthesized, and mass produced in lab-scale fume hoods without the need for vacuum or high-temperature processes. Once prepared on flexible substrates coupled with appropriate flexible charge transport layers and electrodes, OPV devices/modules can demonstrate excellent flexibility, allowing them to be easily rolled up and perfectly adapted to curved surfaces. Since the active layer is only ~100–300 nm thick, 1 g of active layer materials is enough to fabricate modules with an area of up to 2–3 m^2, and the resulting module would be extremely light in weight. The power per weight for flexible OPVs can be as high as 100 W/kg compared to the 5–7 W/kg for typical Si-based PVs prepared on metal substrates, making them ideal for applications with strict weight requirement such as aerospace or military gear.

From a cost perspective, although the current production cost of efficient OPV modules is still relatively high, the roll-to-roll printing technique, along with the vacuum-free, high-temperature-free synthesis of organic materials, can help quickly reduce the cost upon mass production. The recent surge in power conversion efficiency can also decrease the dollar/watt for OPVs. Other than money cost, the ease of processing of organic photovoltaic devices and the resulting low energy needs during their manufacturing will also drastically reduce the energy payback time (EPBT) of this technology, which describes how quickly the technology gains back the energy invested in its making. It has been reported by Espinosa et al. [4] that among various renewable energy technologies, OPVs, even at laboratory scales, demonstrate an EPBT that beats all other PV technologies. The EPBT for OPVs can be as low as 0.2 years, which outperforms technologies involving other energy sources.

Moreover, one of the key benefits of using organic active layer materials is the various synthetic strategies to provide the molecules with desired optical properties, particularly when non-fullerene donor and acceptor materials are used. This offers
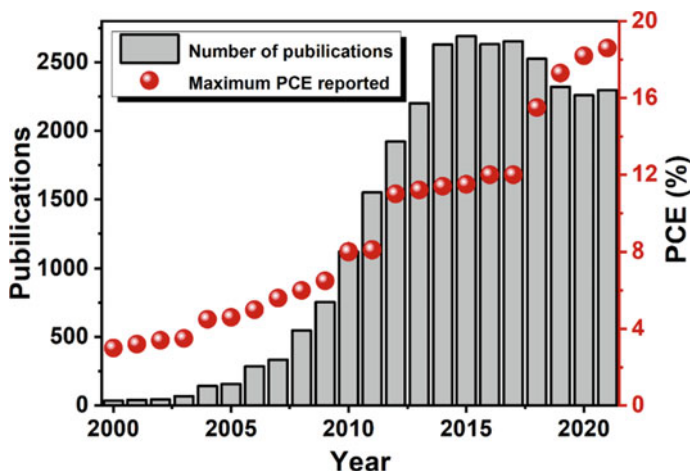
Fig. 5.2 Change in the number of publications and power conversion efficiency (PCE) of organic solar cells from 2000–2021

several additional favorable properties of OPV devices and modules. One could judiciously tune the absorption profile of the device to make it: (1) into almost any color wanted, which allows OPVs to suit application sites with color requirements; (2) semitransparent for glass curtain or automotive window applications; and (3) compatible with the indoor light spectrum to have an extremely high-efficiency for indoor PV applications.

About 10 years ago, researchers estimated that when the PCE of OPV modules reach 10%, the technology would have a chance for commercialization. However, the PCE was only ~2–3% at the time when the best device was based on classic polymer donors and fullerene derivative acceptors. Within the past few years, the development of non-fullerene acceptor materials has quickly changed the field, leading to >18% PCEs for lab-scale devices [5]. To date, the most successful OPVs are based on conjugated polymers and non-fullerene small molecule or polymeric acceptors (Fig. 5.2). To understand what determines the performance of an OPV device, we need to understand how organic solar cells work.

5.2 Working Principles of OPVs

Figure 5.3 shows the structure of a typical OPV device and the main steps for the light-to-current conversion.

In 1986, Tang reported the first example of an organic solar cell based on a bilayer planar heterojunction structure using a CuPc/Perylene derivative as the active component [6]. A typical single-junction OPV device usually consists of a "sandwich" structure: the active layer, where the photon-to-free charge-carrier conversion occurs, is
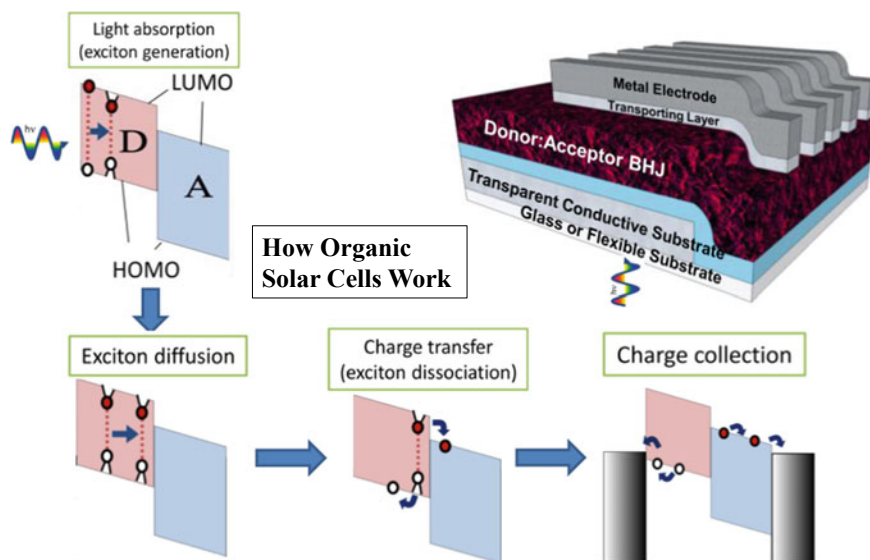
Fig. 5.3 Typical structure of a single-junction OPV device based on the bulk heterojunction (BHJ) active layer and a scheme showing the main light-to-current conversion steps

sandwiched between the anode and cathode layers. To improve the device performance, a hole-transporting layer and an electron-transporting layer are typically placed between the active layer and the anode and cathode, respectively.

Inside the active layer, organic electronic materials such as π-conjugated polymers and small molecular semiconductors with judiciously designed chemical structures are employed as the main active components owing to their excellent light-absorbing abilities such as their absorption coefficients (in the range of ~10^4–10^5 cm^{-1}) and broad absorption bands due to the geometry relaxations in the excited states [7, 8]. The strong light absorptivity over a broad energy range enables efficient light harvesting with much thinner active layers (~100–200 nm) relative to Si-based PVs. With more details about these active layer materials provided in Sect. 1.3, this section briefly introduces the working principle of an OPV device.

5.2.1 Characterization of OPV Devices

Before we introduce the light-to-current processes, we need to know how to characterize an OPV device. As mentioned above, the power conversion efficiency (PCE) is the key parameter for characterization of the performance of a photovoltaic cell. PCE stands for the ratio of electrical power output to incident light power, which can be described as
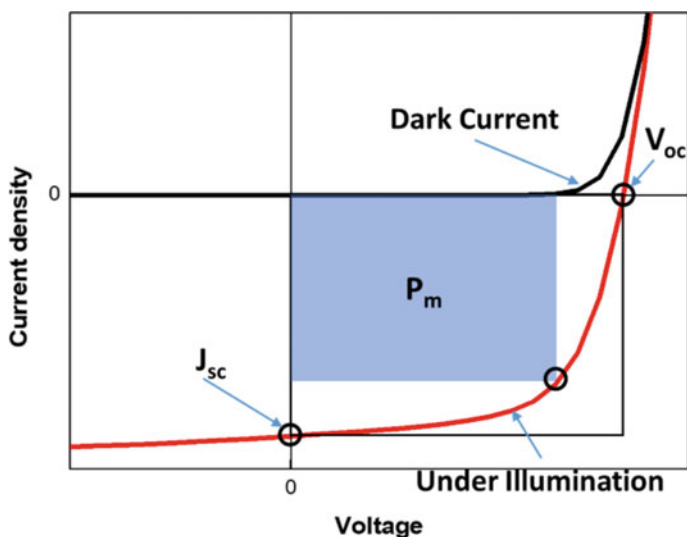
Fig. 5.4 Current density–voltage (*J–V*) characteristics of an organic solar cell

$$\mathrm{PCE} = \frac{P_m}{P_{\mathrm{in}}} = \frac{J_{\mathrm{SC}} \times V_{\mathrm{OC}} \times \mathrm{FF}}{P_{\mathrm{in}}}$$

The parameters in the equation above are exhibited in Fig. 5.4. The value of PCE is calculated from three parameters: short-circuit current density (J_{SC}), open-circuit voltage (V_{OC}), and fill factor (FF). P_m stands for the maximum power point, and P_{in} is the incident light power. J_{SC} is the current density of devices when there is 0 V of applied bias on the two electrodes. V_{OC} is defined when the value of circuit current density reaches zero. FF is the ratio of the maximum power obtainable from the *J–V* curve and the power defined by the product of V_{OC} and J_{SC}.

External quantum efficiency (EQE) is another important parameter for OPVs. As shown in the equation below, EQE represents the percentage of incident photons which convert to charges and are collected by electrodes under short-circuit conditions.

$$\mathrm{EQE} = \frac{I_{\mathrm{SC}}(\lambda)hc}{P_{\mathrm{in}}(\lambda)e\lambda}$$

where I_{SC} denotes photocurrent, h the Planck constant, λ the wavelength, c the vacuum speed of light in vacuum, and e the elementary charge.

5.2.2 Light Absorption and Exciton Generation

In the ground-state configuration of a neutral organic molecule, the highest occupied molecular orbital (HOMO) is filled by two electrons with opposing spins. An incoming photon excites an electron from the HOMO into the lowest unoccupied molecular orbital (LUMO) as a result of the absorption of light, leaving a hole to create an electron–hole pair. The electron–hole pairs created in the preceding stage can readily separate to become free charge carriers with long lifetimes in an ideal photovoltaic system, which will result in a strong photocurrent when they are captured by the corresponding electrodes. However, the OPV community acknowledges that in organic solar cells, the electron–hole pair must overcome their mutual Coulomb attraction V, which is given by

$$V = \frac{e^2}{4\pi \varepsilon_o \varepsilon_r r}$$

where e is the elementary charge, ε_0 is the vacuum permittivity, ε_r is the dielectric constant of the surrounding medium and r is the distance between the electron and hole in the pair. In crystalline silicon based solar cells, the dielectric constant is high ($\varepsilon_r \sim 12$), and the photo excited states are highly delocalized (corresponds to a large r) [7, 9, 10]. However, organic semiconductors used in OPVs generally have low-dielectric constants ($\varepsilon_r \sim 2$–6) and more localized photo excited states, making it more challenging to separate the electron–hole pair.

In addition to the strong Coulomb interaction between the electron and the hole, the electron-lattice and electron–electron interactions of OPV materials are typically strong as well. Because of this, the photoexcitation of the chromophore produces an exciton, which is a bound electron–hole pair, instead of directly creating free charge carriers. To dissociate the exciton and thus generate free charge carriers, it is essential to overcome the exciton binding energy, which is typically ~0.3–0.5 eV [8]. At ambient temperature, its binding energy is significantly more than $k_B T$. This means that additional driving energy is needed to separate the excitons.

The widely used approach for efficiently separating excitons involves creating a heterojunction between an electron-donating (donor) and electron-accepting (acceptor) material. The two materials' different electron affinities (and/or ionization energies) provide an energetic offset at their interface, which acts as a driving energy for exciton dissociation. Initially, vacuum deposition-prepared bilayer heterojunction was used to separate the electron–hole pairs [6]. However, the total efficiency of such a planar heterojunction device is limited, despite achieving more effective exciton dissociation than a single-layer based on a pure material, since a significant portion of the excitons is unable to reach the donor–acceptor interface. Because the rate of photoinduced electron transfer decreases exponentially with the separation between the donor and acceptor molecule, excitons have to migrate to the interface to dissociate [11–13].

Excitons are electrically neutral, therefore electric fields do not drive their movement. In most OPV materials, the excited states are more localized than in inorganic photovoltaic systems, and the excitons generally migrate through the materials by random diffusion that are typically driven by energy transfer. In typical OPV active layers, singlet excitons have a limited lifetime overall, which is consistent with a small exciton diffusion length (5–20 nm). The device based on the bilayer planar heterojunction structure performs poorly due to the short diffusion length. Therefore, with such a bilayer design, a compromise in the layer thickness is required to strike a balance between exciton dissociation (which favors thin layers) and light absorption (favoring thick layers).

The invention of the bulk heterojunction was a turning point in the development of OPVs since it solved the problem of the restricted exciton diffusion length of organic materials and fundamentally altered the way devices are made (BHJ) [14, 15]. A BHJ structure, which has a bicontinuous interpenetrating network generated by the donor and acceptor, can be made by mixing the donor and acceptor materials in one solution or by coevaporating the two components. The BHJ greatly minimizes the distance that the excitons must travel before reaching an interface by enlarging the interfacial region between the donor and acceptor. Therefore, when the nanoscale morphology, particularly the length scales of phase separation, is in agreement with the exciton diffusion lengths, and effective exciton harvesting may be accomplished. Although research into planar heterojunction is still ongoing, the BHJ is currently the predominant structure in efficient OPV devices, and this chapter focuses on OPV devices with BHJ-based active layers.

5.2.3   Charge-Transfer State and Free Carrier Generation

The creation of free charge carriers after exciton dissociation is essential to the functioning of organic solar cells. The mechanism of the generating process, however, has continued to be a controversial topic throughout time. The reason why it is difficult to form a universal theoretical framework for charge generation in OPV is mainly due to the rapid development of OPV materials that leads to significant difference among material systems. Moreover, additional factors like film compositions and morphological characteristics can alter charge generating processes in both major and minor ways. We succinctly review the key experimental findings and theoretical concepts put forth by research teams in this section.

When excitons reach the donor/acceptor interface, the electron from the donor material can transfer to the acceptor material. The hole from the acceptor can also transfer to the donor in a similar manner. This initial electron (or hole) transfer creates an electron–hole pair across the donor/acceptor interface called a charge-transfer state (CTS). The electron and hole are barely 0.5–1 nm apart and are nonetheless connected by the Coulomb force despite being on distinct materials. As a result, the CTS can also geminately recombine, which would result in energy loss, rather of separating into free charges by overcoming its binding energy. The Onsager-Brawn model,

which takes charge hopping via thermal activation into consideration, has frequently been used to explain the dissociation of the CTS. Recent findings in certain efficient OPV devices, however, pose problems for this theoretical paradigm. Experiments have revealed that in some systems, the yield of charge generation is independent of temperature and electric field, and exciton dissociation may occur on timeframes as quick as < 100 fs [16].

Even without a ubiquitous model to describe CTS and its dissociation, the design of OPV materials still has some guidelines to follow [17, 18]. According to conventional wisdom from the energetics point of view, effective charge production necessitates a driving energy offset between the donor and acceptor of > 0.3 eV. This empirical value was summarized from the observation that many OPV material systems (especially those based on fullerene acceptors) suffer from low-charge generation yields in the absence of this energetic offset [19].

Along with energetics, the donor–acceptor interface's morphology can influence charge generation. For instance, experiments demonstrate that when fullerene aggregates grow close to the donor/acceptor interface in fullerene acceptor-based OPV devices, the charge separation efficiency might be improved [20–26]. Aggregates close to the interface boost wavefunction delocalization, which may significantly alter the charge separation process. However, additional research also demonstrates that excessive delocalization might reduce the device's open-circuit voltage by offering more recombination pathways [27, 28]. This implies that in order to balance voltage and current, it might be necessary to optimize the interfacial morphology such as the molecular orientation and aggregate size to realize a favorable CTS delocalization.

The majority of charge generation research has been done on fullerene acceptor-based OPVs, and systematic study of the charge generation process for non-fullerene acceptor-based devices has remained scarce. The device efficiency of OPVs has significantly risen over a very short period of time, i.e., 3–4 years, from 10–12% (fullerene-based) to the present > 19% (non-fullerene based), thanks to the quick development of non-fullerene acceptors and polymer donors that are compatible with these acceptors [29]. It is highly conceivable that the non-fullerene systems cannot be explained by the charge production process seen in fullerene-based material combinations. In fact, research from the past few years has shown that some non-fullerene systems can achieve extremely high-charge dissociation yields without the need for a significant driving energy [30, 31]. There are also reports discussing the possible reasons such as energy transfer between donor and acceptor that removes/reduces the requirement for a significant LUMO-LUMO offset between them [32]. For small molecule and polymer-based material systems, molecular quadrupole moments were also correlated to interfacial energy levels by Leo et al. [33]. These results mark a significant leap in OPV technology since they potentially result in significantly reduced voltage losses and consequently, substantially greater open-circuit voltages than earlier fullerene-based systems.

5.2.4 Charge Transport and Collection

At the donor–acceptor interface, charge carriers known as polarons are produced upon the dissociation of the CTS or the excitons directly. Due to the substantial electron-vibration interactions, polarons polarize their surroundings. Polarons are charged species, and an electric field can assist them travel toward the appropriate electrodes. The main factor used to define the positively charged (p-polarons) and negatively charged (n-polarons) polarons' ability to carry charge is their mobilities. The charge mobilities of organic semiconductors utilized in OPVs are usually lower than those of inorganic semiconductors ($\sim 10^2$ cm^2 V^{-1} s^{-1}) with ordered crystal structures because to weak electronic couplings and disorder effects [8]. In OPVs, charge transport takes place by polarons hopping with mobilities influenced strongly by the nanoscale morphology. The mobilities can range over several orders of magnitude, e.g., from 10^{-6}–10^{-3} cm^{2}V^{-1} s^{-1} to above 1 cm^{2}V^{-1} s^{-1} depending on the nature of the material and the morphology of the film. The mobilities in the BHJ-type active layers in the state-of-the-art OPV devices are typically in the range of 10^{-4}–10^{-3} cm^{2}V^{-1} s^{-1}.

When the polarons reach the "correct" electrodes, i.e., p-polarons reach the anode and n-polarons reach the cathode, photocurrent is produced [34, 35]. In practice, the charge collection efficiency could not be particularly good if the active layer is directly sandwiched between two metal electrodes. Electron and hole carrying layers are frequently used between the active layer and the appropriate electrode to improve charge extraction and increase the electrode's carrier selectivity, which will be covered in more detail in the following section.

During the charge transport process, electrons and holes may encounter near an interface and form a CTS, which then either recombines (through vibronic coupling to the ground state) or dissociates back into free carriers. This recombination process is detrimental to the operation of the device by limiting both photocurrent and photovoltage. There are different types of carrier recombination such as bimolecular versus monomolecular, geminate versus non-geminate, and Langevin versus Shockley–Read–Hall recombination. Each of these terms have a physical meaning behind it. In addition, recombination can also occur through spin-triplet states. The detailed discussion about the recombination mechanism is beyond the scope of this book, and the readers can find reference in the literature if interested [7, 28, 34, 36–42]. While it remains difficult to precisely control mobility, higher OPV efficiencies are typically achieved with higher carrier mobilities [43]. It is clear that recombination is governed by microscopic details of the donor–acceptor interface. To enhance the overall performance of the device, understanding the physics of these processes and developing strategies to limit them are significant.

Through light absorption, exciton diffusion, exciton dissociation, charge transport, and charge collection, the photons are converted to electrical current. As we mentioned, different material systems and the morphology formed by these materials have a dramatic effect on these processes. In the next section, we will summarize the development of OPV materials.

5.3 Development of OPV Materials

Instead of categorizing OPV materials by their chemical structures, this section summarizes the evolution of OPV materials (mainly active components) in a chronological order to show the progress that the OPV field has made, which can also highlight the key structural features that endow the state-of-the-art materials with cutting-edge device performance.

5.3.1 2000–2006: Homopolymer MEH-PPV, P3HT, and Fullerene Derivatives

The donor materials used in the initial development of BHJ solar cells are some classical homopolymers. For instance, the poly(p-phenylene vinylene) polymer MEH-PPV is the first donor used in BHJ solar cells (Fig. 5.5) [15, 44]. In 1995, Heeger et al. combined MEH-PPV with a fullerene acceptor $PC_{61}BM$ and delivered a PCE of 2.5% [15]. Higher efficiency was achieved by a polythiophene-based star material, P3HT. Polymer P3HT mainly absorbs light from 400–600 nm and exhibits high-absorption coefficients [45]. P3HT blended with $PC_{61}BM$ has achieved a certified efficiency of over 4% [46]. On the other hand, due to the high-electron affinity and low-reorganization energy, C_{60} fullerene derivatives, especially $PC_{61}BM$, became the dominating n-type acceptors for OPVs in the early stages of OPV development. $PC_{71}BM$ was then developed in 2003, which further enhanced the light-harvesting capability [47].

5.3.2 ~2007–2015: D-A Copolymer

As it became difficult to make further progress from the homopolymer-based donors, D–A copolymer was introduced into the OPV field. Unlike homopolymer donors, the D–A copolymers consist of alternating electron-donating (D) and electron-withdrawing (A) units. This strategy narrows the bandgap of the material, thus broadening the light-harvesting range and promoting charge transfer among the D–A molecules. As shown in Fig. 5.6, a star polymer, named PTB7, contains an electron-rich D unit named 4,8-bis((2-ethylhexyl)oxy)benzo[1,2-b:4,5-b']dithiophene (BDT) and an electron-deficient A unit named 2-ethylhexyl 3-fluorothieno [3,4-b]thiophene-2-carboxylate (TT). PTB7 exhibits a low bandgap of 1.65 eV with an absorption edge near 800 nm [48]. In 2012, PTB7:$PC_{71}BM$-based solar cells delivered a high PCE of over 9% with an inverted device structure [49]. By introducing an alkylthio-phenyl side chain on the BDT unit, a derivative of PTB7 called PTB7-th (Fig. 5.6) combined with $PC_{71}BM$ further improved the PCE of organic solar cells to almost 10% [50]. In 2013, a pentacyclic aromatic lactam unit, TPTI, emerged as an effective

Fig. 5.5 Chemical structures for MEH-PPV, P3HT, PC$_{61}$BM, and PC$_{71}$BM

MEH-PPV   P3HT

PC$_{61}$BM   PC$_{71}$BM
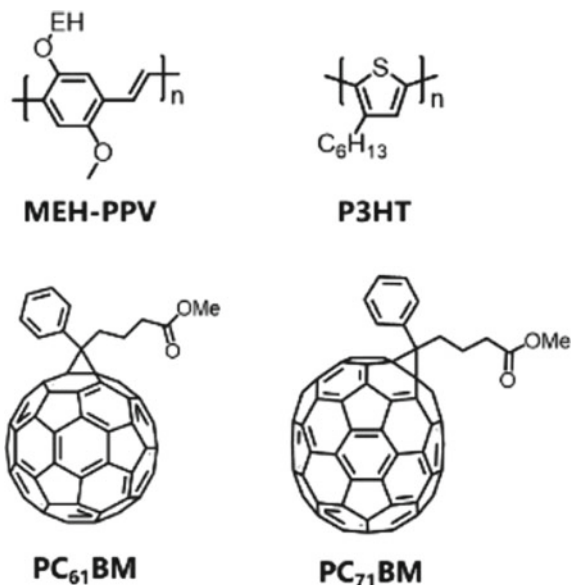
backbone to develop polymer donor [51]. A high V_{OC} of 0.9 V was obtained from the polymer PThTPTI, owing to its high planarity and strong electron-withdrawing property [52]. In 2016, a donor named NT812 with a fused-ring (A) unit exhibited a high-hole mobility of 2.7×10^{-2} cm^{2}V^{-1} s^{-1} [53]. A PCE of 10.3% was achieved from NT812:PC$_{71}$BM cells with an active layer thickness of 340 nm. Since NT812 demonstrates high efficiency at a high-film thickness, it is promising to process this donor material for large-area OPVs. In 2016, a copolymer PffBT4T with a 2-nonyltridecanyl side chain further promoted the PCE to 11.7% when combined with PC$_{71}$BM [54]. This is the best certified efficiency among all the single-junction polymer: fullerene-based solar cells.

5.3.3   ~2015–2021: Non-Fullerene Acceptors

The D–A copolymer donor has promoted the PCE of OPVs to ~12%. However, further improvement of efficiency in the polymer: Fullerene system has become very difficult. The key reason is that fullerenes derivatives have much less contribution to the overall light-harvesting due to their relatively low-absorption coefficients. Moreover, the functionalization of fullerenes is not straightforward, making the optical properties such as the absorption range hard to modify. Along with several additional motivations such as to improve device stability, non-fullerene molecules, particularly those that have electron-accepting tendencies and strong light-harvesting capabilities, have emerged as a novel type of acceptor material. The non-fullerene acceptors
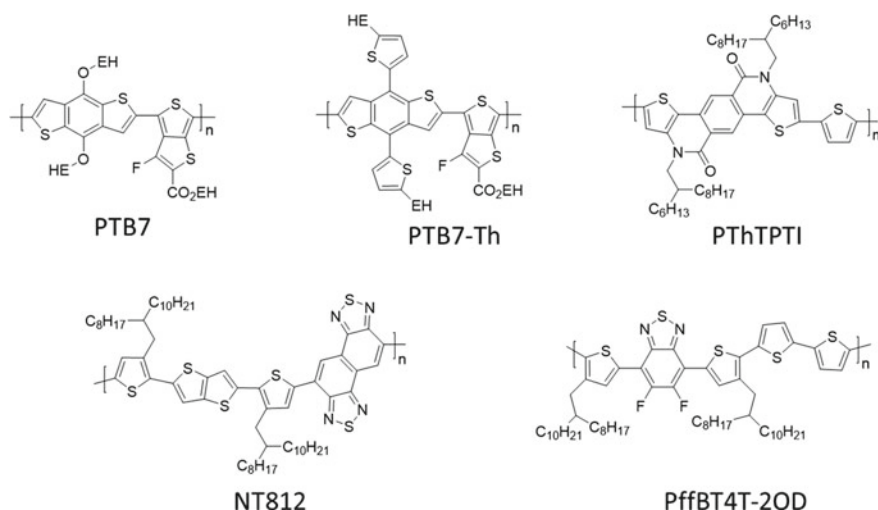
Fig. 5.6 Chemical structures of a few representative D–A copolymers

(NFAs) typically show strong absorptions, and their absorption ranges are readily tunable thanks to the flexible synthetic strategies [29]. Some representative NFAs with an acceptor–donor–acceptor (A-D-A) chemical structure and strong visible or NIR light-harvesting capability are shown in Fig. 5.7. Because of the strong intramolecular charge transfer between the D and A units, the NFAs absorb strongly in the visible and near-infrared regions. In 2015, the famous A-D-A type NFA named ITIC with an optical bandgap of 1.59 eV was developed by Zhan et al. [55]. By compensation of light absorption at 500–800 nm, the PTB7-Th:ITIC-based solar cells gave a PCE of 6.8% [55]. The PCE reached 11% when an indaceno[1,2-b:5,6-b']dithiophene (IDT)-based NFA named IDIC was used as the electron acceptor [56]. Furthermore, after the addition of fluorine substitution to the A units in ITIC, the resulting NFA, namely IT-4F, achieved a PCE of 13.1% [57]. The fluorine substitution enhanced the light absorption and charge mobility in the solar cell. In 2017, a strong electron-donating unit, the ladder-type carbon–oxygen-bridged (CO-bridged) unit, was used for constructing A-D-A acceptors [58]. The COi8DFIC with a CO-bridged unit exhibited a planar molecular structure with a stronger electron-donating effect than traditional carbon-bridged A-D-A acceptors. A low bandgap of 1.26 eV and an absorption range of ~600–1000 nm were demonstrated by COi8DFIC. The PTB7-Th:COi8DFIC-based solar cells delivered a PCE of 12.2% with a high J_{SC} over 26 mA cm^{-2} [59]. The addition of a third component, PC71BM, increased the efficiency of this ternary solar cell to 14.1%, the first time the PCE of an OPV device exceeded 14% [60]. By means of this ternary system, a tandem solar cell with PTB7-Th: COi8DFIC:PC$_{71}$BM as rear subcell delivered a PCE of 17.3% in 2018 [61]. In 2019, the great potential of NFAs was further demonstrated by the report of Y6 [62]. The fused-ring benzo[c][1,2,5]thiadiazole core unit exhibits strong absorption in the 570–920 nm range. Combination of Y6 with various efficient donor materials yielded
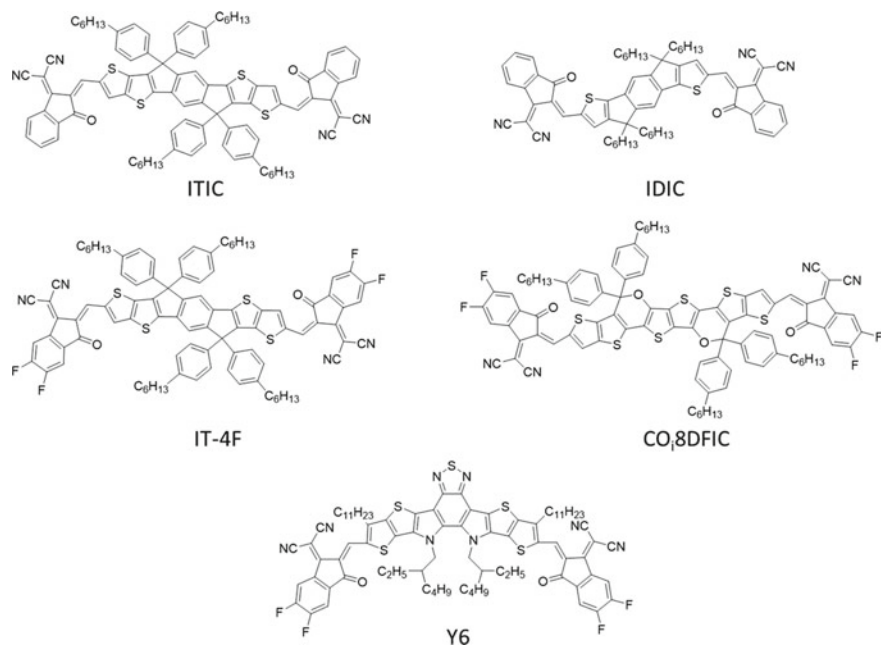
Fig. 5.7 Chemical structures for some high-performance non-fullerene acceptors

PCEs larger than 15% [63–66]. Y6 is one of the best non-fullerene acceptors to date, and there have been various derivatives of Y6 being developed since 2019, such as N3 [67]. The combination of N3 in a single-junction OPV device with a quaternary active layer showed a PCE of 17.7% [68].

5.3.4   Wide-Bandgap Donors

The emergence of NFAs changes the routine of donor material development. When fullerene was still the mainstream acceptors, the promising donors were those with low-bandgap and strong light absorption. However, the NFAs prefer wide-bandgap (WBG) donors with complementary absorption profiles. Recently, some WBG donors with NFAs have achieved good device performance. For example, the widely used donor named PM6 was first developed for a PM6:PC$_{71}$BM system in 2015 and delivered a PCE of 9.2% [69]. In 2019, PM6 was combined with Y6 to realize a much higher PCE of 15.7% [62]. In 2019, a WBG copolymer PTQ10 was developed based on a simple synthetic route [70]. PTQ10:Y6-based organic solar cells demonstrated a PCE of 16.5% [64]. In the same year, a WBG copolymer, P2F-EHp, with an imide-functionalized benzotrizole (TzBI) electron-withdrawing unit was reported. The solar cells based on P3F-EHp offered a PCE of 16.0% in

combination with Y6 [63]. After that, an ultrawide-bandgap copolymer, W1, with a 1,2-difluoro-4,5-bis(octyloxy)benzene electron-withdrawing unit was reported, which exhibited a bandgap of 2.16 eV [65]. The W1:Y6-based solar cells achieved a PCE of 16.2%. Moreover, a 5H-dithieno[3,2-b:2',3'-d]thiopyran-5-one (DTTP) unit was developed and applied in a WBG copolymer called D16. A high PCE of 16.7% was obtained from D16:Y6-based solar cells. In 2020, a much more efficient WBG copolymer named D18 with a fused-ring electron-withdrawing unit named dithieno[3',2':3,4;2',3':5,6]benzo[1,2-c][1,2,5]thiadiazole (DTBT) was developed [71]. High-hole mobility was observed from D18 due to the extended molecular backbone of DTBT relative to that of the DTTP-based D16. The D18:Y6-based solar cells showed a PCE of 18.2%. Those progresses exhibit great potential of WBG copolymer donors for non-fullerene-based OPVs (Fig. 5.8).
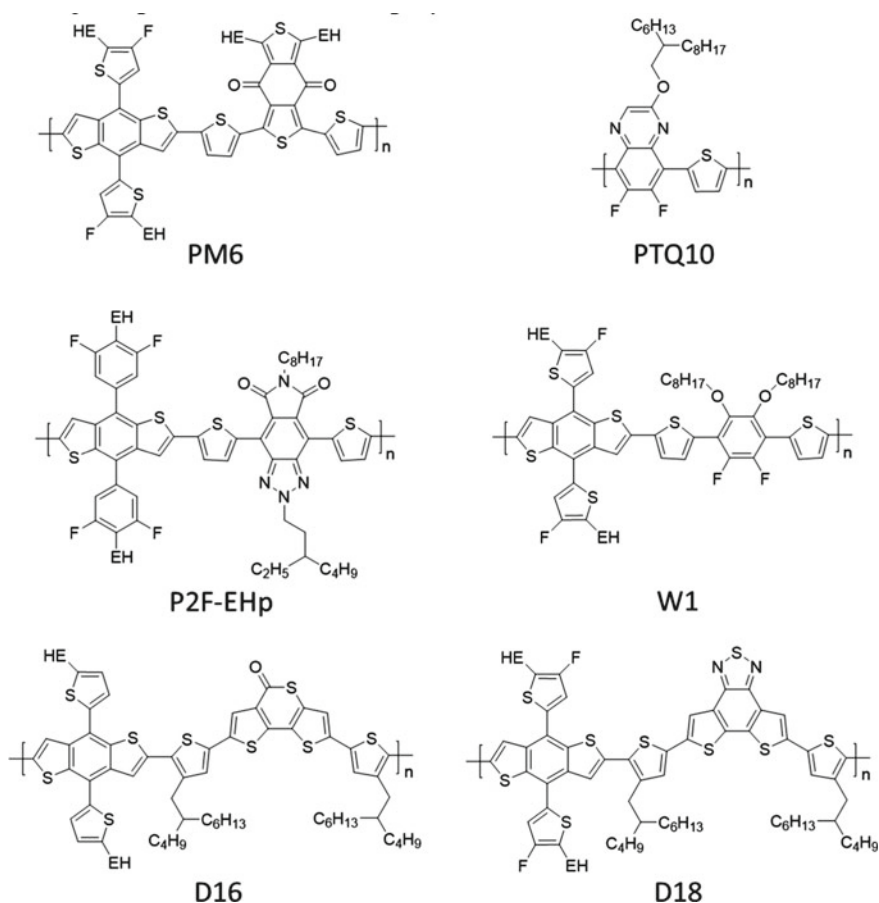
Fig. 5.8 Chemical structures for some high-performance wide-bandgap donors

5.4 Novel Concepts for Better Device Performance

To realize the full potential of an OPV material, device optimization is an inevitable route, which includes but is not limited to device structure engineering, active layer processing method innovation, morphology optimization, multicomponent active layer, and interface engineering. This section begins by discussing the device structure and efficiency upper limit of OPVs. It will then present the effort to improve performance from a device perspective. Different strategies for broadening absorption such as the tandem approach, multicomponent (ternary, quaternary, etc.), and single-junction method will be discussed. All-polymer solar cells and all small molecule solar cells will also be briefly described. In addition, novel techniques for preparing the active layers of organic solar cells, such as the sequential processing method, will also be mentioned.

5.4.1 Upper Limit for Efficiency

In 1961, W. Shockley and H. Queisser calculated the upper limit for the efficiency of p–n junction solar cells using a detailed balanced theory. The authors first assumed that the recombination of electron–hole pairs in the device was all radiative and obtained efficiency limits, and then calculated upper limits by fixing the non-radiative recombination at a certain ratio. By assuming 100% external quantum efficiency for all photons with energies above the bandgap of the semiconductor, they first obtained the relationship between the upper limits of solar cells and the bandgap of the material. Since then, the efficiency limits of solar cells calculated using this model and the revised model (varying by type of solar cell) based on the specific properties of the solar cell have been called Shockley–Queisser (S-Q) limits.

In 2009, when-thiophene-based polymer donors like P3HT and fullerene-based acceptors such as PCBM were still the dominant material combination, Rau et al. calculated the radiative efficiency limits of BHJ-type organic solar cells using the S-Q model [72]. They obtained a theoretical limit of ~23% and explained the difference between laboratory values at the time (3–4%) and the 23% limit by (i) energetic difference between the energy of the exciton in the polymer and the charge-transfer state at the donor/acceptor heterointerface used by bulk heterojunction solar cells (a small efficiency loss of 2%), (ii) insufficient light trapping and parasitic absorption, (iii) low-collection rate of excitons, (iv) a large amount of non-radiative recombination, and (v) insufficiently high-charge-carrier mobilities, where the non-radiative recombination at the donor/acceptor interface was considered the most severe loss channel.

In 2013, the PCE of OPVs increased to over 10%, but some empirical models predicted that the maximum practical PCEs available for OPVs would be in the range of 10–12%, which used an interfacial energy offset, e.g., LUMO-LUMO difference between donor and acceptor, of 0.3–0.5 eV to ensure efficient exciton splitting.

Janssen and Nelson compared various approaches (modified S-Q models) that had been developed to estimate the efficiency limit of OPVs [18]. They mentioned that some of the assumptions in the models used at the time were too pessimistic, which turns out to be correct, of course, starting from the year of 2022 when the current efficiency for single-junction OPVs is nearly 18–29%. They pointed out that the difference of a factor of two compared to the empirical case can largely be explained by differences in ideal and actual internal quantum efficiency (i.e., 1 vs 0.65) and fill factor (i.e., 0.85 vs 0.65).

In 2017, when non-fullerene acceptors were emerging at an unimaginable speed and PCEs of OPVs were improving dramatically, Vandewal et al. studied the relationship between the voltage loss due to non-radiative recombination and the charge-transfer state energy [73]. Using a relatively large number of data sets during the years before 2017, they found that non-radiative voltage loss seems to decrease with increasing charge-transfer state energy, and they claimed that there was an intrinsic link between non-radiative voltage losses and electron-vibration coupling so that these losses are unavoidable. Consequently, a 25.5% PCE limit was calculated by them using a modified S-Q model, and an optimal optical bandgap in the range of 1.45–1.65 eV was suggested, which is 0.2–0.3 eV higher than solar cells with minimized non-radiative voltage losses. The authors also obtained a 19.5% PCE limit for fullerene-based OPVs using non-ideal device parameters, *e.g.*, an EQE of 85% and an FF of 80% in their modified S-Q model.

We note that one of the most fundamental assumptions in the S-Q model is that an excited state, e.g., a singlet exciton, can generate one pair of electrons and a hole, which is true in most cases. However, in some quantum dot solar cells or certain organic semiconductors, multiple exciton generation (MEG) can be realized, which means that the absorption of a photon that has at least twice the bandgap energy produces two or more electron–hole pairs. Such an MEG process in organic semiconductors such as pentacene has been demonstrated. For example, singlet fission is a type of MEG process. In 2013, Baldo et al. showed singlet exciton fission in pentacene, which transforms one singlet state into two triplet states, each with half the energy of the original singlet state [74]. This kind of singlet fission can lead to MEG and can make the solar cell overcome the S-Q limit. In that paper, Baldo et al. demonstrated > 100% external quantum efficiency and 160% internal quantum efficiency using singlet fission. In 2014, Baldo et al. achieved singlet fission in tetracene-based organic solar cells, and a 127% internal quantum efficiency was observed [75]. In 2014, Ehrler et al. incorporated TIPS-pentacene, a solution processed singlet fission organic molecule, into PbSe/PbS-based solar cells and showed that the internal quantum efficiency could reach 170% with PbSe nanocrystals with suitable bandgap [76]. In 2019, Baldo et al. demonstrated the successful sensitization of silicon solar cells using singlet fission in tetracene. The efficient triplet exciton transfer from tetracene to silicon has resulted in a peak total exciton yield of ~133% composed of a singlet transfer yield of ~56% and a triplet transfer yield of ~76% [77]. Nevertheless, how to better utilize MEG processes such as singlet fission of organic semiconductors to promote the efficiency of OPVs or other types of solar cells remains a big challenge, and scientists are trying different strategies to this end [78].

5.4.2   Development of Active Layer Structure

Early OPV devices were fabricated using a simple sandwich structure similar to that of an OLED device, where the active layer composed of only one organic material is placed between a cathode and an anode. Due to the Schottky barrier that typically exists at the organic/metal interface, these early devices are Schottky type OPV devices. Since there is only one component, the excitons generated inside the active layer are difficult to split due to the low-dielectric constant of typical OPV materials. Besides, even if the excitons can split, the charge carriers near the organic/metal interface have a lower chance of being collected due to the Schottky barrier than the state-of-the-art devices with Ohmic contacts. Therefore, these early Schottky devices have low PCEs and are mainly for proof-of-principle purposes. In 1986, C. Tang sequentially vacuum deposited a copper phthalocyanine (CuPc) layer as the electron donor with a thickness of 30 nm and a 50 nm perylene tetracarboxylic derivative layer as the electron acceptor on an ITO coated glass substrate. With Ag evaporated as the top electrode, the bilayer OPV device demonstrated a PCE of almost 1%. This large improvement over the single component device was due to the presence of two different organic layers with a large difference in their electron affinity, which allows excitons to dissociate at the donor/acceptor interface and thus enhances the external quantum efficiency. Nevertheless, the "true" bilayer device, where the donor and acceptor have a relatively clear border that is typically the result of separate vacuum deposition steps, still has issues in exciton harvesting due to the limited interfacial area between the two layers.

In 1995, Heeger et al. and Friend et al. both reported solution processed bulk heterojunction (BHJ) active layer for OPVs where the donor and acceptor are mixed in one solution and processed into a blended thin film. The BHJ structure significantly increases the heterointerface area compared to the bilayer structure. The BHJ structure significantly addresses the low-exciton harvesting yield induced by the short exciton diffusion lengths of typical OPV materials, i.e., 10–20 nm and has been the most unique structure nowadays to realize efficient OPV devices, despite that the route to achieving the BHJ can be different.

5.4.3   Improving the Morphology of Active Layers

Unlike inorganic semiconductor devices with clear crystal structures, the active layers of organic electronic devices represented by organic photovoltaics and organic field-effect transistors not only contain more amorphous states, but also often require more than one organic semiconductor to form active layers in a mixed form to meet the requirements of exciton separation or uniform film formation. Two (or more) organic molecular hybrid films need to form specific morphologies at the nanoscale to meet the requirements of efficient device operation. For example, electron donor and electron acceptor materials in the active layer of organic solar cells must form a nanoscale

bicontinuous interpenetrating network morphology to achieve high-efficiency separation of excitons and efficient charge transport in the meantime. This adds additional morphology complexity to the fabrication, characterization, and optimization of such devices, and the resulting morphological research has also become an important topic in the field of organic optoelectronic devices.

Since BHJ has become the predominant active layer structure, the discussion of morphology becomes even more important. The morphology formed by the donor and acceptor plays an important role in determining the properties of the film, the interface between layers, and the performance of the entire device. As we discussed in the previous section, the morphology of the active layer for a BHJ-type is so crucial that the slightest change in it could lead to essential variations in the electrical, electronic, interfacial, and optical properties of the film. Using phase separation as an example, overly separated donor and acceptor phases may lead to insufficient charge separation, but overly mixed phases reduce charge transport and collection. Therefore, morphology has been intensively studied over the decades along with the evolution of materials and is still the most studied topic in OPV research and even industrial fields. In general, the term "morphology" in thin-film studies refers to the nanoscale structure of the film, involving the spatial arrangement of materials, e.g., the phase segregation of each material, and the internal crystallization property of a material phase domain, e.g., the length of crystal in a certain direction. In the active layer of OPVs, several aspects of the morphology play a strong role in effecting the device performance. For example, the degree of phase segregation among different materials, the domain size and purity, the stacking of conjugated structures in directions such as in-plane and out-of-plane, the orientation of molecular packing, etc.

Methods to study the morphology of OPVs can be roughly categorized into microscopy and scattering techniques. Microscopy is a general term that involves lots of different techniques. Some of the most commonly adopted microscopies to study OPV morphology are scanning electron microscopy (SEM), transmission electron microscopy (TEM), and atomic force microscopy (AFM). These techniques are helpful for more directly revealing the local morphology from phase images. In comparison, scattering techniques use high-flux light beams to probe the structure in Fourier space. Some of the most successful scattering techniques to study OPV morphology include small-angle X-ray scattering (SAXS), resonant soft-X-ray scattering (RSoXS), grazing-incidence X-ray diffraction (GIXD), and small-angle neutron scattering (SANS). In addition, optical measurements can sometimes be useful in revealing the morphology as well, because lots of OPV materials have distinct optical properties such as absorption peaks and their relative intensities. On the basis of steady-state measurements, in situ technologies can also be employed to study the formation process of morphology from liquid state to solid state. For example, in situ synchrotron-based GIXD studies have been carried out to study the morphology evolution of [79]. In situ UV–Vis absorption or photoluminescence spectroscopy has also been used to probe the morphology [80, 81].

Generally speaking, the morphology of a new material and its combination with another material in a BHJ are different whenever the material is changed. Therefore,
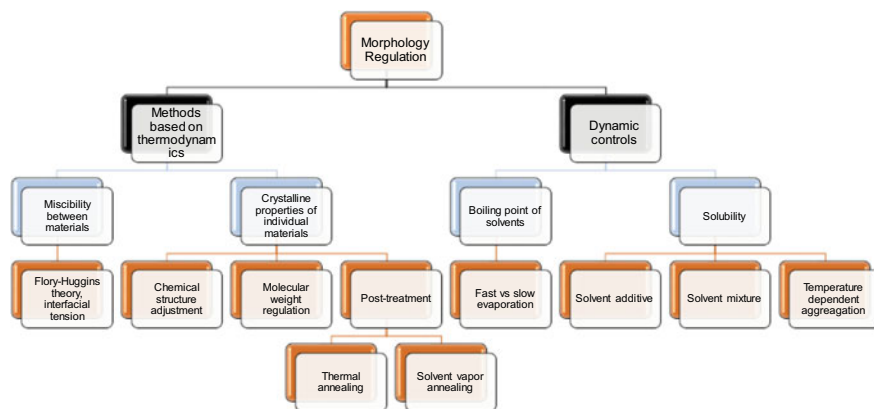
Fig. 5.9 General methods to adjust the morphology of the active layer of OPVs

the investigation into the morphology never stops as long as there are still novel materials being developed. Over the decades, thousands of donor and acceptor materials have been developed for OPV devices, and the number of combinations of them is even greater. Nevertheless, researchers have developed some general methods to tune, control, and eventually improve the morphology of OPVs (Fig. 5.9).

The morphology regulations can be roughly divided into two categories. The first is methods based on thermodynamics: the phase separation between the materials is essentially a thermodynamic question, i.e., whether the donor and acceptor tend to mix or separate is determined by thermodynamics. The Flory–Huggins theory has usually been employed to explain the miscibility between materials. For instance, the Flory–Huggins miscibility parameter, χ, has been used as a figure of merit to signal the miscibility between the materials [82]. Furthermore, some of the materials may tend to separate based on their intrinsic properties determined by their chemical structure. Therefore, to improve the intermixing between the materials, chemists may modify the chemical structure to make them thermodynamically more miscible. Besides, the chemical structure of materials and their interactions with other materials, including solvents, also affect their crystallinity. If a material has an excessive tendency to crystalize, it may form domains that are too large for OPV applications. Therefore, controlling the crystalline behavior is also an important subject in material design and film preparation. Last, post-treatments, i.e., techniques used after the formation of the thin film, can also alter the morphology. For example, simple thermal annealing can greatly improve the morphology of some of the active layers of OPVs. Solvent vapor annealing, which means that the film is placed in a solvent-rich environment for a certain amount of time, is another widely used approach to tune the morphology of the thin film.

In addition to thermodynamics, the solvent evaporation and solute precipitation processes, referred to as dynamics, also play a critical role in the morphology formation process. Not all the morphology formed after the solvent evaporation, and even after post-treatments, is in the thermodynamically equivalent state. In fact, most of

the morphologies formed this way is not thermally stable, which is also the main reason for the morphological instability of OPVs. But this is not always unfavorable. For instance, one can utilize the fast evaporation of solvents to "lock" the morphology in a more OPV-favorable state but not necessarily a thermodynamically equivalent state. There have been multiple reports that high-performance OPV active layers were formed using high-vapor pressure solvents such as chloroform. Solvents such as chloroform not only change the miscibility of materials, but they also evaporate quickly, leaving the solutes in a difficult to change solid state. In comparison with other low-vapor pressure solvents, chloroform may endow the film with more ideal morphology and thus higher PCEs. However, we should note that these high-vapor pressure solvents are not suitable for large-scale device fabrication despite their high performance for lab-scale devices.

5.4.4 Vertical Phase Segregation, Surface Recombination, and Device Architecture

When the term "morphology" is mentioned in the field of OPVs, it generally refers to the bulk morphology, that is, the nanoscale arrangement of materials, their crystalline or amorphous status, their phase separation, etc., within the active layer. However, in the active layer containing two or more organic materials, in addition to the bulk morphology, different materials will also form morphological features with uneven distribution and uneven phase separation scale in the direction perpendicular to the film substrate (longitudinal direction). This phenomenon is called vertical phase separation or vertical phase segregation (VPS). The causes of VPS include both thermodynamic factors such as different surface energies of organic materials and kinetic factors such as phase-lock effects caused by differences in solvent volatilization rates, material crystallization/aggregation rates, and differential solubilities of materials in the solvents [83, 84]. Regardless of the cause, the occurrence of VPS will have varying degrees of influence on device properties. For example, in organic field-effect transistors based on small molecule semiconductors, the vertical phase separation between n-type small molecule organic semiconductors and commonly used polymer film formers such as polystyrene (PS) has a decisive impact on the performance of OFET devices [85]. As another example, in OPV devices, bulk morphology and vertical phase separation of electron donor and electron acceptor both affect the generation, separation, and recombination of photogenerated carriers: the carrier recombination inside the bulk heterojunction is called bulk recombination, while the recombination between the active layer and the interface layer (or electrode) is called surface recombination (or interface recombination).

In the past ten years, research on the morphology of organic active layers has been a research hotspot in the field. However, most of the past researches mainly focused on the bulk morphology of the BHJ and the associated bulk recombination. In contrast, the phase separation in the vertical direction has been less discussed, especially

the changes in surface recombination caused by vertical phase separation. In recent years, with the rapid iteration of organic polymer and small molecule materials and continuous breakthroughs in performance, the research on the vertical phase separation of high-performance material systems and the surface recombination caused by them has lagged behind. Commonly used characterization methods (instruments) include dynamic secondary ion mass spectrometry (D-SIMIS), neutron reflectometry, variable wavelength ellipsometry, cross-sectional scanning (SEM)/transmission electron microscopy (TEM), X-ray photoelectron energy spectroscopy (XPS), near-edge X-ray absorption fine structure (NEXAFS), etc. [88, 89]. Among them, the neutron reflection experiment requires a sufficiently high contrast in the scattering length density (SLD) between the two (or more) materials under study [84]; D-SIMS can track the amount of elements across the film through spectroscopic analysis of secondary ions emanating from the surface of the film by the impact of the high-energy primary ions; ellipsometry is an optical measurements that can easily carried out but it requires complicated mathematical model(s) to obtain satisfactory fitting results in order to extract VPS information; cross-sectional SEM/TEM experiments rely on the contrast between materials (if any) in the vertical direction across the film the gain information on VPS but may not be able to tell the donor from the acceptor in some of the novel organic material combinations that have less signal contrast; XPS and NEXAFS are surface technologies and can only provide compositional information near the surface of the film.

Obviously, the presence or absence of vertical phase separation has a decisive influence on the degree and mechanism of surface recombination: relative to a uniform vertical distribution (top left of Fig. 5.10), if the donor (acceptor) material is more concentrated near the electron (hole) transport layer, the surface recombination of carriers increases, the selectivity of the electrode to carriers decreases, and the device performance is also adversely affected; the opposite vertical phase separation (lower right of Fig. 5.10) can reduce the surface recombination, and the carrier selectivity of the electrode is improved, thereby improving the device performance. The most ideal state of the device is that the surface recombination is extremely low (bottom right of Fig. 5.10), but when the vertical phase separation is not ideal, the surface recombination increases, and this additional surface recombination (rate k_{sf}) will add an extra carrier recombination channel on top of the monomolecular (rate k_{mm}) and bimolecular (rate k_{bm}) bulk recombination (Fig. 5.11a) [90], equivalent to adding a parallel resistance in the equivalent circuit (Fig. 5.11b), which will have a direct negative effect on the V_{OC} of the device. Therefore, adjusting and controlling the vertical phase separation by means of materials and device engineering, eliminating (or weakening) the negative effect of vertical phase separation, and changing the device structure and preparation method to change the negative effect into a positive one are very important for improving device performance.

In crystalline silicon solar cells, surface recombination rates can be derived from effective lifetimes measured on high-quality floating zone wafers with extremely long bulk lifetimes. The feasibility of this approach lies in the fact that the mobility of crystalline silicon is well known, so diffusion to the surface can be easily accounted for,
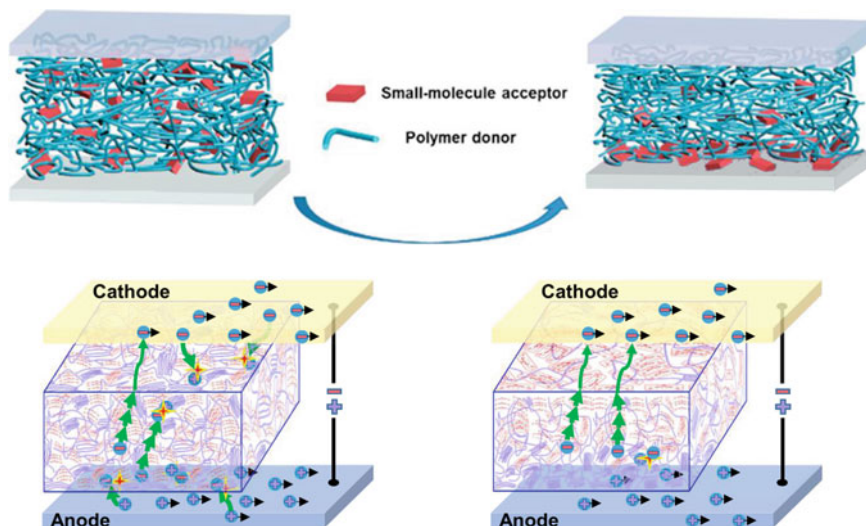
Fig. 5.10 Top (left): The material distribution is relatively uniform, and the vertical phase separation is not obvious in the active layer; (right) the vertical phase separation schematic diagram of the acceptor molecules aggregated to the lower interface and the donor material to the upper interface [86]. Bottom (left): A system in which both bulk and surface recombination are high; (right) a system in which bulk recombination dominates, and surface recombination is less. (Adapted from Ref [87])
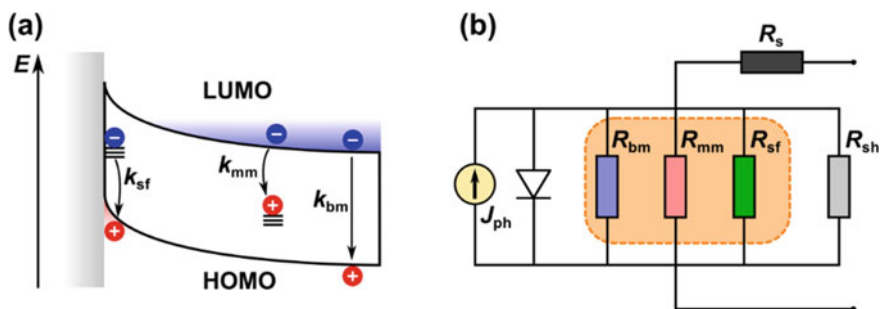
Fig. 5.11 a Schematic representation of surface (k_{sf}), monomolecular (k_{mm}), and bimolecular (k_{bm}) recombination; **b** equivalents including three recombination resistors (orange boxes), shunt resistors, ideal diodes, and series resistors circuit diagram. (Adapted from Ref [90])

thus enabling the assumption of carrier lifetime based on surface recombination limitations. In thin-film solar cells, especially when dealing with new material systems (such as organics and perovskite-based materials), the material absorption, mobility, electrostatic parameters, and carrier bulk lifetime may not have been accurately measured. Their impact on the overall carrier lifetime cannot be quantitatively considered, and surface recombination cannot be isolated for investigation [90]. Another

reason for the lack of research on surface recombination is that surface recombination and monomolecular recombination are difficult to distinguish: The total carrier recombination rate is the superposition of monomolecular recombination, bimolecular recombination, and surface recombination, and the surface recombination and monomolecular recombination rates are both first-order functions of carrier concentration, so it is often impossible to separate them apart. This has led to much research on carrier recombination to combine the two as "trap-assisted recombination."

Nevertheless, there have been studies on the surface recombination of several organic systems [91–93]. In future, in order to better study surface recombination, it is necessary to prepare control groups with similar bulk recombination and different vertical phase separation in high-performance organic solar cells based on the latest generation of donor–acceptor material systems.

5.4.5 Methodology for Active Layer Preparation

As we mentioned earlier, in 1995, Heeger et al. and Friend et al. proposed the concept of bulk heterojunction (BHJ). The proposed method greatly increases the donor/acceptor interface area, which in turn improves the exciton separation efficiency and device performance. The preparation of BHJ structures has been dominated by the blend-casting (BC) method, which involves the preparation of a mixed solution of the electron donor and electron acceptor material, the deposition of this blend solution using thin-film formation techniques such as spin-coating, blade-coating, or slot-die coating, and the formation of an interpenetrated bicontinuous network between the two materials with proper phase separation scales. This blend-casting method provides a convenient way to study the properties of materials. After more than 20 years of experimental verification, BC is still one of the most effective methods for preparing high-performance devices in the field of OPVs [62, 71, 94–101].

Although the BC process is still the mainstream method for the preparation of BHJ, there are still some basic problems in the morphology of the prepared active layer. First, the preparation of BHJ by the BC method relies on the spontaneous phase separation between the donor and acceptor materials to form nanoscale morphology through rapid solvent evaporation and solute precipitation. However, this spontaneously formed morphology is usually not in the best state for achieving high-device performance. To improve the morphology, it usually requires the use of kinetic means or post-treatments. For example, the choice of solvents and additives, processing conditions (e.g., concentration, spin-coating speed, drying time), environmental conditions (e.g., humidity and temperature), and post-annealing steps can all significantly alter performance [102]. Not only are these modifications tedious, but subtle changes in processing conditions or operating environment may cause the transition of active layer to another equilibrium state [103, 104]. Since the morphology formed by the intertwining of the donor and the acceptor is very complex, the optimal morphology requires that the component distribution, crystallinity, phase separation

scale, molecular order, molecular orientation at the interface, and material distribution in the vertical direction (vertical phase separation) must reach a specific state, so the nature of the BC method that the materials are in a mixture makes it difficult for researchers to predict how changing one variable will affect the overall nanoscale morphology. This complexity is further amplified when transitioning from laboratory scale to commercial scale, which is also a significant disadvantage of the BC process. An ideal fabrication process would enable the independent deposition of the donor and acceptor as two separate solutions, allowing each layer to be independently controlled, similar to mimicking traditional layer-by-layer printing processes.

Based on these considerations, Schwartz's research group first explored the way to sequentially prepare the active layer. In 2009, the group published the "sequential processing" method, where the donor and acceptor were processed from independent solutions. This layer-by-layer solution preparation method for the OPV active layer has been referred to as SqP, also known as layer-by-layer (LBL) fabrication, quasi-bilayer, etc. In the original contribution [105], the authors deposited poly(3-hexylthiophene) (P3HT) and [6, 6]-phenyl-C61-butyric acid methyl ester ($PC_{61}BM$) from orthogonal solvents and obtained SqP devices almost as efficient as those processed from the conventional BC method. After a series of characterizations, it was found that the active layer prepared by SqP can form a BHJ structure in the bulk, and at the same time form a vertical structure similar to three layers on the premise of retaining the crystallinity of the underlying polymer. That is, between two relatively pure and thin donor and acceptor layers are a mixed donor/acceptor layer for this material system [106]. This shows that the SqP method cannot only effectively form a BHJ structure like the BC method but also provides an effective solution for the aforementioned vertical phase separation problem (at least for certain donor/acceptor combinations).

The fabrication process of SqP combines the simplicity of a single-junction OPV device with the enlarged material contact area achieved by the BC method (Fig. 5.12). Specifically, in the SqP method, the donor and acceptor solutions are prepared separately and deposited sequentially where the first layer (usually the donor) and the second layer (usually the acceptor) are cast in sequence. Since each material is deposited independently, the crystallization or aggregation process of the bottom layer is not affected by the top layer material, and the top layer material is infiltrated into the bottom layer material through the swelling effect of the solvent on the bottom layer material to form a bicontinuous interpenetrating network, which can achieve individual control and optimization of each layer. Since its development, several research groups have confirmed in different material systems that compared with the BC method, and the SqP method can better control the scale of phase separation, achieve stronger absorption, higher carrier mobility, more efficient charge extraction, and even higher exciton diffusion lengths [107–112]. By controlling the swelling of the donor layer and the degree of mixing with the acceptor, the control on vertical phase separation that cannot be regulated by BC can be achieved [113]. These advantages make the SqP method not only achieve higher efficiency in small-area devices (currently, the highest efficiency of the SqP method has exceeded 18%)

[112], higher thermal stability, and higher reproducibility but also demonstrate superior performance than the BC method in large-area device/module production. The current efficiency of OPV modules based on the large-area SqP method has reached a record of 12% [87], confirming that the SqP method is a more promising mass production technique (Fig. 5.13).

Based on these advantages, the SqP method has been employed as the preparation method for active layer in dozens of material systems, and more than 100 high-quality papers based on the SqP method have been published [115]. However, compared with thousands of OPV works based on the BC method, the SqP method is still relatively slow for being adopted in new material systems. The main problem is not only
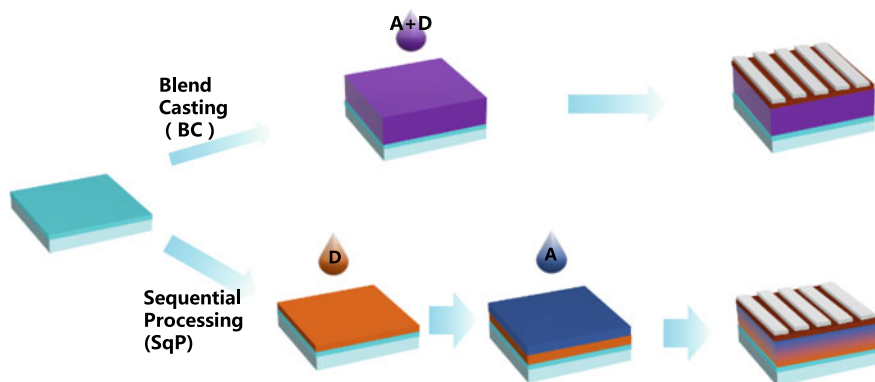
Fig. 5.12 Process comparison between sequential processing (SqP) and blending-casting (BC)
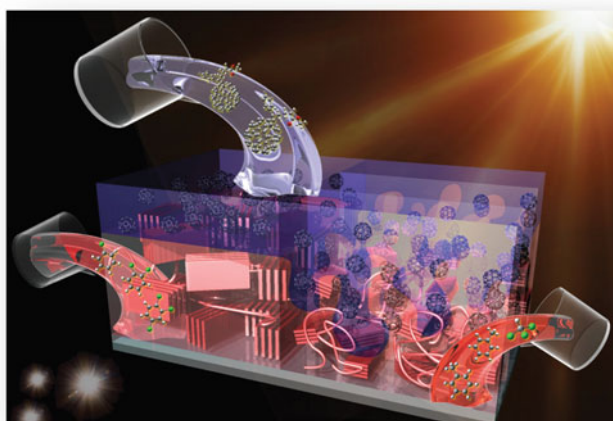
Fig. 5.13 Cartoon showing the SqP method. (Adapted from Ref. [114])

the fast iteration speed of the active layer material system, but also the difficulty of solvent selection (especially the top layer solvent): The ideal top layer solvent cannot have too high solubility for the bottom layer material (otherwise the bottom layer will be destroyed) and must produce sufficient swelling on the bottom layer to inject the top layer material to achieve a bicontinuous and interpenetrating nanoscale network. Therefore, the ideal top layer solvent is not easy to obtain, which limits the promotion of the SqP method. To solve this issue, different research groups have proposed various solutions. For instance, SqP systems that do not require the use of strictly orthogonal solvents have been reported in recent years; some material systems can even use the same solvent for both top and bottom layers [116–119]. In order to make the SqP method more widely accepted, it is still necessary to find a more universal solvent selection route.

5.4.6 Multicomponent Active Layers

To maintain the simplicity of single-junction structure and expand the absorption range at the same time, multicomponent active layer has been proposed and practiced. A typical example is the ternary blend bulk-heterojunction active layer, where two acceptors and one donor or two donors and one acceptor are blended together during active layer fabrication. The initial aim of introducing a third component into the active layer is to broaden the absorption range. Nevertheless, the ternary and multicomponent idea have gradually become a mainstream way to boost efficiency. In particular, ternary solar cells cannot only have increased J_{SC} but also have enhanced V_{OC} or FF, or even concurrently increased all three parameters. Let us take V_{OC} as an example: before, 2012–2013, the conventional wisdom for ternary blend solar cells was that they may have higher J_{SC} due to broadened absorption range, but it is most likely the result of the lowered VOC, and it is overall a trade-off between current and voltage. The reasoning behind this argument was that it was originally predicted that the V_{OC} of ternary or multicomponent active layers is pinned to the smaller V_{OC} of the corresponding binary blends of the constituent components [120], thus increasing the overall energy loss of the device. However, ternary blend organic solar cells have gone beyond expectations since the demonstration of gradual changes in V_{OC} s with the film composition in PCBM and ICBA-based ternary devices [121–123].

The origin of the such almost linearly changed V_{OC} is complicated [126–130]. Mainstream models include the formation of organic alloy inside the active layer [125, 131] and parallel-connected bulk heterojunction [123, 132] have been proposed to explain the compositional dependence of V_{OC}. In 2013, Street et al. revealed that in the ternary solar cell that exhibited such a relationship, the charge-transfer state (CTS) energy also depends strongly on film composition (Fig. 5.14c, d), which indicates the formation of an "alloy"-like structure between the two organic acceptor materials [125]. Gobalasingham et al. [133] studied two different ternary systems where two different pairs of donor polymers have different interfacial tensions and proposed that the interfacial tension between the two polymer donors in such a

donor:donor:acceptor structure is the reason for determining whether they tend to intermix and is therefore the prerequisite for the alloy formation and tunable V_{OC}. Khlyabich et al. [128] further investigated the morphology of these ternary blends and verified the effectiveness of surface energy as a figure of merit to predict intermixing and alloy formation of the organic compounds. In 2018, Jiang et al. [132] studied a series of small molecule acceptor-based non-fullerene ternary blends with PTFB-O as the polymer donor, ITIC-Th as one of the small molecular acceptors, and another A-D-A type or PDI-type small molecule acceptor that has a different LUMO energy level than ITIC-Th. The authors showed that no matter the large chemical structure variation between the two acceptors used in the ternary blend, e.g., PDI-based and A-D-A-based in one blend, as long as the interfacial tension (γ) between them is small, the two acceptors could form an alloy-like mixture that led to almost linearly tuned V_{OC} as a function of film composition. In contrast, the devices showed that when the other acceptor was changed to $PC_{71}BM$, the classical fullerene acceptor with a large surface tension, the large interfacial tension between ITIC-Th and $PC_{71}BM$ resulted in a pinned V_{OC} instead of a linearly tunable V_{OC}. This again confirms that interfacial tension governs the formation of organic alloy. These results manifested that the voltage output of the device may not have to suffer from a large loss due to the trade-off between current and voltage. Instead, they can be tuned between the V_{OC}s of the binary devices, which is a significant bonus on the basis of absorption spectrum broadening for the ternary design. This considerably increases the impact of this device platform (Fig. 5.15).

Another observation that leads to beneficial results for the ternary device when the third component is used is that it could cause energy transfer between materials. *Energy Transfer:* In the excited state, organic conjugated materials can return to the ground state through energy transfer. There are two ways of energy transfer: the Förster type and the Dexter type. First, the Förster-type energy transfer is carried out in a resonance manner. When the energy donor molecule is activated, the energy is transferred to the acceptor in a resonance manner. At this time, at the LUMO level, the donor electron releases energy back to the acceptor. In the ground state, the HOMO level of the acceptor electron absorbs energy and undergoes a transition. Förster energy transfer is resonant, which does not need to go through the overlapping of orbitals and is therefore a relatively longer distance (5–10 nm) interaction. Dexter energy transfer is essentially an electron exchange process. In the excited state, the activated donor transfers electrons from the LUMO to the acceptor's LUMO energy level, and the electrons on the acceptor's HOMO energy level are transferred to the donor's HOMO energy level. In this process, the transfer of energy also occurs. Electron exchange requires spatial overlap of the orbits, and thus close interactions in the range of 0.5–1 nm are required. In some ternary systems, energy transfer can be achieved. The third component could serve either as an energy donor or as an energy acceptor. When it is an energy donor, it transfers energy to the other material(s) after absorbing light; when it is an energy acceptor, the primary energy donor transfers energy to it. The first case, when the third component absorbs photons, it does not directly participate in the separation of charges but converts them into energy and transmits them to the main donor or main acceptor. At this time, its
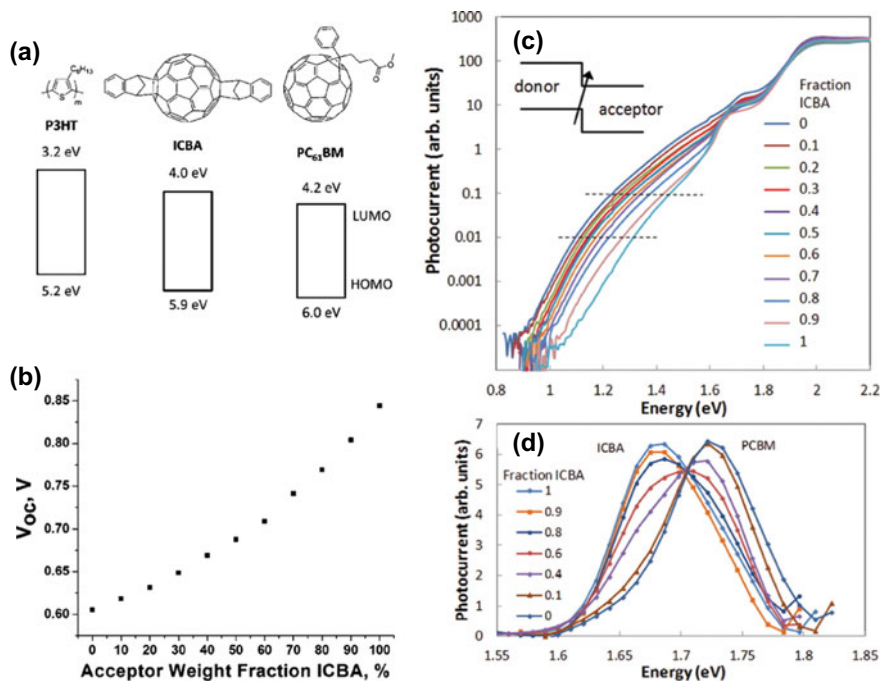
Fig. 5.14 a Structures and corresponding HOMO and LUMO energy levels of P3HT, ICBA, and PC61BM. **b** V_{OC} for the ternary blend BHJ solar cells as a function of the amount of ICBA in the blend (**a**, **b**) (Adapted from Ref [124]). Copyright (2011) American Chemical Society. **c** Photocurrent spectra response data for the P3HT:PCBM:ICBA (D:A1$_x$:A2$_{(1-x)}$) ternary blend solar cells plotted as a function of ICBA fraction in PCBM:ICBA pair. The inset indicates the CT transition or interface band gap that is being measured, and the pair of dashed lines indicates the range over which the interface band gap energy is extracted. **d** Expanded plot of the peaks near 1.7 eV with the background subtracted. The peak centered above 1.7 eV corresponds to PCBM absorption, and the peak centered below 1.7 eV corresponds to ICBA (**c**, **d**). (Adapted from Ref [125])

function is to expand the absorption range and increase the number of absorbed photons, thereby improving the efficiency of the device. The second case is that when the third component participates in the system of charge separation, when the excitons of the energy donor itself cannot sufficiently conduct charge separation, it will transfer energy to the third component, and the third component will separate charges, allowing the donor to absorb more photons or use it to form more excitons, thereby increasing the utilization of excitons.

Gupta et al. [134] reported the ternary blend PCDTBT:PTB7:PC71BM and studied its energy transfer. Using transient fluorescence experiments, they found that the fluorescence lifetime of PCDTs (compared to pure films) was significantly shortened due to energy transfer between the two materials. In the transient absorption spectrum, after blending PCDTBT and PTBT, the ground-state bleaching signal of PTB7 was significantly reduced, and the excited state absorption signal was
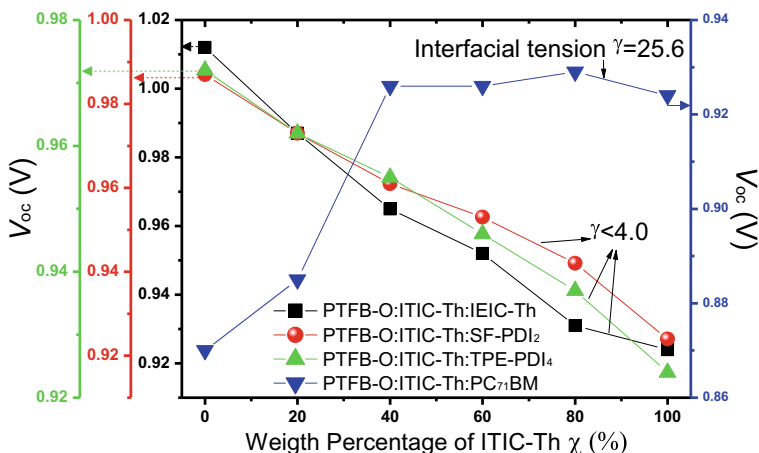
Fig. 5.15 V_{OC} as a function of ITIC-Th weight percentage. The V_{OC} of devices based on four ternary systems with different interfacial tension γ between the two acceptors. PTFB-O:ITIC-Th:IEIC-Th (black square), PTFB-O:ITIC-Th:SF-PDI$_2$ (red circles), PTFB-O:ITIC-Th:TPE-PDI$_4$ (green up triangle), PTFB-O:ITIC-Th:PC$_{71}$BM (blue down triangle). We note that PC$_{71}$BM has a lower LUMO level than ITIC-Th while the other three SMAs have higher LUMO levels than ITIC-Th, which is accounted for the reverse trend in V_{OC}. (Adapted from Ref [132])

enhanced, indicating that the energy transfer to PTB7 through PCDTBT increased the device efficiency from 6.8% to 8.9%. Yu et al. introduced the wide-bandgap polymer donor PID2 into the PTB7-Th:PC$_{71}$BM system [135], which not only improved the morphology and suppressed recombination, but also demonstrated energy transfer between PID2 and PTB7-Th.

Moreover, the addition of the third component could regulate the morphology of the active layer. If such regulation is toward a more favorable direction, then the ternary blend could gain another bonus effect and have improved performance. For instance, Yu et al. used two IDT-based non-fullerene acceptors named IT-M and IEIC-O [136] with different bandgaps in a ternary blend in combination with a large bandgap polymer named J52 [125]. Although the bandgaps are different, the LUMO energy levels between IDT and IT-M are similar, which endowed their binary BHJ devices with almost identical V_{OC}s. Meanwhile, the upshifted HOMO level of IEIC-O led to a redshifted absorption, which better complemented the absorption and increased the J_{SC} and thus the PCE (from 9.4% for the binary to 11.1% for the ternary). Moreover, the structural similarity between IDT and IT-M led to a compatible morphology: The blend morphology of IT-M and IEIC-O can be viewed as the compositional average of morphology formed by the individual material. The authors considered this another reason for the high FF of the ternary solar cell device.

Furthermore, ternary OSCs have been shown to have enhanced stability over their binary counterparts. For instance, Baran et al. reported the use of IDTBR and IDFBR as two non-fullerene acceptors in combination with P3HT or PTB7-Th, the workhorse polymer donors, to fabricate ternary organic solar cells137. Beside

increased efficiency, the authors found that the ternary device outperformed the binary ones in terms of dark and photostability in air.

Since the surge of non-fullerene acceptors, the choices for the third component have been largely increased thanks to the various optical properties of non-fullerene materials. There have been many reports on using either one polymeric donor in combination with two non-fullerene acceptors [138], two donors and one non-fullerene acceptor, one polymer donor and one non-fullerene acceptor together with a fullerene acceptor, etc. Furthermore, quaternary or even five-component active layer has been reported with enhanced photovoltaic performance. For instance, Arunagiri et al. mixed two donors and two acceptors together in one solution for the active layer preparation. The quaternary active layer composing PM6 (donor), PTQ10 (donor), N3 (acceptor), and $PC_{71}BM$ (acceptor) demonstrated a PCE of 17.73%. Through X-ray scattering characterizations, the authors found that the increased performance of the quaternary device can be attributed to a "rivers and streams"-type hierarchical morphology. In this multilength scale morphology, the small domains formed by PTQ10 and $PC_{71}BM$ serve as "separators" that spatially separate the "main river" formed by PM6 and N3, which leads to reduced charge-carrier recombination and improved charge transport properties.

Despite these achievements, it should be noted that morphological and the optoelectronic properties of the multicomponent organic solar cells are extremely complex. There has been no universal model that can elucidate the entire picture of the active layer morphology or the physical meaning behind the electrical behaviors of these films/devices. Nevertheless, this does not hinder the progress of this device platform, and it could be expected that more and more high-performance multicomponent active layer combinations will emerge in future.

5.4.7 All-Polymer Solar Cells

The classic OSC active layer is composed of polymer donors and fullerene derivative acceptors. With the development of non-fullerene acceptor materials, the current research direction has shifted to polymer donors and non-fullerene acceptor-based material systems. Compared with fullerene acceptors, non-fullerene acceptors are flexible in chemical structure design, which can better match the absorbance spectrum and electrical properties of the donors, and the prepared devices also generally exhibit lower voltage loss, which boosted device performance. In terms of material composition, non-fullerene receptors are mainly divided into two categories: small molecule acceptors and polymer acceptors. The development of small molecule acceptors has changed rapidly over the past few years, which currently possesses the highest PCE in the entire OSC field. For the polymer donor-based non-fullerene active layer, when the acceptor is also a polymer, an all-polymer active layer is formed. Such organic solar cells are referred to as all-polymer solar cells (all-PSCs). Besides similar advantages to OSCs based on small molecule acceptors, all-PSCs also possess better mechanical properties [139, 140] such as higher tensile and flexural

toughness and potentially higher thermal stability, which give them better prospects for mass production.

The field of all-PSC has experienced more than 20 years of development, starting from the earliest donor–acceptor polymers based on polyparaphenylene vinylene (PPV) units [14]. The wide application of aromatic imide repeating units (such as NDI, PDI) in developing new polymer acceptors has made great progress in device efficiency for all-PSCs [139, 141–144].

However, polymers are large molecules. From Flory–Huggins theory, the entropy gain for mixing monomers is $S = -R(\phi_1 ln\phi_1 + \phi_2 ln\phi_2)$, where ϕ_1 and ϕ_2 are the volume fractions of monomer 1 and monomer 2, respectively. Whereas, when mixing two polymers, the entropy gain becomes $S = -R\left(\frac{\phi_1}{N_1}ln\phi_1 + \frac{\phi_2}{N_2}ln\phi_2\right)$, where N_1 and N_2 are the degrees of polymerization of polymer 1 and polymer 2, respectively. This indicates that the entropy gain for mixing two polymerized materials is much smaller than that for mixing two monomers or small molecules. This is probably the most crucial reason for the enhanced difficulty in reducing the scale of phase separation in all-PSCs. Therefore, to reduce the overall Gibbs free energy change for mixing two polymers, the enthalpy of mixing, $RT\chi\phi_1\phi_2$, must be minimized, which requires that the Flory–Huggins interaction parameter χ cannot be too large for achieving adequate mixing.

Recently, strategies based on polymerization of high-efficiency small molecule acceptor units have significantly addressed this issue. Organic chemists have transferred the experience of small molecular design to polymer acceptor design. By polymerizing small molecule acceptors, the so-called polymerized small molecules (PSMs) have skyrocketed the performance of all-PSCs [145–147], and the highest efficiency for all-PSCs utilizing PSMAs has surpassed > 17% [148].

However, despite these achievements, due to the rapid iteration of materials, the research on the device preparation method of all-PSCs, the working mechanism of new materials and related device physics may not be synchronized. Several major questions regarding the working principles of all-PSCs need to be answered in future. For example: (1) How to understand the difference between polymer and small molecule acceptors? Do the physical problems facing the small molecule acceptor field apply equally to the all-polymer field? e.g., Does the constraint imposed by the HOMO-HOMO energy difference (ΔHOMO) between the donor polymer and the narrow-bandgap small molecule acceptor on the quantum efficiency of the device also exist in the all-polymer system? [149] (2) How to alleviate the morphology problems caused by the intrinsic factors of the all-polymer such as long-chain entanglement of the polymer to further improve the device performance?

Specifically, for the first question, although the maximum efficiency of small molecule acceptor materials has exceeded 19%, and many systems have shown lower voltage losses than fullerene acceptors, there has always been a hidden concern: Does the continuously decreasing bandgap due to the red-shift of absorption adversely affect device operation? Can the frontier orbital energy level difference between the donor and the donor be infinitely reduced? Not long ago, Laquai et al. [149] prepared a series of solar cell devices based on narrow-bandgap small molecule acceptors and

wider-bandgap polymer donors and found that the internal quantum efficiency (IQE) is directly related to the ΔHOMO between the donor and the acceptor—systems with ΔHOMO values less than about 0.5 eV generally exhibit low IQE. The authors also pointed out that the reason why close to zero ΔHOMO (or ΔLUMO) was observed in higher efficiency systems in some of the previous work was that the measurement method for the energy of frontier orbital was usually cyclic voltammetry, which might not be accurate when measuring the energy level of thin films. These values were not zero and vary widely when measured by more accurate methods. The authors attributed the dependence of IQE on high ΔHOMO to the band bending at the acceptor heterojunction induced by the electrostatic field induced by the quadrupole moment of the small molecule acceptor, which reduces the exciton separation drive energy generated by the original ΔHOMO (before bending). Therefore, without a sufficiently high-original ΔHOMO, efficient hole transfer cannot be formed. Compared with ΔHOMO, IQE has a weaker dependence on ΔLUMO, which was attributed to the energy transfer between wide-bandgap donors and narrow-bandgap acceptors by the authors. These results put more constraints on molecular design: reducing the acceptor bandgap while ensuring a sufficient difference between the acceptor HOMO and the donor HOMO, and the potential band bending further increases the need for the original ΔHOMO, which increases scruples during molecular design and may even limit the maximum efficiency of this material system.

This issue has not been systematically investigated in all-polymer systems. Affected by molecular weight, main and side chain structure, etc., the conformation (affecting the quadrupole moment) presented by the polymer acceptor and the small molecule acceptor at the heterojunction and the potential energy band bending caused by it may be substantially different [150, 151]. It is therefore reasonable to wonder whether the series of problems exhibited by narrow-bandgap small molecules also occurs in narrow-bandgap polymer acceptors, and to what extent if so. If the IQE of the high-efficiency all-polymer given to the acceptor material is also strongly governed by ΔHOMO, the minimum voltage loss achievable by the material system will also increase [25], and the potential maximum efficiency will decrease accordingly. Therefore, answering this question is not only important for all-polymer material design but also for the efficiency limit of this field.

The second problem arises mainly from the intrinsic characteristics of all-polymer active layers. Compared with small molecules, the mixing entropy of the all-polymer system itself is smaller, and factors such as polymer backbone orientation and side chain entanglement may affect the morphology of the all-polymer active layer prepared by traditional blending methods. In order to solve the morphology problem of the active layer of All-PSCs, in addition to improving the chemical structure of the material, there have also been attempts from the perspective of device engineering, such as adjusting the ratio of the acceptor, adding a third component, and changing the intermolecular interaction.

5.5 Market Potential

Clean energy is an important topic in the upcoming decades under the theme of carbon neutralization. Various countries around the world have announced energy development plans that all aim to promote the research, development, and application of clean energy technology. Among them, solar energy utilization, especially the solar cells that can directly convert photons to electricity, is one of the most important categories. Besides centralized PV stations, diversified utilization of solar energy, especially distributed PVs, is considered another major utilization method in modern cities. Different countries and regions have also announced policies to promote the use of distributed photovoltaics. For example, in 2018, Hong Kong announced the highest trade-in tariff rate for PV electricity, which is 5 HKD/kWh (10 kW), about 6–7 times the rest of the world. The "self-generated and self-used" mode of some distributed PVs can reduce the loss due to power transmission and reduce the fluctuation of PV power input for the grid connection mode. The modern city with dense high-rise buildings is the area with the highest electricity density. With the deepening of urbanization, the pace of distributed photovoltaics entering the city is accelerating year by year. However, unlike the vast deserts and plains, the ever-changing application scenarios in cities have put forward new demands for the photovoltaic industry: emerging markets such as power generation glass curtain walls, vehicle photovoltaics, and sensors driven by indoor photovoltaics require photovoltaic technology to be semitransparent, flexible, lightweight, and stylish. These demands have led to the development of a new generation of photovoltaic materials and devices.

However, traditional Si PVs generally have a tedious pattern and color, and they are also opaque, stiff, and fragile, and thus are not suitable for installation on a large scale in modern cities. In contrast, OPVs can offer several attractive features, such as lightweight, flexibility, color, patternability, and semitransparency. Thus, OPV is considered an alternative PV technology for distributed PV in cities.

These new PV markets include, but are not limited to, power-generating stadium shelters, building panoramic sunroofs, power-generation intelligent bus stations, power-generation car films, photovoltaic agricultural greenhouses, and other fields. Thanks to the lightweight and flexibility of OPVs, the installation cost of OPV-based solar panels would be considerably lower than tractional PVs, which require heavy bracketing to ensure mechanical stability.

Automotive PV Market: A typical question asked by the community when it comes to automotive PV is: Is there a need to integrate PV panels on cars? The answer is yes. In fact, some auto makers are actively exploring the use of thin-film PV on cars, not only on electric vehicles but also on conventional gasoline-engine cars. In terms of functionality, the power generated by PV can be used for ventilation, which keeps the car from overheating when parked under sunshine; to prevent battery leakage; and to increase the range per charge for electric vehicles.

Among all types of PVs, c-Si PVs are rigid, fragile, dull-colored and are not suitable for cars with curved surfaces. Cost and semitransparency are two major factors when applying photovoltaics to vehicles. Semitransparency is the biggest

advantage of OPV. Instead of installing an OPV as a separate component into the car, future OPVs should be able to serve as an upgraded version of "window films". Thanks to the wide acceptance and popularity of window films, OPV products would have a chance to enter the market easily. The main functions of traditional car films are to block visible and IR radiation and enhance privacy. OPVs can have these features as well. Therefore, as long as OPV car films in future can be made to have a similar appearance and transparency as the current car films at a relatively low cost, they have great potential to replace them.

BIPV Market: In addition to the vast rural and suburban areas, another important application of distributed grids is in cities. Although modern cities have limited land area, an important way to receive light energy is from the side of the buildings in the city. Compared to the roof, the high-rise office building has a large glass curtain wall on all four sides. According to estimates, the potential glass curtain wall that can be used to generate electricity every year is hundreds of billions of square meters worldwide, which can be translated into a billion dollar market size, assuming only a very small amount of market share. Calculations show that if all glass curtain walls were replaced by power-generation glass curtain walls, the power generation is equivalent to a total installed capacity in the range of tens to hundreds of GW. At the same time, these power glass curtain walls will reduce CO_2 emissions by nearly a million tons, which will greatly contribute to global emission reduction targets. Therefore, power-generation glass curtain walls are an area that many countries strongly support because high-rise buildings in the city are the areas with the highest electricity density. The strategy of "local power generation on site" greatly reduces losses in the power transmission process and is the first step in building a truly green city.

Of course, in addition to a certain power conversion efficiency, the power-generation type glass curtain wall has a rigid requirement for the photovoltaic module: the transmittance of the finished power-generation glass must be as high as the industry requirements. Therefore, traditional photovoltaic technology is not suitable for this application, because the traditional photovoltaic modules are mostly opaque and heavy. The new photovoltaic technology needs to meet the transmittance standard, and it is also best to have color controllability to meet the visual needs of different buildings. These power glass curtain walls will provide a large amount of electricity to the building and will greatly reduce the demand for electricity in the city.

Thanks to the semitransparency, near-IR-absorption (reducing irradiation and thus solar heat to reduce building air-conditioner load), lightweight (easy installation), and mechanical flexibility, OPV is an ideal candidate for BIPV applications such as power-generation glass curtain walls. Not only can OPVs provide extra electrical energy to the building, they can also reduce the overall energy demand of the building since they reduce direct solar heat irradiation in summer or high-temperature regions.

PV-stockbreeding, military PV-tent, and other portable applications: These markets have the following features, including (i) frequent migration; (ii) long sun-hours per day; and (iii) require PVs that are lightweight, flexible, easy to carry, and install. Conventional PVs have obvious limitations because most of them are heavy,

fragile, and hard to carry and install. In comparison, the OPV products of the future are light and flexible, safe, easy to carry and install, which makes them the perfect candidate for this market. Similar to stockbreeding, military tents and beach awnings have similar requirements, which are also potential markets OPVs could aim at.

Indoor applications: OPV for smart home and IoT: The emerging smart home and Internet of things (IoT) industries require a large number of small electronic components such as sensors that do not require a lot of power, but battery replacement is an obstacle to the continued application of sensors. If there is a photovoltaic technology that can generate electricity from indoor light in addition to outdoor light, then these sensors could never need to have their batteries replaced. In contrast to traditional photovoltaics such as c-Si that do not have high-efficiency indoors, the indoor PCE for OPVs can be extremely high, e.g., > 30%.[68] The reason for the high-indoor efficiency is mainly the tunable optical properties of the active layer materials and the decent weak-light performance of thin-film photovoltaics. Combining the flexibility and lightness, OPVs could be fabricated into products such as "photovoltaic tape" and integrated onto these large numbers of sensors. Due to the rapid rise of the IOT and smart home industry in the world, air quality monitoring, temperature/humidity monitoring, surveillance cameras, LED lighting, etc., all require sensors to realize, and the prospect of OPVs in this field is huge.

5.6   Summary and Outlook

OPVs use carbon-based organic semiconductor materials as the active layer, and their easily adjustable chemical structure endows them with flexible and tunable properties including optical, morphological, optoelectronic, and energetical behaviors. One can judiciously design the chemical structure and tailor the properties of the molecules to make them suitable for different applications. They can be prepared into semitransparent or even fully transparent flexible power-generation modules in theory, which makes them perfectly suited to the huge market of BIPV and also meets the needs of vehicle-mounted photovoltaics, portable photovoltaics, military photovoltaics, and other markets. In addition, OPVs can be mass produced by roll-to-roll printing technology without the requirement for vacuum or high-temperature processes. This make them not only have a very short energy payback time but also a low-levelized cost of energy (LCOE) in future.

Although it has been criticized for its low efficiency in the past, in the last 5 years, the power conversion efficiency of OPVs has increased rapidly. From the classic active layer materials such as P3HT and PCBM, which show a typical efficiency of 2–4%, the field has witnessed a surge in PCE since the replacement of fullerenes by non-fullerene acceptors that led to > 19% PCE to date. Different active layer material combinations have led to different mechanisms of morphology formation, charge separation, charge transport, and device stability. The active layer composition has gradually shifted from polymer:fullerene combinations to polymer:small

molecules, all-PSCs, or all small molecules. Each of these combinations has their own advantages and issues, and all of them have a chance to win the competition.

Nevertheless, there are several major tasks for the OPV community before successful commercialization. First, the stability of the device or module needs to be further enhanced. To this end, standards need to be made and accepted by research groups and companies. Without testing standards, different groups may report different numbers under different scenarios, so the numbers become meaningless. To increase the lifetime of a device, researchers must focus more on the stability of the film, the device, and even the encapsulation layers than just on the efficiency. Second, the efficiency gap between small-area and large-area devices needs to be narrowed. Most of the organic active layers with high efficiencies are now prepared by spin-coating with fast-evaporating solvents, which cannot be easily replicated in mass production conditions like slot-die coating with high-boiling-point solvents. Consequently, research in these directions should get more attention.

A relatively new topic in the OPV field is the indoor application. Thanks to the tunable properties of OPV molecules, the absorption of OPV active layers can be tuned to match the indoor illumination spectrum better than traditional Si-based PVs. The high efficiency under indoor light conditions offers OPVs another field that does not need to compete with traditional market dominators directly, which may serve as the driving force for the reduction of the cost of OPV module production. A key link that needs to be considered in the large-scale production of OPVs is the fabrication and processing of active layer films. Especially, how to produce organic active layer films with uniform morphology is crucial for mass production.

References

1. British Petroleum (2020) Energy outlook 2020 edition
2. British Petroleum (2020) Statistical review of world energy 2020
3. Turner JA (1999) A realizable renewable energy future. Science 285(1979):687–689. https://doi.org/10.1126/science.285.5428.687
4. Espinosa N, Hösel M, Angmo D, Krebs FC (2012) Solar cells with one-day energy payback for the factories of the future. Energy Environ Sci 5:5117–5132. https://doi.org/10.1039/c1ee02728j
5. NREL (2020) Best research-cell efficiencies
6. Tang CW (1986) Two-layer organic photovoltaic cell. Appl Phys Lett 48:183–185. https://doi.org/10.1063/1.96937
7. Clarke TM, Durrant JR (2010) Charge photogeneration in organic solar cells. Chem Rev 110:6736–6767. https://doi.org/10.1021/cr900271s
8. Brédas JL, Norton JE, Cornil J, Coropceanu V (2009) Molecular understanding of organic solar cells: the challenges. Acc Chem Res 42:1691–1699. https://doi.org/10.1021/ar900099h
9. Gregg BA (2003) Excitonic solar cells. J Phys Chem B 107:4688–4698. https://doi.org/10.1021/jp022507x
10. Deibel C, Dyakonov V (2010) Polymer-fullerene bulk heterojunction solar cells. Rep Prog Phys 73:096401. https://doi.org/10.1088/0034-4885/73/9/096401
11. Mikhnenko OV, Cordella F, Sieval AB, Hummelen JC, Blom PWM, Loi MA (2008) Temperature dependence of exciton diffusion in conjugated polymers. J Phys Chem B 112:11601–11604. https://doi.org/10.1021/jp8042363

12. Mikhnenko OV, Blom PWM, Nguyen TQ (2015) Exciton diffusion in organic semiconductors. Energy Environ Sci 8:1867–1888. https://doi.org/10.1039/c5ee00925a
13. Menke SM, Holmes RJ (2014) Exciton diffusion in organic photovoltaic cells. Energy Environ Sci 7:499–512. https://doi.org/10.1039/c3ee42444h
14. Halls JJM, Walsh CA, Greenham NC, Marseglia EA, Friend RH, Moratti SC, Holmes AB (1995) Efficient photodiodes from interpenetrating polymer networks. Nature 376:498–500. https://doi.org/10.1038/376498a0
15. Yu G, Gao J, Hummelen JC, Wudl F, Heeger AJ (1995) Polymer photovoltaic cells: enhanced efficiencies via a network of internal donor-acceptor heterojunctions. Science 270:1789–1791. https://doi.org/10.1126/science.270.5243.1789
16. Bässler H, Kohler A (2015) "Hot or cold": how do charge transfer states at the donor-acceptor interface of an organic solar cell dissociate? Phys Chem Chem Phys 17:28451–28462. https://doi.org/10.1039/c5cp04110d
17. Vandewal K, Ma Z, Bergqvist J, Tang Z, Wang E, Henriksson P, Tvingstedt K, Andersson MR, Zhang F (2012) Quantification of quantum efficiency and energy losses in low bandgap polymer: fullerene solar cells with high open-circuit voltage. Adv Func Mater 22:3480–3490. https://doi.org/10.1002/adfm.201200608
18. Janssen RAJ, Nelson J (2013) Factors limiting device efficiency in organic photovoltaics. Adv Mater 25:1847–1858. https://doi.org/10.1002/adma.201202873
19. Li W, Hendriks KH, Furlan A, Wienk MM, Janssen RAJ (2015) High quantum efficiencies in polymer solar cells at energy losses below 0.6 eV. J Am Chem Soc 137:2231–2234. https://doi.org/10.1021/ja5131897
20. Jamieson FC, Domingo EB, McCarthy-Ward T, Heeney M, Stingelin N, Durrant JR (2012) Fullerene crystallisation as a key driver of charge separation in polymer/fullerene bulk heterojunction solar cells. Chem Sci 3:485–492. https://doi.org/10.1039/C1SC00674F
21. Zusan A, Vandewal K, Allendorf B, Hansen NH, Pflaum J, Salleo A, Dyakonov V, Deibel C (2014) The crucial influence of fullerene phases on photogeneration in organic bulk heterojunction solar cells. Adv Energy Mater 4:1400922. https://doi.org/10.1002/aenm.201400922
22. Savoie BM, Rao A, Bakulin AA, Gelinas S, Movaghar B, Friend RH, Marks TJ, Ratner MA (2014) Unequal partnership: asymmetric roles of polymeric donor and fullerene acceptor in generating free charge. J Am Chem Soc 136:2876–2884. https://doi.org/10.1021/ja411859m
23. Bernardo B, Cheyns D, Verreet B, Schaller RD, Rand BP, Giebink NC (2014) Delocalization and dielectric screening of charge transfer states in organic photovoltaic cells. Nat Commun 5:3245. https://doi.org/10.1038/ncomms4245
24. Gélinas S, Rao A, Kumar A, Smith SL, Chin AW, Clark J, Van Der Poll TS, Bazan GC, Friend RH (2014) Ultrafast long-range charge separation in organic semiconductor photovoltaic diodes. Science 343:512–516. https://doi.org/10.1126/science.1246249
25. Poelking C, Tietze M, Elschner C, Olthof S, Hertel D, Baumeier B, Würthner F, Meerholz K, Leo K, Andrienko D (2015) Impact of mesoscale order on open-circuit voltage in organic solar cells. Nat Mater 14:434–439. https://doi.org/10.1038/nmat4167
26. Poelking C, Andrienko D (2015) Design rules for organic donor-acceptor heterojunctions: pathway for charge splitting and detrapping. J Am Chem Soc 137:6320–6326. https://doi.org/10.1021/jacs.5b02130
27. Ndjawa GON, Graham KR, Mollinger S, Wu DM, Hanifi D, Prasanna R, Rose BD, Dey S, Yu L, Brédas JL, McGehee MD, Salleo A, Amassian A (2017) Open-circuit voltage in organic solar cells: the impacts of donor semicrystallinity and coexistence of multiple interfacial charge-transfer bands. Adv Energy Mater 7:1601995. https://doi.org/10.1002/aenm.201601995
28. Burke TM, Sweetnam S, Vandewal K, McGehee MD (2015) Beyond Langevin recombination: how equilibrium between free carriers and charge transfer states determines the open-circuit voltage of organic solar cells. Adv Energy Mater 5:1500123. https://doi.org/10.1002/aenm.201500123

29. Zhang G, Zhao J, Chow PCY, Jiang K, Zhang J, Zhu Z, Zhang J, Huang F, Yan H (2018) Nonfullerene acceptor molecules for bulk heterojunction organic solar cells. Chem Rev 118:3447–3507. https://doi.org/10.1021/acs.chemrev.7b00535

30. Liu J, Chen S, Qian D, Gautam B, Yang G, Zhao J, Bergqvist J, Zhang F, Ma W, Ade H, Inganäs O, Gundogdu K, Gao F, Yan H (2016) Fast charge separation in a non-fullerene organic solar cell with a small driving force. Nat Energy 1:16089. https://doi.org/10.1038/nenergy.2016.89

31. Chen S, Liu Y, Zhang L, Chow PCY, Wang Z, Zhang G, Ma W, Yan H (2017) A wide-bandgap donor polymer for highly efficient non-fullerene organic solar cells with a small voltage loss. J Am Chem Soc 139:6298–6301. https://doi.org/10.1021/jacs.7b01606

32. Karuthedath S, Gorenflot J, Firdaus Y, Chaturvedi N, De Castro CSP, Harrison GT, Khan JI, Markina A, Balawi AH, Dela PTA, Liu W, Liang R-Z, Sharma A, Paleti SHK, Zhang W, Lin Y, Alarousu E, Anjum DH, Beaujuge PM, De Wolf S, McCulloch I, Anthopoulos TD, Baran D, Andrienko D, Laquai F (2021) Intrinsic efficiency limits in low-bandgap non-fullerene acceptor organic solar cells. Nat Mater 20:378–384. https://doi.org/10.1038/s41563-020-00835-x

33. Schwarze M, Schellhammer KS, Ortstein K, Benduhn J, Gaul C, Hinderhofer A, Perdigón Toro L, Scholz R, Kublitski J, Roland S, Lau M, Poelking C, Andrienko D, Cuniberti G, Schreiber F, Neher D, Vandewal K, Ortmann F, Leo K (2019) Impact of molecular quadrupole moments on the energy levels at organic heterojunctions. Nat Commun 10:2466. https://doi.org/10.1038/s41467-019-10435-2

34. Koster LJA, Smits ECP, Mihailetchi VD, Blom PWM (2005) Device model for the operation of polymer/fullerene bulk heterojunction solar cells. Phys Rev B 72:085205. https://doi.org/10.1103/PhysRevB.72.085205

35. Chow PCY, Bayliss SL, Lakhwani G, Greenham NC, Friend RH (2015) In situ optical measurement of charge transport dynamics in organic photovoltaics. Nano Lett 15:931–935. https://doi.org/10.1021/nl503687u

36. Rao A, Chow PCY, Gélinas S, Schlenker CW, Li CZ, Yip HL, Jen AKY, Ginger DS, Friend RH (2013) The role of spin in the kinetic control of recombination in organic photovoltaics. Nature 500:435–439. https://doi.org/10.1038/nature12339

37. Vandewal K, Albrecht S, Hoke ET, Graham KR, Widmer J, Douglas JD, Schubert M, Mateker WR, Bloking JT, Burkhard GF, Sellinger A, Fréchet JMJ, Amassian A, Riede MK, McGehee MD, Neher D, Salleo A (2014) Efficient charge generation by relaxed charge-transfer states at organic interfaces. Nat Mater 13:63–68. https://doi.org/10.1038/nmat3807

38. Faist MA, Kirchartz T, Gong W, Ashraf RS, McCulloch I, De Mello JC, Ekins-Daukes NJ, Bradley DDC, Nelson J (2012) Competition between the charge transfer state and the singlet states of donor or acceptor limiting the efficiency in polymer: fullerene solar cells. J Am Chem Soc 134:685–692. https://doi.org/10.1021/ja210029w

39. Brédas JL, Beljonne D, Coropceanu V, Cornil J (2004) Charge-transfer and energy-transfer processes in π-conjugated oligomers and polymers: a molecular picture. Chem Rev 104:4971–5003. https://doi.org/10.1021/cr040084k

40. Chow PCY, Albert-Seifried S, Gélinas S, Friend RH (2014) Nanosecond intersystem crossing times in fullerene acceptors: implications for organic photovoltaic diodes. Adv Mater 26:4851–4854. https://doi.org/10.1002/adma.201400846

41. Chow PCY, Gélinas S, Rao A, Friend RH (2014) Quantitative bimolecular recombination in organic photovoltaics through triplet exciton formation. J Am Chem Soc 136:3424–3429. https://doi.org/10.1021/ja410092n

42. Menke SM, Sadhanala A, Nikolka M, Ran NA, Ravva MK, Abdel-Azeim S, Stern HL, Wang M, Sirringhaus H, Nguyen TQ, Brédas JL, Bazan GC, Friend RH (2016) Limits for recombination in a low energy loss organic heterojunction. ACS Nano 10:10736–10744. https://doi.org/10.1021/acsnano.6b06211

43. Proctor CM, Love JA, Nguyen TQ (2014) Mobility guidelines for high fill factor solution-processed small molecule solar cells. Adv Mater 26:5957–5961. https://doi.org/10.1002/adma.201401725

44. Shaheen SE, Brabec CJ, Sariciftci NS, Padinger F, Fromherz T, Hummelen JC (2001) 2.5% efficient organic plastic solar cells. Appl Phys Lett 78:841–843

45. Schilinsky P, Waldauf C, Brabec CJ (2002) Recombination and loss analysis in polythiophene based bulk heterojunction photodetectors. Appl Phys Lett 81:3885–3887. https://doi.org/10.1063/1.1521244

46. Li G, Shrotriya V, Huang J, Yao Y, Moriarty T, Emery K, Yang Y (2005) High-efficiency solution processable polymer photovoltaic cells by self-organization of polymer blends. Nat Mater 4:864–868

47. Wienk MM, Kroon JM, Verhees WJH, Knol J, Hummelen JC, van Hal PA, Janssen RAJ (2003) Efficient Methano[70]fullerene/MDMO-PPV bulk heterojunction photovoltaic cells. Angew Chem Int Ed 42:3371–3375. https://doi.org/10.1002/anie.200351647

48. Liang Y, Xu Z, Xia J, Tsai S-T, Wu Y, Li G, Ray C, Yu L (2010) For the bright future-bulk heterojunction polymer solar cells with power conversion efficiency of 7.4%. Adv Mater 22:1–4. https://doi.org/10.1002/adma.200903528

49. He Z, Zhong C, Su S, Xu M, Wu H, Cao Y (2012) Enhanced power-conversion efficiency in polymer solar cells using an inverted device structure. Nat Photonics 6:591–595. https://doi.org/10.1038/nphoton.2012.190

50. Huo L, Zhang S, Guo X, Xu F, Li Y, Hou J (2011) Replacing alkoxy groups with alkylthienyl groups: a feasible approach to improve the properties of photovoltaic polymers. Angew Chem Int Ed Engl 50:9697–9702. https://doi.org/10.1002/anie.201103313

51. Liao SH, Jhuo HJ, Cheng YS, Chen SA (2013) Fullerene derivative-doped zinc oxide nanofilm as the cathode of inverted polymer solar cells with low-bandgap polymer (PTB7-Th) for high performance. Adv Mater 25:4766–4771. https://doi.org/10.1002/adma.201301476

52. Cao J, Liao Q, Du X, Chen J, Xiao Z, Zuo Q, Ding L (2013) A pentacyclic aromatic lactam building block for efficient polymer solar cells. Energy Environ Sci 6:3224. https://doi.org/10.1039/c3ee41948g

53. Jin Y, Chen Z, Dong S, Zheng N, Ying L, Jiang XF, Liu F, Huang F, Cao Y (2016) A novel Naphtho[1,2-c:5,6-c']Bis([1,2,5]Thiadiazole)-based narrow-bandgap pi-conjugated polymer with power conversion efficiency over 10. Adv Mater 28:9811–9818. https://doi.org/10.1002/adma.201603178

54. Zhao J, Li Y, Yang G, Jiang K, Lin H, Ade H, Ma W, Yan H (2016) Efficient organic solar cells processed from hydrocarbon solvents. Nat Energy 1:16089. https://doi.org/10.1038/nenergy.2015.27

55. Lin Y, Wang J, Zhang ZG, Bai H, Li Y, Zhu D, Zhan X (2015) An electron acceptor challenging fullerenes for efficient polymer solar cells. Adv Mater 27:1170–1174. https://doi.org/10.1002/adma.201404317

56. Lin Y, Zhao F, Wu Y, Chen K, Xia Y, Li G, Prasad SK, Zhu J, Huo L, Bin H, Zhang ZG, Guo X, Zhang M, Sun Y, Gao F, Wei Z, Ma W, Wang C, Hodgkiss J, Bo Z, Inganas O, Li Y, Zhan X (2017) Mapping polymer donors toward high-efficiency fullerene free organic solar cells. Adv Mater 29. https://doi.org/10.1002/adma.201604155

57. Zhao W, Li S, Yao H, Zhang S, Zhang Y, Yang B, Hou J (2017) Molecular optimization enables over 13% efficiency in organic solar cells. J Am Chem Soc 139:7148–7151. https://doi.org/10.1021/jacs.7b02677

58. Xiao Z, Liu F, Geng X, Zhang J, Wang S, Xie Y, Li Z, Yang H, Yuan Y, Ding L (2017) A carbon-oxygen-bridged ladder-type building block for efficient donor and acceptor materials used in organic solar cells. Sci Bull 62:1331–1336. https://doi.org/10.1016/j.scib.2017.09.017

59. Xiao Z, Jia X, Li D, Wang S, Geng X, Liu F, Chen J, Yang S, Russell TP, Ding L (2017) 26 mA cm^{-2} Jsc from organic solar cells with a low-bandgap nonfullerene acceptor. Sci Bull 62:1494–1496. https://doi.org/10.1016/j.scib.2017.10.017

60. Xiao Z, Jia X, Ding L (2017) Ternary organic solar cells offer 14% power conversion efficiency. Sci Bull 62:1562–1564. https://doi.org/10.1016/j.scib.2017.11.003

61. Meng L, Zhang Y, Wan X, Li C, Zhang X, Wang Y, Ke X, Xiao Z, Ding L, Xia R, Yip H-L, Cao Y, Chen Y (2018) Organic and solution-processed tandem solar cells with 17.3% efficiency. Science 361:1094–1098

62. Yuan J, Zhang Y, Zhou L, Zhang G, Yip H-L, Lau T-K, Lu X, Zhu C, Peng H, Johnson PA, Leclerc M, Cao Y, Ulanski J, Li Y, Zou Y (2019) Single-junction organic solar cell with over 15% efficiency using fused-ring acceptor with electron-deficient core. Joule 3:1140–1151. https://doi.org/10.1016/j.joule.2019.01.004

63. Fan B, Zhang D, Li M, Zhong W, Zeng Z, Ying L, Huang F, Cao Y (2019) Achieving over 16% efficiency for single-junction organic solar cells. Sci China Chem 62:746–752. https://doi.org/10.1007/s11426-019-9457-5

64. Wu Y, Zheng Y, Yang H, Sun C, Dong Y, Cui C, Yan H, Li Y (2019) Rationally pairing photoactive materials for high-performance polymer solar cells with efficiency of 16.53%. Sci China Chem 63:265–271. https://doi.org/10.1007/s11426-019-9599-1

65. Wang T, Qin J, Xiao Z, Meng X, Zuo C, Yang B, Tan H, Yang J, Yang S, Sun K, Xie S, Ding L (2020) A 2.16 eV bandgap polymer donor gives 16% power conversion efficiency. Sci Bull 65:179–181. https://doi.org/10.1016/j.scib.2019.11.030

66. Wei Q, Liu W, Leclerc M, Yuan J, Chen H, Zou Y (2020) A-DA′D-A non-fullerene acceptors for high-performance organic solar cells. Sci China Chem 63:1352–1366. https://doi.org/10.1007/s11426-020-9799-4

67. Jiang K, Wei Q, Lai JYL, Peng Z, Kim HK, Yuan J, Ye L, Ade H, Zou Y, Yan H (2019) Alkyl chain tuning of small molecule acceptors for efficient organic solar cells. Joule 3:3020–3033. https://doi.org/10.1016/j.joule.2019.09.010

68. Arunagiri L, Peng Z, Zou X, Yu H, Zhang G, Wang Z, Lin Lai JY, Zhang J, Zheng Y, Cui C, Huang F, Zou Y, Wong KS, Chow PCY, Ade H, Yan H (2020) Selective hole and electron transport in efficient quaternary blend organic solar cells. Joule 4:1790–1805. https://doi.org/10.1016/j.joule.2020.06.014

69. Zhang M, Guo X, Ma W, Ade H, Hou J (2015) A Large-bandgap conjugated polymer for versatile photovoltaic applications with high performance. Adv Mater 27:4655–4660. https://doi.org/10.1002/adma.201502110

70. Sun C, Pan F, Bin H, Zhang J, Xue L, Qiu B, Wei Z, Zhang ZG, Li Y (2018) A low cost and high performance polymer donor material for polymer solar cells. Nat Commun 9:743. https://doi.org/10.1038/s41467-018-03207-x

71. Liu Q, Jiang Y, Jin K, Qin J, Xu J, Li W, Xiong J, Liu J, Xiao Z, Sun K, Yang S, Zhang X, Ding L (2020) 18% Efficiency organic solar cells. Sci Bull 65:272–275. https://doi.org/10.1016/j.scib.2020.01.001

72. Habenicht BF, Prezhdo OV (2009) Time-domain Ab initio study of nonradiative decay in a narrow graphene ribbon. J Phys Chem C 113:14067–14070. https://doi.org/10.1021/jp904937c

73. Benduhn J, Tvingstedt K, Piersimoni F, Ullbrich S, Fan Y, Tropiano M, McGarry KA, Zeika O, Riede MK, Douglas CJ, Barlow S, Marder SR, Neher D, Spoltore D, Vandewal K (2017) Intrinsic non-radiative voltage losses in fullerene-based organic solar cells. Nat Energy 2. https://doi.org/10.1038/nenergy.2017.53

74. Congreve DN, Lee J, Thompson NJ, Hontz E, Yost SR, Reusswig PD, Bahlke ME, Reineke S, van Voorhis T, Baldo MA (2013) External quantum efficiency above 100% in a singlet-exciton-fission-based organic photovoltaic cell. Science 340:334–337. https://doi.org/10.1126/science.1232994

75. Wu TC, Thompson NJ, Congreve DN, Hontz E, Yost SR, van Voorhis T, Baldo MA (2014) Singlet fission efficiency in tetracene-based organic solar cells. Appl Phys Lett 104. https://doi.org/10.1063/1.4876600

76. Yang L, Tabachnyk M, Bayliss SL, Böhm ML, Broch K, Greenham NC, Friend RH, Ehrler B (2015) Solution-processable singlet fission photovoltaic devices. Nano Lett 15:354–358. https://doi.org/10.1021/nl503650a

77. Einzinger M, Wu T, Kompalla JF, Smith HL, Perkinson CF, Nienhaus L, Wieghold S, Congreve DN, Kahn A, Bawendi MG, Baldo MA (2019) Sensitization of silicon by singlet exciton fission in tetracene. Nature 571:90–94. https://doi.org/10.1038/s41586-019-1339-4

78. Daiber B, Pujari SP, Verboom S, Luxembourg SL, Tabernig SW, Futscher MH, Lee J, Zuilhof H, Ehrler B (2020) A method to detect triplet exciton transfer from singlet fission materials

into silicon solar cells: comparing different surface treatments. J Chem Phys 152. https://doi.org/10.1063/1.5139486

79. Zhou R, Jiang Z, Yang C, Yu J, Feng J, Adil MA, Deng D, Zou W, Zhang J, Lu K, Ma W, Gao F, Wei Z (2019) All-small-molecule organic solar cells with over 14% efficiency by optimizing hierarchical morphologies. Nat Commun 10. https://doi.org/10.1038/s41467-019-13292-1

80. Bu L, Gao S, Wang W, Zhou L, Feng S, Chen X, Yu D, Li S, Lu G (2016) Film-depth-dependent light absorption and charge transport for polymer electronics: a case study on semiconductor/insulator blends by plasma etching. Adv Electron Mater 2. https://doi.org/10.1002/aelm.201600359

81. Zhang Y, Deng D, Wang Z, Wang Y, Zhang J, Fang J, Yang Y, Lu G, Ma W, Wei Z (2017) Enhancing the photovoltaic performance via vertical phase distribution optimization in small molecule: PC71BM blends. Adv Energy Mater 7. https://doi.org/10.1002/aenm.201701548

82. Ye L, Hu H, Ghasemi M, Wang T, Collins BA, Kim JH, Jiang K, Carpenter JH, Li H, Li Z, McAfee T, Zhao J, Chen X, Lai JLY, Ma T, Bredas JL, Yan H, Ade H (2018) Quantitative relations between interaction parameter, miscibility and function in organic solar cells. Nat Mater 17:253–260. https://doi.org/10.1038/s41563-017-0005-1

83. Wang LM, Wang LM, Li Q, Liu S, Cao Z, Cai YP, Jiao X, Jiao X, Lai H, Xie W, Zhan X, Zhan X, Zhu T (2020) Quantitative determination of the vertical segregation and molecular ordering of PBDB-T/ITIC blend films with solvent additives. ACS Appl Mater Interfaces 12:24165–24173. https://doi.org/10.1021/acsami.0c02843

84. Li Q, Wang LM, Liu S, Zhan X, Zhu T, Cao Z, Lai H, Zhao J, Cai Y, Xie W, Huang F (2019) Impact of donor-acceptor interaction and solvent additive on the vertical composition distribution of bulk heterojunction polymer solar cells. ACS Appl Mater Interfaces 11:45979–45990. https://doi.org/10.1021/acsami.9b15753

85. Pérez-Rodríguez A, Temiño I, Ocal C, Mas-Torrent M, Barrena E (2018) Decoding the vertical phase separation and its impact on C8-BTBT/PS transistor properties. ACS Appl Mater Interfaces 10:7296–7303. https://doi.org/10.1021/acsami.7b19279

86. Cheng HW, Raghunath P, Wang KL, Cheng P, Haung T, Wu Q, Yuan J, Lin YC, Wang HC, Zou Y, Wang ZK, Lin MC, Wei KH, Yang Y (2020) Potassium-presenting zinc oxide surfaces induce vertical phase separation in fullerene-free organic photovoltaics. Nano Lett 20:715–721. https://doi.org/10.1021/acs.nanolett.9b04586

87. Sun R, Wu Q, Guo J, Wang T, Wu Y, Qiu B, Luo Z, Yang W, Hu Z, Guo J, Shi M, Yang C, Huang F, Li Y, Min J (2020) A layer-by-layer architecture for printable organic solar cells overcoming the scaling lag of module efficiency. Joule 4:407–419. https://doi.org/10.1016/j.joule.2019.12.004

88. Duan L, Uddin A (2020) Progress in stability of organic solar cells. Adv Sci 7

89. Park HS, Han YW, Lee HS, Jeon SJ, Moon DK (2020) 13.2% Efficiency of organic solar cells by controlling interfacial resistance resulting from well-distributed vertical phase separation. ACS Appl Energy Mater 3:3745–3754. https://doi.org/10.1021/acsaem.0c00218

90. Vollbrecht J, Brus VV (2020) On the recombination order of surface recombination under open circuit conditions. Org Electron 86. https://doi.org/10.1016/j.orgel.2020.105905

91. Phuong LQ, Hosseini SM, Sandberg OJ, Zou Y, Woo HY, Neher D, Shoaee S (2021) Quantifying quasi-fermi level splitting and open-circuit voltage losses in highly efficient nonfullerene organic solar cells. Solar RRL 5. https://doi.org/10.1002/solr.202000649

92. Riley DB, Sandberg OJ, Wilson NM, Li W, Zeiske S, Zarrabi N, Meredith P, Österbacka R, Armin A (2021) Direct quantification of quasi-fermi-level splitting in organic semiconductor devices. Phys Rev Appl 15. https://doi.org/10.1103/PhysRevApplied.15.064035

93. Poduval GK, Duan L, Hossain MA, Sang B, Zhang Y, Zou Y, Uddin A, Hoex B (2020) High-efficiency nonfullerene organic solar cells enabled by atomic layer deposited zirconium-doped zinc oxide. Solar RRL 4. https://doi.org/10.1002/solr.202000241

94. Yan C, Barlow S, Wang Z, Yan H, Jen AKY, Marder SR, Zhan X (2018) Non-fullerene acceptors for organic solar cells. Nat Rev Mater 3

95. Zhao J, Li Y, Yang G, Jiang K, Lin H, Ade H, Ma W, Yan H (2016) Efficient organic solar cells processed from hydrocarbon solvents. Nat Energy 1. https://doi.org/10.1038/NENERGY.2015.27

96. He Z, Xiao B, Liu F, Wu H, Yang Y, Xiao S, Wang C, Russell TP, Cao Y (2015) Single-junction polymer solar cells with high efficiency and photovoltage. Nat Photonics 9:174–179. https://doi.org/10.1038/nphoton.2015.6

97. Wei R, Chen H, Guo Y, Han H, Zhang D, Zhu Y, He F, Zhao D (2021) Thiophene-fused perylenediimide-based polymer acceptors for high-performance all-polymer solar cells. Macromolecules 54:1499–1506. https://doi.org/10.1021/acs.macromol.0c02558

98. Ma Y, Zhou X, Cai D, Tu Q, Ma W, Zheng Q (2020) A minimal benzo[:C] [1,2,5]thiadiazole-based electron acceptor as a third component material for ternary polymer solar cells with efficiencies exceeding 16.0%. Mater Horiz 7:117–124. https://doi.org/10.1039/c9mh00993k

99. Xu Z, Pan F, Sun C, Hong S, Chen S, Yang C, Zhang Z, Liu Y, Russell TP, Li Y, Wang D (2020) Understanding the morphology of high-performance solar cells based on a low-cost polymer donor. ACS Appl Mater Interfaces 12:9537–9544. https://doi.org/10.1021/acsami.9b22666

100. Hong L, Yao H, Cui Y, Yu R, Lin YW, Chen TW, Xu Y, Qin J, Hsu CS, Ge Z, Hou J (2021) Simultaneous improvement of efficiency and stability of organic photovoltaic cells by using a cross-linkable fullerene derivative. Small 17. https://doi.org/10.1002/smll.202101133

101. Zhang L, Jia T, Pan L, Wu B, Wang Z, Gao K, Liu F, Duan C, Huang F, Cao Y (2021) 15.4% Efficiency all-polymer solar cells. Sci China Chem 64:408–412. https://doi.org/10.1007/s11426-020-9935-2

102. Brabec CJ, Heeney M, Mc Culloch I, Nelson J (2011) Influence of blend microstructure on bulk heterojunction organic photovoltaic performance. Chem Soc Rev 40:1185–1199. https://doi.org/10.1039/c0cs00045k

103. Zhang Y, Xu Y, Ford MJ, Li F, Sun J, Ling X, Wang Y, Gu J, Yuan J, Ma W (2018) Thermally stable all-polymer solar cells with high tolerance on blend ratios. Adv Energy Mater 8. https://doi.org/10.1002/aenm.201800029

104. Schaffer CJ, Palumbiny CM, Niedermeier MA, Jendrzejewski C, Santoro G, Roth SV, Müller-Buschbaum P (2013) A direct evidence of morphological degradation on a nanometer scale in polymer solar cells. Adv Mater 25:6760–6764. https://doi.org/10.1002/adma.201302854

105. Ayzner AL, Tassone CJ, Tolbert SH, Schwartz BJ (2009) Reappraising the need for bulk heterojunctions in polymer-fullerene photovoltaics: the role of carrier transport in all-solution-processed P3HT/PCBM bilayer solar cells. J Phys Chem C 113:20050–20060. https://doi.org/10.1021/jp9050897

106. Clulow AJ, Tao C, Lee KH, Velusamy M, McEwan JA, Shaw PE, Yamada NL, James M, Burn PL, Gentle IR, Meredith P (2014) Time-resolved neutron reflectometry and photovoltaic device studies on sequentially deposited PCDTBT-fullerene layers. Langmuir 30:11474–11484. https://doi.org/10.1021/la5020779

107. He Q, Sheng W, Zhang M, Xu G, Zhu P, Zhang H, Yao Z, Gao F, Liu F, Liao X, Chen Y (2021) Revealing morphology evolution in highly efficient bulk heterojunction and pseudo-planar heterojunction solar cells by additives treatment. Adv Energy Mater 11. https://doi.org/10.1002/aenm.202003390

108. Weng K, Ye L, Zhu L, Xu J, Zhou J, Feng X, Lu G, Tan S, Liu F, Sun Y (2020) Optimized active layer morphology toward efficient and polymer batch insensitive organic solar cells. Nat Commun 11. https://doi.org/10.1038/s41467-020-16621-x

109. Cheng P, Yan C, Wu Y, Dai S, Ma W, Zhan X (2016) Efficient and stable organic solar cells: Via a sequential process. J Mater Chem C 4:8086–8093. https://doi.org/10.1039/c6tc02338j

110. Yang B, Yuan Y, Huang J (2014) Reduced bimolecular charge recombination loss in thermally annealed bilayer heterojunction photovoltaic devices with large external quantum efficiency and fill factor. J Phys Chem C 118:5196–5202. https://doi.org/10.1021/jp500547j

111. Jiang K, Zhang J, Peng Z, Lin F, Wu S, Li Z, Chen Y, Yan H, Ade H, Zhu Z, Jen AKY (2021) Pseudo-bilayer architecture enables high-performance organic solar cells with enhanced exciton diffusion length. Nat Commun 12. https://doi.org/10.1038/s41467-020-20791-z

112. Zhan L, Li S, Xia X, Li Y, Lu X, Zuo L, Shi M, Chen H (2021) Layer-by-layer processed ternary organic photovoltaics with efficiency over 18%. Adv Mater 33. https://doi.org/10.1002/adma.202007231

113. Fontana MT, Aubry TJ, Scholes DT, Hawks SA, Schwartz BJ (2018) 4 (in 4 Volumes)-9in x 6in b3104-v2-ch08 3rd Reading page 1 Sequential processing: a rational route for bulk heterojunction formation via polymer swelling
114. Yi A, Chae S, Hong S, Lee HH, Kim HJ (2018) Manipulating the crystal structure of a conjugated polymer for efficient sequentially processed organic solar cells. Nanoscale 10:21052–21061. https://doi.org/10.1039/c8nr05407j
115. Faure MDM, Lessard BH (2021) Layer-by-layer fabrication of organic photovoltaic devices: material selection and processing conditions. J Mater Chem C 9:14–40. https://doi.org/10.1039/d0tc04146g
116. Dong S, Zhang K, Xie B, Xiao J, Yip HL, Yan H, Huang F, Cao Y (2019) High-performance large-area organic solar cells enabled by sequential bilayer processing via nonhalogenated solvents. Adv Energy Mater 9. https://doi.org/10.1002/aenm.201802832
117. Wei Y, Yu J, Qin L, Chen H, Wu X, Wei Z, Zhang X, Xiao Z, Ding L, Gao F, Huang H (2021) A universal method for constructing high efficiency organic solar cells with stacked structures. Energy Environ Sci 14:2314–2321. https://doi.org/10.1039/d0ee03490h
118. Arunagiri L, Zhang G, Hu H, Yao H, Zhang K, Li Y, Chow PCY, Ade H, Yan H (2019) Temperature-dependent aggregation donor polymers enable highly efficient sequentially processed organic photovoltaics without the need of orthogonal solvents. Adv Funct Mater 29. https://doi.org/10.1002/adfm.201902478
119. Sun R, Guo J, Sun C, Wang T, Luo Z, Zhang Z, Jiao X, Tang W, Yang C, Li Y, Min J (2019) A universal layer-by-layer solution-processing approach for efficient non-fullerene organic solar cells. Energy Environ Sci 12:384–395. https://doi.org/10.1039/c8ee02560f
120. Koppe M, Egelhaaf HJ, Dennler G, Scharber MC, Brabec CJ, Schilinsky P, Hoth CN (2010) Near IR sensitization of organic bulk heterojunction solar cells: towards optimization of the spectral response of organic solar cells. Adv Funct Mater 20:338–346. https://doi.org/10.1002/adfm.200901473
121. Khlyabich PP, Burkhart B, Thompson BC (2012) Compositional dependence of the open-circuit voltage in ternary blend bulk heterojunction solar cells based on two donor polymers. J Am Chem Soc 134:9074–9077. https://doi.org/10.1021/ja302935n
122. Xiao Y, Wang H, Zhou S, Yan K, Xie W, Guan Z, Tsang SW, Xu J bin (2016) Efficient ternary bulk heterojunction solar cells with PCDTBT as hole-cascade material. Nano Energy 19:476–485. https://doi.org/10.1016/j.nanoen.2015.11.016
123. Yang L, Zhou H, Price SC, You W (2012) Parallel-like bulk heterojunction polymer solar cells. J Am Chem Soc 134:5432–5435. https://doi.org/10.1021/ja211597w
124. Khlyabich PP, Burkhart B, Thompson BC (2011) Efficient ternary blend bulk heterojunction solar cells with tunable open-circuit voltage. J Am Chem Soc 133:14534–14537. https://doi.org/10.1021/ja205977z
125. Street RA, Davies D, Khlyabich PP, Burkhart B, Thompson BC (2013) Origin of the tunable open-circuit voltage in ternary blend bulk heterojunction organic solar cells. J Am Chem Soc 135:986–989. https://doi.org/10.1021/ja3112143
126. Mollinger SA, Vandewal K, Salleo A (2015) Microstructural and electronic origins of open-circuit voltage tuning in organic solar cells based on ternary blends. Adv Energy Mater 5. https://doi.org/10.1002/aenm.201501335
127. Wang Z, Zhang Y, Zhang J, Wei Z, Ma W (2016) Optimized "alloy-parallel" morphology of ternary organic solar cells. Adv Energy Mater 6. https://doi.org/10.1002/aenm.201502456
128. Khlyabich PP, Rudenko AE, Thompson BC, Loo YL (2015) Structural origins for tunable open-circuit voltage in ternary-blend organic solar cells. Adv Funct Mater 25:5557–5563. https://doi.org/10.1002/adfm.201502287
129. Kouijzer S, Li W, Wienk MM, Janssen RAJ (2014) Charge transfer state energy in ternary bulk-heterojunction polymer–fullerene solar cells. J Photonics Energy 5:057203. https://doi.org/10.1117/1.jpe.5.057203
130. Cowan SR, Leong WL, Banerji N, Dennler G, Heeger AJ (2011) Identifying a threshold impurity level for organic solar cells: enhanced first-order recombination via well-defined PC84BM traps in organic bulk heterojunction solar cells. Adv Funct Mater 21:3083–3092. https://doi.org/10.1002/adfm.201100514

131. Cheng P, Yan C, Wu Y, Wang J, Qin M, An Q, Cao J, Huo L, Zhang F, Ding L, Sun Y, Ma W, Zhan X (2016) Alloy acceptor: superior alternative to PCBM toward efficient and stable organic solar cells. Adv Mater 28:8021–8028. https://doi.org/10.1002/adma.201602067

132. Jiang K, Zhang G, Yang G, Zhang J, Li Z, Ma T, Hu H, Ma W, Ade H, Yan H (2018) Multiple cases of efficient nonfullerene ternary organic solar cells enabled by an effective morphology control method. Adv Energy Mater 8. https://doi.org/10.1002/aenm.201701370

133. Gobalasingham NS, Noh S, Howard JB, Thompson BC (2016) Influence of surface energy on organic alloy formation in ternary blend solar cells based on two donor polymers. ACS Appl Mater Interfaces 8:27931–27941. https://doi.org/10.1021/acsami.6b10144

134. Gupta V, Bharti V, Kumar M, Chand S, Heeger AJ (2015) Polymer-polymer Förster resonance energy transfer significantly boosts the power conversion efficiency of bulk-heterojunction solar cells. Adv Mater 27:4398–4404. https://doi.org/10.1002/adma.201501275

135. Lu L, Chen W, Xu T, Yu L (2015) High-performance ternary blend polymer solar cells involving both energy transfer and hole relay processes. Nat Commun 6. https://doi.org/10.1038/ncomms8327

136. Yao H, Cui Y, Yu R, Gao B, Zhang H, Hou J (2017) Design, synthesis, and photovoltaic characterization of a small molecular acceptor with an ultra-narrow band gap. Angew Chem 129:3091–3095. https://doi.org/10.1002/ange.201610944

137. Baran D, Ashraf RS, Hanifi DA, Abdelsamie M, Gasparini N, Röhr JA, Holliday S, Wadsworth A, Lockett S, Neophytou M, Emmott CJM, Nelson J, Brabec CJ, Amassian A, Salleo A, Kirchartz T, Durrant JR, McCulloch I (2017) Reducing the efficiency-stability-cost gap of organic photovoltaics with highly efficient and stable small molecule acceptor ternary solar cells. Nat Mater 16:363–369. https://doi.org/10.1038/nmat4797

138. Xu X, Li Y, Peng Q (2022) Ternary blend organic solar cells: understanding the morphology from recent progress. Adv Mater

139. Du J, Hu K, Meng L, Angunawela I, Zhang J, Qin S, Liebman-Pelaez A, Zhu C, Zhang Z, Ade H, Li Y (2020) High-performance all-polymer solar cells: synthesis of polymer acceptor by a random ternary copolymerization strategy. Angew Chem Int Ed 59:15181–15185. https://doi.org/10.1002/anie.202005357

140. Fan Q, Su W, Chen S, Kim W, Chen X, Lee B, Liu T, Méndez-Romero UA, Ma R, Yang T, Zhuang W, Li Y, Li Y, Kim TS, Hou L, Yang C, Yan H, Yu D, Wang E (2020) Mechanically robust all-polymer solar cells from narrow band gap acceptors with hetero-bridging atoms. Joule 4:658–672. https://doi.org/10.1016/j.joule.2020.01.014

141. Fan B, Ying L, Zhu P, Pan F, Liu F, Chen J, Huang F, Cao Y (2017) All-polymer solar cells based on a conjugated polymer containing siloxane-functionalized side chains with efficiency over 10%. Adv Mater 29. https://doi.org/10.1002/adma.201703906

142. Gao L, Zhang ZG, Xue L, Min J, Zhang J, Wei Z, Li Y (2016) All-polymer solar cells based on absorption-complementary polymer donor and acceptor with high power conversion efficiency of 8.27%. Adv Mater 28:1884–1890. https://doi.org/10.1002/adma.201504629

143. Zhu L, Zhong W, Qiu C, Lyu B, Zhou Z, Zhang M, Song J, Xu J, Wang J, Ali J, Feng W, Shi Z, Gu X, Ying L, Zhang Y, Liu F (2019) Aggregation-induced multilength scaled morphology enabling 11.76% efficiency in all-polymer solar cells using printing fabrication. Adv Mater 31. https://doi.org/10.1002/adma.201902899

144. Xu X, Feng K, Yu L, Yan H, Li R, Peng Q (2020) Highly efficient all-polymer solar cells enabled by p-doping of the polymer donor. ACS Energy Lett 5:2434–2443. https://doi.org/10.1021/acsenergylett.0c01010

145. Zhang Z-G, Yang Y, Yao J, Xue L, Chen S, Li X, Morrison W, Yang C, Li Y (2017) Constructing a strongly absorbing low-bandgap polymer acceptor for high-performance all-polymer solar cells. Angew Chem 129:13688–13692. https://doi.org/10.1002/ange.201707678

146. Tang A, Li J, Zhang B, Peng J, Zhou E (2020) Low-bandgap n-type polymer based on a fused-DAD-type heptacyclic ring for all-polymer solar cell application with a power conversion efficiency of 10.7%. ACS Macro Lett 9:706–712. https://doi.org/10.1021/acsmacrolett.0c00234

147. Wang W, Wu Q, Sun R, Guo J, Wu Y, Shi M, Yang W, Li H, Min J (2020) Controlling molecular mass of low-band-gap polymer acceptors for high-performance all-polymer solar cells. Joule 4:1070–1086. https://doi.org/10.1016/j.joule.2020.03.019

148. Sun R, Wang W, Yu H, Chen Z, Xia XX, Shen H, Guo J, Shi M, Zheng Y, Wu Y, Yang W, Wang T, Wu Q, Yang Y, Lu X, Xia J, Brabec CJ, Yan H, Li Y, Min J (2021) Achieving over 17% efficiency of ternary all-polymer solar cells with two well-compatible polymer acceptors. Joule 5:1548–1565. https://doi.org/10.1016/j.joule.2021.04.007

149. Karuthedath S, Gorenflot J, Firdaus Y, Chaturvedi N, de Castro CSP, Harrison GT, Khan JI, Markina A, Balawi AH, dela Peña TA, Liu W, Liang RZ, Sharma A, Paleti SHK, Zhang W, Lin Y, Alarousu E, Anjum DH, Beaujuge PM, de Wolf S, McCulloch I, Anthopoulos TD, Baran D, Andrienko D, Laquai F (2021) Intrinsic efficiency limits in low-bandgap non-fullerene acceptor organic solar cells. Nat Mater 20:378–384. https://doi.org/10.1038/s41563-020-00835-x

150. Ma Y, Zhang M, Wan S, Yin P, Wang P, Cai D, Liu F, Zheng Q (2021) Efficient organic solar cells from molecular orientation control of M-series acceptors. Joule 5:197–209. https://doi.org/10.1016/j.joule.2020.11.006

151. Schwarze M, Schellhammer KS, Ortstein K, Benduhn J, Gaul C, Hinderhofer A, Perdigón Toro L, Scholz R, Kublitski J, Roland S, Lau M, Poelking C, Andrienko D, Cuniberti G, Schreiber F, Neher D, Vandewal K, Ortmann F, Leo K (2019) Impact of molecular quadrupole moments on the energy levels at organic heterojunctions. Nat Commun 10. https://doi.org/10.1038/s41467-019-10435-2

Chapter 6
Organic Semiconductor Laser

A laser is generally composed of three main components: a gain medium, a pump source, and a resonator. Organic lasers are lasers whose gain medium is based on an organic luminophore, usually a conjugated aromatic hydrocarbon molecule, which have long attracted the attention of researchers because of their advantages of simple fabrication, low-cost, easy integration, flexibility, and biocompatibility. Compared with inorganic laser media, organic lasers have a wide range of material sources, which generally exhibit wide emission spectra, large absorption and emission cross-sectional areas, and easy color tunability, thus rendering organic lasers great research and application potential. This chapter starts from the basic principle of lasers; it summarizes the types of organic laser materials and the general characteristics of high-efficiency organic laser materials. Common organic laser microcavities are classified, and their properties are discussed. In addition, the dynamic relationship between gain and loss in organic laser systems is discussed. Moreover, how to further realize current-driven organic laser diodes similar to inorganic lasers instead of optical pumping has become one of the research hotspots and cutting-edge directions in the field of organic lasers for decades. Finally, the overall progress and future research directions of optically pumped organic lasers are summarized, which should hopefully provide new insights for readers.

6.1 Brief History of Lasers and Organic Lasers

The theoretical basis of the laser invention can be traced back to the concept of stimulated radiation, first proposed by Einstein in 1917 when he studied the relationship between optical radiation and transitions. In the article "Quantum Theory of Radiation," the interaction process of light and matter is studied in detail, especially the three basic interaction forms of absorption, spontaneous emission, and stimulated emission, and the famous Einstein relation is derived, which makes the theory of stimulated emission quantitatively describable and lays the basic theory of laser. In

1954, Charles H. Townes (USA), Nikolai Basov (Soviet Union) and others invented the ammonia molecular microwave stimulated radiation amplifier (Maser), which uses the stimulated radiation of atoms and molecules to amplify electromagnetic waves. This breakthrough paved the way for the development of lasers.

The first laser was invented in 1960 by T. H. Maiman of Hughes Company, USA, after the invention of the maser [1]. Since then, a variety of lasers have emerged one after another and competed for development, including gas lasers, liquid lasers, semiconductor lasers, and atomic lasers. The advent of the laser sparked a revolution in science and technology. Lasers have changed the spectrum, giving unprecedented revelations in the fields of physics and chemistry and are used in various fields of technology. For example, the emergence of ultrafast lasers has made it possible for humans to study ultrafast processes in the fields of photochemistry and photophysics; the emergence of high-energy lasers has made a qualitative leap in fine-processing capabilities; and the emergence of inorganic semiconductor lasers has made optical communication and high-density optical storage became reality. Lasers are widely used in medical, telecommunication, national defense, and other fields. The Nobel Prize in Physics in 2014 was awarded to Isamu Akasaki, Hiroshi Amano, and Shuji Nakamura in order to commend their contributions to blue LEDs and GaN lasers [1, 2]. Laser gain media comes from a wide range of sources, and the emission wavelengths of various types of laser light sources can now cover the ultraviolet, visible, and infrared regions, achieving controllable adjustment for different wavelengths, different power levels, and different pulse line widths. This widens the applicability of lasers in different fields.

Although the structure and characteristics of lasers (of different types) are different, the laser must have three basic components: gain medium, pumping source, and resonant cavity. The gain medium makes the light amplified by stimulated emission, which can be a gas, liquid, or solid. The pumping source provides energy for the gain medium to realize the population inversion between higher and lower energy states. The function of the resonant cavity is to realize the feedback of light waves, which determines the spatial and spectral coherence of the emitted light spot.

The history of organic lasers is almost as long as that of the laser itself. Organic materials had already shown an important role within the first decade of lasers, first being widely used in dye lasers. This is very different from OTFT and OLED, in which organic materials came to attention many years after the advent of inorganic semiconductor devices. In the mid-1960s, Schafer first reported that a solution of conjugated dye molecules with high fluorescence efficiency could serve as the gain medium [2]. Because luminescence spectrum of organic dye laser has a very wide adjustable range, the first organic laser phenomenon [3] attracted great attention. However, the original organic dye laser was bulky in design and the solvent used was toxic, which limited its application. To solve these problems, in 1967 [4] scholars suggested that distributing dyes in a solid polymer matrix could be a way to manufacture inexpensive and portable organic lasers. In 1972, a laser based on organic small molecule single crystal has been developed [5], and in 1974, pure small molecule anthracene monocrystalline luminescence has been demonstrated [6]. In 1996, solid organic polymer laser has first been reported [7].

Despite these achievements, commercial products based on organic solid-state lasers have yet to appear. Behind this are both internal and external reasons: The intrinsic disadvantages of organic materials, such as relatively low stability, limited the lifetime of the lasers, while external factors, such as that organic lasers generally require the use of expensive pumping sources (usually pulsed) also contributed. In view of this, researchers in the field of organic lasers have been making continuous efforts to improve the optical stability of dyes and polymer matrices, lower the laser threshold, and find cost-effective alternative pump sources to expand the application of organic lasers. Entering the twenty-first century, semiconductor lasers, which means that the gain medium of the laser is based on semiconductor materials, have become more and more important in both research and application. The rapid development of organic electronics, particularly organic light-emitting diodes and solid-state organic lasers, have ushered in a turning point: the surge of organic semiconductors [9]. Scientists employed organic semiconductors to prepare low-threshold solid-state thin-film organic laser devices, retaining all the advantages of organic materials such as wide emission, simple preparation, and low-cost while making the laser device lightweight, small, and even portable.

Compared to the typically fragile, non-flexible, difficult-to-produce inorganic counterparts, the processing of organic semiconductor materials is typically simpler, and the consequent mechanical flexibility of the devices is also possible. Additionally, devices based on organic emitter materials have demonstrated good biocompatibility. They are frequently less toxic than their inorganic equivalents. Many kinds of organic semiconductors have strong optical gain, which makes them suitable for use as optical amplifiers and laser medium. They are easy to manufacture and compatible with a wide range of optical resonator configurations. In many instances, the resonator may be directly etched onto the organic gain medium, resulting in flexible and reasonably priced laser systems.

Organic solid-state lasers have a wide range of applications including integration into miniature spectroscopic systems, chemical sensing, detection of specific DNA sequences [8], integration into microfluidic devices or lab-on-a-chip sensors [9], optical communication such as short-haul data transfer and optical amplifiers [10].

6.2 Background for Laser, Laser Materials, and Organic Laser Materials

6.2.1 Laser

Laser has the characteristics of high monochromaticity, high directionality, high coherence, and high brightness. If we use φ_2, φ_{21} and φ_{12} to represent the photon density of spontaneous emission, stimulated emission and stimulated absorption of atoms in the system in unit time, respectively, N_1 and N_2 to represent the density of particles (atoms) on the ground state (E_1) and on the excited state (E_2), respectively,

A_{21} to represent Einstein's spontaneous emission coefficient, B_{21} to represent Einstein stimulated emission coefficient, B_{12} to represent stimulated absorption coefficient, and ρ_v to represent the energy density of the applied electromagnetic radiation incident on the system, then the three characteristic quantities A_{21}, B_{21}, and B_{12} of the system are not isolated from each other but have a close relationship. At the same time, the absorption and radiation processes must be balanced, $\varphi_2 + \varphi_{21} = \varphi_{12}$. Furthermore, Maxwell–Boltzmann distribution gives that $\frac{N_i}{N} = \frac{g_i \exp(-E_i/k_T)}{\sum_j g_j \exp(-E_j/k_T)}$, where N_i is the number of particles in state i at equilibrium temperature T, with energy E_i and degeneracy g_i; N is the total number of particles in the system, and k is the Boltzmann constant. Planck's formula for blackbody radiation $\rho v = \frac{8\pi v^2}{c^3} \cdot \frac{hv}{e^{\frac{hv}{k_B T}} - 1}$. From $B_{12} g_1 = B_{21} g_2$, in the case where E_2 and E_1 are not degenerate ($g_1 = g_2 = 1$) or the degree of degeneracy is equal, we have $B_{12} = B_{21}$. That is, Einstein's stimulated emission and stimulated absorption rates are equal. Thus, the ratio of the photon number density of stimulated emission to stimulated absorption can be obtained as: $\frac{\varphi 21}{\varphi 12} = \frac{N_2}{N_1} = e^{-\frac{hv}{k_B T}}$.

In the above formula, if the photon energy corresponding to visible light is taken, the ratio at room temperature is in the order of 10^{-42}. It can be seen that for the thermal equilibrium system the stimulated absorption process and the spontaneous emission process balance each other and the stimulated emission process does not have any significant effect. In order to form the optical amplification of stimulated radiation, the system must be supplied with energy to put the system in a non-equilibrium state, and the applied energy will pump the particles from the ground state to the excited state to achieve population inversion, that is, $\frac{N2}{N1} > 1$.

To generate a laser, there are three necessary requirements:

(1) Light gain medium: The light gain medium not only needs to have strong spontaneous radiation characteristics, but its energy levels must also be conducive to the generation of particle number reversal on the high energy level.
(2) Pump source: An appropriate external excitation source must be provided, which can produce excited states of the light gain medium.
(3) Optical feedback structure: Typically, the structure is based on a resonant cavity, which can make the radiation generated by the light gain material trapped within the resonator while forming self-oscillation in the resonator.

Common laser pump sources include the following:

(1) Light pump: the use of external light sources to illuminate laser substances, usually composed of gas discharge light sources (xenon lamps, krypton lamps, etc.) and lasers. In addition, semiconductor lasers can also be used as a pump source for other lasers.
(2) Electric pumping: electrical power is used to excite the active substance, which includes gas discharge excitation (gas laser), carrier injection excitation (semiconductor laser), and particle accelerator excitation.
(3) Chemical pumping: the use of chemical reaction processes that take place within the active substance to achieve population inversion.

In terms of working mechanism, the working process of the laser can be briefly summarized by the following steps: (1) The pump source provides energy to the active material (light gain medium) to generate the excited state of the active material; (2) Due to the particularity of the energy level structure of the active material, a pump source with certain energy can make the number of particles in the active material reverse, i.e., between the high and low energy levels, where the optical radiation transition occurs, the number of particles on the higher energy level is greater than the number of particles on the lower energy level; (3) At the same time, the spontaneous radiation of the active material incidents onto the active material again after being reflected by the resonator, and the stimulated radiation photons with the same phase, the same wavelength, and the same propagation direction as the spontaneous radiation photons are generated; and (4) Due to the selection effect of the optical resonator, only light of a specific frequency and propagation direction can exist stably while other photons gradually overflow the cavity or are lost. Therefore, these stably existing stimulated radiation photons and spontaneous radiation photons repeatedly irradiate the active material through the reflection of the resonant cavity, so that the number of stimulated radiation photons increases (optical gain). If the photon gain provided by the stimulated radiation exceeds the loss suffered by the beam in one round trip in the cavity, the beam will be amplified, and a self-excited oscillation will be formed in the resonant cavity. Finally, a light beam with good monochromaticity, strong directionality, and high coherence can be formed, that is laser.

6.2.2 Laser Materials

The theoretical basis for judging whether an organic material is suitable as a laser material is mainly discussed in terms of the energy level structure and physicochemical properties of the material medium. First, as a laser active material, it must have strong spontaneous emission characteristics and be able to generate a population inversion between the high and low energy levels of the radiation transition. To achieve population inversion, there are special requirements for the energy level of the material. For systems in which both absorption and radiation are limited to two energy levels, the rate of stimulated emission is equal to the rate of light absorption, and there cannot be more particles at higher energy levels than at lower energy levels, so population inversion is impossible, and such substances are not suitable for use as laser material. And, systems with three and four energy levels have the potential to achieve population inversion and can be used as laser active materials, as shown in Fig. 6.1.

Based on this strict requirement on population inversion, several other factors also determine the suitability of a material being using for lasing. For example, the stimulated emission cross section should be as large as possible; in the host–guest system based on Förster energy transfer, the distribution radius of the host–guest material must be in the range of several nanometers so that the Förster energy transfer can take place; the excited-state absorption should be low so that and the loss
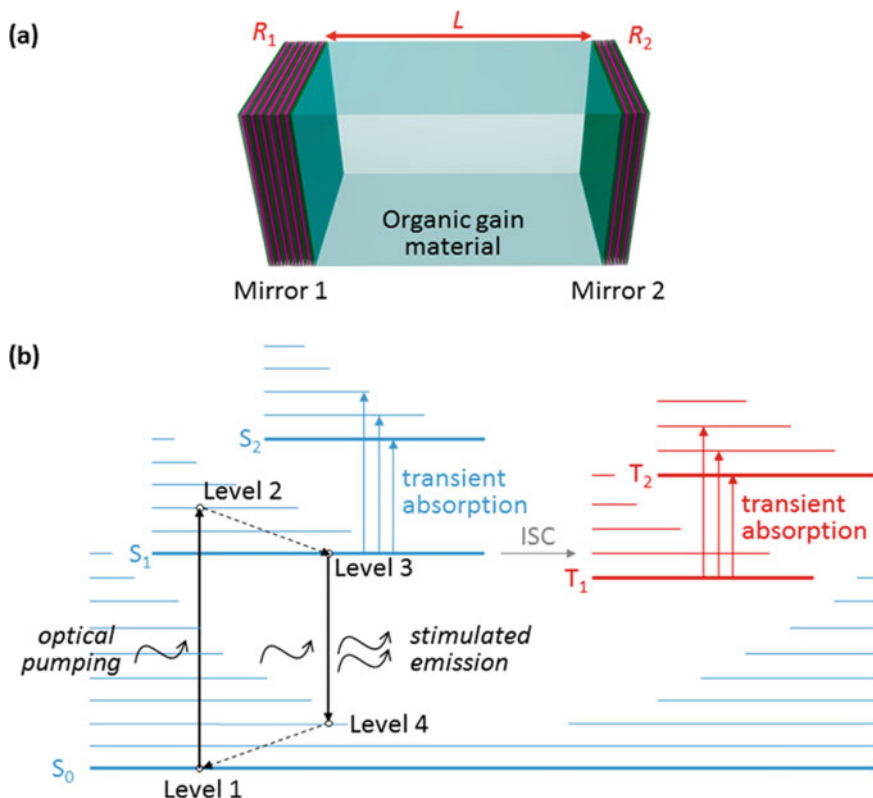
Fig. 6.1 a Archetypical structure of an organic laser, with two mirrors with reflectivity $R1$ and $R2$, separated by distance L, and organic gain medium in between. **b** Generalized Jablonski diagram of an organic luminophore illustrating how the luminophore can act as a quasi-four-level laser system. Fast vibrionic relaxation of most organic luminophores after electronic excitations allows efficient population of the state at the bottom of the $S1$ manifold (level 3) and prevents accumulation of luminophores in higher vibronic states of the $S0$ manifold (level 4). Losses originated from intersystem crossing (ISC) between the first excited singlet state ($S1$) and the $T1$ triplet manifold and from subsequent transient absorption to higher triplet states. (Adapted from Ref. [11])

is relatively low near the wavelength of laser emission; the fluorescence quantum efficiency of the material should be high under solid-state conditions; the material should have good physical and chemical properties, good stability in oxygen and water vapor environments, and good optical stability and uniformity under strong light pumping conditions.

6.2.3   Characteristics of Laser

Output Frequency and Wavelength: The spatial distribution of the photon flow output by the laser can be divided into two parts: horizontal and vertical. Usually, the direction of wave propagation is called the vertical direction, and the mode of the laser output in this direction is called the longitudinal mode; and the direction perpendicular to the propagation direction of the wave is called the transverse direction, and the description of the laser output mode in this direction is called the transverse mode. The transverse mode and the longitudinal mode together constitute the output of the laser. One of the basic pieces of information contained in the laser longitudinal mode is the frequency or wavelength of the laser.

Threshold and Modal Gain: The lowest optical gain is the threshold of the laser. Laser oscillation is generated by spontaneous radiation photons in the gain medium. During the establishment of laser oscillation, the seeds of spontaneous radiation must be amplified in the reciprocating motion in the cavity, which requires gain, whereas there are various types of photon loss in the laser cavity such as the scattering of the beam by the inhomogeneity of the laser medium, the diffraction in the cavity, the absorption of the laser photon by the laser medium, the output of the cavity mirror, etc. Thus, there must be a certain gain to overcome these losses to achieve and maintain the laser oscillation. This lowest gain is the threshold of the laser. The product of the gain cross section (σ) and the density of population inversion is defined as the modal (optical) gain (g): $g = \sigma(n_2 - n_1)$, where n_2 and n_1 are the particle number density at the high energy level and the low energy level, respectively.

Output Power: When the power of the pump source exceeds the threshold pump power, the laser starts to form, and the output power of the laser can be expressed as $P_{\text{out}} =$ transmittance $\times$ energy per output photon $\times$ number of output photons per unit time.

6.2.4   Organic Laser

Although many inorganic solid-state laser (SSL) products have been commercialized, the inherent disadvantages of inorganic materials, such as limited spectral tunability, difficult doping in crystals, and high costs in high-temperature processes, are impeding the further development of inorganic SSLs to meet the increasing higher demands [12, 13]. In contrast, organic molecules have merits that are complementary with their inorganic counterparts, such as low cost in processing, high photoluminescence (PL) wavelength tunability ranging from ultraviolet to infrared, high PL efficiency, and high flexibility in modifying molecular structures. Moreover, there are abundant excited-state processes for most organic materials for which the four-level system can be easily fulfilled for population inversion. Organic lasers have made great progress since the first dye-doped organic solid-state laser (OSSLs) was

demonstrated in 1966 [1]. After that, a great number of organic materials, based on polymers and small organic molecules, have been developed toward laser application.

For organic materials, the π-conjugated organic compounds are all intrinsic four-level systems suitable for population inversion [14]. Furthermore, many organic materials exhibit large Stokes shift between absorption and emission due to the vibrational relaxation during the excitation/emission cycle. This can minimize the reabsorption as there is only weak overlap between the absorption and emission spectra. We note that the molecular conditions still hold in principle for solid-state lasing of organic gain medium, but the photophysical mechanism for solid-state—conjugated material systems is more complicated due to the presence of intermolecular excitonic interactions that could alter the intramolecular properties [15]. In Kasha's molecular exciton model [16], which assumes that intermolecular interactions split molecular electronic transitions, this may be qualitatively described. Due to the modest nearest-neighbor intermolecular separations observed in the solid state, the original model based on point dipoles at a constant center-to-center distance must be furnished more accurately for the solid state for constant intermolecular separation [15]. Since the conformational distribution of conjugated polymers in the film is amorphous, the energy-level distribution of different molecular segments is very broad. When the excitation light is incident on different positions of the material that have different energy levels, the excitation (after absorption) quickly transfers to the molecule or molecular fragment with the lowest energy [17–21]. The experimental results show that most of the redshift occurs within a few picoseconds after excitation. The energy transfer makes the light emission always occur between the excited state and the ground state with the lowest energy, so that the light emission spectrum has a large red shift relative to the absorption spectrum, avoiding the self-absorption of the material at the light emission wavelength, which can effectively reduce the laser threshold. This feature also enables two materials with different energy gaps to form a mixed light-emitting system. After the wide energy gap material absorbs light, the energy will transfer through, e.g., Förster resonant energy transfer mechanism, to the low energy gap material, and emit laser light [22–25].

The existence of triplet excitons in organic molecules will affect the behavior of laser emission. The singlet excitons will change their spin directions through inter-system crossing and finally transform into triplet states. The energy of triplet excitons is usually lower than that of singlet states and the triplet excitons have a longer lifetime, which leads to more accumulation. As shown in Fig. 6.2, the absorption gap from $T1$ to $T2$ excited states is wide and overlaps with the singlet fluorescence emission spectrum [26]. Therefore, solid-state organic lasers can only emit short-pulse lasers (unlike liquid dye lasers, which can emit continuous wavelength lasers, because the presence of the liquid enables the medium to flow continuously). Recent reports have confirmed that after the incidence of the pumping light incident, the laser lasts only a few nanoseconds in the polymer blend host–guest system [27], while in the small molecule system, the laser can last for tens of nanoseconds if it is excited by a long-pulse pump light source [28].

(a) Rohamine 6G   **(b) Coumarin 6H**   **(c) BODIPY**

(d) Cryptocyanine   **(e) Disodium Fluorescein**   **(f) IND-PBI**

(g) 4,4'-diphenylstilbene   **(h) PTPTP (Thiophene-based dyes)**

Typical Dyes for Lasers

(a) Rhodamine   (b) Coumarin   (c) BODIPY   (d) Cyanine   (e) Fluorescein
(f) Rylenes   (g) Stilbene   (h) Thiophene-based dyes
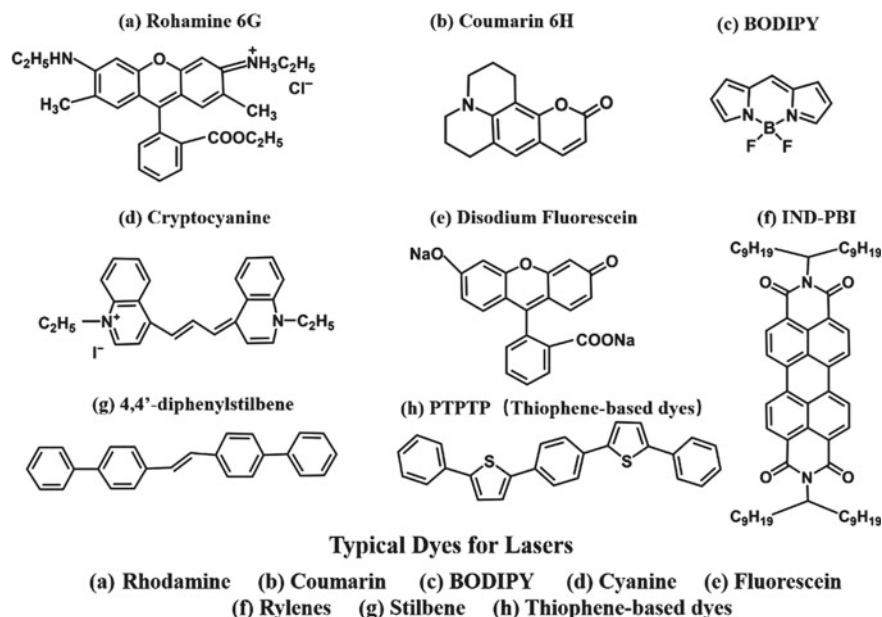
Fig. 6.2 Chemical structures of some representative organic dyes used in organic lasers

6.2.5 Amplifying Spontaneous Emission

Amplifying spontaneous emission (ASE) is a simple process in lasing. ASE test refers to the light generated by spontaneous emission, which is optically amplified in the process of stimulated emission in the gain medium. That is, in the absence of an optical feedback structure, photons from spontaneous fluorescence can still be amplified by stimulated emission by interacting with other excited luminophores in the gain medium. If there is no need to prepare a laser, it is possible to judge whether the material has optical gain characteristics, which will greatly facilitate the screening of laser materials. ASE study of materials is one of the more convenient methods to evaluate the optical gain characteristics of materials. The organic active gain material A planar optical waveguide is fabricated on a quartz substrate. The pumping light passes through diaphragms, slits, and cylindrical mirrors to finally form a narrow strip incident on the surface of the organic film, and the material emits light along the direction of the narrow strip through the organic layer to form a waveguide. The spontaneous emission will be amplified by stimulated emission within the waveguide. If the material has a net gain, there will be outgoing light along the end faces of the narrow strips at the sides of the film. As the intensity of the excitation light increases, we observe a much narrower spectral line than the photofluorescence spectrum, a phenomenon known as specularless lasing. In the ASE test, the spontaneous emission within the film acts like a probe pulse in the transient absorption test. The intensity of the outgoing light exhibits a super-linear

behavior with the length of the strip, and through some simple data processing, the net gain of the material can be obtained: This technique is known as variable stripe length (VSL) [29–31].

6.3   Materials for Organic Lasers

According to the molecular weight and structural characteristics of organic laser materials, they can usually be divided into several categories: organic dyes, organic semiconductors, and other new materials.

6.3.1   Organic Dyes

In the early stage of organic laser development, some of the organic dye materials have been employed because dissolving dye molecules in a liquid solvent is the most common form and most natural choice to construct the laser medium [3]. Organic dye molecules usually refer to organic small molecules containing conjugated double-bond systems with strong absorption properties in the range of ultraviolet to visible light. At the same time, they also exhibit strong stimulated emission properties, with high photoemission quantum efficiency, and their luminescence ranges from near-ultraviolet to infrared to allow the regulation of output laser in the visible spectral range. At present, the technology of dye laser is mature, and it has a wide range of applications in photochemistry, photobiology, spectroscopy, isotope separation, holography, and optical fiber communication.

These organic dyes can be neutral or ionic. Figure 6.2 shows the typical examples of organic dyes used in laser applications including xanthenes (rhodamine and fluorescein family), coumarins, oxazine, pyrromethenes, rylenes, thiophene-based dyes, etc. Because the interaction between adjacent molecules will cause severe concentration quenching of the fluorescence, even if a dye molecule is dispersed in the matrix with strong luminescence, as long as the concentration is too large, the luminescence will be weakened or killed. In organic solid-state lasers, in order to avoid the occurrence of concentration quenching, the most natural way is to dope the dye into the solid matrix. The solid host can be a polymer such as methyl methacrylate (PMMA) and its derivatives [32], or glass and organic–inorganic hybrid materials prepared by the sol–gel method [33–36]. There has also been report on the preparation of two-dimensional photonic crystals by blending two different dyes (DCM and PM567) to obtain low-threshold laser light by interdye energy transfer [37].

6.3.2 Organic Semiconductors

The key commonalities between organic dyes and organic semiconductors are their broad spectra, their strong light emission in the solid state, their ability to be tweaked over the visible spectrum (and beyond), and quasi-four-level laser behavior. There are, however, a few significant variations. One is that even in the pure films (solid state), organic semiconductors can exhibit strong photoluminescence quantum yield. Contrarily, organic dyes require significant dilution in order to make the solid-state quantum yields high. Therefore, in comparison with dyes in the solid state, organic semiconductors have the potential to provide better pump absorption and gain. Another distinction is that many organic semiconductors allow for straightforward processing to produce thin-film laser structures, for instance using solution processing. Furthermore, organic semiconductor solid films have the function of charge transport, which makes electrical pumping a possibility.

If we compare organic semiconductors to inorganic ones, there are similarities between organic and inorganic semiconductors, such as they both have strong light emission in the solid state and they both can transport charges. But there are also many differences between them: On the one hand, organic semiconductors are mostly disordered, so the carrier mobility is much lower than that of inorganic semiconductors; on the other hand, the excitons of organic semiconductors have a larger energy, so the excitons of such materials can exist stably even at room temperature, and the threshold of typical organic semiconductor material is less dependent on temperature [38]; the excited-state lifetime of organic semiconductors is generally only a few nanoseconds, which is much shorter than that of inorganic semiconductors; finally, the device preparation methods of organic semiconductors are relatively simple, such as thermal evaporation, spin coating, and inkjet printing. Based on the difference in structure, we can divide organic semiconductors into three categories: organic crystals, small molecules, and polymers.

6.3.2.1 Organic Crystals

Organic semiconductor materials that can form organic crystals have a lot of overlap with the "organic small molecules" in the next section because both small molecules and macromolecules can form organic crystals. Although self-quenching of luminescence exists in closely packed small molecules, organic single crystals is an active research area because they can offer several distinct advantages that amorphous or less crystalline organic materials do not have. For instance, they typically exhibit large refractive indices and polarized emission due to the high anisotropy of single crystals [39]. The lattice confinement can prevent the entry of oxidants and stabilize the molecular arrangement into a tightly packed structure. This contributes to the material's improved stability [40]. Their enhanced charge transport properties make them be viewed as candidates for electrical pumping [41]. If self-quenching can be prevented, organic single crystals can also provide a high density of luminophores.

Finally, by utilizing internal total reflection at the crystal boundaries, the resulting symmetrical crystal geometries may be used as self-assembled laser resonators. For instance, single crystals with parallel facets function as Fabry-Pérot or microcavity resonators.

However, the growth of such single crystals may not be straightforward, which could make the cost high compared to inorganic counterparts. Further issue of single crystal-based organic lasers is that they typically require high voltage to drive, which limits their practical application.

The chemical structures of several organic single crystal materials are given below (Fig. 6.3). For instance, distyrylbenzene (DSB), its cyano-substituted variants (DCS), and their derivatives are an important family of organic crystal materials. These compounds are more prevalent in terms of substituent variation in part because of their suitable photophysics for lasing and simple, multiple functionalization, which allow for significant variation in the intermolecular arrangement (and the resulting photophysics), particularly through secondary interactions and the twist-elasticity of the flexible DCS backbone. Some of the organic crystals, e.g., DBASDMB, can have intense two-photon absorption and efficient two-photon fluorescence. These properties are appealing for potential applications such as fluorescence microscopy, two-photon-upconversion lasing, optical limiting, and data storage [42].
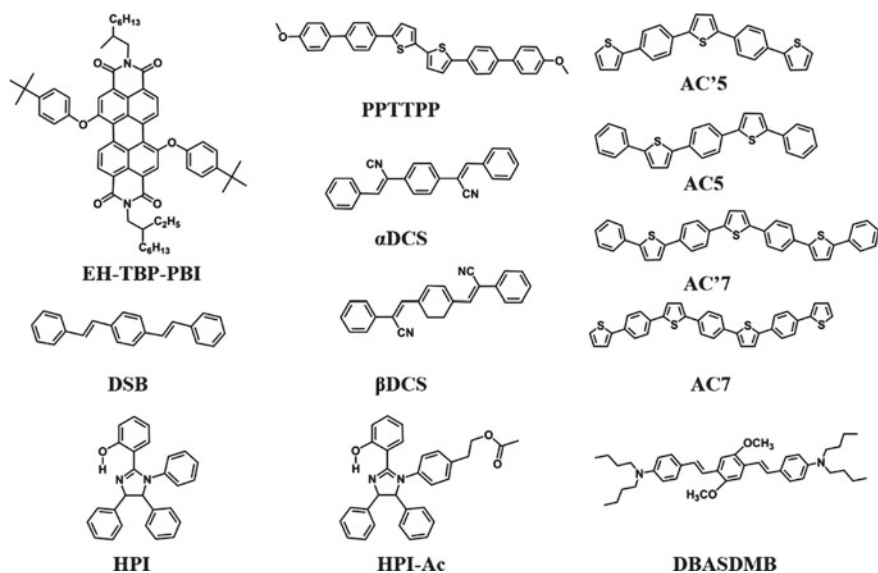
Fig. 6.3   Chemical structures of some organic crystal materials used for constructing organic lasers

6.3.2.2 Organic Small Molecules

Organic small molecule semiconductors, mostly thin films prepared by thermal evaporation, were first employed in organic light-emitting diodes and have been commercialized [43, 44]. In this type of organic semiconductor, part of the materials in the film state is amorphous, while the charge transport is mainly through the hopping mechanism, relying on the overlap of intermolecular orbitals. These small molecule semiconductors have also been utilized in organic lasers with the advantages of batch-to-batch consistency (compared to polymers), easy synthesis and extraction, and thermal evaporation compatibility for most of them. The obtained films have good uniformity and optical quality, whereas some of them exhibit poor stability and incompatibility with flexible substrates. In addition, the $\pi-\pi$ stacking between molecules and the dipole interaction between each unit could lead to intrinsic luminescence quenching. Many approaches in molecular design have been tried to improve the optical emission properties of thin films, such as separating fluorophore units from each other or reducing $\pi-\pi$ overlap [29, 30, 45].

Another method to avoid concentration quenching is to separate the light-emitting units by physical methods. For example, two materials are mixed in a certain ratio to form a host–guest structure, and the active host material transfers energy to the guest through non-radiative transitions. The prototype of this structure is Alq_3:DCM [21, 46]. In this host–guest blend system, the energy of the pump light is absorbed by the host material with a large energy gap, e.g., Alq_3, and then, the energy is passed to the low-energy-gap guest material, e.g., DCM, through Förster energy transfer. Compared with the incorporation of DCM into an inert matrix (such as PMMA), the advantages of the host–guest structure are: (1) the absorption of pumping energy is greater, (2) the charge can be transferred through Alq_3, (3) the Stokes shift between absorption and emission increases, and finally, the self-absorption decreases.

As shown in Fig. 6.4, in addition to the archetypal examples of organic small molecules, e.g., DCM and Alq3, many other structural families have also been adopted such as triphenyldiamines (TPDs) [47], fluorine-based small molecules [11], and unsubstituted specied (nPs) [48, 49].

6.3.2.3 π-Conjugated Polymers

Like we discussed in Chapter 5 and other chapters, conjugated polymer materials are an important branch of organic semiconductor materials [50]. Compared to small molecules, the benefits of polymers include the following. (1) As a polymer, it can obtain a film with good uniformity by spin coating; (2) conjugated polymers, as a typical four-level system material, have the advantages of easier population inversion, wider absorption lines, and lower lasing thresholds; (3) the fluorescence quantum yield of the conjugated polymer is high, and the emission peak position can be changed by changing the side chain structure of the molecule; (4) they can be prepared on rigid substrates as well as large area soft materials; (5) the manufacturing process is simple, the equipment is simple, and the costs are low.
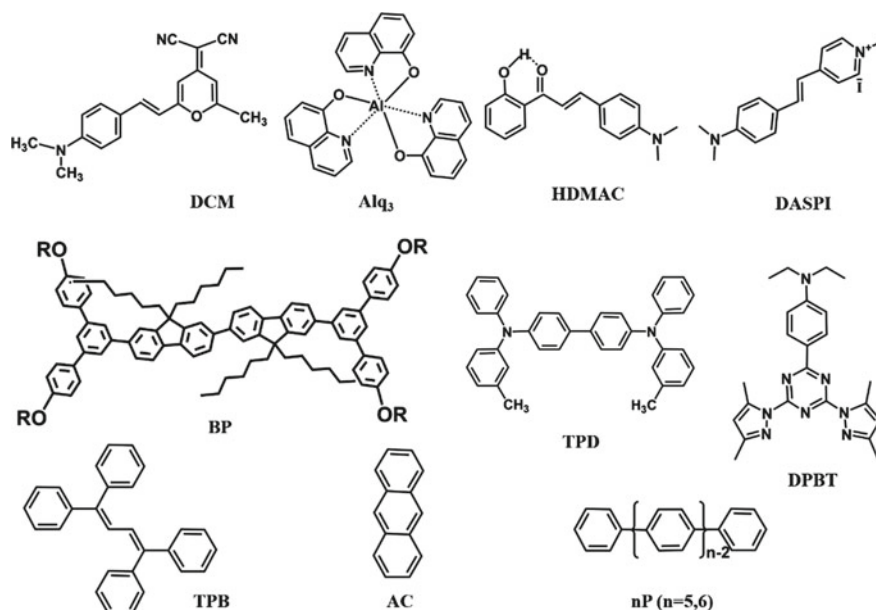
Fig. 6.4 Chemical structures of some organic small molecular semiconductors used for constructing organic lasers

Polymers come in a wide range of morphologies, from entirely amorphous to extremely crystalline. While the former normally has strong optical properties, the latter frequently has better charge transport properties. For laser applications, some conjugated polymers have high photoluminescence quantum yields even in the solid state. Laser emission has been observed in many macromolecular materials. Two of the most important structure families are the PPV-based system [51] and the polyfluorene-based system [47]. First, for the PPVs, ASE has been observed in the PPV and its derivatives, marking the great potential of this structure family. Moreover, the host–guest system based on MEH-PPV-doped with F8BT (two polymers) has been confirmed to have the laser emission [27]. In the polyfluorene family, poly(9,9-dioctylfluorene) (PFO) is the archetype, which has been demonstrated to have different phase properties. The β-phase morphology, in which individual polymer chains adopt an extended conjugation without intermolecular alignment, has the lowest lasing thresholds among the fluorene polymers. Recent research has focused on the refractive index difference between the phase and the amorphous phase of polyfluorene, allowing the creation of novel device designs using both morphologies. In addition to PPVs and polyfluorenes, ternary and higher co-polymers have also demonstrated lasing ability. For example, the blending of poly-(dioctylfluorene-co-benzothiadiazole) F8BT with P3HT, the workhorse electron donor in organic solar cells, enabled P3HT to achieve low-threshold lasing [52] (Fig. 6.5).
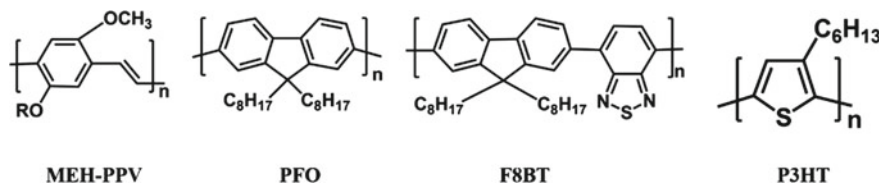
Fig. 6.5 Chemical structures of some conjugated polymers used for constructing organic lasers

6.3.3 Other Organic Lasing Materials

Recently, many new types of materials have also been used in the field of organic lasers. First, biological dyes and fluorescent proteins have been used to construct organic lasers. For example, Gather and Yun [53] reported a more novel laser gain medium, which is a common imaging tracking material in photon biology, namely green light protein, and a laser based on single-cell (in vivo) has been obtained. Moreover, optofluidic lasers have used luciferin, a bioluminescent chemical found in fireflies, bacteria, and marine animals [54]. Second, liquid crystal materials with a highly self-aligned structure [55] can form an optical energy gap suitable for lasers. The gain medium can be an organic dye in the liquid crystal structure, while it can also be the material itself that forms the liquid crystal [56]. In the past few years, in the field of hybrid solar cells as we will discuss in Chap. 11, alkyl ammonium lead halides based perovskite materials have attracted extensive attention due to their unexpectedly optoelectronic, chemical and electrical properties. In addition to the great progress in solar cells, LEDs, X-ray detectors, the application of perovskite materials in lasers has also been demonstrated. As these perovskite materials not only can be vacuum deposited, they can also be solution processed with relatively low-cost procedures. Furthermore, the emission spectra of the perovskite can be regulated by changing the composition of the film, enabling the coverage of the entire visible spectrum from ~400 nm to over 800 nm. More importantly, these perovskite materials have much higher carrier mobilities than typical organic semiconductors, making them great candidates for cost-effective electrically pumped lasers. Xing et al. [57] studied the excited-state behavior of perovskite materials. On this basis, the laser emission behavior of perovskite materials was further reported [58], with an ASE threshold of 10 μJ·cm^{-2}, which expanded the application of perovskite materials in lasers. Optically pumped laser made from perovskite materials was realized in different geometries, such as the sandwich structure of a perovskite layer placed between a DBR and a gold electrode [59]. However, due to the relatively rough surface of perovskite films that results in high optical loss, the threshold of laser emission is still relatively high. In the future, to be used as a laser gain medium, the perovskite materials' stability needs to be further improved, which could become the main research direction of perovskite laser.

6.3.4   Comparison Among Organic Lasing Materials

Over the last few decades, there have been a lot of intriguing advancements in materials for organic lasers. Organic gain materials have been enhanced and optimized for laser performance in a variety of methods throughout the years. Earlier research found that the discovery of novel materials was rather accidental, with advancements made via trial and error. The community then proceeded to develop methods for morphological control by carefully analyzing the most powerful laser materials available, allowing the crystalline and amorphous character of the materials to now be controlled. Organic laser materials including dyes in inert matrices, host–guest systems, conjugated polymers, small molecules, star-shaped dendrimers, oligomers, etc., according to their structural features, exhibit different characteristics in terms of their intermolecular interaction, their solid-state forms, and their optical properties.

First, there are differences in the interaction between dyes and semiconductor molecules, and the effect of this difference on laser behavior can also be distinguished at the macroscopic scale rather than at the molecular scale. Excited states can be quenched by exciton-exciton quenching, exciton diffusion, photogenerated carriers, and the surrounding environment [60–63], which makes the photophysical properties of such lasing media very different from those that exhibit simple four-level structures. These phenomena have been extensively studied in conjugated polymer systems [62, 64] and are observed in host–guest systems. For example, the laser dynamics of Alq_3:DCM hybrid systems are influenced by Förster transfer dynamics [65]. The singlet excitons of the guest DCM are effected by the exciton quenching of the photogenerated triplet excitons of the host Alq_3. On the contrary, if the luminophore is added to the inert matrix, the intermolecular interactions are reduced and the laser physics is relatively simple. In this sense, the difference in the lasing properties of dyes and organic semiconductors in optically inert matrices is closely related to intermolecular interactions.

Second, we can distinguish between bulk gain media and thin film gain media by different preparation methods. Bulk gain materials are rods with a scale of several millimeters to several centimeters, which are ground and polished to a certain optical precision, and then mounted on a microcavity with macroscopic scale [66]. Such rods are generally prepared by embedding organic luminophores into monomers, such as methyl methacrylate, and then polymerizing them [66], or by incorporating the luminophores into glass through a sol–gel method [67]. The thin-film material can be prepared by thermal evaporation or solution methods. If the small molecules (including dyes) are neutral, evaporation may be used, but the polymers cannot be evaporated because the molecular weight is too large. Solution preparation methods include spin coating [68], dip coating, doctor blading [69], or inkjet printing [70]. Most polymers can be prepared by solution methods, as can small molecules as long as they have good solubility. For polymers with poor solubility, functional groups can be added to the side chains, or by copolymerizing some blocks with good solubility on the main chain. In addition, there are some non-conjugated polymers such as

PMMA that are also soluble, so as long as the dye is doped into it, the purpose of preparing the thin film by the solution method can also be achieved.

From an optical point of view, there are many similar properties between dyes and organic semiconductors. For example, the emission spectra of these two materials are very broad and can be adjusted by adjusting the structure; they are all materials with a quasi-quad-level structure. Samuel and Turnbull [14] believed that when discussing the difference between organic semiconductors and dyes, the following three points must be considered: (1) Organic semiconductors still have good photoluminescence quantum yields in thin films, while organic dyes require sufficient dilution, which makes the absorption and gain of the pump light stronger for organic semiconductors than for dyes in the solid state; (2) organic semiconductors can be fabricated into thin-film devices by spin coating or printing; and (3) organic semiconductors can transport charge carriers (although mobility is lower than inorganic semiconductor materials), which is especially important for electrical pumping.

However, in practice, these criteria are not absolute. Some organic molecules may have high fluorescence quantum efficiencies in solution (in line with classic expectations for dyes), but they can also exhibit good luminescence properties and laser behavior in thin films, which also proves that they have semiconductor properties. Historically, the concept of organic semiconductors distinct from dyes has been proposed mainly due to the actual need for transporting carriers for electrical pumping devices. For researches on organic lasers that are carried out under the condition of optical pumping, it does not seem necessary to strictly distinguish between dyes and semiconductors.

6.4   The Photophysical Properties of Organic Laser Materials

6.4.1   Gain Effect

Lasers work because they contain a gain medium that amplifies light waves. Unlike pure photon absorption, if an incident photon interacts with the excited gain material and releases an additional photon from the excited state with a frequency and propagation direction identical to that of the incident photon, the process is called stimulated emission. That is to say, when the light wave propagates through the gain medium, more photons are emitted, a stronger light intensity is generated, and as the distance increases, the stimulated emission increases exponentially. The theory was first proposed by Einstein, and he further pointed out that population inversion is a necessary condition for the realization of stimulated emission and that only in a three-level or four-level system can population inversion be realized.

Fig. 6.6 Schematic of wavelength tuning of organic laser materials by adjusting the chemical structures. Red shift was observed due to the enhancement of electron withdrawing by connecting different functional groups of electron withdrawing on the triphenylamine. (Adapted from Ref. [45])
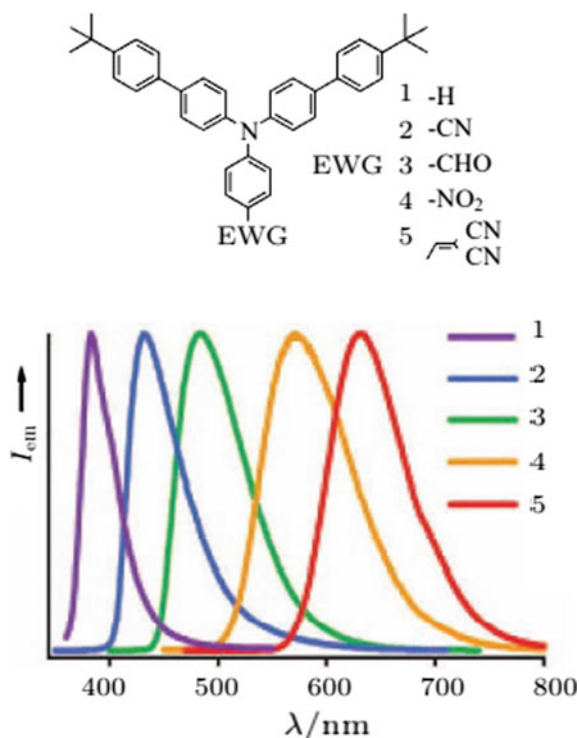
6.4.2 Cross Section of Absorption

The absorption cross section σ_{abs} of organic laser medium is the largest among all materials, generally on the order of 10^{-16} cm^2. In a pure small molecule film, if the molecular density $n \approx \rho \times N_A/M = 1.3 \times 6.10^{23}/460 \approx 10^{21}$ cm^{-3}, (ρ is the density of the film, N_A is the Avogadro constant, M is the molecular weight, and the data of Alq$_3$ is used here), it can be speculated that the light in the organic material is completely absorbed. The typical thickness of this is $L_{abs} = (\sigma_{abs}n)^{-1} \sim 100$ nm. This shows that first thin-film laser devices based on organic gain materials can be realized; Second, since the magnitudes of the absorption and stimulated emission cross-sectional areas are consistent, high gains for organic gain media can be expected [71] (Fig. 6.6).

6.4.3 Emission Spectrum

A large optical gain may be obtained in organic materials. Meanwhile, the gain lifetime is short, only in the order of picoseconds spectrum [72]. Another effective chemical control method is to use an asymmetric push–pull structure to change the

intramolecular electronic properties of the molecule. With the increase of electron-withdrawing groups, the dipole moment of the excited state of the material will increase, and in the thin film or under certain polar conditions, the Stokes shift will increase, which could eventually lead to a red shift of the emission.

6.4.4 Characterization of Organic Laser Materials

To judge whether a certain material has optical gain behavior (i.e., whether it can be used as a laser material) and evaluate the magnitude of the gain, transient absorption experiments or ASE tests are usually employed. The ASE test has been discussed earlier. The transient absorption (TA) experiment is a purely optical test for ultrafast measurement of the transition state change of a photochemical reaction by exciting a substance with light. The principle of TA is not the focus of the chapter, but if there is a net gain in the sample, the probe pulse will be enhanced by stimulated emission after passing through the sample. Ruseckas et al. [73] reported the use of TA to examine poly[3-(2, 5-dioctyl-phenyl)-thiophene] thin films. In TA experiments performed on thin films, the absorption of the excited state contributes to the positive part of ΔA, while the absorption of the ground-state and stimulated emission contributes to the negative part of ΔA. The net gain spectrum of the material depends on the material's gain spectrum and the absorption of the excited and ground states, and the net gain is the gain of the material minus the absorption. There have been a series of reports on the observation of lasing phenomenon of PPV materials, and the kinetics have also been investigated [64, 73, 74]. On the one hand, these studies confirm that a large optical gain may be obtained in organic materials; on the other hand, they also point out that the gain lifetime is short, only in the order of picoseconds.

6.5 Organic Micro-/Nanoscale Lasers

Micro-/nano-lasers, sometimes referred to as small lasers, are a class of miniaturized lasers with a device size or mode volume on the wavelength or subwavelength scale [75], which is the research frontier of the intersection of laser technology and nanotechnology. Micro-/nano-lasers can provide strong coherent optical signals at the micro-/nano-scale. It is expected to bring revolutionary changes to the entire field of science and technology and open up some new application areas. At present, micro-/nano-lasers have been widely used in ultrasensitive chemical and biological sensing and on-chip optical information transmission and processing. [76–78]

Recently, the progress made in the field of microfluidics has enabled the application of organic dyes in small lasers [75]. These organic dye-based fluidic lasers have the unique benefit of being able to adjust the gain spectrum and refractive index of the active medium by altering the solvent or dye that is fed through the device. As an alternative, organic dyes can be incorporated in a solid-state matrix that is transparent

and elastic from a mechanical standpoint (typically a polymer) [75]. Organic semi-conductors are hydrocarbon-based materials having strong optical transitions, much to organic dyes. Their massive conjugated π-electron systems also impart semicon-ducting characteristics, opening the possibility of direct current injection. Fine-tuning the conjugated backbone of polymeric materials or adding long-range order are two methods for producing materials with increased charge mobility and strong optical gain [79]. Configurations of organic semiconductor lasers that are optically pumped have been thoroughly investigated. These devices have immediate uses in addition to serving as a first step toward electrically pumped organic lasers, such as when used in conjunction with affordable LED pump sources [80]. However, when long-term operational stability at high power densities is required, organic materials may suffer photoinduced bleaching of fluorescence and optical gain under high-excitation circumstances.

Despite the relatively weak intermolecular interactions between organic molecules, some organic small molecules or polymers can self-assemble into ordered structures driven by van der Waals force or π-π interactions [81]. These struc-tures can have different dimensions. Among them, one-dimensional (1D) self-assembled organic structures, e.g., nanorods and nanowires, have attracted attention of researchers due to their potential in next-generation optoelectronic devices. 1D organic lasers are simple to fabricate because of the strong cofacial interactions for the majority of organic molecules, which drive axial crystal growth [82]. The cross section for these 1D organic structures can be tuned in the range of a few to up to two hundred nanometers with lengths ranging from hundreds of nanometers to millime-ters. Additionally, the Fabry-Pérot (FP) resonators are inherently embedded within 1D wire or rod-like structures, where the wire or rod serves as a useful optical wave-guide and the end-facets serve as mirrors, demonstrating a length-dependent mode modulating effect and intrinsic lasing performance [13, 83]. The 1D organic solid-state lasers are promising for use in the future generation of optoelectronic devices, notably as the lasing source and interconnects for the on-chip optical circuits since they can lase 1D structures and have the benefits of organic materials. Additionally, by building heterostructures or multiblocks for multifunctional laser applications, the basic 1D morphology may be adaptably changed. Therefore, it is especially crucial to build 1D organic lasers. Nevertheless, many challenges need to be over-come before 1D organic lasers can have practical applications including the limited material choices and not-small-enough crystal size for optical circuits.

6.6   Current Research Status and Outlook

The pump source is one of the laser's three main components. Choosing an appro-priate way to excite the organic material, achieving population inversion, and keeping the number of particles at higher energy levels greater than those at lower energy levels helps assure the laser's continuous output. The present research on organic

lasers is focused on two distinct pumping sources: electrical and optical. Although optical pumping for organic lasers is rather mature, electrically pumped organic lasers have been sought for decades.

6.6.1   Research Status of Electrically Pumped Organic Lasers

Since the discovery of optically pumped organic laser in 1996, the research on solid-state organic laser has been an active spot [84]. As most of the optically pumped organic lasers are driven by strong pulse lasers, their devices are bulky in size, which prevent them from easy integration with other necessary devices for application purposes. Therefore, there has always been a strong demand for the electrically pumped organic solid-state laser, particularly when the portable or Internet-of-Things markets are considered, which sets the requirement for on-chip coherent light sources that can benefit the full integration of organic photonic devices into functional opto-electronic circuits. Electrically pumped OSSL is recognized as the most promising generation of ultralight, cheap, tunable, and flexible laser devices.

As a matter of fact, numerous attempts have been made to pursue electrically pumped organic lasers (EPOLs) [85], especially after the commercialization of OLEDs (see Chap. 3 for details). As we mentioned earlier, the research on PPV-based lasing have already revealed that these polymers are able to transport charges efficiently, signaling the possibility of EPOLs. The same conclusion has been manifested by the small molecule-based organic lasers. In 2009, a light-emitting transistor structure combined with a rib waveguide distributed feedback resonator has been introduced, offering us a viable approach to EPOL with a unique device design and resonator type [66]. Until 2019, Adachi et al. demonstrated a credible experimental example of current injection lasing from an organic small molecule paired with a mixed-order DFB grating, giving the scientific community a strong hint that EPOL is likely to arrive soon [86]. However, despite progresses being made with respect to molecular design, device fabrication and theoretical prediction [87], the electrically pumped organic laser (or called organic laser diode, OLD) has not yet been fully demonstrated.

The realization of electrically pumped organic lasers is a very complex and arduous task [28, 88, 89], which requires a thorough understanding of the working principle of the materials, the device structures, and the device physics. Although OLED devices have achieved great progress in terms of luminescence and efficiency over the past decade, these advances have not been directly transferred to the field of organic lasers. Overall, a full EPOL meeting the following criteria simultaneously has not been successfully demonstrated: (1) sufficient current injection to produce population inversion; (2) a clear threshold of current dependent spectral narrowing and output power enhancement; and (3) the concurrent observation of coherence in space and time (Fig. 6.7) [85].

Nonetheless, this should not stop the pursuit of EPOL because of the bright future EPOL paints for us: The broad color tuning enables the development of active-matrix
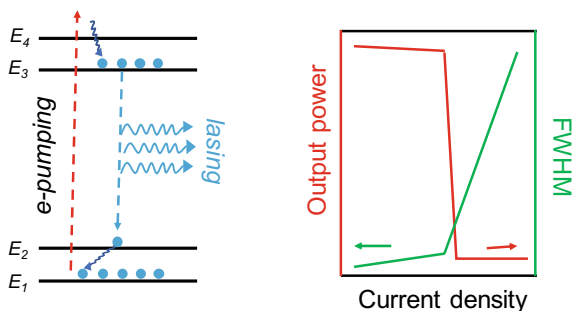
Fig. 6.7 Criteria for an EOPL illustrating for the organic four-level system under electrical excitation. Left: Upon electrical pumping, organic semiconductor undergoes a transition from E_1 to E_4, followed by a quick relaxation to E_3. Due to the development of population inversion between E_3 and E_2, the lasing transition occurs down to E_2, followed by a quick vibrational relaxation to E_1. Right: The relationship between output power and FWHM and current density. Around the lasing threshold, there are noticeable kinks in both the output power and linewidth

flexible laser displays with high saturation, high contrast ratio, and a large attainable color gamut, which offers enormous potential for smart devices and equipment.

6.6.2 Research on Optically Pumped Organic Lasers

Because of the challenges in creating organic laser diodes, researchers began to investigate if an indirect method of achieving electrically pumped organic lasers might be used. That is, charge carriers are not directly injected into conjugated materials, but rather drive a laser diode or LED, and then optically pump organic materials through this diode. The motive behind this notion is the same as it was when we first started researching organic lasers: to give a cheap, practical, and compact alternative to the complex, bulky, and expensive inorganic lasers. The contrast between dyes (in a polymer or semiconductor matrix, such as Alq_3) and organic semiconductors is unimportant under this assumption. To the best of our knowledge, in the next few years or decades, the optically pumped organic lasers may have improvements from the following directions.

The first is indirect electrically pumped organic lasers. The idea of indirect electrically pumped organic lasers is to use an electrical pump light source to optically pump organic materials. Such an approach seeks to capitalize on optical pumping and create tiny devices that nearly resemble the features of a directly electrically driven device. Therefore, the pump light source used in such indirect ways must be a cheap, compact, and efficient system, rather than an expensive flashlamp pumping system such as a Nd:YAG laser, or a Ti:Sapphire laser. GaN-based [90] or InGaN-based [91–93] laser diodes have been proven effective as pump sources for organic lasers.

Meanwhile, inorganic semiconductor-based light-emitting diodes are also an optical pumping source candidate that can achieve indirect electrical pumping [88, 94].

The second is low-threshold organic lasers. The interaction length between the laser pulse and the gain medium, as well as the quality of the cavity mirrors, determines the lasing threshold for a specific organic material. Achieving a low-threshold laser system is an enticing aim since it increases overall electrical-to-optical efficiency and reduces the amount of pump energy required to operate the laser.

Besides, extending the coverage of the wavelength of organic lasers is meaningful [95–99]. As we discussed in Chap. 5, the active research in organic solar cells these past few years has led to the surge of conjugated small molecules or polymers with emission in the near-infrared (NIR) region. These compounds or their derivatives could be considered, if not directly as gain medium, as starting points to design new structures that could extend the emission range.

Finally, improving the wavelength agility or tenability [98, 100–105], the conversion efficiency and thus output power [106–108], the beam quality [106, 107, 109, 110], and the stability (lifetime) [111] of the organic lasers, are all directions with profound significance.

References

1. Sorokin PP, Lankard JR (1966) Stimulated emission observed from an organic dye, chloro-aluminum phthalocyanine. IBM J Res Dev
2. Jiang Y, Liu YY, Liu X, Lin H, Gao K, Lai WY, Huang W (2020) Organic solid-state lasers: a materials view and future development. Chem Soc Rev 49:5885–5944
3. Schäfer FP, Schmidt W, Volze J (1966) Organic dye solution laser. Appl Phys Lett 9:306–309. https://doi.org/10.1063/1.1754762
4. Soffer BH, McFarland BB (1967) Continuously tunable, narrow-band organic dye lasers. Appl Phys Lett 10:266–267. https://doi.org/10.1063/1.1754804
5. Karl N (1972) Laser emission from an organic molecular crystal, p 651
6. Avanesjan OS, Benderskii VA, Brikenstein VK, Broude VL, Korshunov LI, Lavrushko AG, Tartakovskii II (1974) Anthracene crystals under intensive optical pumping. Mol Cryst Liq Cryst 29:165–174. https://doi.org/10.1080/15421407408083197
7. Hide F, Diaz-Garcia MA, Schwartz BJ, Andersson MR, Pei Q, Heeger AJ (1996) Semiconducting polymers: a new class of solid-state laser materials. Science
8. Gaylord BS, Heeger AJ, Bazan GC (2003) DNA hybridization detection with water-soluble conjugated polymers and chromophore-labeled single-stranded DNA. J Am Chem Soc. https://doi.org/10.1021/ja027152
9. Vannahme C, Klinkhammer S, Lemmer U, Mappes T, Janasek D, Franzke J, Manz A (2011) Plastic lab-on-a-chip for fluorescence excitation with integrated organic semiconductor lasers. Opt Express
10. Amarasinghe D, Ruseckas A, Turnbull GA, Samuel IDW (2009) Organic semiconductor optical amplifiers. Proc IEEE 97:1637–1650. https://doi.org/10.1109/JPROC.2009.2023250
11. Kuehne AJC, Gather MC (2016) Organic lasers: recent developments on materials, device geometries, and fabrication techniques. Chem Rev 116:12823–12864
12. Clark J, Lanzani G (2010) Organic photonics for communications. Nat Photonics 4:438–446
13. Eaton SW, Fu A, Wong AB, Ning CZ, Yang P (2016) Semiconductor nanowire lasers. Nat Rev Mater 1
14. Samuel IDW, Turnbull GA (2007) Organic semiconductor lasers. Chem Rev 107:1272–1295

15. Gierschner J, Park SY (2013) Luminescent distyrylbenzenes: tailoring molecular structure and crystalline morphology. J Mater Chem C 1:5818–5832

16. Kasha M, Rawls HR, Ashraf El-Bayoumi M (1965) The exciton model in molecular spectroscopy. Pure Appl Chem

17. Rauscher U, Sassier H, Bradley DDC, Hennecke M (1990) Exciton versus band description of the absorption and luminescence spectra in poly(p-phenylenevinylene). Phys Rev B

18. Rudenko AI, Bässler H (1991) Spectral diffusion in random media: a master equation approach. Chem Phys Lett 182:581–587. https://doi.org/10.1016/0009-2614(91)90128-V

19. Kersting R, Lemmer U, Mahrt RF, Leo K, Kurz H, Bassler H, Gobel EO (1993) Femtosecond energy relaxation in 7r-conjugated polymers. Phys Rev Lett

20. Samuel IDW, Crystall B, Rumbles G, Burn PL, Holmes AB, Friend RH (1993) Time-resolved luminescence measurements in poly(p-phenylenevinylene). Synth Metals 54:281–288. https://doi.org/10.1016/0379-6779(93)91071-9

21. Kozlov VG, Bulović V, Burrows PE, Forrest SR (1997) Laser action in organic semiconductor waveguide and double-heterostructure devices. Nature 389:362–364. https://doi.org/10.1038/38693

22. Gupta R, Stevenson M, Heeger AJ (2002) Low threshold distributed feedback lasers fabricated from blends of conjugated polymers: reduced losses through Förster transfer. J Appl Phys 92:4874–4877. https://doi.org/10.1063/1.1505668

23. Dogariu A, Gupta R, Heeger AJ, Wang H (1999) Time-resolved Förster energy transfer in polymer blends. Synth Metals 100:95–100. https://doi.org/10.1016/S0379-6779(98)00168-4

24. Kozlov VG, Bulovic V, Burrows PE, Baldo M, Khalfin VB, Parthasarathy G, Forrest SR, You Y, Thompson ME (1998) Study of lasing action based on Förster energy transfer in optically pumped organic semiconductor thin films. J Appl Phys 84:4096–4108. https://doi.org/10.1063/1.368624

25. Sheridan AK, Buckley AR, Fox AM, Bacher A, Bradley DDC, Samuel IDW (2002) Efficient energy transfer in organic thin films—implications for organic lasers. J Appl Phys 92:6367–6371. https://doi.org/10.1063/1.1516270

26. Peterson OG, Webb JP, McColgin WC, Eberly JH (1971) Organic dye laser threshold. J Appl Phys 42:1917–1928. https://doi.org/10.1063/1.1660468

27. Lehnhardt M, Riedl T, Weimann T, Kowalsky W (2010) Impact of triplet absorption and triplet-singlet annihilation on the dynamics of optically pumped organic solid-state lasers. Phys Rev B: Condens Matter Mater Phys 81. https://doi.org/10.1103/PhysRevB.81.165206

28. Giebink NC, Forrest SR (2009) Temporal response of optically pumped organic semiconductor lasers and its implication for reaching threshold under electrical excitation. Phys Rev B Condens Matter Mater Phys 79. https://doi.org/10.1103/PhysRevB.79.073302

29. Forget S, Chenais S, Tondelier D, Geffroy B, Gozhyk I, Lebental M, Ishow E (2010) Red-emitting fluorescent organic light emitting diodes with low sensitivity to self-quenching. J Appl Phys 108. https://doi.org/10.1063/1.3481460

30. Rabbani-Haghighi H, Forget Ś, Ch́nais Ś, Siove A, Castex MC, Ishow E (2009) Laser operation in nondoped thin films made of a small-molecule organic red-emitter. Appl Phys Lett 95. https://doi.org/10.1063/1.3182820

31. Jordan G, Flämmich M, Rüther M, Kobayashi T, Blau WJ, Suzuki Y, Kaino T (2006) Light amplification at 501 nm and large nanosecond optical gain in organic dye-doped polymeric waveguides. Appl Phys Lett 88. https://doi.org/10.1063/1.2197314

32. Ahmad M, King TA, Ko D-K, Cha BH, Lee J (2002) Performance and photostability of xanthene and pyrromethene laser dyes in sol-gel phases. J Phys D: Appl Phys

33. Gritsai Y, Sakhno O, Goldenberg LM, Stumpe J (2014) Dye-doped PQ-PMMA phase holographic materials for DFB lasing. J Opt (UK) 16. https://doi.org/10.1088/2040-8978/16/3/035101

34. Faloss M, Canva M, Georges P, Brun A, Dé F, Chaput R, Boilot J-P (1997) Toward millions of laser pulses with pyrromethene-and perylene-doped xerogels. Appl Opt

35. Rahn MD, King TA (1995) Comparison of laser performance of dye molecules in sol-gel, polycom, ormosil, and polyAmethyl methacrylateB host media. Appl Opt

36. Yariv E, Reisfeld R (1999) Laser properties of pyrromethene dyes in sol–gel glasses. Opt Mater (Amst) 13:49–54. https://doi.org/10.1016/S0925-3467(99)00010-5

37. Liu L, Huang W, Diao Z, Peng Z, Mu QQ, Liu Y, Yang C, Hu L, Xuan L (2014) Low threshold of distributed feedback lasers based on scaffolding morphologic holographic polymer dispersed liquid crystal gratings: reduced losses through Forster transfer . Liq Cryst 41:145–152. https://doi.org/10.1080/02678292.2013.845308

38. Kozlov VG, Bulović V, Forrest SR (1997) Temperature independent performance of organic semiconductor lasers. Appl Phys Lett 71:2575–2577. https://doi.org/10.1063/1.120186

39. Spearman P, Borghesi A, Campione M, Laicini M, Moret M, Tavazzi S (2005) Directional dispersion in absorbance spectra of oligothiophene crystals. J Chem Phys 122. https://doi.org/10.1063/1.1826052

40. Rezzonico D, Kwon SJ, Figi H, Kwon OP, Jazbinsek M, Günter P (2008) Photochemical stability of nonlinear optical chromophores in polymeric and crystalline materials. J Chem Phys 128. https://doi.org/10.1063/1.2890964

41. Troisi A (2011) Charge transport in high mobility molecular semiconductors: classical models and new theories. Chem Soc Rev 40:2347–2358

42. Fang HH, Yang J, Feng J, Yamao T, Hotta S, Sun HB (2014) Functional organic single crystals for solid-state laser applications. Laser Photonics Rev 8:687–715

43. Tang CW, Vanslyke SA (1987) Organic electroluminescent diodes. Appl Phys Lett 51:913–915. https://doi.org/10.1063/1.98799

44. Tang CW, Vanslyke SA, Chen CH (1989) Electroluminescence of doped organic thin films. J Appl Phys 65:3610–3616. https://doi.org/10.1063/1.343409

45. Ishow E, Brosseau A, Clavier G, Nakatani K, Tauc P, Fiorini-Debuisschert C, Neveu S, Sandre O, Léaustic A (2008) Multicolor emission of small molecule-based amorphous thin films and nanoparticles with a single excitation wavelength. Chem Mater 20:6597–6599. https://doi.org/10.1021/cm802264c

46. Berggren M, Dodabalapur A, Slusher RE (1997) Stimulated emission and lasing in dye-doped organic thin films with Forster transfer. Appl Phys Lett 71:2230–2232. https://doi.org/10.1063/1.120065

47. Heliotis G, Xia R, Bradley DDC, Turnbull GA, Samuel IDW, Andrew P, Barnes WL (2003) Blue, surface-emitting, distributed feedback polyfluorene lasers. Appl Phys Lett 83:2118–2120. https://doi.org/10.1063/1.1612903

48. Heimel G, Daghofer M, Gierschner J, List EJW, Grimsdale AC, Müllen K, Beljonne D, Brédas JL, Zojer E (2005) Breakdown of the mirror image symmetry in the optical absorption/emission spectra of oligo(para-phenylene)s. J Chem Phys 122. https://doi.org/10.1063/1.1839574

49. Milin-Medina B, Varghese S, Ragni R, Boerner H, Ort E, Farinola GM, Gierschner J (2011) Excited-state switching by per-fluorination of para-oligophenylenes. J Chem Phys 135. https://doi.org/10.1063/1.3643151

50. Heeger AJ (2001) Nobel lecture: semiconducting and metallic polymers: the fourth generation of polymeric materials. Rev Mod Phys

51. Chen Y, Herrnsdorf J, Guilhabert B, Kanibolotsky AL, MacKintosh AR, Wang Y, Pethrick RA, Gu E, Turnbull GA, Skabara PJ, Samuel IDW, Laurand N, Dawson MD (2011) Laser action in a surface-structured free-standing membrane based on a π-conjugated polymer-composite. Org Electron 12:62–69. https://doi.org/10.1016/j.orgel.2010.09.021

52. Xia R, Stavrinou PN, Bradley DDC, Kim Y (2012) Efficient optical gain media comprising binary blends of poly(3-hexylthiophene) and poly(9,9-dioctylfluorene-co-benzothiadiazole). J Appl Phys 111. https://doi.org/10.1063/1.4730041

53. Gather MC, Yun SH (2011) Single-cell biological lasers. Nat Photonics 5:406–410. https://doi.org/10.1038/nphoton.2011.99

54. Wu X, Chen Q, Sun Y, Fan X (2013) Bio-inspired optofluidic lasers with luciferin. Appl Phys Lett 102. https://doi.org/10.1063/1.4807837

55. Coles H, Morris S (2010) Liquid-crystal lasers. Nat Photonics 4:676–685. https://doi.org/10.1038/nphoton.2010.184

56. Muñoz A, Palffy-Muhoray P, Taheri B (2001) Ultraviolet lasing in cholesteric liquid crystals
57. Guichuan X, Nripan M, Shuangyong S, Sien LS, Ming LY, Michael G, Subodh M, Chien ST (2013) Long-range balanced electron- and hole-transport lengths in organic-inorganic $CH_3NH_3PbI_3$. Science 342(1979):344–347. https://doi.org/10.1126/science.1243167
58. Xing G, Mathews N, Lim SS, Yantara N, Liu X, Sabba D, Grätzel M, Mhaisalkar S, Sum TC (2014) Low-temperature solution-processed wavelength-tunable perovskites for lasing. Nat Mater 13:476–480. https://doi.org/10.1038/nmat3911
59. Deschler F, Price M, Pathak S, Klintberg LE, Jarausch DD, Higler R, Hüttner S, Leijtens T, Stranks SD, Snaith HJ, Atatüre M, Phillips RT, Friend RH (2014) High photoluminescence efficiency and optically pumped lasing in solution-processed mixed halide perovskite semiconductors. J Phys Chem Lett 5:1421–1426. https://doi.org/10.1021/jz5005285
60. Gärtner C, Karnutsch C, Lemmer U, Pflumm C (2007) The influence of annihilation processes on the threshold current density of organic laser diodes. J Appl Phys 101. https://doi.org/10.1063/1.2425003
61. List EJW, Kim CH, Naik AK, Scherf U, Leising G, Graupner W, Shinar J (2001) Interaction of singlet excitons with polarons in wide band-gap organic semiconductors: a quantitative study. Phys Rev B Condens Matter Mater Phys 64:1552041–15520411. https://doi.org/10.1103/PhysRevB.64.155204
62. List EJW, Scherf U, Müllen K, Graupner W, Kim CH, Shinar J (2002) Direct evidence for singlet-triplet exciton annihilation in π-conjugated polymers. Phys Rev B Condens Matter Mater Phys 66:1–5. https://doi.org/10.1103/PhysRevB.66.235203
63. Osterbacka R, Wohlgenannt M, Shkunov M, Chinn D, Vardeny ZV (2003) Excitons, polarons, and laser action in poly(p-phenylene vinylene) films. J Chem Phys 118:8905–8916. https://doi.org/10.1063/1.1566937
64. Kraabel B, Klimov V, Kohlman R, Xu S, Wang HL, McBranch D (2000) Unified picture of the photoexcitations in phenylene-based conjugated polymers: universal spectral and dynamical features in subpicosecond transient absorption. Phys Rev B Condens Matter Mater Phys 61:8501–8515. https://doi.org/10.1103/PhysRevB.61.8501
65. Koschorreck M, Gehlhaar R, Lyssenko VG, Swoboda M, Hoffmann M, Leo K (2005) Dynamics of a high-Q vertical-cavity organic laser. Appl Phys Lett 87:1–3. https://doi.org/10.1063/1.2125128
66. Gwinner MC, Khodabakhsh S, Song MH, Schweizer H, Giessen H, Sirringhaus H (2009) Integration of a rib waveguide distributed feedback structure into a light-emitting polymer field-effect transistor. Adv Funct Mater 19:1360–1370. https://doi.org/10.1002/adfm.200801897
67. Deshpande AV, Rane JR, Jathar LV (2009) Comparison of spectroscopic and lasing properties of different types of sol-gel glass matrices containing Rh-6G. J Fluoresc 19:1083. https://doi.org/10.1007/s10895-009-0508-5
68. Chang CC, Pai CL, Chen WC, Jenekhe SA (2005) Spin coating of conjugated polymers for electronic and optoelectronic applications. Thin Solid Films 479:254–260. https://doi.org/10.1016/j.tsf.2004.12.013
69. Ding IK, Melas-Kyriazi J, le Cevey-Ha N, Chittibabu KG, Zakeeruddin SM, Grätzel M, McGehee MD (2010) Deposition of hole-transport materials in solid-state dye-sensitized solar cells by doctor-blading. Org Electron 11:1217–1222. https://doi.org/10.1016/j.orgel.2010.04.019
70. Yoshioka Y, Jabbour GE (2006) Desktop inkjet printer as a tool to print conducting polymers. Synth Met 156:779–783. https://doi.org/10.1016/j.synthmet.2006.03.013
71. McGehee MD, Díaz-García MA, Hide F, Gupta R, Miller EK, Moses D, Heeger AJ (1998) Semiconducting polymer distributed feedback lasers. Appl Phys Lett 72:1536–1538. https://doi.org/10.1063/1.121679
72. Coulson CA (1948) Excited electronic levels in conjugated molecules : I. Long wavelength ultra-violet absorption of naphthalene, anthracene and homologs. Proc Phys Soc (1926–1948)
73. Ruseckas A, Theander M, Valkunas L, Andersson MR, Inganäs O, Sundström V (1998) Energy transfer in a conjugated polymer with reduced inter-chain coupling. J Lumin 76–77:474–477. https://doi.org/10.1016/S0022-2313(97)00238-X

74. Frolov SV, Vardeny ZV, Yoshino K (1998) Cooperative and stimulated emission in polyp-phenylene-vinylene … thin films and solutions

75. Hill MT, Gather MC (2014) Advances in small lasers. Nat Photonics 8:908–918. https://doi.org/10.1038/nphoton.2014.239

76. Ma R-M, Ota S, Li Y, Yang S, Zhang X (2014) Explosives detection in a lasing plasmon nanocavity. Nat Nanotechnol 9:600–604. https://doi.org/10.1038/nnano.2014.135

77. He L, Özdemir ŞK, Zhu J, Kim W, Yang L (2011) Detecting single viruses and nanoparticles using whispering gallery microlasers. Nat Nanotechnol 6:428–432. https://doi.org/10.1038/nnano.2011.99

78. Chuang Z, Chang-Ling Z, Yan Z, Chun-Hua D, Cong W, Hanlin W, Yunqi L, Guang-Can G, Jiannian Y, Sheng ZY (2022) Organic printed photonics: from microring lasers to integrated circuits. Sci Adv 1:e1500257. https://doi.org/10.1126/sciadv.1500257

79. Yap BK, Xia R, Campoy-Quiles M, Stavrinou PN, Bradley DDC (2008) Simultaneous optimization of charge-carrier mobility and optical gain in semiconducting polymer films. Nat Mater 7:376–380. https://doi.org/10.1038/nmat2165

80. Tsiminis G, Wang Y, Kanibolotsky AL, Inigo AR, Skabara PJ, Samuel IDW, Turnbull GA (2013) Nanoimprinted organic semiconductor laser pumped by a light-emitting diode. Adv Mater 25:2826–2830. https://doi.org/10.1002/adma.201205096

81. Zhang W, Yao J, Zhao YS (2016) Organic micro/nanoscale lasers. Acc Chem Res 49:1691–1700. https://doi.org/10.1021/acs.accounts.6b00209

82. Yu H, Bao Z, Oh JH (2013) High-performance phototransistors based on single-crystalline n-channel organic nanowires and photogenerated charge-carrier behaviors. Adv Func Mater 23:629–639. https://doi.org/10.1002/adfm.201201848

83. Wei GQ, Wang XD, Liao LS (2019) Recent advances in 1D organic solid-state lasers. Adv Funct Mater 29

84. Hide F, Diaz-Garcia MA, Schwartz BJ, Andersson MR, Pei Q, Hegger AJ (1996) Semiconducting polymers: a new class of solid-state laser materials. Science 273(1979):1833–1836. https://doi.org/10.1126/science.273.5283.1833

85. Wang K, Zhao YS (2021) Pursuing electrically pumped lasing with organic semiconductors. Chem 7:3221–3231. https://doi.org/10.1016/j.chempr.2022.03

86. Sandanayaka ASD, Matsushima T, Bencheikh F, Terakawa S, Potscavage WJ, Qin C, Fujihara T, Goushi K, Ribierre JC, Adachi C (2019) Indication of current-injection lasing from an organic semiconductor. Appl Phys Express 12. https://doi.org/10.7567/1882-0786/ab1b90

87. Schön JH, Ch K, Dodabalapur A, Batlogg B (2000) An organic solid state injection laser. Science 289(1979):599–601. https://doi.org/10.1126/science.289.5479.599

88. Baldo MA, Holmes RJ, Forrest SR (2002) Prospects for electrically pumped organic lasers. Phys Rev B Condens Matter Mater Phys 66:353211–3532116. https://doi.org/10.1103/PhysRevB.66.035321

89. Tessler N, Pinner DJ, Cleave V, Ho PKH, Friend RH, Yahioglu G, le Barny P, Gray J, de Souza M, Rumbles G (2000) Properties of light emitting organic materials within the context of future electrically pumped lasers. Synth Metals 115:57–62. https://doi.org/10.1016/S0379-6779(00)00301-5

90. Herrnsdorf J, Wang Y, Mckendry JJD, Gong Z, Massoubre D, Guilhabert B, Tsiminis G, Turnbull GA, Samuel IDW, Laurand N, Gu E, Dawson MD (2013) Micro-LED pumped polymer laser: a discussion of future pump sources for organic lasers. Laser Photonics Rev 7:1065–1078. https://doi.org/10.1002/lpor.201300110

91. Riedl T, Rabe T, Johannes HH, Kowalsky W, Wang J, Weimann T, Hinze P, Nehls B, Farrell T, Scherf U (2006) Tunable organic thin-film laser pumped by an inorganic violet diode laser. Appl Phys Lett 88. https://doi.org/10.1063/1.2211947

92. Sakata H, Takeuchi H (2008) Diode-pumped polymeric dye lasers operating at a pump power level of 10 mW. Appl Phys Lett 92. https://doi.org/10.1063/1.2900628

93. Vasdekis AE, Tsiminis G, Ribierre J, Krauss TF, Turnbull GA, W Samuel ID, Díaz-García A, Schwartz BJ, Andersson MR, Pei Q, Heeger AJ (2002) Diode pumped distributed Bragg reflector lasers based on a dye-to-polymer energy transfer blend. Optics

94. Tsiminis G, Wang Y, Shaw PE, Kanibolotsky AL, Perepichka IF, Dawson MD, Skabara PJ, Turnbull GA, Samuel IDW (2009) Low-threshold organic laser based on an oligofluorene truxene with low optical losses. Appl Phys Lett 94. https://doi.org/10.1063/1.3152782

95. Tsiminis G, Ruseckas A, Samuel IDW, Turnbull GA (2009) A two-photon pumped polyfluorene laser. Appl Phys Lett 94. https://doi.org/10.1063/1.3149827

96. Spehr T, Siebert A, Fuhrmann-Lieker T, Salbeck J, Rabe T, Riedl T, Johannes HH, Kowalsky W, Wang J, Weimann T, Hinze P (2005) Organic solid-state ultraviolet-laser based on spiro-terphenyl. Appl Phys Lett 87:1–3. https://doi.org/10.1063/1.2105996

97. del Carro P, Camposeo A, Stabile R, Mele E, Persano L, Cingolani R, Pisignano D (2006) Near-infrared imprinted distributed feedback lasers. Appl Phys Lett 89. https://doi.org/10.1063/1.2387974

98. Yuyama S, Nakajima T, Yamashita K, Oe K (2008) Solid state organic laser emission at 970 nm from dye-doped fluorinated-polyimide planar waveguides. Appl Phys Lett 93. https://doi.org/10.1063/1.2959729

99. Casalboni M, de Matteis F, Merlo V, Prosposito P, Russo R, Schutzmann S (2003) 1.3 µm light amplification in dye-doped hybrid sol-gel channel waveguides. Appl Phys Lett 83:416–418. https://doi.org/10.1063/1.1593227

100. Schütte B, Gothe H, Hintschich SI, Sudzius M, Fröb H, Lyssenko VG, Leo K (2008) Continuously tunable laser emission from a wedge-shaped organic microcavity. Appl Phys Lett 92. https://doi.org/10.1063/1.2913047

101. Mhibik O, Leang T, Siove A, Forget S, Chénais S (2013) Broadly tunable (440–670 nm) solid-state organic laser with disposable capsules. Appl Phys Lett 102. https://doi.org/10.1063/1.4790294

102. Schneider D, Rabe T, Riedl T, Dobbertin T, Kröger M, Becker E, Johannes HH, Kowalsky W, Weimann T, Wang J, Hinze P (2004) Ultrawide tuning range in doped organic solid-state lasers. Appl Phys Lett 85:1886–1888. https://doi.org/10.1063/1.1791742

103. Görrn P, Lehnhardt M, Kowalsky W, Riedl T, Wagner S (2011) Elastically tunable self-organized organic lasers. Adv Mater 23:869–872. https://doi.org/10.1002/adma.201003108

104. Klinkhammer S, Woggon T, Geyer U, Vannahme C, Dehm S, Mappes T, Lemmer U (2009) A continuously tunable low-threshold organic semiconductor distributed feedback laser fabricated by rotating shadow mask evaporation. Appl Phys B: Lasers Opt 97:787–791. https://doi.org/10.1007/s00340-009-3789-0

105. Stroisch M, Woggon T, Teiwes-Morin C, Klinkhammer S, Forberich K, Gombert A, Gerken M, Lemmer U (2010) Intermediate high index layer for laser mode tuning in organic semiconductor lasers. Opt Express

106. Turnbull GA, Andrew P, Barnes WL, Samuel IDW (2003) Operating characteristics of a semiconducting polymer laser pumped by a microchip laser. Appl Phys Lett 82:313–315. https://doi.org/10.1063/1.1536249

107. Heliotis G, Xia R, Turnbull GA, Andrew P, Barnes WL, Samuel IDW, Bradley DDC (2004) Emission characteristics and performance comparison of polyfluorene lasers with one- and two-dimensional distributed feedback. Adv Func Mater 14:91–97. https://doi.org/10.1002/adfm.200305504

108. Rabbani-Haghighi H, Forget S, Siove A, Chénais S (2011) Analytical study of vertical external-cavity surface-emitting organic lasers. EPJ Appl Phys 56:34108-p1–34108-p7. https://doi.org/10.1051/epjap/2011110123

109. Riechel S, Kallinger C, Lemmer U, Feldmann J, Gombert A, Wittwer V, Scherf U (2000) A nearly diffraction limited surface emitting conjugated polymer laser utilizing a two-dimensional photonic band structure. Appl Phys Lett 77:2310–2312. https://doi.org/10.1063/1.1310207

110. Heliotis G, Xia R, Bradley DDC, Turnbull GA, Samuel IDW, Andrew P, Barnes WL (2004) Two-dimensional distributed feedback lasers using a broadband, red polyfluorene gain medium. J Appl Phys 96:6959–6965. https://doi.org/10.1063/1.1811374
111. Guilhabert B, Laurand N, Herrnsdorf J, Chen Y, Mackintosh AR, Kanibolotsky AL, Gu E, Skabara PJ, Pethrick RA, Dawson MD (2010) Amplified spontaneous emission in free-standing membranes incorporating star-shaped monodisperse π-conjugated truxene oligomers. J Opt 12:035503. https://doi.org/10.1088/2040-8978/12/3/035503

Chapter 7
Organic Electrochemical Transistor

7.1 Device Structure of OECT

Organic thin-film transistors (OTFTs) can generally be classified into two types: organic field effect transistors (OFET) and organic electrochemical transistors (OECT). Although both types of devices have been demonstrated for circuit and sensor applications [1–4], their research priorities are very different. The OFETs are promising for applications in the field of low-cost electronic circuits, such as flexible displays and radio frequency identification (RFID) tags [5, 6], while the development of OECT devices is mainly focused for sensing applications because the very low-performance voltage and ion-involved working process [7].

OFET is formed from an organic semiconductor film, dielectrics layer, and three electrodes (source, drain, and gate) (Fig. 7.1a). The charge density at the interface between the semiconductor and dielectrics is modulated by the field generated with applied gate voltage, and consequently, the current flowing between the source and drain electrodes is controlled. For most sensing applications, the semiconductor layers are exposed to the target analytes, where the channel current changes by charge doping or trapping due to the analytes. In an OECT, the dielectrics layer is replaced with a liquid or solid electrolyte (Fig. 7.1b). In this case, the distance between the gate electrode and semiconductor channel is flexible and can be up to few centimeters. The channel current can be modulated by many factors, like electrochemically doing or de-doping the semiconductor from the electrolyte, molecular conformation changes in semiconductor, etc. The analytes are contained in the electrolytes for most OECT-based sensors; the current change is induced by the interaction between the analytes and semiconductor or gate electrode.
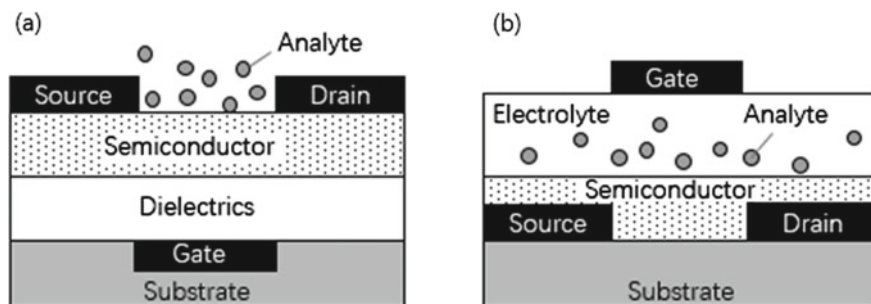
Fig. 7.1 Schematic illustration of OFET (**a**) and OECT (**b**) device structures for sensing applications

7.2 Working Principle of OECT Devices

The first OECT was reported by Wrighton et al. [8] in 1984. Their devices were made with three gold electrodes covered with polypyrrole active layer, and a transistor performance was observed when the device was measured in aqueous electrolyte of $CH_3CN/0.1$ M [n-Bu$_4$N]ClO$_4$ (Fig. 7.2).

When a negative gate voltage was applied, the conductance of polypyrrole was low and the transistor was in "off" state. If the applied gate voltage was positive, the polypyrrole was oxidized and the channel current was increased which turned the device to the "on" state. Compared with OFET devices, OECTs can stably perform in aqueous environment with very low working voltage (less than 1 V). Such devices are suitable for various sensing applications, especially for in situ measurement in biological systems owing to the bio-compatibility of the devices. A device model has been proposed by Bernards et al. [9, 10], and the device current I_{DS} is expressed as:

$$I_{DS} = \frac{q\mu p_0 t W}{LV_p}\left(V_p - V_g^{eff} + \frac{V_{DS}}{2}\right)V_{DS}\left(|V_{DS}| \ll |V_p - V_g^{eff}|\right)$$

$$V_p = qp_0t/c_i$$

$$V_g^{eff} = V_G + V_{offset} \tag{7.1}$$

where q, μ, p_0 are the electronic charge, charge mobility, initial charge density in semiconductor with zero gate voltage, respectively; W and L are device channel width and length; t and c_i are the thickness of the active layer and effective gate capacitance of the device; V_p and V_g^{eff} are the pinch-off voltage and effective gate voltage; V_{offset} is the offset voltage related to the potential drop at the interfaces of gate/electrolyte and electrolyte/channel.

Presently, a commonly used active material for OECD development is poly(styrenesulfonate) (PSS)-doped poly(3,4-ethylenedioxythiophene) (PEDOT). Figure 7.3 illustrates the working process of the OECT made with PEDOT:PSS active
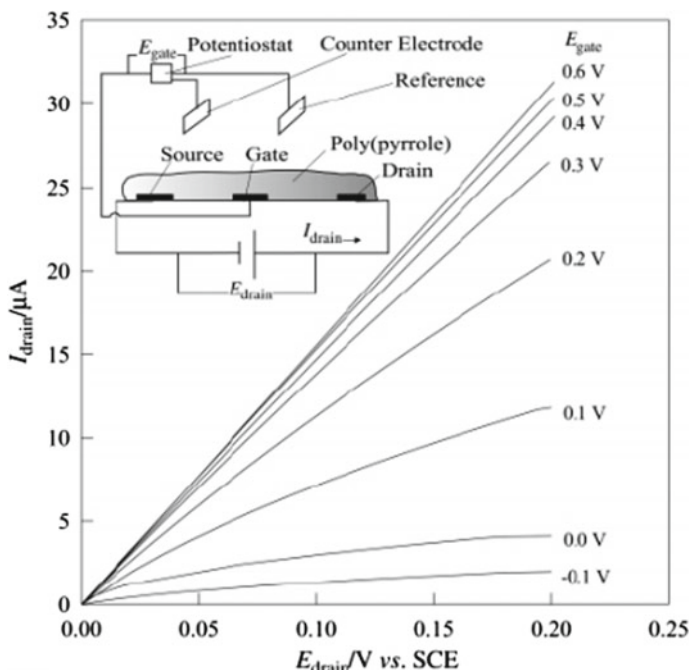
Fig. 7.2 Output curves of device measured in the aqueous electrolyte of $CH_3CN/0.1$ M [n-$Bu_4N]ClO_4$. Inset illustrates the device structure. (Adapted from Ref. [8])

layer and NaCl aqueous solution as electrolyte. The source and drain electrodes are bridged with PEDOT:PSS film and submerged in the electrolyte. If only the source–drain electrodes are biased (no gate voltage is applied), the PEDOT:PSS remains its original high conductance condition as the negatively charged PSS can balance the positive charges in the PEDOT which maintains a high level of hole density of the PEDOT (Fig. 7.3a). When the gate electrode is biased positively, positive ions in the electrolyte move to the active layer and migrate into the polymer network. The positively charged ions will partially neutralize the negative charge of the PSS and consequently reduce the hole density of PEDOT (de-doping); i.e., the positive gate bias turns the OECT device from "on" to "off" state (Fig. 7.3b). Figure 7.4 shows typical performance characteristics of PEDOT:PSS-based OECT device [4]. The device worked in depletion model, i.e., the drain current decreased with the increase of gate voltage applied. In many sensor applications, the devices convert a modulation of the gate voltage ΔV_G to a modulation of the drain current ΔI_D. The figure-of-merit that determines this conversion is the transconductance, defined as $g_m = \Delta I_D/\Delta V_G$. The transconductance is the main parameter of the OECT that governs signal amplification. For sensing applications, the gate electrode should be biased to the value around the maximum transconductance.
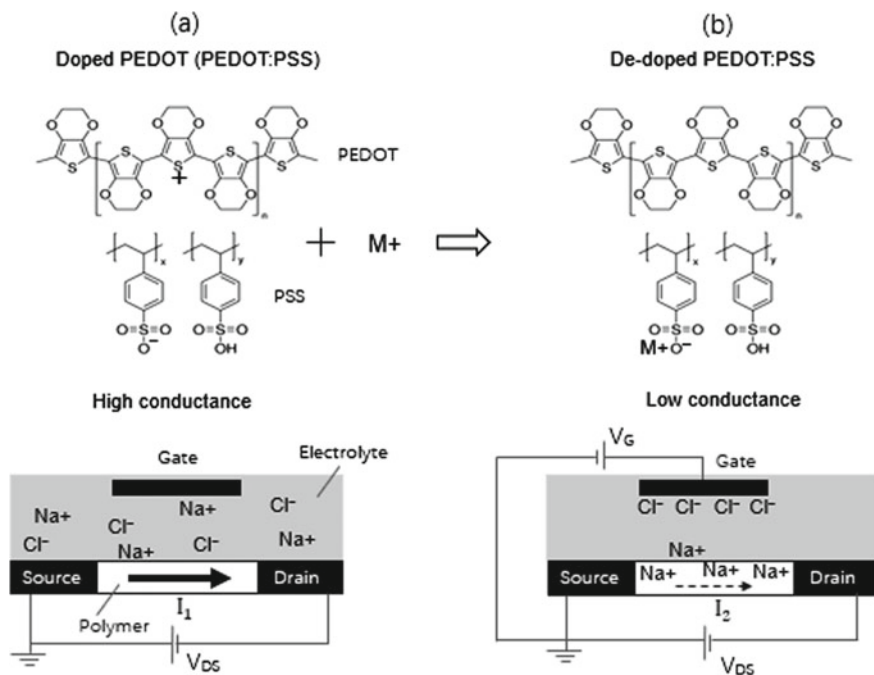
Fig. 7.3 Schematic illustration of working principle of an OECT device made with PEDOT:PSS polymer as active layer and NaCl aqueous solution as electrolyte
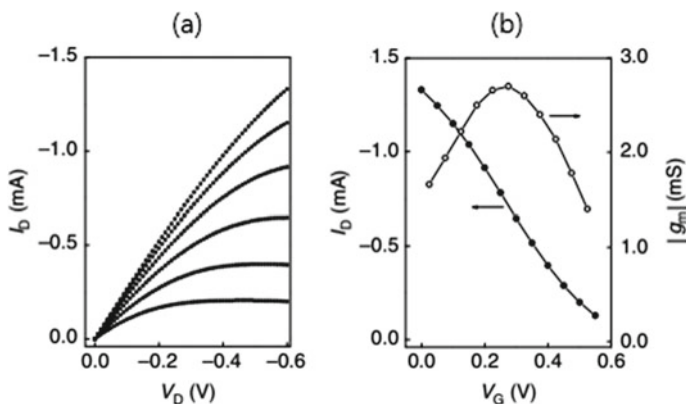
Fig. 7.4 Typical characteristics of PEDOT:PSS-based OECT measured in 0.1 M NaCl aqueous solution with Ag/AgCl wire as gate electrode. **a** Output characteristics for V_G varying from 0 (top curve) to +0.5 V (bottom curve). **b** Transfer curve for $V_D = -0.6$ V, and associated transconductance. (Adapted from Ref. [4])

Presently, sensor applications are the main research focus of the OECT devices. Normally, a sensor based on OECT operates use the principle of changing the potential drop across one of the two interfaces by the effect of analyte: gate/electrolyte and electrolyte/channel [10–13]. Other factors, like change of capacitance c_i, analyte-induced conformation change of semiconducting molecules, etc., may have effects on the device performance.

7.3 Functionalization of OECT Devices

A transistor-based sensor is the combination of a sensor and an amplifier since a small potential change at an interface can induce a substantial variation of the channel current. Therefore, such devices are highly sensitive. The OECT can be easily miniaturized and fabricated on thin flexible substrates, which is essential for some applications in living systems. The gate voltage (V_G) applied on the transistor is dropped on the two interfaces, including the electric double layers (EDL) of electrolyte/gate and electrolyte/channel (Fig. 7.5a). The modification of gate electrode, device channel, and electrolyte could alter the potential distribution and induces a current change of the device. For instance, a higher cation concentration of electrolyte can move the transfer curve horizontally to lower gate voltage for PEDOT:PSS-based OECT as schematically shown in Fig. 7.5b [11]. This can be understood as that when the cation concentration is increased a lower gate voltage is required to achieve the same de-doping level of the channel. Many OECT sensors have similar shift of transfer curve caused by analytes, although the detailed sensing mechanisms might be different.

Typical OECT consists of three components including device channel, electrolyte, and gate electrode. The device functionalization can apply to all these parts for sensing development [14].
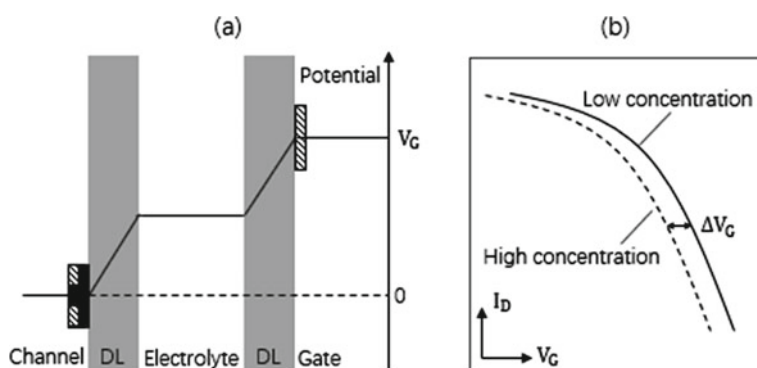
Fig. 7.5 Schematic illustration of potential drops in the two double layers (DL, shadow area) (**a**) and schematical illustration of transfer curve shift induced by variation of cation concentration in the electrolyte of PEDOT:PSS-based OECT (**b**)

(1) **Channel Functionalization**

Functionalization of OECT device channel material or channel surface would lead to a device response to specific analytes when an interaction between the analyte and the channel occurs. Various strategies on engineering of channel/electrolyte interface were applied. For instance, chemical immobilization on the surface of semiconducting layer was applied for bacteria detection [15]. The electrostatic interaction between the bacteria and active layer of the device induced a change of the effective gate voltage that shifted the transfer curve.

(2) **Electrolyte Functionalization**

The formation process and property of the two EDLs are closely related to the properties of the electrolyte. The introduction of various species into the electrolyte (ions, molecules, catalyzers, enzymes, etc.) has great influence on the device properties. Electrolyte functionalization has been used for biosensor development. For instance, bioactive mediators could be incorporated into electrolytes to enhance the capability for specific detections. OECT-based lactate sensor was first realized by incorporating lactate oxidase enzyme into solid-state electrolytes [16].

(3) **Gate Functionalization**

Because the gate is isolated from the channel region in an OECTs, the surface modification on the gate will not influence channel property. A small modification of the gate surface property can result in an obvious change of channel current. Various methods of gate functionalization were reported, such as gate modification for capturing charged molecules, for immobilization of electrochemically active biomolecules, biorecognition elements, etc. The immobilized biomolecules on the gate can selectively capture analyte molecules and consequently influence the electrostatic potential on the gate surface [13]. Antibody can be immobilized on the gate surface to specifically recognize antigen [17].

7.4 Sensor Applications

7.4.1 Ion and pH Sensors

Since the OECTs are a type of transducers that can transfer ion signal to electrical signal, they must be primarily sensitive to ions. Various strategies were adopted to develop ion and pH sensors.

Wrighton et al. [18] reported an polyaniline-based OECT that could be used for sensing redox reagents, such as $Ru(NH_3)_6^{3+/2+}$ and $Fe(CN)_6^{3-/4-}$. The devices were also used for pH sensing. Later, they demonstrated devices based on platinized poly(3-methylthiophene) to sense H_2 and O_2 in aqueous electrolyte [19]. The device current change with addition of analytes was caused by the redox reaction of the polymer through the oxidation of O_2 gas and reduction of H_2 gas catalyzed with

the Pt particles deposited on the poly(3-methylthiophene) active layer. The redox process is sensitive to pH value of the electrolytes; therefrom, they demonstrated a detection of pH with such device at fixed O_2 supplied. Scheiblin et al. [20] reported OECT-based pH sensing through deposition of iridium oxide onto gate electrode. The hydroxyl groups formed on the iridium oxide can capture or release the H^+ which induces an electrical potential change between the oxide and the gate electrode. This causes a change of channel current of the devices.

Dabke et al. [21] reported OECT sensors with polyaniline as active layer to detect metal ions, like K^+, Na^+, Ba^{2+}, Sr^{2+}, Ca^{2+}. The sensing mechanism was attributed to the creation of conformational defects in the polymer. Mousavi et al. [22] reported selective sensing of K^+, Ca^{2+}, Ag^+ with PEDOT:PSS-based OECT through doping/de-doping mechanism. The selectivity was achieved through coating a layer of polymeric membrane with ion-selective ionophores on the top of PEDOT:PSS. Bernards et al. [23] demonstrated OECT sensors with PEDOT:PSS active layer integrated with a bilayer lipid membrane (BLM). They incorporated gramicidin ion channels into the BLMs for selective sensing, and the device could distinguish between solutions containing monovalent and divalent cations.

7.4.2   Humidity Sensors

Chao et al. [24] reported a humidity sensor with polyaniline-based OECT, where poly(vinyl alcohol)/phosphoric-acid acted as solid-state electrolyte. The device can sense humidity level from 0 to 100% which was likely caused by the humidity dependence of the ionic conductivity of the electrolyte. OECT humidity sensors were demonstrated by Nilsson et al. [25] where PEDOT:PSS was used as active layer and electrodes, while proton conductive material was used as solid-state electrolyte. In this work, the PEDOT:PSS electrodes and active channel were patterned on a substrate, and then the solid-state electrolyte layer was defined to cover the area of the device channel and the gate. The ionic conductivity of the electrolyte changed when the device was exposed to various humidity. This caused various reduction level of the PEDOT:PSS channel when positive bias was applied to the gate electrode.

7.4.3   Biosensors

Among all demonstrated OECT-based sensors, the biosensors are the most active research area. The developed devices can sense bio-species at various levels, like biomolecules, cells, and tissues.

7.4.3.1 Glucose Sensors

OECT glucose sensor was first demonstrated with polyaniline as active layer in which glucose oxidase (GOx) was immobilized [26]. The detection limit of the device was about 2 mM of glucose concentration. As the conductivity of polyaniline depends on the pH value of the electrolyte, the sensing mechanism is the change of pH value around the active layer resulted from the enzyme-catalyzed reaction of glucose. Bartlett et al. [27] demonstrated glucose sensors with polyaniline OECTs. In their work, GOx was immobilized in a poly(1,2-diaminobenzene) film covered on polyaniline film and tetrathiafulvalene was used as redox mediator. The mechanism of sensing was attributed to the change of the oxidization state of the active material from lower conductive state to higher conductive state. Malliaras et al. developed glucose sensors based on OECT, where PEDOT:PSS was used as the active channel and Pt as gate electrode [28, 29]. The introduction of glucose in to the GOx contained electrolyte (PBS) led the device current decrease under positive gate voltage. The device was able to detect glucose down to μM concentration which is in the range of the glucose levels in human saliva. The sensing mechanism of the glucose sensors can be explained with the generation of H_2O_2 by the reaction of glucose catalyzed by GOx. Investigation of such devices showed that the transfer curve (I_D–V_G) of the device shifted horizontally to lower gate voltage [10]. This was explained with the Faradic current (i.e., the current induced by redox reaction at electrode) at the Pt gate electrode generated by the reaction of H_2O_2.

$$H_2O_2 \rightarrow 2H^+ + O_2 + 2e^-$$
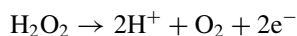
The potential drop at the electrolyte/gate interface decreases with the increase of the glucose concentration due to the increased Faradic current. As the applied gate voltage was mainly dropped at the interfaces of electrolyte/gate (V_{EG}) and electrolyte/channel (V_{EC}), the reduction of V_{EG} increases the V_{EC}, and consequently, the drain current was reduced.

7.4.3.2 Antibody–Antigen Sensors

As an antibody can specifically recognize an antigen, such biological characteristics can be applied for developing sensors with high specificity. Kanungo et al. [30] reported an immunosensor based on OECT through bio-specific binding of antibody–antigen. They immobilized goat antirabbit IgG in PEDOT:PSS polymer matrix for detection of antigen rabbit IgG with various concentrations in PBS solution. Their devices could detect the antigen down to 1×10^{-10} g/ml. The sensing mechanism was attributed to the conformation change of PEDOT caused by the formed antibody–antigen complex.

Kim et al. [31] reported an OECT immunosensor based on PEDOT:PSS for detection of prostate specific antigen/α1-antichymotrypsin (PSA–ACT) complex. The device structure is illustrated in Fig. 7.6. The PEDOT:PSS layer was treated with
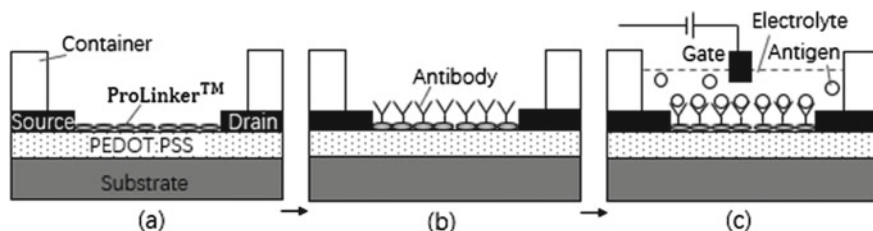
Fig. 7.6 Schematic illustration of OECT immunosensor fabrication and measurement circuit

ProLinker™ molecules (a), and then, PSA monoclonal antibody (PSA-mAb) was immobilized on the ProLinker™ (b). The detection was realized by the selective capture of PSA-ACT complex by the PSA-mAb (c). The sensing mechanism was attributed to the doping effect in the PEDOT:PSS induced by negative surface charge of PSA-ACT complex.

A useful strategy for the antibody–antigen sensor applications is nanoprobe technique. By combination of the nanoprobes and OECT, biosensors with high sensitivity and selectivity can be realized [17, 31]. Cancer biomarker analysis plays an important role in the prognosis, diagnosis, and therapy of cancers. Within numerous biomarkers, protein cancer biomarkers can be found in serum, tissue, or body fluids such as saliva and thus can be conveniently assessed even noninvasively. Yan et al. [17] demonstrated a detection process of human epidermal growth factor receptor (HER2), a key prognostic protein biomarker for the therapeutic treatment of breast cancer patients. HER2 was captured on the surface of the gate electrode by the antibody ($Ab_{capture}$) functionalized on the gate surface (Fig. 7.7). Monoclonal anti-HER2 was used as the $Ab_{capture}$. The capture of the HER2 by the $Ab_{capture}$ on the gate is sensed by electrochemical reaction catalyzed by enzyme which is linked with another type of antibody ($Ab_{detection}$) through Au nanoparticle (i.e., nanoprobe: $Ab_{detection}$-Au-HRP). The enzyme used was horseradish peroxidase (HRP), and polyclonal anti-HER2 was chosen as $Ab_{detection}$. The HER2 caught by the $Ab_{capture}$ anchors the nanoprobes through interaction with the $Ab_{detection}$. The HRP-catalyzed electrochemical reaction of H_2O_2 pre-added in the PBS electrolyte is:

$$H_2O_2 + 2e^- + 2H^+ \overset{HRP}{\Leftrightarrow} 2H_2O$$
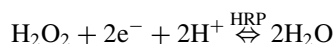
The change of the effective gate voltage V_g^{eff} of the device is proportional to $\log[W_{HRP}]$, while the amount of HRP attracted to the gate electrode W_{HRP} is proportional to the density of HER2 grabbed by the gate. Thus, the change of device current during test will reflect the concentration of HER2 contained in the analyte solution which was used to modify the gate. The gate electrode and nanoprobes were prepared separately before test (Fig. 7.7). The process started from Au electrode patterning (a). Then, mercaptoacetic acid (MAA) was applied to the electrode to form a self-assembled molecular monolayer (SAM) for binding the antibody for antigen capture (b, c). Bovine serum albumin (BSA) solution was used to block the
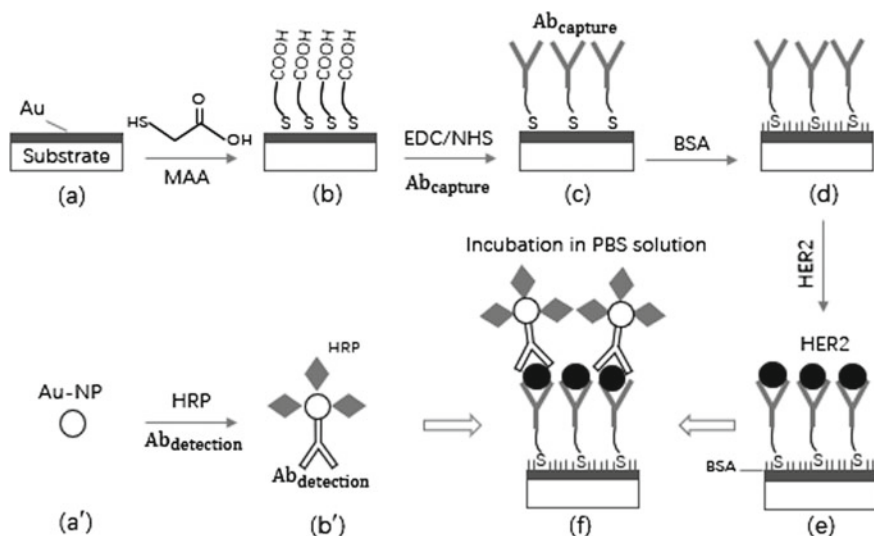
Fig. 7.7 Schematic illustration of gate modification of the proposed devices (**a–e**), nanoprobe preparation (**a′, b′**) and sensing (**f**)

remaining nonspecific binding sites of the electrode (d). Next, the analyte solution (HER2 in PBS) was incubated on the gate electrode for proper time (e). The sensing was done in PBS solution containing appropriate concentration of nanoprobes and H_2O_2 (f). The nanoprobes were prepared by adding $Ab_{detection}$ and HRP into the PBS solution containing Au nanoparticles (a′, b′).

7.4.3.3   DNA Sensors

Krishnamoorthy et al. [32] demonstrated a label-free DNA sensing device with PEDOT as the active channel. Single-strand NDA (ssDNA, probe ssDNA) with low monomeric units was immobilized during the PEDOT formation (polymerization of EDOT in the presence of probe ssDNA) to detect large complementary ssDNA. The sensor response is specific owing to complementary property of DNA double chains. The sensing mechanism was attributed to conformational changes upon duplex formation which induces a decrease in redox charge. DNA sensors based on duplex formation have also been demonstrated by gate electrode functionalization. Lin et al. [13] reported an OECT-based flexible microfluidic system for label-free detection of DNA. Target DNAs were injected into the channel for DNA hybridization with the probe ssDNA functionalized on gate electrode to form double strand NDAs (dsDNA) (Fig. 7.8). The DNA hybridization could decrease the surface potential of the gate electrode because DNA molecules have negative charges due to their low isoelectric point, and this resulted in a shift of the transfer curve of the OECT device.
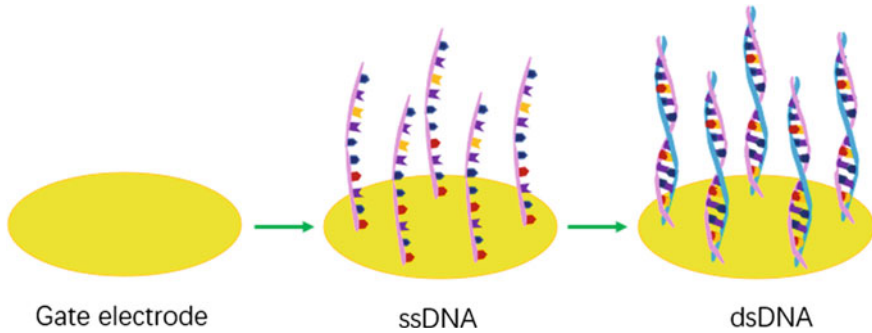
Fig. 7.8 Schematic illustration of gate functionalization with ssDNA and DNA hybridization on the gate electrode

7.4.3.4 Others

Thanks to the inherent low driving voltage and amplification capability, OECTs are highly sensitive transducers that can convert biochemical signals into electronic signals. Apart from ions [21, 22], glucose [10], DNA [13], lactate [16], bacteria [15], protein [17], dopamine [33], cells [12], the OECTs have also been successfully used for many other applications, including electrocardiographic recording [34], brain recording [7], etc. Neurons and brain networks generate small electric potentials, which are difficult to extract from noise when recorded with classical electrodes made of metals such as Ir, Pt, and Au. As OECTs capture ion fluxes, they constitute the optimal solution to measure electrophysiological signals—fluctuation of the electric field generated by the flux of ions through ion channels localized in the cell membrane. Khodagholy et al. [7] demonstrated electrophysiological signal recording on brain surface with flexible PEDOT-PSS OECT device array as recording probe. Optical image of a device channel and surface electrode is shown in Fig. 7.9a. The OECT probe was conformed on the somatosensory cortex for recording, while the surface electrode (E) was used for simultaneous recording. Recording with iridium electrode implanted in the somatosensory cortex has also performed for reference (Fig. 7.9b). The transistor was wired in a common source configuration with a grounded screw used as the gate electrode (Fig. 7.9c). Figure 7.9d shows the recording of spike-and-wave discharges (SWDs) in Genetic Absence Epilepsy Rat from Strasbourg (GAERS) [35]. The OECT device showed to outperform the surface electrode and the implanted conventional metal electrode.
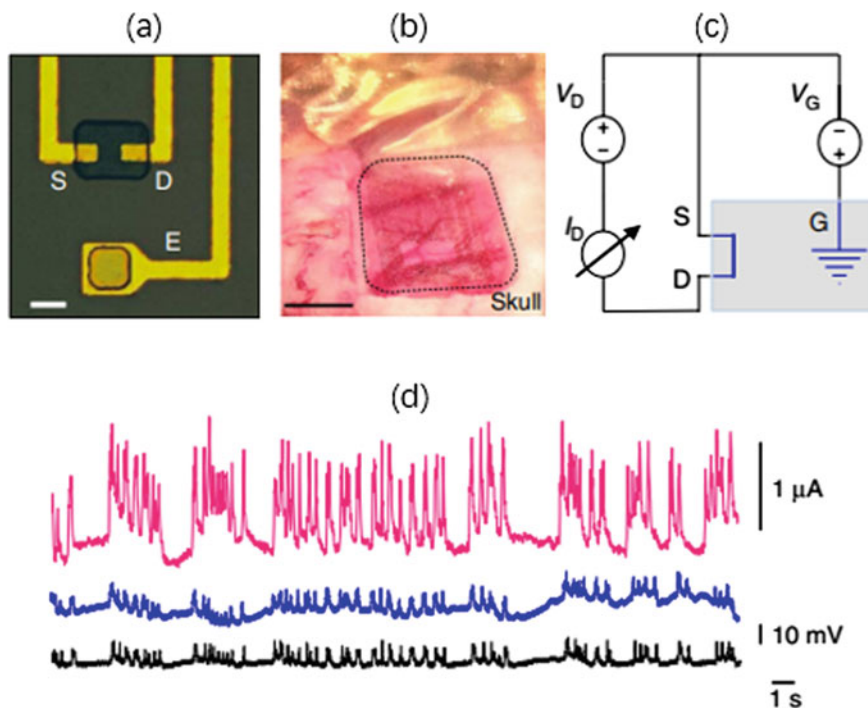
Fig. 7.9 Optical images of devices, measurement circuit, and recorded signals. **a** Optical micrograph of device channel S-D and surface electrode E. Scale bar, 10 μm. **b** Optical image of the OECT probe placed over the somatosensory cortex, with the craniotomy surrounded by dashed lines. Scale bar, 1 mm. **c** Measurement circuit used in the experiment. **d** Recorded signals from an OECT (pink), PEDOT:PSS surface electrode (blue) and Ir-penetrating electrode (black). (Adapted from Ref. [7])

References

1. Brown AR, Pomp A, Hart CM, de Leeuw DM (1995) Logic gates made from polymer transistors and their use in ring oscillators. Science 270:972–974
2. Schwartz G, Tee BCK, Mei J, Appleton AL, Kim DH, Wang H, Bao Z (2013) Flexible polymer transistors with high pressure sensitivity for application in electronic skin and health monitoring. Nat Commun 4:1859
3. van de Burgt Y, Lubberman E, Fuller EJ, Keene ST, Faria GC, Agarwal S, Marinella MJ, Talin AA, Salleo A (2017) A non-volatile organic electrochemical device as a low-voltage artificial synapse for neuromorphic computing. Nat Mater 16:414–419
4. Khodagholy D, Rivnay J, Sessolo M, Gurfinkel M, Leleux P, Jimison LH, Stavrinidou E, Herve T, Sanaur S, Owens RM, Malliaras GG (2013) High transconductance organic electrochemical transistors. Nat Commun 4:2133
5. Gelinck G, Heremans P, Nomoto K, Anthopoulos TD (2010) Organic transistors in optical displays and microelectronic applications. Adv Mater 22:3778–3798
6. Cantatore E, Geuns TCT, Gelinck GH, van Veenendaal E, Gruijthuijsen AFA, Schrijnemakers L, Drews S, de Leeuw DM (2007) A 13.56-MHz RFID system based on organic transponders. IEEE J Solid State Circuits 42:84–92

7. Khodagholy D, Doublet T, Quilichini P, Gurfinkel M, Leleux P, Ghestem A, Ismailova E, Herve T, Sanaur S, Bernard C, Malliaras GG (2013) In vivo recordings of brain activity using organic transistors. Nat Commun 10:1038

8. White HS, Kittlesen GP, Wrighton MS (1984) Chemical derivatization of an array of three gold microelectrodes with polypyrrole: fabrication of a molecule-based transistor. J Am Chem Soc 106:5375–5377

9. Bernards DA, Malliaras GG (2007) Steady-state and transient behavior of organic electrochemical transistors. Adv Funct Mater 17:3538–3544

10. Bernards DA, Macaya DJ, Nikolou M, DeFranco JA, Takamatsu S, Malliaras GG (2008) Enzymatic sensing with organic electrochemical transistors. J Mater Chem 18:116–120

11. Lin P, Yan F, Chan HLW (2010) Ion-sensitive properties of organic electrochemical transistors. ACS Appl Mater Interfaces 2:1637–1641

12. Lin P, Yan F, Yu JJ, Chan HLW, Yang M (2010) The application of organic electrochemical transistors in cell-based biosensors. Adv Mater 22:3655–3660

13. Lin P, Luo X, Hsing IM, Yan F (2011) Organic electrochemical transistors integrated in flexible microfluidic systems and used for label-free DNA sensing. Adv Mater 23:4035–4040

14. Wang N, Yang A, Fu Y, Li Y, Yan F (2019) Functional organic thin film transistors for biosensing. Acc Chem Res 52:277–287

15. He RX, Zhang M, Tan F, Leung PHM, Zhao XZ, Chan HLW, Yang M, Yan F (2012) Detection of bacteria with organic electrochemical transistors. J Mater Chem 22:22072–22076

16. Khodagholy D, Curto VF, Fraser KJ, Gurfinkel M, Byrne R, Diamond D, Malliaras GG, Benito-Lopez F, Owens RM (2012) Organic electrochemical transistor incorporating an ionogel as a solid-state electrolyte for lactate sensing. J Mater Chem 22:4440–4443

17. Fu Y, Wang N, Yang A, Law H, Li L, Yan F (2017) Highly sensitive detection of protein biomarkers with organic electrochemical transistors. Adv Mater 29:1703787

18. Paul EW, Ricco AJ, Wrighton MS (1985) Resistance of polyaniline films as a function of electrochemical potential and the fabrication of polyaniline-based microelectronic devices. J Phys Chem 89:1441–1447

19. Thackeray JW, Wrighton MS (1986) Chemically responsive microelectrochemical devices based on platinized poly(3-methylthiophene): Variation in conductivity with variation in hydrogen, oxygen, or pH in aqueous solution. J Phys Chem 90:6674–6679

20. Scheiblin G, Coppard R, Owens RM, Mailley P, Malliaras GG (2017) Referenceless pH sensor using organic electrochemical transistors. Adv Mater Technol 2:1600141

21. Dabke RB, Singh GD, Dhanabalan A, Lal R, Contractor AQ (1997) An ion-activated molecular electronic device. Anal Chem 69:724–727

22. Mousavi Z, Ekholm A, Bobacka J, Ivaska A (2009) Ion-selective organic electrochemical junction transistors based on poly(3,4-ethylenedioxythiophene) doped with poly(styrene sulfonate). Electroanalysis 21:472–479

23. Bernards DA, Malliaras GG, Toombes GES, Gruner SM (2006) Gating of an organic transistor through a bilayer lipid membrane with ion channels. Appl Phys Lett 89:053505

24. Chao SH, Wrighton MS (1987) Characterization of a "solid-state" polyaniline based transistor: water vapor dependent characteristics of a device employing a poly(vinyl alcohol)/phosphoric acid solid-state electrolyte. J Am Chem Soc 109:6627–6631

25. Nilsson D, Kugler T, Svensson PO, Berggren M (2002) An all-organic sensor transistor based on a novel electrochemical transducer concept printed electrochemical sensors on paper. Sens Actuators B Chem 86:193–197

26. Hoa DT, Kumar TNS, Punekar NS, Srinivasa RS, Lal R, Contractor AQ (1992) Biosensor based on conducting polymers. Anal Chem 64:2645–2646

27. Bartlett PN, Birkin PR (1993) Enzyme switch responsive to glucose. Anal Chem 65:1118–1119

28. Zhu ZT, Mabeck JT, Zhu CC, Cady NC, Batt CA, Malliaras GG (2004) A simple poly(3,4-ethylene dioxythiophene)/poly(styrene sulfonic acid) transistor for glucose sensing at neutral pH. Chem Commun 1556–1557

29. Macaya DJ, Nikolou M, Takamatsu S, Mabeck JT, Owens RM, Malliaras GG (2007) Simple glucose sensors with micromolar sensitivity based on organic electrochemical transistors. Sens Actuators B Chem 123:374–378

30. Kanungo M, Srivastava DN, Kumar A, Contractor AQ (2002) Conductimetric immunosensor based on poly(3,4-ethylenedioxythiophene). Chem Commun 680–681
31. Kim DJ, Lee NE, Park JS, Park IJ, Kim JG, Cho HJ (2010) Organic electrochemical transistor based immunosensor for prostate specific antigen (PSA) detection using gold nanoparticles for signal amplification. Biosens Bioelectron 25:2477–2482
32. Krishnamoorthy K, Gokhale RS, Contractor AQ, Kumar A (2004) Novel labelfree DNA sensors based on poly(3,4-ethylenedioxythiophene). Chem Commun 820–821
33. Tang H, Lin P, Chan HL, Yan F (2011) Highly sensitive dopamine biosensors based on organic electrochemical transistors. Biosens Bioelectron 26:4559–4563
34. Campana A, Cramer T, Simon DT, Berggren M, Biscarini F (2014) Electrocardiographic recording with conformable organic electrochemical transistor fabricated on resorbable bio-scaffold. Adv Mater 26:3874–3878
35. Danober L, Deransart C, Depaulis A, Vergnes M, Marescaux C (1998) Pathophysiological mechanisms of genetic absence epilepsy in the rat. Prog Neurobiol 55:27–57

Chapter 8
Organic Photocatalysts for Water Splitting

This chapter will discuss organic semiconductors for the application of water splitting. The use of fossil fuels in energy generation and propulsion has resulted in the emission of large amounts of carbon dioxide [1], which has caused an increase of earth's surface and air temperature. The conversion of wind, solar, and other renewable energy sources is expected to deliver most of the useful electric energy in the future [2]. However, a major problem with electric energy is its storage, which might be an obstacle for its mass use [3]. Hydrogen has been identified as a possible storable fuel that could overcome these limitations. Solar water splitting offers a potential avenue for the production of clean and storable energy in the form of hydrogen. Organic semiconductors can be used as photocatalysts that enable the simultaneous production of hydrogen and oxygen from water through photoelectrochemical and photochemical processes [4]. This chapter summarizes developments in the field of organic photocatalysts and presents the state of the art in terms of their overall water splitting performance and highlight their potential for future large-scale applications.

8.1 A Brief Introduction of Organic Photocatalysts for Water Splitting

Since the pioneering work on photoelectrochemical water splitting for H_2 evolution over TiO_2 by Fujishima and Honda in 1972 [5], extensive inorganic semiconductor photocatalysts have been exploited, with a particular focus on the d^0 (e.g., Ta^{5+}, Ti^{4+}, Zr^{4+}, Nb^{5+}, Ta^{5+}, W^{6+} and Mo^{6+}) and d^{10} (e.g., In^{3+} and Sn^{4+}, Ga^{3+}, Ge^{4+}, Sb^{5+}) metal-based oxides, sulfides, and nitrides [6]. However, these inorganic photocatalysts exhibited wide bandgap (>3.0 eV), poor solar light utilization (most of them can only absorb UV light), which restrict their solar energy conversion efficiency [7, 8]. Therefore, it is highly desired to introduce earth-abundant materials with optimized compositions, morphologies and optical properties to satisfy the requirements of photocatalytic water splitting with high efficiency.

Organic semiconductor-based photocatalysts have attracted numerous attention due to their tunable structure and properties, low cost, and excellent photo/thermostability. Inorganic photocatalysts are mostly inactive for the hydrogen evolution when the photon wavelengths are around the range of visible light (550–700 nm), while organic photocatalysts have a potential to reach the photons from upper wavelength theoretically. The variation of the geometries, side chain groups, and linking sites of organic materials can derive diverse conjugated polymers, offering great flexibility in the design of the skeletons and porosity for efficient water splitting [9]. Additionally, the tautomerism (e.g., keto-enol) of those conjugated structures endows great diversity to the structure of the conjugated polymers [10]. Thus, their physicochemical properties can be precisely manipulated at the molecular level. Some organic photocatalysts showed remarkable activities for H_2 evolution that is comparable to the inorganic counterparts. In addition, it was theoretically demonstrated that a tandem structure of light-absorbing materials with band gaps in the range of 1.6–1.8 eV would be able to achieve a solar-to-hydrogen (STH) efficiency at >25% when optimum device design related requirements are full-filled [11]. From the materials perspective, conjugated polymers for photocatalysis form a new class of highly porous organic polymers with 2D or 3D network topologies [12, 13].

Historically, the first attempt of using an organic material for water splitting can be dated back to 1985. Yanagida et al. [14] demonstrated linear poly(p-phenylene)s for H_2 evolution under UV-light irradiation ($\lambda > 366$ nm). This discovery suggested a new concept of photocatalysts for H_2 evolution apart from well-known inorganic photocatalysts. However, the structural instabilities under photocatalytic conditions limited the development of organic materials for H_2 evolution at that time. In addition, their poor quantum yield of hydrogen (<0.05%) also suppressed the continuing research interest in organic photocatalysis. There was limited progress on photocatalytic performance until one of the breakthroughs occurred from the report of graphitic carbon nitride (g-C_3N_4) in 2009 [15]. The g-C_3N_4 is highly robust in any pH of the solution. However, the pristine bulk g-C_3N_4 is still unable to fulfill the water splitting process, because it suffers from the low surface area, limited visible light absorption, and poor charge separation/mobility. It is of great significance to design and synthesize more efficient organic conjugated photocatalysts with high activity. Thus, many different kinds of organic photocatalyst materials have been witnessed during the past few years. Carbon sub-nitrides such as (C_2N, C_3N), graphene oxide (GO), microporous polymers networks (MPN), conjugated organic frameworks (COF), conjugated triazine framework (CTF), conjugated microporous polymers (CMPs), silicate conjugate frameworks (SiCOF), and conjugated phosphinine frameworks (CPF), for example, are few notable polymeric photocatalysts [16–24].

Following the introduction, the mechanism of photocatalytic water splitting is discussed. After this, a discussion has been made on material development of organic photocatalysis. We have also mentioned the strategy for overcoming the limitation of a water splitting system. At the end of this chapter, the conclusion and perspectives are discussed.

8.2 Mechanism of Organic Photocatalytic Water Splitting

For the application of photocatalytic water splitting on a large scale, solar-to-hydrogen efficiencies of approximately 10% have been suggested for requirement. This means that 10% of the solar incident light energy that reaches the catalyst surface is used to convert water into hydrogen gas [25]. At present, the current state-of-the-art organic systems are not close to achieving this efficiency, meaning that further effort should be paid on organic semiconductors for water splitting [4].

The direct water splitting process ($H_2O \rightarrow H_2 + 0.5O_2$) is a thermodynamically uphill reaction with a positive Gibbs free energy of 237 kJ mol^{-1}, which corresponds to a minimum energy barrier of 1.23 V to break the water molecule into H_2 and O_2 [26]. Figure 8.1a shows a schematic diagram of water splitting into H_2 and O_2 over photocatalysts. Photocatalysis on semiconductor particles involves three main steps: (i) absorption of photons, (ii) with energies exceeding the semiconductor bandgap, (iii) leading to the generation of electron (e^-) and hole (h^+) pairs and charge separation followed by migration of these photogenerated carriers to active sites; and (iv) surface chemical reactions between these carriers with various compounds (e.g., H_2O); electrons and holes may also recombine with each other without participating in any chemical reactions [27]. When a photocatalyst is used for water splitting, the LUMO level must be more negative than the reduction potential of water to produce H_2, and the HOMO level must be more positive than the oxidation potential of water to produce O_2, as shown in Fig. 8.1b. In other words, the LUMO and HOMO values must be higher and lower than 0 and +1.23 V (vs normal hydrogen electrode (NHE), pH = 0), respectively. In practice, the inevitable energy loss associated with the electron transfer process often requires a bandgap larger than 1.8 eV for photocatalytic water splitting. Moreover, in order to achieve reasonable solar energy conversion efficiency, the bandgap is suggested to be smaller than 2.2 eV to have good light utilization. Therefore, an optimum bandgap should be between 1.8 and 2.2 eV [28].

In principle, semiconductors that fulfill all these requirements are able to drive overall water splitting. However, most of the organic photocatalytic materials are unable to possess both the water oxidation and proton reduction potential with a
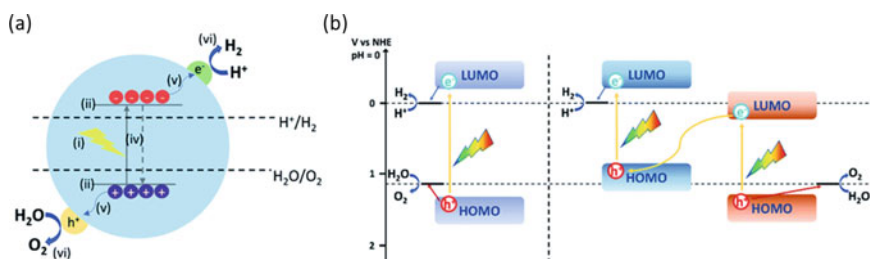
Fig. 8.1 Schematic illustration of water splitting over organic photocatalysts. Reproduced from Ref. [29] (Copyright 2021, The Royal Society of Chemistry)

sufficient overpotential to drive both processes simultaneously, whereas metal co-catalysts are required to facilitate hole and electron transfer reactions. Therefore, often multicomponent systems are used with one component driving proton reduction (H_2 evolution) with a second component performing water oxidation (O_2 evolution) (Fig. 8.1b). This allows matching either component to the required overpotential for the half-reactions but requires twice as many photons as both components have to be excited. These can be systems that rely on direct contact or through a mediator, such as a water-soluble redox active component in a so-called Z-scheme [30], or a solid-state electron mediator, such as carbon nanotubes [31] or reduced graphene oxide [32].

Additionally, some organic semiconductors have act as a sacrificial regent for half-reactions such as proton reduction or water oxidation. Introduction of an organic sacrificial regent promotes proton reduction (water oxidation) and suppresses water oxidation (proton reduction). Systems with good activity for overall water splitting have been developed, which is discussed in next section.

8.3   Material Development of Organic Photocatalysis

The first and second part of this section is about the organic semiconductors for promoting proton reduction (H_2 evolution) and water oxidation (O_2 evolution), respectively. Materials for overall water splitting are discussed in the last part.

8.3.1   Materials for Hydrogen Evolution

As mentioned in last section, organic semiconductors have been far less studied for water splitting compared to inorganic semiconductors. As shown in Fig. 8.2, organic photocatalysis can be classified into non-porous and porous materials. The first widely explored example of a photocatalytic polymer is C_3N_4. It is reported that an organic semiconductor could perform both half-reactions (proton reduction and water oxidation), though not simultaneously and additionally requiring sacrificial reagents to drive both processes [15]. Following this report, many derivatives of carbon nitrides for sacrificial half-reactions have been studied. Materials such as polymeric C_3N_4 can archive high apparent quantum yields (AQYs, defined as percentage of electrons used for the generation of hydrogen per incident photons) of 60% at 420 nm from aqueous 3 wt% NaCl solution [33].

Covalent triazine-based frameworks (CTFs) are related to carbon nitrides with high nitrogen content, which are able to facilitate photocatalytic hydrogen evolution from water with platinum co-catalysts. A large number of structurally diverse CTFs have been reported to be active with quantum yields as high as 15.9% at 420 nm under sacrificial conditions [34].
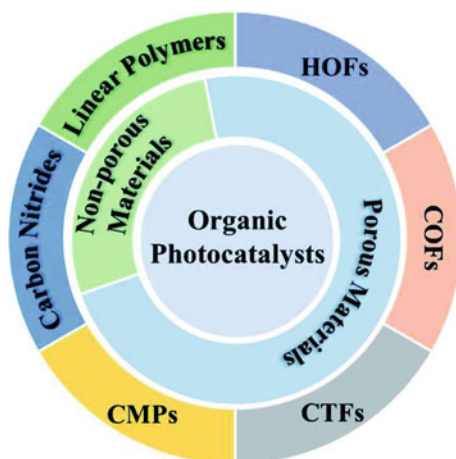
Fig. 8.2 Classes of organic materials that have been studied as photocatalysts for water splitting. CMPs: conjugated microporous polymers; CTFs: covalent triazine-based frameworks, COFs: covalent organic frameworks; HOFs: hydrogen-bonded organic frameworks. Reproduced from Ref. [29] (Copyright 2021, The Royal Society of Chemistry)

Conjugated microporous polymers (CMPs) and covalent organic frameworks (COFs) were reported as members of porous materials. Cooper et al. [35] reported a series of CMPs, where the optical gap was tuned by changing the proportions of phenyl and pyrene building blocks. COFs are porous materials composed of organic molecules linked by covalent bonds, and they show a higher degree of crystallinity compared to carbon nitrides and CTFs. Cooper et al. developed a crystalline COF, FS-COF, leading to a 61% enhancement in the hydrogen evolution rate up to 16.3 mmol g^{-1} h^{-1} [36], which is the highest photocatalytic activity for hydrogen evolution for COFs so far.

The first linear polymers, namely poly(p-phenylene), was reported in 1985, which have been used to be active for sacrificial hydrogen production from water [14]. The photocatalytic activity was low, due to a wide bandgap of 2.9 eV.

Heterojunctions of donor polymers with organic acceptors have also been developed to facilitate intermolecular charge transfer and transport to boost the photocatalytic performance. A high hydrogen evolution rate of 105 mmol h^{-1} g^{-1} was reported using a conjugated polymer donors and fullerene combination in nanohybrid systems [37], which is similar to the BHJ structure in organic solar cells [38, 39]. Systems consisting of two [40] or three [41] different conjugated polymer photocatalysts have also been shown to be efficient for sacrificial hydrogen production by providing an energy offset for charge transfer.

Recently, hydrogen-bonded organic frameworks have been emerged as active photocatalyst [42]. The highly ordered α-phase of tetra(4-carboxyphenyl)pyrene showed a much higher photocatalytic activity for hydrogen evolution combined with ascorbic acid as a sacrificial electron donor, compared with its amorphous analogue

under the same conditions with an AQY of 4.1% at 420 nm showing that a backbone with extended conjugation is not a prerequisite for high activity.

8.3.2   Materials for Water Oxidation

It remains a significant challenge for organic photocatalytic materials to process water oxidation rather than hydrogen evolution due to the required low-lying HOMO levels to facilitate the process and the kinetic barrier that has to be overcome [43]. While oxygen itself has little value, it is an important step forward toward developing photocatalysts for overall water splitting. So far, only a few examples have been presented facilitate water oxidation using organic semiconductors, most requiring a metal co-catalyst to overcome the kinetic barrier of the process and the short lifetime of the holes. The most frequently used co-catalysts are either CoO_x or RuO_x. Impregnation, photodeposition, or calcination methods have been used for deposition of those metal oxides onto the photocatalyst. Alternatively, the co-catalyst can be performed and then coated onto the photocatalyst by ultrasonication [44].

CTFs are materials that are similar to carbon nitrides with respect to their high nitrogen content and low-lying HOMO levels. The meta-links in this material class caused by the triazine core reduce the HOMO levels [45] together with the electronegativity of the nitrogen atoms [46]. After loading with RuO_2, CTFs become active for sacrificial oxygen production with an O_2 evolution rate of 140 μmol h^{-1} g^{-1} [47].

Aza-CMP nanosheets with benzenetetramine and hexaketocyclohexane exhibit activity for oxygen evolution in the presence of $FeCl_3$ without additional metal catalysts [48]. Similar to other materials reported for oxygen evolution, it is nitrogen-rich and has meta-linkages, resulting in the required deep HOMO levels. Addition of cobalt as a co-catalyst has improved the O_2 evolution performance up to 14.3 μmol h^{-1} g^{-1} under visible light. Similarly, a crystalline perylene imide polymer has been reported to facilitate sacrificial oxygen evolution without additional co-catalysts in this system with an evolution rate of 3223.9 μmol h^{-1} g^{-1} [49].

A bipyridine-based covalent organic framework coordinating with Co^{2+} has been reported for photocatalytic water oxidation with an evolution rate of 152 μmol h^{-1} g^{-1} under sacrificial conditions [50]. The co-catalyst was found to be crucial, and no activity was found in the absence of co-catalysts.

Linear conjugated polymer photocatalysts were also found to be active for sacrificial water oxidation [51]. The most active material in this study was the homopolymer of dibenzo[b,d]thiophene sulfone with a rate of 16.6 μmol h^{-1} under broadband irradiation and a rate of 5.2 μmol h^{-1} under visible light. The co-catalysts were loaded onto the materials by photodeposition and found to be crucial with CoO_x giving the highest performance.

Fully planarised nitrogen-containing conjugated ladder polymers have recently been reported to produce oxygen under visible light irradiation with a rate of

$7.16\,\mu\text{mol}\,\text{h}^{-1}$, using AgNO3 as the electron scavenger and La_2O_3 as the pH buffering agent [52].

Overall, only a few reports with relatively low rates when compared to hydrogen production catalysts have been reported; however, the development of these systems is a critical step forward to obtain fully organic photocatalysts for overall water splitting.

8.3.3 Materials for Overall Water Splitting

Unlike the photocatalytic hydrogen production half-reaction that has been extensively studied, there are only a few examples of overall water splitting with organic materials. Z-Schemes endow the coupling of an organic photocatalyst that performs hydrogen production with an inorganic semiconductor to perform overall water splitting by balancing charges through a redox mediator [30].

Carbon nitride was the first to be reported in Z-schemes with WO_3 or $BiVO_4$, acting as the oxygen evolution photocatalyst, in the presence of a redox mediator system (I^-/IO_3^-) [53], which showed H_2 and O_2 evolution of 21.2 and $11.0\,\text{mmol}\,\text{h}^{-1}\,\text{g}^{-1}$, respectively (Fig. 8.3). The Z-scheme concept could also be used for linear conjugated polymers, such as the homopolymer of dibenzo[b,d]thiophene sulfone P10 (Fig. 8.3c) [54]. An optimized system consisting of P10 and $BiVO_4$ produced stoichiometric amounts of hydrogen and oxygen with rates of 5 and $2.7\,\text{mmol}\,\text{h}^{-1}$, respectively. The system was able to reach equilibrium using either $FeCl_3$ or $FeCl_2$. Z-Schemes with mediators have clearly demonstrated that the experiences on organic materials for hydrogen production can be transferred to overall water splitting systems.

A composite of aza-fused microporous polymers and C_2N nanosheets acting as H_2 and O_2 evolution photocatalysts has been reported to facilitate overall water splitting with a rate of $22.5\,\mu\text{mol}\,\text{h}^{-1}$ (Fig. 8.3d) [55], suggesting that the system is able to perform overall water splitting without additional co-catalysts. Systems that do not rely on two separate semiconductors to facilitate overall water splitting is shown in Table 8.1. A nanocomposite of carbon dots and carbon nitride was reported with evolution rates of 8.4 (H_2) and 4.1 (O_2) $\mu\text{mol}\,\text{h}^{-1}$ and an overall solar energy conversion efficiency of 2.0% [56]. An alternative strategy is to optimize co-catalyst system for overall water splitting without using sacrificial reagents [57]. High photocatalytic activities with rates of 2.1 and 1 $\mu\text{mol}\,\text{h}^{-1}$ under visible light were achieved for carbon nitride modified with CoP and Pt as co-catalysts, respectively [58]. Wang et al. [59] reported single crystalline carbon nitride with even higher activities for overall water splitting. Polytriazine imide was synthesized with LiCl and NaCl to improve crystallinity and loaded via photodeposition with Pt/Co exhibiting a high quantum efficiency of 8%. A NiP_x- and Pt-loaded CTFs have also been shown to be able to facilitate overall water splitting [60]. The preformed NiPx was simply mixed with the CFT, which was further loaded with Pt via photodeposition. Two CMPs PTEPB and PTEB were able to facilitate overall water splitting as single
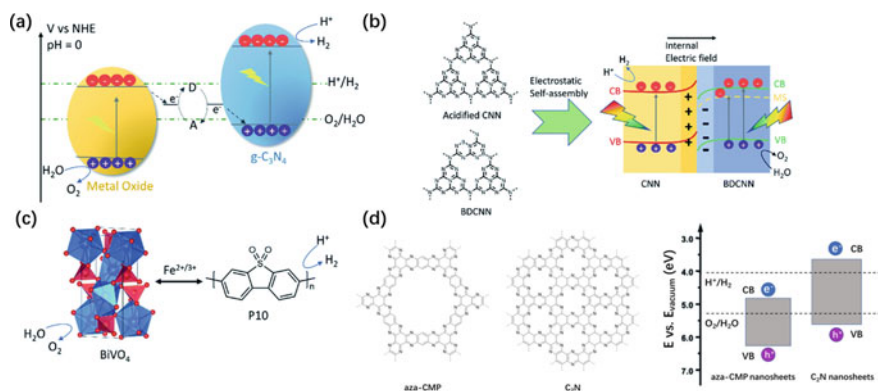
Fig. 8.3 Overall water splitting Z-scheme systems: **a** carbon nitride (C_3N_4) and $BiVO_4$ or WO_3 using a redox mediator; **b** nitrogen-deficient (CNN) and boron-doped (BDCNN) carbon nitride two-dimensional nanosheet heterostructure; **c** linear conjugated polymer P10 coupled with $BiVO4$ using a redox mediator; **d** a conjugated microporous polymer material coupled with a carbon nitride analogue (C_2N). Figures adapted with permission from Ref. [29] (Copyright 2021, The Royal Society of Chemistry)

component systems without introduction of any co-catalysts [61]. A remarkable rate of 218 μmol h^{-1} g^{-1} for H_2 production was achieved. Furthermore, that also delivered a quantum efficiency as high as 10% at 420 nm and a STH of 0.6%.

Table 8.1 Summary of materials for one step excitation overall water splitting

Photocatalyst	Co-catalyst	Amount of photocatalyst (mg)	STH%	Gas evolution rates (μmol h^{-1})		Reference
				H_2	O_2	
C_3N_4	Carbon nanodots	80	2.0	8.4	4.1	[56]
PTEB	Pd	20	0.31	102 (g^{-1})		[61]
PTEPB	Pd	20	0.6	218 (g^{-1})		[61]
C_3N_4	3 wt% Pt, PtOx and 1 wt% CoOx	100	NA	1.2	0.6	[57]
C-TCN	3% Pt and 1 wt% CoOx	10	NA	10.23	5.04	[62]
Sea-urchin-structured C_3N_4	3 wt% Pt	25	NA	41.5(g^{-1})	20.3 (g^{-1})	[63]
CTF-HUST-A1-BuOK	4.5% wt% NixP and 3.0 wt% Pt	50	NA	25.4(g^{-1})	12.9 (g^{-1})	[60]
PTI/Li$^+$Cl$^-$	1% Pt and 0.5% Co	100	NA	189	91	[59]

8.4   Application of Organic Photocatalysis

Large-scale application is one of the major challenges for overall water splitting systems, The water splitting systems are in most cases tested in suspension on a small laboratory scale, which is not fit for large-scale application. Using sheets instead of suspensions is a step forward for large-scale water splitting setup. As suspensions require the use of agitation to prevent the photocatalysts from settling and become inactive as those photocatalysts are no longer exposed to light. Domen et al. [64, 65] developed sheets of multicomponent systems and large-scale panels of single component photocatalysts that can be produced on a larger scale using screen printing (Fig. 8.4b).

Large-scale sacrificial half-reactions have been studied by organic systems rather than overall water splitting, such as device using immobilized carbon nitride loaded
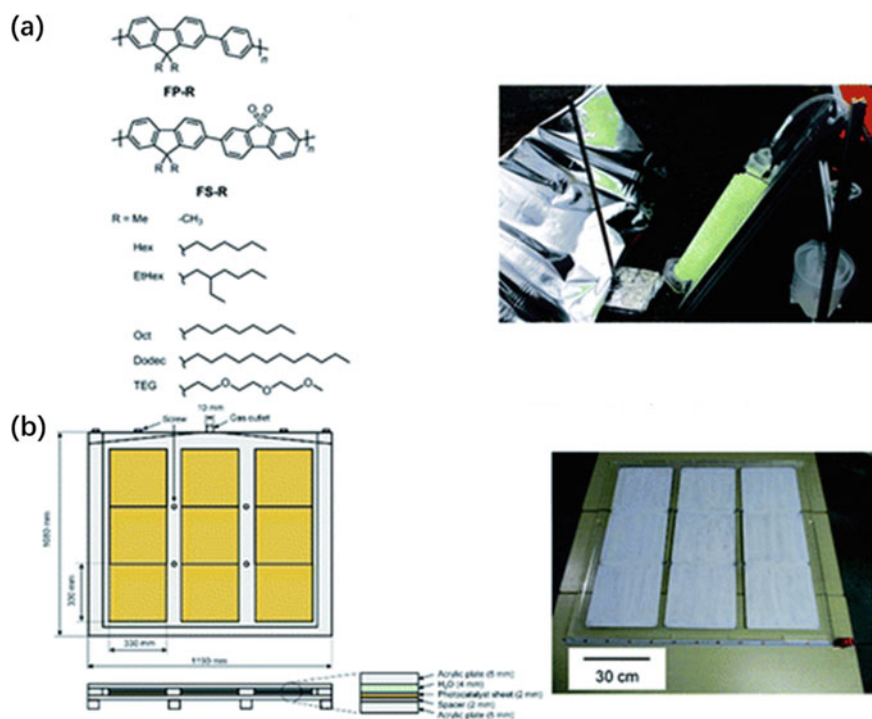
Fig. 8.4 Large-scale water splitting approaches: **a** structures of soluble polymers and the side view of the photoreactor setup with a reflective panel and polymer-coated glass fibers submerged in 5 vol% TEA and connected to a hydrogen collection vessel (right) and **b** photograph of a large-scale system for photocatalytic hydrogen production working under natural sunlight. Figures are adapted from Ref. [64] (Copyright 2018, Elsevier) and Ref. [66] (Copyright 2020, The Royal Society of Chemistry)

with platinum and facilitates hydrogen production in the presence of a hole scavenger [67]. It has been shown that solution-processible polymer photocatalysts FP-R and FS-R retained their activity for sacrificial hydrogen production when cast onto flat supports and onto fibers, allowing for hydrogen production on a larger scale (Fig. 8.4a) [67]. To obtain such systems, further work is required to develop solution processable systems that facilitate overall water splitting with appropriate co-catalysts or two component systems consisting of hydrogen and oxygen production polymers.

8.5   Conclusions and Perspectives

Overall, it is very clear that organic semiconductor-based materials have significant potential as water splitting photocatalysts. The fact that organic semiconductors are easily tunable by structural modification and that they are made from earth-abundant elements makes them ideal candidates for large-scale applications. One of the crucial issues is that more attention needs to be focused on exploring overall water splitting rather than sacrificial hydrogen production.

The water oxidation reaction still remains a significant challenge for organic photocatalysts, and only a few examples have been reported so far. The small number of materials reported in most studies makes it very difficult to establish structure–property relationships. New materials with optical absorption match the solar spectrum need to be developed, while suitable HOMO levels for water oxidation need to be maintained. Thus, the performance of the material should be close to the required STH of 10% [25].

At present, the necessity of co-catalysts for high-performance water splitting is still under debate. It seems that the metal co-catalyst plays a very important role; however, there are metal-free systems among hydrogen, oxygen production, and overall water splitting. A lot of work has to be done to understand the mechanism of organic systems that facilitate water splitting without metal co-catalysts as well as understand the exact role of precious co-catalysts and explore alternative non-precious co-catalysts for scale-up in the future.

It is reported that the lowered performance of overall water splitting is mainly caused by limited exciton separation. To overcome this problem, new concepts of combination of multiple components with synergistic properties such as enhanced both half-reactions and improved electron transfer efficiency. For example, using stacks of molecular crystals, COFs or confining a secondaryphase such as a soluble conjugated polymer in the pore structure of a CMP are able to realize a boost of performance.

Solution-processable materials suggest huge potential for large-scale applications. The potential advantages of organic semiconductors, such as an increasedsurface area by expansion in contact with water, thus promote a larger number of active sites compared toinorganic systems [66]. Further research needs to be done for exploring

large-scale panel systems. For example, polymer photocatalysts processed on transparent substrates such as glass are able to harvest more sunlight as photons that have pass through the surface can be absorbed by photocatalysts in deeper layers [66].

There have been few follow-up studies on the reported organic systems for overall water splitting. To enable this in the future, clear and detailed experimental procedures that allow for the reproduction of materials are needed, combining with the standardization of measurements, which will lead to more efficient overall water splitting systems [68]. To realize reliable and reproducible results of overall water splitting, a standardized efficiency accreditation similar to the existing accreditation of solar cells is needed [69, 70]. Finally, many efforts should be made to explore scale-up and testing water splitting performance under ambient conditions in terms of light intensity, pressure, and stability. We believe that organic semiconductor-based photocatalysts will exhibit remarkable potential for water splitting in the future.

References

1. Hoffert MI (2010) Farewell to fossil fuels? Science 329:1292–1294
2. Stančin H, Mikulčić H, Wang X, Duić N (2020) A review on alternative fuels in future energy system. Renew Sustain Energy Rev 128:109927
3. Koohi-Fayegh S, Rosen MA (2020) A review of energy storage types, applications and recent developments. J Energy Storage 27:101047
4. Wang Z, Li C, Domen K (2019) Recent developments in heterogeneous photocatalysts for solar-driven overall water splitting. Chem Soc Rev 48:2109–2125
5. Fujishima A, Honda K (1972) Electrochemical photolysis of water at a semiconductor electrode. Nature 238:37–38
6. Xing J, Fang WQ, Zhao HJ, Yang HG (2012) Inorganic photocatalysts for overall water splitting. Chem Asian J 7:642–657
7. Ismail AA, Bahnemann DW (2014) Photochemical splitting of water for hydrogen production by photocatalysis: a review. Sol Energy Mater Sol Cells 128:85–101
8. Wang W, Li Y, Kang Z et al (2016) A NIR-driven photocatalyst based on α-NaYF$_4$:Yb, Tm @ TiO$_2$ core–shell structure supported on reduced graphene oxide. Appl Catal B Environ 182:184–192
9. Xu Y, Jin S, Xu H et al (2013) Conjugated microporous polymers: design, synthesis and application. Chem Soc Rev 42:8012–8031
10. Thote J, Aiyappa HB, Deshpande A et al (2014) A covalent organic framework-cadmium sulfide hybrid as a prototype photocatalyst for visible-light-driven hydrogen production. Chem A Eur J 20:15961–15965
11. Hu S, Xiang C, Haussener S et al (2013) An analysis of the optimal band gaps of light absorbers in integrated tandem photoelectrochemical water-splitting systems. Energy Environ Sci 6:2984–2993
12. Banerjee T, Gottschling K, Savasci G et al (2018) H$_2$ evolution with covalent organic framework photocatalysts. ACS Energy Lett 3:400–409
13. Diercks CS, Yaghi OM (2017) The atom, the molecule, and the covalent organic framework. Science 355
14. Yanagida S, Kabumoto A, Mizumoto K et al (1985) Poly(P-phenylene)-catalysed photoreduction of water to hydrogen. J Chem Soc Ser Chem Commun 8:474–475
15. Wang X, Maeda K, Thomas A et al (2009) A metal-free polymeric photocatalyst for hydrogen production from water under visible light. Nat Mater 8:76–80

16. Mahmood J, Lee EK, Jung M et al (2015) Nitrogenated holey two-dimensional structures. Nat Commun 6:4–10
17. Mahmood J, Lee EK, Jung M et al (2016) Two-dimensional polyaniline (C_3N) from carbonized organic single crystals in solid state. Proc Natl Acad Sci U S A 113:7414–7419
18. Mahmood J, Anjum MAR, Baek JB (2019) Fused aromatic network structures as a platform for efficient electrocatalysis. Adv Mater 31:1805062
19. Kuecken S, Acharjya A, Zhi L et al (2017) Fast tuning of covalent triazine frameworks for photocatalytic hydrogen evolution. Chem Commun 53:5854–5857
20. Pachfule P, Acharjya A, Roeser J et al (2018) Diacetylene functionalized covalent organic framework (COF) for photocatalytic hydrogen generation. J Am Chem Soc 140:1423–1427
21. Huang J, Tarábek J, Kulkarni R et al (2019) A π-conjugated, covalent phosphinine framework. Chem A Eur J 25:12342–12348
22. Sprick RS, Jiang JX, Bonillo B et al (2015) Tunable organic photocatalysts for visible-light-driven hydrogen evolution. J Am Chem Soc 137:3265–3270
23. Vogel A, Forster M, Wilbraham L et al (2019) Photocatalytically active ladder polymers. Faraday Discuss 215:84–97
24. Rahman MZ, Moffatt J, Spooner N (2018) Topological carbon nitride: localized photon absorption and delocalized charge carrier separation at intertwined photocatalyst interfaces. Mater Horizons 5:553–559
25. Maeda K (2011) Photocatalytic water splitting using semiconductor particles: history and recent developments. J Photochem Photobiol C Photochem Rev 12:237–268
26. Zhang G, Lan ZA, Wang X (2017) Surface engineering of graphitic carbon nitride polymers with cocatalysts for photocatalytic overall water splitting. Chem Sci 8:5261–5274
27. Tong H, Ouyang S, Bi Y et al (2012) Nano-photocatalytic materials: possibilities and challenges. Adv Mater 24:229–251
28. Le BT, Rérat M, Sautet P (2014) Semiconductors used in photovoltaic and photocatalytic devices: assessing fundamental properties from DFT. J Phys Chem C 118:5997–6008
29. Bai Y, Hippalgaonkar K, Sprick RS (2021) Organic materials as photocatalysts for water splitting. J Mater Chem A 9:16222–16232
30. Martin DJ, Reardon PJT, Moniz SJA, Tang J (2014) Visible light-driven pure water splitting by a nature-inspired organic semiconductor-based system. J Am Chem Soc 136:12568–12571
31. Ng B-J, Putri LK, Tan L-L et al (2017) All-solid-state Z-scheme photocatalyst with carbon nanotubes as an electron mediator for hydrogen evolution under simulated solar light. Chem Eng J 316:41–49
32. Iwase A, Ng YH, Ishiguro Y et al (2011) Reduced graphene oxide as a solid-state electron mediator in Z-scheme photocatalytic water splitting under visible light. J Am Chem Soc 133:11054–11057
33. Zhang G, Lin L, Li G et al (2018) Ionothermal synthesis of triazine–heptazine-based copolymers with apparent quantum yields of 60% at 420 nm for solar hydrogen production from "sea water." Angew Chem Int Ed 57:9372–9376
34. Meier CB, Clowes R, Berardo E et al (2019) Structurally diverse covalent triazine-based framework materials for photocatalytic hydrogen evolution from water. Chem Mater 31:8830–8838
35. Jiang JX, Su F, Trewin A et al (2007) Conjugated microporous poly(aryleneethynylene) networks. Angew Chem Int Ed 46:8574–8578
36. Wang X, Chen L, Chong SY et al (2018) Sulfone-containing covalent organic frameworks for photocatalytic hydrogen evolution from water. Nat Chem 10:1180–1189
37. Yang H, Li X, Sprick RS, Cooper AI (2020) Conjugated polymer donor-molecular acceptor nanohybrids for photocatalytic hydrogen evolution. Chem Commun 56:6790–6793
38. Xie C, Heumüller T, Gruber W et al (2018) Overcoming efficiency and stability limits in water-processing nanoparticular organic photovoltaics by minimizing microstructure defects. Nat Commun 9:5335
39. Xie C, Classen A, Späth A et al (2018) Overcoming microstructural limitations in water processed organic solar cells by engineering customized nanoparticulate inks. Adv Energy Mater 8:1702857

40. Zhang X, Shen F, Hu Z et al (2019) Biomass nanomicelles assist conjugated polymers/Pt cocatalysts to achieve high photocatalytic hydrogen evolution. ACS Sustain Chem Eng 7:4128–4135
41. Liu A, Gedda L, Axelsson M et al (2021) Panchromatic ternary polymer dots involving sub-picosecond energy and charge transfer for efficient and stable photocatalytic hydrogen evolution. J Am Chem Soc 143:2875–2885
42. Aitchison CM, Kane CM, Mcmahon DP et al (2020) Photocatalytic proton reduction by a computationally identified, molecular hydrogen-bonded framework. J Mater Chem A 8:7158–7170
43. Guiglion P, Butchosa C, Zwijnenburg MA (2014) Polymeric watersplitting photocatalysts; a computational perspective on the water oxidation conundrum. J Mater Chem A 2:11996–12004
44. Zhang H, Tian W, Guo X et al (2016) Flower-like cobalt hydroxide/oxide on graphitic carbon nitride for visible-light-driven water oxidation. ACS Appl Mater Interfaces 8:35203–35212
45. Kan Y, Zhu Y, Liu Z et al (2015) Hydrophilic conjugated polymers with large bandgaps and deep-lying HOMO levels as an efficient cathode interlayer in inverted polymer solar cells. Macromol Rapid Commun 36:1393–1401
46. Sprick RS, Wilbraham L, Bai Y et al (2018) Nitrogen containing linear poly(phenylene) derivatives for photo-catalytic hydrogen evolution from water. Chem Mater 30:5733–5742
47. Xie J, Shevlin SA, Ruan Q et al (2018) Efficient visible light-driven water oxidation and proton reduction by an ordered covalent triazine-based framework. Energy Environ Sci 11:1617–1624
48. Wang L, Wan Y, Ding Y et al (2017) Photocatalytic oxygen evolution from low-bandgap conjugated microporous polymer nanosheets: a combined first-principles calculation and experimental study. Nanoscale 9:4090–4096
49. Zhang Z, Chen X, Zhang H et al (2020) A highly crystalline perylene imide polymer with the robust built-in electric field for efficient photocatalytic water oxidation. Adv Mater 32:1907746
50. Chen J, Tao X, Li C et al (2020) Synthesis of bipyridine-based covalent organic frameworks for visible-light-driven photocatalytic water oxidation. Appl Catal B Environ 262:118271
51. Sprick RS, Chen Z, Cowan AJ et al (2020) Water oxidation with cobalt-loaded linear conjugated polymer photocatalysts. Angew Chem 132:18854–18859
52. Ma X, Wang H, Cheng J et al (2021) Fully conjugated ladder polymers as metal-free photocatalysts for visible-light-driven water oxidation. Chin J Chem 39:1079–1084
53. Alivisatos AP, Andrews AM, Boyden ES et al (2013) Nanotools for neuroscience and brain activity mapping. ACS Nano 7:1850–1866
54. Xu Y, Duan J, Yang X et al (2020) Lattice-tailored low-temperature processed electron transporting materials boost the open-circuit voltage of planar $CsPbBr_3$ perovskite solar cells up to 1.654 V. J Mater Chem A 8:11859–11866
55. Wang L, Zheng X, Chen L et al (2018) Van der Waals heterostructures comprised of ultrathin polymer nanosheets for efficient Z-scheme overall water splitting. Angew Chem Int Ed 57:3454–3458
56. Liu J, Li Y, Liu N et al (2015) Metal-free efficient photocatalyst forstable visible water splitting via atwo-electron pathway. Science 347:970–974
57. Zhang G, Lan ZA, Lin L et al (2016) Overall water splitting by Pt/g-C_3N_4 photocatalysts without using sacrificial agents. Chem Sci 7:3062–3066
58. Pan Z, Zheng Y, Guo F et al (2017) Decorating CoP and Pt nanoparticles on graphitic carbon nitride nanosheets to promote overall water splitting by conjugated polymers. Chemsuschem 10:87–90
59. Lin L, Lin Z, Zhang J et al (2020) Molecular-level insights on the reactive facet of carbon nitride single crystals photocatalysing overall water splitting. Nat Catal 3:649–655
60. Zhang S, Cheng G, Guo L et al (2020) Strong-base-assisted synthesis of a crystalline covalent triazine framework with high hydrophilicity via benzylamine monomer for photocatalytic water splitting. Angew Chem Int Ed 59:6007–6014
61. Wang L, Wan Y, Ding Y et al (2017) Conjugated microporous polymer nanosheets for overall water splitting using visible light. Adv Mater 29:1702428

62. Mo Z, Di J, Yan P et al (2020) An all-organic D-A system for visible-light-driven overall water splitting. Small 16:2003914
63. Zeng Y, Li H, Luo J et al (2019) Sea-urchin-structure g-C$_3$N$_4$ with narrow bandgap (~2.0 eV) for efficient overall water splitting under visible light irradiation. Appl Catal B Environ 249:275–281
64. Goto Y, Hisatomi T, Goto Y et al (2018) A particulate photocatalyst water-splitting panel for large-scale solar hydrogen generation. Joule 2:509–520
65. Wang Q, Okunaka S, Tokudome H et al (2018) Printable photocatalyst sheets incorporating a transparent conductive mediator for Z-scheme water splitting. Joule 2:2667–2680
66. Woods DJ, Hillman SAJ, Pearce D et al (2020) Side-chain tuning in conjugated polymer photocatalysts for improved hydrogen production from water. Energy Environ Sci 13:1843–1855
67. Schröder M, Kailasam K, Borgmeyer J et al (2015) Hydrogen evolution reaction in a large-scale reactor using a carbon nitride photocatalyst under natural sunlight irradiation. Energy Technol 3:1014–1017
68. Vignolo-González HA, Laha S, Jiménez-Solano A et al (2020) Toward standardized photocatalytic oxygen evolution rates using RuO$_2$@TiO$_2$ as a benchmark. Matter 3:464–486
69. Wang Z, Hisatomi T, Li R et al (2021) Efficiency accreditation and testing protocols for particulate photocatalysts toward solar fuel production. Joule 5:344–359
70. Green M, Dunlop E, Hohl-Ebinger J et al (2021) Solar cell efficiency tables (version 57). Prog Photovolt Res Appl 29:3–15

Chapter 9
Organic Thermoelectric Devices

Owing to the entropy variation in the internal energy of charge carriers under a temperature difference, thermoelectric (TE) materials can directly convert heat into electricity via the Seebeck effect, and vice versa via the Peltier effect [1]. The recent introduction of organic semiconductors into organic TEs (OTEs) has been of great interest to researchers. In addition to those natural advantages, such as low material cost, mechanical flexibility, low toxicity, and lightweight, OTE materials have two features which are able to overcome the obstacles of traditional inorganic TE materials. Firstly, thermal conductivity of organic materials is typically approaching the lower limit of thermal conductivity of inorganic thermoelectric materials. Second, electronic structures of organic semiconductors are fairly tunable through molecular chemistry and doping treatments [2]. Therefore, organic thermoelectric materials hold much promise in applications at low temperature-based TE generators [3].

In the past decades, OTE materials have been overlooked because of their relatively low TE performance. However, in recent years, great progress has been made in molecular design strategies, nanostructuring, preparation technologies, and TE properties, which provide a broad prospect for the development of OTEs. Therefore, organic TE materials and generators are a promising research field, because they have many attractive characteristics, indicating that OTEs can overcome the shortcomings of existing inorganic TE systems. In the following parts of this chapter, we will briefly introduce the OTE materials and devices, including a brief introduction of the OTE, the carrier energy and heat transport theory in the OTE system, the organic semiconductor materials in the OTE, and the future prospects of the OTE devices.

9.1 A Brief Introduction of OTE

TE power generation is becoming increasingly important as a result of global efforts to find new sources of energy. It has been found that approximately 70% of primary energy consumption is wasted as heat, and efforts are being made to use this energy

more efficiently [4]. The first work on TE materials is the report of the Seebeck effect by Thomas Johann Seebeck in 1822. Subsequently, the Peltier effect and Thomson effect were reported by Jean Charles Peltier in 1834. Since then, the development of highly efficient thermoelectric materials and devices is widespread not only in the laboratory but also in industry. At present, inorganic TE materials have shown excellent thermoelectric properties, and with the development of temperature difference generators and refrigerators, some of these materials have been commercialized. Historically, all commercially available TE generators have been produced from doped narrow bandgap semiconductors. Goldsmid et al. discovered bismuth telluride (Bi_2Te_3) in 1954, which is considered as a representative inorganic TE material with high performance [5]. Since the twenty-first century, due to the improvement of atomic-scale synthesis and manufacturing techniques, new materials with high TE properties have been reported [6]. Firstly, the composing elements such as Bi, Te, Sb, and Pb are toxic and not abundant. Secondly, laboratory processing of inorganic materials, including melt-spinning, ball milling, and hot pressing, is costly in terms of energy and instruments, and requires a long payback time. Lastly, most inorganic materials are not just too heavy but also brittle to be used in daily life [7].

Due to the aforementioned obstacles faced by current inorganic TE materials, more and more attention has been paid on organic candidates. In addition to being potentially abundant, low-cost and lightweight, the unique advantage of organic TE materials over their inorganic counterparts is their poor thermal conductivity. Due to the disordered and amorphous nature, the conductivity of OTEs exhibit an order of magnitude lower than that of inorganic materials such as Bi_2Te_3, which is suitable for thermoelectric applications in low temperature. Organic semiconductors are unique because the inherent tunability in their structure and processing can enable thermoelectric property optimization that is not achievable with traditional inorganic semiconductors. The film-forming nature of organic materials also opens new application opportunities such as flexible and wearable electronics. Despite all the above advantages, further development in OTE materials is impeded by bottleneck problems including low electrical carrier mobilities and inferior Seebeck coefficients (thermopower).

Research of organic thermoelectric materials dates back to 1970s, which was mainly about thermoelectric measurement of organic semiconductors and conducting polymers [8]. Since then, Seebeck coefficients of various types of organic electronic materials were studied, including organic photoconductive dyes, [9] organic charge transfer salts, [10] derivatives of phthalocyanines [11], and conducting polymers [12]. Nevertheless, thermoelectric measurements were carried out at that time to study the electronic structure, rather than looking for potential OTE materials. Similarly, in the 1990s, the doping process of small molecule semiconductor films prepared by thermal deposition was solved by characterizing the Seebeck coefficient, and the device performance of OLED or OPV was improved by doping [13]. Therefore, there are both practical and fundamental interests in the research of OTE materials.

Since the early twenty-first century, there have been ongoing efforts to employ organics for TE applications. In the early stage of OTE research, conjugated polymers

were studied due to their specific TE properties such as reasonable electrical conductivity, good chemical stability, and easy processability [14]. Meanwhile, pentacene [15] and fullerene [16] and other small molecules are also doped as p-type and n-type TE generators, respectively. After more than ten years of research, so far, the highest values of ZT for p-type and n-type OTE materials are 0.42 [17] and 0.34 [18], respectively. Moreover, TE devices fabricated by printing using organic thermoelectric materials have been realized. Furthermore, hybrid materials of organic and inorganic thermoelectric materials have also been developed, and their thermoelectric properties are better than those of materials without any component [19]. This hybrid strategy demonstrate TE performance approaching that of state-of-the-art inorganic materials while maintaining the appeal of low thermal conductivity and flexible form factors that incorporating organic species impart. All the detailed content will be introduced in next sections.

9.2 Working Principles of Organic Thermoelectrics

9.2.1 Basic Principles of Thermoelectrics

TEs are devices that directly convert heat to electricity. These devices are composed of p-type and n-type semiconductors (thermoelectric legs), which are electrically connected in series and thermally connected in parallel, and are sandwiched between the heat source and the radiator. Under an applied temperature difference, the carriers in these semiconductors diffuse from the hot side to the cold side, producing a voltage consistent with the Seebeck effect (Fig. 9.1), which can be demonstrated as follows:

$$S_{12} = (V_1 - V_2)/(T_1 - T_2) \tag{9.1}$$

where S_{12} is the Seeback coefficient (thermopower) and V represents the voltages of the two semiconductors. Generally, a TE device starts with a pair of n-(electron-rich) and p-type (electron-deficient) semiconducting materials which are known as a TE couple. The Seebeck coefficients generally vary as function of temperature and depend strongly on the composition of the conductor. For ordinary materials at room temperature, the Seebeck coefficient may range in value from $-100\ \mu V\ K^{-1}$ to $+1000\ \mu V\ K^{-1}$.

Conversely, if the current is applied, exothermic and endothermic reactions can occur at the semiconductor–metal junctions via the Peltier effect (Fig. 9.1b). The Peltier heat generated at the junction per unit time is

$$Q = (\pi_1 - \pi_2)I \tag{9.2}$$
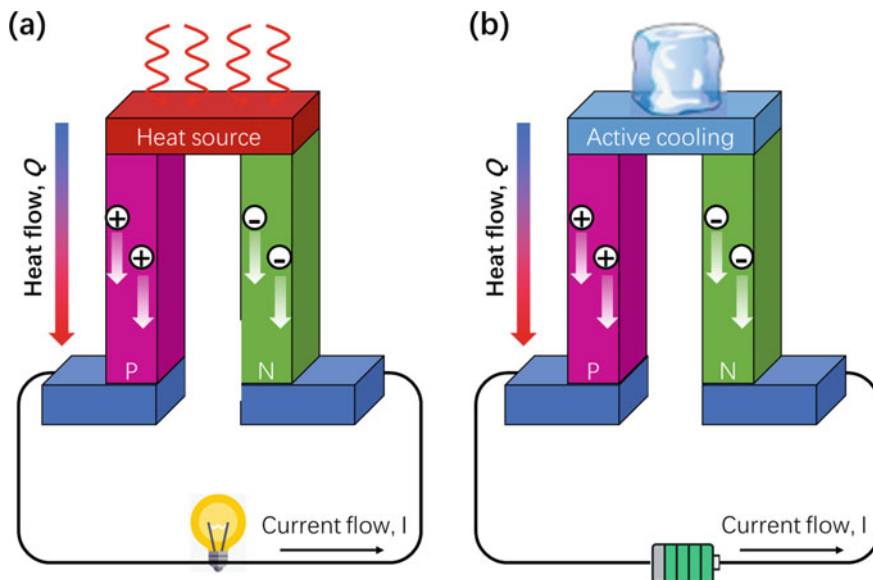
Fig. 9.1 Schematic diagram of thermoelectric module for **a** power generation (Seebeck effect) and **b** active cooling (Peltier effect). **a** The applied temperature difference makes the carriers in the material (electrons or holes) diffuse from the hot side to the cold side, causing current to flow through the circuit. **b** When current flows through the circuit, heat is absorbed at the upper junction and propagated to the lower junction

where π is the Peltier coefficients of the two semiconductors and I is the electric current from 1 to 2. The Seebeck and Peltier effects are different manifestations of the same physical process.

In different materials, the Seebeck coefficient is not constant in temperature, and so a spatial gradient of temperature will lead to a gradient of Seebeck coefficient. If a current is driven through this gradient, then a continuous version of the Peltier effect will occur. Thomson effect refers to the phenomenon that there is a temperature gradient in the heating or cooling of a current-carrying conductors. If a current I is passed through a homogeneous conductor, the Thomson effect predicts a heat production rate per unit volume

$$Q = \beta I \Delta T \qquad (9.3)$$

where ΔT is the temperature gradient, and β is the Thomson coefficient. The Thomson coefficient is unique among the three main thermoelectric coefficients because it is the only one directly measurable for individual materials. The Peltier and Seebeck coefficients can only be easily determined for pairs of materials. Thomson, Peltier, and Seebeck effects are different manifestations of one effect. The relation among those three effects can be shown in the first Thomson relation

$$\beta = \mathrm{d}\pi/\mathrm{d}T - S \tag{9.4}$$

where β is the Thomson coefficient, π is the Peltier coefficient, and S is the Seebeck coefficient. This relationship is easily shown given that the Thomson effect is a continuous version of the Peltier effect.

The second Thomson relation is

$$\pi = \mathrm{TS} \tag{9.5}$$

This relation expresses a subtle and fundamental connection between the Peltier and Seebeck effects. Using the second relation, the first Thomson relation becomes

$$\beta/T = \mathrm{d}S/\mathrm{d}T \tag{9.6}$$

It is difficult to find absolute Seebeck or Peltier coefficient values for individual materials. If the Thomson coefficient of the material is measured in a wide temperature range, the Thomson coefficient can be integrated by using the Thomson relation, so as to determine the absolute values of Peltier coefficient and Seebeck coefficient. Only one material needs to be measured, because other values can be determined by measuring the paired Seebeck coefficient in the thermocouple containing the reference material, and then adding back the absolute Seebeck coefficient of the reference material.

9.2.2 Performance Parameters of OTEs

The energy conversion efficiency of a thermoelectric material depends on its electrical and thermal transfer characteristics. It should be a good electrical conductor to effectively transmit carriers and a good insulator to maintain a large temperature difference between the cold and hot sides, resulting in a class of materials. Together, these properties of TE materials is evaluated by a dimensionless figure of merit (ZT), which is shown as follows,

$$\mathrm{ZT} = S^2 \sigma T/\kappa \tag{9.7}$$

where S, σ, T, and κ are the Seebeck coefficient (thermopower), electrical conductivity, absolute temperature, and thermal conductivity, respectively. It can be seen that, at a specific temperature, the high Seebeck coefficient, large electrical conductivity, and low thermal conductivity are the key factors for achieving excellent thermoelectric materials. However, it is found that these parameters are strongly interrelated and interdependent, which makes it extremely difficult to optimize and improve the thermoelectric efficiency (ZT) of bulk materials [20]. Due to the low thermal conductivity of polymer-based organic thermoelectric devices, the power factor (PF $= S^2\sigma$) is adopted to evaluate its thermoelectric efficiency [21, 22].

To improve thermoelectric performance, the electrical conductivity can be enhanced by increasing the carrier concentration and mobility. The electrical conductivity is typically expressed as follows [23]:

$$\sigma = \mu q n = \mu q N \exp(-|E_{\mathrm{Tr}} - E_F|/k_B T) \tag{9.8}$$

where μ is the electron mobility, q is the elementary charge, n is the charge carrier density, k_B is the Boltzmann constant, N is the density of state (DOS) in transport band, E_{Tr} is the transport band edge energy (HOMO for p-type and LUMO for n-type) and E_F is the Fermi level. σ and n are correlated with the energy offset between E_{Tr} and E_F. Organic semiconductors are relatively insulating with very low n due to their wide bandgaps. n can be drastically increased by doping to move E_F toward E_{Tr}. Thus, n is related to the doping level of conductive polymer [24] μ is affected by the morphology and packing of organic film [25]. When a semiconductor contains both electrons and holes, the conductivity is the sum of p-type and n-type conductivity. Although doping is accompanied by an increase in the electrical conductivity, the Seebeck coefficient is expected to decrease, which is demonstrated as follows:

$$S = \frac{k_B}{q} \left(\frac{E_{\mathrm{Tr}} - E_F}{k_B T} + A \right) \tag{9.9}$$

A is a dimensionless numerical factor and related to the weighted conductivity density of states. Here, A can be neglected because the Fermi level is at a large distance to the corresponding energy band edge ($E_{\mathrm{Tr}} - E_F >> kT$) [26]. Thus, we obtained the simplified version of the mobility edge model equation: $S = (E_{\mathrm{Tr}} - E_F/qT)$. The equation also shows an inverse ratio of S to σ and a coupling that makes it difficult for most thermoelectric materials to obtain a high-power factor. Moving the Fermi level away from the conduction band enhances S, but decreases σ because there are fewer carriers to transport. This also explains why metals have low thermal power and high conductivity, while insulators have high thermal power and low conductivity, making doped semiconductors an ideal class of thermoelectric materials. Consequently, there should be an optimal doping level to obtain the highest PF value.

The anti-correlated trends among Seebeck coefficient, electric conductivity, and thermal conductivity are shown in Fig. 9.2. The increase of carrier concentration not only causes an increase in electrical conductivity but thermal conductivity. This is because the thermal conductivity is comprised of a contribution from both electrons (κ_e) and phonons or the lattice (κ_L), which is expressed as:

$$\kappa = \kappa_e + \kappa_L = L\sigma T + (1/3)C_V \upsilon l \tag{9.10}$$

where L, C_v, υ, and l are the Lorentz number, constant-volume specific heat, phonon speed, and phonon mean free path, respectively. The electronic contribution is related to the electrical conductivity through the Wiedemann–Franz law: $\kappa_e = L\sigma T$. Upon increasing the carrier concentration, κ_e increases as σ increases, and this results in an enhancement of the overall thermal conductivity. κ_L represents energy transport
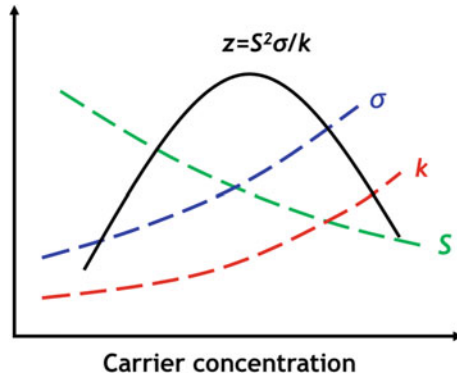
Fig. 9.2 Thermoelectric properties are inversely correlated and competitive with doping. The increase of carrier concentration leads to the increase of conductivity and the decrease of Seebeck coefficient. The thermal conductivity increases with the increase of carrier concentration

by phonons. Typically, organic materials have a low thermal conductivity in the range of 0.1–0.7 W m^{-1} K^{-1}, [27] because their electrical conductivities are often lower than 1 S cm^{-1}. The low electrical conductivity leads to orders of magnitude lower κ_e compared with the κ_L of organic materials. The electrical and thermal conductivities are often anisotropic in organic thin films. The inherent coupling between the thermoelectric properties leads to the optimal carrier concentration, which maximizes ZT (Fig. 9.2). When the carrier concentration is between 10^{19} and 10^{21} per cm^3, this optimal value appears, making heavily doped semiconductors the preferred thermoelectric material [1].

9.2.3 Performance Parameters of TE Generators (TEGs)

Thermoelectric generators (TEGs) are able to realize energy conversion from thermal to electrical power, which are composed of simple two-leg structures and are advantageous for fabricating low-cost and disposable energy conversion devices. Organic TEGs are ideal for applications to support wearable devices such as watches, health monitors, and toys.

The energy conversion efficiency is applied to determine the performance of a TEG as follows:

$$\eta = \frac{T_{\text{hot}} - T_{\text{cold}}}{T_{\text{hot}}} \frac{\sqrt{1 + ZT} - 1}{\sqrt{1 + ZT} + \frac{T_{\text{cold}}}{T_{\text{hot}}}} \tag{9.11}$$

where T_{hot} and T_{cold} represent the absolute temperature of the hot side and the cold side, respectively. It should be mentioned that Eq. (9.11) is under an ideal condition.

The energy conversion efficiency is affected by many different factors such as joule heating, heat loss, the electrical and thermal contact resistances [28, 29].

The power output is another important parameter, which has been used as one of the main factors in the evaluation of TEGs. When the resistance of an external load (R_L) is close to the internal resistance of the device (R_{TEG}), $R_L \approx R_{TEG}$, the maximum power output of a TEG (P_{max}) can be obtained. Then, the output voltage (V_L) is half of the open-circuit voltage (V_{OC}), and the maximum power output can be written as

$$P_{max} = \frac{V_L^2}{R_L} = \frac{V_{OC}^2}{4R_L} = \frac{S^2(T_{hot} - T_{cold})^2}{4R_L} \tag{9.12}$$

When estimation of a TEG performance, the power density and efficiency are two important parameters for consideration. However, for practical applications, working environment, space, and mass should also be considered, because these are the main limitations for integration of TEGs into existing systems and architectures [30].

9.3   Organic Semiconductors for OTEs

Organic materials exhibit very low thermal conductivities compared to inorganic materials due to their naturally weak van der Waals bonding and disordered microstructures. This is accompanied by rather poor intrinsic electrical conductivities, and thus, organic materials have not been introduced for thermoelectric applications for a long time [31]. Organic semiconductors for TE applications require even higher electrical conductivities than those applied for OPV or OFET applications. Recent development in the doping techniques enables improvements in the electrical conductivity of organic semiconductors through control over the charge carrier concentration, [32, 33] optimization of the nanoscopic morphology, [34] modulation of transport pathways, [35] low-dimensional compounds with pronounced spatially anisotropic correlations of their electronic systems, [36] and control over the structural anisotropy in copolymer thin films [37, 38]

At present, most of the OTE materials are polymers. Recently, hybrid TE systems have demonstrated remarkable improvements where different types of materials are systematically combined to effectively guide the leading parameters of thermoelectric transport. All the OTE materials can be divided into three categories, polymers, small molecules, and organic–inorganic hybrid materials. Three subcategories of polymers part have been established in the form of conjugated polymers, coordination polymers and carbon nanotubes (CNT)/polymer composites.

9.3.1 Polymers

9.3.1.1 Conjugated Polymers
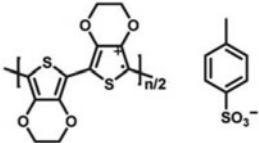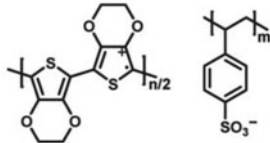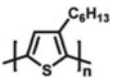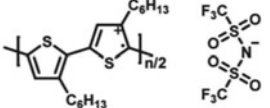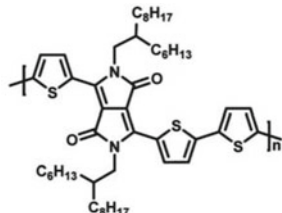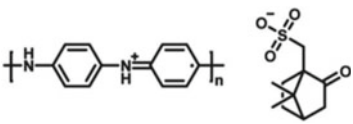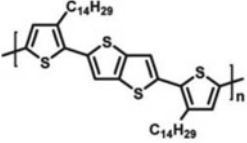
In the early research of organic TE, conjugated polymers such as polystyrene, polyaniline, polypyridine, polyacetylene, and metallized polymers have been studied because of their reasonable conductivity, good chemical stability, and ease of processing. Some of the recent OTE materials are shown in Tables 9.1 and 9.2. Among these studied conjugated polymers, PEDOT and its derivatives have high conductivity (around 300 S cm^{-1}) and high stability, so they have significant properties and play a leading role in electrical and electronic applications [39]. Poly(styrene sulfonic acid) (PSS) is always introduced as the charge-balancing dopant with PEDOT for high solubility in water. However, an intrinsically low carrier concentration in conjugated polymers leads to poor electrical conductivity.

Doping is a common approach to increase carrier concentration, which provides an effective method to improve conductivity and PF. In a doping process, carriers are considered as polarons and bipolarons, which lead to local deformation of carriers in molecular structures. The doping level has an important influence on the local hopping or delocalized diffusion of molecules, which is related to the morphology and stacking behavior of molecules. A small amount of doping can significantly improve the conductivity of the polymer [40]. For PEDOT, due to the positive charge, the counter ion of the dopant is used to balance the charge, which affects the electrical properties [41]. PEDOT with iron tosylate (Tos) as the dopant forms a PEDOT-Tos complex. In this study, the ZT value reached 0.25. With the increase of doping level, the conductivity increases from around 6×10^{-4} S cm^{-1} to 300 S cm^{-1}. However, due to the contradict trend between the electrical conductivity and the Seebeck coefficient, precisely controlling the oxidation level of PEDOT is very important for doping and optimizing PF. It has been reported an electrochemical method to control the carrier concentration of PEDOT [42]. A maximum *PF* of up to 1270 mW m^{-1} K^{-2} was obtained when the electrical conductivity was around 1000 S cm^{-1}, which is only half of the highest electrical conductivity of PEDOT. The electrochemical method shows the possibility of the precise control of the oxidation level and the optimization of polymerization conditions.

Apart from doping, solvent treatment is also used to optimize the polymer's PF. Formamide, [43] dimethyl sulfoxide (DMSO), [17] polyethylene glycol (PEG), [44]. N,N-dimethylformamide (DMF), [45] and salt solution [46] instead of water can significantly increase the conductivity of PEDOT:PSS to 2000 S cm^{-1}.
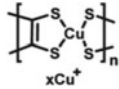
It has been confirmed that p-type polymers have been more widely studied than n-type polymers. The power factor of n-type polymer is significantly lower than that of p-type material. The conductivity of p-type polymer is more than 1000 S cm^{-1}, and the power factor is about 500 μWm^{-1} K^{-2}. In contrast, very few n-type counterparts have conductivity greater than 10 S cm^{-1} and power factor greater than 10 μWm^{-1} K^{-2}, [58, 59] which indicates the need to better develop n-type organic TE materials. The LUMO energy level of n-type polymer has an important influence

Table 9.1 Summary of thermoelectric properties of selected p-type organic semiconductors

Material	Structure	σ (S cm^{-1})	PF (μW mK^{-2})	Ref.
PEDOT-tosylate		117	1270	[42]
PEDOT:PSS		72.6	469	[17]
P3HT		39.5	31	[47]
P3HT:TFST		51	23.9	[47]
PDPP3T		70	25	[48]
PANI:CSA		34	19	[49]
PBTTT-C$_{14}$		32.7	109	[50]

Table 9.1 (continued)
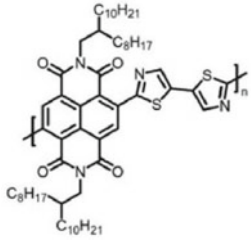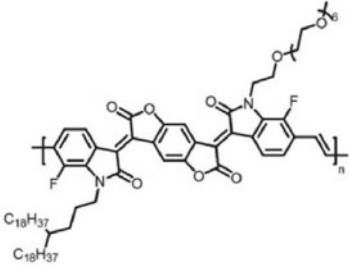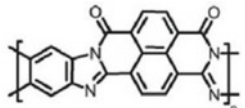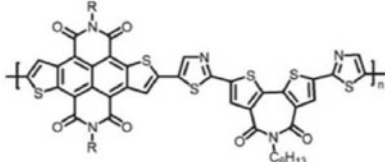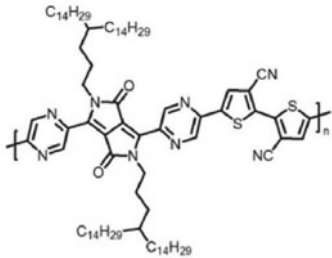
Material	Structure	σ (S cm^{-1})	PF (μW mK^{-2})	Ref.
Poly[Cux(Cu-ett)]		83	6.5	[51]

on the nitrogen doping efficiency. Reducing the LUMO energy level of conjugated polymer can expand the energy offset between polymer and n-dopant and promote electron transfer in thermodynamics, resulting in effective n-doping [59]. In addition, the miscibility between polymer and dopant has a great influence on the phase separation of doped film, which affects the optimal loading of dopant. Improving the miscibility between polymer and dopant is considered to be an effective strategy to improve the conductivity and TE properties of n-type polymer [60].

Table 9.2 shows some typical n-type polymer for TE applications. One of the representative systems is doping the recent developed n-type polymer, poly{N,N'-bis(2-octyl-dodecyl)-1,4,5,8-napthalenedicarboximide-2,6-diyl]-alt-5,5'-(2,2'-bithiophene)} (P(NDI2OD-T2)), which is the pioneer of n-type material with enhanced performance after doping [61]. Since then, various types of n-type polymers have been developed as well as improved TE performance [53, 55, 56]. Those new n-type TE polymer can be classified into seven categories as follows: poly(p-phenylene vinylene) (PPV) derivatives, [53, 62, 63]. NDI derivatives, [52, 64, 65] benzimidazo-based ladder-type (BBL) polymer, [54] naphthodithiophene diimide (NDTI)-based copolymers, [55, 66] bithiazolothienyl-tetracarboxydiimide (DTzTI)-based homopolymer, [67] diketopyrrolopyrrole (DPP)-based copolymers [56, 68], and emerging organoboron polymers [57] The dopant is a crucial factor to affect device performance. Most of them are based on TAM, TDAE, or N-DMBI [58].
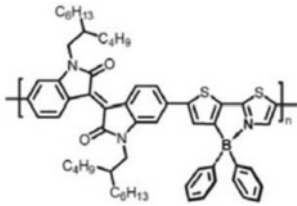
For NDI derivatives, Chabinyc et al. firstly introduced 4-(1,3-dimethyl-2,3-dihydro-1H-benzoimidazol-2-yl)-N,N-dimethylaniline (N-DMBI) as a dopant. After optimization of backbone and side chain, planar configurated PNDI2TEG-2Tz was developed with a maximum conductivity of 1.8 S cm^{-1} and a PF of 4.5 μW m^{-1} K^{-2} after doping N-DMBI [64]. Pei et al. used an n-dopant, trisaminomethane (TAM) with UFBDPPV and achieved a PF of u 92.0 μWm^{-1} K^{-2} and a conductivity of 25.0 S cm^{-1}, which is the highest performance reported for n-type polymers. A polymer LPPV-1 with high stability was also reported, the PF of which only degraded 2% after exposing in air for 7 days [53]. A typical n-type ladder polymer BBL was developed and exhibited a maximum conductivity of 2.4 S cm^{-1} after doping with TDAE. Homopolymer PDTzTI with high crystallinity was developed, which facilitates charge transport [69]. P(PzDPP-CT2) was developed with the lowest LUMO level among those copolymers based on DPP, which delivered a conductivity of 8.4 S cm^{-1} and a PF of 57.3 μWm^{-1} K^{-2} after doping with N-DMBI [56]. Furthermore, organoboron polymers based on the boron nitrogen coordination bond (B $\leftarrow$ N) were

Table 9.2 Summary of thermoelectric properties of selected n-type organic semiconductors

Material	Structure	S (μV K^{-1})	σ (S cm^{-1})	Ref.
P(NDI2OD-Tz2)		0.1	1.5	[52]
UFBDPPV		25	92	[53]
BBL		2.4	0.43	[54]
pNB-TzDP		11.6	53.4	[55]
P(PzDPP-CT2)		8.4	57.3	[56]

Table 9.2   (continued)

Material	Structure	S (μV K^{-1})	σ (S cm^{-1})	Ref.
PI-BN		0.001	0.02	[57]

used for TE application. The LUMO level of polymer PI-BN with B $\leftarrow$ N exhibited a drop of 0.3 eV and delivered a PF of 0.02 μW m^{-1} K^{-2} and conductivity of 0.001 S cm^{-1} [57].

9.3.1.2   Coordination Polymers

Coordination polymers (CPs) are complexes based on metal ions and organic ligands. In this case, metal ions act as connectors and ligands act as linkers. Since the 1960s, the research of coordination polymers has mainly focused on many topics, such as chirality, luminescence, magnetism, catalysis, and conductivity, while there are few studies related to the thermoelectric properties of CPs [70, 71]. The first promising CPs for thermoelectrical application were a series of ligands based on 4,40-dihydroxy- 3,30-diacetyl biphenyl bis-thiosemicarbazone (L-1) and 4,40-dihydroxy-3,30-dipropionyl biphenyl bis-thiosemicarbazone (L-2) [72]. However, poor thermoelectric properties of the synthesized CPs Cu(L-1) and Cu(L-2) was observed and their conductive characters are close to insulator. Zhu et al. developed a representative CP poly[Ax(M-ett)]. in 2012, which exhibited a high electrical conductivity of 63 S cm^{-1} and a Seebeck coefficients around -200 mV K^{-1} [51].

Recently, the family of metal–organic frameworks (MOFs) has aroused further interest in TE research. When the iron framework and the 1,2,3-triazolate (tri) ligand in Fe (TRI) 2 are oxidized to Fe(tri)$_2$(BF$_4$)$_{0.33}$ state, the conductivity increases by 8 orders of magnitude [73]. Moreover, these materials have broad application prospects not only in the field of thermoelectricity, but also in the field of organic electronics.

9.3.1.3   Carbon Nanotubes/polymer Composites

Carbon nanotubes have a unique one-dimensional structure, which has attracted extensive attention in the preparation of thermoelectric materials. It was mentioned that one-dimensional nanomaterials theoretically give better thermoelectric performance than multi-dimensional materials [74, 75]. Thermoelectric efficiency can be

significantly improved by increasing the mobility of carbon nanotubes in the rectangular direction, or by reducing the diameter of carbon nanotubes to reduce the thermal conductivity. CNTs have extremely high mobilities and thermal conductivities [76]. Optimizing the synergistic effect and reducing the conductivity and thermal conductivity are the most crucial factors in the preparation of high-efficiency thermoelectric materials.

Because holes are the main carriers, CNTs are considered to be a typical p-type TE material. However, it was reported that CNT demonstrates the properties of n-type TE materials under a vacuum environment [77]. Their research suggests that the Seebeck coefficient is sensitive to the concentration of ambient oxygen [78]. CNT can also show n-type TE properties in an atmospheric environment with different dopants. Therefore, the flexible transformation of carbon nanotubes from p-type to n-type broadens the potential applications of carbon nanotubes in the field of organic electronics.

In most cases, after being doped by oxidative dopant, CNT has been considered as a p-type TE material. PANI/MWCNT polymer composite nanofibers was developed and CNT and polymer nanofibers exhibit alignment and orientation along the same axis, exhibiting superior anisotropic thermoelectric performance [79]. Meng et al. developed a simple method to prepare high-performance PANI/CNT sheet composites. At 300 K, compared with neat carbon CNTs ($12.2\,\mu V\,K^{-1}$) and pure cyanamide ($2.74\,\mu V\,K^{-1}$), its Seebeck coefficient is as high as $22.4\,\mu V\,K^{-1}$, which shows that PANI coating is a promising and effective method to improve the properties of TE materials [80]. Gao et al. used in situ oxidation reaction to oxidize thiophene [3,4-b] pyrazine (TP) to TP dinitroxide (TPNO) on the surface of SWCNT and proposed a new synthesis strategy. With the decrease of TPNO/SWCNT mass ratio, the conductivity increased from 2.0 to $382\,S\,cm^{-1}$. The Seebeck coefficient decreases with the increase of SWCNTs concentration. DMSO-treated samples have the highest conductivity, $185\,S\,cm^{-1}$, and the highest power factor, $17\,\mu W\,m^{-1}\,K^{-2}$ [81]. The Seebeck coefficient of P3HT/CNT devices prepared by Hong et al. through spray printing is $97\,\mu V\,k^{-1}$, conductivity $345\,s\,cm^{-1}$, PF $325\,W\,mK^{-2}$; the Seebeck coefficient of thermoelectric material prepared by drip method is $102\,\mu V\,k^{-1}$, conductivity $224\,S\,cm^{-1}$, power factor $234\,\mu\,WmK^{-2}$ [82]. The improvement of the performance of the spay-printing device is attributed to the improvement of the beam connection density among CNTs. Lee et al., fabricated a DWCNT/PEDOT:PSS nanocomposite film and used ethylene glycol (EG) for post-treatment [83]. The EG treatment removed most of the uncomplicated PSS molecular chains, effectively reduced the distance between DWCNTS and bundles in the composite film, and significantly improved the conductivity of the composite. Hsu et al. prepared PEDOT:PSS/CNT and post-treating in dimethyl sulfoxide (DMSO) or formic acid (FA) [83]. After DMSO or FA treatment, the conductivity of PEDOT:PSS/CNT increased from 0.31 $S\,cm^{-1}$ to $1.8 \times 10^3\,S\cdot cm^{-1}$. The CNT network with good permeability and connectivity is formed in the complex, which is conducive to the transportation of the carrier. The Seebeck coefficient and PF value of the PEDOT:PSS/CNT composites reached the maximum value of $59\,\mu V\,K^{-1}$ and $464\,\mu W\,m^{-1}\,K^{-2}$, respectively.

Strategies to convert p-type CNTs into n-type carbon nanotubes include chemical reduction and low molecular doping. After doping, due to the charge transfer between CNTs and dopants, the Fermi level moves upward to the conduction band of CNTs. Therefore, the Fermi level is close to the conduction band, which realizes the conversion from p-type CNTs to n-type CNTs, and finally reduces the conductivity [84]. N-type dopant polyethyleneimine (PEI) was introduced into the p-type composites of CNT and poly(vinylidene fluoride) (PVDF) to realize the conversion from p- to n-type. From p-type to n-type, the final Seebeck coefficient reaches $-32.5\,\mu V\,K^{-1}$ [85]. CNT can also be doped with conjugated polyelectrolytes (CPEs). It was found that n-type and p-type can be prepared by doping the cationic CPEs and anionic CPEs to the CNT, respectively [86]. Kim et al. fabricated SWCNT/PEDOT:PSS composite fibers in a methanol/coagulation system. The samples were immersed in hydrazine solutions and PEI-infiltration and the transformation from p-type to n-type was realized, in which the PF of p-type is $83.2\,\mu W\,m^{-1}\,K^{-2}$ and an PF of n-type is $113\,\mu W\,m^{-1}\,K^{-2}$ [87]. SWCNT/PEDOT composites treated with TDAE can obtain a high PF of $1050\,\mu W\,m^{-1}\,K^{-2}$. TDAE treatment convert the PEDOT into n-type and the Seebeck coefficient became $-4.3\,mV\,K^{-1}$ [88].

CNTs/conductive polymer composites are considered to be very promising materials because of the high conductivity of CNTs, the low thermal conductivity of polymers and the improved Seebeck coefficient through structural optimization. The TE properties of CNTs/polymer composites can be further improved by post-treatment and doping. Besides, a lot of attention was paid on CNT-based composites for further TE application in wearable devices, due to their properties of easier processability and good flexibility.

9.3.2 Small Molecules

The research in the field of small molecules lags behind the field of conductive polymers. However, there are few exceptions, such as pentacene, C_{60} and some thiobenzene derivatives, which can transfer the Seebeck coefficient in the range of $mV\,K^{-1}$. However, small molecular TE materials are very attractive is because of easy purification and crystallization. Besides, it may be more feasible to achieve n-type conduction in small molecules.

TE interest is increasingly on so-called strong charge transfer complexes. In parallel with polymers, charge transfer complexes are another type of highly conducting organic material. Most of these complexes are based on derivatives of tetrathiafulvalenes (TTFs) which were in the focus of organic semiconductor research during the 1980–90 s [89]. In one of the organic conductors TTF-TCNQ, a charge transfer complex is formed between electron donor TTF and electron acceptor tetracyanoquinodimethane (TCNQ), and the donor and acceptor molecules are stacked into a one-dimensional column separately. TTF-TCNQ single crystals exhibit high electrical conductivities but low Seebeck coefficient ($-28\,mV\,K^{-1}$). The ZT value of TTF-TCNQ crystal was calculated to be $0.7–1.1 \times 10^{-2}$. The

ZT values of iodine-doped tetrathiotetraene (TTT_2I_3) and copper dicyanoquinone diamine ($Cu(DCNQI)_2$) single crystals are 0.03 and 0.2, respectively, and their p-type conductivity and n-type conductivity are about 103 s cm-1, respectively. A ZT value of more than 0.15 is then achieved by $Cu(DCNQI)_2$, which is one of the highest values for n-type OTE materials [90]. Recently, apart from charge transfer complexes, DPP or fullerene derivatives were further introduced for high-performance OTE devices. Huang et al. developed two DPP derivatives with aromatic and quinoid structures, respectively. The chemically doped A-DCV-DPPTT with aromatic structure exhibits an electrical conductivity of 5.3 S cm^{-1} and a PF up to 236 μW m^{-1} K^{-2}, which is 50 times higher than that of Q-DCM-DPPTT with a quinoid structure. Due to the low thermal conductivity, a ZT of 0.23 was achieved by DCV-DPPTT [91]. Liu et al. reported molecular n-doped fullerene derivatives, whose side chain design is meticulous and are close to organic "PGEC" TE materials. [18]. The conductivity of this "PGEC" is over 10 S cm^{-1}, the thermal conductivity is lower than 0.1 W m^{-1} K^{-1}, and its best value ZT = 0.34, which is the best reported ZT value of n-type TE material. This study shows the great potential of fullerenes as TE materials.

9.3.3 Organic–Inorganic Hybrid Materials

Recently, another method to promote TE research is to combine organic materials with nanoparticles to form a nanocomposite hybrid system. The design of polymer-inorganic TE composites provides a promising method to overcome the low conductivity, low Seebeck coefficient, low PF of polymers and the high cost of inorganic reagents.

PANI–inorganic thermoelectric nanomaterials have been reported, in which PANI is mixed with various metal oxides, such as $BaTiO_3$, V_2O_5, $Ca_3Co_4O_9$, Bi, BiCuSeO, Bi_2Te_3, PbTe, and $NaFe_4P_{12}$ [92]. Toshima et al. synthesized PANI-$Bi2Te_3$ nanohybrids, in which the device showed an increase in the Seebeck coefficient and TE performance [93]. They have also prepared hybrid materials of PANI with Au nanoparticles. The conductivity of the obtained hybrid nanostructure is as high as 330 S cm^{-1} and the Seebeck coefficient is 15 μV m^{-1} K^{-1} [94]. In 2013, Toshima et al. also hybridized PANI with Pt and Au nanoparticles. They used PVP-protected Pt and Au nanoparticles (NPs) to mix with PANI to prepare a hybrid material, which doubled the ZT values [95].

Apart from CNT, inorganic materials, such as Bi_2Te_3, $Ca_3Co_4O_9$ compounds, Au noble-metal nanoparticles and Te nanorods, are frequently mixed with PEDOT:PSS to form hybrid composites. Hybrids of Te nanorods and PEDOT:PSS was synthesized. The Seebeck coefficient of the hybrids was found to be 144.1 V m^{-1} K^{-1}, which is much higher than that of the polymer [19]. The high electrical conductivity of these hybrid films (19.3 S cm^{-1}) has been attributed to the improvement of particle to particle contact as well as the prevention of oxidation of Te nanorod by PEDOT:PSS. ZT reached a high value of 0.1 at room temperature. Zhang et al. found that the PF of PEDOT:PSS can be enhanced by incorporating either p- or n-type Bi_2Te_3 powders

into the composites, a result of the enhancement of the Seebeck coefficient and the electrical conductivity, respectively [96]. Liu et al. mechanically blended $Ca_3Co_4O_9$ powder with a PEDOT:PSS solution to synthesize PEDOT:PSS/$Ca_3Co_4O_9$ composite films [97]. The effect of Au nanoparticles on the TE performance of PEDOT polymers was investigated. Hybrid films of PEDOT:PSS with Au nanoparticles were prepared, which were protected by two kinds of ligands (terthiophenethiol and dodecanethiol). The Au nanoparticles, which was protected by dodecanethiol, had improved electrical conductivity and ZT value from 104 S cm^{-1} to 241 S cm^{-1} and from 0.62×10^{-2} to 1.63×10^{-2}, respectively [94]

The above research shows that the incorporation of inorganic semiconducting materials provides a promising method to improve the ZT and PF of polymers. However, this type of composite still has some limitations. Firstly, the addition of inorganic nanoparticles may introduce some toxic elements. Secondly, inorganic nanoparticles have a significant impact on the flexibility of the composite, significantly increasing the density of the composite. Thirdly, the practical application of some complex superlattice processes should be limited. Therefore, more problems need to be considered in the process of material design and synthesis.

9.4 Strategies for Better Performance of TE Devices

As mentioned in previous sections, high Seebeck coefficient, high electrical conductivity, and low thermal conductivity are required for maximizing the ZT value of an OTE device. However, the decoupling of S, σ and κ (Fig. 9.2) values requires OTE materials with balanced molecular structures and proper fabrication techniques. This section will discuss the molecular design and fabrication strategies for enhancement of PF and ZT values in OTE devices.

9.4.1 Molecular Design of Organic Thermoelectric Materials

From the relationship between structure and properties, an ideal OTE material should have tunable carrier concentration and high carrier mobility, which is closely related to the interaction between host molecules and dopant, energy-level position, and intermolecular stacking order. The energy level is directly related to the main chain structure of the molecule, while the miscibility and self-assembly order are related to the properties of the side chain. Therefore, the molecular design of new backbone and side chains is essential for the fine-tuning of TE performance.

The energy-level and doping efficiency are the key to determine electrical conductivity. Electrical conductivity is affected by π-electron coupling level, which requires close contact between molecules to promote effective charge transfer. Therefore, the conjugated framework with planar structure can achieve more efficient electronic coupling. In principle, the conjugated skeleton will strongly affect the electronic

structure, energy-level shift, and planarity of conjugated molecules, which is very important for improving intermolecular interaction, carrier density (n, Eq. (9.8)), and charge transfer between host materials and dopants. Obviously, the reasonable design of conjugated backbone is very important for the study of high-performance OTE materials.

9.4.1.1 Backbone and Substituent Effect

The conjugated backbone is the key factor to determine the molecular energy level, doping efficiency, and the planarity of conjugated molecules. By adding electron-rich or electron-deficient units for molecular modulation, targeted n-type and p-type OTE materials can be achieved. The conjugated units are connected by two structures: One is in the aromatic mode of single bond connection between monomers, and the other is in the quinone form of double bond connection [91]. Although the molecular geometry is similar, the two different connection methods will lead to significant differences in the distribution of electrons along the framework, which will cause differences in energy levels and doping efficiency [91].

By introducing electron withdrawing elements (such as halogen atoms) into the electron-rich part, the electronic structure can be fine-tuned to make the LUMO level deeper and the n-type doping efficiency higher. [98]. For example, the absorption ability of electrons can be improved by fluorine atoms electrostatic effect and sigma induction effect. In addition, the addition of fluorine substituents not only gives the stability of doped materials, but also provides low surface energy, high rigidity and various properties of self-assembly in solid state. Low LUMO levels can be observed from poly(p-styrene) (BDPPV) derivatives, which make them the most electron-deficient polymers [65]. Other studies have shown that TE performance can be affected by electron-withdrawing modification of donor units. Pei et al. reported two DPP-based D-A copolymers, PDPH and PDPF, in which the halogen atom is the electron withdrawing group. PDPF has low LUMO level and multi-polymer filling orientation. Different transition regions are introduced to accommodate more dopants and doped cations, so as to improve the doping efficiency and avoid phase separation [68]

9.4.1.2 Side Chain Engineering

In OTE materials, the engineering of side chain causes solubility enhancement as well as the intermolecular packing and the optoelectronic properties. Side chain length, polarity, and self-doping properties could affect the miscibility, self-doping properties, and self-assembly packing order of OTE materials.

Wang et al. demonstrated naphthodithiophene diimide (NDTI)-based copolymers, in which the side chain was modified from 2-decyltetradecyl (DT) to 3-decylpentadecyl (DP) [55]. Due to the increased length, the polymer with DP exhibited improved packing order and resulted in perpendicular orientations of the π–π

stacking planes. In addition, the bimodal orientation provides better accommodation of dopant molecules.

Polar side chains are of interest because they can enhance the solubility of ionic free groups in polar solvents and are easy to complex with metal ions. For example, hydrophilic oligomer (ethylene glycol) chains have been widely used to improve the processability of solutions. From the perspective of chemical doping, the good miscibility between dopant and matrix can improve the doping efficiency [18, 99]

The materials with electron-rich and electron-deficient parts realize self-doping and obtain high conductivity without external doping. Self-doping is a novel approach, which can avoid the disadvantages of doping without interrupting the order of packing. Designing stable radical molecules and incorporating ionic side chains are two main approaches for self-doping. Radical molecules based on perylene imide (PDI) can show a very small energy band gap, promoting free carriers through thermal activation and facilitating carrier transport by enhancing orbital overlap [100]. Ionic side chains with conjugated backbone can generate conjugated polyelectrolytes (CPEs), which provides a unique method for developing water-soluble or polar-soluble OTE materials [101]. Compared with conventional-doped organic semiconductors, the doping level of self-doped materials is still too low for high-performance OTE materials. However, these materials still have the potential to develop the most advanced and stable OTE materials through alternative methods.

9.4.2   Fabrication Strategy of Organic Thermoelectric Generators

Compared to inorganic counterparts, organic TEGs can be processed by printing, because solution processing can be used for polymers at room temperature. In recent years, several printing technologies have been studied.

PEDOT:PSS and silver paste were deposited on paper by screen printing [102]. OTE modules can be fabricated by the screen printing technique, which is simple and easy to use [103]

It was reported that ink-jet printing was applied to fabricate TEG modules from PEDOT:Tos and TTF-TCNQ, [32] which achieved a maximum power output of 0.128 mW at a temperature gradient of 10 K and a power density of around 0.27 mW cm^{-2}.

Roll-to-roll (R2R) printing technique was also applied for printing large-scale OTE generators [104]. Although only a low power output was estimated in this device, the potential for mass production of organic TE devices at low cost is promising.

Production of OTEG pellets is another method of fabricating TE devices, because the OTE materials are difficult to be printed [105]. Due to the poor crystallinity of pellets and their low conductivity, TE performance is usually lower than that of thin films.

9.5   Conclusions and Perspectives

Organic semiconductor-based TE materials have developed rapidly in recent years. However, their molecular types are limited, their stability is relatively low, and their performance is not ideal. Many challenges must be overcome to unleash their inherent potential. Tremendous efforts should be paid on molecular design of OTE materials bearing conjugated backbones with balanced molecular doping and ordered assembly as well as side chains with new functionality.

At the molecular level, S, σ, and κ optimization is the key to prepare high-performance OTE materials. The traditional molecular design relies on taking the backbone composed of conjugated units and introducing variation to study the afore-mentioned effects. The comparison results show that the proposed design concept is justified without systematically considering the doping effect. It should be concerned that the dopant should be taken into account when investigating relevant structure–property relationships. A synthetic approach to systematically modify the structure of the host molecules and dopants should be required. We are committed to creating new molecular engineering approaches for high-performance, multifunctional, and stable OTE materials. We hope to convey some exciting opportunities of designing next-generation OTE materials in this chapter.

In addition to the performance optimization of OTE, future application of OTE devices is a practical consideration. So far, due to the high performance of inorganic materials, most commercial TE research and applications are mainly achieved by inorganic materials, but its inherent brittleness is a key obstacle to wearable applications and shape compatibility of uneven heat source surfaces. For these innovative applications, OTE is one of the most promising ways to realize new functions such as flexibility, portability, and stability. Therefore, in addition to the need for performance optimization through material design, there is also an increasing need for novel concept for device processing. The flexibility and solution processability of organic semiconductors enable OTEs to have huge potential in wearable uses. In conclusion, although organic semiconductors have shown comparable performance with inorganic semiconductors, the research and development field of OTE is still in its infancy. We believe that further research in OTE field could realize commercial applications of this technology with green sustainable energy.

References

1. Snyder GJ, Toberer ES (2008) Complex thermoelectric materials. Nat Mater 7:105–114
2. Heeger AJ (2001) Semiconducting and metallic polymers: the fourth generation of polymeric materials (nobel lecture). Angew Chem Int Ed 40:2591–2611
3. Zhang Q, Sun Y, Xu W, Zhu D (2014) Organic thermoelectric materials: emerging green energy materials converting heat to electricity directly and efficiently. Adv Mater 26:6829–6851
4. Forman C, Muritala IK, Pardemann R, Meyer B (2016) Estimating the global waste heat potential. Renew Sustain Energy Rev 57:1568–1579

5. Br RWD, Phys JA (1954) The use of semiconductors in thermoelectric refrigeration the use of semiconductors in thermoelectric refrigeration. Br J Appl Phys 5:386
6. Heremans JP, Dresselhaus MS, Bell LE, Morelli DT (2013) When thermoelectrics reached the nanoscale. Nat Nanotechnol 8:471–473
7. Environ E, Zebarjadi M, Esfarjani K et al (2012) Perspectives on thermoelectrics: from fundamentals to device applications. Energy Environ Sci 5:5147–5162
8. Coninunications SS, Park YW, Denenstein A et al (1979) Semiconductor-metal transition in doped (CH)x:thermoelectric power. Solid State Commun 29:747–751
9. Dyes P (2004) Thermoelectric power of some organic photoconducting dyes. J Chem Phys 42:3922
10. Blythe BYAR, Boon MK, Wright PG (1971) Measurement of seebeck and hall effects in compactions of TCNQ salts. Discuss Faraday Soc 51:110–115
11. Marks BTJ (1990) Interfaces between molecular and polymeric "metals": electrically conductive, structure-enforced assemblies of metallomacrocycles. Angew Chem Int Ed 29:857–879
12. Kaiser AB (1989) Thermoelectric power and conductivity of heterogeneous conducting polymers. Phys Rev B 40:2806–2813
13. Walzer K, Maennig B, Pfeiffer M, Leo K (2007) Highly efficient organic devices based on electrically doped transport layers. Chem Rev 107:1233–1271
14. He M, Feng Qiu ZL (2013) Towards high-performance polymer-based thermoelectric materials. Energy Environ Sci 6:1352–1361
15. You A, Be MAY, In I (2015) Thermoelectric and bulk mobility measurements in pentacene thin films. Appl Phys Lett 093303:96–99
16. Sumino M, Harada K, Ikeda M et al (2011) Thermoelectric properties of n-type C60 thin films and their application in organic thermovoltaic devices. Appl Phys Lett 99:093304
17. Kim GH, Shao L, Zhang K, Pipe KP (2013) Engineered doping of organic semiconductors for enhanced thermoelectric efficiency. Nat Mater 12:719–723
18. Liu J, van der Zee B, Alessandri R et al (2020) N-type organic thermoelectrics: demonstration of ZT>0.3. Nat Commun 11:5694
19. See KC, Feser JP, Chen CE et al (2010) Water-processable polymer-nanocrystal hybrids for thermoelectrics. Nano Lett 10:4664–4667
20. Fahrnbauer F, Souchay D, Wagner G, Oeckler O (2015) High thermoelectric figure of merit values of germanium antimony tellurides with kinetically stable cobalt germanide precipitates. J Am Chem Soc 137:8–13
21. Qu S, Ming C, Yao Q et al (2018) Understanding the intrinsic carrier transport in highly oriented poly(3-hexylthiophene): effect of side chain regioregularity. Polymers (Basel) 10:815
22. Cho C, Stevens B, Hsu J et al (2015) Completely organic multilayer thin film with thermoelectric power factor rivaling inorganic tellurides. Adv Mater 27:2996–3001
23. Dai X, Meng Q, Zhang F et al (2021) Electronic structure engineering in organic thermoelectric materials. J Energy Chem 62:204–219
24. Xu Y, Sun H, Liu A et al (2018) Doping: a key enabler for organic transistors. Adv Mater 30:1801830
25. Yao H, Fan Z, Cheng H et al (2018) Recent development of thermoelectric polymers and composites. Macromol Rapid Commun 39:1700727
26. Zou Y, Huang D, Meng Q et al (2018) Correlation between seebeck coefficient and transport energy level in poly. Org Electron 56:125–128
27. You A, Be MAY, In I (2015) In-plane thermal conductivity of nanoscale polyaniline thin films. Appl Phys Lett 95:033113
28. Yee SK, Leblanc S, Goodson KE, Dames C (2013) $ per W metrics for thermoelectric power generation: beyond ZT. Energy Environ Sci 6:2561–2571
29. Leblanc S, Yee SK, Scullin ML et al (2014) Material and manufacturing cost considerations for thermoelectrics. Renew Sustain Energy Rev 32:313–327
30. Leblanc S (2014) Thermoelectric generators: linking material properties and systems engineering for waste heat recovery applications. Sustain Mater Technol 1–2:26–35

31. Zevalkink A, Smiadak DM, Blackburn JL et al (2018) A practical field guide to thermoelectrics : Fundamentals, synthesis, and characterization. Appl Phys Rev 5:021303
32. Bubnova O, Khan ZU, Malti A et al (2011) Optimization of the thermoelectric figure of merit in the conducting polymer poly(3,4-ethylenedioxythiophene). Nat Mater 10:429–433
33. Park T, Park C, Kim B et al (2013) Flexible PEDOT electrodes with large thermoelectric power factors to generate electricity by the touch of fingertip. Energy Environ Sci 6:788–792
34. Nanowires UEP, Taggart DK, Yang Y et al (2011) Enhanced thermoelectric metrics in ultra-long electrodeposited PEDOT nanowires. Nano Lett 11:125–131
35. Sun J, Yeh ML, Jung BJ et al (2010) Simultaneous increase in seebeck coefficient and conductivity in a doped poly(alkylthiophene) blend with defined density of states. Macromolecules 43:2897–2903
36. Kodak E, Fork W (1978) Magnetic susceptibility, electrical resistivity, and thermoelectric power measurements of bis(tetrathiotetracene)-triiodide. Phys Rev B 18:439
37. Hiroshige Y, Ookawa M, Toshima N (2006) High thermoelectric performance of poly(2,5-dimethoxyphenylenevinylene) and its derivatives. Synth Met 156:1341–1347
38. Hiroshige Y, Ookawa M, Toshima N (2007) Thermoelectric figure-of-merit of iodine-doped copolymer of phenylenevinylene with dialkoxyphenylenevinylene. Synth Matals 157:467–474
39. Wang H, Hsu J, Yi S et al (2015) Thermally driven large N-type voltage responses from hybrids of carbon nanotubes and poly (3, 4- ethylenedioxythiophene) with tetrakis (dimethylamino) ethylene. Adv Mater 27:6855–6861
40. Chiang CK, Fincher CR, Park YW et al (1978) Electrical conductivity in doped polyactylene—erratum. Phys Rev Lett 40:1472
41. Wan C, Tian R, Kondou M et al (2017) Ultrahigh thermoelectric power factor in flexible hybrid inorganic-organic superlattice. Nat Commun 8:1024
42. Park T, Park C, Kim B et al (2013) Flexible PEDOT electrodes with large thermoelectric power factors to generate electricity by the touch of fingertips. Energy Environ Sci 6:788–792
43. Kyaw AKK, Yemata TA, Wang X et al (2018) Enhanced thermoelectric performance of PEDOT:PSS films by sequential post-treatment with formamide. Macromol Mater Eng 303:1700429
44. Sun Z, Shu M, Li W et al (2020) Enhanced thermoelectric performance of PEDOT:PSS self-supporting thick films through a binary treatment with polyethylene glycol and water. Polymer (Guildf) 192:122328
45. Wei Q, Mukaida M, Naitoh Y, Ishida T (2013) Morphological change and mobility enhancement in PEDOT:PSS by adding co-solvents. Adv Mater 25:2831–2836
46. Fan Z, Du D, Yu Z et al (2016) Significant enhancement in the thermoelectric properties of PEDOT:PSS films through a treatment with organic solutions of inorganic salts. ACS Appl Mater Interfaces 8:23204–23211
47. Zhang Q, Sun Y, Xu W, Zhu D (2012) Thermoelectric energy from flexible P3HT films doped with a ferric salt of triflimide anions. Energy Environ Sci 5:9639–9644
48. Zhang Q, Sun Y, Xu W, Zhu D (2014) What to expect from conducting polymers on the playground of thermoelectricity: lessons learned from four high-mobility polymeric semiconductors. Macromolecules 47:609–615
49. Yan H, Ohta T, Toshima N (2001) Stretched polyaniline films doped by ($\pm$)-10-camphorsulfonic acid: anisotropy and improvement of thermoelectric properties. Macromol Mater Eng 286:139–142
50. Patel SN, Glaudell AM, Kiefer D, Chabinyc ML (2016) Increasing the thermoelectric power factor of a semiconducting polymer by doping from the vapor phase. ACS Macro Lett 5:268–272
51. Sun Y, Sheng P, Di C et al (2012) Organic thermoelectric materials and devices based on p- and n-type poly(metal 1,1,2,2-ethenetetrathiolate)s. Adv Mater 24:932–937
52. Wang S, Sun H, Erdmann T et al (2018) A chemically doped naphthalenediimide-bithiazole polymer for n-type organic thermoelectrics. Adv Mater 30:1801898

53. Lu Y, Di YuZ, Liu Y et al (2020) The critical role of dopant cations in electrical conductivity and thermoelectric performance of n-doped polymers. J Am Chem Soc 142:15340–15348

54. Wang S, Sun H, Ail U et al (2016) Thermoelectric properties of solution-processed n-doped ladder-type conducting polymers. Adv Mater 28:10764–10771

55. Wang Y, Takimiya K (2020) Naphthodithiophenediimide-bithiopheneimide copolymers for high-performance n-type organic thermoelectrics: significant impact of backbone orientation on conductivity and thermoelectric performance. Adv Mater 32:2002060

56. Yan X, Xiong M, Li JT et al (2019) Pyrazine-flanked diketopyrrolopyrrole (DPP): a new polymer building block for high-performance n-type organic thermoelectrics. J Am Chem Soc 141:20215–20221

57. Dong C, Meng B, Liu J, Wang L (2020) B ← N unit enables n-doping of conjugated polymers for thermoelectric application. ACS Appl Mater Interfaces 12:10428–10433

58. Meng B, Liu J, Wang L (2021) Recent development of n-type thermoelectric materials based on conjugated polymers. Nano Mater Sci 3:113–123

59. Lu Y, Wang JY, Pei J (2019) Strategies to enhance the conductivity of n-type polymer thermoelectric materials. Chem Mater 31:6412–6423

60. Boyle CJ, Upadhyaya M, Wang P et al (2019) Tuning charge transport dynamics via clustering of doping in organic semiconductor thin films. Nat Commun 10:2827

61. Schlitz RA, Brunetti FG, Glaudell AM et al (2014) Solubility-limited extrinsic n-type doping of a high electron mobility polymer for thermoelectric applications. Adv Mater 26:2825–2830

62. Shi K, Zhang F, Di CA et al (2015) Toward high performance n-type thermoelectric materials by rational modification of BDPPV backbones. J Am Chem Soc 137:6979–6982

63. Lu Y, Di YuZ, Zhang RZ et al (2019) Rigid coplanar polymers for stable n-type polymer thermoelectrics. Angew Chemie - Int Ed 58:11390–11394

64. Liu J, Ye G, van der Zee B et al (2018) N-type organic thermoelectrics of donor-acceptor copolymers: improved power factor by molecular tailoring of the density of states. Adv Mater 30:1804290

65. Kiefer D, Giovannitti A, Sun H et al (2018) Enhanced n-doping efficiency of a naphthalenediimide-based copolymer through polar side chains for organic thermoelectrics. ACS Energy Lett 3:278–285

66. Wang Y, Nakano M, Michinobu T et al (2017) Naphthodithiophenediimide-benzobisthiadiazole-based polymers: versatile n-type materials for field-effect transistors and thermoelectric devices. Macromolecules 50:857–864

67. Liu J, Shi Y, Dong J et al (2019) Overcoming coulomb interaction improves free-charge generation and thermoelectric properties for n-doped conjugated polymers. ACS Energy Lett 4:1556–1564

68. Yang CY, Jin WL, Wang J et al (2018) Enhancing the n-type conductivity and thermo-electric performance of donor-acceptor copolymers through donor engineering. Adv Mater 30:1802850

69. Shi Y, Guo H, Qin M et al (2018) Thiazole imide-based all-acceptor homopolymer: achieving high-performance unipolar electron transport in organic thin-film transistors. Adv Mater 30:1705745

70. Kaiser AB, Skákalováb V (2011) Electronic conduction in polymers, carbon nanotubes and graphene. Chem Soc Rev 40:3786–3801

71. Dubey N, Leclerc M (2011) Conducting polymers: efficient thermoelectric materials. J Polym Sci Part B Polym Phys 49:467–475

72. D'Sa JT, Rao VJ, Patel KC, Patel RD (1979) A study on the synthesis and electrical properties of chelate polymers. Die Angew Makromol Chemie 79:133–145

73. Park JG, Aubrey ML, Oktawiec J et al (2018) Charge delocalization and bulk electronic conductivity in the mixed-valence metal-organic framework Fe(1,2,3-triazolate)2 (BF4)x. J Am Chem Soc 140:8526–8534

74. Hong CT, Kang YH, Ryu J et al (2015) Spray-printed CNT/P3HT organic thermoelectric films and power generators. J Mater Chem A 3:21428–21433

75. Moriarty GP, Briggs K, Stevens B et al (2013) Fully organic nanocomposites with high thermoelectric power factors by using a dual-stabilizer preparation. Energy Technol 1:265–272

76. Lee W, Kang YH, Lee JY et al (2016) Improving the thermoelectric power factor of CNT/PEDOT:PSS nanocomposite films by ethylene glycol treatment. RSC Adv 6:53339–53344

77. Chen YC, Lee SC, Liu TH, Chang CC (2015) Thermal conductivity of boron nitride nanoribbons: anisotropic effects and boundary scattering. Int J Therm Sci 94:72–78

78. Liu FS, Zheng JX, Huang MJ et al (2010) Enhanced thermoelectric performance of single-walled carbon nanotubes/polyaniline hybrid nanocomposites. ACS Nano 4:2445–2451

79. Wang Q, Yao Q, Chang J, Chen L (2012) Enhanced thermoelectric properties of CNT/PANI composite nanofibers by highly orienting the arrangement of polymer chains. J Mater Chem 22:17612–17618

80. Hu X, Chen G, Wang X (2017) An unusual coral-like morphology for composites of poly(3,4-ethylenedioxythiophene)/carbon nanotube and the enhanced thermoelectric performance. Compos Sci Technol 144:43–50

81. Gao C, Chen G (2018) In Situ oxidation synthesis of p-type composite with narrow-bandgap small organic molecule coating on single-walled carbon nanotube: flexible film and thermoelectric performance. Small 14:1703453

82. Wang L, Yao Q, Xiao J et al (2016) Engineered molecular chain ordering in single-walled carbon nanotubes/polyaniline composite films for high-performance organic thermoelectric materials. Chem - An Asian J 11:1804–1810

83. Seo MK, Lee JR, Park SJ (2005) Crystallization kinetics and interfacial behaviors of polypropylene composites reinforced with multi-walled carbon nanotubes. Mater Sci Eng A 404:79–84

84. Wu G, Gao C, Chen G et al (2016) High-performance organic thermoelectric modules based on flexible films of a novel n-type single-walled carbon nanotube. J Mater Chem A 4:14187–14193

85. Montgomery DS, Hewitt CA, Barbalace R et al (2016) Spray doping method to create a low-profile high-density carbon nanotube thermoelectric generator. Carbon N Y 96:778–781

86. Mai CK, Russ B, Fronk SL et al (2015) Varying the ionic functionalities of conjugated polyelectrolytes leads to both p- and n-type carbon nanotube composites for flexible thermoelectrics. Energy Environ Sci 8:2341–2346

87. Kim JY, Lee W, Kang YH et al (2018) Wet-spinning and post-treatment of CNT/PEDOT:PSS composites for use in organic fiber-based thermoelectric generators. Carbon N Y 133:293–299

88. Wang H, Hsu JH, Yi SI et al (2015) Thermally driven large N-type voltage responses from hybrids of carbon nanotubes and poly(3,4-ethylenedioxythiophene) with Tetrakis(dimethylamino)ethylene. Adv Mater 27:6855–6861

89. Jérome D (2004) Organic conductors: From charge density wave TTF-TCNQ to superconducting (TMTSF)2PF6. Chem Rev 104:5565–5591

90. Huewe F, Steeger A, Bauer I et al (2015) Energy exchange between phononic and electronic subsystems governing the nonlinear conduction in DCNQI2Cu. Phys Rev B—Condens Matter Mater Phys 92:155107

91. Huang D, Yao H, Cui Y et al (2017) Conjugated-backbone effect of organic small molecules for n-Type thermoelectric materials with ZT over 0.2. J Am Chem Soc 139:13013–13023

92. Jin H, Li J, Iocozzia J et al (2019) Hybrid organic—inorganic thermoelectric materials and devices angewandte. Angew Chem Int Ed 58:15206–15226

93. Toshima N, Imai M, Ichikawa S (2011) Organic—inorganic nanohybrids as novel thermoelectric materials : hybrids of polyaniline and bismuth (III) telluride nanoparticles. J Electron Mater 40:898–902

94. Toshima N, Jiravanichanun N (2012) Organic thermoelectric materials composed of conducting polymers and metal nanoparticles. J Electron Mater 41:1735–1742

95. Toshima N (2013) Metal nanoparticles for energy conversion. Pure Appl Chem 85:437–451

96. Zhang B, Sun J, Katz HE et al (2010) Promising thermoelectric properties of commercial PEDOT: PSS materials and their Bi 2 Te 3 powder composites. Appl Mater Interfaces 2:3170–3178

97. Liu C, Jiang F, Huang M et al (2011) Free-standing PEDOT-PSS / Ca 3 Co 4 O 9 composite films as novel thermoelectric materials. J Electron Mater 40:948–952

98. Feng K, Guo H, Wang J et al (2021) Cyano-functionalized bithiophene imide-based n-type polymer semiconductors: synthesis, structure-property correlations, and thermoelectric performance. J Am Chem Soc 143:1539–1552

99. Liu J, Ye G, Potgieser HGO et al (2021) Amphipathic side chain of a conjugated polymer optimizes dopant location toward efficient n-type organic thermoelectrics. Adv Mater 33:2006694

100. Russ B, Robb MJ, Brunetti FG et al (2014) Power factor enhancement in solution-processed organic n-type thermoelectrics through molecular design. Adv Mater 26:3473–3477

101. Mai C, Schlitz RA, Su GM et al (2014) Side-chain effects on the conductivity, morphology, and thermoelectric properties of self-doped narrow-band-gap conjugated polyelectrolytes. J Am Chem Soc 136:13478–13481

102. Wei Q, Mukaida M, Kirihara K, Naitoh Y (2014) Polymer thermoelectric modules screen-printed on. RSC Adv 4:28802–28806

103. Wei Q, Mukaida M, Kirihara K et al (2015) Recent progress on PEDOT-based thermoelectric materials. Materials (Basel) 8:732–750

104. Espinosa N, Jørgensen M, Krebs FC et al (2013) Practical evaluation of organic polymer thermoelectrics by large-area R2R processing on flexible substrates. Energy Sci Eng 1:81–88

105. Miles MG, Wilson JD (1975) Semiconducting metal-organic salts. Inorg Chem 14:2357–2360

Chapter 10
Organic Memory Devices

Memory devices are used for storage of data and programs in modern technologies. Normally, a memory consists of many storage units/bits each of which has two stable states expressed as "0" and "1." The two states can convert to each other reversibly or irreversibly by applying electrical field to realize information storage or erase.

10.1 Common Memory Devices

With the ways of writing and erasing, the memory devices can be categorized as random access memory (RAM) and read-only memory (ROM). For the ROM, the information stored can only be read out and cannot be modified or deleted. ROM is often used to store fixed programs or tables. RAM is used to store input and output data on site, like results of calculation, exchange information with external memory devices. The memory units of RAM can be read, written, and modified. It can be used to store programs and data, once the electrical power is cutoff, the stored data will be lost. Presently, there are two types of RAMs dominated on the market: dynamic RAM (DRAM) and static RAM (SRAM). For the SRAM, the storage is realized with bistable flip-flops. While, for the DRAM, the information is stored with gate capacitance in MOS circuits. As the stored charge can leak, and it needs to be supplemented regularly with refresh circuit. But DRAM has high density, low-power consumption, and low-manufacturing cost property.

10.1.1 Capacitor-Based Memory

Capacitor-based memory mainly includes RAM and ROM, where DRAM is the particularly important type. The DRAM has following characteristics:

(1) Random access: Random access means that one can write and read information into/from any address at any time.
(2) Volatility: When the supplied electrical power is off, the stored information will be lost. For permanent storage, the data needs to be stored in other system, like hard disks.
(3) Sensitive to static electricity: Static electricity can interfere the charge stored in the devices which can lead data loss and even circuit burning out.
(4) High-access speed.

10.1.2   Field-Effect Transistor-Based Flash Memory

Flash memory is a non-volatile memory, where the stored information will not be lost if the supplied electrical power is switched off.

10.1.3   Other Types of Memory

There are other types of memory which are based on non-electronic devices, like hard disk and optical disks. A hard disk uses magnetic medium to store information. Information is stored in densely spaced permanent magnetic bits embedded in thin-film coated on a disk. A hard disk driver is formed with a stack of such disks and magnetic recording head. The magnetic head stores/erases information through switching the magnetization polarity of the bits and reads the information through sensing the local field of each bit. Optical disks are media where the stored information can be read out with light. Optical disks can be divided to non-erasable (CD-ROM, DVD-ROM, etc.) and erasable (CD-RW, DVD-RAM, etc.).

10.2   Organic Memory Devices

Organic memory devices are important for organic integrated circuits, like radio frequency identification (RFID) tags, large-area displays. There are mainly two types of organic memory devices: organic diode memory and organic field-effect transistor memory devices.

10.2.1 *Organic Diode Memory Devices*

10.2.1.1 Structure and Classification of Organic Diode Memory Devices

Diode memory device has sandwich structure, i.e., organic function layer (or layers) is sandwiched between two electrodes.

With the mechanism of electrical-current change, organic diode memory device (ODMD) can be classified into capacitance type and resistance type. For the capacitance type, the memory states are defined use stored electrical charges. The functional materials are organic dielectric materials, and the devices are mainly used for DRAM application. For general dielectrics materials, the stored charges may leak with time, and the stored states cannot remain for long time, i.e., the devices are volatile. To stabilize the stored information, charges need to be supplemented regularly to the capacitance devices with refresh circuit. If the functional materials of the devices are ferroelectrics, the information can be stored for much longer as a stable electrical polarization is generated in the ferroelectrics with applied electrical field. Such ferroelectrics-based diode memory devices are named as FeRAM. For the resistance-type devices, the states are signified with resistance, and the resistance states can be stably switched with externally applied field.

According to electrical characteristics, the memory devices can be classified into two types: volatile and non-volatile memory (Fig. 10.1). The volatile memory includes DRAM and SRAM. The DRAM requires a periodic refreshment with circuit, while the SRAM only needs continuous power supplying. The organic non-volatile memory mainly includes flash memory and write-once read-many memory (WORM). Flash memory is a type of devices that can be reprogrammed and erased electrically. WORM memory allows only to write information once and read out repeatedly, but the stored information cannot be modified. The main parameters used to evaluate the quality of memory devices are write voltage, memory window, retention time, write and erase speed, duration cycles, ON/OFF current ratio, etc. Among them, the memory window and retention time are the basic parameters. Generally, a low-write voltage is preferable, and less than 10 V operation voltage is required for non-volatile memory devices.

10.2.1.2 Working Mechanism of Organic Diode Memory Devices

For the capacitance type of ODMD, the memory states are signified use stored electrical charges. Such type of devices faces the problem of charge storage failure with the device size shrinking. Thus, resistance memory is considered as one of the most promising candidates for next-generation memories because of its simple structure, low cost, and high-density integration. Resistance change of device materials is mainly induced by the variation of charge density or mobility, or both. A series of mechanisms of resistance switch were proposed based on charge generation, charge traps, charge conduction processes.
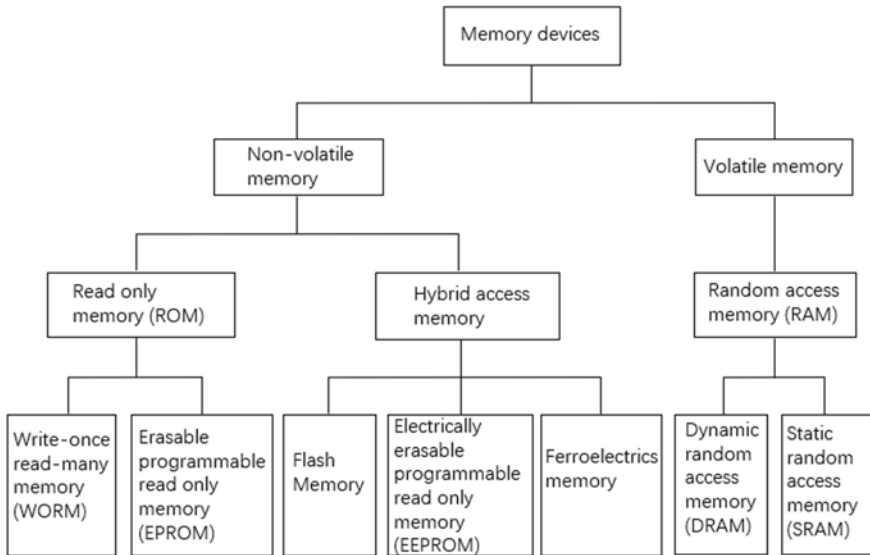
Fig. 10.1 Types of memory devices

(1) **Filamentary path conduction**

When a series of voltage pulses is applied to a diode formed with two metal electrodes and an organic film sandwiched between them, some metal atoms of the anode will be oxidized and migrate through the organic film to the cathode and be reduced there. With the increase of time, the reduced ions accumulate and form filaments gradually in the organic film. When a filament bridges the two electrodes, the device switches from a high-resistance state (HRS) to low-resistance state (LRS). After formation of the nanofilament, if the electrical field direction is reversed, the atoms of the filament will move back to the original active electrode through the same mechanism, which leads a fracture of the filament and the device occupies high-resistance state again. The formation and fracture of the nanofilament are reversible; therefore, the device is non-volatile and rewritable.

Joo et al. have reported a device with P3HT layer sandwiched between Cu and Al electrodes carried on Si substrate with 200 nm SiO_2 cover layer (Cu/P3HT/Al/SiO$_2$/Si) [1]. Al electrode was grounded during the device test, and typical switching behavior of the device is represented in Fig. 10.2. A sudden decrease in the device resistance was observed at -2 V as a result of the metal filament formation between two metal electrodes. The low-resistive state (set state) showed typical metal characteristics confirmed by low-temperature experiment where the resistance linearly increased with temperature. The set state was switched back to the initial high-resistive state (reset state) due to the fracture of filament by joule heating. Lee et al. have observed Ag filament formation and fracture in Ag/WPF-BT-FEO/P$^+$-Si device with TEM observation [2].

Fig. 10.2 Current–voltage (I-V) curve of Cu/P3HT/Al device which shows the non-volatile memory behavior. (Adopted from ref [1])
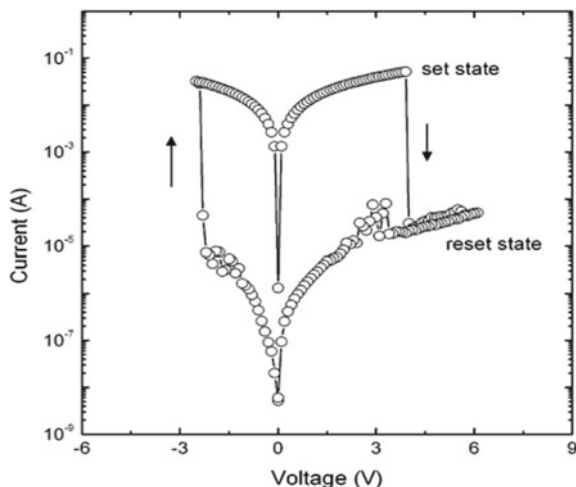
(2) **Space charge limitation and charge trapping**

As the electrical conductance of organic materials is much lower than metals, the injected charges from an electrode may accumulate in the organic layer nearby the electrode. These charges will introduce a field to screen the external field and induce a change of the device current. Figure 10.3 shows typical I-V curves of an organic diode made with a conjugated P6OMe polymer layer and ITO/Al electrodes [3]. A pronounced feature of the I-V curves is the hysteresis caused by space charges. The size of the hysteresis loop depends on the amplitude of scanning voltage. During the initial sweep from 0 to a positive voltage, a space charge layer of holes was established in the polymer film near the ITO electrode. With an increased voltage, space charges were stored in the device, and spatial distribution of such charges was established. When the voltage-sweep direction was reversed (from positive to 0), the device retained its spatial distribution of charge carriers. The stored charge induces a small positive voltage, open-circuit voltage (V_{OC}, clockwise sense of loop), which is required to balance the effect of the charges to maintain zero current. At zero voltage, a non-zero current was observed (short-circuit current I_{SC}), which is caused by the flow of stored charges. When the voltage was swept to a reversed bias, the negative current increased due to the injection of holes from the Al electrode, and space charges begin to form in the polymer layer near the Al electrode. During reversal of the sweep (from negative voltage to 0), the stored charges caused an open-circuit voltage and short-circuit current. The magnitudes of both V_{OC} and I_{SC} were higher when the voltage was swept with higher amplitudes (see the two loops in Fig. 10.3) because more charges are stored.

The space charges can be caused for many reasons, including charge injection from electrode, accumulation of mobile ions at surfaces of electrodes, etc. Such hysteresis loops can be used to make memory devices. The writing and erasing of the devices are realized through application of pulsed positive/negative voltage, while the
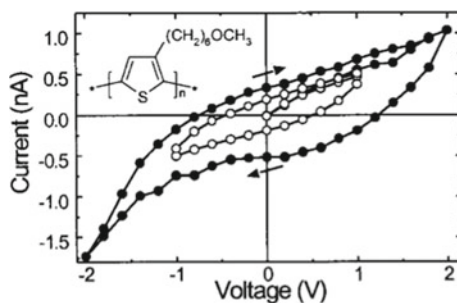
Fig. 10.3 Hysteresis behavior of current in a device with structure ITO/P6OMe/Al. Measurements were performed with voltage scan amplitudes of ± 1 V and ± 2 V at a 2.5 mV/s sweep rate. The inset shows the molecular structure of the polymer. (Adapted from ref [3])

reading is done by measuring the current under a small probe voltage. Traps formed at surface or inside of organic materials can be used for memory device development as the traps induce a change of charge mobility. Oxygen molecules in organic films [4], donor–acceptor structures in the film [5], metal, or semiconductor nanoparticles [6, 7] et al. can serve as trapping centers. With increase of applied voltage, more electrical charges are injected into polymer film to fill the traps gradually. When all the traps are filled, the charge injection will no longer be affected by the traps [8], and consequently, a sudden increase of current defines a switch from HRS to LRS.

(3) **Field-induced charge transfer**

The mechanism of field-induced charge transfer mainly applies in donor–acceptor (D-A) and organic/inorganic-nanoparticle hybrid systems. For the D-A systems, electron transfer occurs from donor to acceptor under external field which defines a switching between resistance states. Donor and acceptor can be in the same molecule or in different molecules. Charge transfer between donor molecule and acceptor molecule can form charge-transfer complex. Sun et al. have fabricated memory devices with device structure of ITO/PI-NT COF/LiF/Al, where the organic layer (PI-NT COF) contains TAPA donor and NTCDA acceptor [9]. Figure 10.4 shows the result of device characterization.

When the applied voltage gradually swept from 0 to 3 V, an abrupt increase of current occurred (curve 1 in Fig. 10.4a), switching from HRS to LRS state. The LRS was retained in the subsequent sweeps from positive to negative (curves 2, 3). Therefore, the ITO/PI-NT COF/LiF/Al devices behaved as non-volatile WORM memories. A high-ON/OFF current ratio was obtained for the devices which is a favorable feature to facilitate reading and writing information with high fidelity. A stable switching behavior was obtained in the voltage window of ± 2 V for READ process (curves 4, 5). Figure 10.4b shows the retention characteristics for LRS and HRS obtained with reading at $+ 1$ V. A similar WORM behavior was obtained when the measurement was initiated with negative scan (Fig. 10.4c). A slightly larger setting voltage was found (curve 1), and the devices performed stably as sweeping the READ voltage in the range of -2 to 1.5 V (curves 2, 3). The origin of the
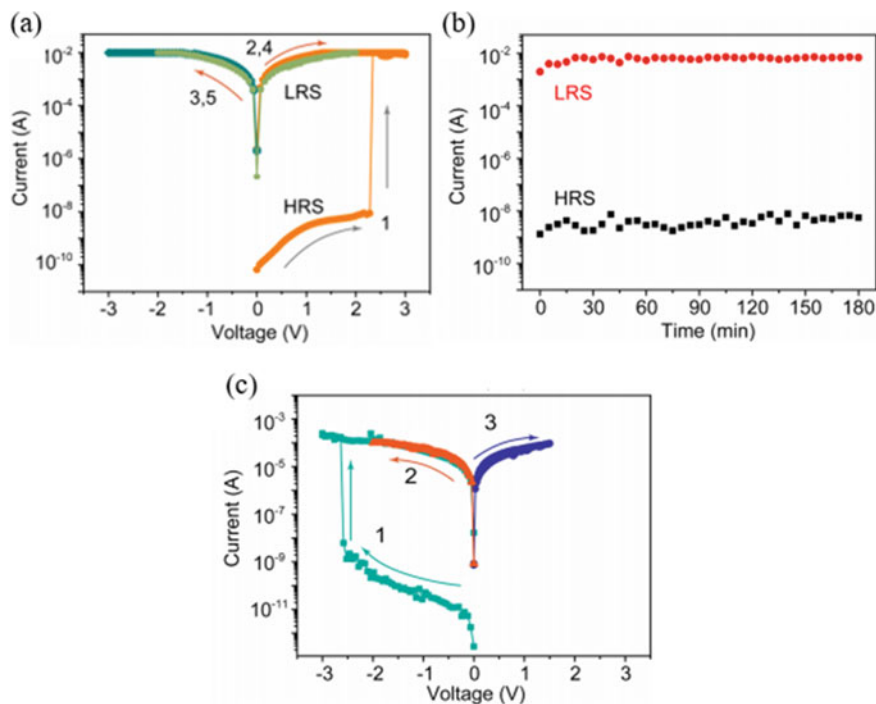
Fig. 10.4 **a** I − V curves of the PI-NT COF memory device for various voltage scans. Curve 1 corresponds to voltage scan from 0 to + 3 V; curve 2: from + 3 V to 0; curves 3: from 0 to − 3 V; curve 4: from 0 to + 2 V; curve 5: from 0 to − 2 V. **b** Retention characteristics for LRS and HRS at + 1 V (read). **c** I − V characteristics on the negative scan for the device. Curve 1 corresponds to voltage scan from 0 to − 3 V; curve 2: from 0 to −2 V; and curve 3: reversing scan between 0 and + 1.5 V. (Adapted from Ref. [9])

device behavior was ascribed to formation of $NTCDA^{-\bullet}/TAPA^{+\bullet}$ complex through charge-transfer under applied field. The formation of the complex results in electron localization in LUMO and holes in HOMO, forming stable charge-transfer channels. A very similar memory devices have also been demonstrated in other D-A systems [10]. Many other memory devices were explained with charge-transfer mechanism, for instance organometallic complex [11], fullerene or carbon-nanotube composite [12, 13], metal nanoparticles-polymer composites [14, 15].

(4) **Molecular conformation and phase transition**

Molecular conformation change with external condition variation can be used for storage. For example, rotaxanes and catenanes are the two types of bistable molecules which were explored for ultrahigh-density information storage (Fig. 10.5a). In such a molecule, the ring can rotate around the rod or slide along it. A bulky stopper is located at each end of the bar to prevent the ring from slipping off. Two recognition sites are introduced on the bar which correspond to the two states for the ring to dwell. Feng et al. have developed rotaxane molecules (H1), where a ring chemical
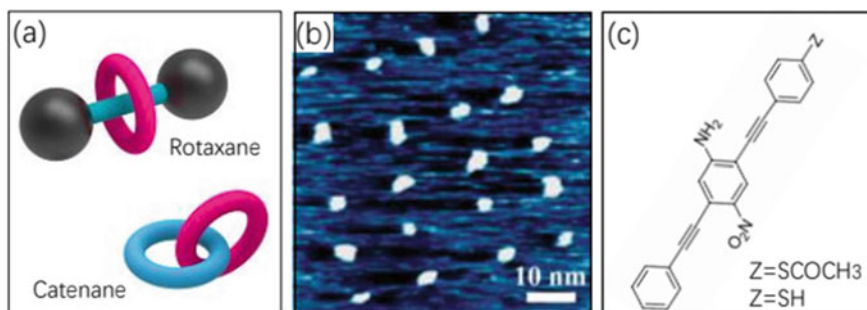
Fig. 10.5 a Schematic illustration of rotaxane and catenane molecules. **b** STM image of the recording dots written in the H1 rotaxane thin film (Adapted from Ref.[16]). **c** Schematic structure of phenylacetylene oligomer used to fabricate erasable molecule memory devices

group CBPQT$^+$ can move between TTF and DNP sites, and two stable resistance states were defined [16–18]. Under external bias, the redox reaction induces the ring-movement through attraction or repulsion between charged chemical groups. The interaction between the ring and the recognition sites causes a conductance change of the molecule. The conductance switch is reversible, non-volatile, and very promise for high-density storage application. Figure 10.5b shows STM image of the recording dots written in the H1 rotaxane film. Similar effect can be found with catenane molecules, where a ring with recognition sites can rotate under applied bias, and a conductance change is caused by the interaction between the recognition sites and another ring nested with this ring [19].

Reed et al. have reported another type of conductance switch induced by molecular conformation change [20]. They fabricated erasable molecular memory devices use phenylacetylene oligomer. Chemical groups -NO$_2$ and -NH$_2$ were introduced on the middle benzene ring (Fig. 10.5c). Such asymmetric structure leads a sensitivity of the electron cloud to external perturbation. Under an applied field, such molecules that bridged between two electrodes will twist and deform, and the conductivity decreases. The devices are electronically programmable and erasable with bit retention times greater than 15 min at room temperature.

Another strategy proposed is to control π-π stacking in organic semiconductor molecules. Huang et al. have developed memory devices use PVK-PF molecules, a derivative of PVK [21]. Under an applied field, the carbazole groups that branched from the main chain become ordered through π-π stacking in the PVK-PK molecules, and the conductance increases. Since rigid steric groups were introduced in the PVK-PK molecules, the stacked carbazole groups will not return to disorder when the external field was removed. Reversed bias can return the order of carbazole groups to disorder due to thermal effect. The developed devices were worked as non-volatile flash memory.
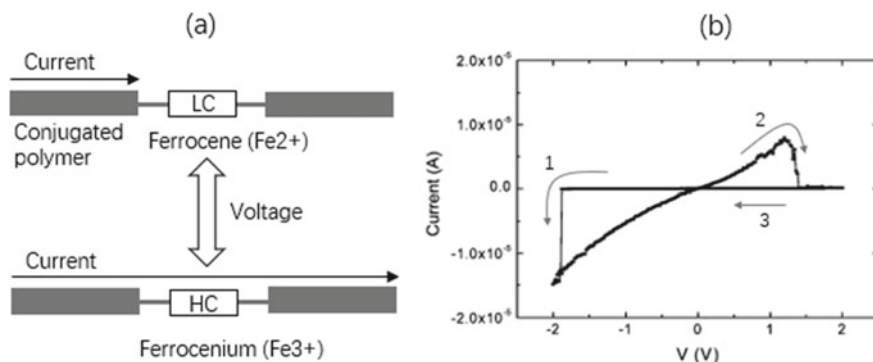
Fig. 10.6 **a** Proposed memory device based on redox reaction mechanism. **b** Measured I-V curve taken from a device with structure of ITO/PFT2-Fc/LiF/Al. (Adapted from Ref. [22])

(5) **Redox reaction mechanism**

Redox reaction mechanism has been observed in organic diode memory devices [22, 23]. It is known that many materials can change its conductivity by oxidation, like photooxidation and chemical oxidation. This has motivated researchers to use redox phenomena to synthesis molecules for memory devices. Choi et al. have proposed and demonstrated memory devices made with ferrocene linked with conjugated polymer PFT2 (Fig. 10.6a) [22]. With the newly synthesized polymer, PFT2-Fc devices with structure ITO/PFT2-Fc/LiF/Al were fabricated and characterized with the Al electrode grounded (Fig. 10.6b). When a negative bias is applied, initially, the device was at low-conducting state (off-state), then a sudden increase of current was found at around -1.9 V (on-state) which indicates an oxidation of ferrocene (arrow 1), because the ferrocenium is more conductive. The high conductance persisted until the device was switched to low-conductance state again at around 1.4 V (arrow 2). The low conductance retained until the voltage is scanned to 2 V and reversed to −2 V (arrow 3).

## 10.2.2 Organic Field-Effect Transistor Memory Devices

10.2.2.1 Classification of OFET Memory Devices and Mechanism of Device Performances

According to charge storage mechanisms, the OFET memory devices can be classified into three types: floating gate OFET memory, polymer electret OFET memory, and ferroelectric OFET memory.

(1) Floating gate OFET memory

In 1967, Kahng and Sze have proposed the concept of floating gate non-volatile memory [24]. They have inserted floating gate, which was made of doped conductive silicon, into dielectrics layer, and charge storage in the floating gate was achieved. Floating gate OFET memory devices have similar structure [25]. Floating gate can be formed with conductive nanoparticles imbedded in dielectrics (Fig. 10.7a). The dielectrics layer between the floating gate and semiconductor is called tunneling layer. The function of tunneling layer is to prevent the stored charges to vanish and to ensure the charges can tunnel through it to enter the floating gate from semiconductor. The dielectrics layer between the floating gate and gate electrode is called blocking layer or controlling dielectrics layer. The blocking layer is relatively thicker to avoid loss of charges in the floating gate when the gate voltage is removed. If a pulsed voltage is applied to the gate electrode, the charges in the semiconductor channel are injected into the floating gate through direct tunneling or thermal emission. The charges can be stored in the floating gate because it is isolated with dielectrics. The stored charges partially screen the field of the gate electrode which will lead a shift of the transfer curve of the device, i.e., a shift of threshold voltage ΔV_T (Fig. 10.7b). The newly obtained threshold voltage of the device with stored charge (V_{TW}, threshold voltage after writing) does not change if the stored charge remains. When a reversed gate voltage-pulse is applied, the stored charge returns to semiconductor channel, and the threshold voltage shifts back to original value (V_{TE}, threshold voltage after erasing).

For thin-film floating gate, device minimization is greatly restricted due to the increased leakage current. To solve this problem, nanoparticle materials were used as floating gates. The particle's physical and chemical properties, like dispersity and density of distribution etc., can bring huge impact to device properties [26–28]. Li and Yan have fabricated flexible devices with structure of PET/P(NDI2OD-T2)/PVA/Au-particles/P(VDF-TrFE-CFE)/Al-gate [29]. The P(NDI2OD-T2) is a well-known n-type polymer semiconductor. PVA and P(VDF-TrFE-CFE) polymer layers acted as the tunneling and blocking layers, respectively. The device structure and images of nanoparticles are shown in Fig. 10.8. All polymer layers were defined by spin-coating, and the nanoparticles were formed by thermal evaporation. For comparison,
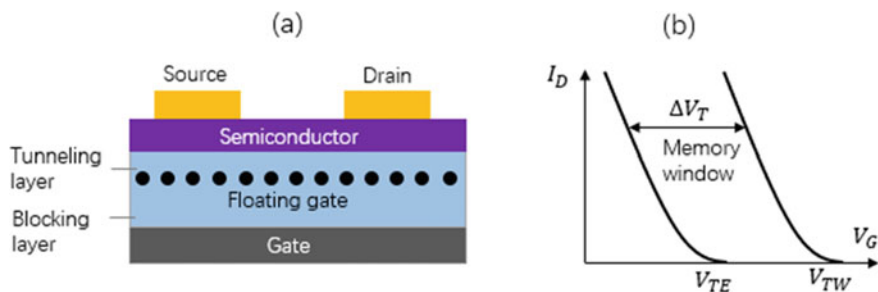

Fig. 10.7 Schematic illustration of floating gate OFET memory device (**a**) and threshold voltage before and after tunneling of charges into the floating gate (**b**)

similar device without the nanoparticle floating gate was fabricated and character-ized. Figure 10.9a shows transfer curves of the fabricated device without the Au nanoparticles. The device without nanoparticles performed as normal OTFT with very little hysteresis behavior. The carrier mobility, threshold voltage, and on/off ratio of the device at operational voltage of 3 V were $0.32cm^2/VS$, 0.32 V, and 10^5, respectively. For the devices with Au nanoparticles (Fig. 10.9b), electron injection from the channel to the Au nanoparticles occurs with increased gate voltage. The electrons stored in the Au floating gate induce a shift of the threshold voltage of the devices to a more positive value. The threshold voltage can be recovered to its orig-inal value when -6 V was applied on the gate, indicating that the electrons in the Au nanoparticles can be removed by applying a proper negative gate voltage. Therefore, a flash device with programmable memory behavior was realized, which is attributed to charging/discharging of the Au nanoparticles during the program/erase operations. The device had little degradation after 10^5 program/erase cycles, and good retention after 10^5 s, which suggest great promise in the application of non-volatile memories. Other nanomaterials can also be used to fabricate floating gate of OFET memory devices, like organic semiconductor nanoparticles [30], graphene oxide [31], small molecule semiconductors [32–34].

(2) **Polymer Electret-Based OFET memories**

In polymer electret OFET memory devices, the charges are stored within the bulk of the dielectrics film or at the interface between the gate dielectrics and the semi-conductor channel. Electret is a functional dielectric material exhibiting a quasi-permanent electrostatic field caused by trapped charges. The OTFT channel conduc-tance can be modulated by trapping charge inside the polymer electret with applied gate voltage (V_G) through which the devices are programmed or erased. When a bias is applied on the gate above a specific range, charges are stored in the polymer electret layer. The stored charges can move back to the channel or recombined with charges of opposite polarity through an applied reverse voltage bias.

Singh et al. have reported first polymer electret OFET memory device with poly (vinyl alcohol) (PVA) as charge trapping layer [35]. Baeg et al. have fabricated such devices with poly(α-methylstyrene) (PαMS). The device showed excellent memory characteristics with reversible shifts in threshold voltage by programming and erasing process [36]. They have fabricated devices with a series of charge trapping materials and found that the size of memory window is proportional to contact angle of the trapping layer materials and is inversely proportional to dielectric constants [37]. At a given applied gate voltage, the smaller dielectric constant of the dielectrics, the larger tunnel field is produced. This is favorable for charge injection. They have also found that non-polarized and hydrophobic electret materials have more stable retention time. The reason is that hydrophilic materials can absorb moisture which can carry ions and impurities to form conductive channels for charge dissipation. Apart from polymer materials, polymer composites formed by embedding functional moieties
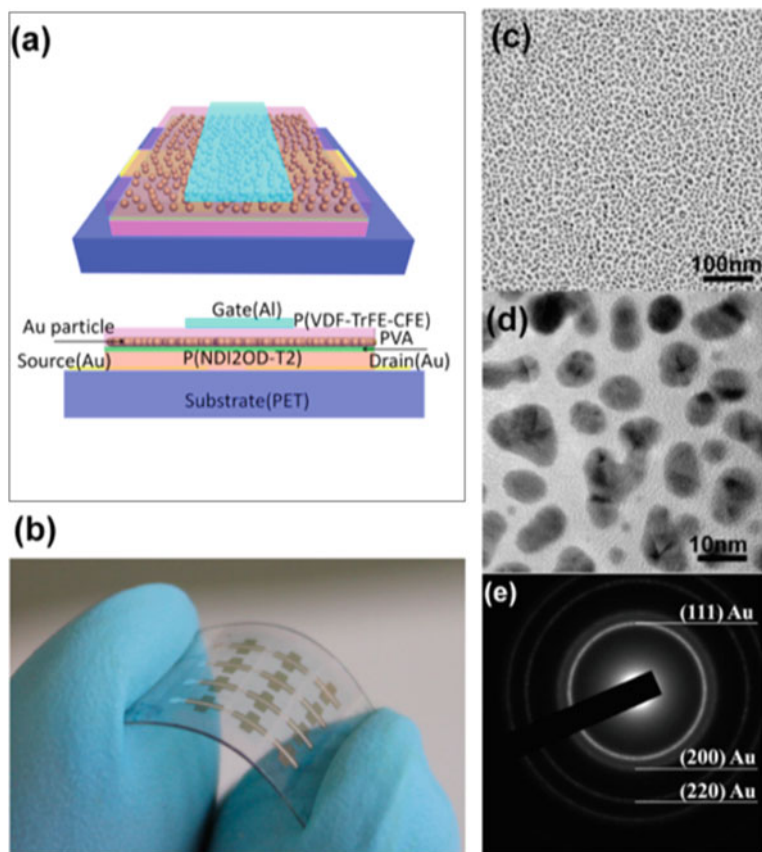
Fig. 10.8 **a** Schematical diagram of a floating gate field-effect transistor with a top-gate and bottom-contact structure. **b** Photograph of the memory on a flexible PET substrate. **c**, **d** TEM images of Au nanoparticles on a PVA films. **e** Electron diffraction pattern of Au nanoparticles under TEM. (Adapted from Ref. [29])
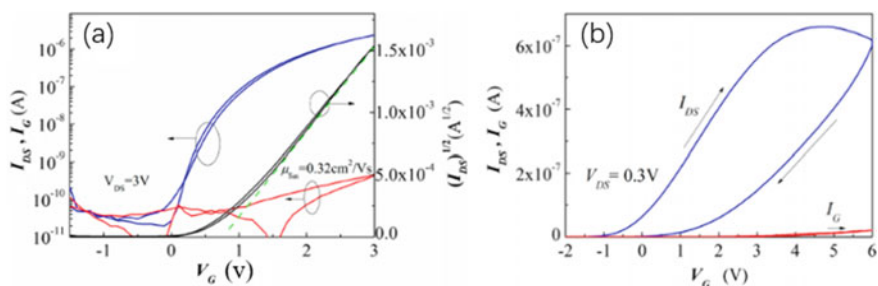
Fig. 10.9 Transfer curves of P(NDI2OD-T2)/PVA/P(VDF-TrFE-CFE)/Al-gate organic TFT without (**a**) and with (**b**) Au nanoparticles between the PVA and P(VDF-TrFE-CFE) layers. (Adopted from Ref. [29])

into the polymer matrix can also be used as charge trapper in OFET memory devices [38, 39].

(3)   **Organic ferroelectric OFET memories**

Ferroelectric materials have spontaneous electric polarization, i.e., they naturally possess dipole moments that can orient in the direction normal to film surface. The polarization can be generated and switched by applying an external electrical field. The ferroelectric property can be proved by measuring field dependence of charge transfer in thin-film capacitor. Ferroelectric OFET memory devices are formed by replacing the dielectrics layer in a normal OFET with ferroelectric film [40]. The ferroelectric polarization switch induced by applied gate voltage can modulate the charge density in the device channel, and consequently, the device can present different conductive states. In 1986, Yamauchi et al. reported first FET memory device with organic ferroelectric polymer as dielectrics layer [41], but the device needed a high-performance voltage and writing time. In 2004, Schroeder et al. fabricated all-organic ferroelectric OFET memory device with poly(m-xylylene adipamide) as dielectrics layer [42]. The device showed 20 V memory window and ON/OFF current ratio 200. In the same year, Unni et al. reported all-organic ferroelectric OFET memory device with P(VDF-TrFE) (70:30), and the device showed reasonably good retention. The ON-current dropped to 81% of its initial value after 5 h [43]. In 2005, Naber et al., made further progress in this area [40]. They have fabricated bottom gate OFET memory device use P(VDF-TrFE) (65:35) as ferroelectric dielectrics and MEH-PPV as semiconductor layer. The retention time was large than one week, and duration cycles was greater than 1000. Roy et al. have reported such devices with device structure shown in Fig. 10.10a [44]. P(VDF-TrFE) ferroelectrics film was spin-coated on p-doped Si substrate with oxidized layer. Copper phthalocyanine (CuPc) active layer was deposed by thermal evaporation on the top of P(VDF-TrFE). Au source and drain electrodes were defined by thermal evaporation through shadow mask. Device with a ferroelectric capacitance structure was made through spin-coating P(VDF-TrFE) on glass substrate with indium tin oxide (ITO) layer and subsequent deposition of Al layer. The spin-coated P(VDF-TrFE) films in both types of devices were annealed at 75 °C, 135 °C and subsequently quenched to 6 °C with ice-cooled metallic platform. Figure 10.10b shows polarization-electrical field (P-E) hysteresis loop taken from the fabricated device with capacitance structure. A non-volatile memory character is seen from the transfer curve measured from the organic FeFET device (Fig. 10.10c). The memory window of the device was ~20 V.

10.3   Synapse Devices

The development of artificial neural networks (ANNs) that can match the efficiency of their biological counterparts in information processing remains a major challenge in computing. The mammalian brain outperforms computers in many computational
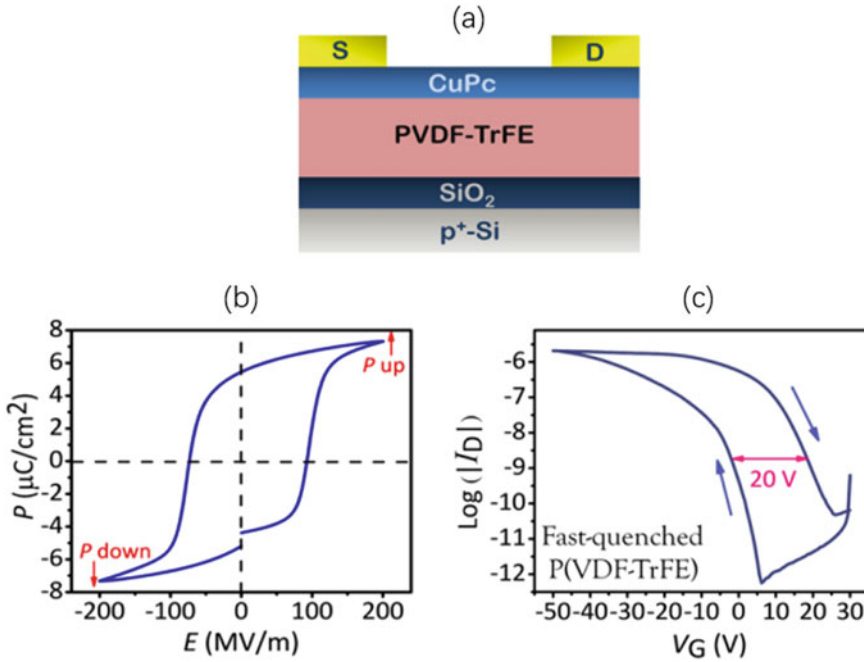
Fig. 10.10 **a** Schematic illustration of organic ferroelectric FET device structure. **b** Ferroelectric hysteresis plot of the P(VDF-TrFE) thin-film capacitor. **c** Transfer curve of organic ferroelectric FET memory device. The arrows show the directions of voltage sweep. (Adapted from Ref. [44])

tasks. For instance, it can recognize complex images faster with better fidelity, while it consumes only a small fraction of the energy that computers require to accomplish such a task. Today, the need for efficient ANNs is greater than ever, given the growing needs of information processing for the coming era of robotics, bioinformatics, distributed sensor networks, etc. In the mammalian central nervous systems, signal transmission is carried out by interconnected networks of nerve cells, or neurons. When an action potential is generated from the soma (cell body), it travels down the neuron along the axon toward the synapses, which link the axon terminals of one neuron (i.e., a pre-synapse neuron) and the dendrites of the next neuron (i.e., a post-synapse neuron) (Fig. 10.11a). The action potential triggers Ca^{2+} to flood the pre-synaptic membrane and bind to specific proteins in the cytoplasm, which in turn trigger the fusion of the synaptic vesicles with the cellular membrane to release neurotransmitter chemicals into the synapse cleft (Fig. 10.11b). The neurotransmitter chemicals are picked up by the dendrites of the post-synaptic neuron via receptors and generate an action potential, which is analogous to the output signal in neuron computation.

Biological research shows that the connection-synapses between neurons can be strengthened or weakened, depending on their inputs. Single synapse can undergo long-term potentiation (LTP) or long-term depression (LTD), and the strengthening
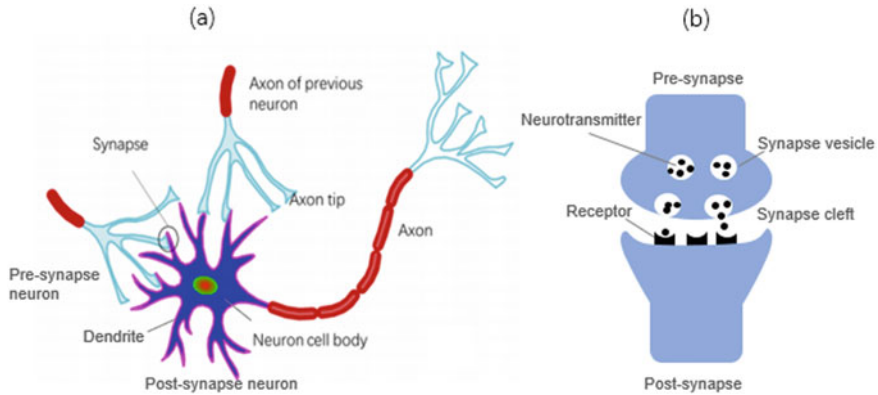
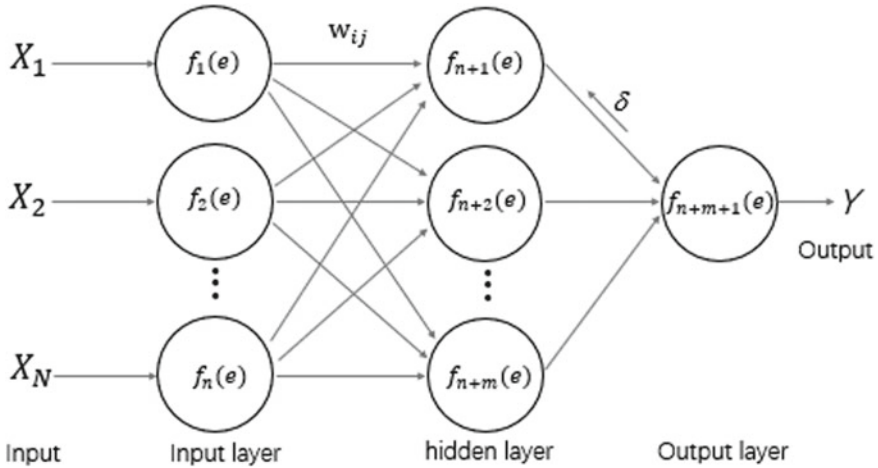**Fig. 10.11** Schematic illustration of synapse structure. **a** Pre-synaptic and post-synaptic neurons linked with synapses. (Adapted from Ref. [45]). **b** Scheme of a synapse, where the signal process between neurons is processed via the transfer of neurotransmitter chemicals

of interconnections between neurons is an essential process of learning. A unique feature of neuron systems in the brain is that massive parallel network processing and storing of information can be performed simultaneously by modulating the connection strength of synapses. This inspired researchers to develop devices/systems that enable to tune the connections (synapses) between signal processing units (neurons): artificial neural networks. Therefore, developing electronic devices that can imitate the functions of synapses is of great significance to the development of artificial intelligence (AI) technology.

The fundamental principle of neuron computing is that of continuously updating connection weights between neuron units, which is analogous to the biological LTP/LTD process: strengthening/weakening synapse connections in the nervous system of the human brain [46]. Figure 10.12 shows a schematic drawing of basic working principle of ANNs. ANNs are computational models based on parallel processing. An ANN can be defined as a pool of simple processing units (neurons) that communicate among themselves by sending signals. The system has layered structure of neurons: input layer, hidden layer, and output layer. Signals travel through pre-synapse neurons (i) and post-synapse neurons (j) linked by synapses which tune the weight value (w_{ij}) of the connections. With a set of pre-defined weight values w_{ij} (i = 1, 2, 3···, j = 1, 2, 3···) input data, like a picture, X_i is entered into the system through pre-synapse neurons to initiate the computation. The output result "Y" is compared with the expected result "Z" (a comparative standard, like a pattern, image, numbers, etc.) to obtain a deviation value δ = Z-Y. If the δ value is large than the tolerance error, the w_{ij} values are readjusted, and new of w_{ij} values are set and repeat the computation. Compare the obtained new δ value with the tolerance error again. If the δ value is still large than the tolerance error, repeat the computation until the δ value is small enough. Such a repeated computation process is called training. During the signal propagation, a neuron needs to perform two functions: (i) to find

Fig. 10.12 Schematic illustration of simplified ANN

weighted sum of all input information and (ii) to obtain an output of the neuron through a non-linear activation function $f(e)$.

To date, several efforts have been made to implement appropriate synaptic devices/circuits by exploiting CMOS technology and emerging nanoelectronic devices. Although the capability of CMOS circuits is enough to capture synaptic functionalities [47], the chip area and power consumption required would be prohibitively large for large-scale integration. To overcome the challenges of CMOS-based approaches, attention has turned to the emerging adaptive devices. The states of such adaptive device(synapse device)vary with applied voltages, and each state remains after removing the applied field, i.e., a memory device with multilevel states or consecutively varied states. Usually, the states of synapse device refer to the resistances controlled by electrical field, although other physical parameters and control mechanisms can also be used.

According to device structures, the synapse devices can be divided into two categories: two-terminal and three-terminal devices. The well-known two-terminal devices are memristors, which was postulated by Chua in 1971[48] and demonstrated in 2008 [49–51]. Such devices can be generalized to include any class of two-terminal devices whose electrical resistance depends on the internal states of the system [52]. Many systems belong to this class, including the thermistor [53], certain spintronic devices [54, 55], ionic motion-induced resistance change, etc. [56]. Figure 10.13a illustrates the working principle of the devices demonstrated by Williams et al. from Hewlett–Packard. The devices were formed with titanium dioxide layer sandwiched between two metal electrodes, where the titanium dioxide layer was formed with a stoichiometric TiO_2 and oxygen-deficient TiO_{2-x} sublayers. The stoichiometric TiO_2 is a high-resistive compound. The oxygen vacancies in the oxide can act as positive charge carriers, as a result the TiO_{2-x} layer is more conductive than the TiO_2 layer. If a positive pulse voltage is applied to the top electrode, the vacancies in the TiO_{2-x} are
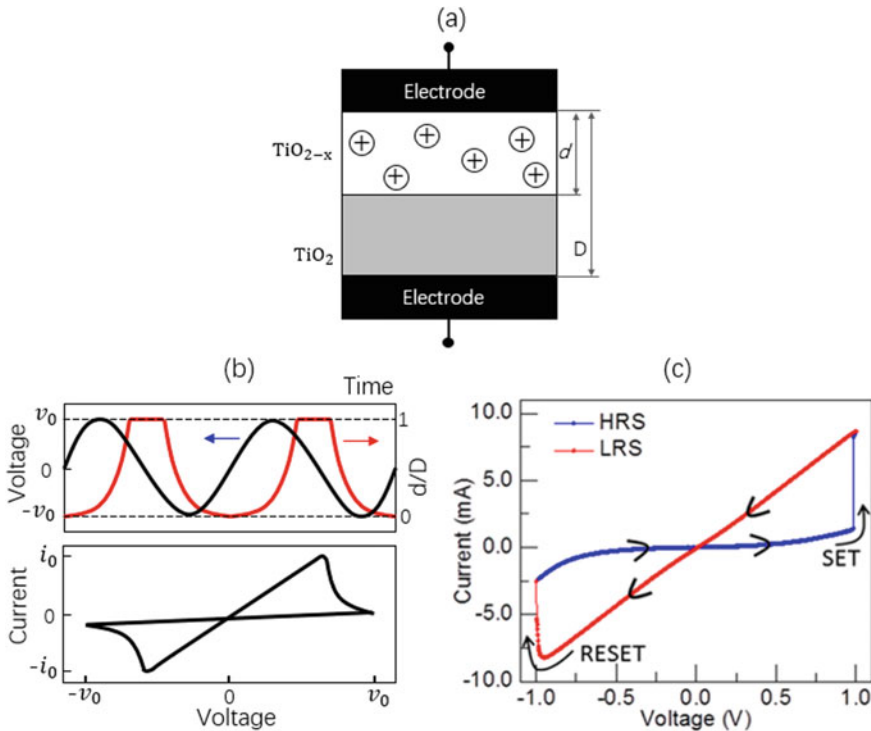
Fig. 10.13 a Schematic illustration of device structure for memristor developed by Hewlett–Packard. **b** Schematic illustration of voltage-driven memristive behavior of device with non-linear drift of charged species (ions, defects, etc.). Upper panel: applied sinusoidal voltage and corresponding response of d/D. Lower panel: Current–voltage loop caused by the charge-drift behavior shown in the upper panel [49]. **c** Switching behavior of a Pt/TiOx/Pt device made with nanocrystalline oxygen-deficient TiOx film. (Adapted from Ref. [57])

pushed downwards for a distance Δd. Consequently, the resistance measured between the two terminals will decrease accordingly. When a negative pulsed bias is applied to the top electrode, the resistance between the two terminals will increase. Therefore, the conductance of such devices can be tuned by pulsed voltages consecutively, which is similar to synapses in neuron system where potentiation and depression are controlled by biological electrical signals. Memristors with such resistive switch mechanism shown in Fig. 10.13a are categorized as bias-driven interface type [57]. The moving of charged species depends on the device materials, device geometry, device size, etc., thus a rich hysteretic current–voltage curves can be observed. For instance, when a non-linear drift of oxygen vacancies happens (if d is close to zero or D) as shown in the Fig. 10.13a, hysteresis curves shown in Fig. 10.13b (bottom panel) and Fig. 10.13c can be observed [49, 57]. Another popular resistive switch mechanism, involving formation/dissolution of one or more conducting filaments,

is called filament type switching [58, 59]. Many other inorganic oxides/compounds-based memristors were developed, for instance NiO_x, WO_x, VO_2, NbO_2 [60–64], AgS_2, and CuS_2 [65, 66].

Organic materials have also been used to develop memristors, since organic materials are low cost, easy to fabricate, flexible, and electrical property can be tuned by molecule design. Synaptic plasticity and learning behavior with Ag/PEDOT:PSS/Ta memristors were demonstrated which is related to the formation and growth of Ag filament induced by a redox reaction under electric bias [67]. Liu et al. have reported memristors with structure $Ta/EV(ClO_4)_2/BTPA-F/Pt$, and a series of synaptic behaviors were demonstrated by using electrochemical redox reaction of the $EV(ClO_4)_2/BTPA-F$ bilayer [68]. Another approach that has attracted much attention is three-terminal organic devices, i.e., adaptive transistors, whereby the channel conductance of a transistor is modulated by tuning signals applied to the gate or drain electrodes. Several methods have been used to realize the adaptation of channel conductance of transistors, including FET with floating gate imbedded in dielectrics layer [69], charge trapping/de-trapping in the channel use metal nanoparticles embedded in semiconductor layer [70, 71], ion trapping at the interface between the semiconductor and ion-conductive dielectric layer to form a charged double layer (CDL: ions/electrons or ions/holes) [72], and reversibly doping and de-doping of polymer semiconductors with ions in organic electrochemical transistors [73].

References

1. Joo W, Choi T, Lee K, Chung Y (2007) Study on threshold behavior of operation voltage in metal filament-based polymer memory. J Phys Chem B 111:7756–7760
2. Cho B, Yun JM, Song S, Ji Y, Kim D, Lee T (2011) Direct observation of Ag filamentary paths in organic resistive memory devices. Adv Funct Mater 21:3976–3981
3. Majumdar HS, Bandyopadhyay A, Bolognesi A, Pal AJ (2002) Memory device applications of a conjugated polymer: role of space charges. J Appl Phys 91:2433–2437
4. Sadaoka Y, Sakai Y (1976) Switching in poly(N-vinylcarbazole) thin films. J Chem Soc Faraday Trans 2(72):1911–1915
5. Meyyappan M, Han J, Zhou CW (2004) Multilevel memory based on molecular devices. Appl Phys Lett 84(11):1949–1951
6. Li F, Son DI, Cha HM, Seo SM, Kim BJ, Kim HJ, Jung JH, Kim TW (2007) Memory effect of CdSe/ZnS nanoparticles embedded in a conducting poly[2-methoxy-5-(2-ethylhexyloxy)-1, 4-phenylene-vinylene] polymer layer. Appl Phys Lett 90(22):222109
7. Bozano LD, Kean BW, Rice PM, Beinhoff M, Scott JC, Carter KR (2005) Organic materials and thin-film structures for cross point memory cells based on trapping in metallic nanoparticles. Adv Funct Mater 15(12):1933–1939
8. Song Y, Tan YP, Teo EYH, Zhu C, Chan DSH, Ling QD, Neoh KG, Kang ET (2006) Synthesis and memory properties of a conjugated copolymer of fluorene and benzoate with chelated europium complex. J Appl Phys 100(8):084508
9. Sun B, Li X, Feng T, Cai S, Chen T, Zhu C, Zhang J, Wang DY, Liu Y (2020) Resistive switching memory performance of two-dimensional polyimide covalent organic framework films. ACS Appl Mater Interfaces 12:51837–51845

10. Arunagirinathan RN, Gopikrishna P, Das D, Iyer PK (2019) Solution processed donor-acceptor polymer based electrical memory device with high on/off ratio and tunable properties. ACS Appl Electron Mater 1:600–607

11. Gong JP, Osada Y (1992) Preparation of polymetric metal-tetracyanoquinodimethane film and its bistable switching. Appl Phys Lett 61(23):2787–2789

12. Lian SL, Liu CL, Chen WC (2011) Conjugated fluorene-based rod-coil block copolymers and their PCBM composites for resistive memory switching devices. ACS Appl Mater Interfaces 3(11):4504–4511

13. Liu G, Ling QD, Teo EYH, Zhu C, Chan S, Neoh K, Kang E (2009) Electrical conductance tuning and bistable switching in poly(N-vinylcarbazole)-Carbon nanotube composite films. ACS Nano 3(7):1929–1937

14. Prakash A, Ouyang J, Lin JL, Yang Y (2006) Polymer memory device based on conjugated polymer and gold nanoparticles. J Appl Phys 100(5):409–503

15. Song Y, Ling QD, Lim SL, Teo EYH, Tan YP, Li L, Kang E, Chan D, Zhu C (2007) Electrically bistable thin-film device based on PVK and GNPs polymer material. IEEE Electron Device Lett 28(2):107–110

16. Feng M, Gao X, Lin X, He XB, Ji W, Du S, Zhang D, Zhu D, Gao H (2005) Stable, reproducible nanorecording on rotaxane thin films. J Am Chem Soc 127:15338–15339

17. Feng M, Gao L, Du S, Deng Z, Cheng Z, Ji W, Zhang D, Guo X, Lin X, Chi L (2007) Observation of structural and conductance transition of rotaxane molecules at a submolecular scale. Adv Funct Mater 17:770–776

18. Feng M, Gao L, Deng Z, Ji W, Guo X, Du S, Shi D, Zhang D, Zhu D, Gao H (2007) Reversable, erasable, and rewritable nanorecording on an H2 rotaxane thin film. J Am Chem Soc 129:2204–2205

19. Collier CP, Mattersteig G, Wong EW, Luo Y, Beverly K, Sampaio J, Raymo FM, Stoddart JF, Heath JR (2000) A catenane-based solid state electronically reconfigurable switch. Science 289:1172–1175

20. Chen J, Reed MA (2002) Electronic transport of molecular systems. Chem Phys 281:127–145

21. Xie L, Ling Q, Hou X, Huang W (2008) An effective friedel-crafts postfunctionalization of poly (N-vinylcarbazole) to tune carrier transportation of supramolecular organic semiconductors based on π-stacked polymers for nonvolatile flash memory cell. J Am Chem Soc 130:2120–2121

22. Choi TL, Lee KH, Joo WJ, Lee S, Lee TW, Mi YC (2007) Synthesis and nonvolatile memory behavior of redox-active conjugated polymer-containing ferrocene. J Am Chem Soc 129:9842–9843

23. Ling QD, Song Y, Ding SJ, Zhu C, Chan DSH, Kwong D, Kang E, Neoh K (2005) Non-volatile polymer memory device based on a novel copolymer of N-vinylcarbazole and Eu-complexed vinylbenzoate. Adv Mater 17:455–459

24. Kahng D, Sze SM (1967) A floating gate and its application to memory devices. Bell Lab Technical Journal 46(6):1288–1295

25. Shih CC, Lee WY, Chen WC (2016) Nanostructured materials for non-volatile organic transistor memory applications. Mater Horiz 3:294–308

26. Han ST, Zhou Y, Xu ZX, Roy VAL, Hung TF (2011) Nanoparticle size dependent threshold voltage shift in organic memory transistors. J Mater Chem 21(38):14575–14580

27. Wang SM, Leung CW, Chan PK (2010) Nonvolatile organic transistor-memory devices using various thicknesses of silver nanoparticle layers. Appl Phys Lett 97(2):023511

28. Wang W, Shi JW, Ma DG (2009) Organic thin film transistor memory with nanoparticles floating gate. IEEE Trans Electron Devices 56(5):1036–1039

29. Li J, Yan F (2014) Solution-processable low-voltage and flexible floating-gate memories based on an n-type polymer semiconductor and high-k polymer gate dielectrics. ACS Appl Mater Interfaces 6:12815–12820

30. Shih CC, Chiu YC, Lee WY, Chen JY, Chen WC (2015) Conjugated polymer nanoparticles as nano floating gate electrets for high performance nonvolatile organic transistor memory devices. Adv Funct Mater 25(10):1511–1519

31. Jang S, Hwang E, Lee JH, Park HS, Cho JH (2015) Graphene-graphene oxide floating gate transistor memory. Small 11(3):311–318
32. Baeg KJ, Khim D, Kim DY, Jung S, Koo JB, Noh Y (2010) Organic nano-floating-gate memory with polymer:[6, 6]-phenyl-C_{61} butyric acid methyl ester composite films. Jpn J Appl Phys 49(5): 05EB01–05EB05
33. Zhou Y, Han ST, Yan Y, Huang L, Zhou L, Huang J, Roy VAL (2013) Solution processed molecular floating gate for flexible flash memories. Sci Rep 3(1):3093
34. Han ST, Zhou Y, Wang CD, He L, Zhang W, Roy VAL (2013) Layer-by-layer-assembled reduced graphene oxide/gold nanoparticle hybrid double-floating-gate structure for low-voltage flexible flash memory. Adv Mater 25(6):872–877
35. Singh TB, Marjanovic N, Matt GJ, Sariciftci NS, Schwödiauer R, Bauer S (2004) Nonvolatile organic field-effect transistor memory element with a polymeric gate electret. Appl Phys Lett 85(22):5409–5411
36. Baeg KJ, Noh YY, Ghim J, Kang S, Lee H, Kim D (2006) Organic non-volatile memory based on pentacene field-effect transistors using a polymeric gate electret. Adv Mater 18(23):3179–3183
37. Baeg KJ, Noh YY, Ghim J, Lim B, Kim DY (2008) Polarity effects of polymer gate electrets on non-volatile organic field-effect transistor memory. Adv Funct Mater 18(22):3678–3685
38. Wu W, Zhang H, Wang Y, Ye S, Guo Y, Di C, Yu G, Zhu D, Liu Y (2008) High performance organic transistor memory elements with steep flanks of hysteresis. Adv Funct Mater 18:2593–2601
39. Chiu Y, Chen T, Chen Y, Satoh T, Kakuchi T, Chen W (2014) High-performance nonvolatile organic transistor memory devices using the electrets of semiconducting blends. ACS Appl Mater Interfaces 6:12780–12788
40. Naber RCG, Tanase C, Blom PWM, Gelinck GH, Marsman AW, Touwslager FJ, Setayesh S, de Leeuw DM (2005) High-performance solution-processed polymer ferroelectric field-effect transistors. Nat Mater 4(3):243–248
41. Yamauchi N (1986) A metal-insulator-semiconductor (MIS) device using a ferroelectric polymer thin film in the gate insulator. Jpn J Appl Phys Part–1 Regular Papers Brief Commun Rev Papers 25(4):590–594
42. Schroeder R, Majewski LA, Grell M (2004) All-organic permanent memory transistor using an amorphous, spin-cast ferroelectric-like gate insulator. Adv Mater 16(7):633–636
43. Unni KNN, de Bettignies R, Dabos-Seignon S, Nunzi JM (2004) A nonvolatile memory element based on an organic field-effect transistor. Appl Phys Lett 85(10):1823–1825
44. Roy D, Pattader PSG, Bandyopadhyay CM, Wang C, Yang Y, Mukherjee M (2020) Dipolar alignment in a ferroelectric dielectric layer of FeFETs to boost charge mobility and nonvolatile memory. ACS Appl Electron Mater 2:3187–3198
45. Li J, Chang X, Li S, Shrestha PK, Tan EKW, Chu D (2020) High-resolution electro-chemical transistors defined by mould-guided drying of PEDOT:PSS liquid suspension. ACS Appl Electron Mater 2:2611–2618
46. Sun B, Guo T, Zhou G, Ranjan S, Jiao Y, Wei L, Zhou YN, Wu YA (2021) Synaptic devices based neuromorphic computing applications in artificial intelligence. Mater Today Phys 18:100393
47. Mead C (1990) Neuromorphic electronic systems. Proc IEEE. 78(10):1629–1636
48. Chua LO (1971) Memristor—the missing circuit element. IEEE Trans Circuit Theory CT-18:507–519
49. Strukov DB, Snider GS, Stewart DR, Williams RS (2008) The missing memristor found. Nature 453:80–83
50. Prezioso M, Merrikh-Bayat F, Hoskins BD, Adam GC, Likharev KK, Strukov DB (2015) Training and operation of an integrated neuromorphic network based on metal-oxide memristors. Nature 521:61–64
51. Yang JJ, Strukov DB, Stewart DR (2013) Memristive devices for computing. Nat Nanotech 8:13–24
52. Chua LO, Kang SM (1976) Memrisive devices and systems. Proc IEEE 64:209–223
53. Sapoff M, Oppenheim RM (1963) Theory and application of self-heated thermistors. Proc IEEE 51:1292–1305

54. Pershin YV, Di VM (2008) Spin memristive systems: spin memory effects in semiconductor spintronics. Phys Rev B 78:113309

55. Wang XB, Chen YR, Xi HW, Dimitrov D (2009) Spintronic memristor through spin-torque-induced magnetization motion. IEEE Electron Device Lett 30(3):294–297

56. Yang Y, Zhang X, Qin L, Zeng Q, Qiu X, Huang R (2017) Probing nanoscale oxygen ion motion in memristive systems. Nat Commun 8:15173

57. Srivastava S, Thomas JP, Heinig NF, Leung KT (2017) High-performance single-active-layer memristor based on an ultrananocrystalline oxygen-deficient TiO_x film. ACS Appl Mater Interfaces 9:36989–36996

58. Kwon DH, Kim KM, Jang JH, Jeon JM, Lee MH, Kim GH, Li XS, Park GS, Lee B, Han S, Kim M, Hwang CS (2010) Atomic structure of conducting nanofilaments in TiO_2 resistive switching memory. Nat Nanotechnol 5:148–153

59. Celano U, Goux L, Belmonte A, Opsomer K, Franquet A, Schulze A, Detavernier C, Richard O, Bender H, Jurczak M, Vandervorst W (2014) Three-dimensional observation of the conductive filament in nanoscaled resistive memory devices. Nano Lett 14:2401–2406

60. Hu SG, Liu Y, Chen TP, Liu Z, Yu Q, Deng LJ, Yin Y, Hosaka S (2013) Emulating the paired-pulse facilitation of a biological synapse with a NiO_x-based memristor. Appl Phys Lett 102:183510

61. Yang JJ, Pickett MD, Li X (2008) Memristive switching mechanism for metal/oxide/metal nanodevices. Nat Nanotech 3(7):429–433

62. Chang T, Jo SH, Kim KH, Sheridan P, Gaba S, Wei L (2011) Synaptic behaviour and modelling of a metal oxide memristive device. Appl Phys A 102(4):857–863

63. Lappalainen J, Mizsei J, Huotari M (2019) Neuromorphic thermal-electric circuits based on phase-change VO2 thin-film memristor elements. J Appl Phys 125:044501

64. Kumar S, Strachan JP, Williams RS (2017) Chaotic dynamics in nanoscale NbO_2 Mott memristors for analogue computing. Nature 548:318–321

65. Ohno T, Hasegawa T, Tsuruoka T, Terabe K, Gimzewski JK, Aono M (2011) Short-term plasticity and long-term potentiation mimicked in single inorganic synapses. Nat Mater 10(8):591–595

66. Nayak A, Ohno T, Tsuruoka T, Terabe K, Hasegawa T, Gimzewski JK, Aono M (2012) Controlling the synaptic plasticity of a Cu_2S gap-type atomic switch. Adv Funct Mater 22:3606–3613

67. Li S, Zeng F, Chen C (2013) Synaptic plasticity and learning behaviours mimicked through Ag interface movement in an Ag/conducting polymer/Ta memristive system. J Mater Chem C 1(34):5292–5298

68. Liu G, Wang C, Zhang W, Pan L, Zhang C, Yang X, Fan F, Chen Y, Li R (2016) Organic biomimicking memristor for information storage and processing applications. Adv Electron Mater 2:1500298

69. Kim S, Choi B, Lim M, Yoon J, Lee J, Kim H, Choi S (2017) Pattern recognition using carbon nanotube synaptic transistors with an adjustable weight update protocol. ACS Nano 11:2814–2822

70. Alibart F, Pleutin S, Guerin D, Novembre C, Lenfant S, Lmimouni K, Gamrat C, Vuillaume D (2010) An organic nanoparticle transistor behaving as a biological spiking synapse. Adv Funct Mater 20:330–337

71. Alibart F, Pleutin S, Bichler O, Gamrat C, Serrano-Gotarredona T, Linares-Barranco B, Vuillaume D (2012) A memristive nanoparticle/organic hybrid synapstor for neuroinspired computing. Adv Funct Mater 22:609

72. Zang Y, Shen H, Huang D, Di C-A, Zhu D (2017) A dual-organic-transistor-based tactile-perception system with signal-processing functionality. Adv Mater 29:1606088

73. van de Burgt Y, Lubberman E, Fuller EJ, Keene ST, Faria GC, Agarwal S, Marinella MJ, Talin AA, Salleo A (2017) A non-volatile organic electrochemical device as a low-voltage artificial synapse for neuromorphic computing. Nat Mater 16:414–419

Chapter 11
Organic–Inorganic Hybrid Devices—Perovskite-Based Devices

As one of the most promising photovoltaic materials, the organic–inorganic metal halide perovskites have gained great attention worldwide during the past decade due to their outstanding optoelectronic properties. In particular, the perovskite solar cells (PSCs) have undergone great success and progress, achieving a certified cell efficiency of 25.7%. In this chapter, we comprehensively introduced the hybrid perovskite materials as well as perovskite-based optoelectronic devices. Fundamentals of the perovskite materials, like crystal structures, composition/bandgap tuning, optoelectronic properties, and film deposition methods, are summarized in the first part. The second part focuses on the revolution history, device architectures, state-of-the-art technologies, stability, and upscaling issues of PSCs. Some other important perovskite-based optoelectronic devices are briefly discussed in the following part. Finally, perspectives about future development of perovskite-based devices are proposed.

11.1 Organic–Inorganic Hybrid Perovskite Materials

As one of the emerging photovoltaic technologies, organic–inorganic hybrid metal halide perovskite solar cells (PSCs) have undergone great success and progress during the past decade. The hybrid perovskite materials have risen to stardom due to their extraordinary optoelectronic properties, such as high optical absorption coefficient, high carrier mobility, long free carrier diffusion length, low exciton binding energy, and easy solution processability. According to the best research-cell efficiency chart obtained from the Web site of National Renewable Energy Laboratory (NREL), [1] a certified champion power conversion efficiencies (PCE) of 25.7% have been obtained for PSCs. The high PCEs and low fabrication costs of the PSCs make it a promising candidate to replace silicon cells. In this chapter, we first summarize briefly the basic properties and fabrication approaches of the organic–inorganic hybrid perovskite materials. The second part mainly introduces the state-of-the-art organic–inorganic

hybrid PSCs and some key challenges for commercialization. Some other important perovskite-based optoelectronic devices beyond PSCs are briefly discussed in the following part. Last, perspectives about future development of perovskite-based devices are proposed.
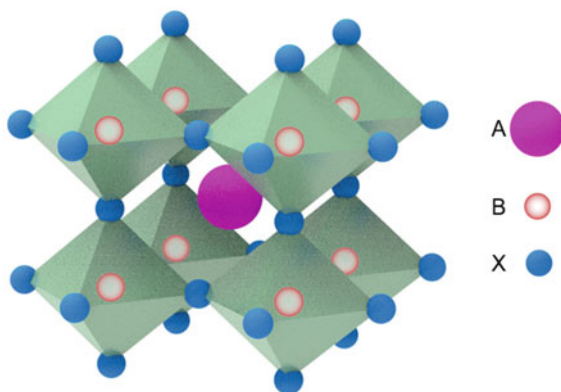
11.1.1   Crystal Structures

The organic–inorganic halide perovskite crystals share the same crystal structure with calcium titanium oxide ($CaTiO_3$), which possesses the typical perovskite crystal structure, named after the Russian mineralogist Perovski (1792–1856). The general chemical formula of the hybrid perovskites is ABX_3, where A represents monovalent inorganic or organic cations like cesium (Cs^+), methylammonium (MA^+), formamidinium (FA^+), MA = $CH_3NH_3^+$, and FA = $CH(NH_2)_2^+$; B represents divalent metal cations like Pb^{2+} or Sn^{2+}; and X represents halide anions like Cl^-, Br^-, or I^-. In an ideal perovskite crystal structure (cubic), the body-centered B-site cation is coordinated with 6 nearest X-site anions, forming BX_6 octahedra, while the A-site cations located at vertex positions filling the voids formed by BX_6 octahedrons, as shown in Fig. 11.1. The crystal structure can be changed to lower symmetric phases (tetragonal, orthorhombic, hexagonal, etc.) through tuning the ionic radii or rotation/distortion of the BX_6 octahedrons [2, 3]. The crystal structure formation and stability of perovskites can be speculated by the well-known Goldschmidt tolerance factor (t) [3].

$$t = \frac{R_A + R_X}{\sqrt{2}(R_B + R_X)}$$

where R_A, R_B, and R_X represent the effective ionic radii for the mentioned ions at A, B, and X sites, respectively. Generally, a t value between 0.81 and 1.11 is found

Fig. 11.1 The ideal cubic crystal structure of typical organic–inorganic metal halide perovskites with chemical formula of ABX_3

favorable for the formation of stable 3D organometal semiconducting perovskites [4]. The cubic structure in Fig. 11.1 is likely when t value lies between 0.89 and 1.0, while lower t values will give lower symmetric crystal structures [4]. Besides, phase transition happens with temperature increasing, and the high-temperature phase of the hybrid halide perovskites generally has cubic crystal structure. For the most frequently used perovskites, the room-temperature crystal symmetries of MAPbI$_3$ and FAPbI$_3$ are tetragonal and cubic, respectively.

11.1.2 Compositional Engineering and Bandgap Tuning

In general, organometal halide perovskites have direct-bandgap structure. The bandgaps of halide perovskites can be easily tuned by replacing A/B-site cations and X-site anions in the composition, covering the entire visible spectral range and part of the near-infrared region. At the early stage, the most widely used halide perovskite material for PSCs was MAPbI$_3$, which has low crystallization temperature (~100 °C) and high efficiencies (>22%). However, its high-temperature (e.g., 85 °C) operating stability is not good enough, which is related with the low crystal formation energy [5]. Currently, most of the reported high efficiencies of PSCs are based on FAPbI$_3$-dominated mixed perovskites, with incorporation like Cs, K, MA, and MDA cations and Br anion for partial substitution of FA and I in FAPbI$_3$. Use of larger A-site cations has been proved to be useful for enhancing light absorption due to associated higher symmetry and smaller bandgap. Therefore, the bandgap of FAPbI$_3$ perovskite (~1.45 eV) is slightly smaller than that of MAPbI$_3$ (~1.55 eV), because of the larger ionic radius of FA cation than that of MA. The bandgap of FAPbI$_3$ perovskite is closer to the "ideal" single-junction solar cell bandgap (1.1~1.4 eV), [6] demonstrating higher light current. As widely reported in the literature, by simultaneously incorporating serval cations (like FA, MA, MDA, Cs, etc.), the perovskite lattice strain can be relaxed and the resulting mixed-cation perovskites are generally thermally more stable and show higher PCEs with better reproducibility.

Regarding B-site metal cations, the two most widely studied ions are Pb^{2+} and Sn^{2+}. Although Sn-based lead-free perovskites possess more ideal (smaller) bandgap than that of Pb-based perovskites, the performance of Sn-based devices lags far behind that of Pb-based PSCs, due to the inherent chemical instability of Sn^{2+} ions, which are prone to be oxidized into Sn^{4+} upon exposure in the air [7–12]. Recently, Sn–Pb mixed perovskites with narrow bandgaps (tunable from 1.2 eV to 1.3 eV) have enabled the construction of all-perovskite tandem solar cells, which are promising to exceed the PCEs of single-junction PSCs [13–16]. However, it is still challenging to prepare highly efficient and stable Sn–Pb mixed PSCs due to the easy oxidation of Sn^{2+} to Sn^{4+}.

Besides, the bandgap of the hybrid perovskites can also be continuously tuned by using mixed halides (I, Br, Cl). Previous studies have shown that the bandgap of MAPbI$_x$Br$_{3-x}$ perovskites can be tuned between 1.55 eV (MAPbI$_3$) and 2.30 eV (MAPbBr$_3$) by varying the halide composition between iodide (I) and bromide (Br),

while $FAPbI_xBr_{3-x}$ perovskites have tunable bandgap between 1.45 eV ($FAPbI_3$) and 2.23 eV ($FAPbBr_3$), thus enabling perovskite films with a variety of colors [17, 18]. The introduction of Br element also enhances the crystal stability of the perovskite films in ambient conditions. Similarly, the bandgap of $MAPbCl_xBr_{3-x}$ perovskites can be tuned between 2.30 eV ($MAPbBr_3$) and 3.16 eV ($MAPbCl_3$) by adjusting the composition ratio of Br and Cl [19].

In addition to the three-dimensional (3D) perovskites discussed above, the so-called two-dimensional (2D) metal halide perovskites (or layered perovskites), as an important category of perovskite materials, have attracted much attention of researchers for their desirable optoelectronic properties and improved stability compared to their 3D counterparts. The 2D layered perovskites have a general chemical formula of $L_2A_{n-1}B_nX_{3n+1}$, where L is a long-chain organic cation (spacer), A is a small organic cation, B is a metal cation, and X is a halide anion [20–22]. The 2D perovskites possess a very unique architecture, with n layers of inorganic BX_6 octahedral sheets sandwiched between two layers of organic chains. And their corresponding optoelectronic properties depend greatly on the value of n. Compared with their 3D counterparts, a wide variety of large organic cations (*L*) are suitable for the 2D crystal structure. Generally, the 2D perovskites are not a good choice as solar cell absorbers directly, because of their wide bandgaps and limited charge transport abilities of the 2D layers. Nevertheless, 2D perovskites are recently proved to be an excellent choice for 3D perovskite surface passivation.

11.1.3 Optoelectronic Properties

The outstanding optical and electronic properties of perovskite light absorbers are important fundamentals for their success and superior performance in photovoltaic and other optoelectronic applications. Being direct-bandgap semiconductors, the organic–inorganic hybrid perovskites have high light-absorption coefficients ($\sim 10^5$ cm^{-1}), [23, 24] long carrier diffusion lengths (micrometer scale),[25–27] long carrier lifetimes (microsecond scale),[28] low trap density ($\sim 10^{10}$ cm^{-3}) [25, 29], and modest carrier mobilities ($10^2 \sim 10^3$ cm^{2}V^{-1} s^{-1}) [30] Owing to their high optical absorption coefficients, a perovskite film less than 1 μm-thick is generally sufficient to absorb almost all the sunlight, [23] which can greatly reduce the material costs. Moreover, the exciton binding energy (E_b) for the iodide-based perovskite materials commonly used in PSCs was measured to be only a few millielectronvolts at room temperature, [31–33] which means that no high-electric fields across the absorber are required for the generation of free charges upon light illumination. Therefore, these superior optoelectronic properties ensure that charge carriers can be freely transported across the entire perovskite film (<1 μm) before recombination. However, for the polycrystalline perovskite films, it is noteworthy that the surface recombination (non-radiative, trap-assisted recombination at grain boundaries and film surface) is a major mechanism for losses in PSCs in compassion with bulk recombination inside perovskite crystals or grains [34, 35].

11.1.4 Deposition Methods of Perovskite Thin Films

In most cases, polycrystalline organic–inorganic metal halide perovskite thin films work as the core part of the perovskite-based optoelectronic devices. The film surface coverage, morphology, uniformity, crystallinity, etc., are closely related to the opto-electronic properties of the perovskite films. Therefore, depositing high-quality perovskite thin films is crucial for fabricating high-performance perovskite-based electronic devices. The most widely used lab-scale deposition methods of perovskite thin films generally include one-step route, two-step route, and vapor deposition route, as shown in Fig. 11.2. Among them, both one-step route and two-step route are solution-based processes (e.g., spin-coating), which are simple and less costly compared to the vapor deposition route.

(1) One-step Route

In the one-step route, stoichiometric metal halides (PbI_2, $PbBr_2$, SnI_2, etc.) and organic halides (MAI, FAI, etc.) are firstly dissolved in organic solvents like dimethyl formamide (DMF), dimethyl sulfoxide (DMSO), γ-butyrolactone (GBL), and N-methyl pyrrolidone (NMP), and then, the precursor solution is spin-coated on substrates directly, followed by thermal annealing on hotplates for complete crystallization of the perovskite films (see Fig. 11.2a). However, since all these solvents have high viscosities and high boiling points (150 ~ 200 °C), the slow evaporation of the solvents limits the perovskite nucleation rate, which consequently leads to low coverage (with pinholes) and high surface roughness of the prepared perovskite films [36]. In order to address this problem, an anti-solvent-assisted one-step route has been widely adopted by researchers, i.e., dripping volatile anti-solvents (such as chlorobenzene, toluene, diethyl ether, ethyl acetate) on the spinning substrate during the one-step perovskite spin-coating process. These anti-solvents cannot dissolve the solute but are miscible with the perovskite solvents (DMF, DMSO, etc.). Therefore, the dripped anti-solvents can extract perovskite solvents quickly, reduce the solute solubility, and create supersaturation conditions, leading to rapid precipitation or
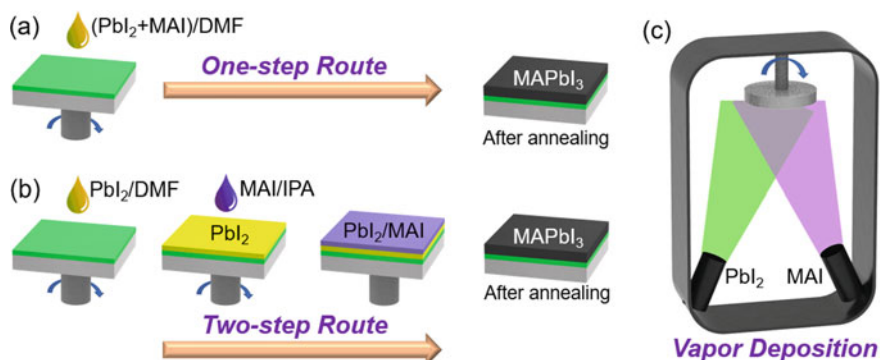

Fig. 11.2 Schematic deposition methods of perovskite thin films

crystallization of perovskite films. Additionally, the anti-solvents can also wash away part of the perovskite solvents since they are miscible with each other, which can further promote the rapid crystallization process. Consequently, the anti-solvent-assisted method increases the nucleus density during the film formation process, so that smooth, uniform, and pinhole-free perovskite films can be produced [37, 38]. Notably, the anti-solvent volume, dripping time, duration, flow speed, etc., are important influence factors of perovskite film quality.

In order to further improve the film quality, a solvent-engineering strategy (using mixed perovskite solvents, e.g., DMF/DMSO or GBL/DMSO) has been successfully used. In terms of $MAPbI_3$ perovskite, a $MAI-PbI_2-DMSO$ intermediate phase is formed during the anti-solvent-assisted spin-coating process due to the strong interaction between and DMSO [39]. The presence of the intermediate phase can retard the rapid reaction between MAI and PbI_2 during the spin-coating process, which leads to the formation of the uniform and smooth perovskite layer with comparatively larger grain size than that without DMSO. Besides, for $FAPbI_3$-based perovskites, using methylammonium chloride (MACl) as additive in perovskite solution has been demonstrated an effective strategy to dramatically increase the grain size and crystallinity of perovskite films prepared through the above-discussed anti-solvent-assisted one-step route [40–42]. It is noteworthy that the addition of MACl can also enlarge the time window for dripping anti-solvents, which ensures good device reproducibility. In addition to the anti-solvent-based method, some other approaches have also been studied for one-step fabrication of perovskite films, such as hot-casting, [43] vacuum pumping[44, 45], and gas quenching techniques, [46] which have their own pros and cons.

(2) Two-step Route

For the two-step sequential deposition route in early stages, a lead halide (like PbI_2) layer is first spin-coated on substrate, followed with immersing in organic halide salts (like MAI) solution (dissolved in 2-propanol) and subsequent thermal annealing for the conversion to perovskite phase [47, 48]. Later, an improved two-step route was developed, i.e., sequential spin-coating of lead halide and organic salt bilayer film, followed by a subsequent thermal interdiffusion-driven process for the reactions between the lead halide and organic salts and complete crystallization (see Fig. 11.2b). However, one of the most common problems for the two-step route is the incomplete conversion of PbI_2, with some residual insulating PbI_2 material at the substrate/perovskite interface, which will definitely hinder the charge transport and increase the device sheet resistance. Regarding to this puzzle, Sang Il Seok et al. exploited an intramolecular exchange process (IEP) approach, wherein the $PbI_2(DMSO)$ film (instead of PbI_2 film) was first deposited, followed by the coating of FAI and subsequent thermal annealing [49]. During annealing, DMSO was exchanged with FAI, consequently forming highly oriented $FAPbI_3$ films with large grains and flat surfaces without residual PbI_2. The resultant cells get a certified efficiency of 20.2%. Furthermore, mixed organic salts dissolved in 2-propanol, e.g., FAI:MAI:MACl or FAI:MABr:MACl, are often used for the fabrication of mixed perovskite films through two-step route [50, 51].

(3) Thermal Vapor Deposition Route

The thermal vapor deposition of perovskite films involves the simultaneous or alternate thermal evaporation of the solid metal halides (e.g., PbI_2, $PbBr_2$) and the organic halide salts powder (e.g., MAI, FAI, MABr) onto a rotating substrate by using a dual-source evaporation system (see Fig. 11.2c). In 2013, Henry J. Snaith et al. first adopted vapor-deposited $CH_3NH_3PbI_{3-x}Cl_x$ perovskite film as the absorbing layer, with which the first planar heterojunction PSC was prepared successfully and a PCE up to 15.4% was achieved [52]. The precise controlling of the deposition rates, substrate temperature, and the molar ratio of the two precursor materials are crucial for the preparation of high-quality vapor-deposited perovskite films. Compared with perovskite films prepared through solution processes, the vapor-deposited ones were extremely flat and uniform without pinholes or voids; thus, the vapor deposition route is applicable to the large-area perovskite deposition and perovskite-based tandem solar cell applications. However, this vapor deposition method is the least frequently used one these days, because the perovskite deposition conditions are complicated and expensive high-vacuum equipment is required [53].
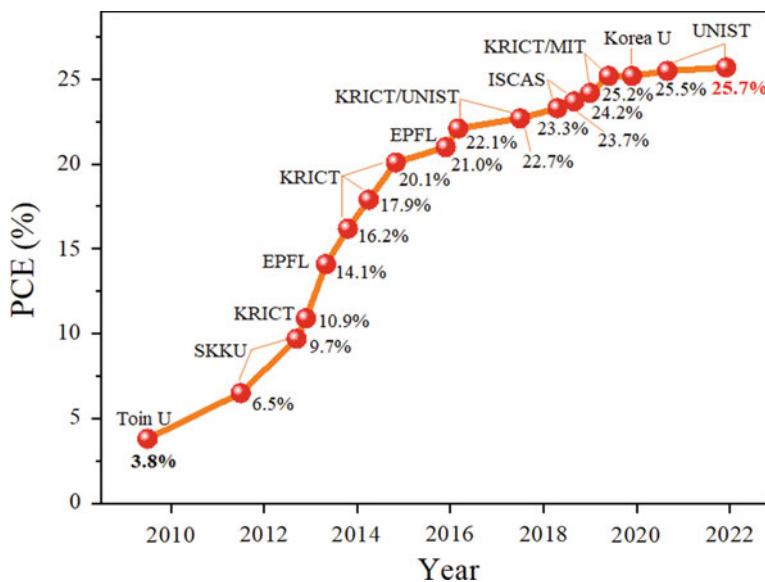
11.2 Perovskite Solar Cells (PSCs)

11.2.1 Evolution of PSCs

Referring to the best research-cell efficiencies chart downloaded from the Web site of National Renewable Energy Laboratory (NREL), [1] it is noteworthy that the efficiency growth rate of PSCs is faster than that of other PV technologies. Some of the important landmark efficiencies of PSCs are summarized in Fig. 11.3.

In 2009, Tsutomu Miyasaka and coworkers reported the photovoltaic application of metal halide perovskites for the first time, by depositing $MAPbBr_3$ and $MAPbI_3$ nanocrystalline particles on the ~10 μm-thick mesoporous TiO_2 film as visible-light sensitizers in the dye-sensitized solar cells (DSSCs) configuration with liquid hole-conducting electrolyte [54]. A champion efficiency of only 3.8% was obtained for $MAPbI_3$-sensitized cells at that time, while the cells were quite unstable, owing to the usage of the liquid hole-conducting electrolytes. Two years later, Nam-Gyu Park and colleagues prepared DSSCs with similar device structures based on $MAPbI_3$-quantum-dot-sensitized TiO_2 film (3.6 μm-thick), and they realized a cell efficiency of 6.5% in 2011 [55]. Similarly, the perovskite quantum-dot-sensitized solar cells possess very short lifetime (~10 min) due to the easy dissolution of the perovskite nanocrystals in the liquid electrolyte. This stimulated the replacement of the liquid electrolyte with solid-state hole transport materials (HTMs). Later in 2012, Nam-Gyu Park and Michael Gratzel et al. introduced a solid-state spiro-OMeTAD (2,2',7,7'-tetrakis(N,N-di-p-methoxyphenylamine)-9,9'-spirobifluorene) hole conductor and successfully fabricated the first all-solid-state perovskite sensitized mesoscopic solar cell with dramatically improved device efficiency (9.7%) and

Fig. 11.3 The efficiency roadmap of perovskite solar cells

shelf stability [56]. Herein, MAPbI$_3$ nanoparticles were deposited onto a submicron-thick mesoporous TiO$_2$ films (600 nm-thick), whose pores were infiltrated with spiro-OMeTAD solution, leaving only solid spiro-OMeTAD after solvent evaporation. Almost simultaneously in the same year, Henry J. Snaith et al. also reported success with spiro-OMeTAD hole conductor [36]. They replaced the TiO$_2$ mesoporous layer and MAPbI$_3$ absorber with an insulating Al$_2$O$_3$ scaffold and an iodide-chloride mixed-halide perovskite (MAPbI$_2$Cl), respectively. As a result, the newly developed hybrid solar cell, termed as "meso-superstructured solar cell" (MSSC), delivered a higher PCE of 10.9% with increased photovoltage. This mixed-halide perovskite material was reported to have remarkably better stability and carrier transport property than its pure iodide equivalent. Notably, only perovskite nanoparticles or quantum dots, instead of perovskite thin films or capping layer, were employed up to that time. Therefore, those cells, essentially, still belong to the category of sensitized solar cells.

In 2013, Sang Il Seok and Michael Gratzel et al. reported a PCE up to 12% by using a polymeric hole conductor (poly-triarylamine, denoted as PTAA) in the device structure of mp-TiO$_2$(600 nm-thick)/MAPbI$_3$/PTAA/Au [57]. Specifically, a solid perovskite capping layer was found on top of the mp-TiO$_2$/MAPbI$_3$ composites. By using similar device structures (with mp-TiO$_2$ and PTAA) and MAPb(I$_{1-x}$Br$_x$)$_3$ perovskites, Seok's group further improved the device efficiency to 12.3% (when x = 0.2) with greatly improved stability. Later in 2013, Gratzel's group reported a sequential deposition route (i.e., the two-step method), permitting much better control over

the perovskite formation [47]. PbI_2 solution is first infiltrated into a mp-TiO_2 scaffold film and subsequently transformed into the $MAPbI_3$ perovskite after exposing in MAI solution. The resultant mesoscopic solar cells got a PCE of 15.0% (certified efficiency of 14.1%). This two-step method has been widely adopted by researchers ever after for its better reproducibility. Subsequently, Snaith's group reported similar efficiency (15.4%, without certification) by employing a compact vapor-deposited $MAPbI_{3-x}Cl_x$ perovskite film and a simple planar heterojunction thin-film device architecture (FTO/compact-TiO_2/perovskite/spiro-OMeTAD/Ag) [52]. It is noteworthy that the vapor-deposited perovskite films were extremely uniform and flat in comparison with the solution-processed ones. Moreover, the innovative planar device structure (without the mesoporous scaffold) developed by Snaith et al. exerted a profound effect on the subsequent evolution of PSC structures, although this device structure at that time tends to have significant I-V hysteresis phenomenon.

Soon afterward in 2014, Seok's group reported a certified PCE of 16.2% (certified in 2013) without I-V hysteresis by using a bilayer solar cell architecture: FTO/compact-TiO_2/mp-TiO_2 + perovskite(200 nm-thick)/perovskite capping layer/PTAA/Au [39]. Extremely uniform and dense mixed-halide $MAPbI_{3-x}Br_x$ perovskite films were prepared by using a solvent-engineering technique (GBL/DMSO mixed solvents) and anti-solvent quenching approach, which became very popular in the PSC community afterward. Subsequently in early 2015, a higher certified efficiency of 17.9% (certified in early 2014) was reported also by Seok's group by using the $(FAPbI_3)_{1-x}(MAPbBr_3)_x$ mixed perovskites [58]. The incorporation of $MAPbBr_3$ was found capable of stabilizing the $FAPbI_3$ perovskite phase for efficient and stable PSCs.

Later in 2015, the first confirmed efficiency of over 20% (20.1%, certified in late 2014) was reported by Seok's group [49]. They prepared high-quality $FAPbI_3$-based perovskite films through the IEP process (as discussed in 11.1.4). Then in early 2016, Gratzel's group reported a certified efficiency ~21% (certified in late 2015), enabled by cesium (Cs)-containing triple cation perovskite compositions, i.e., $Cs_x(FA_{0.83}MA_{0.17})_{1-x}Pb(I_{0.83}Br_{0.17})_3$ [59]. The device structure used is a stack of FTO/compact-TiO_2/Li-doped mp-TiO_2/perovskite/spiro-OMeTAD/Au. Subsequently in 2017, Seok et al. reported an iodide management strategy based on the previously adopted IEP process and achieved a certified PCE of 22.1% (certified in early 2016), which was further improved to 22.7% (certified in mid-2017) [60]. The introduction of additional iodide ions into the FAI (MABr) solution decreases the concentration of deep-level defects.

Further progress was reported by Jingbi You's group from China in 2019 [51]. They used an organic salt phenethylammonium iodide (PEAI) for the surface passivation of $FA_{1-x}MA_xPbI_3$ perovskites (prepared by two-step route) to suppress the surface defects. As a result, certified efficiencies of 23.3% and 23.7% (both certified in 2018) were obtained, respectively. Also in 2019, Seok's team got the same certified efficiency of 23.7% by stabilizing α-$FAPbI_3$ perovskite with the incorporation of methylenediammonium dichloride ($MDACl_2$, 3.8 mol%) [41]. Later, an increased efficiency of 24.4% (certified in early 2019) was reported in 2020 by the same group

through simultaneous substitution of Cs and MDA in $FAPbI_3$ perovskite for lattice strain relaxation [42].

Strikingly, a few efficiencies exceeding the 25% mark were obtained independently by several different research groups from 2019 to 2021. Moungi G. Bawendi1 and Jangwon Seo et al. reported a certified PCE of 25.2% by using a chemical-bath-deposited SnO_2 electron transport layer, [61] while Jin Young Kim and colleges achieved an equal certified efficiency by pseudo-halide anion engineering of $FAPbI_3$ perovskite using formate ($HCOO^-$), both of which were certified in 2019 [62]. Dong Suk Kim et al. adopted polyacrylic acid-stabilized SnO_2 quantum dots on the compact-TiO_2 (QD-SnO2@c-TiO2) as electron transport layer, which enabled a certified efficiency of 25.4% [63]. Soek's group obtained a certified PCE of 25.5% in mid-2020 by coupling Cl-bonded SnO_2 with a Cl-containing perovskite precursor [64]. Besides, the very recent new champion efficiency of 25.7% (certified in late 2021) [1] is likely still from Seok's group. Therefore, the SnO_2-based planar PSCs seem to have great potential for achieving new record efficiencies.

11.2.2   Device Architectures

PSCs are usually composed of perovskite light absorbers, charge transport layers, and electrodes. Currently, the most often adopted device architectures for PSCs can be categorized into three types: [65] mesoporous n-i-p structure, planar n-i-p structure, and planar p-i-n structure, as shown in Fig. 11.4. Among them, n-i-p and p-i-n architectures correspond to normal structure and inverted structure, respectively. Herein, n and p denote n-type (e.g., TiO_2, ZnO, SnO_2, PCBM) and p-type (e.g., spiro-OMeTAD, PTAA, PEDOT:PSS, NiO_X, CuSCN) semiconducting material films, [66] working as electron transport layers (ETLs) and hole transport layers (HTLs), respectively, while I represent the perovskite light-absorbing layer. In principle, charge transport layers should have good energy level alignment with perovskite layer and electrodes, for efficient charge transport and collection.

The mesoporous n-i-p structure first evolved from the dye-sensitized solar cells (DSSCs) configuration with a thick mesoporous metal-oxide scaffold layer (like mp-TiO_2) [54]. The mesoporous layer allows the infiltration of perovskite precursor solution and the formation of mp-TiO_2/perovskite intermixed layer. In the very early stage, the mesoporous TiO_2 layer (mp-TiO_2) usually has a thickness of more than one micrometer for sufficient light absorption, which however impedes the cell efficiency because the perovskite grains are confined by the dimensions of the pores and cannot grow into larger ones. Currently, mesoporous layer with thickness less than 300 nm is often utilized for the mesoporous n-i-p devices, and a dense and uniform perovskite capping layer with large perovskite grains will form on top of the mesoporous layer (see Fig. 11.4a). PSCs with device structure of FTO/compact-TiO_2/mp-TiO_2/perovskite/spiro-OMeTAD/Au now can achieve certified efficiencies higher than 25% [62, 67]. However, the high-temperature sintering process of the
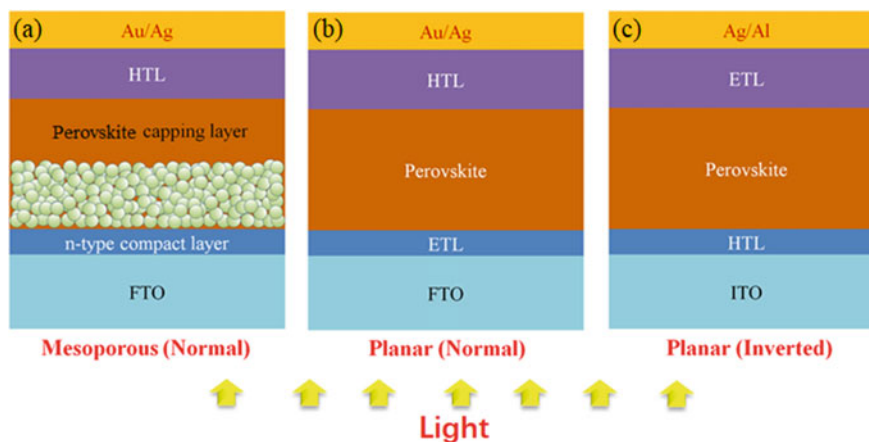
Fig. 11.4 Schematic illustrations of the most commonly used device architectures of PSCs. Reprinted with permission from Ref. [78]

mesoporous layer hampers the development of PSCs since it is unfavorable for scaling.

In planar structures, the mesoporous layer is omitted; therefore, there is no mesoporous/perovskite intermixed layer in the device structure, which not only simplifies the device preparation processes, but also allows for the low-temperature preparation. In the planar n-i-p architecture, the perovskite layer is directly deposited on the thin ETL (~30 nm), followed by the coating of HTL and top electrodes (see Fig. 11.4b). To date, the best n-i-p PSCs normally employ SnO_2 as ETL, with device structure of FTO/SnO_2/perovskite/spiro-OMeTAD/Au, and can attain similar or even slightly higher efficiencies (>25%) than that of mesoporous devices [61, 63, 64]. Notably, the I-V hysteresis is negligible for well-prepared planar PSCs based on SnO_2 ETL. In contrast with the planar n-i-p structure, in the planar p-i-n structure, the perovskite layer is deposited on top of ultrathin HTL (mostly PTAA or NiO_X), as shown in Fig. 11.4c. High-performance planar p-i-n PSCs generally possess device structure of ITO/PTAA/perovskite/PCBM/BCP/Ag, and the champion cell efficiencies are ~24% [68–76]. In addition, the simple planar device structure enables the easy preparation of semitransparent (using transparent electrodes like graphene) and flexible PSCs (on flexible substrates) through low-temperature solution processes [77–79].

11.2.3   State-Of-The-Art PSC Technologies

To date, the champion cell efficiencies of single-junction PSCs (25.7%) have crossed the 25% threshold, approaching the highest certified efficiencies of single-crystal silicon solar cells (26.1%) and silicon heterostructure cells (26.7%) [1]. Currently, the state-of-the-art PSCs are usually based on organic–inorganic lead halide PSCs

with normal device architectures, either mesoporous n-i-p structure (with mp-TiO$_2$ layer) or planar n-i-p structure (SnO$_2$ as ETL).

In terms of the perovskite active layers for the state-of-the-art PSCs, FAPbI$_3$-dominated mixed perovskites are generally prepared through the above-mentioned anti-solvent-assisted one-step route, with DMSO incorporation for Lewis acid–base adduct formation. Notably, methylammonium chloride (MACl) is commonly utilized as additive in perovskite precursor solution to help mediate the crystallization process of perovskites [41, 42, 61, 62, 64, 80]. The MACl additive is shown to induce the formation of intermediate phase with pure α-phase FAPbI$_3$ perovskite films without annealing [40, 81–83]. Then, the intermediates disappear quickly and transform into perovskite phase during later thermal annealing process, because of the volatile property of MACl. Notably, almost no MACl exists in the annealed perovskite films. By tuning the incorporation amount of MACl (optimized value ~35 mol%), high-quality and stable perovskite film with enlarged grain size, enhanced crystallinity, and increased carrier lifetime can be obtained.

As discussed above, photoinactive δ-phase FAPbI$_3$ (yellow phase) is prone to form during the film deposition process; meanwhile, the α-phase FAPbI$_3$ (black phase) film is intrinsically unstable and can spontaneously transform into the undesirable δ-phase, which will both greatly deteriorate the performance of PSCs [84, 85]. In order to fabricate and also stabilize phase-pure α-phase FAPbI$_3$ (black phase) films, a series of compositional engineering strategies have been developed, such as the incorporation of MAPbBr$_3$ and Cs$^+$, i.e., (FAMA)Pb(IBr)$_3$ or (FAMACs)Pb(IBr)$_3$,[58, 59] whereas the introduction of MA, bromine, and caesium components (normally < 15 mol%) will widen the mixed perovskite bandgap, which is unfavorable for the light absorption and photocurrent generation. To maximize the light-absorption region, Sang Il Seok et al. used the inherent bandgap of α-phase FAPbI$_3$ (~1.45 eV) to increase the photocurrent of PSCs [41]. They stabilized the α-FAPbI$_3$ phase by doping with only 3.8 mol% methylenediammonium dichloride (MDACl$_2$) while inducing only a slight change in the perovskite bandgap; therefore, they achieved certified short-circuit current densities of over 26 mA/cm^2 and a certified efficiency of 23.7%. Further optimization of the FAPbI$_3$-MDA strategy by Cs-MDA codoping, as well as the replacement of compact-TiO$_2$/mp-TiO$_2$ double layer with atomically coherent SnO$_2$ thin film, contributes to the much higher certified efficiencies of 24.43% and 25.5%, respectively [42, 64]. Except for the above cation-doping strategies, Jin Young Kim et al. also introduced an anion engineering concept using pseudo-halide anion formate (HCOO −, 2 mol% addition) to suppress anion-vacancy defects located at perovskite film surface and grain boundaries, with enhanced film crystallinity [62]. The resulting PSCs attain a certified PCE of 25.2% and maintain excellent operational stability.

In addition to the stabilizing of perovskite absorbers, interfacial engineering at perovskite/HTL and perovskite/ETL interfaces is also of crucial importance for achieving highly efficient and stable PSCs. As is known, the interfaces between the perovskite and charge transport layers contain much higher concentrations of defects than that within the perovskite layer, specifically deep-level defects, which seriously hamper the device efficiencies [29, 86, 87]. Currently, the most popular

perovskite surface (perovskite/HTL interface) passivation materials are alkylam-monium halides bearing long alkyl chains, such as phenethylammonium (PEA^+), ethylammonium (EA^+), and n-butylammonium (BA^+), which improve the device efficiencies and stabilities by forming 2D perovskite capping layers [28, 42, 51, 61, 62, 64, 88, 89]. The so-called 2D/3D passivation strategy nowadays has been widely used for perovskite surface passivation. However, it is difficult to effectively passivate the underlying perovskite/ETL interface, because the passivation materials deposited on ETL may be dissolved by perovskite solution during perovskite film spin-coating process. In view of this issue, Sang Il Seok et al. reported the formation of an ultrathin atomically coherent interlayer at the SnO_2/perovskite interface, achieved by coupling Cl-bonded SnO_2 with a Cl-containing perovskite precursor [64]. This interlayer leads to the decreased interfacial defects and enhanced charge extraction and transport from the perovskite layer, resulting in a certified high efficiency of 25.5% under standard light illumination. The Cl-bonded SnO_2 films used here were deposited by using either spin-coating or chemical bath deposition methods, from either $SnCl_2 \cdot 2H_2O$ solution in ethanol or $SnCl_4$ solution in deionized water.

11.2.4 Stability of PSCs

Although PSCs have lots of advantages in competition with silicon and other thin-film solar cells, poor long-term operating stability of PSCs remains a main issue that hinders their commercialization. Generally, there are intrinsic and extrinsic factors that influence the device degradation processes of PSCs. The intrinsic device instabil-ities of PSCs are closely correlated with the intrinsic crystallographic and chemical instability of the perovskite absorbers, as well as other negative effects like ion migration, electrode-perovskite reactions, residual strains, and the instable nature of organic charge transport layers [90–94]. On the other hand, various extrinsic environ-mental factors, like UV-light, moisture, oxygen, thermal stress, etc., will accelerate the decomposition of ABX_3 crystal into its constituents and additional by-products, which tend to magnify the intrinsic instabilities of perovskites and further aggravate the perovskite and device degradation processes [8, 95, 96].

At present, the majority of the PSC stability studies are focusing on $FAPbI_3$-based devices. While $FAPbI_3$ has better thermal stability than $MAPbI_3$ perovskite, the black $FAPbI_3$ perovskite phase (α-phase) is not stable at room temperature, due to the easy formation of the undesirable photoinactive δ-phase (yellow phase). There-fore, many recent researches have been conducted with regard to the stabilizing of the $FAPbI_3$ perovskite phase, and outstanding progress has been made. Inter-estingly, many above-mentioned strategies for achieving high efficiencies (>24%), e.g., compositional engineering, additive engineering, 2D/3D interfacial engineering, and charge transport layer design, in most cases, can also help achieve and main-tain α-$FAPbI_3$ phase in PSCs [40, 62, 64]. For example, based on the principle of tolerance factor adjustment, the incorporation of inorganic cations (Cs^+, Rb^+) with smaller ionic radius to A-site can suppress phase transition processes to yellow

phase and improves crystal stability [59, 97]. Moreover, 2D perovskite surface passivation layer has been proved to be quite effective for stabilizing the underlying 3D perovskites, because 2D perovskites exhibit better humidity stability compared with 3D perovskites, and enhanced activation energy barrier for phase transition (black phase to yellow phase) [98]. The hydrophobic alkane chain in 2D perovskites can also help suppress the influence of humidity on 3D perovskites. Recently, Wei Huang and coworkers reported the synthesis of stable α-FAPbI$_3$ in ambient air, irrespective of atmosphere humidity (20~90%) and temperature (25~100 °C), based on vertically aligned PbI$_2$ thin films grown from an ionic liquid methylamine formate (MAFa), instead of using the commonly used solvents like DMF and DMSO [99]. The vertically grown PbI$_2$ film has numerous nanometer-scale ion channels, which facilitate the diffusion of FAI into the PbI$_2$ thin films for fast and robust transformation to α-FAPbI$_3$. PCEs of over 24% were achieved for the PSCs prepared in ambient air. The unencapsulated cells can retain 80% and 90% of their initial efficiencies after operation at maximum power point for 500 h at 85 °C and continuous light stress, respectively.

11.2.5   Upscaling of PSCs

At present, the efficiencies of large-area PSCs (>1 cm^2) still lag behind that of small-sized devices (mostly around 0.1 cm^2). The development of large-area PSCs and modules is essential to their mass production and commercialization; thus, more and more researchers and companies have been devoted to the upscaling of PSCs over the past decade. The main challenge for the manufacture of high-performance large-scale PSCs is the scalable fabrication of high-quality large-area perovskite films with uniform and dense surfaces. Here for large-area films, the laboratory-scale spin-coating method is not applicable any more, due to the poor reproducibility and the non-uniformity of films from center to edge, while some other scalable deposition approaches are utilized instead by researchers, such as blade (bar) coating, slot-die coating, inkjet printing, spray coating, screen printing, vacuum deposition methods, and roll-to-roll printing (for flexible substrates) [100–104]. To date, many notable results on large-area PSCs have been achieved. For example, a certified stabilized efficiency of 18.6% with an aperture area of ~30 cm^2 (corresponding to an active area efficiency of 20.2%) has been obtained for minimodules with blade-coated perovskite layer, [101] and a PCE of 17.9% has been achieved by inkjet printing for perovskite module with area ~800 cm^2, according to the Champion Photovoltaic Module Efficiency Chart plotted by National Renewable Energy Laboratory (NREL) [105]. The increasing module efficiencies indicate large potential for practical use in the future. However, the perovskite module stability is also a main challenge in for large-scale manufacturing and applications [106].

When it comes to commercialized perovskite solar modules, it is necessary to pattern the ITO or FTO electrodes and divide the full-sized bottom electrodes into multiple subcells, because of the relatively low sheet resistances of ITO or FTO

electrodes (7~15 Ω/sq). Two main architectures are normally employed, i.e., series-connected and parallel-connected architectures. To realize interconnections of such architectures, laser-scribing techniques (known as P1, P2, and P3 scribing processes) are generally used in industrial production [107]. The P1, P2, and P3 scribing steps are conducted for the patterning of bottom electrodes, charge transport layers/active layer, and top electrodes, respectively. Additionally, the deposition of metal grid on ITO or FTO electrodes is often employed as an strategy to increase the charge collection on the bottom electrodes [108].

11.3 Other Perovskite-Based Devices

The organic–inorganic hybrid metal halide perovskite materials, which have led to unprecedented success in photovoltaic devices, have also been proved to be promising candidates for many other optoelectronic applications, such as light-emitting diodes, lasers, photodetectors, sensors, photocatalytic devices, thermoelectric devices, and memory devices. These perovskite-based devices normally inherit the typical device architectures and working principles of the organic devices discussed in previous chapters, while demonstrating many special advantages due to the extraordinary optoelectronic features and low-cost fabrication of the metal halide perovskites. In this part, several representing types of perovskite-based devices will be introduced briefly.

11.3.1 Perovskite Light-Emitting Diodes and Lasers

Apart from the great advances of PSCs, the perovskite light-emitting diodes (PeLEDs) with perovskite emitting layers have become another hot topic and witnessed great progress in recent years. The effective light emission from the hybrid perovskites originates from their remarkable characteristics, including: (i) high photoluminescence quantum yield (PLQY), (ii) narrow emission linewidth, (iii) wide bandgap tunability through composition engineering, (iv) low defect density, (v) low non-radiative recombination, (vi) easy solution processability, and (vii) negligible Stokes shifts. Light emissions of various color (from visible to near-infrared region) with high brightness can be obtained due to the wide-range tunable bandgaps of the hybrid perovskites, which may help surmount some of the shortcomings of both traditional LEDs (suboptimal color quality) and OLEDs (low maximum brightness and color quality). The demonstration of effective perovskite electroluminescence offers scope for developing efficient and color-tunable light emitters for low-cost lighting, display, and other optical applications.

The electroluminescence performance of PeLEDs can be quantified via the external quantum efficiency (EQE), that is, the ratio between emitted photons to the electrons flowing in the circuit. In general, to maximize the EQE of the PeLEDs,

important factors like leakage current, non-radiative recombination, charge balance, and photon recycling should be carefully considered [109, 110]. Highly efficient PeLEDs will result from the combination of an optimized perovskite emitter with suppressed non-radiative recombination, as well as the device architecture designs favoring the radiative charge recombination in the perovskite layer and the extraction of the emitted photons. Generally, halide perovskites with different dimensionalities, including 3D (bulk, nanocrystals, and quantum dots) and quasi-2D perovskites, are utilized as the perovskite emitting layer. In contrast to 3D perovskites with very low exciton binding energies (a few meV), the quasi-2D layered perovskites possess very large exciton binding energies (several hundreds of meV) due to enhanced electron–hole interactions originating from their special natural quantum-well structures, where the inorganic layers act as "wells" and the organic molecules act as "barriers."

In 2014, Richard H. Friend et al. reported the first room-temperature operating PeLED based on solution-processed organometal halide perovskites [111]. They prepared infrared ($MAPbI_{3-x}Cl_x$) and green ($MAPbBr_3$) light-emitting devices, with very low EQEs of 0.76% and 0.1%, respectively. Since then, the device performances have experienced rapid progressing. So far, the EQEs of PeLEDs have surpassed 20% for green, red, and near-infrared (NIR) emission and more than 10% for blue and white emission [112–116].

Along with the rapid performance enhancements for PeLEDs, extensive efforts are focusing on resolving their instable issue, which is mainly caused by chemical reactions and ion migration in the perovskite emitting layers and at interfaces [117]. The device stability of PeLEDs mainly suffers from moisture, temperature, photodegradation, and bias-induced degradation. To date, the champion operating half-life (T_{50}) of PeLEDs is 2400 h, [118] while most of the reported T_{50} values are less than 100 h under operation, which still lag far behind that of the state-of-the-art inorganic LEDs and OLEDs (up to a million hours). More studies on device optimization strategies and degradation mechanisms are required before achieving industry-ready operational stability.

For luminescent applications beyond LEDs, the metal halide perovskites have also shown great potential as gain media for solution-processed laser diodes, in consideration of their excellent carrier mobilities, low non-radiative recombination, sharp absorption onsets, and large gain cross section at the emission wavelength [119]. In fact, optically pumped lasers with high-quality perovskite gain media have already been demonstrated successfully through Fabry–Perot cavities or whispering mode cavities [120–122]. However, to date, the realization of electrically driven perovskite lasers remains a great challenge, mainly because of the low stability of the metal halide perovskites, especially at the lasing working conditions with high temperatures induced at the lasing regime.

11.3.2   Perovskite Photodetectors

In terms of light detection, high-performance perovskite photodetectors (PePDs) could be obtained by using lead halide perovskites in device forms of photodiodes, photoconductors, and phototransistors. Recently, PePDs have gained increasing attention and research interests due to their fast response speeds, high specific detectivities, high responsivities, wide response wavelength range, low noise, and controllable wavelength-dependent response [123, 124]. Compared with traditional silicon-based photodetectors, the hybrid perovskite films with thickness of only a few-hundred nanometers in PePDs can absorb a much greater number of photogenerated charge carriers per unit of thickness, leading to improved EQEs and low response time. The detection wavelengths of PePDs cover a wide range of the electromagnetic spectrum from visible to near-infrared and even to X-ray band. Therefore, PeLEDs have many promising applications, including imaging, communication, medical sensors, automatic control, etc.

Recently, hybrid PePDs based on perovskite/2D material heterojunctions have attracted increasing attention [125]. Herein, the perovskite films with large absorption coefficients are mainly responsible for light harvesting, while high-mobility ultrathin 2D materials work as charge transport layer/channel. This heterojunction structure increases the device performance greatly, with ultrafast interfacial charge transfer (based on the photogating effect) and high responsivity along with fast response. A variety of 2D materials, such as graphene or its derivatives, transition-metal dichalcogenides, transition-metal nitrides, black phosphorous, and MXene, have also been successfully integrated with perovskites for PePDs applications.

11.3.3   Perovskite X-ray Detectors

As a special branch of photodetectors, X-ray detectors and imagers are widely applied in our daily life, such as being used for medical diagnostics, security check, and non-destructive product inspection. Generally, highly sensitive and low-dose imaging is desired to reduce the side effects and risks caused by X-ray irradiation. The metal halide perovskites naturally with high Z atoms (e.g., Cs, Pb) could attenuate X-ray effectively. Perovskite X-ray detectors with lower fabrication cost have showed much higher sensitivity and lower detectable X-ray dose than the commercial α-Se X-ray imagers in recent reports [126–129]. Moreover, the low-temperature solution growth of large perovskite single crystals offers the opportunity of fabricating large-area single-crystal X-ray imagers, which could suppress the ghosting or image lags with the absence of grain boundaries. These superior properties establish the potential of perovskite X-ray detectors to be the next-generation X-ray imagers. However, there is still lots of work that needs to be done before the commercialization of perovskite X-ray imagers. Except for the stability issue, some commercially concerned parameters,

such as detective quantum efficiency (DQE), image lag, and ghosting, should be further optimized for better comparison with the commercial detectors.

In addition to the above-discussed applications, the organometal halide perovskites have also been employed for a variety of other optoelectronic applications, such as photocatalytic, thermoelectric, sensing, and memory devices. When it comes to the photocatalysis research and applications, the metal halide perovskites have been employed for solar water splitting, hydrogen generation, organic contaminants degradation, etc. For sensor applications, the hybrid perovskite materials have been used for a variety of analytes, such as gases, solvents, metal ions, organic compounds, humidity, and temperature. However, the perovskite stability issue needs to be further addressed to achieve high-performance optoelectronic devices.

11.4   Summary and Perspectives

As one of the most promising photovoltaic materials, the organic–inorganic metal halide perovskites have gained great attention worldwide during the past decade, showing promising potential in many kinds of optoelectronic devices. In particular, the perovskite photovoltaic devices (PSCs) have undergone great success and progress. The hybrid perovskite materials have risen to stardom due to their extraordinary optoelectronic properties, such as high optical absorption coefficient, high carrier mobility, long free carrier diffusion length, low exciton binding energy, and easy solution processability. To date, the highest certified cell efficiency (25.7%) of PSCs is already very close to 26%. And the reported PCEs of perovskite/silicon tandem solar cells have reached 29.8% [1]. The excellent device performance and low fabrication costs of the PSC technology make it a promising candidate to compete with silicon-based solar panels. However, some issues like long-term stability, lead toxicity, and upscaling fabrication are critical challenges to face for PSCs. Due to the excellent defect tolerance of perovskite, its applications expand not only to photoelectric conversion but also to LEDs, photodetectors, etc.

In order to achieve highly efficient PSCs with long-term operational stability, it is essential to have high-quality perovskite films with smooth surface, full coverage (pinhole-free), high crystallinity (large grain size), stable photoactive crystal phase, low defect density on surface and at grain boundaries, and good heterojunction contacts. Therefore, improving the crystal quality of perovskite films, defect passivation and suppression of non-radiative recombination at interfaces (interface engineering), and rational selection of charge transport layers are expected to further improve the device efficiency. Notably, for the widely adopted $FAPbI_3$-based mixed perovskites, the formation of photoactive yellow phase, as well as phase segregation phenomenon, often occurs during the film fabrication process, which has not been well solved to date.

Currently, progress in crystal growth, compositional engineering, solvent engineering, intermediate phase engineering, and film deposition approaches have made it possible to prepare organometal halide perovskite thin films with minimized bulk

trap density, such that defects are predominantly located at the interfaces and grain boundaries. This has motivated the development of interfacial defect passivation. The perovskite top and bottom interface engineering through surface treatment is often adopted in the literature for defect passivation. For example, some organic halide salts are widely used to modify the perovskite surface and form an interfacial 2D perovskite layer (2D/3D heterostructure), which can dramatically stabilize the perovskite surface. However, a recent study shows that surface treatments may induce a negative work function shift (i.e., more n-type), which activates halide migration to aggravate PSC instability [130]. Therefore, despite the beneficial effects of surface passivation, this detrimental side effect may limit the maximum device stability attainable for PSCs. In view of this phenomenon, some new interfacial modification materials that will not change perovskite work function are desired. One important choice is 2D materials. As reported, high-mobility 2D flakes like black phosphorous are promising for perovskite surface modification, which can greatly enhance charge transport and device performance [96]. Therefore, the heterointerfaces in PSCs, as well perovskite grain boundaries, should be optimized carefully to achieve better device performance.

In addition to device efficiency and stability, recently, research topics on reducing lead toxicity and lead leakage have entered people's vision. Since the heavy metal Pb (Pb^{2+}) is soluble in water, lead leakage from the cracked perovskite solar panels will show serious potential threat to the environment and human health. Moreover, due to the ionic nature of the organometal halide perovskites, they tend to decompose quickly in the presence of water, which accelerates the leakage of Pb. In some recent studies, perovskite surface layers, like metal–organic framework, 2D perovskites, and polymers, are employed to help slow down the perovskite film dissolution speed and reduce lead leakage, while the long-term operational stability can also be substantially improved [131–134]. Besides, the development of more reliable cell encapsulation techniques is also very important for improving device stability and preventing lead leakage.

Further development of PSCs also calls for solutions for the upscaling fabrication issue. For PSCs, the slight increase in area (e.g., from $0.1cm^2$ to $1cm^2$) will lead to a dramatic drop of the cell efficiency (e.g., from 25% to less than 22%). In literature, PSCs with active area of $1cm^2$ are often described as large-area device. However, such small area ($1cm^2$) is still far from the requirements of practical solar panel products. Perovskite modules with larger area show even lower efficiencies. For example, the highest certified module efficiency to date is as low as 17.9% (802 cm^2, Panasonic) [105]. Therefore, minimizing the efficiency loss between small-area cells and large-area modules still remains a great challenge for PSCs. The wide gap between small-area cells and large-area modules comes from several reasons. Firstly, the quality of perovskite films fabricated by using scalable approaches (e.g., blade coating, inject printing, roll-to-roll printing) is poorer with more defects. Secondly, the relatively high resistance of the transparent conducting electrode (ITO or FTO) used in PSCs is another key aspect that accused for the loss of the module efficiency. Normally, this effect can be relieved by dividing a large panel into many small subcells, which are serial or parallel-connected through interconnections. Therefore,

the contact resistance of these interconnections will also contribute to the series resistance increase and efficiency loss of the perovskite module. Although the development of PSC is facing a variety of great challenges, it has already shown great promise toward large-scale production and applications in the near future.

References

1. National Renewable Energy Laboratory (NREL), Best research-cell efficiency chart, https://www.nrel.gov/pv/cell-efficiency.html. Accessed June, 2022
2. Baikie T et al (2013) Synthesis and crystal chemistry of the hybrid perovskite (CH3NH3)PbI3 for solid-state sensitised solar cell applications. J Mater Chem A 1(18):5628–5641
3. Kim HS, Im SH, Park NG (2014) Organolead halide perovskite: new horizons in solar cell research. J Phys Chem C 118(11):5615–5625
4. Green MA, Ho-Baillie A, Snaith HJ (2014) The emergence of perovskite solar cells. Nat Photonics 8:506–514
5. Conings B et al (2015) Intrinsic thermal instability of methylammonium lead trihalide perovskite. Adv Energy Mater 5(15):1500477
6. Meillaud F et al (2006) Efficiency limits for single junction and tandem solar cells. Sol Energy Mater Sol Cells 90(18–19):2952–2959
7. Bernal C, Yang KS (2014) First-principles hybrid functional study of the organic-inorganic perovskites CH3NH3SnBr 3 and CH3NH3SnI3. J Phys Chem C 118(42):24383–24388
8. Tai QD et al (2019) Antioxidant grain passivation for air-stable tin-based perovskite solar cells. Angewandte Chemie-International Edition 58(3):806–810
9. Tai QD et al (2019) Recent advances toward efficient and stable tin-based perovskite solar cells. Ecomat 1(1):e12004
10. Cao JP et al (2019) Enhanced performance of tin-based perovskite solar cells induced by an ammonium hypophosphite additive. J Mater Chem A 7(46):26580–26585
11. Wang TY et al (2021) 2D WSe2 flakes for synergistic modulation of grain growth and charge transfer in tin-based perovskite solar cells. Adv Sci 8(11):2004315
12. Tang GQ et al (2021) Synergistic effects of the zinc acetate additive on the performance enhancement of Sn-based perovskite solar cells. Mater Chem Frontiers 5(4):1995–2000
13. Cao JP et al (2022) High-performance tin-lead mixed-perovskite solar cells with vertical compositional gradient. Adv Mater 34(6):2107729
14. Yu Z et al (2022) Gradient doping in Sn-Pb perovskites by barium ions for efficient single-junction and tandem solar cells. Adv Mater e2110351
15. Prasanna R et al (2019) Design of low bandgap tin-lead halide perovskite solar cells to achieve thermal, atmospheric and operational stability. Nat Energy 4(11):939–947
16. Bandara RMI et al (2022) Progress of Pb-Sn mixed perovskites for photovoltaics: a review. Energy Environ Mater 5(2):370–400
17. Eperon GE et al (2014) Formamidinium lead trihalide: a broadly tunable perovskite for efficient planar heterojunction solar cells. Energy Environ Sci 7(3):982–988
18. Noh JH et al (2013) Chemical management for colorful, efficient, and stable inorganic-organic hybrid nanostructured solar cells. Nano Lett 13(4):1764–1769
19. Kumawat NK et al (2015) Band gap tuning of CH3NH3Pb(Br 1-xClx)(3) hybrid perovskite for blue electroluminescence. ACS Appl Mater Interfaces 7(24):13119–13124
20. Dou LT et al (2015) Atomically thin two-dimensional organic-inorganic hybrid perovskites. Science 349(6255):1518–1521
21. Liang C et al (2020) Two-dimensional Ruddlesden-popper layered perovskite solar cells based on phase-pure thin films. Nat Energy 6(1):38–45
22. Zhang F et al (2020) Advances in two-dimensional organic-inorganic hybrid perovskites. Energy Environ Sci 13(4):1154–1186

23. Yin WJ, Shi TT, Yan YF (2014) Unique properties of halide perovskites as possible origins of the superior solar cell performance. Adv Mater 26(27):4653–4658
24. De Wolf S et al (2014) Organometallic halide perovskites: sharp optical absorption edge and its relation to photovoltaic performance. J Phys Chem Lett 5(6):1035–1039
25. Dong QF et al (2015) Electron-hole diffusion lengths >175 mu m in solution-grown CH3NH3PbI3 single crystals. Science 347(6225):967–970
26. Stranks SD et al (2013) Electron-hole diffusion lengths exceeding 1 micrometer in an organometal trihalide perovskite absorber. Science 342:341–344
27. Shi D et al (2015) Low trap-state density and long carrier diffusion in organolead trihalide perovskite single crystals. Science 347(6221):519–522
28. Kim JY et al (2020) High-efficiency perovskite solar cells. Chem Rev 120(15):7867–7918
29. Ni Z et al (2020) Resolving spatial and energetic distributions of trap states in metal halide perovskite solar cells. Science 367(6484):1352–1358
30. Brenner TM et al (2016) Hybrid organic-inorganic perovskites: low-cost semiconductors with intriguing charge-transport properties. Nat Rev Mater 1(1)
31. Miyata A et al (2015) Direct measurement of the exciton binding energy and effective masses for charge carriers in organic-inorganic tri-halide perovskites. Nat Phys 11(7):582–594
32. Lin QQ et al (2015) Electro-optics of perovskite solar cells. Nat Photonics 9(2):106–112
33. D'Innocenzo V et al (2014) Excitons versus free charges in organo-lead tri-halide perovskites. Nat Commun 5:3586
34. Sherkar TS et al (2017) Recombination in perovskite solar cells: significance of grain boundaries, interface traps, and defect ions. ACS Energy Lett 2(5):1214–1222
35. Yang Y et al (2017) Top and bottom surfaces limit carrier lifetime in lead iodide perovskite films. Nat Energy 2(2):16207
36. Lee MM et al (2012) Efficient hybrid solar cells based on meso-superstructured organometal halide perovskites. Science 338:643–647
37. Ghosh S, Mishra S, Singh T (2020) Antisolvents in perovskite solar cells: importance, issues, and alternatives. Adv Mater Interfaces 7(18):2000950
38. Xiao MD et al (2014) A fast deposition-crystallization procedure for highly efficient lead iodide perovskite thin-film solar cells. Angewandte Chemie-International Edition 53(37):9898–9903
39. Jeon NJ et al (2014) Solvent engineering for high-performance inorganic-organic hybrid perovskite solar cells. Nat Mater 13(9):897–903
40. Kim M et al (2019) Methylammonium chloride induces intermediate phase stabilization for efficient perovskite solar cells. Joule 3(9):2179–2192
41. Min H et al (2019) Efficient, stable solar cells by using inherent bandgap of alpha-phase formamidinium lead iodide. Science 366(6466):749–753
42. Kim G et al (2020) Impact of strain relaxation on performance of alpha-formamidinium lead iodide perovskite solar cells. Science 370(6512):108–112
43. Nie WY et al (2015) High-efficiency solution-processed perovskite solar cells with millimeter-scale grains. Science 347(6221):522–525
44. Li X et al (2016) A vacuum flash-assisted solution process for high-efficiency large-area perovskite solar cells. Science 353(6294):58–62
45. Ding B et al (2017) Material nucleation/growth competition tuning towards highly reproducible planar perovskite solar cells with efficiency exceeding 20%. J Mater Chem A 5(15):6840–6848
46. Yu Y et al (2021) A review on gas-quenching technique for efficient perovskite solar cells. Solar Rrl 5(10):2100386
47. Burschka J et al (2013) Sequential deposition as a route to high-performance perovskite-sensitized solar cells. Nature 499(7458):316–319
48. Luo SQ et al (2016) The influence of chloride on interdiffusion method for perovskite solar cells. Mater Lett 169:236–240
49. Yang WS et al (2015) High-performance photovoltaic perovskite layers fabricated through intramolecular exchange. Science 348:1234–1237

50. Jiang Q et al (2017) Planar-structure perovskite solar cells with efficiency beyond 21%. Adv Mater 29(46):1703852
51. Jiang Q et al (2019) Surface passivation of perovskite film for efficient solar cells. Nat Photonics 13(7):460–466
52. Liu M, Johnston MB, Snaith HJ (2013) Efficient planar heterojunction perovskite solar cells by vapour deposition. Nature 501(7467):395–398
53. Hsiao SY et al (2016) Efficient all-vacuum deposited perovskite solar cells by controlling reagent partial pressure in high vacuum. Adv Mater 28(32):7013–7019
54. Kojima A et al (2009) Organometal halide perovskites as visible-light sensitizers for photovoltaic cells. J Am Chem Soc 131(17):6050–6051
55. Im JH et al (2011) 6.5% efficient perovskite quantum-dot-sensitized solar cell. Nanoscale 3(10):4088–4093
56. Kim H-S et al (2012) Lead iodide perovskite sensitized all-solid-state submicron thin film mesoscopic solar cell with efficiency exceeding 9%. Sci Rep 2:591
57. Heo JH et al (2013) Efficient inorganic–organic hybrid heterojunction solar cells containing perovskite compound and polymeric hole conductors. Nat Photonics 7:486–491
58. Jeon NJ et al (2015) Compositional engineering of perovskite materials for high-performance solar cells. Nature 517(7535):476–480
59. Saliba M et al (2016) Cesium-containing triple cation perovskite solar cells: improved stability, reproducibility and high efficiency. Energy Environ Sci 9:1989–1997
60. Yang WS et al (2017) Iodide management in formamidinium-lead-halide-based perovskite layers for efficient solar cells. Science 356(6345):1376–1379
61. Yoo JJ et al (2021) Efficient perovskite solar cells via improved carrier management. Nature 590(7847)
62. Jeong J et al (2021) Pseudo-halide anion engineering for alpha-FAPbI(3) perovskite solar cells. Nature 592(7854):381–385
63. Kim M et al (2022) Conformal quantum dot-SnO2 layers as electron transporters for efficient perovskite solar cells. Science 375(6578):302–306
64. Min H et al (2021) Perovskite solar cells with atomically coherent interlayers on SnO_2 electrodes. Nature 598(7881):444–450
65. Li Z et al (2018) Scalable fabrication of perovskite solar cells. Nat Rev Mater 3(4):18017
66. Li S et al (2021) A brief review of hole transporting materials commonly used in perovskite solar cells. Rare Met 40(10):2712–2729
67. Kim M et al (2021) Enhanced electrical properties of Li-salts doped mesoporous TiO_2 in perovskite solar cells. Joule 5(3):659–672
68. Wu SF et al (2020) 2D metal-organic framework for stable perovskite solar cells with minimized lead leakage. Nat Nanotechnol 15(11):934-+
69. Alsalloum AY et al (2021) 22.8% efficient single-crystal mixed-cation inverted perovskite solar cells with a near-optimal bandgap. Energy Environ Sci 14(4):2263–2268
70. Degani M et al (2021) 23.7% efficient inverted perovskite solar cells by dual interfacial modification. Sci Adv 7(49):eabj 7930
71. Wang S et al (2022) Critical role of removing impurities in nickel oxide on high-efficiency and long-term stability of inverted perovskite solar cells. Angew Chem Int Ed Engl 61(18):e202116534
72. Li X et al (2022) Constructing heterojunctions by surface sulfidation for efficient inverted perovskite solar cells. Science 375(6579):434–437
73. Azmi R et al (2022) Damp heat-stable perovskite solar cells with tailored-dimensionality 2D/3D heterojunctions. Science eabm5784
74. Tang G et al (2019) Solution-phase epitaxial growth of perovskite films on 2D material flakes for high-performance solar cells. Adv Mater 31(24):e1807689
75. Tang GQ et al (2018) Performance enhancement of perovskite solar cells induced by lead acetate as an additive. Solar RRL 2(6):1800066
76. Cao JP et al (2020) Enhanced performance of planar perovskite solar cells induced by van der waals epitaxial growth of mixed perovskite films on WS2 flakes. Adv Func Mater 30(38):2002358

77. You P et al (2015) Efficient semitransparent perovskite solar cells with graphene electrodes. Adv Mater 27(24):3632–3638

78. You P, Tang GQ, Yan F (2019) Two-dimensional materials in perovskite solar cells. Mater Today Energy 11:128–158

79. Liu ZK et al (2016) Ultrathin and flexible perovskite solar cells with graphene transparent electrodes. Nano Energy 28:151–157

80. Jeong M et al (2020) Stable perovskite solar cells with efficiency exceeding 24.8% and 0.3-V voltage loss. Science 369(6511):1615–1620.

81. Kosmatos KO et al (2019) Methylammonium chloride: a key additive for highly efficient, stable, and up-scalable perovskite solar cells. Energy Environ Mater 2(2):79–92

82. Mateen M et al (2020) MACl-induced intermediate engineering for high-performance mixed-cation perovskite solar cells. ACS Appl Mater Interfaces 12(9):10535–10543

83. Xiang WC et al (2022) Intermediate phase engineering of halide perovskites for photovoltaics. Joule 6(2):315–339

84. Huang YM et al (2022) Recent progress on formamidinium-dominated perovskite photovoltaics. Adv Energy Mater 12(4):2100690

85. Wu TH et al (2021) The main progress of perovskite solar cells in 2020–2021. Nano-Micro Letters 13(1):152

86. Ono LK, Liu SZ, Qi YB (2020) Reducing detrimental defects for high-performance metal halide perovskite solar cells. Angewandte Chemie-International Edition 59(17):6676–6698

87. Schulz P, Cahen D, Kahn A (2019) Halide perovskites: is it all about the interfaces? Chem Rev 119(5):3349–3417

88. Jung EH et al (2019) Efficient, stable and scalable perovskite solar cells using poly(3-hexylthiophene). Nature 567(7749):511–515

89. McGott DL et al (2021) 3D/2D passivation as a secret to success for polycrystalline thin-film solar cells. Joule 5(5):1057–1073

90. Park BW, Seok SI (2019) Intrinsic instability of inorganic-organic hybrid halide perovskite materials. Adv Mater 31(20)

91. Cheng YH, Ding LM (2021) Pushing commercialization of perovskite solar cells by improving their intrinsic stability. Energy Environ Sci 14(6):3233–3255

92. Qiu ZW et al (2020) Recent advances in improving phase stability of perovskite solar cells. Small Methods 4(5):1900877

93. Jiang JK et al (2020) Atomistic and electronic origin of phase instability of metal halide perovskites. Acs Appl Energy Mater 3(12):11548–11558

94. You P et al (2020) Ultrafast laser-annealing of perovskite films for efficient perovskite solar cells. Energy Environ Sci 13(4):1187–1196

95. Tai QD et al (2016) Efficient and stable perovskite solar cells prepared in ambient air irrespective of the humidity. Nat Commun 7:11105

96. You P et al (2021) 2D materials for conducting holes from grain boundaries in perovskite solar cells. Light-Sci Appl 10(1):68

97. Saliba M et al (2016) Incorporation of rubidium cations into perovskite solar cells improves photovoltaic performance. Science 354(6309):206–209

98. Liu YH et al (2019) Ultrahydrophobic 3D/2D fluoroarene bilayer-based water-resistant perovskite solar cells with efficiencies exceeding 22%. Sci Adv 5(6):eaaw2543

99. Hui W et al (2021) Stabilizing black-phase formamidinium perovskite formation at room temperature and high humidity. Science 371(6536):1359–1364

100. Liu P, Tang GQ, Yan F (2022) Strategies for large-scale fabrication of perovskite films for solar cells. Solar Rrl 6(1):2100683

101. Deng YH et al (2021) Defect compensation in formamidinium-caesium perovskites for highly efficient solar mini-modules with improved photostability. Nat Energy 6(6):633–641

102. Li HY et al (2020) Recent progress towards roll-to-roll manufacturing of perovskite solar cells using slot-die processing. Flexible Printed Electron 5(1):014006

103. Kim YY et al (2020) Roll-to-roll gravure-printed flexible perovskite solar cells using eco-friendly antisolvent bathing with wide processing window. Nat Commun 11(1):5146

104. Deng YH et al (2018) Surfactant-controlled ink drying enables high-speed deposition of perovskite films for efficient photovoltaic modules. Nat Energy 3(7):560–566
105. National Renewable Energy Laboratory (NREL), Champion photovoltaic module efficiency chart, https://www.nrel.gov/pv/module-efficiency.html. Accessed Jun 2022
106. Perini CAR et al (2021) Pressing challenges in halide perovskite photovoltaics-from the atomic to module level. Joule 5(5):1024–1030
107. Brooks KG, Nazeeruddin MK (2021) Laser processing methods for perovskite solar cells and modules. Adv Energy Mater 11(29):2101149
108. da Silva Filho JMC et al (2021) A review on the development of metal grids for the upscaling of perovskite solar cells and modules. Solar RRL
109. Ji KY et al (2021) Halide perovskite light-emitting diode technologies. Adv Optical Mater 9(18):2002128
110. Liu XK et al (2021) Metal halide perovskites for light-emitting diodes. Nat Mater 20(1):10–21
111. Tan ZK et al (2014) Bright light-emitting diodes based on organometal halide perovskite. Nat Nanotechnol 9(9):687–692
112. Wu SF et al (2021) The evolution and future of metal halide perovskite-based optoelectronic devices. Matter 4(12):3814–3834
113. Liu Z et al (2021) Perovskite light-emitting diodes with EQE exceeding 28% through a synergetic dual-additive strategy for defect passivation and nanostructure regulation. Adv Mater 33(43):2103268
114. Zhu L et al (2021) Unveiling the additive-assisted oriented growth of perovskite crystallite for high performance light-emitting diodes. Nat Commun 12(1):5081
115. Chen ZM et al (2021) Utilization of trapped optical modes for white perovskite light-emitting diodes with efficiency over 12%. Joule 5(2):456–466
116. Liu Y et al (2022) Wide-bandgap perovskite quantum dots in perovskite matrix for sky-blue light-emitting diodes. J Am Chem Soc 144(9):4009–4016
117. Li N et al (2022) Ion Migration in perovskite light-emitting diodes: mechanism, characterizations, and material and device engineering. Adv Mater 34(19):2108102
118. Liu Y et al (2021) Bright and stable light-emitting diodes based on perovskite quantum dots in perovskite matrix. J Am Chem Soc 143(38):15606–15615
119. Sutherland BR, Sargent EH (2016) Perovskite photonic sources. Nat Photonics 10(5):295–302
120. Stylianakis MM et al (2019) Inorganic and hybrid perovskite based laser devices: a review. Materials 12(6)
121. Yang DC et al (2018) Lasing characteristics of CH3NH3PbCl3 single-crystal microcavities under multiphoton excitation. Adv Optical Mater 6(3):1700992
122. Yang DC et al (2016) Amplified spontaneous emission from organic-inorganic hybrid lead iodide perovskite single crystals under direct multiphoton excitation. Adv Optical Mater 4(7):1053–1059
123. Xie C et al (2017) Ultrasensitive broadband phototransistors based on perovskite/organic-semiconductor vertical heterojunctions. Light Sci. Appl. 6:e17023
124. Zou X et al (2019) Schottky barrier-controlled black phosphorus/perovskite phototransistors with ultrahigh sensitivity and fast response. Small 15(25):e1901004
125. Ghosh J, Giri PK (2021) Recent advances in perovskite/2D materials based hybrid photodetectors. J Phys: Mater 4(3):032008
126. Kim YC et al (2017) Printable organometallic perovskite enables large-area, low-dose X-ray imaging. Nature 550(7674):87–91
127. Zhao J et al (2020) Perovskite-filled membranes for flexible and large-area direct-conversion X-ray detector arrays. Nat Photonics 14(10):612–617
128. He Y et al (2022) Sensitivity and detection limit of spectroscopic-grade perovskite CsPbBr 3 crystal for hard X-ray detection. Adv Func Mater 32(24):2112925
129. Zhang P et al (2022) Ultrasensitive and robust 120 keV hard X-ray imaging detector based on mixed-halide perovskite CsPbBr 3- n In single crystals. Adv Mater 34(12):e2106562
130. Tan S et al (2022) Stability-limiting heterointerfaces of perovskite photovoltaics. Nature 605(7909):268–273

131. Wu SF et al (2020) 2D metal-organic framework for stable perovskite solar cells with minimized lead leakage. Nat Nanotechnol 15(11):934–940
132. Wei X et al (2022) Avoiding structural collapse to reduce lead leakage in perovskite photovoltaics. Angew Chem Int Ed Engl e202204314
133. Liang Y et al (2021) Lead leakage preventable fullerene-porphyrin dyad for efficient and stable perovskite solar cells. Adv Func Mater 32(14):2110139
134. Cao Q et al (2022) Environmental-friendly polymer for efficient and stable inverted perovskite solar cells with mitigating lead leakage. Adv Funct Mater